Frequency Metrology with Optimal Ramsey Interferometry for Optical Atomic Clocks

Von der Fakultät für Mathematik und Physik
der Gottfried Wilhelm Leibniz Universität Hannover
genehmigte Dissertation zur Erlangung des Grades

Doktor der Naturwissenschaften
Dr. rer. nat.

von

M. Sc. Timm Kielinski

geboren am 8. März 1997 in Hannover

2025

Referent: Prof. Dr. Klemens Hammerer
Institut für Theoretische Physik
Leibniz Universität Hannover

Korreferent: Prof. Dr. Piet O. Schmidt
Institut für Quantenoptik
Leibniz Universität Hannover

Korreferent: Prof. Dr. Akimasa Miyake
Department of Physics and Astronomy
University of New Mexico

Tag der Promotion: 29.08.2025

Abstract

Frequency metrology represents a cornerstone of modern precision measurements and optical atomic clocks, in particular, have emerged as one of the most precise measurement devices. Correlated quantum states and measurements promise further improvements in the accuracy of frequency metrology and the stability of atomic clocks by reducing quantum projection noise below the standard quantum limit imposed by uncorrelated atoms. However, developing strategies robust under realistic conditions remains challenging. This thesis addresses this research question by investigating the trade-off between achieving entanglement-enhanced sensitivity and maintaining robustness against decoherence processes and noise sources. Specifically, we consider frequency metrology tailored to single-ensemble clocks, in which the atomic reference is periodically interrogated utilizing identical Ramsey protocols in each clock cycle. In this framework, this thesis aims to provide theoretical guidance for the development of next-generation optical atomic clocks. After establishing a comprehensive theoretical foundation for atomic clock operation, we identify optimal Ramsey interrogation schemes primarily focusing on regimes limited by spontaneous decay and laser noise.

In the first part, we show that maximally entangled GHZ-like states – in conjunction with a correlated measurement and nonlinear estimation strategy – achieve gains of up to 2.25 dB in the presence of spontaneous decay, comparable to fundamental bounds for up to several tens of atoms. This result is particularly surprising since GHZ states do not provide any enhancement under dephasing due to white frequency noise compared to the standard quantum limit. The gain arises from a veto signal, which allows for the detection and mitigation of errors caused by spontaneous decay events. We demonstrate the robustness of these GHZ-like protocol through comprehensive Monte-Carlo simulations of atomic clocks.

In the second part, we present progress on frequency metrology tailored to optical atomic clocks primarily limited by laser noise. By consolidating and extending previous findings on laser noise limited atomic clocks and variational quantum circuits, we identify optimal Ramsey interrogation schemes across a variety of scenarios, including different experimental platforms, ensemble sizes and a broad range of interrogation durations and dead times. The optimal Ramsey protocols strongly depend on the specific experimental parameters, as clock stability generally reflects a trade-off between quantum projection noise, the coherence time limit, fringe hops and dead time effects. Although variational quantum circuits with low complexity promise substantial enhancements in idealized settings, practical constraints in realistic scenarios limit these advantages. As a result, only tweezer arrays with several tens of atoms – operating in the regime dominated by quantum projection noise – benefit significantly from these protocols, while standard protocols – utilizing coherent spin states, spin-squeezed states and GHZ states – represent robust interrogation schemes in a variety of experimental setups, closely approaching the ultimate lower limit.

Keywords: Frequency metrology, Optical atomic clocks, Ramsey interferometry, Entanglement, Spontaneous decay, Laser noise, Dead time, Bayesian phase estimation, GHZ states, Spin-squeezed states, Variational quantum circuits

Zusammenfassung

Die Frequenzmetrologie bildet einen Grundstein moderner Präzisionsmessungen und optische Atomuhren gehören derzeit zu den genauesten Messinstrumente. Korrelierte Quantenzustände und Messstrategien versprechen eine weitere Steigerung der Stabilität, indem das Quantenprojektionsrauschen unter das Standard-Quanten-Limit unkorrelierter Atome gesenkt wird. Die Entwicklung robuster Strategien unter realistischen Bedingungen ist jedoch weiterhin eine zentrale Herausforderung. Diese Dissertation widmet sich dieser Fragestellung, indem der Kompromiss zwischen verschränkungsbasierter Sensitivitätssteigerung und Robustheit gegenüber Dekohärenzprozessen und Rauschen untersucht wird. Dabei werden Uhren mit einzelnen Ensemblen betrachtet, bei denen die atomare Referenz in jedem Uhrenzyklus periodisch mittels identischer Ramsey-Protokolle abgefragt wird. In diesem Kontext stellt diese Arbeit einen theoretischen Ratgeber für die Entwicklung optischer Atomuhren der nächsten Generation dar. Aufbauend auf einer umfassenden theoretischen Beschreibung von Atomuhren werden optimale Ramsey-Strategien identifiziert, mit dem Fokus auf Regimen, die durch spontane Emission und Laserrauschen limitiert sind.

Im ersten Teil wird gezeigt, dass maximal verschränkte GHZ-ähnliche Zustände in Kombination mit korrelierten Messungen und nichtlinearen Schätzstrategien unter spontaner Emission einen Gewinn von bis zu 2.25 dB ermöglichen – vergleichbar mit fundamentalen Schranken für Ensemble mit mehreren Dutzend Atomen. Dieses Ergebnis ist insbesondere bemerkenswert, da GHZ-Zustände unter Dephasierung infolge von weißem Frequenzrauschen keine Vorteile gegenüber dem Standard-Quanten-Limit bieten. Der beobachtete Gewinn beruht auf einem Veto-Signal, das Fehler durch spontane Emission erkennt und reduziert. Die Robustheit dieser GHZ-ähnlichen Protokolle wird durch umfassende Monte-Carlo-Simulationen demonstiert.

Der zweite Teil präsentiert einen Fortschrittsbericht zur Frequenzmetrologie in optischen Atomuhren, die primär durch Laserrauschen limitiert sind. Durch Konsolidierung und Erweiterung früherer Erkenntnisse zu laserrauschlimitierten Uhren und variationellen Abfrageprotkollen werden optimale Ramsey-Protokolle für eine Vielzahl realistischer Szenarien identifiziert – darunter verschiedene experimentelle Plattformen, Ensemblegrößen, sowie unterschiedliche Abfragedauern und Totzeiten. Die optimalen Protokolle hängen stark von den experimentellen Bedingungen ab, da die Uhrenstabilität im Allgemeinen einen Kompromiss zwischen Quantenprojektionsrauschen, Kohärenzzeitlimit, Frequenzsprüngen und Totzeiteffekten darstellt. Aufgrund dieser experimentellen Einschränkungen bieten variationelle Abfrageprotokolle lediglich für Tweezer-Arrays mit mehreren Dutzend Atomen signifikante Vorteile, sofern Quantenprojektionsrauschen die dominante Limitierung darstellt. Währenddessen repräsentieren Standardprotokolle – unter Verwendung kohärenter Zustände, gequetschter Zustände und GHZ Zustände – in vielen Experimenten robuste Strategien und erreichen Stabilitäten nahe der fundamentalen Stabilitätsgrenzen.

Schlagwörter: Frequenzmetrologie, Optische Atomuhren, Ramsey Interferometrie, Verschränkung, Spontane Emission, Laserrauschen, Totzeit, Bayessche Phasenschätzung, GHZ Zustände, Gequetschte Zustände, Variationale Quantenprotokolle

Author contributions

Parts of this thesis have appeared elsewhere, as peer-reviewed publications or on pre-print servers. Here I summarize my personal contributions to these works. Note that contributions of other co-authors without my involvement are not explicitly listed. In order of the corresponding chapter, they are:

Chapter 3:
T. Kielinski, P. O. Schmidt and K. Hammerer, *GHZ protocols enhance frequency metrology despite spontaneous decay.* [1]

Author contribution: Methodology and formal analysis were conducted by **TK** and KH. **TK** carried out the analytic calculations and the optimization with input from KH. **TK** identified the optimal interrogation schemes and was responsible for numerical analysis and visualization. All authors contributed to the writing, review and editing of the manuscript.

Chapter 4:
T. Kielinski and K. Hammerer, *Bayesian frequency metrology with optimal Ramsey interferometry in optical atomic clocks.* [2]

Author contribution: **TK** contributed to the idea of the manuscript together with all authors. The analytic calculations and optimizations were performed by **TK**, with input from KH. **TK** was responsible for numerical analysis and visualization. **TK** and KH interpreted the optimal interrogation schemes. **TK** prepared the manuscript with contributions from KH.

All chapters:
T. Kielinski, *Monte Carlo simulations of atomic clocks [Data set].* [3]

Author contribution: **TK** built upon existing code to implement extensive generalizations, enabling the simulation of arbitrary Ramsey protocols and a wide range of feedback strategies. **TK** prepared the corresponding documentation.

For completeness I add that the following articles, which were published during my time as a PhD student, but are not included in this thesis:

K. Dietze, L. Pelzer, L. Krinner, F. Dawel, J. Kramer, N. C. H. Spethmann, **T. Kielinski**, K. Hammerer, K. Stahl, J. Klose, S. Dörscher, C. Lisdat, E. Benkler and P. O. Schmidt, *Entanglement-enhanced optical ion clock.* [4]

M. S. Scharnagl, **T. Kielinski** and K. Hammerer, *Optimal Ramsey interferometry with echo protocols based on one-axis twisting.* [5]

Contents

1 Introduction 1
- 1.1 A brief history of clocks . . . 3
- 1.2 What is a clock? . . . 5
- 1.3 Qualitative requirements for clocks . . . 6

2 Basics of Atomic Clocks 9
- 2.1 Allan Deviation - A Stability Measure . . . 9
- 2.2 Local Oscillator . . . 15
  - 2.2.1 Noise Characterization . . . 15
  - 2.2.2 Coherence Time . . . 17
- 2.3 Atomic Reference . . . 18
  - 2.3.1 Spin Systems . . . 19
  - 2.3.2 Unitary Dynamics . . . 26
  - 2.3.3 Decoherence Processes . . . 31
  - 2.3.4 Measurements . . . 37
  - 2.3.5 Ramsey Interferometry . . . 38
  - 2.3.6 Quantum Projection Noise (QPN) . . . 40
  - 2.3.7 Coherent Spin States (CSS) . . . 43
  - 2.3.8 GHZ States . . . 47
  - 2.3.9 Spin-Squeezed States (SSS) . . . 49
- 2.4 Feedback and Servo . . . 55
  - 2.4.1 Double-Integrating Servo . . . 57
  - 2.4.2 General Linear Integrator . . . 58

3 Frequency metrology limited by spontaneous decay 61
- 3.1 Motivation and research problem . . . 61
- 3.2 Atomic clocks and Ramsey interferometry . . . 63
- 3.3 Dynamics . . . 65
- 3.4 Local frequency metrology . . . 67
  - 3.4.1 Local phase estimation . . . 68
  - 3.4.2 Local frequency estimation . . . 70
  - 3.4.3 Clock stability and Allan deviation . . . 71

3.5 Bounds in local phase estimation theory 73
  3.5.1 Cramér-Rao Bound (CRB) 73
  3.5.2 Quantum Cramér-Rao Bound (QCRB) 77
  3.5.3 Optimal Quantum Interferometer (OQI) 79
3.6 Bounds in local frequency metrology 83
3.7 Optimal Ramsey protocols in frequency metrology limited by spontaneous decay 84
  3.7.1 Separable and maximally entangled states 85
  3.7.2 Beating the standard quantum limit with GHZ states 87
  3.7.3 Saturating the optimal quantum interferometer 92
  3.7.4 Spontaneous decay events in GHZ(-like) states 94
  3.7.5 Performance in atomic clocks 96
  3.7.6 Unique features of GHZ(-like) states in the presence of spontaneous decay 97
3.8 Crossover to regimes limited by dephasing 100
3.9 Conclusion 103
3.10 Outlook 105
  3.10.1 Incoherent pumping 106
  3.10.2 Spontaneous decay events as erasure errors 108

4 Bayesian frequency metrology limited by laser noise **113**
4.1 Motivation and research problem 113
4.2 Bayesian phase estimation 116
4.3 Bounds in Bayesian phase estimation theory 119
  4.3.1 Bayesian Cramér-Rao Bound (BCRB) 120
  4.3.2 Bayesian Quantum Cramér-Rao Bound (BQCRB) 121
  4.3.3 Optimal Quantum Interferometer (OQI) 122
4.4 Estimators 125
  4.4.1 Linear estimator 125
  4.4.2 Optimal Bayesian estimator 126
4.5 Bayesian frequency metrology 126
  4.5.1 Clock stability and Allan deviation 127
  4.5.2 Qualitative scaling 128
  4.5.3 Interrogation time and prior width 129
4.6 Optimal Ramsey protocols in Bayesian frequency metrology 131
  4.6.1 Standard protocols 131
  4.6.2 Variational Ramsey protocols 136
  4.6.3 Optimal protocols 140

4.7 Application in the full feedback loop of an atomic clock 144
4.7.1 Limitation due to fringe hops 145
4.7.2 Clock stability 146
4.7.3 Comparison of linear and optimal Bayesian estimation 149
4.8 Dead time 152
4.8.1 Dead time in Bayesian frequency metrology 153
4.8.2 General results 154
4.8.3 Setup specific dead times 158
4.9 Conclusion 164
4.10 Outlook 165

5 Summary 171

A Numerical routines 175
A.1 Optimization 176
A.1.1 Local frequency metrology 176
A.1.2 Bayesian frequency metrology 178
A.2 Monte Carlo clock simulation 180
A.2.1 Feedback loop 181
A.2.2 Local Oscillator Noise 182
A.2.3 Reference 183
A.2.4 Servo 186
A.2.5 Long-term stability 186
A.3 Prior width 188
A.3.1 Iterative prior width 188
A.3.2 Prior width and dead time 190

B Rotations of Collective Spin Operators and States 191

C Decoherence processes 195
C.1 Independence of the processes 196
C.2 Time evolution 203

D Derivations of bounds in local phase estimation 207
D.1 Cramér-Rao Bound (CRB) 207
D.2 Fisher information 208
D.2.1 Convexity 208
D.2.2 Additivity 209
D.3 Method of moments 211
D.4 Quantum Cramér-Rao Bound (QCRB) 213

D.5 Quantum Fisher information (QFI) 215
D.5.1 Convexity 215
D.5.2 Additivity 215
D.5.3 Unitary phase evolution 216
D.5.4 Pure states 217
D.5.5 Decoherence-free scenario 219

E Calculations for protocols in local frequency metrology 221
E.1 Mapping the decoherence processes to the measurement 221
E.1.1 Projective spin measurement 222
E.1.2 Parity measurement 229
E.2 Coherent spin states (CSS) 232
E.3 Parity-GHZ protocol 235
E.4 QCRB of the GHZ state 238
E.5 GHZ transformation $\mathcal{U}_{\mathrm{GHZ}}$ 240
E.6 Linear-GHZ protocol 243
E.7 Heralded-GHZ protocol 245
E.8 Heralded-uGHZ protocol 248
E.8.1 General uGHZ state 248
E.8.2 Optimal uGHZ state 252
E.8.3 Gain over SQL 255
E.9 Spontaneous decay events in GHZ(-like) states 256
E.10 Incoherent pumping 261
E.10.1 Non-commutativity of the master equation 262
E.10.2 Solution of the master equation 263
E.10.3 Projective spin measurements 264
E.10.4 Parity measurement 266
E.10.5 Heralded-(u)GHZ protocol 267
E.11 Spontaneous decay events as erasure errors 271
E.11.1 Spontaneous decay events in CSS 271
E.11.2 Conversion of spontaneous decay events into erasure errors . . 272

F Derivations of bounds and estimators in Bayesian phase estimation 277
F.1 Bayesian Cramér-Rao Bound (BCRB) 277
F.2 Bayesian Quantum Cramér-Rao Bound (BQCRB) 279
F.2.1 Unitary phase evolution and Gaussian prior distribution . . . 281
F.3 Optimal Quantum Interferometer (OQI) 282
F.3.1 Coherence time limit (CTL) 282

F.3.2 Asymptotic limit . . . 283
F.3.3 Phase operator based interferometer (POI) . . . 284
F.4 Estimators . . . 285
F.4.1 Linear estimator . . . 285
F.4.2 Optimal Bayesian estimator . . . 286

G Calculations for protocols in Bayesian frequency metrology 287
G.1 Coherent Spin States (CSS) . . . 287
G.2 Spin-Squeezed States (SSS) . . . 288
G.3 GHZ States . . . 289

Acknowledgements 292

List of Figures 294

List of Tables 296

Bibliography 297

Abbreviations and Acronyms

ADEV	Allan deviation
AVAR	Allan variance
BCRB	Bayesian Cramér-Rao bound
BMSE	Bayesian mean squared error
BQCRB	Bayesian quantum Cramér-Rao bound
CRB	Cramér-Rao bound
CSS	coherent spin state
CTL	coherence time limit
FN	flicker frequency noise
GHZ	Greenberger-Horne-Zeilinger
HL	Heisenberg limit
LO	local oscillator
MSE	mean squared error
OAT	one-axis-twisting
OAVAR	overlapping Allan variance
OADEV	overlapping Allan deviation
OQI	optimal quantum interferometer
POI	phase operator based interferometer
POVM	positive operator-valued measure
PSD	power spectral density
PVM	projection-valued measure
QCRB	quantum Cramér-Rao bound
QFI	quantum Fisher information
QPN	quantum projection noise
RWN	random walk frequency noise
SLD	symmetric logarithmic derivative
SQL	standard quantum limit
SSS	spin-squeezed state
uGHZ	unbalanced GHZ
WN	white frequency noise
π**HL**	π-corrected Heisenberg limit

1

Introduction

Frequency metrology constitutes a fundamental pillar in modern precision measurements, driving advancements across a broad range of scientific and technological fields [6–11]. At the forefront of this discipline are optical atomic clocks, which exploit narrow-linewidth atomic transitions in the optical domain [12, 13]. This new generation of clocks was spurred by technological advances over the past decades, including breakthroughs in laser technology [12], the invention of the optical frequency comb [14, 15], and the development of highly controllable platforms such as ion traps [16–18], tweezer arrays [19–22], and optical lattices [23–26]. Today, state-of-the-art optical atomic clocks are among the most precise measurement devices ever built, achieving stabilities on the order of 10^{-18} and below [18, 27–37]. To illustrate this extraordinary precision, such clocks would gain or lose less than a second over the age of the universe. They have surpassed traditional microwave-based Caesium atomic clocks, which had long served as the standard for timekeeping, thereby paving the way for the redefinition of the SI second [12, 38]. This unprecedented stability renders optical clocks indispensable tools for a broad spectrum of applications. In research, they are instrumental in probing fundamental physics, from testing general relativity through gravitational redshift measurements [36, 38–42] to exploring variations in fundamental constants [43, 44] and searching for new physics beyond the Standard Model [45–47]. In technology, optical atomic clocks foster potential applications ranging from enhancing global navigation satellite systems [48, 49] and synchronizing large-scale networks [50] to supporting precision geodesy [51–54].

Quantum projection noise (QPN) is the most fundamental process limiting clock stability, arising from the stochastic nature of quantum measurements and the discrete outcomes inherent in finite-size ensembles [55, 56]. For separable states of many atoms, namely uncorrelated or classically-correlated states, the standard quantum limit (SQL) imposes a fundamental bound on QPN [6, 12, 13, 57]. However, stability beyond this classical limit can be achieved by introducing entanglement within the atomic ensemble [6, 13, 57]. Three decades ago, Wineland et al. proposed in seminal works [58, 59] to entangle cold ions via their common coupling to collective modes of motion to suppress projection noise in frequency metrology, thereby overcoming the SQL and enhancing atomic clock stability. With the momentous advancements in optical atomic clocks and programmable quantum processors since then, this vision now encounters new opportunities and challenges. In recent years, entanglement on optical clock transitions has been demonstrated in various setups, including the generation of spin squeezing in trapped ions [60] and in neutral atoms mediated by cavities [32, 61] or Rydberg interactions [62]. Recently, also maximally entangled GHZ states and cascades thereof have been realized in optical clocks based on tweezer arrays [63, 64] and ion traps [4]. In an ideal scenario, GHZ states saturate the Heisenberg limit, which represents the ultimate bound on quantum projection noise and yields a quadratic improvement over the SQL in the scaling of the sensitivity with the ensemble size [6].

However, in realistic scenarios, decoherence processes and external noise degrade the coherence of the quantum system, impairing the stability and preventing the achievement of the Heisenberg limit [65–68]. While entanglement promises to overcome the SQL and thereby improving clock stability, the detrimental effects of decoherence are particularly pronounced in entangled states, since they are highly susceptible to the loss of coherence. Thus, a trade-off emerges between achieving entanglement-enhanced sensitivity, which enables surpassing the SQL, and ensuring robustness against the decoherence and noise processes. As a consequence, incorporating decoherence effects and external noise is essential for identifying optimal interrogation protocols in frequency metrology.

This inherent challenge – advancing frequency metrology with entangled states in the presence of decoherence and noise – precisely defines the central objective of this thesis. To this end, we establish a comprehensive theoretical framework for Ramsey interferometry and identify the optimal interrogation schemes in a variety of scenarios. Consequently, this work essentially provides guidance for the development of next-generation optical atomic clocks, particularly in regimes limited by spontaneous decay and laser noise. Specifically, we focus on single-ensemble clocks in which the atomic reference is periodically interrogated using the same protocol in each clock cycle. Although this work is tailored to frequency metrology in atomic clocks, the developed tools and techniques extend beyond this specific application. In particular, they are broadly applicable to general frequency metrology and Ramsey interferometry, including implementations in atom interferometry and magnetometry.

This thesis is organized as follows:

- Chapter 1: In the remainder of this introduction, we outline the general concept of clocks, as they represent the primary application of frequency metrology considered in this work.

- Chapter 2: We introduce the theoretical foundations for describing atomic clock operation, with a particular emphasis on the atomic reference. This chapter is designed to provide a comprehensive background and self-contained introduction accessible to graduate students.
- Chapter 3: We investigate the impact of decoherence processes during the Ramsey sequence within the framework of local frequency metrology and identify optimal interrogation schemes. In particular, we focus on spontaneous decay, as the finite lifetime of the excited state imposes a fundamental limit, and additionally examine the crossover to regimes constrained by external noise sources described by dephasing.
- Chapter 4: We incorporate frequency fluctuations of the laser in the framework of Bayesian frequency metrology. In this context, we determine optimal schemes that are robust to laser noise for a variety of scenarios, including different experimental platforms, ensemble sizes and regimes characterized by a wide range of interrogation durations and dead times.

At this point, we intentionally kept the introduction general, framing the central research topics within a broader context. Each chapter is written to be self-contained to facilitate independent reading. Consequently, we explicitly motivate the specific regimes of frequency metrology at the beginning of Chapter 3 and Chapter 4. Moreover, in both chapters we present the primary results and insights, while detailed proofs and derivations are provided in the appendix.

1.1 A brief history of clocks

The quest for accurate timekeeping and measuring time with high precision has been an integral aspect of human civilization, evolving from the natural rhythms observed in celestial bodies to the sophisticated technology that underpins modern atomic clocks. Early societies relied on nature's clocks, solar cycles, lunar phases, and seasonal changes to organize their lives. Although these natural indicators provided rudimentary yet effective means of measuring time, their inherent variability limited precision and reliability. As civilizations advanced, so did the mechanisms of timekeeping, evolving from sundials to the first human-made clocks. The invention of sand glasses and water clocks provided more structured methods for measuring time, independent of sunlight or other natural phenomena. The advent of mechanical clocks in the Middle Ages further refined this pursuit. In particular, the invention of the pendulum clock by Huygens in the 17th century marked a significant leap in precision, achieving stabilities around ten seconds a day (corresponding to a relative uncertainty of 10^{-4}). In the 18th century, the development of marine chronometers by Harrison enabled precise navigation and spurred advances in exploration, trade and science, reaching stabilities of up to a hundredth of a second a day (10^{-7}). The invention of quartz oscillators in the 1920s revolutionized timekeeping by utilizing the piezoelectric properties of quartz crystals. The benefits of quartz oscillators include their high stability of around 1 ms a day (10^{-8}), along with low cost and compact size, which enabled their widespread adoption in consumer electronics, telecommunications, and computing applications. Despite this impressive progress and precision, human-made clocks, whether mechanical or electrical, remain inherently imperfect due to variations in the components across different devices and inevitable drifts over time. This ultimately created the need for a consistent and accurate standard to synchronize global timekeeping: atomic clocks. In fact, Maxwell and Thomson [69] already envisioned the concept of atomic clocks in the 1870s by arguing that atoms of a particular species are identical and immutable, and thus, in theory, constitute the building blocks to perfect clocks. However, it was not until the mid-twentieth century that this concept became reality. With advances in the generation of microwaves and Rabi's development of the molecular beam magnetic resonance technique in 1939 [70] (Nobel Prize 1944), the first atomic clocks were realized in the late 1940s. Within a century, Caesium beam clocks were established in several national laboratories around the world, employing the method of separated oscillatory fields proposed by Ramsey in 1949 [71] (Nobel Prize 1989) and achieving uncertainties of around 10^{-11}. In subsequent years, the precision of Caesium clocks was continuously improved and this unprecedented stability led to a redefinition of the second in 1967 by the General Conference on Weights and Measures as "the duration of 9 192 631 770 periods of the radiation corresponding to the transition between the two hyperfine levels of the ground state of the Caesium 133 atom" [72]. Moreover, atomic clocks have driven advances in various fields such as communication, metrology, advanced positioning and navigation systems. With progress in cooling techniques and extended interrogation times achieved through the development of atomic fountains, Caesium fountain clocks reached uncertainties around 10^{-15} by the end of the twentieth century and nowadays are approaching the 10^{-16} level. Over the past decades, technological improvements in laser systems [12], highly controllable platforms for trapping and manipulating atoms [16–26] and the invention of the frequency comb [14, 15] have paved the way for optical clocks using various atomic species. Operating at optical frequencies, several orders of magnitude higher than the microwave transition in Caesium clocks, these new-generation clocks achieve uncertainties of 10^{-18} and below, gaining or losing less than a second over the age of the universe [18, 27–37]. As a consequence, in

2022 the General Conference on Weights and Measures voted to redefine the second based on optical clocks in the future [73]. Yet, the pursuit of even better clocks is far from over. While optical atomic clocks still offer significant potential for improvement, the recent laser excitation of the ^{229}Th nucleus [74] already heralds the advent of the next generation of clocks: nuclear clocks. [11, 75–81]

1.2 What is a clock?

A clock, at its core, consists of two essential components (cf. Fig. 1.1): a frequency standard – a device which generates a continuous and consistent frequency signal – and a mechanism that counts the oscillations over time. While the clockwork device essentially translates the frequency signal into measurable time intervals, the frequency standard represents the true heart of a clock. Frequency standards are commonly classified as either active or passive, depending on their operational principle. Active frequency standards generate their own oscillation at a given frequency, as the hydrogen maser or the Helium-Neon laser, where stimulated emission results in a highly coherent signal. Conversely, passive frequency standards require an external source to stimulate their oscillation. While active frequency standards typically excel in short-time stability, passive frequency standards often achieve superior long-term stability and accuracy, because the frequency can be precisely monitored and corrected against the reference response over time. Consequently, passive frequency standards are commonly preferred for clocks. [9–11]

The concept of a passive frequency standard can be illustrated by imagining two pendulums. The first pendulum is our primary noisy pendulum, whose fluctuating frequency we aim to stabilize. The second pendulum serves as an (almost) ideal reference, though it does not oscillate on its own. Hence, the task of a passive frequency standard is to periodically adjust the primary pendulum's frequency to match with the reference pendulum by repeatedly measuring the frequency difference between the two. However, each measurement introduces some noise into the system. Hence, it is desirable to extend the interrogation time as long as possible, thereby reducing the relative impact of this measurement noise and ultimately enhancing stability. However, if the interrogation time is extended too far we risk missing a "tick" of the reference, leading to synchronization errors that may accumulate over repeated measurements. Therefore, while longer interrogation times improve stability, there is an optimal duration beyond which stability is compromised. [10–12]

In (passive) atomic clocks (cf. Fig. 1.1), the local oscillator (LO), representing the primary pendulum, generates an inherently noisy frequency signal $\omega_{\mathrm{LO}}(t)$ that varies over time t. The LO is stabilized to an atomic transition frequency ω_0, acting

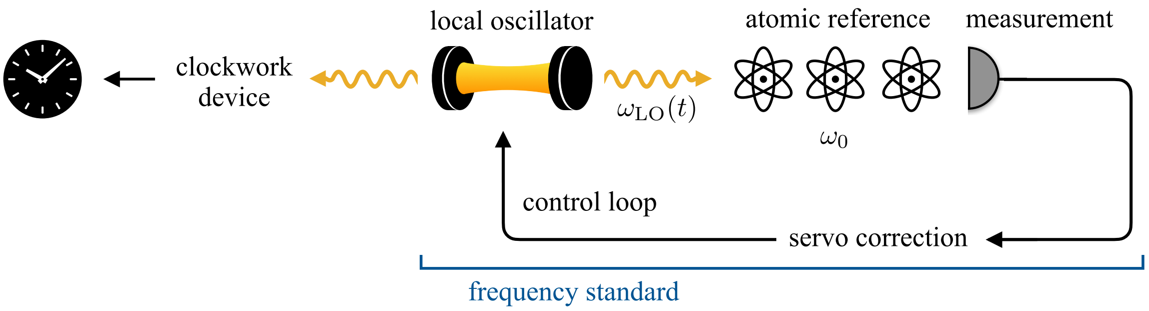

Figure 1.1: **Basic principle of an atomic clock:** A local oscillator (LO) with fluctuating frequency $\omega_{\mathrm{LO}}(t)$ is stabilized to an atomic transition ω_0 by repeatedly measuring the frequency difference. Based on these measurements, the servo applies corrections to the LO frequency. This control loop constitutes the frequency standard, while the clockwork device translates the frequency signal into measurable time intervals.

as the reference pendulum, through repeated interrogations of the atomic ensemble, effectively measuring the frequency difference $\omega(t) = \omega_0 - \omega_{\mathrm{LO}}(t)$. Based on this measurement, the servo applies feedback to correct the LO frequency, thereby completing the control cycle and resulting in a stabilized frequency signal. In optical atomic clocks, the LO is realized by an ultra-stable laser, while a frequency comb serves as a clockwork device, converting optical frequencies to the microwave regime. [6, 9–12]

In the remainder of this thesis, we exclusively consider such passive atomic clocks.

1.3 Qualitative requirements for clocks

Despite the diverse applications of frequency standards and clocks, each with distinct specific demands, three fundamental requirements are universal [9–12, 82]:

- **Reproducibility** refers to the degree of agreement among a set of independent devices of the same type, ensuring that they generate comparable frequency signals. As discussed in Sec. 1.1, human-made clock references are inherently subject to imperfections arising from natural variations in manufacturing processes. Consequently, the advent of atomic clocks represented a significant milestone, as all atoms of a particular species are identical.

- **Accuracy** characterizes how closely the generated (mean) frequency aligns with the true reference frequency, thereby quantifying the absolute deviation. Corresponding systematic uncertainties refer to predictable, repeatable errors that cause the clock frequency to deviate consistently from the true value. These errors stem from environmental noise or clock-specific characteristics, such as

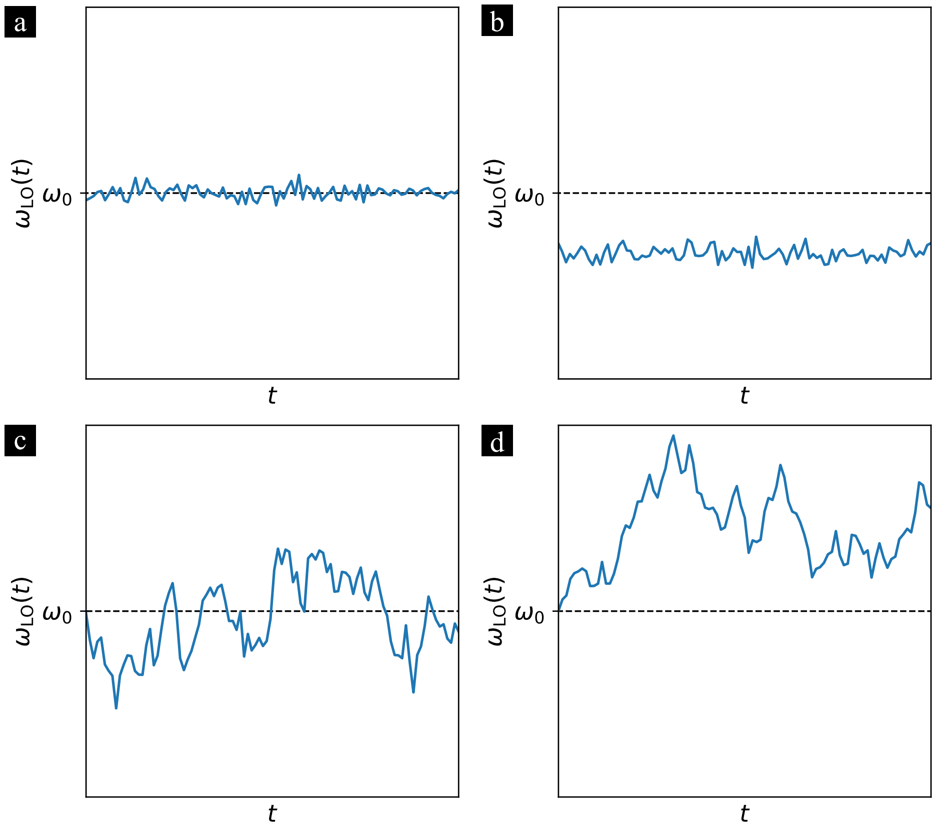

Figure 1.2: **Accuracy and stability:** Generic variations of the local oscillator (LO) frequency $\omega_{\mathrm{LO}}(t)$ over time t, illustrating frequency traces that are (a) accurate and stable, (b) not accurate but stable, (c) accurate but not stable and (d) neither accurate nor stable.

magnetic fields, temperature fluctuations, imperfections in laser alignment or Stark shifts induced by electric fields. Therefore, systematic uncertainties require careful calibration and correction to align the clock signal with the true reference frequency. To this end, there exist generally accepted procedures to characterize systematic uncertainties [11, 12].

- **Stability**, or precision, describes the consistency with which a frequency standard maintains its frequency over time, characterizing fluctuations relative to its mean value. It is associated with statistical uncertainties arising from random, unpredictable fluctuations, such as quantum projection noise or short-term laser noise. These fluctuations typically vary between individual clock cycles and consequently, statistical uncertainties are generally minimized by performing repeated measurements, as they tend to average out over time.

The difference between accuracy and stability is illustrated in Fig. 1.2. In this work, we focus exclusively on the performance of atomic clocks as determined by statistical uncertainties, while systematic uncertainties are neglected.

2

Basics of Atomic Clocks

This chapter, as motivated in the introduction, is designed to provide a comprehensive background, facilitating an easier introduction for future (graduate) students. Hence, the knowledgeable reader may choose to proceed directly to the main results in Chapter 3 and Chapter 4.

Here, we outline the theoretical foundations for describing atomic clock operation. To start with, in Sec. 2.1 we introduce the Allan deviation, the primary metric for clock stability. Subsequently, we describe the three fundamental components of an atomic clock (as presented in Sec. 1.2):

- Sec. 2.2: The local oscillator, which produces the inherently noisy frequency signal.
- Sec. 2.3: The atomic reference, to which the local oscillator is stabilized by repeated interrogations.
- Sec. 2.4: The servo, which applies feedback to correct the local oscillator.

As the primary objective of this thesis is the identification of optimal interrogation schemes, a particular emphasis is placed on the atomic reference. Note that throughout this thesis we set $\hbar \equiv 1$ for simplicity, except when explicitly discussing relations between frequencies and energies.

2.1 Allan Deviation - A Stability Measure

Before we describe the individual components of an atomic clock in detail, we first introduce methods for characterizing atomic clocks and frequency standards. The focus will be on the primary metric in this work: the Allan deviation, characterizing the clock stability. This measure is essential for understanding the performance and limitations of atomic clocks.

Model— The output of an ideal local oscillator would be a pure sine wave of an electromagnetic field $E(t) = E_0 \sin(\omega_0 t)$ with amplitude E_0 and frequency ω_0 being constant in time. In any realistic device, however, various unavoidable physical processes introduce deviations from a purely sinusoidal waveform. Consequently, both the amplitude and frequency of the oscillator fluctuate over time, and as a result, the output signal cannot be described analytically in general. These fluctuations – collectively referred to as noise – affect the stability of the oscillator. Since amplitude fluctuations have no significant impact on the stability analysis [83], we model the output of the local oscillator as

$$E(t) = E_0 \sin(\omega_0 t - \phi(t)), \tag{2.1}$$

where the fluctuations of the phase $\phi(t)$ arise from random noise processes. The corresponding local oscillator frequency $\omega_{\mathrm{LO}}(t)$ is linked to the phase fluctuations by a derivative

$$\omega_{\mathrm{LO}}(t) = \omega_0 - \frac{\mathrm{d}\phi(t)}{\mathrm{d}t} \tag{2.2}$$

and thus, the frequency difference $\omega(t)$ reads

$$\omega(t) = \frac{\mathrm{d}\phi(t)}{\mathrm{d}t} = \omega_0 - \omega_{\mathrm{LO}}(t). \tag{2.3}$$

Accordingly, the phase fluctuations can be obtained by integrating the frequency deviation

$$\phi(t) = \int_{t_0}^{t} \mathrm{d}t' \, \omega(t'). \tag{2.4}$$

To facilitate a comparison between oscillators with different nominal frequencies ω_0, it is advantageous to introduce the dimensionless relative frequency deviation

$$y(t) = \frac{\omega(t)}{\omega_0} = \frac{\omega_0 - \omega_{\mathrm{LO}}(t)}{\omega_0}. \tag{2.5}$$

Similarly, we can define relative phase fluctuations

$$x(t) = \frac{\phi(t)}{\omega_0}. \tag{2.6}$$

To be precise, $x(t)$ represents effective time fluctuations in seconds, resulting from phase fluctuations. However, they are usually called relative phase fluctuations for clarity and to ease the distinction from the independent time variable t. The relation between relative frequency and phase deviations follows directly from the definition, yielding

$$y(t) = \frac{\mathrm{d}x(t)}{\mathrm{d}t} \qquad \text{or} \qquad x(t) = \int_{t_0}^{t} \mathrm{d}t'\, y(t'). \tag{2.7}$$

Already from Eq. (2.5) and Eq. (2.6) it becomes evident that higher frequencies are advantageous considering the stability of frequency standards and atomic clocks, as the relative contribution of deviations is suppressed for larger ω_0.

Naturally, the local oscillator produces a continuous noisy frequency trace $y(t)$, as illustrated in Fig. 2.1(a). However, in many applications – including the operation of an atomic clock – only a sequence of discrete frequency measurements averaged over individual clock cycles of duration T_C is recorded. In general, each clock cycle can be decomposed into two parts: the interrogation time T and the dead time T_D. During the interrogation time T, the frequency of the local oscillator is effectively compared to the atomic transition frequency to determine deviations arising from various noise sources. In contrast, frequency fluctuations during dead time T_D – originating from processes such as probe preparation, measurement and the application of feedback – are not monitored and thus cannot be corrected. Although dead time will be discussed in detail in Chapter 4 and we assume a negligible dead time in the first part of this thesis, at this point we aim to treat the frequency trace in its most general form. Accordingly, the frequency trace is divided into equal intervals of duration $T_C = T_D + T$ and the frequency value recorded at the end of cycle k is obtained by averaging over this particular cycle

$$y_k = \frac{1}{T_C} \int_{(k-1)T_C}^{kT_C} \mathrm{d}t\, y(t) = \frac{1}{T_C} \left[\int_{(k-1)T_C}^{(k-1)T_C+T_D} \mathrm{d}t\, y(t) + \int_{(k-1)T_C+T_D}^{kT_C} \mathrm{d}t\, y(t) \right], \tag{2.8}$$

as depicted in Fig. 2.1(b). Accordingly, the relative phase deviation is given by $x_k = y_k T_C$. Moreover, we will consider the frequency averaged over a total duration $\tau = nT_C$, corresponding to n cycles,

$$\overline{y}_j = \frac{1}{\tau} \int_{(j-1)\tau}^{j\tau} \mathrm{d}t\, y(t) = \frac{1}{\tau} \sum_{k=(j-1)n+1}^{jn} \int_{(k-1)T_C}^{kT_C} \mathrm{d}t\, y(t) = \frac{1}{n} \sum_{k=(j-1)n+1}^{jn} y_k. \tag{2.9}$$

In the following, we introduce statistical measures used to characterize the fluctuations of the frequency.

Standard deviation— A common approach for characterizing statistical processes involves calculating the mean value $\overline{y}$ and the variance s^2, defined by

$$\overline{y} = \frac{1}{m}\sum_{k=1}^{m} y_k \tag{2.10}$$

$$s^2 = \frac{1}{m-1}\sum_{k=1}^{m} (y_k - \overline{y})^2, \tag{2.11}$$

where m denotes the total number of fractional frequency values y_k. The standard variance often is expressed in terms of its square root, the standard deviation s. However, the standard deviation is only a meaningful measure for uncorrelated noise. If the noise is correlated, the deviation from its mean value is no longer stationary [84] and thus, the standard deviation might be non-convergent. Consequently, it is not recommended to characterize frequency standards or atomic clocks using the standard deviation. An indication of correlated noise is that fluctuations over an averaging time τ are significantly smaller than over the entire data set (cf. Fig. 2.1(a)).

Allan deviation— The Allan variance (AVAR) [85, 86] is the most widely used time-domain metric for evaluating the stability of frequency standards and atomic clocks [11, 83, 84, 87]. It is defined as [11, 84–86]

$$\sigma_y^2(\tau) = \frac{1}{2}\langle(\overline{y}_{j+1} - \overline{y}_j)^2\rangle, \tag{2.12}$$

where $\langle\cdot\rangle$ denotes statistical averaging. To be precise, the Allan variance measures frequency instability and thus, a lower value indicates reduced instability, or equivalently, improved stability. It serves as a measure of fractional frequency fluctuations – similar to the standard variance – but with the crucial benefit of converging for most types of noise encountered in atomic clocks. The Allan variance is calculated from the difference between two consecutive averaged frequency values $\overline{y}_j$ and $\overline{y}_{j+1}$, each averaged over a time interval τ, as illustrated in Fig. 2.1(c). This is in contrast to the standard variance, which quantifies deviations from the mean value $\overline{y}$. It is remarkable that variation of the averaging time τ provides insight to the noise on different time scales. While small $\tau \sim T_C$ provide information on the short-term stability, large $\tau \gg T_C$ describe the long-term stability. Consequently, the full dependence $\sigma_y(\tau)$ has to be considered to compare the performance of different local oscillators.

For finite data sets, the statistical averaging is practically realized as [84]

$$\sigma_y^2(\tau) = \frac{1}{2(M-1)}\sum_{j=1}^{M-1} (\overline{y}_{j+1} - \overline{y}_j)^2, \tag{2.13}$$

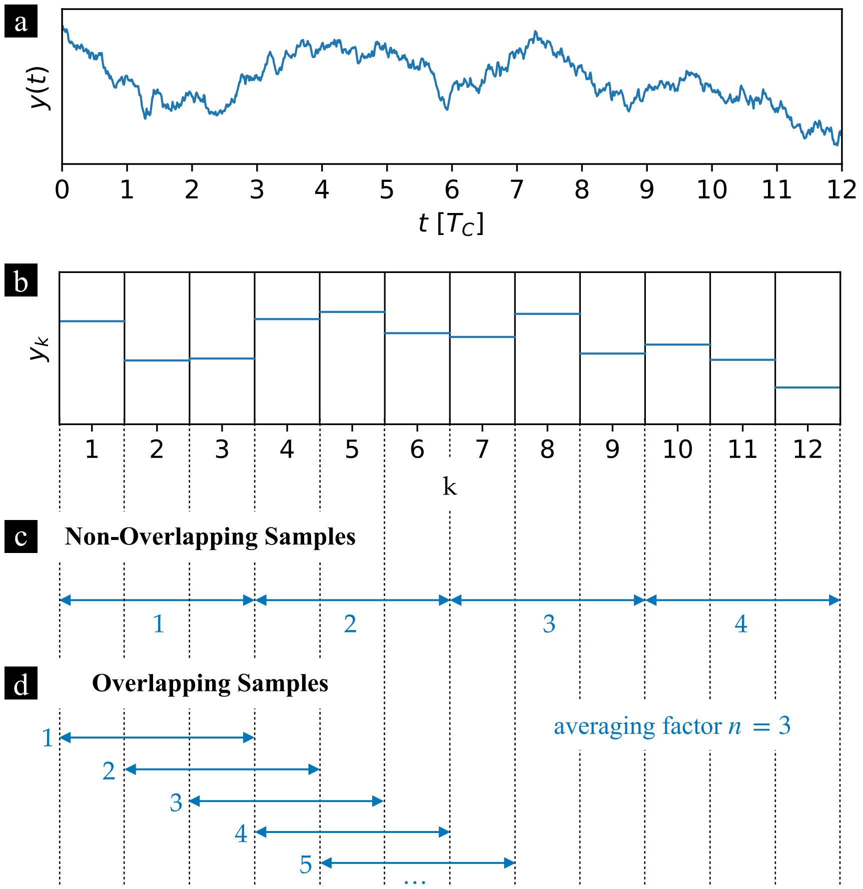
a
$y(t)$
0
1
2
3
4
5
6
7
8
9
10
11
12
$t\ [T_C]$
b
y_k
1
2
3
4
5
6
7
8
9
10
11
12
k
c
Non-Overlapping Samples
1
2
3
4
d
Overlapping Samples
averaging factor $n = 3$
1
2
3
4
5
...

Figure 2.1: **Allan deviation:** (a) Generic continuous relative frequency difference $y(t)$ as a function of t. (b) Corresponding discrete time series y_k sampled in each clock cycle with duration T_C. (c) Non-Overlapping samples for the (standard) Allan deviation (ADEV) with averaging factor $n = 3$ ($\tau = 3T_C$). (d) Overlapping samples for the overlapping Allan deviation (OADEV) with averaging factor $n = 3$ ($\tau = 3T_C$).

where $M = \frac{m}{n}$ represents the number of consecutive frequency intervals with length $\tau = nT_C$. The quantity usually addressed is the square root of the Allan variance, namely the Allan deviation (ADEV). In terms of fractional phase deviations, the Allan variance can alternatively be calculated as [84]

$$\sigma_y^2(\tau) = \frac{1}{2(K-2)\tau^2} \sum_{j=1}^{K-2} (\overline{x}_{j+2} - 2\overline{x}_{j+1} + \overline{x}_{j+1})^2, \tag{2.14}$$

where $\overline{y}_j = \frac{\overline{x}_{j+1} - \overline{x}_j}{\tau}$ and $K = M + 1$ is the total number of phase data.

The confidence interval – or error – of the Allan deviation is typically estimated as $\pm\sigma_y(\tau)/M$ although it depends on the specific noise type in general [84].

Overlapping Allan deviation— The overlapping Allan variance (OAVAR) extends the standard Allan variance by incorporating all possible overlapping intervals of length $\tau = nT_C$, as illustrated in Fig. 2.1(d), thereby making maximal use of the data set. While it yields the same value as the standard Allan variance, this approach improves the statistical confidence of the resulting stability estimate by significantly increasing the effective number of samples, even though the overlapping intervals are not entirely independent [84]. This enhanced confidence comes with a trade-off in computational complexity, as the calculations involve all possible combinations within the data set. Nevertheless, the overlapping Allan variance is the preferred choice in stability analysis for high-precision measurements. The overlapping Allan variance is defined by [84]

$$\sigma_y^2(\tau) = \frac{1}{2n^2(M-2n+1)} \sum_{j=1}^{M-2n+1} \left[\sum_{l=j}^{j+n-1} (\overline{y}_{l+n} - \overline{y}_l) \right]^2 , \tag{2.15}$$

where M denotes the number of all possible overlapping intervals of length $\tau = nT_C$. Consequently, M is significantly larger compared to the standard Allan variance (see comparison of Fig. 2.1(c) and (d)), resulting in a substantially lower confidence interval. Unfortunately, this expression is demanding in terms of computational complexity due to the double summation. The necessary overhead can be reduced by integrating the frequency data first and using [84]

$$\sigma_y^2(\tau) = \frac{1}{2(K-2n)\tau^2} \sum_{j=1}^{K-2n} (\overline{x}_{j+2n} - 2\overline{x}_{j+n} + \overline{x}_j)^2 \tag{2.16}$$

for fractional phase deviations with $K = M+1$. Again, the result is usually expressed as the square root, which is denoted as overlapping Allan deviation (OADEV).

Note that although various other types of variances are available for stability analysis, in this thesis we will focus exclusively on the overlapping Allan deviation. For simplicity, we refer to it as the Allan deviation and implicitly assume the overlapping variant considering confidence intervals.

Although relative frequency deviations are the most widely used convention in frequency metrology, absolute frequency deviations are also frequently encountered. Furthermore, particularly in experimental contexts, frequencies ν are often used instead of angular frequencies $\omega = 2\pi\nu$. Fortunately, with the relation

$$y(t) = \frac{\omega(t)}{\omega_0} = \frac{\omega_0 - \omega_{\mathrm{LO}}(t)}{\omega_0} = \frac{\nu_0 - \nu_{\mathrm{LO}}(t)}{\nu_0} = \frac{\nu(t)}{\nu_0}, \tag{2.17}$$

the conversion between these conventions is straightforward to derive and reads

$$\sigma_y(\tau) = \frac{\sigma_\omega(\tau)}{\omega_0} = \frac{\sigma_\nu(\tau)}{\nu_0}. \tag{2.18}$$

2.2 Local Oscillator

Depending on the specific application and type of clock, various local oscillators are employed, each with its characteristic noise composition. In the following section, we introduce methods for characterizing these noise processes and relate them to the stability, quantified by the previously introduced Allan deviation. By combining both time-domain and frequency-domain approaches, we gain a comprehensive understanding of the noise contributions and their impact on frequency stability. Additionally, we introduce a single time scale that allows for the comparison of different local oscillators, regardless of their specific noise characteristics and mean frequency.

2.2.1 Noise Characterization

Frequency domain— In the previous section, we introduced the Allan deviation as the primary measure for the stability of frequency standards and atomic clocks, by quantifying frequency fluctuations in the time domain. However, because the Allan deviation averages over fluctuations, some information about the noise characteristics is inherently lost. A more comprehensive characterization of the noise processes is provided by the (single-sided) power spectral noise density[1] (PSD) $S_y(f)$, in units of 1/Hz, of the frequency fluctuations, defined for Fourier frequencies $0 \leq f < \infty$. State-of-the-art clock lasers can be modeled by a power law [11, 12, 83–85, 87, 88]

$$S_y(f) = \sum_\alpha h_\alpha f^\alpha \tag{2.19}$$

with coefficients h_α, where $\alpha = 0, -1, -2$ corresponds to white frequency noise (WN), flicker frequency noise (FN) and random walk frequency noise (RWN), respectively. This model is valid for $0 \leq f \leq f_c$, where f_c is an upper cutoff frequency to maintain integrability and can be physically motivated by finite bandwidth and duration [83]. Furthermore, it is assumed that any potential slow frequency drifts can always be corrected. For a more detailed discussion and characterization or origins of the particular noise contributions, we refer to the pertinent literature as Refs. [11, 12, 83–85, 87, 88].

---

[1] In theoretical studies, the two-sided PSD $S_y^{(2)}(f)$, defined over Fourier frequencies $-\infty < f < \infty$, is often employed. In experimental settings, however, only positive frequencies are typically relevant. Since the PSD is a real, non-negative, and even function, these two variants are related by $S_y(f) = 2S_y^{(2)}(f)$. Accordingly, in this work, we focus on the single-sided PSD $S_y(f)$. [11]

In practice, for a given frequency trace, the PSD can be calculated as [89, 90]

$$S_y(f) = 2 \lim_{\mathcal{T}\to\infty} \frac{1}{\mathcal{T}} \left| \int_0^{\mathcal{T}} \mathrm{d}t\, y(t) e^{-i2\pi f t} \right|^2 \tag{2.20}$$

and thus involves a Fourier transform. Again, we can convert between different frequency conventions by

$$S_y(f) = \frac{S_\omega(f)}{\omega_0^2} = \frac{S_\nu(f)}{\nu_0^2} \tag{2.21}$$

where $S_\omega(f)$ and $S_\nu(f)$ represent the spectral noise densities for angular and absolute frequencies, respectively.

Time domain— After characterizing the frequency stability in the time domain by the Allan deviation and the frequency noise through the spectral noise density in the Fourier frequency domain, we aim to link these two approaches. Based on a given spectral noise density, the Allan variance can be inferred according to [11, 83, 84]

$$\sigma_y^2(\tau) = 2 \int_0^\infty \mathrm{d}f\, S_y(f) \frac{\sin^4(\pi\tau f)}{(\pi\tau f)^2}. \tag{2.22}$$

Assuming a power law model for the spectral noise density as introduced in Eq. (2.19), an explicit form for the Allan variance of a local oscillator is given by

$$\begin{aligned} \sigma_{y,\mathrm{LO}}^2(\tau) &= \sigma_{y,\mathrm{WN}}^2(\tau) + \sigma_{y,\mathrm{FN}}^2(\tau) + \sigma_{y,\mathrm{RWN}}^2(\tau) \\ &= \frac{\tilde{h}_{-1}}{\tau} + \tilde{h}_0 + \tilde{h}_1\tau = \sum_{\beta=-1}^{1} \tilde{h}_\beta \tau^\beta. \end{aligned} \tag{2.23}$$

Consequently, the Allan variance likewise can be modeled by a power law with scaling $\beta = -\alpha - 1$, depending on the averaging time τ. For white, flicker and random walk frequency noise, the corresponding coefficients are $\tilde{h}_{-1} = \frac{h_0}{2}$, $\tilde{h}_0 = 2\ln(2)h_{-1}$ and $\tilde{h}_1 = \frac{2\pi^2}{3}h_{-2}$, respectively, which can be derived using the integrals

$$\int_0^\infty \mathrm{d}f\, \frac{\sin^4(af)}{a^2 f^4} = \frac{a\pi}{3} \tag{2.24}$$

$$\int_0^\infty \mathrm{d}f\, \frac{\sin^4(af)}{a^2 f^3} = \ln(2) \tag{2.25}$$

$$\int_0^\infty \mathrm{d}f\, \frac{\sin^4(af)}{a^2 f^2} = \frac{\pi}{4a}. \tag{2.26}$$

Hence, the different noise contributions can be identified by investigating the scaling behavior of the Allan variance with the averaging time τ. For clarity, the individual noise contributions to the spectral noise density and Allan variance are summarized in Tab. 2.1. Generic examples are illustrated in Fig. 2.2(a-c).

Noise type	α	$S_y(f)$	$\beta = -\alpha - 1$	$\sigma_y^2(\tau)$	$\tilde{h}_\beta$
WN	0	$h_0 f^0$	-1	$\tilde{h}_{-1}\tau^{-1}$	$\frac{h_0}{2}$
FN	-1	$h_{-1} f^{-1}$	0	$\tilde{h}_0\tau^0$	$2\ln(2)h_{-1}$
RWN	-2	$h_{-2} f^{-2}$	1	$\tilde{h}_1\tau^1$	$\frac{2\pi^2}{3}h_{-2}$

Table 2.1: **Noise contributions to the Allan variance:** Power law scaling of the spectral noise density and Allan variance of fractional frequency fluctuations for white frequency noise (WN), flicker frequency noise (FN) and random walk frequency noise (RWN).

2.2.2 Coherence Time

In the previous section we have seen that frequency fluctuations of a local oscillator originate from a complex mixture of different noise processes. Therefore, thorough characterization requires a comprehensive analysis of the measures introduced. In terms of the Allan deviation, a broad range of averaging times has to be considered, while for the spectral noise density it involves investigating a broad band of Fourier frequencies. Nevertheless, each unique combination of noise contributions introduces a characteristic time scale to the system, ultimately limiting the clock stability, as we will discuss in detail in Chapter 4. Hence, it is convenient to define a coherence time Z to facilitate a conceptual comparison of different local oscillators with distinct noise characteristics and mean frequency. While there are several possibilities motivated by different applications, we follow Ref. [92] and define the coherence time Z implicitly by

$$\sigma_{y,\mathrm{LO}}(Z_C)\omega_0 Z = 1 \text{ rad} \tag{2.27}$$

where $Z_C = Z + T_D$ is the corresponding cycle duration, including dead time T_D. Intuitively, the coherence time is determined by the intersection of the local oscillator stability $\sigma_{y,\mathrm{LO}}(\tau)$ and $1/\omega_0\tau$ at $\tau = Z$. Consequently, as we will derive in the next section, the coherence time can be interpreted as the interrogation time at which the Allan deviation of the local oscillator at a single clock cycle coincides with the stability arising from quantum projection noise of a single particle in an ideal scenario.

An exemplary evaluation of the coherence time Z is shown in Fig. 2.2(d). While each specific noise profile $\sigma_{y,\mathrm{LO}}(\tau)$ uniquely determines Z, the reverse is not necessarily true. Distinct noise compositions can yield the same coherence time. Hence, a given coherence time Z may arise from various noise compositions.

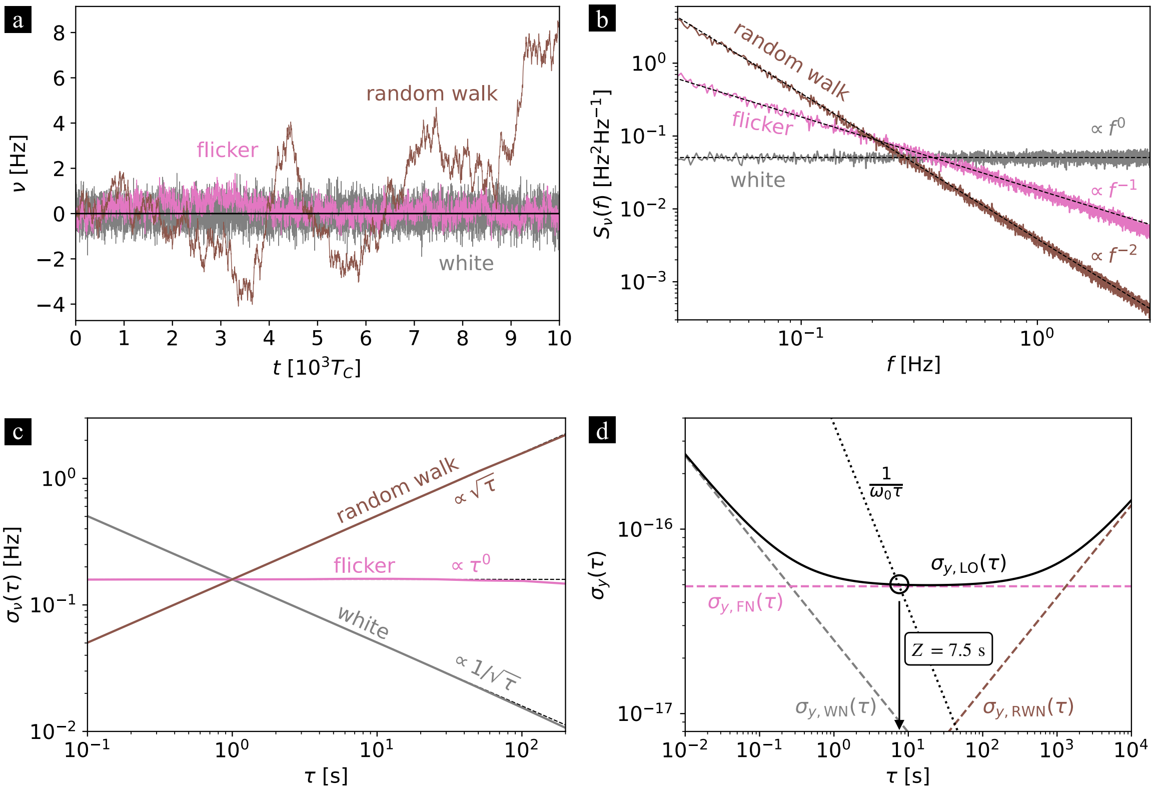

Figure 2.2: **Stability analysis of local oscillators:** (a) Frequency traces simulated over 10^4 cycles for white (gray), flicker (pink) and random walk (brown) frequency noise. (b) Corresponding spectral noise density $S_\nu(f)$ showing the characteristic scaling with Fourier frequency f for the three noise processes. (c) Corresponding Allan deviation $\sigma_\nu(\tau)$, highlighting the characteristic scaling with the averaging time τ for the three noise processes. (d) Allan deviation $\sigma_{y,\mathrm{LO}}(\tau)$ of a state-of-the-art clock laser as considered in Ref. [91], with white frequency noise $\sigma_{y,\mathrm{WN}}(\tau) = 2.5 \times 10^{-17} \left(\frac{\tau}{\mathrm{s}}\right)^{-1/2}$, flicker frequency noise $\sigma_{y,\mathrm{FN}}(\tau) = 4.9 \times 10^{-17}$ and random walk frequency noise $\sigma_{y,\mathrm{RWN}}(\tau) = 1.35 \times 10^{-18} \left(\frac{\tau}{\mathrm{s}}\right)^{1/2}$, based on the laser described in Ref. [88]. Dashed colored lines indicate the individual noise contributions. The intersection of $\sigma_{y,\mathrm{LO}}(\tau)$ (solid black) with the dashed black line visualizes the laser coherence time Z. We use $\nu_0 = 429.228$ THz considering ^{87}Sr for calculations.

2.3 Atomic Reference

Atomic sensors are the preferred choice in frequency metrology as they represent ideal references: they are identical, their transition frequencies are constants of nature, and they are well described mathematically, enabling comprehensive comparisons between theory and experiment.

In this section, we introduce the fundamental concepts and notations required to describe the interrogation of the atomic reference. We begin by reviewing essential properties of spin systems in Sec. 2.3.1. Subsequently, we discuss the time evolution of spin systems: Sec. 2.3.2 derives the unitary dynamics, while Sec. 2.3.3 addresses the impact of decoherence processes. Furthermore, the notion of quantum measurements is considered in Sec. 2.3.4. Building on these fundamental aspects, we introduce Ramsey interferometry in Sec. 2.3.5, which represents the primary interrogation scheme considered throughout this thesis. In this context, we discuss quantum projection noise (QPN) in Sec. 2.3.6, which imposes a fundamental limit in interferometry due to the indeterministic nature of quantum mechanics. Finally, the three standard Ramsey protocols are presented utilizing coherent spin states (CSS) in Sec. 2.3.7, GHZ states in Sec. 2.3.8 and spin-squeezed states (SSS) in Sec. 2.3.9.

2.3.1 Spin Systems

The generally complex electronic structure of atoms used in precision spectroscopy can often be reduced to a two-level system by focusing on a single, isolated atomic transition. This simplification is valid when all other transitions are sufficiently separated in energy and are thus effectively off-resonant, allowing them to be neglected. Additionally, ideal transitions for atomic clock application are both narrow – minimizing the effects of a finite excited-state lifetime – and offer precise coherent control. These properties are crucial for achieving high stability and accuracy, which are essential for reliable interrogation and long-term frequency stability in metrological applications.

Two level system— The Hilbert space of a two-level system, mathematically equivalent to a (pseudo-) spin-1/2 particle [6, 59, 93], is given by $\mathcal{H} = \mathbb{C}^2$. In this space, we use two orthonormal basis states: $|{\downarrow}\rangle = |\mathrm{g}\rangle = |0\rangle$, representing the ground state (or lower energy level, corresponding to “spin-down”), and $|{\uparrow}\rangle = |\mathrm{e}\rangle = |1\rangle$, representing the excited state (or higher energy level, corresponding to “spin-up”). Any pure state of the system can thus be expressed as a linear combination of these basis states $|\psi\rangle = c_\downarrow |{\downarrow}\rangle + c_\uparrow |{\uparrow}\rangle$ where the complex coefficients $c_\downarrow, c_\uparrow \in \mathbb{C}$ satisfy the normalization condition $|c_\downarrow|^2 + |c_\uparrow|^2 = 1$. These states can also be conveniently represented as two-dimensional complex vectors, typically by adopting the standard (canonical) basis vectors vectors $|{\uparrow}\rangle \doteq \binom{1}{0}$ and $|{\downarrow}\rangle \doteq \binom{0}{1}$.

Correspondingly, observables of two-level systems are represented by hermitian (self-adjoint) 2×2-matrices. A convenient basis for the space of observables is provided by the identity matrix $\mathbb{1} = |\uparrow\rangle\langle\uparrow| + |\downarrow\rangle\langle\downarrow|$ and the three Pauli matrices

$$\begin{aligned}
\sigma_x &= |\uparrow\rangle\langle\downarrow| + |\downarrow\rangle\langle\uparrow| = \sigma_+ + \sigma_- \\
\sigma_y &= -i\,|\uparrow\rangle\langle\downarrow| + i\,|\downarrow\rangle\langle\uparrow| = -i(\sigma_+ - \sigma_-) \\
\sigma_z &= |\uparrow\rangle\langle\uparrow| - |\downarrow\rangle\langle\downarrow| = \sigma_{\mathrm{ee}} - \sigma_{\mathrm{gg}}
\end{aligned} \tag{2.28}$$

where $\sigma_+ = \sigma_{\mathrm{eg}} = |\uparrow\rangle\langle\downarrow|$ and $\sigma_- = \sigma_{\mathrm{ge}} = |\downarrow\rangle\langle\uparrow|$ are the raising and lowering operators – which induce transitions between the ground and excited states – effectively flipping the spin. The operators $\sigma_{\mathrm{ee}} = |\uparrow\rangle\langle\uparrow|$ and $\sigma_{\mathrm{gg}} = |\downarrow\rangle\langle\downarrow|$ are projectors onto the excited and ground states, respectively, and give rise to the z-component, representing the population difference. Moreover, the spin observable is expressed in terms of the Pauli operators $\mathbf{S} = \frac{1}{2}\boldsymbol{\sigma}$, where $\mathbf{S} = (S_x, S_y, S_z)^T$ and $\boldsymbol{\sigma} = (\sigma_x, \sigma_y, \sigma_z)^T$, respectively,

Likewise, any mixed state of a two-level system, described by a density matrix ρ, can be written as a linear combination of the Pauli operators

$$\rho = \frac{1}{2}\left(\mathbb{1} + \mathbf{r}^T\boldsymbol{\sigma}\right) = \frac{1}{2}\left(\mathbb{1} + r_1\sigma_x + r_2\sigma_y + r_3\sigma_z\right) \tag{2.29}$$

where $\mathbf{r} = (r_1, r_2, r_3)^T = (\langle\sigma_x\rangle, \langle\sigma_y\rangle, \langle\sigma_z\rangle)^T \in \mathbb{R}^3$, with $|\mathbf{r}| \leq 1$, forms the so called Bloch vector. The components of $\mathbf{r}$ represent the expectation values of the Pauli operators and fully characterize the mixed state ρ. In this framework, pure states are represented by points on the Bloch sphere, since $|\mathbf{r}| = 1$. Alternatively, pure states can also be parametrized by the azimuthal angle θ and polar angle φ

$$|\psi\rangle = \cos\left(\tfrac{\theta}{2}\right)|\downarrow\rangle + e^{-i\varphi}\sin\left(\tfrac{\theta}{2}\right)|\uparrow\rangle\,. \tag{2.30}$$

In this representation, the Bloch vector is given by

$$\mathbf{r} = \begin{pmatrix} \sin(\theta)\cos(\varphi) \\ \sin(\theta)\sin(\varphi) \\ -\cos(\theta) \end{pmatrix} \tag{2.31}$$

since $\sin(\pi - \theta) = \sin(\theta)$ and $\cos(\pi - \theta) = -\cos(\theta)$. Note that the azimuthal angle θ is measured from the negative z-axis, in contrast to the commonly used definition of spherical coordinates. The concept of Bloch vectors on the Bloch sphere provides a geometric representation of spin states, with $\mathbf{r}$ effectively describing the polarization of the state. Consequently, it also facilitates intuitive insights into the dynamics of spin-1/2 systems. Representative states on the Bloch sphere are illustrated in Fig. 2.3.

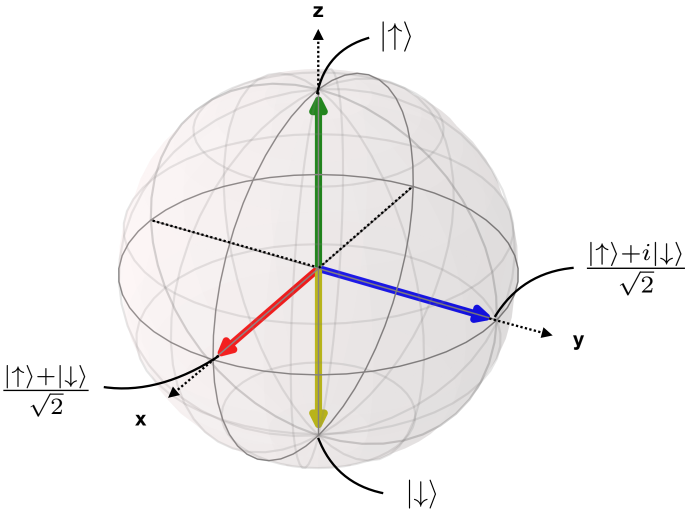
z
$|\uparrow\rangle$
$\frac{|\uparrow\rangle+i|\downarrow\rangle}{\sqrt{2}}$
y
$\frac{|\uparrow\rangle+|\downarrow\rangle}{\sqrt{2}}$
x
$|\downarrow\rangle$

Figure 2.3: **Visualization of states on the Bloch sphere:** The ground (yellow) and excited (green) states are aligned along the $\mp z$-axis, while red ($\theta = \frac{\pi}{2}$, $\varphi = 0$) and blue ($\theta = \frac{\pi}{2}$, $\varphi = \frac{\pi}{2}$) states are polarized in x- and y-direction, respectively.

Collective spin— The generalization of the presented formalism to N spin-1/2 systems is straightforward. The composite Hilbert space $\mathcal{H} = \bigotimes_{k=1}^{N} \mathcal{H}_k = \bigotimes_{k=1}^{N} \mathbb{C}^2$ is formed by the tensor product of N single particle Hilbert spaces $\mathcal{H}_k = \mathbb{C}^2$. A basis for this 2^N dimensional Hilbert space can be constructed from tensor products of single particle basis elements $|i_1, \ldots, i_N\rangle = \bigotimes_{i=1}^{N} |i_k\rangle^{(k)}$ with $i_k \in \{\downarrow, \uparrow\} \forall k$. For example, the collective ground and excited states are represented by $|\downarrow\rangle^{\otimes N}$ and $|\uparrow\rangle^{\otimes N}$, respectively. However, numerical simulations in this full Hilbert space are limited to relatively small particle numbers N, as the dimension of $\mathcal{H}$ scales exponentially with the ensemble size N, making numerical computations increasingly demanding. This exponential scaling presents a significant challenge in studying systems with larger ensembles, motivating the need for efficient representations or the exploitation of symmetries to reduce the effective dimensionality of the problem.

The collective spin operator $\mathbf{S} = \sum_{k=1}^{N} \mathbf{S}^{(k)}$ is constructed from single particle spin operators $\mathbf{S}^{(k)}$. The spin components form an angular momentum algebra defined by

$$[S_j, S_k] = i\epsilon_{jkl} S_l, \tag{2.32}$$

where $[A, B] = AB - BA$ denotes the commutator and ϵ_{jkl} is the fully anti-symmetric Levi-Civita tensor. Consequently, the total spin operator $\mathbf{S}^2 = S_x^2 + S_y^2 + S_z^2$ commutes with each spin component $[\mathbf{S}^2, S_k] = 0$ for $k \in \{x, y, z\}$. Therefore, simultaneous eigenstates of the total spin and one spin component can be found. Typically, eigenstates of $\mathbf{S}^2$ and S_z are chosen, while the corresponding states in a different basis can be obtained by a unitary transformation (cf. App. B). The eigenstates $|S, M\rangle_z$ are labeled by the quantum numbers S and M, representing the total spin magnitude and the spin projection along the z-axis, respectively. In the following, we omit the index z for simplicity, referring implicitly to the z-basis. If a different basis is used, we will indicate this explicitly. The states $|S, M\rangle$ are often referred to as Dicke states [94] and satisfy the eigenvalue equations

$$\mathbf{S}^2 |S, M\rangle = S(S+1) |S, M\rangle , \tag{2.33}$$

$$S_z |S, M\rangle = M |S, M\rangle , \tag{2.34}$$

where $S \in \{N/2, N/2-1, \ldots, S_{\text{min}}\}$ and $M \in \{-S, -S+1, \ldots, S-1, S\}$. The minimal total spin is $S_{\text{min}} = 0$ for N even and $S_{\text{min}} = 1/2$ for N odd. To move between states with different projections M, ladder operators can be constructed from the spin components

$$S_\pm = S_x \pm iS_y, \tag{2.35}$$

which act as

$$S_\pm |S, M\rangle = \sqrt{S(S+1) - M(M \pm 1)}\, |S, M \pm 1\rangle \tag{2.36}$$

and are often called raising and lowering or creation and annihilation operators, since they increase or decrease the number of excited atoms by one. They obey the commutation relations

$$[S_z, S_\pm] = \pm S_\pm, \qquad [S_+, S_-] = 2S_z, \qquad \left[\mathbf{S}^2, S_\pm\right] = 0. \tag{2.37}$$

Permutational symmetry— Already for $N > 2$, we observe that the Dicke states are degenerate and the quantum numbers S and M do not determine $|S, M\rangle$ uniquely. In fact, the total number of Dicke states is

$$n_{\text{DS}} = \sum_{S=S_{\text{min}}}^{N/2} 2S + 1 = \left(\frac{N}{2} + 1\right)^2 - \frac{1}{4}\text{mod}_2(N), \tag{2.38}$$

where the modulo term takes ensembles with N odd into account. This expression can be derived by separately evaluating the sum for even and odd ensemble sizes. While n_{DS} grows quadratically with N, the dimension of the full Hilbert space increases exponentially as 2^N. Hence, each Dicke state $|S, M\rangle$ has a degeneracy [95–100]

$$d_N^S = (2S+1)\frac{N!}{(\frac{N}{2} + S + 1)!(\frac{N}{2} - S)!}. \tag{2.39}$$

This degeneracy bridges from n_{DS} to $\dim(\mathcal{H})$ via

$$\dim(\mathcal{H}) = 2^N = \sum_{S=S_{\min}}^{N/2} d_N^S(2S+1). \tag{2.40}$$

For example, for $N=4$ we find $d_4^0=2$, $d_4^1=3$ and $d_4^2=1$, showing that the Dicke states for $S<N/2$ are degenerate.

The Dicke states with maximal spin $S=N/2$ are uniquely defined, as any Dicke state represents a symmetric superposition of $N_+ = N/2+M$ excited two-level systems

$$\left|\tfrac{N}{2}, M\right\rangle = \frac{1}{\sqrt{\binom{N}{N_+}}}\mathcal{S}\left[\left|\uparrow\right\rangle^{\otimes N_+} \otimes \left|\downarrow\right\rangle^{\otimes(N-N_+)}\right], \tag{2.41}$$

where $\mathcal{S}$ is the symmetrization operator and the binomial coefficient $\binom{N}{N_+}$ accounts for all possible combinations and ensures normalization. This symmetric subspace, denoted as $\mathcal{H}_{\mathrm{S}}$, is permutationally invariant and has dimension $\dim(\mathcal{H}_{\mathrm{S}}) = N+1$. The states $\left|\frac{N}{2}, M\right\rangle$ can be constructed from the collective ground state $\left|\frac{N}{2}, -\frac{N}{2}\right\rangle = \left|\downarrow\right\rangle^{\otimes N}$ by repeated application of S_+

$$\left|\tfrac{N}{2}, M\right\rangle = \frac{1}{(\frac{N}{2}+M)!}\begin{pmatrix} N \\ \frac{N}{2}+M \end{pmatrix}^{-1/2} S_+^{\frac{N}{2}+M}\left|\tfrac{N}{2}, -\tfrac{N}{2}\right\rangle. \tag{2.42}$$

The states $\left|\frac{N}{2}, M\right\rangle$ with maximal spin $S=N/2$ are commonly referred to as $|M\rangle$ for simplicity.

For $S<N/2$ however, there exist d_N^S degenerate, non-symmetric superpositions of the N two level systems. To determine the action of single particle operators on collective states, for example necessary for individual decoherence processes (cf. Sec. 2.3.3), the Dicke states have to be explicitly expressed in terms of the tensor product basis. Hence, we have to introduce more general Dicke states $|S, M, \alpha_S\rangle$ [94], where the additional quantum number α_S accounts for the degeneracy. Unfortunately, finding all 2^N representations of this basis is computationally demanding, similar to computations in the tensor product basis. However, permutational symmetry of the system and its dynamics – which is assumed throughout this thesis and typically applies to a good approximation – enables a crucial simplification, as discussed in detail in Refs. [95–100]. In this case, the matrix elements for different α_S are identical and thus, the states $|S, M, \alpha_S\rangle$ cannot be distinguished. Therefore, effective basis states $|S, M\rangle$ can be defined, and the degeneracy is eliminated. Hence, any arbitrary density operator can then be expressed as

$$\rho = \sum_{S,M,S',M'} \rho_{SM,S'M'}\left|S, M\right\rangle\!\left\langle S', M'\right|, \tag{2.43}$$

with matrix elements $\rho_{SM,S'M'} = \langle S, M|\,\rho\,|S', M'\rangle$. If the dynamics additionally does not create any coherences between Dicke states with $S \neq S'$, i.e. $\langle S, M|\,\rho\,|S', M'\rangle = 0$, which will be the case throughout this thesis, the density operator further simplifies to

$$\rho = \sum_{S,M,M'} \rho_{SMM'}\,|S, M\rangle\langle S, M'|\,, \tag{2.44}$$

with matrix elements $\rho_{SMM'} = \langle S, M|\,\rho\,|S, M'\rangle$. Therefore, ρ has block-diagonal form, as illustrated in Fig. 2.4. While the blocks become smaller with increasing S, the number d_N^S of degenerate states represented by each block increases, except for $d_j^{S_{\min}}$. Consequently, permutational invariance allows to reduce the dimension of the problem significantly, yielding a smaller Hilbert space $\mathcal{H}_{\mathrm{PS}}$ with $\dim(\mathcal{H}_{\mathrm{PS}}) = n_{\mathrm{DS}} \in \mathcal{O}(N^2)$, rather than $\dim(\mathcal{H}) = 2^N$. Additionally assuming the particular form in Eq. (2.44), the total number of non-zero matrix elements reduces to

$$\sum_{S=S_{\min}}^{N/2} = (2S+1)^2 = \frac{1}{6}(N+1)(N+2)(N+3) = \mathcal{O}(N^3), \tag{2.45}$$

providing a substantial reduction compared to the 4^N elements in the tensor product or generalized Dicke basis. This reduction enables numerical studies of significantly larger ensembles (cf. App. A for a detailed discussion).

Wigner function— Considering collective spin systems, the concept of the Bloch sphere can be generalized to a Bloch sphere with radius $S = N/2$. Hence, collective spin states can be illustrated by the Bloch vector, providing a geometrical representation of the mean spin vector. Although this visualization is intuitive, it only describes the polarization and thus, lacks the ability to capture quantum correlations of more complex spin states, especially entangled or non-classical states. A comprehensive representation is provided by the Wigner function, a quasi-probability distribution on the Bloch sphere that reveals deeper insights into the quantum nature of a state. Additionally, this approach also applies to spin operators. Below, we briefly present the concept following Refs. [101, 102] for an arbitrary density or spin operator G.

Assuming fixed total spin S, we expand G as

$$G = \sum_{k=0}^{2S} \sum_{q=-k}^{+k} G_{kq} T_{kq} \tag{2.46}$$

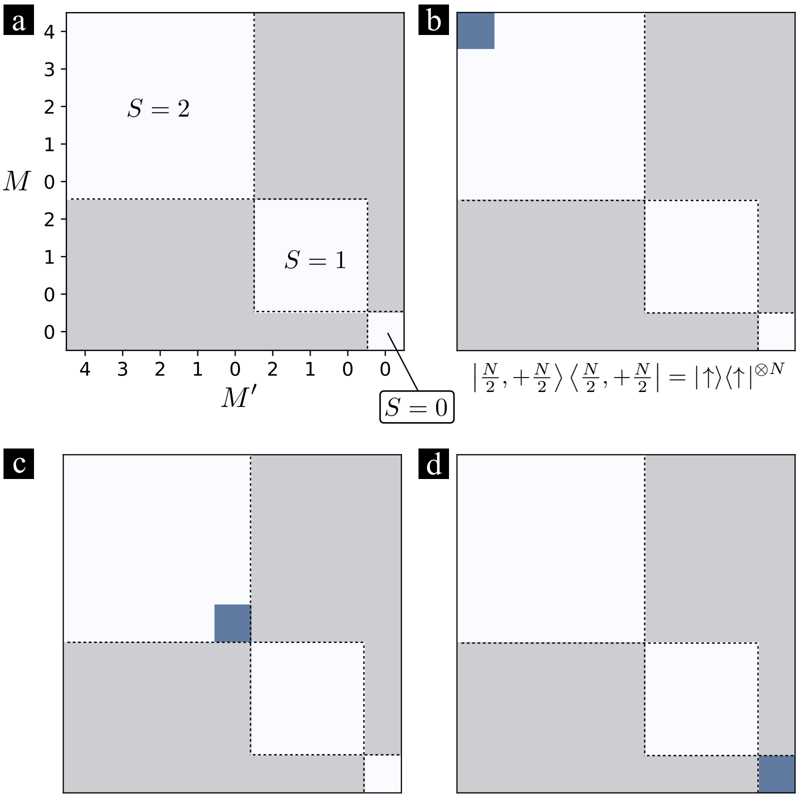

$\left|\frac{N}{2},+\frac{N}{2}\right\rangle\left\langle\frac{N}{2},+\frac{N}{2}\right| = |\uparrow\rangle\langle\uparrow|^{\otimes N}$

$\left|\frac{N}{2},-\frac{N}{2}\right\rangle\left\langle\frac{N}{2},-\frac{N}{2}\right| = |\downarrow\rangle\langle\downarrow|^{\otimes N}$

$|0,0\rangle\langle 0,0|$

Figure 2.4: **Block-diagonal structure in the Dicke basis:** (a) The density matrix in the Dicke basis $|S,M\rangle\langle S,M'|$ for $N=4$. Each block corresponds to a distinct spin quantum number S, decreasing from the top left to the bottom right ($S = N/2, N/2-1, \ldots$). Within each block, the projections M, M' decrease from left (top) to right (bottom) according to $M = +S, \ldots, -S$. The gray area outside of the diagonal blocks represents matrix elements with $S \neq S'$, which are not populated as discussed in the main text. (b) The fully excited state $\left|\frac{N}{2},+\frac{N}{2}\right\rangle = |\uparrow\rangle^{\otimes N}$. (c) The ground state $\left|\frac{N}{2},-\frac{N}{2}\right\rangle = |\downarrow\rangle^{\otimes N}$. (d) The state $|0,0\rangle$.

in terms of the multipole operators

$$\begin{aligned} T_{kq} &= \sum_{M=-S}^{+S}\sum_{M'=-S}^{+S}(-1)^{S-M}\sqrt{2k+1}\begin{pmatrix} S & k & S \\ -M & q & M' \end{pmatrix}|S,M\rangle\langle S,M'| \\ &= \sum_{M=-S}^{+S}\sum_{M'=-S}^{+S}(-1)^{S-M'}\langle S,M;S,-M'|k,q\rangle\,|S,M\rangle\langle S,M'|\,. \end{aligned} \tag{2.47}$$

Here, $\left(\begin{smallmatrix} S & k & S \\ -M & q & M' \end{smallmatrix}\right)$ and $\langle S,M;S,-M'|k,q\rangle$ are the Wigner 3-j symbols and Clebsch-Gordan coefficients, respectively [103]. The coefficients of the multipole expansion are given by

$$G_{kq} = \mathrm{Tr}\left(GT_{kq}^{\dagger}\right) \tag{2.48}$$

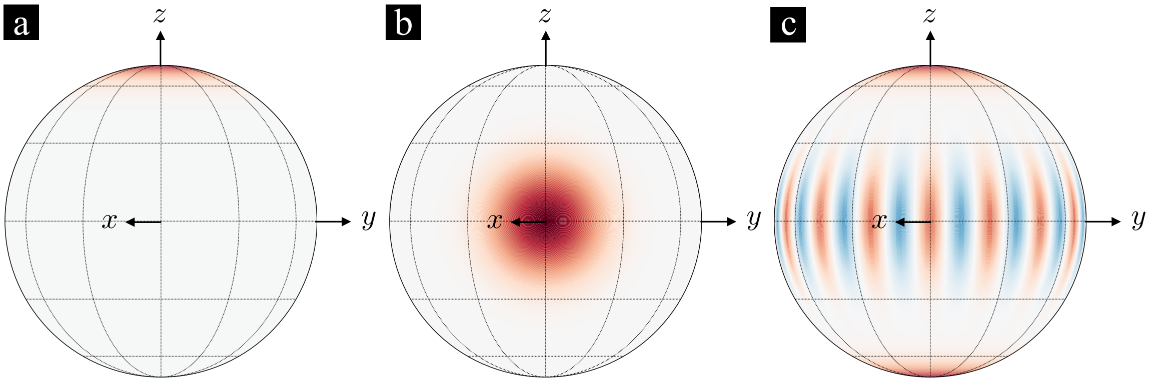

Figure 2.5: **Wigner function:** Bloch sphere visualization of the Wigner function W for $N = 16$, illustrating (a) the collective excited state $|\uparrow\rangle^{\otimes N}$, (b) the coherent spin state (CSS) polarized along the x-direction (cf. Sec. 2.3.7) and (c) the GHZ state (cf. Sec. 2.3.8). In particular, (b) reflects (a) rotated by $\frac{\pi}{2}$ around the y-axis. Red regions correspond to positive quasi-probability, while blue areas depict negative values and thus indicate quantum correlations.

and the Wigner function associated with G is defined by

$$W(\theta, \varphi) = \sum_{k=0}^{2S} \sum_{q=-k}^{+q} G_{kq} Y_{kq}(\theta, \varphi), \tag{2.49}$$

where $Y_{kq}(\theta, \varphi)$ are the spherical harmonics.

In Fig. 2.5, Wigner functions for generic states are illustrated. Quantum correlations between atoms manifest as regions of negative quasi-probability, whereas classical states display a uniform distribution, a distinction we will explore further in the following sections.

2.3.2 Unitary Dynamics

Hamiltonian of atom-field interaction— Rather than presenting the complete derivation, which can be found in detail in standard literature such as Refs. [104,105], we will briefly outline the main steps and approximations relevant for understanding the atom-field interaction in this context. For a comprehensive introduction, we also recommend Ref. [106].

As motivated before, we model the atom as a two level system. In contrast, we treat the electromagnetic field classically, assuming an electric field of the form

$$\mathbf{E}(t) = \boldsymbol{\mathcal{E}} E_0 \left[e^{-i(\omega_{\mathrm{LO}}(t)t+\varphi_{\mathrm{LO}})} + e^{i(\omega_{\mathrm{LO}}(t)t+\varphi_{\mathrm{LO}})} \right] \tag{2.50}$$

with amplitude E_0, polarization $\boldsymbol{\mathcal{E}}$, fluctuating frequency $\omega_{\mathrm{LO}}(t)$ and phase φ_{LO}. Here, we have already applied the dipole approximation, which neglects the spatial variation

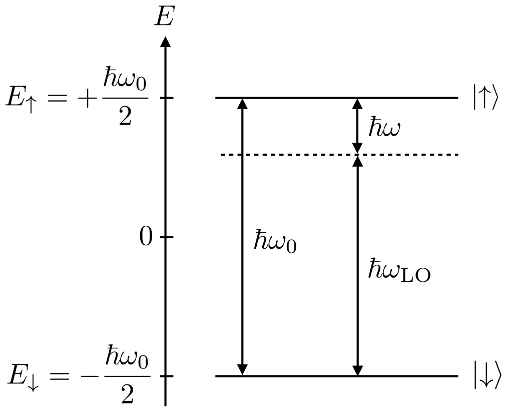
E
$E_\uparrow = +\frac{\hbar\omega_0}{2}$
0
$E_\downarrow = -\frac{\hbar\omega_0}{2}$
$|\uparrow\rangle$
$|\downarrow\rangle$
$\hbar\omega$
$\hbar\omega_0$
$\hbar\omega_{\mathrm{LO}}$

Figure 2.6: **Energy level structure in a two level system:** Schematic energy splitting between ground and excited states in a two level system and the relation between the atomic transition frequency ω_0, laser frequency ω_{LO} and frequency difference ω, as defined in the main text.

of the field. This is a valid assumption when the wavelength of the field is much longer than the atomic scale and thus, effectively does not vary over the extend of the atom. This is the case in optical atomic clocks, as atomic dimensions are on the order of Å, while the laser wavelengths are hundreds of nm. In this semi-classical approach, the total Hamiltonian for the atom and field

$$H = H_{\mathrm{A}} + H_{\mathrm{AF}} \tag{2.51}$$

can be written as a sum of the Hamiltonian of the free atom H_{A} and the atom-field interaction Hamiltonian H_{AF}. With atomic transition frequency $\omega_0 = (E_\uparrow - E_\downarrow)/\hbar$ and defining zero energy by $E_\downarrow + \frac{\hbar\omega_0}{2} = 0$, as illustrated in Fig. 2.6, the Hamiltonian of the free atom reads

$$H_{\mathrm{A}} = \frac{\omega_0}{2}\sigma_z. \tag{2.52}$$

The atom-field interaction Hamiltonian is given by

$$H_{\mathrm{AF}} = -\mathbf{d}^T\mathbf{E}(t) \tag{2.53}$$

with atomic dipole operator $\mathbf{d}$, which can be expressed in terms of Pauli operators. We proceed by moving to a rotating frame at frequency $\omega_{\mathrm{LO}}(t)$, in which the terms oscillate at frequencies $\pm(\omega_0 \pm \omega_{\mathrm{LO}}(t))$. Applying the rotating wave approximation (RWA), we assume $|\omega_0 - \omega_{\mathrm{LO}}(t)| \ll \omega_0 + \omega_{\mathrm{LO}}(t)$ and neglect the fast oscillating terms $\pm(\omega_0 + \omega_{\mathrm{LO}}(t))$ as they average to zero over relevant timescales.

The resulting Hamiltonian that governs the dynamics of the atom reads

$$H = \frac{\omega(t)}{2}\sigma_z + \frac{\Omega_R}{2}\left[\sin(\varphi_{\mathrm{LO}})\sigma_x - \cos(\varphi_{\mathrm{LO}})\sigma_y\right], \tag{2.54}$$

where $\omega(t) = \omega_0 - \omega_{\mathrm{LO}}(t)$ denotes the detuning between the atomic transition frequency ω_0 and the local oscillator frequency $\omega_{\mathrm{LO}}(t)$. The Rabi frequency

$$\Omega_R = |2E_0 \mathbf{d}^T \boldsymbol{\mathcal{E}}| \tag{2.55}$$

quantifies the strength of the coherent driving, which is assumed to be strong and near-resonant. Hence, we consider the frequency hierarchy $|\omega(t)| \ll \Omega_R \ll \omega_{\mathrm{LO}}(t) \approx \omega_0$.

Extending the description from a single atom to an ensemble of N identical and independent two-level systems interacting with a common field, we construct the total Hamiltonian as the sum of the individual single-particle Hamiltonians. This yields

$$\begin{aligned} H &= \sum_{k=1}^{N} \frac{\omega(t)}{2} \sigma_z^{(k)} + \frac{\Omega_R}{2} \left[\sin(\varphi_{\mathrm{LO}}) \sigma_x^{(k)} - \cos(\varphi_{\mathrm{LO}}) \sigma_y^{(k)} \right] \\ &= \omega(t) S_z + \Omega_R \left[\sin(\varphi_{\mathrm{LO}}) S_x - \cos(\varphi_{\mathrm{LO}}) S_y \right], \end{aligned} \tag{2.56}$$

where we introduced the collective spin components. Therefore, the dynamics of a single two-level system can be generalized seamlessly to an ensemble of N atoms by replacing individual Pauli operators with the collective spin operators, effectively capturing the collective response of the system to the field.

Equations of motion— The time evolution of a state vectors $|\psi\rangle$ is determined by the Schrödinger equation

$$i\partial_t |\psi\rangle = H(t) |\psi\rangle . \tag{2.57}$$

Rather than solving the Schrödinger equation directly, it is often useful to express the time evolution in terms of the unitary time evolution operator $\mathcal{U}(t, t_0)$, namely

$$|\psi(t)\rangle = \mathcal{U}(t, t_0) |\psi(t_0)\rangle . \tag{2.58}$$

Assuming that the Hamiltonian commutes with itself at different times, $[H(t), H(t')] = 0$, which will be the case throughout this thesis, the unitary time evolution operator is defined by

$$\mathcal{U}(t, t_0) = \exp\left(-i \int_{t_0}^{t} \mathrm{d}t' \, H(t') \right) . \tag{2.59}$$

Hence, the time evolution effectively corresponds to a unitary transformation generated by the mean Hamiltonian, averaged over the time interval $[t_0, t]$. The corresponding Schrödinger equation for $\mathcal{U}(t, t_0)$ reads

$$\partial_t \mathcal{U}(t, t_0) = -iH(t) \mathcal{U}(t, t_0). \tag{2.60}$$

In several situations, we will use the density operator ρ to describe mixed states or statistical ensembles. Its time evolution is governed by the von Neumann equation

$$\partial_t \rho = -i[H, \rho]. \tag{2.61}$$

A formal solution, in the same context as for the Schrödinger equation, is obtained by

$$\rho(t) = \mathcal{U}(t, t_0)\rho(t_0)\,\mathcal{U}^\dagger(t, t_0). \tag{2.62}$$

For some applications, it is convenient to switch to the Heisenberg picture, where the states are time independent, while the operators evolve in time. In this picture, an arbitrary operator A_H at time t is related to its counterpart $A_S \equiv A$ in the Schrödinger picture by

$$A_H(t) = \mathcal{U}^\dagger(t, t_0) A_S\, \mathcal{U}(t, t_0) \tag{2.63}$$

and follows the equation of motion

$$\partial_t A_H = i[H, A_H]. \tag{2.64}$$

The time evolution has the same form as the von Neumann equation, however, differing by a minus sign. Hence, operators in the Heisenberg picture evolve with the adjoint time evolution operator of states or density operators in the Schrödinger picture. This relation can intuitively be understood by considering the expectation value of an arbitrary operator A with respect to a state $|\psi(t)\rangle$

$$\langle A(t)\rangle = \langle\psi(t)|\, A\, |\psi(t)\rangle = \langle\psi|\, \mathcal{U}^\dagger(t, t_0) A\, \mathcal{U}(t, t_0)\, |\psi\rangle = \langle\psi|\, A_H(t)\, |\psi\rangle\,. \tag{2.65}$$

Therefore, depending on the problem, we may choose to apply the time evolution to either the states or the operators, based on which approach is more convenient.

Unitary dynamics of the system— The unitary dynamics of the system is obtained by applying the equations of motion to the Hamiltonian of our system. Essential to the evaluation of the time evolution operator is the integration of the Hamiltonian over time. For the atom-field interaction Hamiltonian H_{AF}, which is time independent, the integral reduces to a multiplication by the elapsed time

$$\int_{t_0}^{t} \mathrm{d}t'\, H_{\mathrm{AF}}(t') = \Omega_R(t - t_0)\left[\sin(\varphi_{\mathrm{LO}}) S_x - \cos(\varphi_{\mathrm{LO}}) S_y\right]. \tag{2.66}$$

In contrast, the frequency fluctuations of the local oscillator vary in time and thus, we explicitly have to integrate over the frequency difference $\omega(t)$ for the Hamiltonian of the free atom

$$\int_{t_0}^{t} \mathrm{d}t'\, H_{\mathrm{A}}(t') = \left(\int_{t_0}^{t} \mathrm{d}t'\, \omega(t')\right) S_z = \omega(t-t_0) S_z, \tag{2.67}$$

where we introduced the time averaged frequency deviation

$$\omega = \frac{1}{t-t_0} \int_{t_0}^{t} \mathrm{d}t'\, \omega(t'), \tag{2.68}$$

which is consistent with the notation developed in Sec. 2.1 for the Allan deviation. By introducing the average frequency deviation ω and implicitly incorporating the averaging into the Hamiltonian, we effectively make the Hamiltonian $H_A = \omega S_z$ independent of time and the time evolution operator simplifies to $\mathcal{U}(t, t_0) = \exp(-i(t-t_0)H)$.

To investigate the action of the time evolution operator, we further rewrite the Hamiltonian as

$$H = \omega S_z + \Omega_R \left[\sin(\varphi_{\mathrm{LO}}) S_x - \cos(\varphi_{\mathrm{LO}}) S_y\right] = \Omega_{\mathrm{eff}} \mathbf{n}^T \mathbf{S} = \Omega_{\mathrm{eff}} S_{\mathbf{n}} \tag{2.69}$$

by defining an effective Rabi frequency Ω_{eff} and direction $\mathbf{n}$

$$\begin{aligned} \Omega_{\mathrm{eff}} &= \sqrt{\omega^2 + \Omega_R^2 \sin^2(\varphi_{\mathrm{LO}}) + \Omega_R^2 \cos^2(\varphi_{\mathrm{LO}})} = \sqrt{\omega^2 + \Omega_R^2} \\ \mathbf{n} &= \frac{1}{\Omega_{\mathrm{eff}}} \left(\Omega_R \sin(\varphi_{\mathrm{LO}}), -\Omega_R \cos(\varphi_{\mathrm{LO}}), \omega\right)^T . \end{aligned} \tag{2.70}$$

Furthermore, we have introduced the notation $S_{\mathbf{n}} = n_x S_x + n_y S_y + n_z S_z$, representing the projection of the spin vector $\mathbf{S}$ along a particular direction $\mathbf{n}$, $|\mathbf{n}| = 1$. As the spin $\mathbf{S}$ corresponds to the angular momentum operator of the system, it is the generator of rotations. Hence, the time evolution operator

$$\mathcal{U}(t, t_0) = \exp(-i\Omega_{\mathrm{eff}}(t-t_0) S_{\mathbf{n}}) \tag{2.71}$$

represents a rotation around axis $\mathbf{n}$ by the angle $\Omega_{\mathrm{eff}}(t-t_0)$. This type of dynamics implements the interrogation sequence invented by Rabi [70], where the population for each atom oscillates between the ground and excited states (Rabi flopping) – driven by an external field – and effectively results in the optical Bloch equations (without spontaneous decay) [106].

In more general terms, we will denote rotations around an arbitrary axis $\mathbf{n}$ by the angle θ as

$$\mathcal{R}_{\mathbf{n}}(\theta) = \exp(-i\theta S_{\mathbf{n}}), \tag{2.72}$$

a notation frequently used throughout this thesis. Exploiting properties of the Pauli matrices, we can derive an explicit expression for a single particle rotation

$$\begin{aligned} \mathcal{R}_{\mathbf{n}}^{(k)}(\theta) &= \exp\bigl(-i\theta S_{\mathbf{n}}^{(k)}\bigr) = \exp\left(-i\tfrac{\theta}{2}\mathbf{n}^T\boldsymbol{\sigma}^{(k)}\right) \\ &= \cos\left(\tfrac{\theta}{2}\right)\mathbb{1} - i\sin\left(\tfrac{\theta}{2}\right)\mathbf{n}^T\boldsymbol{\sigma}^{(k)}. \end{aligned} \tag{2.73}$$

It is interesting to note that this explicitly shows that, in contrast to classical vectors, the spin of a two level system has to be rotated by 4π instead of 2π to return to its original state. The corresponding collective rotation is given by $\mathcal{R}_{\mathbf{n}}(\theta) = \bigotimes_{k=1}^{N}\mathcal{R}_{\mathbf{n}}^{(k)}(\theta)$.

Two regimes are of particular interest throughout this thesis. In the strong driving regime $|\omega| \ll \Omega_R$, typically corresponding to pulses and transformations for state preparation and measurement, effects of the frequency detuning ω can be neglected. Therefore, the unitary time evolution can be approximated by

$$\begin{aligned} \mathcal{U}(t,t_0) &= \exp\left(-i\Omega_R(t-t_0)\left[\sin(\varphi_{\mathrm{LO}})S_x - \cos(\varphi_{\mathrm{LO}})S_y\right]\right) \\ &= \left(\cos\left(\tfrac{\Omega_R(t-t_0)}{2}\right)\mathbb{1} - i\sin\left(\tfrac{\Omega_R(t-t_0)}{2}\right)\left[\sin(\varphi_{\mathrm{LO}})\sigma_x - \cos(\varphi_{\mathrm{LO}})\sigma_y\right]\right)^{\otimes N}. \end{aligned} \tag{2.74}$$

Conversely, if no external field is applied, the system evolves freely and the time evolution is governed solely by H_A, resulting in

$$\begin{aligned} \mathcal{U}(t,t_0) &= \exp\left(-i\omega(t-t_0)S_z\right) \\ &= \left(\cos\left(\tfrac{\omega(t-t_0)}{2}\right)\mathbb{1} - i\sin\left(\tfrac{\omega(t-t_0)}{2}\right)\sigma_z\right)^{\otimes N}. \end{aligned} \tag{2.75}$$

In certain situations, it is also convenient to express the free evolution as

$$\begin{aligned} \mathcal{U}(t,t_0) &= \left(e^{-i\frac{\omega(t-t_0)}{2}}\sigma_{\mathrm{ee}} + e^{i\frac{\omega(t-t_0)}{2}}\sigma_{\mathrm{gg}}\right)^{\otimes N} \\ &= \left(e^{-i\frac{\omega(t-t_0)}{2}}\left|\uparrow\right\rangle\left\langle\uparrow\right| + e^{i\frac{\omega(t-t_0)}{2}}\left|\downarrow\right\rangle\left\langle\downarrow\right|\right)^{\otimes N}. \end{aligned} \tag{2.76}$$

For free evolution times $T = t - t_0$, the accumulated phase is given by $\phi = \omega T$. Therefore, the corresponding time evolution represents a rotation around the z-axis by an angle ϕ, denoted by $\mathcal{R}_z(\phi)$. Consequently, in the remainder of this thesis, for a unitary time evolution with duration T, we typically assume $t_0 = 0$ and $t = T$, and refer to the time evolution operator $\mathcal{U}(t,t_0) = \exp(-i\omega T S_z)$ as $\mathcal{R}_z(\phi) = \exp(-i\phi S_z)$.

2.3.3 Decoherence Processes

The unitary dynamics described in the previous section strictly applies to isolated quantum systems, evolving independently of any external influences. In reality, however, virtually all systems interact to some extent with an external environment, resulting in a non-unitary evolution. Even in a highly controlled laboratory setting, residual couplings to the surroundings, including electromagnetic fields, thermal fluctuations and material imperfections, are unavoidable. These interactions lead to decoherence, where the system gradually loses its quantum coherence due to the continuous exchange of information with its environment. The study of open quantum systems is a well-established field, extensively investigated in the literature, such as Refs. [107–112]. In this section, we introduce the fundamental concepts and tools required to model and analyze decoherence processes relevant to the framework of this thesis, building on these references.

The general approach in studying open quantum systems is to consider the system and its environment as a single closed composite system. Within this framework, the dynamics of the total system is unitary. However, in many practical scenarios, explicitly describing both subsystems together becomes unfeasible due to the vast number of degrees of freedom in the environment and the intricate nature of their interactions. Furthermore, in most cases, we are primarily interested in the dynamics of the system itself, as the evolution of the environment is either irrelevant or inaccessible. This perspective motivates a framework where the environment is eliminated, yielding an effective equation of motion for the system. This reduced approach allows to focus exclusively on the system of interest, while capturing the influence of the environment in an indirect yet effective manner.

Quantum channels— Physical processes that transform quantum states into other quantum states can be described by maps known as quantum channels. A quantum channel is a linear, completely positive, trace preserving map Λ that represents the evolution of a quantum state. Every quantum channel has a decomposition

$$\rho \mapsto \Lambda[\rho] = \sum_j K_j \rho K_j^\dagger \tag{2.77}$$

with a set of Kraus operators $\{K_j\}$ satisfying the completeness relation

$$\sum_j K_j^\dagger K_j = \mathbb{1}. \tag{2.78}$$

The unitary dynamics described in the previous section implements a quantum channel with a single Kraus operator $\mathcal{U}$.

Within the general approach of open quantum systems, the quantum channel can be interpreted as follows: Considering the combination of system S and environment E as a single closed system, described by the joint density operator ρ_{SE}, the dynamics is given by a unitary evolution $\mathcal{U}_{SE}$. The quantum channel of the system is obtained by tracing out the environment, i.e. $\Lambda[\rho] = \mathrm{Tr}_E(\mathcal{U}_{SE}\rho_{SE}\mathcal{U}_{SE}^{\dagger})$. This approach highlights how quantum channels capture the effects of environmental interactions while focusing on the reduced dynamics of the system of interest.

Master equations— Suppose two quantum systems: the system S, our primary system of interest, and its environment (often referred to as the reservoir or bath) E. For instance, S represents the atom and E corresponds to the electromagnetic field. The Hilbert spaces associated with these systems are denoted as $\mathcal{H}_S$ and $\mathcal{H}_E$, respectively. The combined system $S+E$ is then described by the joint Hilbert space $\mathcal{H}_{SE} = \mathcal{H}_S \otimes \mathcal{H}_E$. The total Hamiltonian is given by

$$H_{SE} = H_S + H_E + H_I, \tag{2.79}$$

where H_S and H_E are the Hamiltonians of the system and the environment, respectively, and H_I describes their interaction. This interaction reflects an exchange of information between S and E, leading to the emergence of decoherence and dissipation.

Since the total system evolves unitarily, its dynamics is described by the von Neumann equation

$$\partial_t \rho_{SE} = -i[H_{\mathrm{SE}}, \rho_{SE}] \tag{2.80}$$

with density operator ρ_{SE} for $S+E$. While we already derived the dynamics of the system H_S in the previous section, now we are primarily interested in the interaction H_I. Hence, we transform to an interaction picture, where the rapid dynamics generated by $H_S + H_E$ are separated from the comparatively slower dynamics induced by H_I. In the interaction picture, denoted by the explicit time dependence, the equation of motion reads $\partial_t \rho_{SE}(t) = -i[H_{\mathrm{SE}}(t), \rho_{SE}(t)]$. Integrating the von Neumann equation formally

$$\rho_{SE}(t) = \rho_{SE}(0) - i\int_0^t \mathrm{d}t' \, [H_{SE}(t'), \rho_{SE}(t')] \tag{2.81}$$

and substituting $\rho_{SE}(t)$ back into the von Neumann equation results in an integro-differential equation for the dynamics

$$\dot{\rho}_{SE}(t) = -i[H_{\mathrm{SE}}(t), \rho_{SE}(0)] - \int_0^t \mathrm{d}t' \, [H_{SE}(t), [H_{SE}(t'), \rho_{SE}(t')]]. \tag{2.82}$$

Taking the partial trace over the environment, we obtain an equation of motion for the system $\rho_S = \mathrm{Tr}_E(\rho_{SE})$ given by

$$\dot{\rho}_S(t) = -i\mathrm{Tr}_E\left([H_{\mathrm{SE}}(t), \rho_{SE}(0)]\right) - \int_0^t \mathrm{d}t' \, \mathrm{Tr}_E\left([H_{SE}(t), [H_{SE}(t'), \rho_{SE}(t')]]\right). \tag{2.83}$$

Assuming a small system and large environment as well as a weak coupling, the perturbations to the environment are small and can be neglected on the relevant time scales. If we further assume no correlations between the system and environment at $t = 0$, the environment is virtually stationary and the total state factorizes according to

$$\rho_{SE}(t) \approx \rho_S(t) \otimes \rho_E, \tag{2.84}$$

which is referred to as the Born approximation. Additionally, we will assume that the first term in Eq. (2.83) vanishes, i.e. $\mathrm{Tr}_E\left([H_{\mathrm{SE}}(t), \rho_S(0) \otimes \rho_E]\right) = 0$, which can always be arranged by a shift in the energy scale [106, 107]. Nevertheless, the equation of motion Eq. (2.83) remains complicated since the evolution of ρ_S depends on its past history through the integration over $\rho_{SE}(t') \approx \rho_S(t')\rho_E$. To address this, we apply the Markov approximation, which assumes that the system evolves slowly compared to the correlation time of the environment and thus, we can substitute $\rho_S(t')$ by $\rho_S(t)$ [106, 107], yielding

$$\dot{\rho}_S(t) = -\int_0^t \mathrm{d}t' \, \mathrm{Tr}_E\left([H_{SE}(t), [H_{SE}(t'), \rho_S(t) \otimes \rho_E]]\right). \tag{2.85}$$

If the dynamics is governed by a completely positive, trace preserving quantum channel represented by Kraus operators – as introduced above – that arises from a time evolution forming a one-parameter semigroup, then Lindblad's theorem [106–108, 110] states that it is generated by a Lindblad superoperator. This yields the master equation

$$\dot{\rho}_S = -i[H_S, \rho_S] + \sum_k \mathcal{L}_k[\rho], \tag{2.86}$$

where the Lindblad superoperators $\mathcal{L}_k[\rho]$ are defined by

$$\mathcal{L}_k[\rho] = C_k \rho_S C_k^\dagger - \frac{1}{2} C_k^\dagger C_k \rho_S - \frac{1}{2} \rho_S C_k^\dagger C_k, \tag{2.87}$$

with collapse or jump operators C_k.

In the following, we omit the index S for the system. Furthermore, in Chapter 3, we will consider three different decoherence processes, namely spontaneous decay with rate Γ and $C_k = \sqrt{\Gamma}\sigma_-^{(k)}$, individual dephasing with rate γ and $C_k = \frac{\sqrt{\gamma}}{2}\sigma_z^{(k)}$, and collective dephasing with rate γ_c and $C_k = \sqrt{\gamma_c} S_z$. Hence, the master equation for N atoms reads

$$\begin{aligned}\dot{\rho} = -i[H, \rho] &+ \Gamma \sum_{k=1}^{N} \left(\sigma_-^{(k)} \rho \sigma_+^{(k)} - \frac{1}{2} \sigma_+^{(k)} \sigma_-^{(k)} \rho - \frac{1}{2} \rho \sigma_+^{(k)} \sigma_-^{(k)} \right) \\ &+ \frac{\gamma}{4} \sum_{k=1}^{N} \left(\sigma_z^{(k)} \rho \sigma_z^{(k)} - \rho \right) + \gamma_c \left(S_z \rho S_z - \frac{1}{2} S_z^2 \rho - \frac{1}{2} \rho S_z^2 \right)\end{aligned} \tag{2.88}$$

with Hamiltonian H and where we already used that $\sigma_z^2 = \mathbb{1}$. Although Eq. (2.88) involves single particle operators, it preserves permutational symmetry as all atoms are affected identically. Moreover, no coherences between Dicke states with $S \neq S'$ are created [99], resulting in the block-diagonal form in the Dicke basis illustrated in Fig. 2.4.

Quantum trajectories and quantum jumps— The Lindblad master equation provides a comprehensive framework for describing the dynamics of open quantum systems. In particular, it captures the ensemble-average evolution of the system as it interacts with its environment. However, it inherently lacks the capability to describe and interpret individual realizations of this dynamics, where stochastic processes constitute an essential component. Such realizations, representing the evolution of single quantum systems, often exhibit discrete, probabilistic events intertwined with continuous processes. The framework of quantum trajectories and quantum jumps unravels the master equation into individual stochastic paths that represent the possible outcomes of individual evolutions of the system.

The dynamics based on a general master equation is governed by

$$\dot{\rho} = -i[H, \rho] + \left(C\rho C^\dagger - \frac{1}{2} C^\dagger C \rho - \frac{1}{2} \rho C^\dagger C \right) \tag{2.89}$$

with Hamiltonian H and collapse (jump) operator C, representing an arbitrary dissipative process (quantum jump). For simplicity, we consider a single jump operator, though this formalism readily extends to multiple noise processes. It is instructive to rewrite the master equation according to

$$\dot{\rho} = -i(H_{\text{eff}}\rho - \rho H_{\text{eff}}^\dagger) + C\rho C^\dagger \tag{2.90}$$

with

$$H_{\text{eff}} = H - \frac{i}{2} C^\dagger C. \tag{2.91}$$

The dynamics can be interpreted as a combination of a continuous and a stochastic evolution. The continuous evolution is determined by the effective Hamiltonian H_{eff} and does not imply any quantum jumps, i.e. no quanta are exchanged with the environment. Nevertheless, an effective decay is caused by the non-hermitian part of H_{eff}. In contrast, the stochastic contribution is characterized by the term $C\rho C^\dagger$ and results in sudden quantum jumps, interrupting the continuous evolution. These jumps reflect discrete events like the emission of a photon.

The formal solution of the master equation can be expressed as

$$\begin{aligned}\rho(t,t_0) &= e^{-iH_{\mathrm{eff}}(t-t_0)}\rho(t_0)e^{iH^\dagger_{\mathrm{eff}}(t-t_0)} \\ &\quad + e^{-iH_{\mathrm{eff}}(t-t_0)}\left(\int_{t_0}^{t}\mathrm{d}t'\, e^{iH_{\mathrm{eff}}(t'-t_0)}C\rho(t',t_0)C^\dagger e^{-iH^\dagger_{\mathrm{eff}}(t'-t_0)}\right)e^{iH^\dagger_{\mathrm{eff}}(t-t_0)} \\ &= \mathcal{G}(t,t_0)\rho(t_0) + \int_{t_0}^{t}\mathrm{d}t'\,\mathcal{G}(t,t')\mathcal{J}\rho(t',t_0),\end{aligned} \tag{2.92}$$

where the superoperators $\mathcal{G}(t,t_0)A = e^{-iH_{\mathrm{eff}}(t-t_0)}Ae^{iH^\dagger_{\mathrm{eff}}(t-t_0)}$ and $\mathcal{J}A = CAC^\dagger$ represent the continuous non-unitary time propagation and the quantum jump, respectively. Iteratively expanding this solution leads to a series

$$\begin{aligned}\rho(t,t_0) = \mathcal{G}(t,t_0)\rho(t_0) &+ \int_{t_0}^{t}\mathrm{d}t_1\,\mathcal{G}(t,t_1)\mathcal{J}\mathcal{G}(t_1,t_0)\rho(t_0) \\ + \int_{t_0}^{t}\mathrm{d}t_2\int_{t_0}^{t_2}&\mathrm{d}t_1\,\mathcal{G}(t,t_2)\mathcal{J}\mathcal{G}(t_2,t_1)\mathcal{J}\mathcal{G}(t_1,t_0)\rho(t_0) + \ldots\end{aligned} \tag{2.93}$$

with terms involving an increasing number of quantum jumps in the time interval $[t_0,t]$. The individual terms, characterized by the number k of quantum jumps $\mathcal{J}$, can be denoted by

$$\tilde{\rho}_k(t,t_0) = \int_{t_0}^{t}\mathrm{d}t_k\int_{t_0}^{t_k}\mathrm{d}t_{k-1}\ldots\int_{t_0}^{t_2}\mathrm{d}t_1\,\mathcal{G}(t,t_k)\mathcal{J}\mathcal{G}(t_k,t_{k-1})\mathcal{J}\ldots\mathcal{G}(t_2,t_1)\mathcal{J}\mathcal{G}(t_1,t_0)\rho(t_0) \tag{2.94}$$

which generally are not normalized. In particular, the first term $\tilde{\rho}_0(t,t_0) = \mathcal{G}(t,t_0)\rho(t_0)$ does not include a single quantum jump and thus is referred to as 'no-jump dynamics'.

In this framework, the solution of the master equation, given by

$$\rho(t,t_0) = \sum_{k=0}^{\infty} p_k(t,t_0)\rho_k(t,t_0), \tag{2.95}$$

represents a mixture of the normalized states

$$\rho_k(t,t_0) = \frac{\tilde{\rho}_k(t,t_0)}{\mathrm{Tr}(\tilde{\rho}_k(t,t_0))} = \frac{\tilde{\rho}_k(t,t_0)}{p_k(t,t_0)} \tag{2.96}$$

with probability $p_k(t,t_0) = \mathrm{Tr}(\tilde{\rho}_k(t,t_0))$ for the occurrence of k quantum jumps in the time interval $[t_0,t]$, satisfying the completeness relation $\sum_{k=0}^{\infty} p_k(t,t_0) = 1$. Consequently, in each individual evolution of the system, effectively one of the states or quantum trajectories ρ_k is realized with probability p_k.

Sampling quantum trajectories, commonly referred to as the Monte Carlo wavefunction method [113, 114], is straightforward to implement and a powerful tool for studying open quantum systems. This approach provides deep insights into the interplay between the discrete stochastic events and the continuous evolution, characterizing the dynamics of individual quantum systems interacting with its environment. Importantly, it is fully equivalent to the Lindblad master equation, as the ensemble average over many trajectories exactly reproduces the results of the master equation.

2.3.4 Measurements

In the following, we briefly present the concept of quantum measurements based on Ref. [108], establishing the conventions and notation that will be used throughout this thesis.

General measurements— In general, quantum measurements are described by a set of measurement operators $\{E_x\}$ acting on the Hilbert space $\mathcal{H}$, where x denotes the measurement outcomes. For a quantum system in state $|\psi\rangle$ or with density operator ρ, the probability of obtaining outcome x is given by

$$P(x) = \langle\psi| E_x^\dagger E_x |\psi\rangle = \mathrm{Tr}\left(\rho E_x^\dagger E_x\right). \tag{2.97}$$

This measurement results in the updated (or post-measurement) state

$$|\psi\rangle \mapsto \frac{E_x |\psi\rangle}{\sqrt{\langle\psi| E_x^\dagger E_x |\psi\rangle}} \tag{2.98}$$

$$\rho \mapsto \frac{E_x \rho E_x^\dagger}{\mathrm{Tr}\left(\rho E_x^\dagger E_x\right)}. \tag{2.99}$$

Hence, this process can be interpreted as a quantum channel that acts on the system state, where each measurement outcome is associated with a specific Kraus operator E_x. Here, the operators E_x satisfy the completeness relation

$$\sum_x E_x^\dagger E_x = \mathbb{1}, \tag{2.100}$$

ensuring normalization of the probabilities

$$\sum_x P(x) = 1. \tag{2.101}$$

Positive operator-valued measure (POVM)— In many scenarios, particularly when the final state of the system after the measurement is irrelevant, only the probabilities $P(x)$ are of interest. In this case, the positive operators

$$\Pi_x = E_x^\dagger E_x \tag{2.102}$$

with $\sum_x \Pi_x = \mathbb{1}$, yielding $P(x) = \langle\psi| \Pi_x |\psi\rangle = \mathrm{Tr}\,(\rho\Pi_x)$, are sufficient to describe the measurement probabilities. The set $\{\Pi_x\}$ is referred to as a positive operator-valued measure (POVM). This formulation captures the probability structure of measurements without requiring the specification of the post-measurement state, which is particularly useful when the focus is explicitly on the measurement statistics.

Projection-valued measure (PVM)— A special class of POVMs is represented by projective measurements, described by an observable X with spectral decomposition

$$X = \sum_x x P_x, \tag{2.103}$$

where $P_x = |x\rangle\langle x|$ are the projectors onto the eigenstates of X with eigenvalues x. The probability of measurement outcome x is given by $P(x) = \langle\psi| P_x |\psi\rangle = \mathrm{Tr}\,(\rho P_x)$. Rather than characterizing the projective measurement by its observable X, the set of projectors $\{P_x\}$ can be specified. The projectors satisfy the completeness relation $\sum_x P_x = \mathbb{1}$ and are orthogonal, i.e. $P_x P_{x'} = \delta_{xx'} P_x$. Since each projector $P_x = |x\rangle\langle x|$ can be expressed in terms of an orthonormal basis state $|x\rangle$, a PVM can be understood as a measurement in the basis $|x\rangle$. This type of measurement, described by an observable X or, equivalently, by a set of orthogonal projectors P_x, is denoted as a projection-valued measure (PVM).

Although POVMs provide the more general framework, in the remainder of this thesis typically PVMs are considered, unless explicitly stated otherwise.

2.3.5 Ramsey Interferometry

Historically, Rabi's molecular beam magnetic resonance technique [70] – nowadays commonly referred to as the Rabi method or Rabi flopping – was first proposed to realize Maxwell's vision of atomic clocks. Although it remains a valuable tool in specific experimental setups, Rabi's method exhibits inherent limitations due to its reliance on a continuous interaction between the atoms and the driving field. In particular, resolving small frequency splittings requires long interaction times, which introduce challenges such as maintaining uniform fields over large regions, avoiding apparatus constraints, and mitigating energy shifts (e.g. Stark shifts). Ramsey's method of separated oscillatory fields [71] addresses these issues by replacing the continuous interaction with two short $\pi/2$ pulses separated by a long interaction-free evolution period. This approach minimizes inhomogeneities and perturbations, resulting in narrower resonance linewidths and enhanced precision, which makes it a widely adopted technique in modern atomic clocks.

For a single atom in the absence of decoherence, the conventional Ramsey protocol comprises three steps, as illustrated in Fig. 2.7:

(i) Starting from the ground state $|{\downarrow}\rangle$, a first Ramsey pulse is performed, represented by a rotation around the negative y-axis by an angle $\Omega_R t = \pi/2$. Hence, the time evolution is given by $\mathcal{R}_y\left(-\frac{\pi}{2}\right) = \frac{1}{\sqrt{2}}\left(\mathbb{1} + i\sigma_y\right)$ and can be realized by an application of the Hamiltonian in the strong driving regime with $\varphi_{\mathrm{LO}} = 0$ (cf. Eq. (2.74)). The effective initial state

$$|\psi_0\rangle = \frac{|{\downarrow}\rangle + |{\uparrow}\rangle}{\sqrt{2}} \tag{2.104}$$

represents an equal superposition of the ground and excited states. On the Bloch sphere, $|\psi_0\rangle$ corresponds to a vector pointing in the x-direction, since $\langle\sigma_x\rangle = 1$.

(ii) During the free evolution time T, no external field is applied and the atom evolves according to Eq. (2.76). Hence, a phase $\phi = \omega T$, arising from the average frequency difference ω of the local oscillator and atomic reference, is accumulated, which is represented by a rotation around the z-axis $\mathcal{R}_z(\phi)$. The state after the free evolution time – commonly referred to as Ramsey dark time – is given by

$$|\psi_\phi\rangle = \frac{1}{\sqrt{2}}\left[e^{i\frac{\phi}{2}}|{\downarrow}\rangle + e^{-i\frac{\phi}{2}}|{\uparrow}\rangle\right] = \frac{1}{\sqrt{2}}e^{i\frac{\phi}{2}}\left[|{\downarrow}\rangle + e^{-i\phi}|{\uparrow}\rangle\right], \tag{2.105}$$

where the global phase $e^{i\frac{\phi}{2}}$ can be neglected as it is redundant and has no physical meaning. Consequently, the information on the phase ϕ, and thus the frequency difference ω, is encoded in terms of a relative phase shift between the ground and excited states.

(iii) To complete the interferometry sequence, a measurement is performed. In the conventional Ramsey protocol, this is accomplished by applying a second $\pi/2$-pulse with $\varphi_{\mathrm{LO}} = \pi/2$, corresponding to a rotation around the x-axis by an angle $\Omega_R t = \pi/2$, given by $\mathcal{R}_x\left(\frac{\pi}{2}\right) = \frac{1}{\sqrt{2}}\left(\mathbb{1} - i\sigma_x\right)$. Hence, the final state reads

$$|\psi_f\rangle = \frac{1}{2}e^{i\frac{\phi}{2}}\left[\left(1 - ie^{-i\phi}\right)|{\downarrow}\rangle + \left(e^{-i\phi} - i\right)|{\uparrow}\rangle\right]. \tag{2.106}$$

A consecutive measurement of the observable σ_z, representing the population difference of the ground and excited states, results in the signal

$$\langle\sigma_z\rangle = |\langle{\uparrow}|\psi_f\rangle|^2 - |\langle{\downarrow}|\psi_f\rangle|^2 = \sin(\phi) \tag{2.107}$$

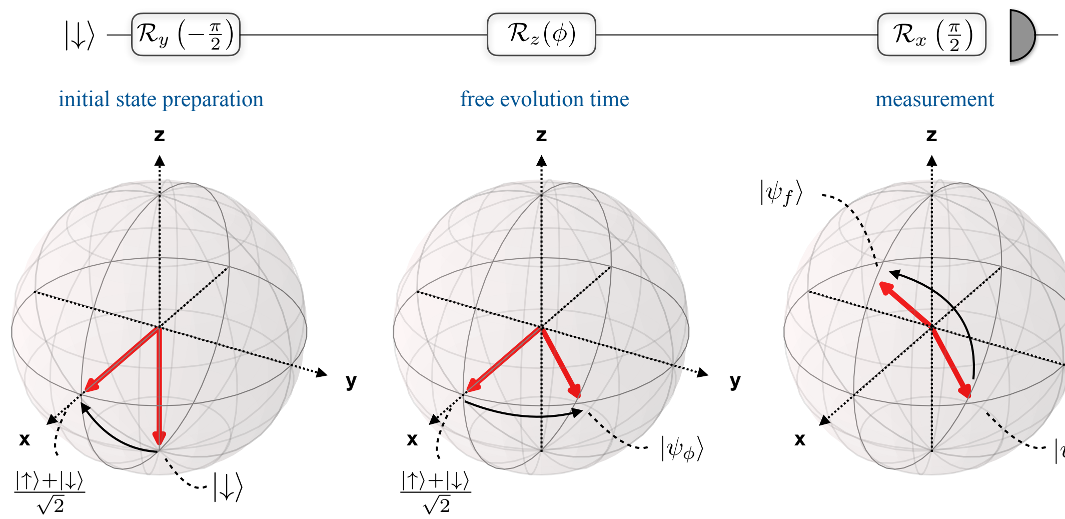
$|\downarrow\rangle$
$\mathcal{R}_y\left(-\frac{\pi}{2}\right)$
$\mathcal{R}_z(\phi)$
$\mathcal{R}_x\left(\frac{\pi}{2}\right)$
initial state preparation
free evolution time
measurement
z
x
y
$\frac{|\uparrow\rangle+|\downarrow\rangle}{\sqrt{2}}$
$|\downarrow\rangle$
z
x
y
$\frac{|\uparrow\rangle+|\downarrow\rangle}{\sqrt{2}}$
$|\psi_\phi\rangle$
z
x
y
$|\psi_f\rangle$
$|\psi_\phi\rangle$

Figure 2.7: **Conventional Ramsey interferometry:** Schematic illustration of the conventional Ramsey protocol and visualization on the Bloch sphere for a single atom.

with variance

$$(\Delta\sigma_z)^2 \equiv \left\langle \sigma_z^2 \right\rangle - \left\langle \sigma_z \right\rangle^2 = 1 - \sin^2(\phi) = \cos^2(\phi), \tag{2.108}$$

since $\sigma_k^2 = \mathbb{1}$ holds for all Pauli matrices. The corresponding excitation probabilities are given by

$$p_\uparrow(\phi) = \left|\langle\uparrow|\psi_f\rangle\right|^2 = \frac{1}{2}\left[1 + \sin(\phi)\right] \tag{2.109}$$

$$p_\downarrow(\phi) = \left|\langle\downarrow|\psi_f\rangle\right|^2 = \frac{1}{2}\left[1 - \sin(\phi)\right]. \tag{2.110}$$

Consequently, the second Ramsey pulse maps the relative phase to a population difference, making it detectable in a spin measurement.

Note that instead of applying the second $\pi/2$-pulse and measuring σ_z, equivalently a measurement of σ_y could be performed after the free evolution time (cf. App. B).

2.3.6 Quantum Projection Noise (QPN)

Atomic sensors offer numerous advantages in quantum metrology, but simultaneously impose fundamental precision limits. This limitation arises from the inherent indeterminism of quantum mechanics, which is a probabilistic rather than deterministic theory. In particular, quantum mechanics does not predict specific measurement outcomes with certainty, but instead provides probabilities for different outcomes.

To illustrate this indeterminism, we consider the measurement process of a two level system. Any pure state $|\psi\rangle = c_\downarrow |\downarrow\rangle + c_\uparrow |\uparrow\rangle$ can be expressed as a linear combination of the basis states $\{|\downarrow\rangle, |\uparrow\rangle\}$, where $c_\downarrow, c_\uparrow \in \mathbb{C}$ are normalized coefficients satisfying $|c_\downarrow|^2 + |c_\uparrow|^2 = 1$. Consequently, a measurement of the observable σ_z yields one of the two eigenvalues. The eigenvalues -1 (corresponding to $|\downarrow\rangle$) and $+1$ (corresponding to $|\uparrow\rangle$) occur with probabilities $p_\downarrow = |c_\downarrow|^2$ and $p_\uparrow = |c_\uparrow|^2$, respectively. Except in cases where either $c_\downarrow$ or $c_\uparrow$ vanishes, the outcome cannot be predicted with certainty. Hence, the measurement process is mathematically equivalent to a Bernoulli trial with binary outcomes -1 and $+1$ and does not give direct access to $p_\uparrow$ and $p_\downarrow$. Importantly, this indeterminism does not arise from imperfections in the state preparation or the measurement, but is a fundamental feature of quantum mechanics. The resulting fluctuations in measurement outcomes, known as quantum projection noise (QPN) [55], stem from the probabilistic nature of state projections onto the eigenstates of the measurement operator. The expectation (or mean) value $p_\uparrow$, which can be expressed as $p_\uparrow = \langle P_\uparrow \rangle$ with $P_\uparrow = |\uparrow\rangle\langle\uparrow|$, fluctuates with variance

$$(\Delta p_\uparrow)^2 \equiv (\Delta P_\uparrow)^2 = \left\langle P_\uparrow^2 \right\rangle - \left\langle P_\uparrow \right\rangle^2 = p_\uparrow(1 - p_\uparrow) \tag{2.111}$$

since $P_\uparrow = P_\uparrow^2$ is a projector. This variance quantifies the inherent quantum noise associated with probabilistic measurements.

Since the spin measurement on single atoms provides only a binary output, more accurate estimates can be obtained by either repeating the measurement on a single atom multiple times or using N uncorrelated and identically prepared atoms. In the latter case, it is beneficial to consider the operator $N_\uparrow = \sum_{k=1}^{N} P_\uparrow^{(k)}$, counting the number of atoms in the excited state, where $P_\uparrow^{(k)} = |\uparrow\rangle\langle\uparrow|^{(k)}$ denotes the projector onto the excited state for atom k. Assuming that the atoms are uncorrelated, the mean and variance follow directly from the single atom analysis

$$\langle N_\uparrow \rangle = N p_\uparrow \tag{2.112}$$

$$(\Delta N_\uparrow)^2 = N p_\uparrow (1 - p_\uparrow). \tag{2.113}$$

Hence, the measurement outcomes are distributed according to a binomial distribution, as depicted in Fig. 2.8(a). To estimate the probability $p_\uparrow$, an estimator $p_\uparrow^{\mathrm{est}} = x/N$ can be defined, where x denotes a particular measurement outcome of $N_\uparrow$. The expectation value $\left\langle p_\uparrow^{\mathrm{est}} \right\rangle = p_\uparrow$ coincides with the true probability and the corresponding variance reads $(\Delta p_\uparrow^{\mathrm{est}})^2 = (\Delta N_\uparrow)^2/N^2 = p_\uparrow(1 - p_\uparrow)/N$ and thus is reduced by a factor N compared to a single atom. The same result is obtained for N repeated measurements with a single atom.[2] The preceding discussion was based on the probability $p_\uparrow$, as it is an intuitive quantity and highlights the benefits of using an ensemble of N atoms. However, in this thesis we will primarily focus on spin measurements.

---

[2] Since the choice of quantization axis is arbitrary, these properties apply for spin measurements along any direction, not only restricted to S_z.

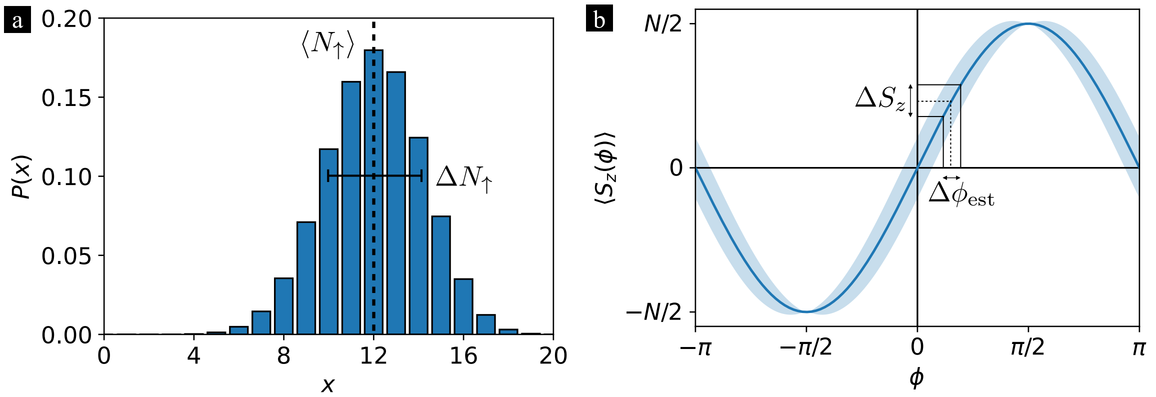

Figure 2.8: **Quantum projection noise:** (a) Binomial distribution $P(x)$ for a measurement of $N_\uparrow$, where x denotes the number of atoms detected in the excited state. For $N = 20$ and $p_\uparrow = 0.6$, the distribution is centered around the mean value $\langle N_\uparrow \rangle = 12$ with standard deviation $\Delta N_\uparrow \approx 2.19$. (b) Error propagation from the measurement signal $\langle S_z(\phi) \rangle$ to the phase estimation uncertainty $\Delta\phi_{\mathrm{est}}$.

In the context of an atomic clock, the ultimate goal of the interferometry sequence is to estimate the phase ϕ as precisely and accurately as possible, since it comprises the frequency difference ω, which we aim to correct for. Unfortunately, the parameter ϕ cannot be measured directly, but has to be encoded onto an appropriate observable. In the previous section, we have seen that in the case of Ramsey interferometry, the phase is mapped to a population difference characterized by the spin component S_z. Generalizing the single atom result to N uncorrelated atoms, the expectation value of the observable reads $\langle S_z(\phi) \rangle = \frac{N}{2} \sin(\phi)$. If $\langle S_z(\phi) \rangle$ could be obtained exactly, the phase ϕ in the interval $\left[-\frac{\pi}{2}, +\frac{\pi}{2}\right]$ would be determined by an inversion of the signal $\phi_{\mathrm{est}} = \arcsin\left(\frac{2\langle S_z(\phi)\rangle}{N}\right)$. However, the measurement outcome of S_z is a random variable and fluctuates with variance $(\Delta S_z(\phi))^2 = \frac{N}{4}\cos^2(\phi)$. Consequently, quantum projection noise causes the estimator ϕ_{est} to become a random variable as well.

In a small region around a particular phase value ϕ_0, the variance of ϕ_{est} can be derived from the mean and variance of S_z according to error propagation

$$\Delta\phi_{\mathrm{est}} = \left. \frac{\Delta S_z(\phi)}{\left|\partial_\phi \langle S_z(\phi) \rangle\right|} \right|_{\phi=\phi_0} \tag{2.114}$$

as illustrated in Fig. 2.8(b), where $\Delta S_z(\phi) \equiv \sqrt{(\Delta S_z(\phi))^2}$ denotes the standard deviation of S_z. Consequently, fluctuations of estimations of the phase ϕ are a direct consequence of quantum projection noise. The working point ϕ_0 is chosen to minimize $\Delta\phi_{\mathrm{est}}$, which typically coincides with the point of maximal slope of the signal.[3]

---

[3] While the phase dependence of the numerator and denominator in Eq. (2.114) cancels out mathematically for the conventional Ramsey protocol, any additional technical noise makes it necessary

Considering a single atom, the phase estimation uncertainty is given by $\Delta\phi_{\text{est}} = 1$, whereas N uncorrelated atoms improve the uncertainty by a factor $\sqrt{N}$ yielding $\Delta\phi_{\text{SQL}} = \Delta\phi_{\text{est}} = 1/\sqrt{N}$. This result represents the standard quantum limit (SQL) – the lower limit on the phase estimation uncertainty considering uncorrelated atoms. Since $(\Delta\phi_{\text{est}})^2$ arises from quantum projection noise of S_z, the phase estimation uncertainty is often referred to as quantum projection noise as well. A more rigorous framework for the phase estimation uncertainty and its fundamental bounds is presented in Chapter 3, providing a detailed discussion of phase estimation theory in this context.

2.3.7 Coherent Spin States (CSS)

Coherent spin states (CSS) provide a compact and elegant framework to describe states and dynamics of uncorrelated spin systems with maximal total spin $S = N/2$, which corresponds to the fully symmetric subspace. They offer an intuitive interpretation of the conventional Ramsey sequence and serve as a powerful tool for understanding collective spin dynamics. In the following, we define coherent spin states and outline a selection of their key properties. For a more comprehensive discussion, we refer to Refs. [115–117].

In the strong driving regime of atom-field interactions – effectively corresponding to short pulses – the unitary transformation represents a rotation of the form

$$R_{\theta,\varphi} = e^{-i\theta[\sin(\varphi)S_x - \cos(\varphi)S_y]} \tag{2.115}$$

with rotation angle $\theta = \Omega_R t$ and axis $\mathbf{n} = (\sin(\varphi), -\cos(\phi), 0)^T$. Coherent spin states are defined by the application of the rotation $R_{\theta,\varphi}$ to the collective ground state $\left|\frac{N}{2}, -\frac{N}{2}\right\rangle = |{\downarrow}\rangle^{\otimes N}$, i.e.

$$|\theta,\varphi\rangle = R_{\theta,\varphi}\left|\tfrac{N}{2}, -\tfrac{N}{2}\right\rangle = \bigotimes_{k=1}^{N}\left[\cos\left(\tfrac{\theta}{2}\right)|{\downarrow}\rangle^{(k)} + e^{-i\varphi}\sin\left(\tfrac{\theta}{2}\right)|{\uparrow}\rangle^{(k)}\right], \tag{2.116}$$

where $|\cdot\rangle^{(k)}$ denotes the eigenstate of σ_z of atom k. CSS are therefore product states with no correlations between the atoms, representing the N particle version of the single atom state described by Eq. (2.30). Generalizing the concept of the Bloch

---

to choose the optimal working point at $\phi_0 = 0$. This choice aligns the working point with the inflection point of the signal, thereby maximizing the sensitivity to small phase fluctuations and ensuring that these fluctuations can be accurately resolved in experimental measurements.

sphere to an ensemble of N atoms, CSS can be illustrated by the Bloch vector[4]

$$\mathbf{r}(\theta,\varphi) = \langle \mathbf{S} \rangle = \begin{pmatrix} \langle S_x \rangle \\ \langle S_y \rangle \\ \langle S_z \rangle \end{pmatrix} = \frac{N}{2} \begin{pmatrix} \sin(\theta)\cos(\varphi) \\ \sin(\theta)\sin(\varphi) \\ -\cos(\theta) \end{pmatrix} \tag{2.117}$$

on a Bloch sphere with radius $S = N/2$. Consequently, the CSS $|\theta,\varphi\rangle = \left|\frac{N}{2},\frac{N}{2}\right\rangle_{\mathbf{r}}$ is the eigenstate of $S_{\mathbf{r}}$ with maximal eigenvalue $M = +N/2$. By comparison, coherent spin states can be understood in analogy to coherent states $|\alpha\rangle$ of the harmonic oscillator, which are defined as the eigenstates of the annihilation operator a. In this analogy, the rotation $R_{\theta,\varphi}$, which generates $|\theta,\varphi\rangle$ from the collective ground state, serves as the counterpart to the displacement operator $D(\alpha)$ for coherent states of the harmonic oscillator $|\alpha\rangle = D(\alpha)\,|0\rangle$.

Properties— Beyond the mean polarization, the variances of coherent spin states are of particular interest, especially for evaluating the sensitivity of the conventional Ramsey protocol. On the one hand, the variances can be derived from a single two level system, as shown above. On the other hand, they can be inferred from the collective ground state $\left|\frac{N}{2},-\frac{N}{2}\right\rangle$, since CSS are rotated versions of this state and thus, the variances can be adopted accordingly. For the collective ground state, we evaluate

$$\begin{aligned} \left\langle S_x^2 \right\rangle &= \frac{1}{4}\left\langle \tfrac{N}{2},-\tfrac{N}{2}\right| \left(S_+^2 + S_-^2 + S_+S_- + S_-S_+\right) \left|\tfrac{N}{2},-\tfrac{N}{2}\right\rangle \\ &= \frac{1}{4}\left\langle \tfrac{N}{2},-\tfrac{N}{2}\right| S_-S_+ \left|\tfrac{N}{2},-\tfrac{N}{2}\right\rangle = \frac{N}{4} \end{aligned} \tag{2.118}$$

and similarly $\left\langle S_y^2 \right\rangle = N/4$. Hence, the variances of coherent spin states along any direction $\mathbf{k} \perp \mathbf{r}$ are given by $V_{\mathrm{CSS}} = (\Delta S_{\mathbf{k}})^2 = N/4$. As a result, CSS exhibit an isotropic quasi-probability distribution in spherical phase space, as illustrated in Fig. 2.5(b) by the Wigner function. Consequently, coherent spin states $|\theta,\varphi\rangle$ form minimum-uncertainty states with respect to the uncertainty relation

$$(\Delta S_{\mathbf{k}})^2\,(\Delta S_{\mathbf{l}})^2 \geq \frac{1}{4}\left|\langle S_{\mathbf{r}}\rangle\right|^2 \tag{2.119}$$

for all $\mathbf{k} \perp \mathbf{l}$ in the orthogonal plane to $\mathbf{r}$, i.e. $\mathbf{k} \perp \mathbf{r}$ and $\mathbf{l} \perp \mathbf{r}$.

Again, an analogy can be drawn to coherent states of the harmonic oscillator, which are minimum uncertainty states with respect to the uncertainty relation of position x and momentum p. Furthermore, coherent spin states overlap and are overcomplete as well. Coherent states of the harmonic oscillator are widely regarded as the most classical-like states in quantum mechanics because their properties closely resemble those of classical harmonic oscillations. Accordingly, coherent spin states are the most classical-like spin states, as they represent product state with no correlations between the atoms and achieve the standard quantum limit (SQL). This limit, already mentioned in the previous section and further discussed in Chapter 3, defines the lower bound for the phase estimation uncertainty $\Delta\phi_{\text{est}}$ using uncorrelated (i.e. classical) states.

---

[4] Note that the azimuthal angle θ is still measured from the negative z-axis.

Moreover, coherent spin states can be expressed as a superposition of Dicke basis states $\left|\frac{N}{2}, M\right\rangle$. The disentangling theorem [115] allows us to write the rotation $R_{\theta,\varphi}$ as

$$R_{\theta,\varphi} = e^{-i\theta(\sin(\varphi)S_x - \cos(\varphi)S_y)} = e^{\tau S_+} e^{\ln\left(1+|\tau|^2\right)S_z} e^{-\tau^* S_-} \tag{2.120}$$

with $\tau = e^{-i\varphi}\tan\left(\frac{\theta}{2}\right)$. The term $e^{-\tau^* S_-}$ has no effect on the collective ground state, i.e. $e^{-\tau^* S_-}\left|\frac{N}{2}, -\frac{N}{2}\right\rangle = \left|\frac{N}{2}, -\frac{N}{2}\right\rangle$, since $S_-\left|\frac{N}{2}, -\frac{N}{2}\right\rangle = 0$. Application of the eigenvalue equation yields $e^{\ln\left(1+|\tau|^2\right)S_z}\left|\frac{N}{2}, -\frac{N}{2}\right\rangle = e^{-\frac{N}{2}\ln\left(1+|\tau|^2\right)}\left|\frac{N}{2}, -\frac{N}{2}\right\rangle = (1+|\tau|^2)^{-N/2}\left|\frac{N}{2}, -\frac{N}{2}\right\rangle$. Using Eq. (2.42) to compute $e^{\tau S_+}\left|\frac{N}{2}, -\frac{N}{2}\right\rangle$, coherent spin states can be written as

$$\begin{aligned} |\theta,\varphi\rangle =& R_{\theta,\varphi}\left|\tfrac{N}{2}, -\tfrac{N}{2}\right\rangle = \sum_{M=-S}^{S} \binom{2S}{S+M}^{1/2} \frac{\tau^{S+M}}{\left(1+|\tau|^2\right)^S}\left|\tfrac{N}{2}, M\right\rangle \\ =& \sum_{M=-\frac{N}{2}}^{\frac{N}{2}} \binom{N}{\frac{N}{2}+M}^{1/2} \sin^{\frac{N}{2}+M}\left(\tfrac{\theta}{2}\right)\cos^{\frac{N}{2}-M}\left(\tfrac{\theta}{2}\right) e^{-i\left(\frac{N}{2}+M\right)\varphi}\left|\tfrac{N}{2}, M\right\rangle . \end{aligned} \tag{2.121}$$

Another convenient property of coherent spin states emerges when calculating expectation values of spin components. The anti-normally ordered characteristic function (with respect to the set of spin operators $\{S_-, S_z, S_+\}$) is defined by [115]

$$\begin{aligned} X_A(\theta,\varphi) &= \langle\theta,\varphi| e^{\gamma S_-} e^{\beta S_z} e^{\alpha S_+} |\theta,\varphi\rangle \\ &= \left[e^{-\beta/2}\cos^2\left(\tfrac{\theta}{2}\right) + e^{\beta/2}\left(\sin\left(\tfrac{\theta}{2}\right)e^{-i\varphi} + \alpha\cos\left(\tfrac{\theta}{2}\right)\right)\left(\sin\left(\tfrac{\theta}{2}\right)e^{i\varphi} + \gamma\cos\left(\tfrac{\theta}{2}\right)\right)\right]^N . \end{aligned} \tag{2.122}$$

Consequently, expectation values of combinations of spin operators and their exponentials with respect to coherent spin states can be calculated according to

$$\langle\theta,\varphi| S_-^c e^{\tilde{\gamma}S_-} S_z^b e^{\tilde{\beta}S_z} S_+^a e^{\tilde{\alpha}S_+} |\theta,\varphi\rangle = \partial_\alpha^a \partial_\beta^b \partial_\gamma^c X_A(\theta,\varphi)\Big|_{\alpha=\tilde{\alpha},\beta=\tilde{\beta},\gamma=\tilde{\gamma}} \tag{2.123}$$

where $a, b, c \in \mathbb{N}$ and $\tilde{\alpha}, \tilde{\beta}, \tilde{\gamma} \in \mathbb{C}$ are arbitrary coefficients.

Conventional Ramsey protocol— The discussion of N uncorrelated atoms can, in principle, be directly inferred from the results of a single atom, as each atom is independent and subject to identical transformations and measurements. However, studying conventional Ramsey interferometry using coherent spin states and collective rotations provides an intuitive interpretation of the conventional Ramsey protocol and prepares for potential extensions.

Starting with the collective ground state $\left|\frac{N}{2},-\frac{N}{2}\right\rangle = \left|\downarrow\right\rangle^{\otimes N}$, the first Ramsey pulse is implemented by a rotation around the negative y-axis by an angle $\Omega_R t = \pi/2$. Within the framework of coherent spin states, this corresponds to the rotation $\mathcal{R}_{\theta=\pi/2,\varphi=0} = \mathcal{R}_y(-\pi/2) = e^{i\pi S_y/2}$. Therefore, the initial state $|\psi_0\rangle$ is given by

$$\begin{aligned} |\psi_0\rangle = |\theta=\pi/2,\varphi=0\rangle &= \mathcal{R}_{\theta=\pi/2,\varphi=0}\left|\tfrac{N}{2},-\tfrac{N}{2}\right\rangle_z \\ &= \left[\frac{1}{\sqrt{2}}\left(|\downarrow\rangle + |\uparrow\rangle\right)\right]^{\otimes N} = \left|\tfrac{N}{2},\tfrac{N}{2}\right\rangle_x, \end{aligned} \tag{2.124}$$

which corresponds to a coherent spin state with mean spin polarization $\mathbf{r} = \mathbf{e}_x$. During the free evolution time, the phase is imprinted by a collective rotation $\mathcal{R}_z(\phi)$ around the z-axis. In principle, the initial state $|\psi_0\rangle$ can be expressed in terms of Dicke states according to Eq. (2.121) and thus, the action of $\mathcal{R}_z(\phi)$ becomes trivial. However, it is conceptually instructive to interpret the free evolution time as a transformation of the observable, rather than of the initial state. This approach aligns with the Heisenberg picture, as discussed in Sec. 2.3.2. Likewise, the second Ramsey pulse $\mathcal{R}_x(\pi/2)$ can be assigned to the observable S_z. Following this approach, we effectively measure the operator

$$S_z(\phi) = \mathcal{R}_z^\dagger(\phi)\mathcal{R}_x^\dagger\left(\tfrac{\pi}{2}\right) S_z \mathcal{R}_x\left(\tfrac{\pi}{2}\right)\mathcal{R}_z(\phi). \tag{2.125}$$

Applying the rotation properties derived in App. B, the observable transforms according to $\mathcal{R}_x^\dagger(\pi/2)S_z\mathcal{R}_x(\pi/2) = S_y$ and $\mathcal{R}_z^\dagger(\phi)S_y\mathcal{R}_z(\phi) = \cos(\phi)S_y + \sin(\phi)S_x$. Thus, the first and second moments of the observable are given by

$$\langle S_z(\phi)\rangle = \cos(\phi)\langle S_y\rangle + \sin(\phi)\langle S_x\rangle \tag{2.126}$$

$$\left\langle S_z^2(\phi)\right\rangle = \cos^2(\phi)\left\langle S_y^2\right\rangle + \sin(\phi)\cos(\phi)\langle S_xS_y + S_yS_x\rangle + \sin^2(\phi)\left\langle S_x^2\right\rangle. \tag{2.127}$$

Evaluating these expectation values with respect to the initial state $\left|\frac{N}{2},\frac{N}{2}\right\rangle_x$ using the properties of coherent spin states results in

$$\langle S_z(\phi)\rangle = \frac{N}{2}\sin(\phi) \tag{2.128}$$

$$\left\langle S_z^2(\phi)\right\rangle = \frac{N}{4}\cos^2(\phi) + \frac{N^2}{4}\sin^2(\phi). \tag{2.129}$$

With variance $(\Delta S_z(\phi)) = \frac{N}{4}\cos^2(\phi)$, the phase estimation uncertainty reads $\Delta\phi_{\text{est}} = 1/\sqrt{N}$, as already derived before. This calculation demonstrates the utility of coherent spin states combined with collective rotations and spin measurements. In particular, the expectation values of the observable can be traced back to fundamental properties of coherent spin states.

It is worth noting that the first Ramsey pulse could also be assigned to the observable, allowing the expectation values to be evaluated with respect to the collective ground state. However, presenting both approaches provides pedagogical value by offering a broader perspective. Furthermore, separating the initial state preparation from the free evolution and measurement will be advantageous for the analysis of generalized Ramsey protocols (cf. Chapter 3 and Chapter 4).

2.3.8 GHZ States

As demonstrated in the previous sections, coherent spin states saturate the standard quantum limit (SQL), achieving a phase estimation uncertainty $\Delta\phi_{\text{SQL}} = 1/\sqrt{N}$. To further enhance sensitivity and reduce the estimation error, it is necessary to employ entangled states. As a brief reminder, entanglement emerges when quantum correlations between particles prevent the state from being expressed as a product of individual particle states. More precisely, a pure state $|\psi\rangle \in \mathcal{H} = \bigotimes_k \mathcal{H}^{(k)}$ is separable if it can be factorized into single-particle states $\left|\psi^{(k)}\right\rangle \in \mathcal{H}^{(k)}$, such that

$$|\psi_{\text{sep}}\rangle = \bigotimes_{k=1}^{N} \left|\psi^{(k)}\right\rangle = \left|\psi^{(1)}\right\rangle \otimes \left|\psi^{(2)}\right\rangle \otimes \ldots \otimes \left|\psi^{(N)}\right\rangle . \tag{2.130}$$

Similarly, a mixed state is separable if it can be written as a mixture of separable pure states [118]

$$\rho_{\text{sep}} = \sum_k p_k \, |\psi_{\text{sep},k}\rangle\langle\psi_{\text{sep},k}| \, , \tag{2.131}$$

where $p_k \geq 0$ and $\sum_k p_k = 1$. States that cannot be decomposed in this way are classified as entangled [119, 120].

In Chapter 3, we will demonstrate that by employing entangled states, the ultimate lower bound for the phase estimation uncertainty in the absence of decoherence is given by the Heisenberg limit (HL) $\Delta\phi_{\text{HL}} = 1/N$, resulting in an improvement by a factor of $\sqrt{N}$ compared to the SQL. The HL can be saturated using the maximally entangled Greenberger-Horne-Zeilinger (GHZ) states [121]

$$|\text{GHZ}\rangle = \frac{1}{\sqrt{2}}\left[|{\downarrow}\rangle^{\otimes N} + |{\uparrow}\rangle^{\otimes N}\right] = \frac{1}{\sqrt{2}}\left[\left|\tfrac{N}{2}, -\tfrac{N}{2}\right\rangle + \left|\tfrac{N}{2}, \tfrac{N}{2}\right\rangle\right] , \tag{2.132}$$

representing an equal superposition of the collective ground and excited states, as illustrated in Fig. 2.5(c). The corresponding Ramsey sequence, initially proposed by Wineland et al. in Ref. [122], is denoted as the standard GHZ or 'parity-GHZ' protocol. During the free evolution time, the accumulated phase is amplified by a factor of N due to the maximal entanglement in the GHZ state. The evolved state reads

$$|\psi_\phi\rangle = \mathcal{R}_z(\phi)\,|\mathrm{GHZ}\rangle = \frac{1}{\sqrt{2}}\left[e^{i\frac{N\phi}{2}}\,|{\downarrow}\rangle^{\otimes N} + e^{-i\frac{N\phi}{2}}\,|{\uparrow}\rangle^{\otimes N}\right]. \tag{2.133}$$

The second Ramsey pulse, represented by a rotation $\mathcal{R}_y(\pi/2)$ around the y-axis by an angle $\pi/2$, results in the final state

$$|\psi_f\rangle = \mathcal{R}_y\left(\tfrac{\pi}{2}\right)|\psi_\phi\rangle = \frac{1}{\sqrt{2}^{N+1}}\left[e^{i\frac{N\phi}{2}}(|{\downarrow}\rangle - |{\uparrow}\rangle)^{\otimes N} + e^{-i\frac{N\phi}{2}}(|{\uparrow}\rangle + |{\downarrow}\rangle)^{\otimes N}\right], \tag{2.134}$$

where we used $\mathcal{R}_y^{(k)}(\pi/2) = \frac{1}{\sqrt{2}}(\mathbb{1}^{(k)} - \sigma_+^{(k)} + \sigma_-^{(k)})$ according to Eq. (2.73). Finally, the parity operator $\sigma_z^{\otimes N}$ is measured. Its eigenvalues are $(-1)^{\frac{N}{2}-M} = (-1)^{N_-}$, where N_- denotes the number of atoms in the ground state. Consequently, the parity has a binary outcome ±1, quantifying if there is an even $(+1)$ or odd (-1) number of atoms in the ground state. The expectation value of the observable is given by

$$\left\langle\sigma_z^{\otimes N}\right\rangle = \langle\psi_f|\,\sigma_z^{\otimes N}\,|\psi_f\rangle = (-1)^N\cos(N\phi). \tag{2.135}$$

Unlike the conventional Ramsey protocol, the GHZ protocol yields a symmetric signal with respect to the origin. Alternatively, as for the conventional Ramsey protocol, the second Ramsey pulse can be absorbed in the measurement. Hence, by employing Eq. (2.73) once again, the effective observable

$$\Pi = \mathcal{R}_y^\dagger(\pi/2)\sigma_z^{\otimes N}\mathcal{R}_y(\pi/2) = (-1)^N\sigma_x^{\otimes N} \tag{2.136}$$

can be defined. Π is also commonly denoted as parity measurement and has expectation value $\langle\Pi(\phi)\rangle = (-1)^N\cos(N\phi)$. With $\sigma_k^2 = \mathbb{1}$ for all Pauli matrices, the second moment simply reads $\langle\Pi^2(\phi)\rangle = 1$. Thus, the variance is given by

$$(\Delta\Pi(\phi))^2 = 1 - \cos^2(N\phi) = \sin^2(N\phi). \tag{2.137}$$

Finally, with the slope of the signal $\partial_\phi\langle\Pi(\phi)\rangle = (-1)^{N+1}N\sin(N\phi)$, the phase estimation uncertainty becomes

$$\Delta\phi_{\mathrm{est}} = \left.\frac{\Delta\Pi(\phi)}{|\partial_\phi\langle\Pi(\phi)\rangle|}\right|_{\phi=\phi_0} = \frac{1}{N} \tag{2.138}$$

and thus saturates the HL.[5] The enhanced sensitivity of the GHZ protocol, in comparison to the conventional Ramsey protocol, can be understood from two different perspectives: (i) In the context of N identically prepared single atoms, as discussed in Sec. 2.3.6, the variance is reduced by a factor N using uncorrelated atoms. In contrast, the variance is independent of N for the GHZ protocol due to the binary nature of the parity measurement. At the same time, the N fold increased accumulated phase in the GHZ protocol directly leads to an N times steeper slope of the signal and thus, results in a gain of $\sqrt{N}$ in the phase estimation uncertainty $\Delta\phi_{\text{est}}$ compared to the SQL. (ii) Considering the collective description using coherent spin states (CSS), as discussed in Sec. 2.3.7, the slope of the signal for both protocols scales linearly with N. For the GHZ protocol, this originates from the N fold increased accumulated phase, while it naturally arises from the collective behavior of N uncorrelated atoms for the CSS. However, the binary outcomes of the measurement in the GHZ protocol ensures that the variance remains independent of N, unlike for CSS, where it scales linearly with N. Hence, the GHZ protocol achieves the HL, whereas the conventional Ramsey protocol remains limited by the SQL.

Intuitively, the GHZ protocol can be interpreted as an artificial single atom with an effective transition frequency amplified by a factor N, leading to an enhanced phase accumulation. However, this advantage comes with a significant trade-off. The binary nature of the parity measurement and the increased oscillation frequency of the Ramsey fringes make the protocol extremely susceptible to decoherence and phase noise originating from frequency fluctuations, as will be discussed in Chapter 3 and Chapter 4, respectively.

2.3.9 Spin-Squeezed States (SSS)

A promising approach to surpass the SQL is represented by spin squeezing. Spin-squeezed states (SSS) form a subclass of entangled states characterized by a reduced (squeezed) variance along one axis of the collective spin compared to coherent spin states – at the cost of an increased (anti-squeezed) variance along an orthogonal axis. These states have been extensively studied theoretically and implemented in various experimental setups, establishing them as a cornerstone of modern quantum metrology. [6, 12, 58, 59, 123, 124]

In this section, we introduce squeezing parameters to define and identify SSS. To emphasize their relevance in quantum metrology and, in particular, their role in improving the performance of optical atomic clocks, we relate the phase estimation uncertainty to the squeezing parameter. Finally, we explore the generation of SSS through one-axis twisting (OAT) [125], a paradigmatic model allowing comprehensive theoretical insights and experimental implementation in various setups [62, 126–133].

---

[5] Here, the phase dependence cancels again. By the same arguments as for the conventional Ramsey protocol, the optimal working point should be chosen at $\phi_0 = \frac{\pi}{2N}$. Alternatively, an additional rotation $\mathcal{R}_z(-\frac{\pi}{2N})$ can be applied directly before or after the free evolution time to shift the optimal working point to $\phi_0 = 0$.

Spin Squeezing Parameters— In analogy to squeezed states of the harmonic oscillator [105], an intuitive definition of spin squeezing arises from the spin uncertainty relation Eq. (2.119). In this context, a natural criterion for spin squeezing is given by $(\Delta S_{\mathbf{k}})^2 < |\langle S_{\mathbf{l}} \rangle|/2$ for orthogonal directions **k** and **l**, with corresponding squeezing parameter defined as [123, 134–136]

$$\xi_n = \frac{\Delta S_{\mathbf{k}}}{\sqrt{|\langle S_{\mathbf{l}} \rangle|/2}}. \tag{2.139}$$

Spin squeezing occurs if $\xi_n < 1$. However, this parameter depends on the choice of the coordinate system and thus can yield $\xi_n < 1$ even for coherent spin states [58, 59, 125]. Consequently, ξ_n does not adequately capture quantum correlations between the atoms. Additionally, squeezing in spin systems is inherently more complex than in the harmonic oscillator due to the fundamentally different commutation relations.

Addressing these issues, Kitagawa and Ueda [125] proposed that a spin state is regarded as squeezed if the variance of a spin component $S_\perp$, orthogonal to the mean spin vector $\mathbf{r} = \langle \mathbf{S} \rangle$, is smaller than the variance of a coherent spin state, since they are minimum uncertainty states and most classical-like states. With the variance of a CSS $V_{\mathrm{CSS}} = (\Delta S_\perp)^2_{\mathrm{CSS}} = N/4$, the condition for spin squeezing becomes $(\Delta S_\perp)^2_{\mathrm{min}} < \frac{N}{4}$, leading to the spin squeezing parameter

$$\xi_S^2 = \frac{4(\Delta S_\perp)^2_{\mathrm{min}}}{N}, \tag{2.140}$$

where $(\Delta S_\perp)_{\mathrm{min}}$ denotes the minimum variance of a spin component orthogonal to **r**.

However, squeezing of the variance in a particular direction does not necessarily indicate an enhanced sensitivity, as reflected by the trade-off between variance and polarization of the estimation error in Eq. (2.114). To account for this trade-off, Wineland et al. [58, 59] defined a spin squeezing parameter tailored to quantum metrology in the context of Ramsey interferometry

$$\xi^2 = N\frac{(\Delta S_{\mathbf{m}})^2}{\langle S_{\mathbf{r}} \rangle^2}, \tag{2.141}$$

where the measurement direction **m** is orthogonal to both the mean spin vector **r** and the free evolution rotation axis **n**. A value $\xi^2 < 1$ indicates spin squeezing useful for Ramsey interferometry. States satisfying $\xi^2 < 1$ exhibit reduced variance $(\Delta S_{\mathbf{m}})^2$, while preserving the uncertainty relation Eq. (2.119) through an increased variance $(\Delta S_{\mathbf{n}})^2$. Notably, $\xi^2 < 1$ implies $\xi_S^2 < 1$, since $\langle S_{\mathbf{r}} \rangle \leq N/2$, but the converse does not hold. Moreover, $\xi^2 < 1$ is a sufficient condition for entanglement [130]. For a Ramsey protocol where $\mathbf{r}, \mathbf{n}, \mathbf{m}$ are mutually orthogonal, the squeezing parameter ξ^2 is related to quantum projection noise, described in Eq. (2.114), by

$$(\Delta\phi_{\text{est}})^2 = \frac{\xi^2}{N}. \tag{2.142}$$

In the conventional Ramsey protocol, with $\mathbf{r} = \mathbf{e}_x$, $\mathbf{n} = \mathbf{e}_z$, and $\mathbf{m} = \mathbf{e}_y$, the SQL is recovered. A fundamental lower limit for ξ^2 can be derived from the uncertainty relation. From Eq. (2.119), $(\Delta S_{\mathbf{m}})^2 \geq \langle S_{\mathbf{r}} \rangle^2 / 4(\Delta S_{\mathbf{n}})^2$ and with $(\Delta S_{\mathbf{n}})^2 \leq N^2/4$, this yields

$$\xi^2 \geq \frac{1}{N}, \tag{2.143}$$

which reflects the Heisenberg limit.

It is important to note that not all entangled states are spin squeezed, as SSS merely form a subset of non-separable states. Alternative squeezing parameters and their applications are discussed in Refs. [137, 138]. While numerous methods for generating SSS have been proposed (see Refs. [6, 124, 138] for examples), this work focuses on SSS generated through one-axis-twisting (OAT) interactions.

One-Axis-Twisting (OAT)— In the previous sections, we have seen that Hamiltonians linear in the spin operators lead to collective rotations, resulting in the notion of coherent spin states. Hence, non-linear interactions are required to generate entanglement among the atoms. The simplest non-linear interaction is represented by one-axis-twisting (OAT), discussed in detail by Kitagawa and Ueda in Ref. [125]. One-axis-twisting interactions receive much attention, since they give enhanced sensitivity by generating spin-squeezed states or echo protocols and can be reliably implemented in several experimental setups [5, 62, 126–133, 139–143]. Below, we outline the fundamental concept of OAT and discuss its metrologically relevant properties.

The one-axis-twisting Hamiltonian is quadratic in S_z and reads

$$H = \chi S_z^2 \tag{2.144}$$

where χ is the interaction strength. The corresponding dynamics is governed by the unitary operator

$$\mathcal{T}_z(\mu) = \exp\left(-i\tfrac{\mu}{2} S_z^2\right) \tag{2.145}$$

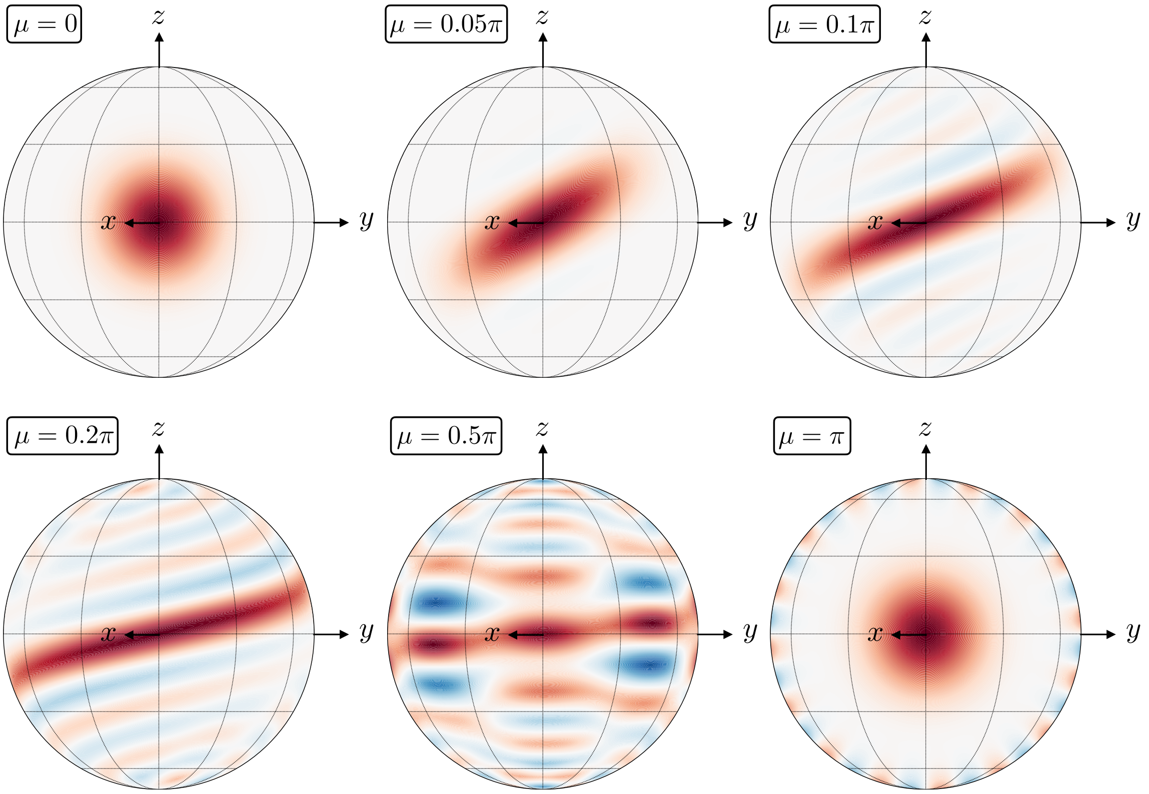

Figure 2.9: **One-axis-twisting interaction:** Bloch sphere visualization of the one-axis-twisting (OAT) interaction acting on the coherent spin state (CSS) polarized along the x-direction, illustrated by the Wigner function for $N = 16$. The quasi-probability distribution is presented for several squeezing strengths μ, ranging from a CSS ($\mu = 0$) via spin-squeezed states (SSS) to a rotated GHZ state ($\mu = \pi$), as discussed in the main text.

with squeezing strength $\mu = 2\chi t$. This dynamics generates a variety of entangled states. For small squeezing strengths μ, one-axis-twisting results in spin-squeezed states by shearing the initial CSS $\left|\frac{N}{2}, \frac{N}{2}\right\rangle_x$ around the z-axis, as illustrated in Fig. 2.9. As μ increases, the regime of spin-squeezed states is surpassed, indicated by the Wigner function bending around the Bloch sphere, and strongly entangled states are generated. In particular, rotated versions of the GHZ state are created for the maximal twisting strength $\mu = \pi$. For $\mu > \pi$, the dynamics reverses. Explicit evaluations of the properties of SSS generated by OAT are provided in Ref. [125].

As already observed in Fig. 2.9, the minimal spin variance for states generated via one-axis-twisting (OAT) lies in the y-z-plane. To enable a direct comparison with the conventional Ramsey protocol, the spin-squeezed states can be rotated by an angle θ around the x-axis. The resulting state $|\psi_0\rangle = \mathcal{R}_x(\theta)\mathcal{T}_z(\mu)\left|\frac{N}{2}, \frac{N}{2}\right\rangle_x$ exhibits a squeezed variance V_- aligned along the y-direction, while the variance along the z-axis

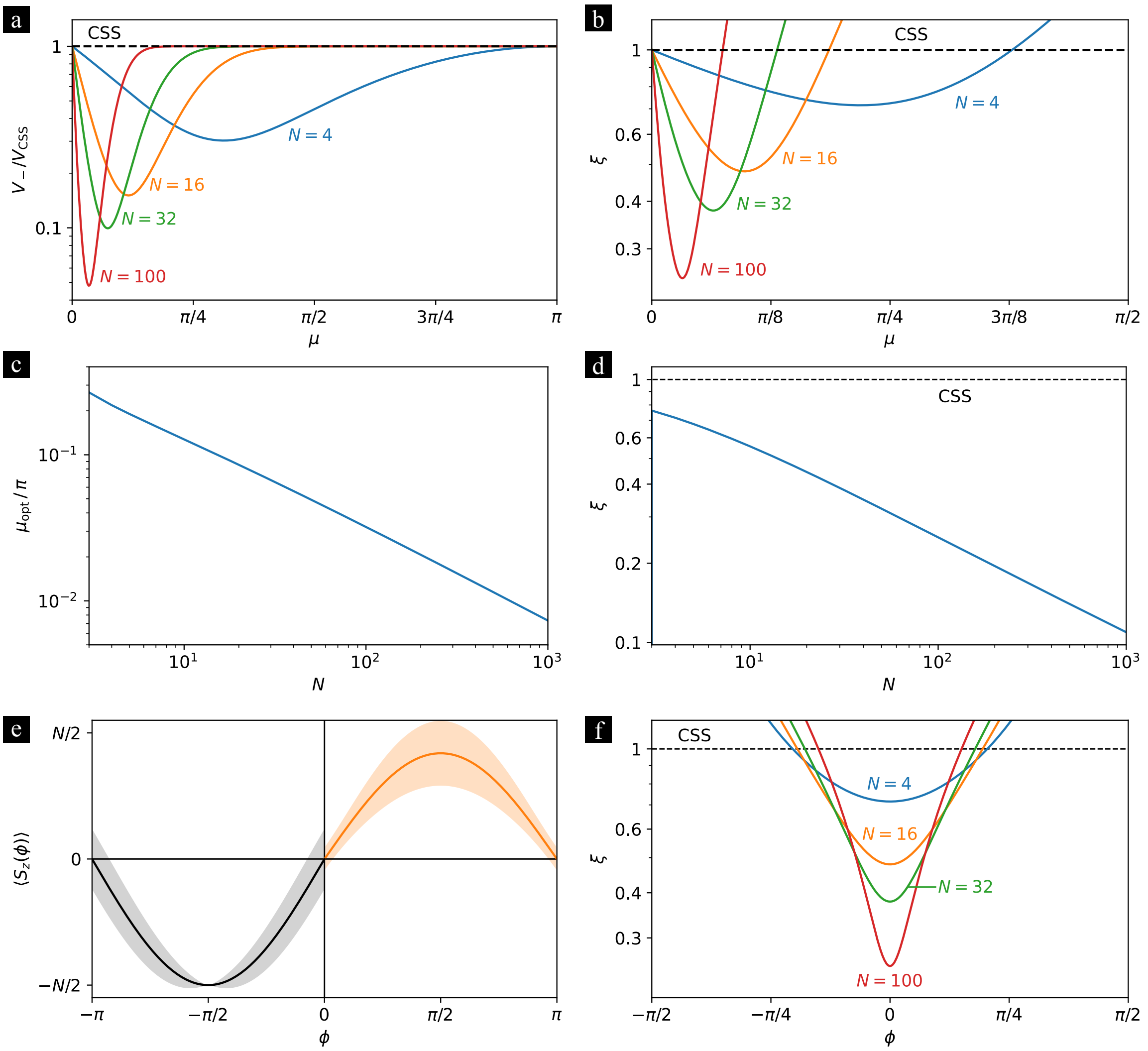

Figure 2.10: **Spin-squeezed states:** (a) Comparison of the squeezed variance V_- to the coherent spin state variance $V_{\rm CSS} = N/4$ for various N, showing $V_- \leq V_{\rm CSS}$ for all squeezing strengths μ. (b) Squeezing parameter ξ as a function of the squeezing strength μ for several N. Metrological spin squeezing is obtained only for small μ due to the trade-off between squeezed variance and reduced contrast. (c) Optimal squeezing strength $\mu_{\rm opt}$ that minimizes the squeezing parameter ξ, plotted against the ensemble size N. (d) Corresponding optimal squeezing parameter ξ. (e) Measurement signals $\langle S_z(\phi)\rangle$ for a coherent spin state (black) and an optimally spin squeezed state (orange) for $N = 16$. The shaded areas represent the corresponding standard deviations $\Delta S_z(\phi)$. (f) Dependence of the squeezing parameter ξ on the accumulated phase ϕ for optimally spin squeezed states. The sensitivity is enhanced in the vicinity of $\phi_0 = 0$ compared to CSS, but this region diminishes with increasing ensemble size.

is anti-squeezed with variance V_+. Explicit calculations yield the variances [125]

$$V_\pm = \frac{N}{4}\left\{1 + \frac{1}{4}(N-1)\left[A \pm \sqrt{A^2+B^2}\right]\right\}, \tag{2.146}$$

where $A = 1 - \cos^{N-2}(\mu)$ and $B = 4\sin\left(\frac{\mu}{2}\right)\cos^{N-2}(\frac{\mu}{2})$. The squeezed variance V_- is depicted in Fig. 2.10(a) for various ensemble sizes N, demonstrating that $V_- \leq V_{\text{CSS}} = N/4$ for all squeezing strengths $\mu > 0$. However, as pointed out before, the sensitivity to accumulated phases in Ramsey interferometry depends not only on the variance V_- but also on the contrast of the signal, which is given by [125]

$$\langle S_x \rangle = \frac{N}{2}\cos^{N-1}\left(\frac{\mu}{2}\right). \tag{2.147}$$

This contrast decreases with increasing μ, which becomes more pronounced for larger ensembles. The squeezing parameter is given by [125]

$$\xi^2 = N\frac{V_-}{\langle S_x \rangle^2} = \frac{\left\{1 + \frac{1}{4}(N-1)\left[A - \sqrt{A^2 + B^2}\right]\right\}}{\cos^{2N-2}\left(\frac{\mu}{2}\right)}. \tag{2.148}$$

Metrological spin squeezing, characterized by $\xi < 1$, is achieved only for small μ due to the trade-off between reduced variance and decreasing contrast, as illustrated in Fig. 2.10(b). In this regime, the phase estimation uncertainty $\Delta\phi_{\text{est}} = \xi/\sqrt{N} < 1/\sqrt{N}$ is reduced compared to CSS, yielding a sensitivity below the SQL. One-axis-twisted states are spin squeezed for $\mu \lesssim 4/\sqrt{N}$ [125, 139], with optimal sensitivities achieved for squeezing strengths that scale with the ensemble size N according to $\mu_{\text{opt}} \sim N^{-3/5}$, as illustrated in Fig. 2.10(c). The corresponding sensitivities – characterized by the squeezing parameter ξ – scale as $\xi \sim N^{-1/3}$, as schown in Fig. 2.10(d).

In atomic clocks, frequency fluctuations require a high sensitivity not only at the optimal working point ($\phi_0 = 0$), but also in its vicinity. The measurement signal for an optimally squeezed state compared to a CSS is shown in Fig. 2.10(e), where shaded areas represent the corresponding variance. For spin-squeezed states, the variance is significantly reduced close to the optimal working point ϕ_0, providing enhanced sensitivity. However, the region offering this enhancement diminishes as the atom number N increases. This behavior is further illustrated in Fig. 2.10(f), where the squeezing parameter ξ is plotted as a function of the accumulated phase ϕ. While stronger squeezing reduces the phase variance around ϕ_0, it simultaneously narrows the region where this enhanced sensitivity is maintained. This imposes additional constraints on the squeezing strength μ for the application in atomic clocks. In particular, for long interrogation times, a broad dynamic range is essential for stable clock operation, as we will discuss in detail in Chapter 4. Consequently, spin-squeezed states generated by one-axis-twisting enhance the sensitivity compared to coherent spin states at the cost of reduced dynamic range.

2.4 Feedback and Servo

After characterizing the two primary components in an atomic clock – the local oscillator (LO) and the atomic reference – this section describes the servo mechanism, which implements a feedback loop to correct the LO frequency based on the Ramsey interrogation. We begin by reviewing the basic clock operation, as presented in Sec. 1.2, by considering a single clock cycle and introducing the relevant frequency notation. As before, we assume identical clock cycles with total duration $T_C = T_D + T$, comprising a potential dead time T_D and the Ramsey dark time T.

In each clock cycle, the atomic reference is interrogated according to a specific Ramsey sequence for duration T. The frequency of the LO at the end of the interrogation time in cycle k, prior to the measurement, is denoted by $\omega_{\mathrm{LO},k}$. This frequency reflects stabilization in preceding cycles ($j < k$), but still incorporates the intrinsic (new) noise introduced during the current cycle k. Consequently, $\omega_{\mathrm{LO},k}$ gives rise to the phase shift ϕ_k accumulated by the atomic ensemble, as dicussed in Sec. 2.3. Therefore, this frequency is of primary interest for the interrogation of the atomic reference and we refer to $\omega_{\mathrm{LO},k}$ as the LO frequency throughout this thesis when considering individual clock cycles. At the end of the Ramsey sequence, ϕ_k is estimated as $\phi_{\mathrm{est},k}$ based on the measurement outcome (cf. Sec. 2.3). Accordingly, an estimation of the frequency $\omega_{\mathrm{LO},k}$ is obtained via $\omega_{\mathrm{est},k} = \phi_{\mathrm{est},k}/T$. Finally, to complete the feedback loop, the servo applies a correction $\omega_{\mathrm{corr},k}$ based on the estimate $\omega_{\mathrm{est},k}$.[6] The resulting stabilized clock frequency is given by

$$\omega_{\mathrm{clock},k} = \omega_{\mathrm{LO},k} - \omega_{\mathrm{corr},k}. \tag{2.149}$$

In an experiment, the LO frequency is dynamically adapted during clock operation as described above. However, to employ the methods presented in Ref. [92] and to establish the notation required to describe the Monte Carlo simulations (cf. App. A and Ref. [3]), we extend the model in the following. In particular, we aim to relate the clock frequency to the free-running local oscillator. Although the free-running LO frequency is not directly accessible in practice due to continuous stabilization, this perspective provides a comprehensive understanding of the control loop and, in particular, the feedback strategy.

The free-running LO generates a time-dependent frequency $\omega_{\mathrm{LO}}^{\mathrm{free}}(t)$, with fluctuations entirely determined by the intrinsic noise characteristics of the LO, as detailed in Sec. 2.2. In cycle k, the average free-running LO frequency is given by

---

[6] To be precise, only the frequency fluctuations of the LO during the Ramsey interrogation time T are monitored and therefore can be estimated and corrected, while dead time leads to undetected aliased frequency deviations, as we discuss further in Chapter 4.

$$\omega_{\mathrm{LO},k}^{\mathrm{free}} = \frac{1}{T_C} \int_{(k-1)T_C}^{kT_C} \mathrm{d}t' \omega_{\mathrm{LO}}^{\mathrm{free}}(t'). \tag{2.150}$$

Consequently, the LO frequency $\omega_{\mathrm{LO},k}$ can be expressed as

$$\omega_{\mathrm{LO},k} = \omega_{\mathrm{clock},k-1} + (\omega_{\mathrm{LO},k}^{\mathrm{free}} - \omega_{\mathrm{LO},k-1}^{\mathrm{free}}) = \omega_{\mathrm{clock},k-1} + \omega_{\mathrm{LO},k}^{\mathrm{new}}, \tag{2.151}$$

where we have introduced the new noise of the k-th cycle $\omega_{\mathrm{LO},k}^{\mathrm{new}} = \omega_{\mathrm{LO},k}^{\mathrm{free}} - \omega_{\mathrm{LO},k-1}^{\mathrm{free}}$.

To express the stabilized clock frequency $\omega_{\mathrm{clock},k}$ in terms of the free-running LO frequency $\omega_{\mathrm{LO},k}^{\mathrm{free}}$, we define the total (or cumulative) correction

$$\omega_{\mathrm{corr},k}^{\mathrm{tot}} = \sum_{j=1}^{k} \omega_{\mathrm{corr},j}, \tag{2.152}$$

which additionally accounts for all past frequency corrections in clock cycles $j < k$. Accordingly, $\omega_{\mathrm{corr},k}^{\mathrm{tot}}$ represents the total correction that would hypothetically be required to correct the free-running LO up to the k-th cycle. Hence, the clock frequency $\omega_{\mathrm{clock},k}$ can be expressed as

$$\omega_{\mathrm{clock},k} = \omega_{\mathrm{LO},k}^{\mathrm{free}} - \omega_{\mathrm{corr},k}^{\mathrm{tot}}. \tag{2.153}$$

Similarly, the LO frequency $\omega_{\mathrm{LO},k}$ can be rewritten as

$$\omega_{\mathrm{LO},k} = \omega_{\mathrm{LO},k}^{\mathrm{free}} - \omega_{\mathrm{corr},k-1}^{\mathrm{tot}}. \tag{2.154}$$

Finally, we define an effective prediction for the free-running LO frequency in the current clock cycle – prior to the correction – as

$$\omega_{\mathrm{pred},k} = \omega_{\mathrm{corr},k-1}^{\mathrm{tot}} + \omega_{\mathrm{est},k}, \tag{2.155}$$

which is determined by the total correction of the previous clock cycle $\omega_{\mathrm{corr},k-1}^{\mathrm{tot}}$ and the current frequency estimation $\omega_{\mathrm{est},k}$ of the LO frequency $\omega_{\mathrm{LO},k}$.

Ultimately, the stabilization of the local oscillator to the atomic reference requires a specific choice of the servo corrections $\omega_{\mathrm{corr},k}$, or equivalently the total corrections $\omega_{\mathrm{corr},k}^{\mathrm{tot}}$. From a theoretical perspective, optimal feedback is achieved by adjusting the correction to precisely match the estimated frequency, i.e. $\omega_{\mathrm{corr},k} = \omega_{\mathrm{est},k}$ or $\omega_{\mathrm{corr},k}^{\mathrm{tot}} = \omega_{\mathrm{pred},k}$, as this approach maximizes the use of the available information. However, practical clock operation has demonstrated that a weaker feedback is often advantageous, as it provides more robust clock performance against various disturbances and imperfections [11, 12, 91, 92, 144]. In the remainder of this section, we present two particular feedback strategies following Ref. [92].

2.4.1 Double-Integrating Servo

Since the exact correction with $\omega_{\text{est},k}$ is unfavorable, as argued above, a natural generalization is represented by a simple integrator, with feedback corrections given by [11, 91, 92, 144]

$$\omega_{\text{corr},k} = g \cdot \omega_{\text{est},k}, \tag{2.156}$$

where the dimensionless gain factor $0 < g < 1$ determines the strength of the feedback. Accordingly, the total correction reads

$$\omega_{\text{corr},k}^{\text{tot}} = \omega_{\text{corr},k-1}^{\text{tot}} + \omega_{\text{corr},k} = \omega_{\text{corr},k-1}^{\text{tot}} + g\omega_{\text{est},k} = g\sum_{j=1}^{k} \omega_{\text{est},j}. \tag{2.157}$$

In terms of the predictions $\omega_{\text{pred},k}$ of the free-running LO frequency, defined in Eq. (2.155), this can be expressed as

$$\begin{aligned} \omega_{\text{corr},k}^{\text{tot}} &= \omega_{\text{corr},k-1}^{\text{tot}} + g\omega_{\text{est},k} \\ &= \omega_{\text{corr},k-1}^{\text{tot}} + g\left(\omega_{\text{pred},k} - \omega_{\text{corr},k-1}^{\text{tot}}\right) \\ &= g\omega_{\text{pred},k} + (1-g)\omega_{\text{corr},k-1}^{\text{tot}}. \end{aligned} \tag{2.158}$$

Recursively substituting this expression for $\omega_{\text{corr},k-1}^{\text{tot}}$, we obtain

$$\begin{aligned} \omega_{\text{corr},k}^{\text{tot}} &= g\omega_{\text{pred},k} + (1-g)\omega_{\text{corr},k-1}^{\text{tot}} \\ &= g\omega_{\text{pred},k} + g(1-g)\omega_{\text{pred},k-1} + (1-g)^2\omega_{\text{corr},k-2}^{\text{tot}} \\ &= \dots \\ &= \sum_{j=1} g(1-g)^{k-j}\omega_{\text{pred},j}. \end{aligned} \tag{2.159}$$

Typically, the gain factor g is chosen heuristically, depending on the specific experimental setup [91, 92, 144]. Relevant parameters include the noise profile of the LO, quantum projection noise (QPN), interrogation time and dead time. Alternatively, g may be determined via the optimization method for general linear integrators presented in the next section or by the approximate analytical expression provided for known noise models in the appendix of Ref. [92].

For some local oscillators exhibiting strongly correlated noise processes, such as slow frequency drifts or random walk frequency noise, a single integrator is insufficient to achieve reliable stabilization of the LO. In these cases, a second integrator incorporating averages on longer time scales has to be implemented [11, 92, 144]. For the double integrator, the feedback corrections are given by

$$\omega_{\text{corr},k} = g\omega_{\text{est},k} + g_{\text{dr}}\sum_{i=1}^{k} \omega_{\text{est},j}, \tag{2.160}$$

or equivalently

$$\omega_{\text{corr},k}^{\text{tot}} = \omega_{\text{corr},k-1}^{\text{tot}} + \omega_{\text{corr},k} = \omega_{\text{corr},k-1}^{\text{tot}} + g\omega_{\text{est},k} + g_{\text{dr}} \sum_{i=1}^{k} \omega_{\text{est},j}, \tag{2.161}$$

where g_{dr} denotes the secondary gain factor associated with the slow integrator. To avoid undesired servo oscillations, it is essential to ensure that $g_{\text{dr}} \ll g$ [92]. The additional term effectively aims to predict and compensate for potential long-term drifts in the LO frequency.

2.4.2 General Linear Integrator

A more general strategy is provided by the broader class of linear integrators, discussed in detail by Leroux in Ref. [92] and briefly outlined below. In this framework, the total correction represents a weighted linear combination of all past frequency estimations

$$\omega_{\text{corr},k}^{\text{tot}} = \sum_{j=1}^{k} \tilde{w}_j \cdot \omega_{\text{est},j}, \tag{2.162}$$

with coefficients $\tilde{w}_j$. In particular, the simple integrator discussed in the previous section emerges as a special case with uniform weights $\tilde{w}_j = g$.

To apply the optimization method presented in Ref. [92] and to align the theoretical description with the implementation of the Monte Carlo simulations (cf. App. A and Ref. [3]), we adapt the notation as follows. We define the total correction in terms of the predictions of the free-running LO according to

$$\omega_{\text{corr},k}^{\text{tot}} = \sum_{j=1}^{k} w_j \cdot \omega_{\text{pred},j}, \tag{2.163}$$

where we additionally require the weights w_j to satisfy the normalization condition $\sum_j w_j = 1$. Comparison to Eq. (2.159) shows that the simple integrator of the previous section is realized in the special case $w_j = g(1-g)^{k-j}$.[7]

The optimization of such general linear integrators has been extensively investigated in the literature, such as in Ref. [145], building on fundamental studies of Wiener [146] and Kolmogorov [147]. For the servo corrections as defined in Eq. (2.163), the optimal weights are explicitly derived in Ref. [92].

Due to the large number of clock cycles in realistic clock operation, it is unfeasible to incorporate all preceding estimates or predictions to calculate the subsequent correction. Therefore, typically only the last n_{w} estimates are used. For example, in the numerical simulations presented throughout this thesis, we take the most recent $n_\mathrm{w} = 50$ estimates into account. While the optimal weights, in principle, need to be computed for each individual clock cycle, they can be evaluated once in advance if the frequency fluctuations of the local oscillator are stationary and sufficiently well characterized. Specifically, the optimal weights depend on the LO noise, quantum projection noise, interrogation duration and dead time. Leveraging prior knowledge of the system, Ref. [92] provides an explicit evaluation of these optimal weights in this context. Moreover, this method can also be used to determine an appropriate gain for the simple integrator by identifying $g = w_{n_w}$, where w_{n_w} denotes the weight associated with the most recent estimation or prediction [92].

---

[7] Note, however, that this choice does not satisfy the normalization condition.

As before, a second integrator has to be added to address strongly correlated noise processes

$$\omega_{\mathrm{corr},k}^{\mathrm{tot}} = \sum_{j=1}^{k} w_j \cdot \omega_{\mathrm{pred},j} + g_\mathrm{dr} \sum_{i=1}^{k} \omega_{\mathrm{est},j}. \tag{2.164}$$

If the condition $g_\mathrm{dr} \ll \max_j w_j$ is ensured, the contribution of the additional integrator can be neglected in the optimization of the weights [92].

3

Frequency metrology limited by spontaneous decay

3.1 Motivation and research problem

Current efforts to further improve the stability of optical clocks involve exploring the use of entanglement in atomic systems to reduce quantum projection noise (QPN) and overcome the standard quantum limit (SQL) imposed by uncorrelated atoms [6,12,13]. Unfortunately, decoherence presents a substantial obstacle in frequency metrology, impairing the precision of measurements by compromising the coherence of quantum systems essential for achieving entanglement-based enhancement [65–67, 148–150]. In particular, Huelga et al. have demonstrated that GHZ protocols, which are optimal in the absence of decoherence, suffer significantly from individual dephasing associated with random phase changes, ultimately showing no improvement over the SQL [149]. To address this susceptibility of entanglement-enhanced protocols, various noise sources have been taken into account to determine optimal interrogation sequences [5, 91, 98, 139–142, 148, 149, 151]. Unlike magnetic field fluctuations or laser noise, the finite lifetime of qubits in the excited state represents a fundamental limit rather than an external noise source. Nevertheless, in contrast to the extensive treatment of dephasing and frequency fluctuations, the effects of spontaneous decay have received comparatively little attention.

State-of-the-art clock lasers achieve coherence times of several seconds [88], entering the regime of the excited-state lifetime of various clock candidates, such as In^+-ions (0.2 s), Sr^+-ions (0.4 s), Ca^+-ions (1.1 s) and Hg-atoms (1.6 s). With further technological improvements in the short-term laser stabilization, coherence times will potentially approach lifetimes of further clock species as Yb-atoms (15.9 s) or Al^+-ions (20.7 s). Consequently, it is highly relevant to investigate the impact of spontaneous decay for the development of future clocks and identify optimal interrogation schemes for specific setups. This aspect becomes particularly important when employing strongly entangled states, which are generally more susceptible to decoherence.

Spontaneous decay arises from the inherent instability of excited atomic states when interacting with the quantum fluctuations of the electromagnetic field, even in a vacuum [107,152,153]. This process manifests as probabilistic transitions to a lower energy state, releasing the energy difference by emitting a photon. In spin systems, or equivalently two level systems, this results in discrete quantum jumps from the excited to the ground state. Spontaneous decay is fundamentally explained within the framework of quantum electrodynamics (QED) and can be rigorously described by Wigner-Weisskopf theory [154]. For a comprehensive derivation of spontaneous decay in this context, we refer to the literature such as Refs. [106,153–155].

Additionally, we consider individual dephasing, as this process has been the predominant focus in studies of decoherence effects throughout the literature. Individual dephasing in spin systems is typically associated with random fluctuations in the local environment, affecting each spin independently. Such environmental noise can originate from a variety of sources, including stray magnetic fields, spatially varying laser noise, atomic collisions or fluctuations in trap properties. These effects induce random phase shifts, for instance by causing instantaneous variations in the energy levels of each spin and, consequently, in their precession frequencies. As a result, different spins accumulate distinct quantum phases over time, leading to a gradual loss of coherence within the ensemble, without affecting the populations. [6,56,108,149,156]

Furthermore, we explore the effect of collective dephasing on the Ramsey protocols investigated in this chapter. Collective dephasing occurs when all spins in an ensemble experience correlated phase fluctuations due to a common noise source, such as laser phase noise or fluctuations in a global magnetic field. In this scenario, the dephasing acts uniformly across the ensemble, leading to a simultaneous loss of coherence that critically undermines collective quantum correlations. [12,56,157–159]

To start with, we introduce the fundamental principles of atomic clocks and Ramsey interferometry, establishing the connection between frequency metrology and phase estimation theory. To set the theoretical foundation for this chapter, we outline the framework of local frequency metrology and examine lower bounds on the sensitivity in the first sections. The primary results of this chapter are discussed in Sec. 3.7. Here, we present a protocol with quantum operations of low complexity and a highly nonlinear estimator that saturates the quantum Cramér-Rao bound (QCRB) of the GHZ state. Surprisingly, and in contrast to dephasing, we find that GHZ states provide a substantial enhancement compared to the SQL in the presence of spontaneous decay. Moreover, we compare the sensitivity of this protocol to the ultimate lower limit and to spin-squeezed states (SSS), which are optimal in the asymptotic limit of large particle numbers. In addition, we present a variation of this protocol with a GHZ-like initial state, which achieves the ultimate lower limit for ensembles with several tens of atoms and outperforms SSS for up to 80 atoms. To demonstrate the robustness of the measurement and estimation scheme, we perform comprehensive Monte-Carlo simulations of the full feedback loop in an atomic clock. Finally, in Sec. 3.8 we examine the crossover between regimes dominated by spontaneous decay and dephasing.

To implement the low complexity protocols, we employ single one-axis-twisting (OAT) [125] operations for both state preparation and as an effective measurement, since they give rise to a variety of entangled states, ranging from spin-squeezed states (SSS) to the GHZ state, as well as variational classes of generalized Ramsey spectroscopy saturating the ultimate limit in sensitivity [5, 139–143]. Furthermore, OAT interactions are accessible in several setups as in ion traps via Mølmer-Sørensen gates [126–128], in tweezer arrays via Rydberg interactions [62, 129] or Bose-Einstein condensates via elastic collisions [130–133].

3.2 Atomic clocks and Ramsey interferometry

In atomic clocks (cf. Fig. 3.1(a)), a local oscillator (LO) generates an inherently noisy frequency signal $\omega_{\mathrm{LO}}(t)$ that varies over time t. The LO is stabilized to an atomic transition frequency ω_0 through repeated interrogations of the atomic ensemble according to a specific Ramsey interferometry scheme. Throughout this thesis we focus on single-ensemble clocks in which the atomic reference is periodically interrogated using the same protocol in each clock cycle. During the Ramsey time T, the atoms accumulate a phase $\phi = \omega T$, which effectively reflects the average of the frequency deviation over the interrogation period

$$\omega = \frac{1}{T}\int_t^{t+T} \mathrm{d}t'[\omega_0 - \omega_{\mathrm{LO}}(t')]. \tag{3.1}$$

At the end of each interrogation sequence, a measurement with outcome x is performed, from which an estimate $\phi_{\mathrm{est}}(x)$ of the monitored phase ϕ is inferred. The control cycle is completed by the servo that applies feedback to correct the LO frequency by ω_{corr} based on the phase estimate $\phi_{\mathrm{est}}(x)$, resulting in a stabilized LO signal. Consequently, frequency metrology is directly connected to phase estimation theory.

In interferometry, the objective is to estimate an unknown parameter ϕ as precise and accurate as possible. In generalized Ramsey spectroscopy (cf. Fig. 3.1(b)), the phase ϕ is encoded onto the initial probe state ρ_{in} during the free evolution time T (Ramsey dark time) via a completely-positive trace-preserving map $\Lambda_{\phi,T}$. Additionally, this quantum channel $\Lambda_{\phi,T}$ may also account for decoherence processes such as

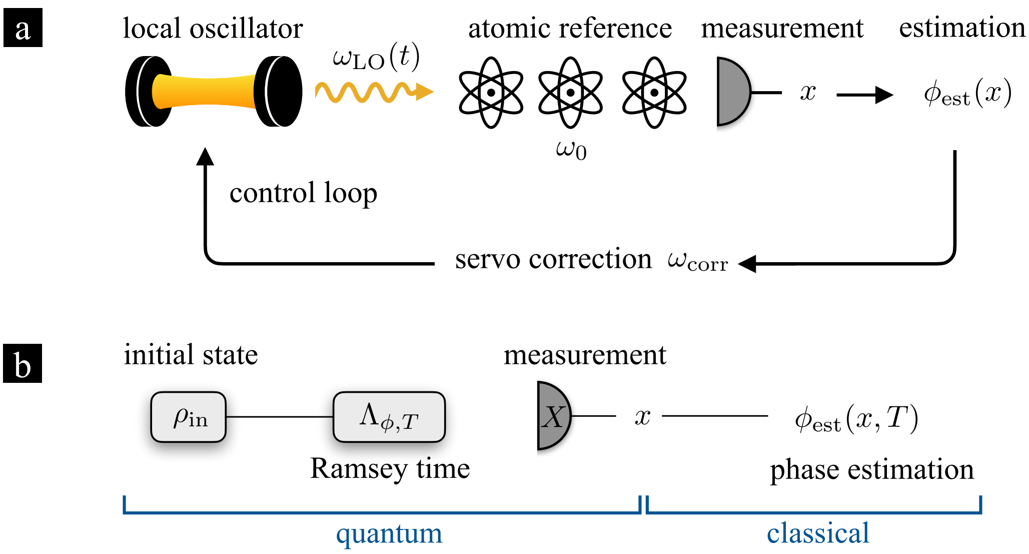
a
local oscillator
$\omega_{\mathrm{LO}}(t)$
atomic reference
ω_0
measurement
x
estimation
$\phi_{\mathrm{est}}(x)$
control loop
servo correction ω_{corr}
b
initial state
ρ_{in}
$\Lambda_{\phi,T}$
Ramsey time
measurement
X
x
$\phi_{\mathrm{est}}(x,T)$
phase estimation
quantum
classical

Figure 3.1: **Atomic clock and Ramsey interferometry:** (a) Basic principle of an atomic clock: A local oscillator (LO) with fluctuating frequency $\omega_{\mathrm{LO}}(t)$ is stabilized in a control loop to an atomic transition ω_0. During the free evolution time T, the probe state accumulates a phase ϕ arising from the frequency deviation. Based on the measurement outcome x, the phase is estimated by ϕ_{est} and the LO frequency is corrected according to ω_{corr} by the servo. (b) Generalized Ramsey interferometry: The phase ϕ is encoded during the interrogation time T onto the initial state ρ_{in} via $\Lambda_{\phi,T}$. Based on the measurement outcome x of the observable X, an estimation ϕ_{est} of the phase is conducted.

dephasing or spontaneous decay, with their impact depending on T. Unfortunately, the phase itself is not an observable and therefore, cannot be measured directly. Consequently, after the free evolution, an appropriately chosen observable X is measured. The measurement is described by a positive operator-valued measure (POVM) $\{\Pi_x\}$, with $\Pi_x \geq 0$ and $\sum_x \Pi_x = \mathbb{1}$, where x denotes the measurement outcome. Due to the inherent indeterministic nature of quantum measurements, the outcomes x are random and occur with conditional probability

$$P(x|\phi) = \mathrm{Tr}\left(\Pi_x \Lambda_{\phi,T}[\rho_{\mathrm{in}}]\right), \tag{3.2}$$

also referred to as the likelihood or statistical model. Finally, based on the measurement outcome x (of X), an estimation $\phi_{\mathrm{est}}(x)$ of the parameter ϕ is performed. Note that since the quantum channel depends on the interrogation time T, the conditional probabilities $P(x|\phi)$ and the estimator $\phi_{\mathrm{est}}(x)$ generally likewise depend on T. Unlike state preparation, free evolution, and measurement, which are governed by quantum mechanics, the estimation process involves classical post-processing of measurement data and is thus addressed within the framework of classical phase estimation theory.

While the free evolution $\Lambda_{\phi,T}$ is determined by the experimental setup, the estimation strategy $\phi_{\mathrm{est}}(x)$, the measurement $\{\Pi_x\}$, and the initial state ρ_{in} can be chosen arbitrarily.[1] Consequently, generalized Ramsey interferometry offers three control parameters that can be adjusted to optimally determine the phase ϕ. Naturally, some choices are better than others. In general, effective choices exhibit a high sensitivity to changes in ϕ. This raises fundamental questions: How can we characterize the sensitivity to changes in the phase? What distinguishes good choices from bad ones? How precise can we ultimately become? To address these questions, we introduce a cost function that precisely quantifies the sensitivity to changes in the phase. We further derive bounds on this sensitivity and investigate various interrogation schemes designed to achieve these limits.

Although we explore frequency metrology in the context of atomic clocks, we emphasize that the majority of the results and techniques are broadly applicable to a wide range of scenarios within the field.

3.3 Dynamics

Considering a unitary phase evolution with Hamiltonian $H = \omega S_z$, spontaneous decay with rate Γ, individual dephasing with rate γ and collective dephasing with rate γ_c, the dynamics of the system during the free evolution time T, represented by the quantum channel $\Lambda_{\phi,T}$, is described by a master equation of the form (cf. Sec. 2.3.3)

$$\dot{\rho} = -i\omega\,[S_z, \rho] + \frac{\Gamma}{2}\sum_{k=1}^{N} \mathcal{L}_{S_-^{(k)}}[\rho] + \frac{\gamma}{2}\sum_{k=1}^{N} \mathcal{L}_{S_z^{(k)}}[\rho] + \frac{\gamma_c}{2}\mathcal{L}_{S_z}[\rho], \tag{3.3}$$

where $S_-^{(k)} = \sigma_-^{(k)}$, $S_z^{(k)} = \frac{1}{2}\sigma_z^{(k)}$ and $S_z = \sum_k S_z^{(k)}$, with single particle Pauli operators σ_j. The Lindblad superoperators are defined as $\mathcal{L}_A[\rho] := 2A\rho A^\dagger - A^\dagger A\rho - \rho A^\dagger A$.

---

[1] In principle, a specific experimental setup typically imposes constraints on the available transformations for initial state preparation and measurement. However, to allow for a general investigation, we assume that arbitrary states and measurements can be realized.

Explicitly expanding Eq. (3.3), the master equation is expressed as

$$\begin{aligned}\dot{\rho} &= -i\omega[S_z,\rho] + \frac{\Gamma}{2}\sum_{k=1}^{N}\left(2\sigma_-^{(k)}\rho\sigma_+^{(k)} - \sigma_+^{(k)}\sigma_-^{(k)}\rho - \rho\sigma_+^{(k)}\sigma_-^{(k)}\right) \\ &\quad + \frac{\gamma}{8}\sum_{k=1}^{N}\left(2\sigma_z^{(k)}\rho\sigma_z^{(k)} - \left(\sigma_z^{(k)}\right)^2\rho + \rho\left(\sigma_z^{(k)}\right)^2\right) + \frac{\gamma_c}{2}\left(2S_z\rho S_z - S_z^2\rho - \rho S_z^2\right) \\ &= -i\omega[S_z,\rho] + \frac{\Gamma}{2}\sum_{k=1}^{N}\left(2\sigma_-^{(k)}\rho\sigma_+^{(k)} - \sigma_{\mathrm{ee}}^{(k)}\rho - \rho\sigma_{\mathrm{ee}}^{(k)}\right) \\ &\quad - \frac{\gamma}{2}\sum_{k=1}^{N}\left(\sigma_{\mathrm{ee}}^{(k)}\rho\sigma_{\mathrm{gg}}^{(k)} + \sigma_{\mathrm{gg}}^{(k)}\rho\sigma_{\mathrm{ee}}^{(k)}\right) + \frac{\gamma_c}{2}\left(2S_z\rho S_z - S_z^2\rho - \rho S_z^2\right),\end{aligned} \tag{3.4}$$

where we used $\sigma_z^2 = \mathbb{1}$ and $\sigma_+\sigma_- = \sigma_{\mathrm{ee}}$. Furthermore, since $\sigma_z = \sigma_{\mathrm{ee}} - \sigma_{\mathrm{gg}}$ and $\mathbb{1} = \sigma_{\mathrm{ee}} + \sigma_{\mathrm{gg}}$, we obtained $\sigma_z\rho\sigma_z - \rho = -2\sigma_{\mathrm{ee}}\rho\sigma_{\mathrm{gg}} - 2\sigma_{\mathrm{gg}}\rho\sigma_{\mathrm{ee}}$. Here, $\sigma_{\mathrm{gg}} = |\downarrow\rangle\langle\downarrow|$ and $\sigma_{\mathrm{ee}} = |\uparrow\rangle\langle\uparrow|$ represent the projectors onto the ground and excited states, respectively. Starting with an initial state ρ_{in}, the state after evolution for duration T according to Eq. (3.4) is denoted as $\rho_{\mathrm{in}}(\phi,T) = \Lambda_{\phi,T}[\rho_{\mathrm{in}}]$, with phase $\phi = \omega T$ arising from the average frequency deviation ω defined in Eq. (3.1). In general, solving master equations with multiple distinct terms, such as Eq. (3.4), is a complex and intricate task. However, since all four terms of the master equation (super-)commute pairwise (cf. App. C), the dynamics associated with each component can be solved independently, thereby significantly simplifying the problem.

In particular, it is convenient to treat the unitary part and the decoherence processes separately. The first term of Eq. (3.4) effectively describes the unitary phase evolution, which is determined by the von Neumann equation

$$\frac{\mathrm{d}\rho}{\mathrm{d}\phi} = -i[S_z,\rho]. \tag{3.5}$$

The corresponding solution is represented by a collective rotation $\mathcal{R}_z(\phi) = \exp(-i\phi S_z)$ by an angle ϕ around the z-axis and is given by

$$\rho_{\mathrm{in}}(\phi) = \Lambda_\phi[\rho_{\mathrm{in}}] = \Lambda_{\phi,T=0}[\rho_{\mathrm{in}}] = \mathcal{R}_z(\phi)\rho_{\mathrm{in}}\mathcal{R}_z^\dagger(\phi), \tag{3.6}$$

where Λ_ϕ denotes the quantum channel associated with Eq. (3.5). Although the quantum channel Λ_ϕ (and likewise $\Lambda_{\phi,T}$) is 2π-periodic with respect to the phase, i.e. $\Lambda_\phi = \Lambda_{\phi+2\pi}$, phases $\phi + 2\pi k$ (with $k \in \mathbb{Z}$) originate from a different frequency deviation ω than ϕ, and thus have a distinct physical interpretation, especially in the context of frequency metrology, where the primary objective is to determine the frequency deviation ω.

Identifying the first term in Eq. (3.4) as the phase imprint, the effective time evolution associated with the decoherence processes is governed by the master equation

$$\begin{aligned}\dot{\rho} = &\frac{\Gamma}{2}\sum_{k=1}^{N}\left(2\sigma_{-}^{(k)}\rho\sigma_{+}^{(k)} - \sigma_{\mathrm{ee}}^{(k)}\rho - \rho\sigma_{\mathrm{ee}}^{(k)}\right) \\ &+ \frac{\gamma}{4}\sum_{k=1}^{N}\left(\sigma_{z}^{(k)}\rho\sigma_{z}^{(k)} - \rho\right) + \frac{\gamma_c}{2}\left(2S_z\rho S_z - S_z^2\rho - \rho S_z^2\right).\end{aligned} \tag{3.7}$$

The formal solution is given by $\rho_{\mathrm{in}}(T) = \Lambda_T[\rho_{\mathrm{in}}] = \Lambda_{\phi=0,T}[\rho_{\mathrm{in}}]$, where Λ_T denotes the quantum channel associated with Eq. (3.7). Explicit solutions for the individual terms are provided in App. C. In general, all three decoherence processes cause the coherences to gradually diminish over time. Additionally, in the presence of spontaneous decay, the populations of the excited state progressively decay to the ground state.

In this chapter, we primarily focus on spontaneous decay and additionally consider individual dephasing, as the impact of decoherence processes has typically been investigated using the example of individual dephasing (cf. Sec. 3.1). In contrast, we address collective dephasing only in Sec. 3.8, where we discuss the crossover between regimes with distinct dominant decoherence processes.

3.4 Local frequency metrology

In the local (frequentist) approach to frequency metrology, additional assumptions are taken into account. Specifically, probabilities, such as the conditional probabilities $P(x|\phi)$, are defined as the infinite sample limit of an event. Furthermore, the frequency is regarded as a fixed, though unknown, variable. In contexts where the frequency fluctuates – such as in atomic clocks – this assumption is generally not valid. However, in local frequency metrology it is assumed that the frequency fluctuations are not the dominant noise source. This assumption is reasonable when the frequency fluctuations are comparatively small, and the primary limitations arise from spontaneous decay or dephasing. Therefore, we assume that the frequency of the local oscillator $\omega_{\mathrm{LO}}(t)$ is tightly centered around the atomic resonance frequency ω_0 and thus, the spread $\delta\omega$ of the average frequency deviations ω, as defined in Eq. (3.1), around $\omega = 0$ is sufficiently small, ensuring $\delta\omega \cdot T \ll 1$. The regime beyond this assumption – where laser noise imposes the dominant limitation and frequency fluctuations introduce estimation ambiguities – is discussed in detail in Chapter. 4.

3.4.1 Local phase estimation

As motivated in Sec. 3.2, phase estimation theory constitutes an essential component of frequency metrology. Accordingly, the assumptions inherent in local frequency metrology also apply to local (frequentist) phase estimation theory. In particular, perfect resonance $\omega = 0$ corresponds to $\phi = 0$, resulting in no phase accumulation during the Ramsey time. Therefore, we assume that the phases ϕ are tightly centered around $\phi = 0$, characterized by a small spread $\delta\phi \ll 1$, which allows us to effectively treat them as fixed.

As the estimator depends on the measurement outcomes x, which are distributed according to the conditional probabilities $P(x|\phi)$ defined in Eq. (3.2), ϕ_{est} likewise constitutes a random variable. Consequently, the estimator can be characterized by a ϕ-dependent statistical mean value

$$\overline{\phi}_{\text{est}} = \sum_x P(x|\phi)\phi_{\text{est}}(x) \tag{3.8}$$

and variance

$$(\Delta\phi_{\text{est}})^2 = \sum_x P(x|\phi)\left[\phi_{\text{est}}(x) - \overline{\phi}_{\text{est}}\right]^2 . \tag{3.9}$$

In principle, the estimator can be chosen arbitrarily. However, to quantify whether a particular estimator is a good or bad choice – and ultimately identify optimal estimation schemes – it is convenient to restrict the analysis to a specific class of estimators. To give an example, consider the constant estimator $\phi_{\text{est}}(x) = \varphi = \text{const.}$, independent of the measurement result. If we are lucky, $\phi = \varphi$ and our guess coincides with the true phase ϕ, resulting in an estimator with zero variance $(\Delta\phi_{\text{est}})^2 = 0$. However, for all other $\phi \neq \varphi$, this estimator is wrong and introduces a random bias to the estimation. Hence, such estimators are useless in practice. To exclude these pathological cases, in the following we require the estimators to be unbiased.

An estimator $\phi_{\text{est}}(x)$ is unbiased if and only if $\overline{\phi}_{\text{est}} = \phi$ for all ϕ, or in words: The mean estimator returns the true value ϕ for all phases. In this case, the variance of the estimator coincides with the mean squared error (MSE)

$$(\Delta\phi)^2 = \sum_x P(x|\phi)\left[\phi_{\text{est}}(x) - \phi\right]^2 , \tag{3.10}$$

which quantifies the mean squared deviation of the estimation $\phi_{\text{est}}(x)$ from the true phase ϕ and therefore is denoted as phase estimation uncertainty.

Unfortunately, since the phase originates from the average frequency deviation ω, it can, in principle, take arbitrary values within the range $-\infty < \phi < +\infty$. However, a specific interrogation and estimation scheme generally provides only a limited dynamic range within which the phase can be uniquely resolved. As a consequence there generally exists no estimator that is unbiased – or even optimal – for all possible phases ϕ. However, this stringent condition can be relaxed in the context of local phase estimation, as this approach assumes that the phases ϕ are tightly centered around $\phi = 0$. In practice, atomic clocks are operated at a specific working point ϕ_0, which does not necessarily coincide with perfect resonance $\phi = 0$ and thus reflects a constant offset. In general, the optimal working point ϕ_0 is characterized by the phase that provides the highest sensitivity to variations in ϕ. Hence, it corresponds to the phase that minimizes the MSE, defined in Eq. (3.10), with respect to all values of ϕ. Within local phase estimation for Ramsey protocols, this optimal working point typically corresponds to the inflection point of the signal. Thus, anti-symmetric signals exhibit $\phi_0 = 0$, while for symmetric signals ϕ_0 usually aligns with half the period of the signal. Consequently, although the goal is to stabilize the clock at $\omega = 0$, or equivalently $\phi = 0$, an artificial shift ϕ_0 is frequently introduced to maximize the sensitivity for a given Ramsey sequence. As a result, frequency fluctuations manifest as variations in the phase ϕ around ϕ_0.[2] Nevertheless, the phase is tightly centered around ϕ_0, i.e. $(\phi - \phi_0)^2 \ll 1$. As a consequence, it is instructive to introduce a weaker condition on the estimator, which specifically focuses on the relevant domain around ϕ_0.

An estimator $\phi_{\mathrm{est}}(x)$ is locally unbiased at $\phi = \phi_0$ if and only if

$$\overline{\phi}_{\mathrm{est}}|_{\phi=\phi_0} = \sum_x P(x|\phi_0)\phi_{\mathrm{est}}(x) = \phi_0 \tag{3.11}$$

$$\frac{\mathrm{d}\overline{\phi}_{\mathrm{est}}}{\mathrm{d}\phi}\Big|_{\phi=\phi_0} = \sum_x \frac{\mathrm{d}P(x|\phi)}{\mathrm{d}\phi}\Big|_{\phi=\phi_0} \phi_{\mathrm{est}}(x) = 1, \tag{3.12}$$

or in words: The mean estimator returns the true phase value at $\phi = \phi_0$ and tracks its variation up to the first order. Fortunately, local unbiasedness is sufficient to derive bounds on the phase estimation uncertainty, as we demonstrate in Sec. 3.5. With a locally unbiased estimator at ϕ_0, the phase estimation uncertainty is characterized by the MSE

$$(\Delta\phi(T))^2 = \sum_x P(x|\phi_0)\left[\phi_{\mathrm{est}}(x) - \phi_0\right]^2, \tag{3.13}$$

---

[2] In principle, ω and thus ϕ could be redefined such that the optimal working point always equals $\phi_0 = 0$. However, with this redefinition, $\omega = 0$ would not necessarily imply $\omega_0 = \omega_{\mathrm{LO}}$ and therefore, we choose to consider cases where potentially $\phi_0 \neq 0$.

which represents the most common cost function in local (frequentist) phase estimation. In the following, we will consistently present T explicitly as a parameter of the MSE, since the dependence of the phase estimation uncertainty on the Ramsey time T is essential for the investigations in this chapter. In general, like any variance, the phase estimation uncertainty is bounded by $0 \leq (\Delta\phi(T))^2 < +\infty$. Here, the limit $\Delta\phi(T) \to +\infty$ would represent a completely ineffective interrogation and typically would result in severe additional consequences on the clock stability. Conversely, a hypothetical perfect phase estimation (precluded by quantum mechanics due to its intrinsic indeterminism) would result in a vanishing phase estimation uncertainty $\Delta\phi(T) = 0$.

Up to this point, we have considered only a single interrogation sequence. By performing n independent Ramsey schemes on identical copies, a statistical gain in the phase estimation uncertainty according to

$$(\Delta\phi_n(T))^2 = \frac{(\Delta\phi(T))^2}{n} \tag{3.14}$$

is obtained, where we implicitly introduced the notation $(\Delta\phi(T))^2 = (\Delta\phi_{n=1}(T))^2$. This gain is sometimes referred to as Bienaymé's identity [160]. Throughout this chapter, we will primarily focus on the single-cycle phase estimation uncertainty $(\Delta\phi(T))^2$ and predominantly refer to $(\Delta\phi_n(T))^2$ in the context of the asymptotic limit of many repetitions $n \gg 1$.

3.4.2 Local frequency estimation

After characterizing the sensitivity to phase estimation, we relate the associated uncertainty to frequency estimation, which is the ultimate goal in frequency metrology, such as with atomic clocks. For discrete Ramsey times T, phase and frequency are related through $\phi = \omega T$, as discussed in Sec. 3.2. Consequently, averaging over n independent and identical repetitions of a Ramsey interrogation sequence results in an uncertainty in frequency estimation given by

$$\Delta\omega(T) = \frac{\Delta\phi(T)}{\sqrt{\tau T}}, \tag{3.15}$$

where we fix the total averaging time $\tau = nT$ to allow for comparisons across different interrogation times T. Here, $\Delta\phi(T)$ represents the phase estimation uncertainty of a single Ramsey interrogation, as introduced in the previous section.

At this point, before delving further into details, we discuss the scaling of $\Delta\omega(T)$ with the interrogation time T based on the general form of Eq. (3.15). In an ideal, decoherence-free scenario, $\Delta\phi(T) \equiv \Delta\phi$ is independent of T and the frequency estimation uncertainty appears to decrease monotonically with longer interrogation times. Unfortunately, this figure is severely compromised by decoherence effects [65–67, 148–150]. In particular, a loss of coherence causes $\Delta\phi(T)$ to increase with T. As a consequence, the frequency estimation uncertainty can only be improved by longer interrogation times T as long as the decoherence effects remain negligible. In contrast, sensitivity is lost once decoherence processes become relevant. Consequently, $\Delta\omega(T)$ features a trade-off between increased sensitivity, i.e. decreased frequency estimation uncertainty, achieved through long interrogation times and the limitations imposed by decoherence. Therefore, a compromise must be found for the optimal interrogation time T_{min} that results in the minimal frequency estimation uncertainty $\Delta\omega_{\text{min}}$. Indeed, optimizing $\Delta\omega_{\text{min}}$ by identifying optimal Ramsey schemes to achieve the associated lower bounds is the central goal of this chapter. Since frequency and phase estimation are related via Eq. (3.15), lower bounds derived in phase estimation theory can be directly applied to frequency metrology and ultimately determine limits on $\Delta\omega_{\text{min}}$. Therefore, in Sec. 3.5, we first establish lower bounds in local phase estimation theory and then apply these limits to determine lower bounds on the frequency estimation uncertainty in Sec. 3.6.

3.4.3 Clock stability and Allan deviation

Naturally, the error in frequency estimation $\Delta\omega(T)$, or equivalently the phase estimation uncertainty $\Delta\phi(T)$, will ultimately affect the clock stability. Hence, in this section, we establish a connection between the frequency estimation uncertainty and the clock stability characterized by the Allan deviation, introduced in detail in Sec. 2.1.

As a reminder, the Allan variance is defined as [11, 84–86]

$$\sigma_y^2(\tau) = \frac{1}{2}\langle(\overline{y}_{j+1} - \overline{y}_j)^2\rangle, \tag{3.16}$$

where $\langle\cdot\rangle$ denotes statistical averaging. It is calculated from the difference between two consecutive frequency values $\overline{y}_j$ and $\overline{y}_{j+1}$, each averaged over n clock cycles with duration T_C, corresponding to a total averaging time $\tau = nT_C$. Here, the clock cycle duration $T_C = T_D + T$ additionally accounts for potential dead time T_D. The averages $\overline{y}_j$ are given by

$$\overline{y}_j = \frac{T_C}{\tau} \sum_{k=(j-1)n+1}^{jn} y_k, \tag{3.17}$$

where $y_k = \omega_k/\omega_0$ denotes the average frequency deviation ω_k in cycle k relative to the atomic transition frequency ω_0. Explicitly expanding Eq. (3.16) yields

$$\begin{aligned}\sigma_y^2(\tau) = \frac{T_C^2}{2\tau^2}\Bigg[&\sum_{k=jn+1}^{(j+1)n}\sum_{l=jn+1}^{(j+1)n}\langle y_k y_l\rangle + \sum_{k=(j-1)n+1}^{jn}\sum_{l=(j-1)n+1}^{jn}\langle y_k y_l\rangle \\ &+2\sum_{k=jn+1}^{(j+1)n}\sum_{l=(j-1)n+1}^{jn}\langle y_k y_l\rangle\Bigg].\end{aligned} \tag{3.18}$$

Assuming that the feedback loop of the atomic clock stabilizes the local oscillator reliably to the atomic transition in the limit $\tau \gg 1$ s, the residual frequency fluctuations primarily originate from the estimation uncertainty, effectively characterizing quantum projection noise (QPN). Consequently, these fluctuations are independent in each cycle, i.e. $\langle y_k y_l\rangle = \delta_{kl}\langle y_k^2\rangle$. Therefore, we obtain

$$\sigma_y^2(\tau) = \frac{T_C^2}{2\tau^2}\left[\sum_{k=jn+1}^{(j+1)n}\langle y_k^2\rangle + \sum_{k=(j-1)n+1}^{jn}\langle y_k^2\rangle\right]. \tag{3.19}$$

To establish the relation between the Allan variance and frequency estimation, we identify y_k with the residual average frequency fluctuations $y_k = (\omega_k - \omega_{\text{est}})/\omega_0$ after the Ramsey sequence with duration T. For a (locally) unbiased estimator, as assumed in local frequency metrology, the statistical average effectively results in

$$\langle y_k^2\rangle = \frac{(\Delta\omega(T))^2}{\omega_0^2}, \tag{3.20}$$

yielding

$$\sigma_y^2(\tau) = \frac{T_C^2}{\tau^2}\frac{n(\Delta\omega(T))^2}{\omega_0^2} = \frac{T_C}{\tau}\frac{(\Delta\omega(T))^2}{\omega_0^2} = \frac{T_C}{\tau}\frac{(\Delta\phi(T)^2}{(\omega_0 T)^2}. \tag{3.21}$$

Consequently, the clock stability characterized by the Allan deviation is expressed as

$$\sigma_y(\tau) = \frac{\Delta\omega(T)}{\omega_0}\sqrt{\frac{T_C}{T}} = \frac{\Delta\phi(T)}{\omega_0 T}\sqrt{\frac{T_C}{\tau}} \tag{3.22}$$

and thus represents the frequency estimation uncertainty $\Delta\omega(T)$ relative to the atomic transition ω_0, with an additional correction factor $\sqrt{T_C/T}$ to account for potential dead time. However, throughout this chapter, we restrict the analysis to the dead time-free scenario, corresponding to $T_C/T = 1$. Hence, the Allan deviation reads

$$\sigma_y(\tau) = \frac{\Delta\omega(T)}{\omega_0} = \frac{\Delta\phi(T)}{\omega_0\sqrt{\tau T}}. \tag{3.23}$$

As a result, investigating the frequency estimation uncertainty $\Delta\omega(T)$ directly provides profound insight into the clock stability.

3.5 Bounds in local phase estimation theory

The goal in phase estimation is to estimate the phase as precisely as possible by minimizing the cost function, the phase estimation uncertainty $\Delta\phi(T)$ defined in Eq. (3.13). For a generalized Ramsey sequence, as introduced in Sec. 3.2, there are three control parameters to optimize: the initial state ρ_{in}, the measurement $\{\Pi_x\}$, and the estimation strategy $\phi_{\text{est}}(x)$. To determine the ultimate precision with which the phase can be estimated based on these control parameters, we review the literature and collect a hierachy of lower bounds on the phase estimation uncertainty $\Delta\phi(T)$. In particular, we present the relevant bounds from Refs. [6, 161–170], while detailed proofs are provided in App. D. The discussion in this section remains general, allowing for arbitrary quantum channels $\Lambda_{\phi,T}$, while specific assumptions and asymptotic results will be explicitly noted.

3.5.1 Cramér-Rao Bound (CRB)

The primary objective in classical estimation theory is to determine the (locally) unbiased estimator that minimizes the phase estimation uncertainty $\Delta\phi(T)$ for a given statistical model $P(x|\phi)$, as defined in Eq. (3.2), with fixed initial state ρ_{in} and measurement $\{\Pi_x\}$. In this context, a lower bound on $(\Delta\phi(T))^2$ is represented by the Cramér-Rao bound (CRB) $(\Delta\phi_{\text{CRB}}(T))^2$, which implicates an optimization over all possible estimation strategies ϕ_{est}. Assuming a locally unbiased estimator at ϕ_0 and standard regularity conditions

$$\sum_x \frac{\mathrm{d}P(x|\phi)}{\mathrm{d}\phi} = \frac{\mathrm{d}}{\mathrm{d}\phi}\sum_x P(x|\phi) = 0, \tag{3.24}$$

which allows us to exchange summation and derivative, thereby trivially satisfying the second equality due to the normalization of the conditional probabilities $P(x|\phi)$, the CRB reads [161, 162, 164, 165]

$$(\Delta\phi(T))^2 \geq (\Delta\phi_{\text{CRB}}(T))^2 = \min_{\phi_{\text{est}}}(\Delta\phi(T))^2 = \frac{1}{\mathcal{F}[\Lambda_{\phi,T}[\rho_{\text{in}}], \{\Pi_x\}]}, \tag{3.25}$$

with Fisher information [171, 172] defined as

$$\mathcal{F}[\Lambda_{\phi,T}[\rho_{\text{in}}], \{\Pi_x\}] = \sum_x \frac{1}{P(x|\phi)}\left(\frac{\mathrm{d}P(x|\phi)}{\mathrm{d}\phi}\right)^2. \tag{3.26}$$

Unfortunately, the CRB is generally not helpful in constructing an optimal estimation strategy ϕ_{est}.

In principle, the Fisher information $\mathcal{F}$ depends on the phase ϕ. However, we are primarily interested in the sensitivity at the optimal working point ϕ_0, where the

Fisher information is maximized, i.e. $\phi_0 = \underset{\phi}{\operatorname{argmax}} \mathcal{F}[\Lambda_{\phi,T}[\rho_{\text{in}}], \{\Pi_x\}]$. Therefore, in the following we omit the dependence on ϕ and implicitly refer to the Fisher information at the optimal working point.

Fisher information (FI)— At this point, we address two important properties of the Fisher information that have profound consequences for phase estimation.

Assuming that the state $\rho_{\text{in}}(\phi, T)$ represents an arbitrary mixture

$$\rho_{\text{in}}(\phi, T) = \sum_k p_k \rho_k(\phi, T), \tag{3.27}$$

with weights $p_k \geq 0$ satisfying $\sum_k p_k = 1$, the associated Fisher information is convex [163, 164]

$$\mathcal{F}[\rho_{\text{in}}(\phi, T), \{\Pi_x\}] \leq \sum_k p_k \, \mathcal{F}[\rho_k(\phi, T), \{\Pi_x\}], \tag{3.28}$$

where $\mathcal{F}[\rho_k(\phi, T), \{\Pi_x\}]$ denotes the Fisher information associated with the state $\rho_k(\phi, T)$ and measurement $\{\Pi_x\}$. As a consequence, mixing quantum states cannot increase the Fisher information and thus does not decrease the phase estimation uncertainty, since equality in Eq. (3.28) is achieved for pure states $\rho_{\text{in}}(\phi, T)$.

Assuming a separable time evolved state with N independent systems $\rho_{\text{in}}(\phi, T) = \bigotimes_{j=1}^N \rho_{\text{in}}^{(j)}(\phi, T)$, where $\rho_{\text{in}}^{(j)}(\phi, T)$ denotes the state of the j-th system, and independent measurements $\Pi_x = \bigotimes_{j=1}^N \Pi_{x_j}^{(j)}$, with measurement outcomes x_j and POVMs $\Pi_{x_j}^{(j)}$ for each system, the Fisher information is additive [164]

$$\mathcal{F}[\rho_{\text{in}}(\phi, T), \{\Pi_x\}] = \sum_{j=1}^N \mathcal{F}[\rho_{\text{in}}^{(j)}(\phi, T), \{\Pi_x^{(j)}\}], \tag{3.29}$$

where $\mathcal{F}[\rho_{\text{in}}^{(j)}(\phi, T), \{\Pi_x^{(j)}\}]$ denotes the Fisher information of the j-th system. In particular, in the case of identical systems and identical measurements, the N-system Fisher information simply is given by N times the Fisher information of a single system $\mathcal{F}[\rho_{\text{in}}^{(1)}(\phi, T), \{\Pi_x^{(1)}\}]$, i.e. $\mathcal{F}[\rho_{\text{in}}(\phi, T), \{\Pi_x\}] = N\mathcal{F}[\rho_{\text{in}}^{(1)}(\phi, T), \{\Pi_x^{(1)}\}]$.

Estimators— In general, within the framework of local phase estimation theory, any estimator that is (locally) unbiased can be employed. Naturally, however, we aim to identify estimators that saturate the CRB, which are known as efficient estimators. Unfortunately, the CRB itself provides no recipe to determine an efficient estimation strategy. Indeed, there is no guarantee that efficient estimators exist for an arbitrary total number of measuerment repetitions n. Nevertheless, we are interested in some universal estimation strategies that perform well across a variety of scenarios. In this context, we examine the maximum likelihood estimator and a linear estimator associated with the so-called method of moments.

The maximum likelihoood (ML) estimator is defined as

$$\phi_{\text{est}}^{\text{ML}}(x) = \underset{\phi}{\operatorname{argmax}}\, P(x|\phi), \tag{3.30}$$

which – as indicated by its name – maximizes the conditional probability (likelihood) for a particular measurement outcome x. Hence, it selects the phase value for which the event is most likely. Nevertheless, $\phi_{\text{est}}^{\text{ML}}$ remains a random variable since the measurement outcomes x are inherently random. Because the ML estimator relies on the full statistical model $P(x|\phi)$, its sensitivity is not easily accessible in general. However, as one of the most important theorems of classical estimation theory, the ML estimator becomes asymptotically unbiased and efficient [164–166].[3] Thus, it saturates the CRB in the limit of many measurements $n \to \infty$ (or $N \to \infty$ if systems, dynamics and measurements are independent and identical). In particular, in this regime, the distribution of the ML estimator converges to a Gaussian centered around the true phase value ϕ_0 with variance equal to the inverse of the Fisher information, i.e. $\phi_{\text{est}}^{\text{ML}} \sim \mathcal{N}(\phi_0, (n\mathcal{F}(\phi_0))^{-1})$ [164–166]. However, a priori it is not known how large the sample size n has to be such that the CRB is approached.

Unfortunately, the ML estimator requires the knowledge of the full statistical model $P(x|\phi)$. However, the evaluation of the conditional probabilities can become difficult in several scenarios, especially for large ensembles and entanglement-enhanced Ramsey schemes. In these cases, an analytical evaluation is typically not possible, while numerical evaluation becomes computationally costly with increasing ensemble size N. For instance, the conditional probabilities of entanglement enhanced protocols even with relatively low complexity, as spin-squeezed states (SSS), are not accessible in general. This raises the question of how to perform phase estimation when only limited information about the system is available. The most prominent alternative is represented by the method of moments, which – as the name suggests – only takes advantage of the moments of a measurement. In particular, it solely relies on the first two moments, effectively corresponding to the mean value and variance.

In the following, we outline the general concept, while a more detailed discussion is provided in App. D.3 based on Refs. [6, 164, 167]. In particular, we consider an observable X with known mean value $\langle X(\phi, T)\rangle$ and variance $(\Delta X(\phi, T))^2$. Suppose n measurements of X with outcomes $x_1, \ldots, x_n$, defining the random variable $X_n = \frac{1}{n}\sum_{j=1}^{n} x_j$, which represents the sample mean of the measurement outcomes.

---

[3] The proof of this theorem is rather technical and since we do not make use of the ML estimator within this work, we refer to the literature such as Refs. [164–166].

Although the conditional probabilities are unknown, and thus the ML estimator cannot be employed, the central limit theorem provides the asymptotic probability distribution of X_n in the limit of many repetitions $n \to \infty$, or equivalently large ensembles $N \gg 1$. In this regime, $X_n \overset{n\to\infty}{\sim} \mathcal{N}(\langle X(\phi,T)\rangle, (\Delta X(\phi,T))^2/n)$, representing a Gaussian distribution with mean $\langle X(\phi,T)\rangle$ and variance $(\Delta X(\phi,t))^2/n$. However, this only works sufficiently well if $\partial_\phi \langle X(\phi,T)\rangle \gg \partial_\phi(\Delta X(\phi,T))^2$, ensuring that the changes of $P(x|\phi)$ are primarily captured in the shift of the mean value. Conveniently, in this asymptotic limit, the concept of the ML estimation strategy can be applied to X_n, as we know its asymptotic probability distribution. Defining $f(\phi) = \langle X(\phi,T)\rangle$, the corresponding estimator is given by the inverse of the signal $\phi_{\text{est}}^{\text{mom}}(X_n) = f^{-1}(X_n)$. In particular, this provides an asymptotically unbiased and efficient estimator for X_n, i.e. when we only have access to the mean and variance of the observable X. In general however, it is not optimal for measurements of X and thus does not saturate the CRB, especially considering single Ramsey sequences rather than $n \gg 1$. Nevertheless, due to its simplicity and general applicability, it is both theoretically and experimentally commonly used.

Additionally assuming that the signal can be linearized around the optimal working point ϕ_0 and that $\langle X(\phi_0,T)\rangle = 0$, which always can be achieved by shifting the signal appropriately, application of this concept to individual interrogations yields the linear estimator associated with the method of moments

$$\phi_{\text{est}}^{\text{mom}}(x) = \frac{x}{\partial_\phi \langle X(\phi,T)\rangle \,|_{\phi=\phi_0}} + \phi_0. \tag{3.31}$$

Here, the linear scaling factor is given by the inverse of the slope at the optimal working point. Since $\langle X(\phi_0,T)\rangle = \sum_x xP(x|\phi_0) = 0$, local unbiasedness of $\phi_{\text{est}}^{\text{mom}}$ at ϕ_0 is ensured. The corresponding phase estimation uncertainty directly follows from Eq. (3.13) and, using $\langle X(\phi_0,T)\rangle = 0$ as argued above, can be expressed as

$$(\Delta\phi_{\text{mom}}(T))^2 = \frac{(\Delta X(\phi,T))^2}{(\partial_\phi \langle X(\phi,T)\rangle)^2}\Big|_{\phi=\phi_0}. \tag{3.32}$$

Intuitively, Eq. (3.32) represents the inverse of the signal to noise ratio and equivalently can be derived through error propagation (cf. Sec. 2.3.6). In the case of projective spin measurements, the method of moments is related to the Wineland squeezing parameter ξ [58, 59], introduced in Sec. 2.3.9, via

$$(\Delta\phi_{\text{mom}}(T))^2 = \frac{(\Delta S_{\mathbf{m}}(\phi,T))^2}{(\partial_\phi \langle S_{\mathbf{r}}(\phi,T)\rangle)^2}\Big|_{\phi=\phi_0} = \frac{\xi^2}{N}, \tag{3.33}$$

where $\mathbf{m}$, $\mathbf{r}$ and the rotation axis of the signal (pointing in z-direction within this chapter) are mutually orthogonal directions. In general, however, the linear estimator

$\phi_{\text{est}}^{\text{mom}}$ is not optimal, i.e.

$$(\Delta\phi_{\text{mom}}(T))^2 \geq \frac{1}{\mathcal{F}[\Lambda_{\phi,T}[\rho_{\text{in}}], \{\Pi_x\}]}, \tag{3.34}$$

where $\{\Pi_x\}$ describes the measurement of observable X. In the remainder of this chapter, when considering a linear estimator or the method of moments, we specifically refer to the estimator $\phi_{\text{est}}^{\text{mom}}$.

3.5.2 Quantum Cramér-Rao Bound (QCRB)

In classical estimation theory, the goal is to identify the optimal inference strategy ϕ_{est} based on measurement outcomes x, given the statistical model $P(x|\phi)$. In quantum estimation theory, we additionally ask what the optimal measurement $\{\Pi_x\}$ is for a given initial state ρ_{in}, resulting in the statistical model $P(x|\phi) = \text{Tr}(\Pi_x \Lambda_{\phi,T}[\rho_{\text{in}}])$, as defined in Eq. (3.2). Consequently, the quantum Cramér-Rao bound (QCRB) extends the (classical) Cramér-Rao bound (CRB) by additionally optimizing over all possible measurements $\{\Pi_x\}$. Hence, for a given initial state ρ_{in}, the QCRB

$$(\Delta\phi_{\text{QCRB}}(T))^2 = \min_{\{\Pi_x\}} (\Delta\phi_{\text{CRB}}(T))^2 = \min_{\{\Pi_x\},\phi_{\text{est}}} (\Delta\phi(T))^2 \tag{3.35}$$

provides a lower bound on the CRB and thus establishes the hierachy

$$(\Delta\phi(T))^2 \geq (\Delta\phi_{\text{CRB}}(T))^2 \geq (\Delta\phi_{\text{QCRB}}(T))^2. \tag{3.36}$$

While the (classical) Cramér-Rao bound (CRB) is expressed in terms of the (classical) Fisher information, likewise, the quantum Cramér-Rao bound (QCRB) [161, 162, 164, 168, 169]

$$(\Delta\phi_{\text{QCRB}}(T))^2 = \frac{1}{\mathcal{F}_Q[\Lambda_{\phi,T}[\rho_{\text{in}}]]} \tag{3.37}$$

is determined by the quantum Fisher information (QFI)

$$\mathcal{F}_Q[\rho] = \text{Tr}\big(\rho L^2\big), \tag{3.38}$$

where the symmetric logarithmic derivative (SLD) L is implicitly defined by

$$\frac{\mathrm{d}\rho}{\mathrm{d}\phi} = \frac{1}{2}(\rho L + L\rho). \tag{3.39}$$

The optimal measurement is provided by the projection-valued measure (PVM) associated with the orthonormal eigenstates of L. In contrast to the (classical) Fisher information, the quantum Fisher information is independent of the phase ϕ for unitary time evolution, as the optimal measurement adapts accordingly, yielding the same value for all phases.

In analogy to the phase estimation uncertainty, the quantum Fisher information establishes an upper bound to the (classical) Fisher information by optimizing over all measurements $\{\Pi_x\}$, such that

$$\mathcal{F}_Q[\rho] = \max_{\{\Pi_x\}} \mathcal{F}[\rho, \{\Pi_x\}]. \tag{3.40}$$

Quantum Fisher information (QFI)— The quantum Fisher information (QFI), similar to the (classical) Fisher information, exhibits both convexity and additivity:

For a mixed state $\rho_{\text{in}}(\phi, T) = \sum_k p_k \rho_k(\phi, T)$, as defined in Eq. (3.27), with weights $p_k \geq 0$ satisfying $\sum_k p_k = 1$, the QFI is convex [164]

$$\mathcal{F}_Q[\rho_{\text{in}}(\phi, T)] \leq \sum_k p_k \mathcal{F}_Q[\rho_k(\phi, T)]. \tag{3.41}$$

Consequently, despite optimizing over all possible measurements, mixing quantum states cannot enhance the estimation precision, since equality in Eq. (3.41) is achieved for pure states $\rho_{\text{in}}(\phi, T)$.

If we assume N independent systems $\rho_{\text{in}}(\phi, T) = \bigotimes_{j=1}^N \rho_{\text{in}}^{(j)}(\phi, T)$, the QFI is additive [164]

$$\mathcal{F}_Q[\rho_{\text{in}}(\phi, T)] = \sum_{j=1}^N \mathcal{F}_Q[\rho_{\text{in}}^{(j)}(\phi, T)]. \tag{3.42}$$

In the case of identical systems, this simplifies to $\mathcal{F}_Q[\rho_{\text{in}}(\phi, T)] = N\mathcal{F}_Q[\rho_{\text{in}}^{(1)}(\phi, T)]$. Hence, the QFI of separable states scales linearly with the ensemble size N at most.

Unitary phase evolution— Assuming a general unitary phase evolution with generator G according to

$$\rho_{\text{in}}(\phi) = e^{-i\phi G} \rho_{\text{in}}\, e^{i\phi G} \tag{3.43}$$

and corresponding von Neumann equation

$$\frac{\mathrm{d}\rho}{\mathrm{d}\phi} = -i[G, \rho], \tag{3.44}$$

the quantum Fisher information (QFI) can be expressed as [164, 168]

$$\mathcal{F}_Q[\rho_{\text{in}}(\phi, T)] = 2 \sum_{\substack{j,k \\ p_j + p_k > 0}} \frac{(p_j - p_k)^2}{p_j + p_k} |\langle j| G |k\rangle|^2, \tag{3.45}$$

where p_k and $|k\rangle$ are the eigenvalues and eigenstates of $\rho_{\text{in}}(\phi, T)$, respectively. The associated optimal measurement is given by

$$L = 2i \sum_{\substack{j,k \\ p_j + p_k > 0}} \frac{p_j - p_k}{p_j + p_k} |j\rangle\langle j| G |k\rangle\langle k| \,. \tag{3.46}$$

Pure states— For pure states $\rho_{\text{in}}(\phi, T) = |\psi_\phi\rangle\langle\psi_\phi|$ and a unitary phase evolution according to Eq. (3.44), the QFI simplifies to [164]

$$\mathcal{F}_Q[\rho_{\text{in}}(\phi, T)] = \mathcal{F}_Q[|\psi_\phi\rangle\langle\psi_\phi|] = 4(\Delta G)^2 \tag{3.47}$$

and thus is given by four times the variance of the generator G.

Furthermore, since the QFI is convex and thus mixing states can only decrease the QFI, for an arbitrary state $\rho_{\text{in}}(\phi, T)$ and unitary dynamics with generator G, as described by Eq. (3.44), the QFI is bounded by [164]

$$\mathcal{F}_Q[\rho_{\text{in}}(\phi, T)] \leq 4(\Delta G)^2, \tag{3.48}$$

with equality holding for pure states $\rho_{\text{in}}(\phi, T)$.

3.5.3 Optimal Quantum Interferometer (OQI)

The ultimate lower bound to the phase estimation uncertainty is represented by the optimal quantum interferometer (OQI), completing the hierachy

$$(\Delta\phi(T))^2 \geq (\Delta\phi_{\text{CRB}}(T))^2 \geq (\Delta\phi_{\text{QCRB}}(T))^2 \geq (\Delta\phi_{\text{OQI}}(T))^2. \tag{3.49}$$

The OQI simultaneously optimizes over all three control parameters: the initial state ρ_{in}, measurement $\{\Pi_x\}$ and estimator ϕ_{est}:

$$(\Delta\phi_{\text{OQI}}(T))^2 = \min_{\rho_{\text{in}}} (\Delta\phi_{\text{QCRB}}(T))^2 = \min_{\rho_{\text{in}}, \{\Pi_x\}} (\Delta\phi_{\text{CRB}}(T))^2 = \min_{\rho_{\text{in}}, \{\Pi_x\}, \phi_{\text{est}}} (\Delta\phi(T))^2. \tag{3.50}$$

Unfortunately, general expressions for the sensitivity of the OQI for arbitrary ensemble sizes only exist in the ideal, decoherence-free scenario. In contrast, in the presence of decoherence, complex optimization procedures are required. In the following, we begin by discussing the ideal scenario, introducing the prominent standard quantum limit (SQL) and the Heisenberg limit (HL). Afterwards, we present an iterative optimization algorithm that efficiently determines the OQI numerically at least for small ensembles.

Decoherence-free scenario— In the ideal scenario, no decoherence processes are present and thus, the dynamics is exclusively determined by the unitary evolution described by Eq. (3.43). Consequently, the phase estimation uncertainty $\Delta\phi(T) \equiv \Delta\phi$ is independent of the interrogation time T. As demonstrated in the previous sections, the Fisher information and quantum Fisher information (QFI) are convex and consequently, mixing states cannot improve the sensitivity. Therefore, we restrict our analysis to pure states $\rho_{\text{in}} = |\psi_{\text{in}}\rangle\langle\psi_{\text{in}}|$ as the unitary dynamics preserves purity and thus, pure initial states are optimal. Furthermore, we have seen that the QFI for a pure state equals four times the variance of the generator G (cf. Eq. (3.47)). Consequently, maximizing the variance $(\Delta G)^2$ yields the optimal input probe state, given by [164]

$$|\psi_{\text{in}}\rangle = \frac{1}{\sqrt{2}}\left[|g_{\text{min}}\rangle + e^{i\theta}|g_{\text{max}}\rangle\right], \tag{3.51}$$

where $|g_{\text{min}}\rangle$ and $|g_{\text{max}}\rangle$ denote the eigenvectors corresponding to the minimal and maximal eigenvalues g_{min} and g_{max} of G, respectively, and θ is an arbitrary phase. The associated QFI reads [164]

$$\mathcal{F}_Q[|\psi_{\text{in}}\rangle] = (g_{\text{max}} - g_{\text{min}})^2. \tag{3.52}$$

Suppose N identical probe systems subject to the unitary evolution described by Eq. (3.43), representing N identical and independent quantum channels that act in parallel on these probe systems. In this case, the phase is imprinted by the unitary $e^{-i\phi G} = \bigotimes_{j=1}^{N} \exp\left(-i\phi G^{(j)}\right) = \exp\left(-i\phi \sum_j G^{(j)}\right)$, where $G^{(j)}$ denotes the respective generators of the individual systems.

For separable states, which are represented by uncorrelated product states of the form $|\psi_{\text{in}}\rangle = \bigotimes_{j=1}^{N} |\psi_{\text{in}}^{(j)}\rangle$, the QFI is maximized if each system is in the state described by Eq. (3.51). In this case, due to its additivity, the QFI of separable states is bounded by

$$\mathcal{F}_Q^{\text{separable}}[|\psi_{\text{in}}\rangle] \leq N(g_{\text{max}} - g_{\text{min}})^2, \tag{3.53}$$

where g_{min} and g_{max} represent the minimal and maximal eigenvalues of the single system generator $G^{(j)}$, respectively. The corresponding lower bound on the phase estimation uncertainty is expressed as

$$\Delta\phi_{\text{separable}} \geq \Delta\phi_{\text{SQL}} = \frac{1}{\sqrt{N}}\frac{1}{|g_{\text{max}} - g_{\text{min}}|}, \tag{3.54}$$

commonly referred to as the standard quantum limit (SQL). Here, the particle number N plays the role of a statistical gain and thus is equivalent to N repetitions of the measurement on a single particle. As a consequence, the SQL is often referred to as the classical limit, as it relies solely on classical correlations within the ensemble and therefore does not achieve any quantum improvement.

A natural question that arises is whether entangled input probe states can enhance the QFI. A condition that indicates metrologically useful entangled states can be directly derived from Eq. (3.53), namely

$$\mathcal{F}_Q[|\psi_{\text{in}}\rangle] > N(g_{\text{max}} - g_{\text{min}})^2. \tag{3.55}$$

In fact, not all entangled states prove to be metrologically useful. While any state that satisfies Eq. (3.55) is entangled, the converse is not true [6]. Not every entangled state satisfies Eq. (3.55) and thus is metrologically useful. The maximal and minimal eigenvalues of the generator of the dynamics $G = \sum_{j=1}^{N} G^{(j)}$, denoted by $g_{\text{max}}^{(N)} = Ng_{\text{max}}$ and $g_{\text{min}}^{(N)} = Ng_{\text{min}}$, correspond to the eigenvectors $|g_{\text{max}}\rangle^{\otimes N}$ and $|g_{\text{min}}\rangle^{\otimes N}$, respectively. Consequently, the optimal input probe state is given by

$$|\psi_{\text{in}}\rangle = \frac{1}{\sqrt{2}}\left[|g_{\text{min}}\rangle^{\otimes N} + e^{i\theta}\,|g_{\text{max}}\rangle^{\otimes N}\right], \tag{3.56}$$

resulting in the QFI of entangled states being bounded by

$$\mathcal{F}_Q^{\text{entangled}}[|\psi_{\text{in}}\rangle] \leq N^2(g_{\text{max}} - g_{\text{min}})^2. \tag{3.57}$$

This represents a potential gain of a factor N in the scaling with the ensemble size compared to the SQL. The corresponding lower bound on the phase estimation uncertainty, known as the Heisenberg limit (HL), is given by

$$\Delta\phi_{\text{entangled}} \geq \Delta\phi_{\text{HL}} = \frac{1}{N}\frac{1}{|g_{\text{max}} - g_{\text{min}}|}. \tag{3.58}$$

Unlike the SQL, where the ensemble size N reflects a purely statistical gain that can be equally achieved by repeating the interrogation sequence N times with a single particle, the improvement at the Heisenberg limit arises from quantum correlations and cannot be attained through classical strategies alone. This enhancement is thus a genuine quantum effect.

For two level systems where the phase is imprinted by a unitary rotation around a fixed axis, as introduced in Sec. 3.3, we specifically have $g = g_{\text{max}} = -g_{\text{min}} = 1/2$. Consequently, the bounds on the QFI and phase estimation uncertainty are explicitly given by

$$\mathcal{F}_Q^{\text{separable}}[|\psi_{\text{in}}\rangle] \leq N \tag{3.59}$$

$$\Delta\phi_{\text{separable}} \geq \Delta\phi_{\text{SQL}} = \frac{1}{\sqrt{N}} \tag{3.60}$$

$$\mathcal{F}_Q^{\text{entangled}}[|\psi_{\text{in}}\rangle] \leq N^2 \tag{3.61}$$

$$\Delta\phi_{\text{entangled}} \geq \Delta\phi_{\text{HL}} = \frac{1}{N}. \tag{3.62}$$

While the concept of coherent spin states (CSS) (see Sec. 2.3.7) provides a compact framework for separable states with identical single-particle states, thereby achieving the standard quantum limit (SQL), GHZ states (see Sec. 2.3.8) saturate the Heisenberg limit (HL).

Decoherence— In the presence of decoherence processes, the time evolved state $\Lambda_{\phi,T}[\rho_{\text{in}}]$ generally is no longer pure but instead represents a mixture. Consequently, the SQL and HL are typically not saturable, since the convexity of the QFI causes mixed states to achieve lower sensitivities. While the SQL can be redefined for specific noise processes to provide a tight bound for separable states, as we will discuss in Sec. 3.7, unfortunately, no explicit expressions exist for the lower bound in entanglement-enhanced protocols, represented by the OQI, and thus numerical optimization is required.

Iterative optimization algorithm— In the following, we outline an algorithm presented in Ref. [170], which iteratively optimizes the initial probe state ρ_{in} and the measurement $\{\Pi_x\}$. Although numerical optimization becomes challenging with increasing ensemble size, this algorithm enables efficient computation at least for small N.

For a given input probe state ρ_{in}, the dynamics during the Ramsey dark time T results in the state $\Lambda_{\phi,T}[\rho_{\text{in}}]$. In Sec. 3.5.2, we demonstrated that the measurement achieving optimal sensitivity, i.e. maximal QFI, is determined by the projection-valued measure (PVM) associated with the eigenbasis of the symmetric logarithmic derivative (SLD). Conversely, for a given SLD L, we have to examine the optimal input probe state ρ_{in}. To address this, we effectively have to map the dynamics from the state to the measurement. By defining the adjoint quantum channel $\Lambda^{\dagger}_{\phi,T}$ via

$$\operatorname{Tr}\left(\Lambda_{\phi,T}[\rho_{\text{in}}]A\right) = \operatorname{Tr}\Big(\rho_{\text{in}}\Lambda^{\dagger}_{\phi,T}[A]\Big) \tag{3.63}$$

for arbitrary operators A, we can rewrite the QFI, defined in Eq. (3.38), as

$$\mathcal{F}_Q[\rho_{\text{in}}] = \operatorname{Tr}\left(\Lambda_{\phi,T}[\rho_{\text{in}}]L^2\right) = \operatorname{Tr}\Big(\rho_{\text{in}}\Lambda^{\dagger}_{\phi,T}[L^2]\Big). \tag{3.64}$$

Consequently, the optimal input probe state $\rho_{\text{in}} = |\psi_{\text{in}}\rangle\langle\psi_{\text{in}}|$ corresponds to the eigenvector $|\psi_{\text{in}}\rangle$ of the operator $\Lambda^{\dagger}_{\phi,T}[L^2]$ associated with its maximal eigenvalue.[4] In the iterative algorithm, starting from an arbitrary state, the optimal measurement and the corresponding optimal probe state are iteratively determined until the phase estimation uncertainty $(\Delta\phi(T))^2$ converges to the OQI [170]. As a result, this finally demonstrates that the optimal input probe state is pure. In contrast, convexity of the QFI merely indicates that pure time-evolved states $\Lambda_{\phi,T}[\rho_{\text{in}}]$ are optimal, which, however, strongly depends on the particular dynamics and generally cannot be attained.

---

[4] Ref. [170] additionally suggests to rewrite this expression using the definition of the SLD in Eq. (3.39), leading to $\operatorname{Tr}\Big(\rho_{\text{in}}\Lambda^{\dagger}_{\phi,T}[2i[G,L] - L^2]\Big)$. Within this reformulation, however, the fundamental principle remains unchanged.

3.6 Bounds in local frequency metrology

As discussed before, frequency and phase estimation are related via Eq. (3.15) and therefore, lower bounds derived in phase estimation theory can be directly applied to frequency metrology. Additionally, the optimal interrogation time T_{min} has to be identified, achieving the minimal frequency estimation uncertainty $\Delta\omega_{\text{min}}$. Since numerical optimization was already required for the optimal quantum interferometer (OQI) in phase estimation theory, it is likewise necessary to determine the ultimate lower bounds in frequency metrology.

Although the iterative algorithm is efficient for small ensembles, it becomes computationally costly with increasing N (cf. App. A). Fortunately, in the asymptotic limit of large ensembles $N \gg 1$, explicit expressions for the ultimate lower bound – representing the optimal quantum interferometer (OQI) – can be derived for various decoherence processes [173–179]. In the presence of dephasing [66, 67, 149] with rate γ and spontaneous decay [68] with rate Γ, the asymptotic ultimate lower bound is given by

$$(\Delta\omega_{\text{min}})^2 \geq (\Delta\omega_{\text{asym}})^2 \geq \frac{\Gamma + \gamma}{N\tau}. \tag{3.65}$$

Interestingly, this bound scales linearly with N, providing only a constant enhancement compared to the standard quantum limit (SQL) imposed by separable states. In contrast, the decoherence-free scenario achieves the Heisenberg limit, which offers an improvement of N and thus scales quadratically with the ensemble size.

In Ref. [149], $(\Delta\omega_{\text{asym}})^2$ was derived for individual dephasing, considering arbitrary input states and a projective measurement of the spin in a suitable direction. The extension to spontaneous decay yields Eq. (3.65), as we demonstrate in App. E.1, where we additionally derive this bound considering arbitrary input states and a parity measurement. Interestingly, this already represents the asymptotic ultimate lower bound as derived in Refs. [66–68, 176, 179, 180], where the tightness of this bound has also been demonstrated.[5]

---

[5] Note that in the presence of spontaneous decay, a lower bound smaller by a factor of 4 compared to Eq. (3.65) was derived in Refs. [66, 180], which might be achievable by means of additional

3.7 Optimal Ramsey protocols in frequency metrology limited by spontaneous decay

In the previous sections, we established the theoretical framework for local frequency metrology and introduced lower bounds on the frequency estimation uncertainty. In the remainder of this section, our goal is to achieve the ultimate lower bound – represented by the optimal quantum interferometer (OQI) – in the context of local frequency metrology limited by spontaneous decay. Consequently, this section presents the central results of this chapter. To draw parallels to the well-studied scenario involving individual dephasing, we additionally include it in our analysis. To start with, we investigate the performance of coherent spin states (CSS) and GHZ states in Sec. 3.7.1, as they achieve the standard quantum limit (SQL) and Heisenberg limit (HL), respectively, in the decoherence-free scenario. However, evaluating the quantum Cramér-Rao bound (QCRB) for GHZ states reveals that the parity measurement is not optimal in the presence of spontaneous decay, achieving at best a frequency uncertainty equivalent to the SQL. To address this, in Sec. 3.7.2, we identify an alternative interrogation scheme that saturates the QCRB for GHZ states employing a correlated measurement and a highly nonlinear estimator. Furthermore, in Sec. 3.7.3, we compare the sensitivity of this protocol to the optimal quantum interferometer (OQI) and to spin-squeezed states (SSS) generated through one-axis-twisting (OAT) interactions [125], as SSS are optimal in the asymptotic limit for large ensembles and OAT interactions are accessible in several experimental setups [62, 126–133]. Although the protocol that saturates the QCRB of the GHZ state provides a substantial gain over the SQL, it does not saturate the OQI. In addition, we present a variation of this protocol with a GHZ-like initial state that approximates the OQI for small ensembles. For the investigated GHZ(-like) states, it is essential to identify terms associated with a specific number of spontaneous decay events, which we examine in Sec. 3.7.4. In Sec. 3.7.5, we demonstrate the robustness of the measurement and estimation schemes by performing Monte-Carlo simulations of the full feedback loop in an atomic clock. Finally, we discuss the unique features of GHZ(-like) states in the presence of spontaneous decay in Sec. 3.7.6. In the following, we present the primary results, while detailed derivations are provided in App. E.

The trade-off between the increased sensitivity achieved through long interrogation times and the limitations imposed by decoherence, as discussed in Sec. 3.4.2, emerges for all Ramsey schemes. For the interrogation protocols we explore in the

---

ancilla systems or adaptive quantum feedback strategies, such as quantum error correction schemes. However, saturability remains an open question and is beyond the scope of this work. Refs. [150, 181] give a comprehensive overview over different quantum control strategies and corresponding bounds.

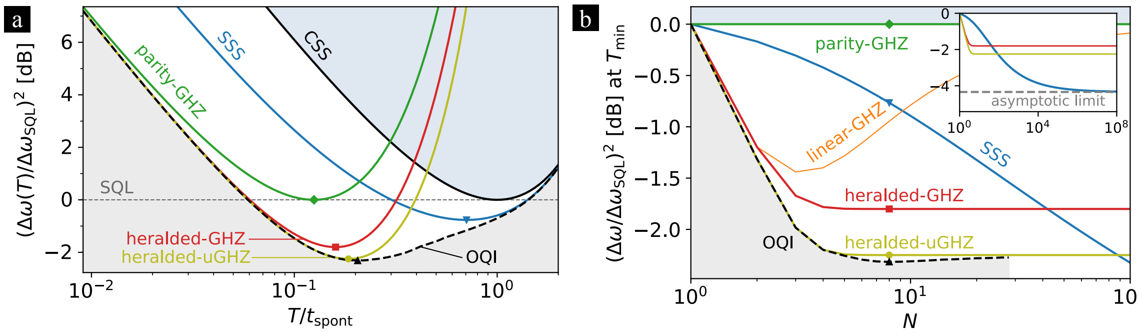

Figure 3.2: **Enhancement of protocols with GHZ(-like) states compared to the SQL:** (a) Generic frequency estimation uncertainty $\Delta\omega(T)$ in the presence of spontaneous decay for $N = 8$, scaled to the SQL defined in Eq. (3.69), for the indicated protocol types (see main text), $\gamma = 0$. The interrogation time is rescaled by the excited-state lifetime of the atoms $t_{\mathrm{spont}} = 1/\Gamma$. Symbols indicate the optimal interrogation time T_{min}. The gray shaded area represents the inaccessible sensitivity region set by the OQI limit, while the blue shaded area indicates achievable frequency estimation uncertainties using uncorrelated atoms. (b) Scaling of the relative frequency estimation uncertainty at the optimal interrogation time T_{min} with the ensemble size N. The ratio $\Delta\omega/\Delta\omega_{\mathrm{SQL}}$ is independent of the decay rate Γ due to the comparison with the SQL. As discussed in the main text, numerical evaluation of the OQI with the employed algorithm is only feasible for $N \lesssim 30$. Symbols correspond to the minima in (a). The inset illustrates the asymptotic scaling for large ensembles N, using the same axes and protocols.

following, the generic dependence of the frequency estimation uncertainty $\Delta\omega(T)$ on the interrogation time T is illustrated in Fig. 3.2(a). Additionally, the scaling of the minimal frequency estimation uncertainty $\Delta\omega_{\mathrm{min}}$ with the ensemble size N at optimal interrogation time T_{min} is presented in Fig. 3.2(b). While investigating frequency metrology in the presence of spontaneous decay and individual dephasing, we are primarily interested in the regime where spontaneous decay constitutes the dominant limitation, as argued before. Consequently, we set $\gamma = 0$ in the results depicted in the figures. To enable comparability between various setups, the interrogation time T is rescaled by the excited-state lifetime of the atoms $t_{\mathrm{spont}} = 1/\Gamma$ and the frequency estimation uncertainty $\Delta\omega(T)$ is presented relative to the SQL (see below). Hence, the ratios are independent of the particular decoherence strength and ensure that the results are transferable to specific experimental parameters.

3.7.1 Separable and maximally entangled states

Coherent Spin States (CSS)— Coherent spin states (CSS) [115–117], introduced in detail in Sec. 2.3.7, are product states of N qubits, with each qubit prepared identically. As indicated by the additivity of the quantum Fisher information (QFI), they represent the optimal separable states for phase estimation and frequency metrology (cf. Sec. 3.5.2). As a result, the minimal frequency estimation uncertainty achieved with CSS and an uncorrelated measurement determines the standard quantum limit (SQL). In particular, the conventional Ramsey protocol employs CSS, complemented by a collective projective spin measurement and a linear estimation strategy. The phase estimation uncertainty is given by

$$(\Delta\phi_{\mathrm{CSS}}(T))^2 = \frac{e^{(\Gamma+\gamma)T}}{N}, \tag{3.66}$$

which coincides with the QCRB for CSS. The corresponding frequency estimation uncertainty reads

$$(\Delta\omega_{\mathrm{CSS}}(T))^2 = \frac{e^{(\Gamma+\gamma)T}}{N\tau T}. \tag{3.67}$$

The trade-off with respect to the interrogation time is illustrated in Fig. 3.2(a). In the limit $\Gamma+\gamma \to 0$ or equivalently $T \to 0$, the SQL of the decoherence-free scenario $(\Delta\phi_{\mathrm{SQL}})^2 = 1/N$ is recovered. Conversely, when the interrogation time approaches $T \sim 1/(\Gamma+\gamma)$, the decoherence processes become relevant and ultimately limit the sensitivity. Minimization with respect to T yields the optimal interrogation time

$$T_{\mathrm{CSS}} = \frac{1}{\Gamma+\gamma} \tag{3.68}$$

and minimal frequency estimation uncertainty

$$(\Delta\omega_{\mathrm{SQL}})^2 = (\Delta\omega_{\mathrm{CSS}})^2 = \frac{\mathrm{e}\,(\Gamma+\gamma)}{N\tau}, \tag{3.69}$$

which represents the lower bound attainable with separable states, thus defining the SQL, as argued before. For $\Gamma = 0$, this reproduces the result determined by Huelga et al. [149]. Consequently, despite being inherently different, spontaneous decay and individual dephasing constrain the sensitivity of separable states in the same way, thereby leading to the respective SQL.

GHZ States— In the decoherence-free scenario, a dramatic improvement over separable states can be gained by preparing atoms in a GHZ state [121]

$$|\mathrm{GHZ}\rangle = \frac{1}{\sqrt{2}}\left(|\uparrow\rangle^{\otimes N} + |\downarrow\rangle^{\otimes N}\right) \tag{3.70}$$

and measuring the parity $\Pi = (-1)^N \sigma_x^{\otimes N}$ after the free evolution time (cf. Sec. 2.3.8), as initially proposed by Wineland et al. [122]. This strategy, to which we refer in the following as 'parity-GHZ' protocol, achieves a phase estimation uncertainty of

$$(\Delta\phi_{\mathrm{GHZ}}(T))^2 = \frac{e^{(\Gamma+\gamma)NT}}{N^2} \tag{3.71}$$

and corresponding frequency estimation uncertainty of

$$(\Delta\omega_{\mathrm{parity-GHZ}}(T))^2 = \frac{e^{(\Gamma+\gamma)NT}}{N^2\tau T}. \tag{3.72}$$

The dependence of $\Delta\omega_{\mathrm{parity-GHZ}}(T)$ on T is illustrated in Fig. 3.2(a). For short interrogation times $T \ll t_{\mathrm{spont}}$, or equivalently small decoherence rates $\Gamma + \gamma \ll 1$, the parity-GHZ protocol surpasses CSS and achieves the Heisenberg limit (HL) $(\Delta\phi_{\mathrm{HL}})^2 = 1/N^2$, which represents the ultimate lower bound in the decoherence-free scenario. However, GHZ states collapse N times faster than uncorrelated states, as decoherence processes become relevant at proportionally shorter T. This results in the optimal interrogation time

$$T_{\mathrm{parity-GHZ}} = \frac{1}{(\Gamma+\gamma)N}, \tag{3.73}$$

exactly compensating for the gain in phase estimation, yielding the minimal frequency estimation uncertainty

$$(\Delta\omega_{\mathrm{parity-GHZ}})^2 = \frac{\mathrm{e}\,(\Gamma+\gamma)}{N\tau}. \tag{3.74}$$

Consequently, the parity-GHZ protocol completely loses its gain due to spontaneous decay and individual dephasing, achieving at best a frequency estimation uncertainty equivalent to the SQL, as depicted in Fig. 3.2(b). This is consistent with the result derived for vanishing spontaneous emission rate $\Gamma = 0$ by Huelga et al. [149]. As a consequence, this statement has often been generalized without further investigation in the sense that GHZ states generally do not lead to any improvement in the presence of decoherence.

3.7.2 Beating the standard quantum limit with GHZ states

Indeed, performing a parity measurement on the GHZ state in the presence of spontaneous decay is not optimal, as it does not saturate the QCRB. The QCRB for the phase estimation uncertainty with a GHZ state is given by

$$(\Delta\phi^{\mathrm{GHZ}}_{\mathrm{QCRB}}(T))^2 = \frac{\mathrm{e}^{(\Gamma+\gamma)NT}}{2N^2}\left[1 + e^{-\Gamma NT} + \left(1 - e^{-\Gamma T}\right)^N\right]. \tag{3.75}$$

The corresponding bound for the optimal frequency estimation uncertainty follows from minimization with respect to the interrogation time

$$(\Delta\omega^{\mathrm{GHZ}}_{\mathrm{QCRB}})^2 = \min_T \frac{(\Delta\phi^{\mathrm{GHZ}}_{\mathrm{QCRB}}(T))^2}{\tau T}. \tag{3.76}$$

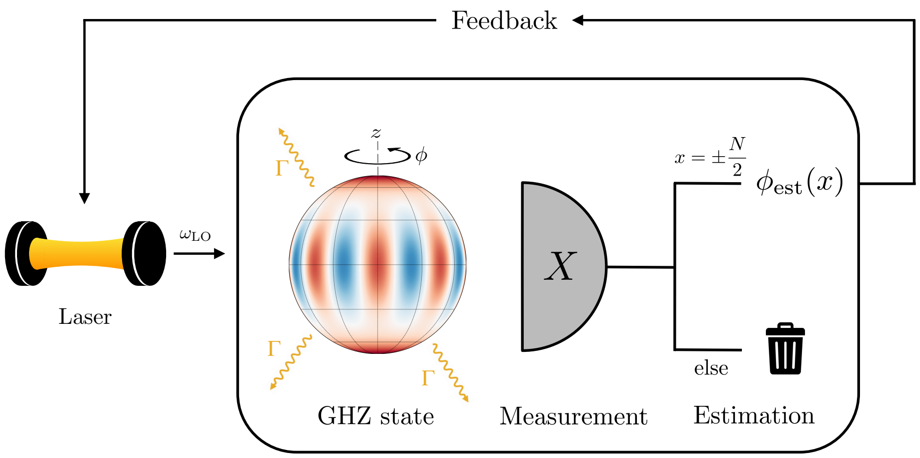

Figure 3.3: **Schematic illustration of the heralded-GHZ protocol:** The laser with fluctuating frequency ω_{LO} is stabilized to the atomic reference. During the free evolution time T, the GHZ state accumulates a phase ϕ through a rotation around the z-axis and is subject to spontaneous decay with rate Γ. Based on the measurement outcome x of the observable X, an estimation ϕ_{est} of the phase is conducted to correct the laser accordingly. The estimation strategy exclusively selects the maximal measurement outcomes $x = \pm\frac{N}{2}$, effectively implementing an error detection and mitigation scheme for spontaneous decay events.

In the absence of spontaneous decay ($\Gamma = 0$), this reproduces the findings of Huelga et al. [149] that the QCRB equals the SQL. However, for $\Gamma > 0$ one finds $(\Delta\omega_{\mathrm{QCRB}}^{\mathrm{GHZ}})^2 < (\Delta\omega_{\mathrm{SQL}})^2$. Somewhat surprisingly, GHZ states do admit gains beyond the SQL when the relevant decoherence process is spontaneous decay rather than dephasing noise. Since these gains are not realized by parity measurements, the question arises as to which alternative measurements do saturate the QCRB of the GHZ state described by Eq. (3.75).

This can be achieved as follows (cf. Fig. 3.3): At the end of the Ramsey interrogation time T, atoms are subject to a unitary operation

$$\mathcal{U}_{\mathrm{GHZ}} = \begin{cases} \mathcal{T}_x(\pi) & \text{if } N \text{ is even} \\ \mathcal{R}_x\left(\frac{\pi}{2}\right)\mathcal{T}_x(\pi) & \text{if } N \text{ is odd} \end{cases} \tag{3.77}$$

where $\mathcal{T}_x(\mu) = \exp\left(-i\frac{\mu}{2}S_x^2\right)$ denotes an one-axis-twisting (OAT) interaction with twisting strength $\mu = \pi$ along x, whereas $\mathcal{R}_x(\theta)$ represents a rotation around the x-axis by an angle $\theta = \frac{\pi}{2}$. We note that the unitary $\mathcal{U}_{\mathrm{GHZ}}$ also corresponds to the operation that may be used to generate the GHZ state from the ground state $|{\downarrow}\rangle^{\otimes N}$ initially. Subsequently, the spin is measured projectively along the z-direction, effectively resulting in a measurement of the observable

$$X = \mathcal{U}_{\mathrm{GHZ}}\, S_z\, \mathcal{U}_{\mathrm{GHZ}}^{\dagger} \tag{3.78}$$

with outcomes $x \in \{-\frac{N}{2}, \ldots, \frac{N}{2}\}$. This procedure corresponds to the one explored in the experiment reported by Leibfried et al. [128] and essentially implements an exact Loschmidt echo [182], since the state preparation with $\mathcal{U}_{\mathrm{GHZ}}$ is complemented by its corresponding adjoint transformation $\mathcal{U}_{\mathrm{GHZ}}^{\dagger}$ for the measurement. Any such measurement has to be accompanied by a suitable rule for estimating the phase ϕ for a given outcome x. In order to saturate the QCRB, the nonlinear estimator

$$\phi_{\mathrm{est}}(x) = \begin{cases} \pm\frac{1}{N}\mathrm{e}^{\frac{(\Gamma+\gamma)}{2}NT} & \text{if } x = \pm\frac{N}{2} \\ 0 & \text{else} \end{cases} \tag{3.79}$$

has to be applied. ϕ_{est} estimates the phase for the maximal outcomes $x = \pm\frac{N}{2}$ according to the standard linear estimator in local phase estimation, namely scaled linearly with the inverse signal slope, while all other measurement outcomes are simply discarded. In the context of atomic clocks, an estimated phase $\phi_{\mathrm{est}} = 0$ corresponds to inferring no frequency deviation, and correspondingly, no error signal is generated.

Physical interpretation— The fact that this measurement and estimation strategy performs well under spontaneous decay can be understood from two reasons, which we motivate physically in the following. Additionally, they are reflected in the conditional probabilities

$$P\left(x|\phi\right) = \frac{1}{4}\left[1 + e^{-\Gamma NT} + \left(1 - e^{-\Gamma T}\right)^{N} \mp 2e^{-\frac{\Gamma+\gamma}{2}NT}\cos(N\phi)\right] \tag{3.80}$$

if $x = \pm\frac{N}{2}$ and

$$P\left(x|\phi\right) = \frac{1}{4}\binom{N}{N_-}\left[e^{-\Gamma T(N-N_-)}\left(1 - e^{-\Gamma T}\right)^{N_-} + e^{-\Gamma TN_-}\left(1 - e^{-\Gamma T}\right)^{N-N_-}\right] \tag{3.81}$$

if $x = \frac{N}{2} - N_-$, where $N_- \in \{1, \ldots, N-1\}$ denotes the number of particles in the ground state $|{\downarrow}\rangle$.

Firstly, the measurement outcomes can be interpreted as a flag for spontaneous decay. If none of the particles decays, a relative phase between the states $|{\downarrow}\rangle^{\otimes N}$ and $|{\uparrow}\rangle^{\otimes N}$ is accumulated during the free evolution time. Although these coherences decrease over time due to the decoherence effects, the state remains in the subspace spanned by the two maximal Dicke states and effectively one of the two GHZ-like states $\mathcal{U}_{\mathrm{GHZ}}|{\uparrow}\rangle^{\otimes N}$ or $\mathcal{U}_{\mathrm{GHZ}}|{\downarrow}\rangle^{\otimes N}$ is measured, corresponding to outcomes $x = \pm\frac{N}{2}$, respectively. Conversely, if a particle decays, the subspace spanned by the maximal Dicke states is left and we obtain a measurement outcome $x \neq \pm\frac{N}{2}$ that depends on the number of particles that decayed. Hence, measurement outcomes $x \neq \pm\frac{N}{2}$ can only occur if at least one spontaneous decay event has taken place (cf. Sec. 3.7.4), such that selecting the $x = \pm\frac{N}{2}$ events, as is done by the estimator Eq. (3.79), in essence filters out all such cases.

Secondly, and quite remarkably, for the particular observable X, introduced in Eq. (3.78), the conditional probabilities $P(x|\phi)$ turn out to be independent of ϕ for all outcomes $x \neq \pm\frac{N}{2}$. Thus, these cases do not provide any information on ϕ. Hence, we only infer information about the phase for $x = \pm\frac{N}{2}$, while for $x \neq \pm\frac{N}{2}$ we effectively measure noise with a binomial(-like) distribution characterized by the spontaneous decay rate Γ and interrogation time T. In particular, the conditional probabilities $P(x|\phi)$ for $x = \frac{N}{2} - N_- \neq \pm\frac{N}{2}$ are directly associated to the probabilities of N_- decay events, as we will show in Sec. 3.7.4. Consequently, trying to estimate the phase for outcomes $x \neq \pm\frac{N}{2}$ effectively corresponds to random estimates based on this binomial(-like) noise distribution. Metaphorically speaking, this would essentially result in a blind guess and spoil the sensitivity.

Together, these two features allow to implement an error detection and mitigation scheme [183] tailored to frequency metrology. On the one hand, outcomes $x \neq \pm\frac{N}{2}$ can be considered as heralded errors signifying an unsuccessful, decohered Ramsey interrogation. Conversely, outcomes $x = \pm\frac{N}{2}$ signal a no-jump dynamics (see Sec. 3.7.4) delivering maximal phase information. On the other hand, exclusively selecting these events during (classical) post-processing results in enhanced sensitivity, saturating the QCRB Eq. (3.75).[6] We therefore refer to this scheme as 'heralded-GHZ' protocol in the following.

Frequency estimation uncertainty— The dependence of the frequency estimation uncertainty of the heralded-GHZ protocol $\Delta\omega_{\mathrm{heralded-GHZ}}(T)$, which coincides with the QCRB for the GHZ state given by Eq. (3.75), on the interrogation time T is illustrated in Fig. 3.2(a). For short interrogation times $T \ll t_{\mathrm{spont}}$, or equivalently small decoherence rates $\Gamma \ll 1$, the heralded-GHZ protocol performs similarly to the parity-GHZ protocol, with both achieving the HL. However, as T approaches $T_{\mathrm{parity-GHZ}} = \frac{1}{(\Gamma+\gamma)N}$, the heralded-GHZ protocol demonstrates its advantage and achieves a lower frequency estimation uncertainty. Although the optimal interrogation time for the heralded-GHZ protocol is slightly longer than for the parity-GHZ protocol, the maximal entanglement of the GHZ state still leads to $T_{\mathrm{heralded-GHZ}} \ll T_{\mathrm{CSS}}$. Thus, $T_{\mathrm{heralded-GHZ}}$ approximately remains in the regime of $T_{\mathrm{parity-GHZ}}$.

---

[6] Instead of emphasizing a gain compared to the parity-GHZ protocol, we can interpret the situation from the perspective of a decoherence-free scenario. In this context, this measurement and estimation strategy is less susceptible to decoherence and thus suffers less from its effects than the parity-GHZ protocol. In particular, it effectively extracts the maximum phase information from the decohered state, as indicated by saturating the QCRB.

In Fig. 3.2(b), we present the minimal frequency estimation uncertainty as a function of the ensemble size N, optimized with respect to the interrogation time T and scaled to the SQL. The heralded-GHZ protocol shows a substantial enhancement over the SQL for all N. In particular, a constant gain of 1.8 dB relative to the SQL is achieved for $N \geq 5$ and thus, no loss in improvement is observed for large N. Especially considering the scaling of small and intermediate ensembles, the resulting increase in sensitivity is quite remarkable.

Unfortunately, the minimization of $\Delta\omega_{\text{heralded}-\text{GHZ}}(T)$ with respect to the interrogation time T generally is not analytically possible. However, an explicit expression can be obtained if the term $(1-e^{-\Gamma T})^N$ in Eq. (3.75) is negligible. This contribution reflects the probability of N spontaneous decay events occurring during the interrogation time T (cf. Sec. 3.7.4), in which case the time evolved state would collapse to $|{\downarrow}\rangle^{\otimes N}$. However, this scenario becomes increasingly unlikely for larger ensemble sizes N. In this limit, the minimal frequency estimation uncertainty is given by

$$\Delta\omega_{\text{heralded}-\text{GHZ}} = \Delta\omega_{\text{QCRB}}^{\text{GHZ}} = \frac{\Delta\omega_{\text{SQL}}}{\sqrt{2eW(1/e)}}. \tag{3.82}$$

Here, W denotes the Lambert-W function (cf. App. E.7). The resulting gain over the SQL of $\frac{1}{\sqrt{2eW(1/e)}} < 1$ corresponds to the observed 1.8 dB. In particular, this approximation proves to be appropriate already for small ensembles $N \geq 5$, as a constant gain compared to the SQL is achieved (cf. Fig. 3.2(b)).

Linear-GHZ protocol— To highlight the importance of the nonlinear estimator presented in Eq. (3.79), we compare it to the standard linear estimation strategy

$$\phi_{\text{est}}(x) = \frac{2x}{N^2}\mathrm{e}^{\frac{(\Gamma+\gamma)}{2}NT}, \tag{3.83}$$

which we denote as 'linear-GHZ' protocol. As argued before, measurement outcomes $x \neq \frac{N}{2}$ provide no phase information (cf. Eq. (3.81)), leading to random phase guesses that degrade the sensitivity. Consequently, the frequency estimation uncertainty associated with the linear-GHZ protocol, given by

$$\left(\Delta\phi(T)_{\text{linear}-\text{GHZ}}\right)^2 = \frac{e^{(\Gamma+\gamma)NT}}{N^3}\left[1+(N-1)\left(1-2e^{-\Gamma T}+2e^{-2\Gamma T}\right)\right], \tag{3.84}$$

is compromised relative to the heralded-GHZ protocol for $N > 2$, as illustrated in Fig. 3.2(b). Nevertheless, an improvement over the SQL is achieved, with maximal gain observed for $N = 3$. However, this enhancement diminishes with increasing ensemble size and the sensitivity ultimately converges to the SQL, resulting in a vanishing advantage in the asymptotic limit.

Two immediate concerns arise regarding the heralded-GHZ protocol. Firstly, how well does it compare to other potential strategies where, beyond measurements and estimators, the initial state is also optimally chosen and may differ from a GHZ state? Secondly, one may question the effectiveness of a strategy that ignores all but two measurement outcomes in each interrogation cycle, particularly in the context of atomic clocks, where the ultimate challenge is to stabilize the constantly drifting phase of a local oscillator. We address both of these issues in the remainder of this section.

3.7.3 Saturating the optimal quantum interferometer

The performance of the optimal quantum interferometer (OQI) is determined by optimizing over all entangled initial states, measurements, and estimators. Unfortunately, as discussed in Sec. 3.5.3, no general expressions for the OQI sensitivity exist for arbitrary ensemble sizes and thus complex optimization procedures are required. In particular, the iterative algorithm presented in Ref. [170] and outlined in Sec. 3.5.3 allows an efficient computation at least for small ensembles (cf. App. A). However, numerical optimization becomes challenging with increasing N. In the asymptotic limit ($N \gg 1$), the ultimate lower bound is given by (cf. Sec. 3.6)

$$(\Delta\omega_{\text{asym}})^2 \geq \frac{\Gamma + \gamma}{N\tau}, \tag{3.85}$$

which results in a maximal improvement of 1/e over the SQL Eq. (3.69), corresponding to a gain of 4.3 dB. Interestingly, individual dephasing and spontaneous decay exhibit the same asymptotic limit despite their fundamentally different nature. For individual dephasing, it was demonstrated in Ref. [148] that this bound is asymptotically saturated by spin-squeezed states (SSS) generated by one-axis-twisting (OAT) interactions [125], introduced in detail in Sec. 2.3.9. Likewise, SSS prove to be asymptotically optimal in the presence of spontaneous decay, as shown in the inset of Fig. 3.2(b). As a consequence, we focus on small ensembles where the OQI can be evaluated numerically and benchmark the heralded-GHZ protocol against SSS generated by OAT due to their asymptotic optimality.

Although the heralded-GHZ protocol provides a substantial enhancement compared to the SQL, it does not saturate the OQI, which likewise represents a constant improvement with respect to the SQL in the regime where numerical evaluation is feasible ($N \leq 30$), as illustrated in Fig. 3.2(b). Furthermore, in this regime, the heralded-GHZ protocol achieves sensitivities relatively close to the OQI, despite its low complexity. Conversely, the enhancement of SSS over the SQL increases with N. In particular, for larger ensembles ($N \geq 42$), SSS surpass the heralded-GHZ protocol in sensitivity and ultimately approximate the lower bound Eq. (3.85) asymptotically (cf. inset of Fig. 3.2(b)). Consequently, the gain of the OQI over the SQL will increase likewise for larger ensembles.

The gap between the heralded-GHZ protocol and the OQI for small ensembles raises the question of which protocol could be used to close it and what resources would be required to do so. The fact that the gap is independent of the number of particles suggests that this could be possible with a fixed protocol that varies little or not at all with N. Furthermore, the optimal interrogation time T_{OQI} is close to the one of the heralded-GHZ protocol (cf. Fig. 3.2(a)) and thus indicates that GHZ-like states might be optimal. Indeed, we have identified a particular interrogation scheme that reaches the level of the OQI for several tens of atoms and outperforms SSS for up to about 80 atoms. Surprisingly, no deep circuit depths are necessary, but a simple extension of the heralded-GHZ protocol involving one more twisting operation for state preparation is sufficient. The initial state

$$|\psi_{\mathrm{in}}\rangle = \mathcal{U}_{\mathrm{GHZ}}\,\mathcal{R}_z(\theta)\,\mathcal{U}_{\mathrm{GHZ}}|{\downarrow}\rangle^{\otimes N} = \alpha_\theta|{\downarrow}\rangle^{\otimes N} + \beta_\theta|{\uparrow}\rangle^{\otimes N} \tag{3.86}$$

is generated by an additional OAT interaction $\mathcal{U}_{\mathrm{GHZ}}$ and rotation $\mathcal{R}_z(\theta)$ with optimal rotation angle θ depending on the ensemble size N and the dimensionless parameter ΓT (cf. App. E.8). Essentially, the additional transformation only modifies the coefficients α_θ and β_θ, generating an unbalanced GHZ-like state (referred to as 'uGHZ' in the following). As limiting cases, the GHZ state is reproduced for $\theta_{\mathrm{GHZ}} = \frac{\pi}{2N}$, rendering the additional transformation redundant, while the collective excited state $|{\uparrow}\rangle^{\otimes N}$ and ground state $|{\downarrow}\rangle^{\otimes N}$ are obtained for $\theta_{\uparrow} = 0$ and $\theta_{\downarrow} = \pi/N$, respectively. In particular, the optimal rotation angle features a trade-off between two contrary aspects. On the one hand, based on the ideal scenario, one would expect the highest sensitivity if the time evolved state comprises an equal superposition of both maximal Dicke states, which is achieved for θ_{equal} with $\theta_{\uparrow} \leq \theta_{\mathrm{equal}} \leq \theta_{\mathrm{GHZ}}$. Hence, this strategy effectively aims to compensate for spontaneous decay during the free evolution time. On the other hand, however, a higher population in the excited state at the same time increases the decoherence effects due to spontaneous decay, counteracting the aforementioned benefit. Ultimately, a compromise is found with the optimal rotation angle θ_{opt} in the range $\theta_{\mathrm{equal}} \leq \theta_{\mathrm{opt}} \leq \theta_{\mathrm{GHZ}}$, as illustrated in Fig. 3.4(a), assigning a higher weight to the excited state.

Due to its GHZ-like nature, the measurement defined in Eq. (3.77) remains optimal, ensuring that the phase is encoded exclusively onto the maximal Dicke states. Consequently, the nonlinear estimation strategy proposed in Eq. (3.79), with an appropriately adapted scaling factor corresponding to the inverse of the signal slope, is employed to filter out measurement outcomes $x \neq \pm\frac{N}{2}$, which are associated with

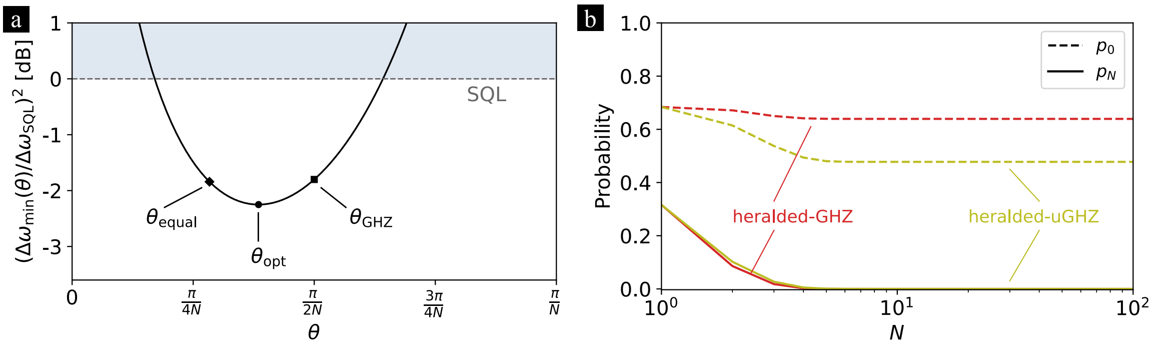

Figure 3.4: **Optimal rotation angle and probability of no-jump dynamics:** (a) Dependence of the minimal frequency estimation uncertainty $\Delta\omega_{\rm min}(\theta)$, scaled to the SQL, at optimal interrogation time $T_{\rm min}$ on the rotation angle θ in the interval $\theta_\uparrow = 0 \leq \theta \leq \theta_\uparrow = \frac{\pi}{N}$ for $N = 8$. Symbols indicate the three special cases discussed in the main text. The blue shaded area represents achievable frequency estimation uncertainties using uncorrelated atoms. (b) Probability of the no-jump dynamics p_0 (dashed) and the quantum trajectory involving N spontaneous decay events p_N (solid) at optimal interrogation time $T_{\rm min}$ as a function of the ensemble size N.

spontaneous decay events (cf. Sec. 3.7.4). Therefore, this protocol exhibits characteristics similar to the heralded-GHZ protocol. The corresponding phase estimation uncertainty is given by

$$(\Delta\phi_{\rm heralded-uGHZ}(T))^2 = \frac{e^{(\Gamma+\gamma)NT}}{4N^2}\left[1+\sqrt{e^{-N\Gamma T}+\left(1-e^{-\Gamma T}\right)^N}\right]^2, \tag{3.87}$$

which coincides with the QCRB of the uGHZ state. Fig. 3.2(b) shows that this 'heralded-uGHZ' protocol saturates the OQI for small ensemble sizes ($N \leq 4$) and achieves a constant gain of 2.25 dB compared to the SQL for $N \geq 5$, remaining close to the OQI for intermediate N. Analogous to the heralded-GHZ protocol, an explicit expression can be determined if the term $\left(1-e^{-\Gamma T}\right)^N$ is negligible, yielding

$$\Delta\omega_{\rm heralded-uGHZ} = \Delta\omega_{\rm SQL}\frac{\sqrt{1+2W(1/2\sqrt{e})}}{4\sqrt{e}W(1/2\sqrt{e})}, \tag{3.88}$$

where the gain of $\frac{\sqrt{1+2W(1/2\sqrt{e})}}{4\sqrt{e}W(1/2\sqrt{e})} < 1$ over the SQL corresponds to the observed 2.25 dB. Again, the asymptotically optimal SSS are advantageous for larger ensembles ($N > 87$).

3.7.4 Spontaneous decay events in GHZ(-like) states

In the preceding sections, we identified specific expressions in the conditional probabilities and estimation uncertainties with distinct numbers of spontaneous decay events. At this point, we aim to illustrate this association based on the framework of quantum trajectories and quantum jumps, outlined generally in Sec. 2.3.3 and applied to GHZ(-like) states in the presence of spontaneous decay in App. E.9.

To determine the aforementioned expressions associated with a particular number of spontaneous decay events for GHZ(-like) states, we consider the generic initial state

$$\rho_{\mathrm{in}} = \rho_{\mathrm{gg}}^{(N)} |{\downarrow}\rangle\langle{\downarrow}|^{\otimes N} + \rho_{\mathrm{ge}}^{(N)} |{\downarrow}\rangle\langle{\uparrow}|^{\otimes N} + \rho_{\mathrm{eg}}^{(N)} |{\uparrow}\rangle\langle{\downarrow}|^{\otimes N} + \rho_{\mathrm{ee}}^{(N)} |{\uparrow}\rangle\langle{\uparrow}|^{\otimes N}. \tag{3.89}$$

The dynamics according to the master equation, Eq. (3.4), leads to the time evolved state

$$\begin{aligned} \rho_{\mathrm{in}}(\phi, T) = \rho_{\mathrm{gg}}^{(N)} |{\downarrow}\rangle\langle{\downarrow}|^{\otimes N} + e^{-\frac{\Gamma N T}{2}} \left(\rho_{\mathrm{ge}}^{(N)} e^{iN\phi} |{\downarrow}\rangle\langle{\uparrow}|^{\otimes N} + \rho_{\mathrm{eg}}^{(N)} e^{-iN\phi} |{\uparrow}\rangle\langle{\downarrow}|^{\otimes N}\right) \\ + \rho_{\mathrm{ee}}^{(N)} \left(e^{-\Gamma T} |{\uparrow}\rangle\langle{\uparrow}| + \left[1 - e^{-\Gamma T}\right] |{\downarrow}\rangle\langle{\downarrow}|\right)^{\otimes N}. \end{aligned} \tag{3.90}$$

In the framework of quantum trajectories and quantum jumps, the state $\rho_{\mathrm{in}}(\phi, T)$ is expressed as a mixture

$$\rho_{\mathrm{in}}(\phi, T) = \sum_{k=0}^{\infty} p_k(\phi, T) \rho_k(\phi, T), \tag{3.91}$$

where $\rho_k(\phi, T)$ denotes the normalized state involving k quantum jumps occurring with probability $p_k(\phi, T)$. For spontaneous decay, at most N quantum jumps can occur, as this scenario would map the collective excited state $|{\uparrow}\rangle^{\otimes N}$ to the collective ground state $|{\downarrow}\rangle^{\otimes N}$. Thus, the mixture in Eq. (3.91) contains $N+1$ terms with $k \in \{0, \dots, N\}$.

Of particular interest for the GHZ(-like) protocols investigated in this thesis is the 'no-jump' dynamics, characterized by the absence of any spontaneous decay events. This contribution is determined by

$$\begin{aligned} \rho_0(\phi, T) = \frac{1}{p_0(\phi, T)} \Big[\rho_{\mathrm{gg}}^{(N)} |{\downarrow}\rangle\langle{\downarrow}|^{\otimes N} + e^{-\frac{\Gamma N T}{2}} \left(\rho_{\mathrm{ge}}^{(N)} e^{iN\phi} |{\downarrow}\rangle\langle{\uparrow}|^{\otimes N} + \rho_{\mathrm{eg}}^{(N)} e^{-iN\phi} |{\uparrow}\rangle\langle{\downarrow}|^{\otimes N}\right) \\ + \rho_{\mathrm{ee}}^{(N)} e^{-\Gamma N T} |{\uparrow}\rangle\langle{\uparrow}|^{\otimes N} \Big]. \end{aligned} \tag{3.92}$$

Consequently, the subspace of the maximal Dicke states in the time evolved state described by Eq. (3.90), ultimately resulting in outcomes $x = \pm\frac{N}{2}$ for measurements of the observable X, is not solely governed by the no-jump dynamics, as the term $\rho_{\mathrm{ee}}^{(N)} \left(1 - e^{-\Gamma T}\right)^N |{\downarrow}\rangle\langle{\downarrow}|^{\otimes N}$ is not captured in $\rho_0(\phi, T)$. The probability of the no-jump dynamics reads

$$p_0(\phi, T) = \rho_{\mathrm{gg}}^{(N)} + \rho_{\mathrm{ee}}^{(N)} e^{-\Gamma N T}. \tag{3.93}$$

In contrast, states in the expansion Eq. (3.91) with $k > 0$ involve k spontaneous decay events and are given by

$$\rho_k(\phi, T) = \frac{\rho_{\mathrm{ee}}^{(N)}}{p_k(\phi, T)} e^{-\Gamma T(N-k)} \left(1 - e^{-\Gamma T}\right)^k \mathcal{P}\left(|{\downarrow}\rangle\langle{\downarrow}|^{\otimes k} \otimes |{\uparrow}\rangle\langle{\uparrow}|^{\otimes N-k}\right), \qquad (3.94)$$

where the permutation operator $\mathcal{P}$ generates the $\binom{N}{k}$ distinct permutations of the state $|{\downarrow}\rangle\langle{\downarrow}|^{\otimes k} \otimes |{\uparrow}\rangle\langle{\uparrow}|^{\otimes N-k}$, with k particles in the ground state and $N-k$ particles in the excited state. The corresponding probabilities of dynamics with $k > 0$ decay events read

$$p_k(\phi, T) = \rho_{\mathrm{ee}}^{(N)} \binom{N}{k} e^{-\Gamma T(N-k)} \left(1 - e^{-\Gamma T}\right)^k \qquad (3.95)$$

and are directly connected to the conditional probabilities associated with measurement outcomes $x \neq \pm\frac{N}{2}$ in the GHZ(-like) protocols investigated in the previous sections (cf. Eq. (3.81)).

In particular, the scenario of N spontaneous decay events occurs with probability

$$p_N(\phi, T) = \rho_{\mathrm{ee}}^{(N)} \left(1 - e^{-\Gamma T}\right)^N \qquad (3.96)$$

and results in the system being in the collective ground state $|{\downarrow}\rangle^{\otimes N}$. Therefore, to be precise, the nonlinear estimator in Eq. (3.79) does not exclusively select the no-jump dynamics, but additionally takes the scenario involving N spontaneous decay events into account. However, the probability of this event becomes increasingly unlikely for larger ensemble sizes N. In particular, this contribution can be effectively disregarded already for $N \geq 5$, as shown in Fig. 3.4(b). Consequently, both the heralded-GHZ and heralded-uGHZ protocols achieve their maximal gain of 1.8 dB and 2.25 dB over the SQL, respectively, once the scenario of N spontaneous decay events becomes negligibly unlikely and thus, the nonlinear estimator in Eq. (3.79) indeed selects the no-jump dynamics $\rho_0(\phi, T)$. Furthermore, Fig. 3.4(b) illustrates that a higher initial population in the excited state increases the decoherence effects caused by spontaneoud decay, as discussed in Sec. 3.7.3. This is reflected in the reduced probability of the no-jump dynamics for the heralded-uGHZ protocol compared to the heralded-GHZ protocol.

3.7.5 Performance in atomic clocks

To investigate the robustness of the presented measurement and estimation schemes to spontaneous decay in a realistic scenario of frequency metrology, we perform numerical Monte Carlo simulations of the full feedback loop in an atomic clock and compare the results to the theoretical predictions. The Monte Carlo simulation implements the basic principles of an atomic clock, as described in Sec. 3.2. Further implementation details are provided in App. A and Ref. [3].

As discussed in Sec. 3.4.3, the long term stability of an atomic clock in a dead time-free scenario is well approximated by

$$\sigma_y(\tau) = \frac{1}{\omega_0} \frac{\Delta\phi(T)}{\sqrt{\tau T}} = \frac{\Delta\omega(T)}{\omega_0} \tag{3.97}$$

and thus corresponds to the frequency estimation uncertainty rescaled with ω_0. Consequently, in Fig. 3.5, we present our results in two complementary ways: Lower x-axis and left y-axis refer to general frequency estimation where the uncertainty is rescaled to be independent of the particular averaging time τ and lifetime $t_{\text{spont}} = 1/\Gamma$. Thus, it allows for an application to several experimental setups and atomic species as long as spontaneous decay remains the dominating decoherence effect. Upper x-axis and right y-axis illustrate results in an atomic clock for the particular example of Ca$^+$-ions with lifetime $t_{\text{spont}} = \frac{1}{\Gamma} \simeq 1.1\,\text{s}$ [184] and transition frequency $\omega_0 = 2\pi\nu_0 \simeq 2\pi \times 411.042\,\text{THz}$ [37, 185, 186]. Furthermore, we consider frequency fluctuations corresponding to a state-of-the-art clock laser. In particular, we assume a flicker noise limited laser with coherence time $Z \simeq 7.5\text{ s} \gg t_{\text{spont}}$ [88] (cf. Sec. 2.2.2). Results of numerical simulations (symbols) in comparison to theoretical predictions (lines) of the investigated protocols are shown in Fig. 3.5 for the representative cases of (a) $N = 4$ and (b) $N = 16$ particles, while the results and conclusions generally apply to other ensemble sizes as well. As Monte Carlo simulations are stochastic processes, resulting stabilities fluctuate around the average value. Overall, numerical simulations of all discussed interrogation schemes show very good agreement with theoretical predictions. Therefore, all schemes, including the heralded-GHZ and heralded-uGHZ protocols in particular, are robust and thus suited for realistic scenarios as in the context of atomic clocks. At interrogation times $T \gtrsim T_{\text{min}}$, fringe hops occur due to the impact of decoherence effects, where the feedback loop passes to an adjacent fringe resulting in the clock running systematically wrong and consequently spoiling the clock stability. Moreover, the comparison of $N = 4$ and $N = 16$ already indicates the transition between the optimality of GHZ-like protocols and squeezing protocols.

3.7.6 Unique features of GHZ(-like) states in the presence of spontaneous decay

Finally, we want to emphasize that both the measurement of the observable X (cf. Eq. (3.78)) and the application of the nonlinear flag estimator (cf. Eq. (3.79)) are specifically designed for GHZ(-like) states limited by spontaneous decay, achieving

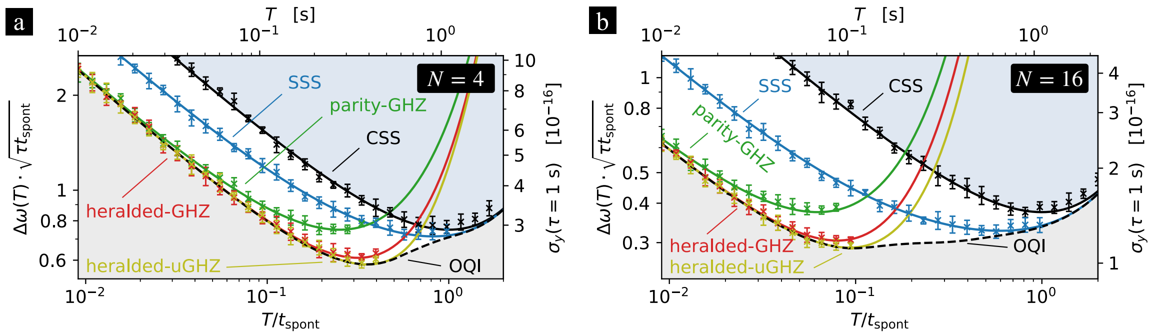

Figure 3.5: **Monte-Carlo simulations of the full feedback loop in an atomic clock:** Simulation results for (a) $N = 4$ and (b) $N = 16$ are displayed by symbols, while theoretical predictions are shown as lines. Data points denote the average over 10 independent clock runs. Error bars indicate the corresponding standard deviations. Upper x-axis and right y-axis illustrate results in an atomic clock for the particular example of Ca^+-ions with lifetime $t_{\text{spont}} = \frac{1}{\Gamma} \simeq 1.1$ s [184] and transition frequency $\omega_0 = 2\pi\nu_0 \simeq 411.042$ THz [37]. In each clock run, 10^7 cycles were performed and the corresponding Allan deviation was evaluated. The presented values are obtained by extrapolating the Allan deviation at $\tau = 1$ s based on the long term stability Eq. (3.97) at $\tau \gg 1$ s. The gray shaded area represents the inaccessible sensitivity region set by the OQI limit, while the blue shaded area indicates achievable frequency estimation uncertainties using uncorrelated atoms.

substantial enhancements over the SQL and approximating the OQI for small ensembles. Unfortunately, the underlying concepts cannot be easily transferred to other scenarios to obtain comparable improvements, as we will discuss below. In particular, we examine the impact of (i) the measurement, (ii) the initial state and (iii) the decoherence process.

(i) Investigating measurements for GHZ(-like) states, primarily two key aspects are essential. First, the measurement has to distinguish between different Dicke states to detect spontaneous decay events. In particular, the parity measurement, with its binary outcomes, does not satisfy this condition and thus is inadequate for this purpose, as it only indicates whether there is an even or odd number of particles in the ground state. Consequently, no estimator can be constructed which exclusively selects the no-jump term. Second, the phase has to be imprinted solely onto the maximal Dicke states, otherwise, phase information is lost when selecting the measurement outcomes $x = \pm\frac{N}{2}$, as done by the flag estimator. Both requirements are addressed by measurements of the observable X.

(ii) The implicit detection of spontaneous decay events solely based on the measurement outcomes x is a key aspect of the presented protocols with GHZ(-like) states. This feature originates from the superposition of only two Dicke states, which are well separated in terms of the quantum number M (cf. Fig. 3.6(a) and (b)). This separation allows to identify measurement outcomes $x \neq \pm\frac{N}{2}$ as indicators for spontaneous decay events. In contrast, without such separation, measurement outcomes cannot be uniquely associated with spontaneous decay events, preventing the detection of these quantum jumps and ultimately degrading sensitivity. Indeed, the GHZ state is not the only state that enables this capability. In principle, superpositions of multiple Dicke states can pursue a similar strategy, provided that there is negligible overlap in the distributions of each time-evolved Dicke state. Conversely, CSS exhibit a binomial-like distribution of Dicke states, preventing the unique identification of spontaneous decay events, as no separation of the distributions of the time-evolved Dicke states is ensured, as illustrated in Fig. 3.6(c) and (d). To identify spontaneous decay events for CSS would require to detect them explicitly, which is further discussed in Sec. 3.10.2. However, states featuring such distinct separation are typically highly entangled and, as indicated by Fig. 3.2(b), become less favorable for large ensembles due to their susceptibility to decoherence processes. In contrast, weakly entangled states, such as SSS with binomial(-like) distributions, benefit substantially from larger ensembles due to their resilience to decoherence effects and thus become asymptotically optimal.

(iii) In Ramsey interferometry, although entangling transformations – effectively generating correlated measurements – may be applied after the free evolution time, typically a projective spin measurement is performed in the end (cf. Eq. (3.78)), yielding the population difference. Consequently, only quantum jumps that affect the populations, such as spontaneous decay events, are detectable. Conversely, if the decoherence process only degrades the coherences over time, as in the case of dephasing, changes in the measurement statistics may originate from either the decoherence process or the phase evolution, without means to distinguish between them. To give an example, this ambiguity also becomes evident for the heralded-GHZ and heralded-uGHZ protocols. For dephasing, quantum jumps effectively manifest as random phase shifts between the ground and excited states of the particles. Hence, only the contrast of the phase information decreases, while the state remains in the subspace spanned by the maximal Dicke states (cf. Eq. (3.80) and Eq. (3.81) for $\Gamma = 0$). However, changes in the signal can likewise arise from variations in the phase ϕ, despite the fundamentally different nature of these processes. Consequently, in such cases, the changes in the measurement statistics cannot be uniquely attributed to either quantum jumps or variations in the phase, thereby compromising sensitivity.[7] In the worst-case scenario, this ambiguity can lead to a complete loss of the

---

[7] To be precise, the coherences likewise decrease for spontaneous decay and thus this particular effect of the decoherence process cannot be detected. However, this contribution originates from the continuous non-unitary time evolution (cf. App. E.9), while quantum jumps indeed can be detected, as discussed before. This feature represents the fundamental difference between spontaneous decay

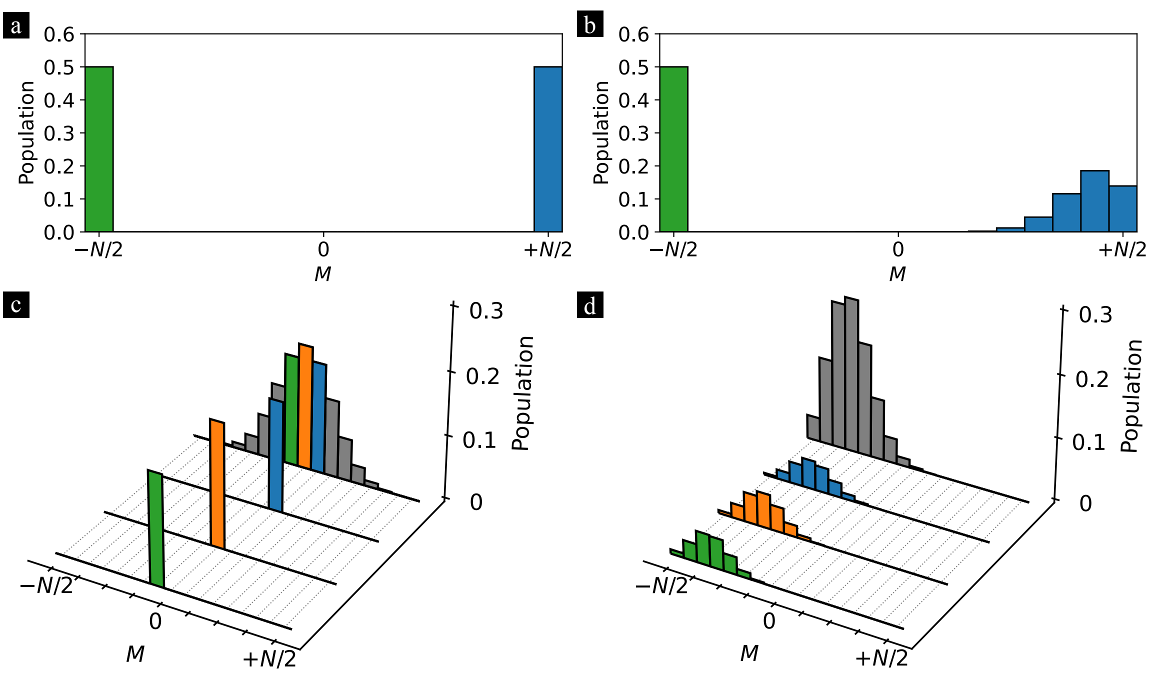

Figure 3.6: **Separation of Dicke states and detection of spontaneous decay events:** Population of the GHZ state (top) and the CSS (bottom) at $T = 0$ (left) and optimal interrogation time T_{min} (right). The GHZ state represents an equal superposition of the two maximal Dicke states with $M = \pm\frac{N}{2}$ (depicted in blue and green, respectively). Consequently, the distribution of the time evolved state remains distinctly separated with respect to M. In contrast, the CSS comprises a superposition of several adjacent Dicke states. At T_{min}, the contributions of three generic Dicke states, indicated by corresponding colors at $T = 0$, to the overall distribution (gray) are shown. In particular, these contributions exhibit a substantial overlap, preventing the implicit detection of spontaneous decay events.

entanglement-induced enhancement, as observed for GHZ states in the presence of dephasing.

3.8 Crossover to regimes limited by dephasing

In the previous section, we primarily focused on scenarios where spontaneous decay with rate Γ imposed the dominant limitation. However, in experimental setups, additionally dephasing processes may be present. To evaluate the robustness of the presented protocols employing GHZ(-like) states in the presence of both individual and collective dephasing with rates γ and γ_c, respectively, we investigate the crossover between regimes dominated by spontaneous decay and those where dephasing becomes the primary limitation. In particular, we assess the minimal frequency estimation

---

and dephasing.

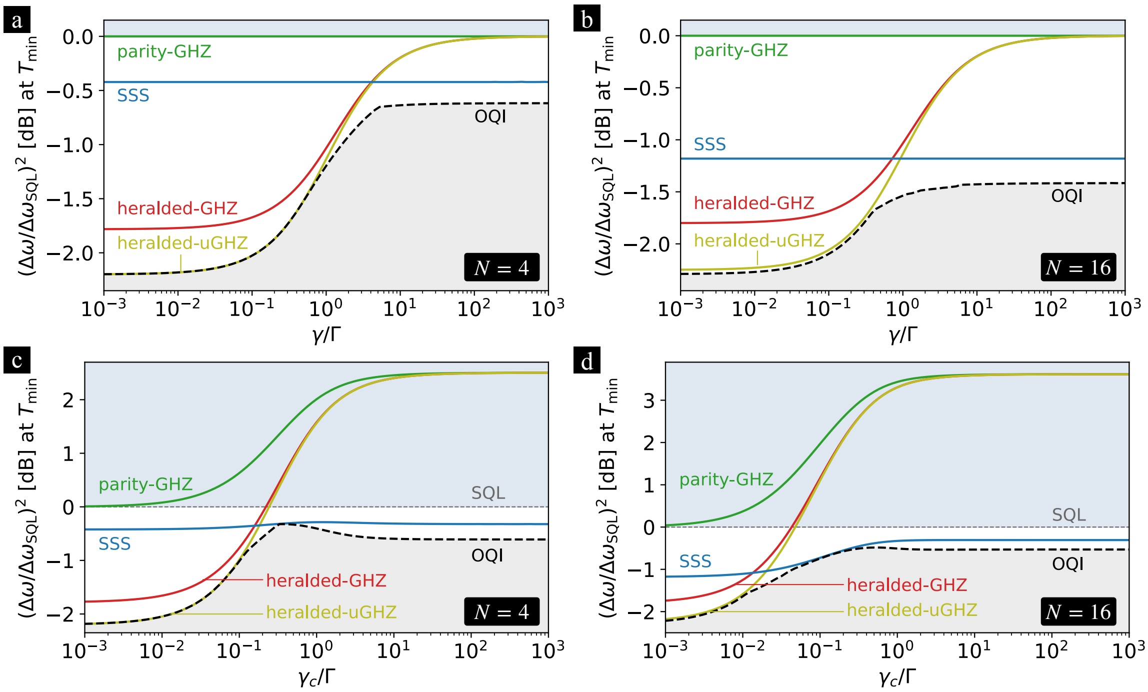

Figure 3.7: **Crossover to dephasing:** Crossover between regimes limited by spontaneous decay with rate Γ and (top) individual dephasing with rate γ and (bottom) collective dephasing with date γ_c. Minimal frequency estimation uncertainty $\Delta\omega_{\min}$, relative to the SQL, for (left) $N = 4$ and (right) $N = 16$ as a function of γ/Γ and γ/Γ, respectively. The ratio $\Delta\omega/\Delta\omega_{\mathrm{SQL}}$ is independent of the decoherence rates due to the comparison with the SQL.

uncertainty $\Delta\omega_{\min}$ relative to the SQL for a given ensemble size N, while systematically varying the ratios γ/Γ and γ_c/Γ, as shown in Fig. 3.7. Small ratios correspond to the regime where spontaneous decay is dominant, thereby reproducing the results of the previous section, while large ratios represent regimes dominated by dephasing. As before, we focus on small ensembles, where the OQI can be evaluated numerically and GHZ(-like) states perform close to it due to the detection and mitigation of spontaneous decay events. This results in a pronounced difference between both regimes since quantum jumps arising from dephasing cannot be uniquely identified, as discussed in detail in the previous section. Consequently, the OQI demonstrates a significantly increased gain over the SQL in the regime dominated by spontaneous decay. For both types of dephasing, this enhancement diminishes with increasing ratios γ/Γ and γ_c/Γ, respectively, as the contribution of undetectable decoherence effects from dephasing grows. In contrast, for large ensembles ($N \gg 1$), weakly entangled states become optimal, as discussed in Sec. 3.7.6, and detecting quantum jumps becomes less relevant.

Individual dephasing— For individual dephasing and small ensembles, as illustrated in Fig. 3.7(a) and (b), the difference in the enhancement of the OQI over the SQL between both regimes is particularly pronounced. Surprisingly, the heralded-uGHZ protocol performs close to the OQI limit approximately until both decoherence processes contribute comparably, i.e. $\Gamma \simeq \gamma$. The sensitivity of SSS remains independent of the ratio γ/Γ, since spontaneous decay and individual dephasing affect projective spin measurements with a linear estimation strategy in the same way (cf. App. E.1.1). With increasing ensemble size, the enhancement of SSS over the SQL grows. Although SSS become optimal only in the asymptotic limit of large ensembles ($N \gg 1$), the gain of the OQI in the regime dominated by individual dephasing increases likewise. Consequently, the difference between the OQI in both regimes diminishes and the heralded-uGHZ protocol loses its optimality at slightly smaller ratios γ/Γ. For $\gamma \gtrsim \Gamma$, the sensitivity of the GHZ(-like) protocols converges towards the SQL, as they lose their advantage when individual dephasing becomes dominant, consistent with the findings in Ref. [149] for $\Gamma = 0$.

Collective dephasing— In comparison, GHZ(-like) states exhibit a substantially enhanced susceptibility to collective dephasing, as illustrated in Fig. 3.7(c) and (d). In particular, these states collapse N-times faster compared to individual dephasing (cf. App. E). As a result, the critical ratio at which the heralded-(u)GHZ protocols lose their optimality decreases accordingly with the ensemble size N and thus, GHZ(-like) states become unfavorable for large ensembles in the presence of collective dephasing. Furthermore, for $\gamma_c/\Gamma \gg 1$, the sensitivity does not even converge to the SQL – as it does for individual dephasing – but instead degrades substantially below the classical limit. Consequently, the heralded-uGHZ protocol performs close to the OQI limit only in the regime dominated by spontaneous decay $\Gamma \gg \gamma_c$, while losing its optimality already when $\Gamma > \gamma_c$. Moreover, the gain of SSS over the SQL diminishes with increasing ratio γ_c/Γ. In contrast to spontaneous decay and individual dephasing, the enhancement of SSS remains approximately independent of the ensemble size in the regime constrained by collective dephasing. Interestingly, while the gain of the OQI over the SQL diminishes with increasing γ_c/Γ, as discussed before, it unexpectedly exhibits a minimal enhancement in the crossover region before increasing again as collective dephasing becomes dominant. Although this gain remains smaller than in the contrary regime – where spontaneous decay imposes the primary limitation (i.e. $\gamma_c \ll \Gamma$) – this behavior differs fundamentally from the scaling observed under individual dephasing.

Phenomenologically, this can be understood as follows: For spontaneous decay and individual dephasing, the sensitivity is primarily determined by the degree of entanglement in the initial state. Although correlated measurements can enhance the sensitivity – by facilitating a higher entanglement depth in the initial state or by enabling phase information to be encoded onto particular Dicke states, as observed for the heralded-(u)GHZ protocol – they influence the frequency estimation uncertainty only implicitly. In contrast, for collective dephasing, the measurement explicitly affects the sensitivity by substantially increasing the dynamic range – primarily characterized by the optimal interrogation time $T_{\min}$. This qualitative distinction is already evident for CSS. While a conventional projective spin measurement suffices to saturate the QCRB in the presence of spontaneous decay and individual dephasing (cf. App E.2), this is not the case for collective dephasing, where a correlated measurement is required. This behavior is generically illustrated for $N = 8$ and $\Gamma = \gamma_c$ in Fig. 3.8(a). The QCRB of CSS exhibits a substantial enhancement compared to CSS with a projective spin measurement – which imposes the SQL – achieved at a longer optimal interrogation time $T_{\min}$. To demonstrate that this effect genuinely arises from collective dephasing, the QCRB of CSS is compared to the SQL as a function of the ratio γ_c/Γ in Fig. 3.8(b). Furthermore, the scaling of the minimal frequency estimation uncertainty $\Delta\omega_{\min}$ and the corresponding optimal interrogation time $T_{\min}$ with the ensemble size N in the regime where collective dephasing imposes the primary limitation ($\Gamma/\gamma_c \to 0$) are shown in Fig. 3.8(c) and (d), respectively. Interestingly, the maximal gain of the QCRB of CSS over the SQL is obtained for $N = 4$, whereas it decreases for larger ensembles. In contrast, the ratio of the optimal interrogation time for the QCRB of CSS and CSS with a projective spin measurements steadily increases with N.

Consequently, the crossover between the regimes where spontaneous decay and collective dephasing limit the sensitivity reflects a trade-off between enhancements through initial states and measurements, ultimately resulting in the particular scaling observed in Fig. 3.7(c) and (d). Since collective dephasing is phenomenologically similar to the treatment of laser noise within the Bayesian framework, it affects clock stability similarly and we refer to Chapter 4 for further details.

3.9 Conclusion

We have presented a protocol with low complexity that saturates the QCRB of GHZ states and thus, unexpectedly, results in a substantial enhancement of 1.8 dB compared to the SQL in the presence of spontaneous decay. This is achieved by a measurement and estimation scheme that allows to identify and exclude spontaneous decay events in the Ramsey sequence and thus implements an error detection and mitigation scheme to improve frequency metrology. Additionally, we have identified

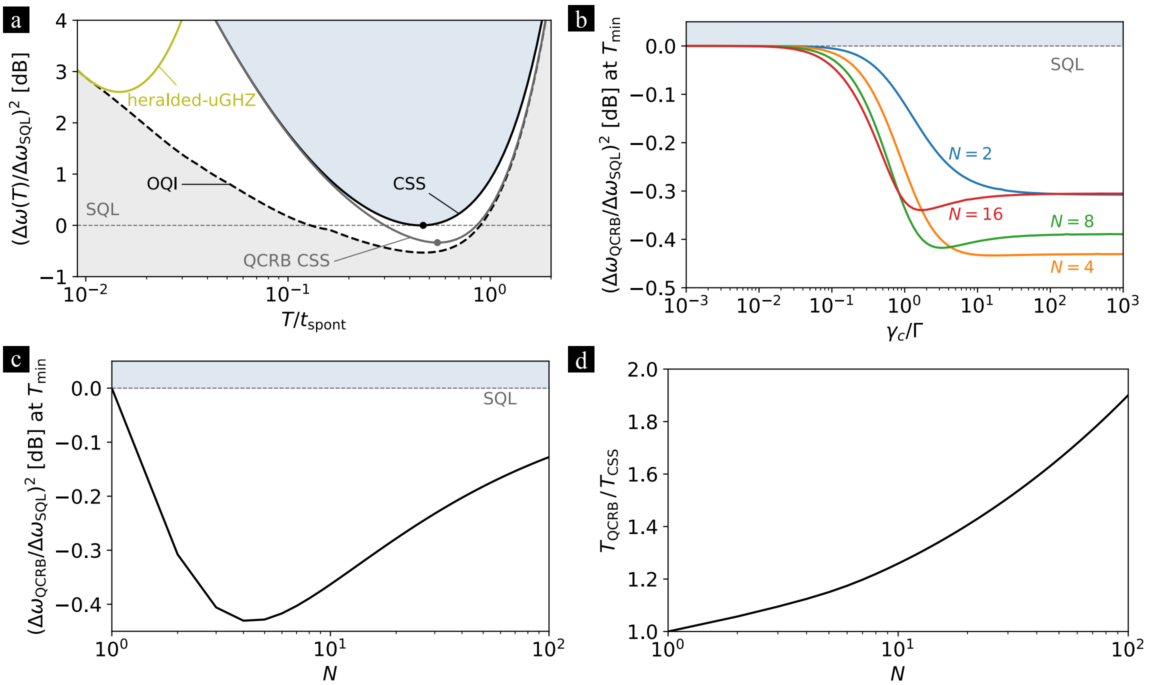

Figure 3.8: **QCRB of CSS in the presence of collective dephasing:** (a) Frequency estimation uncertainty $\Delta\omega(T)$ relative to the SQL for $N = 8$ and $\Gamma = \gamma_c$. The QCRB for CSS demonstrates a substantial enhancement compared to the SQL, represented by CSS with a projective spin measurement, achieved at a longer optimal interrogation time T_{min}. (b) Enhancement of the QCRB for CSS over the SQL at optimal interrogation time T_{min} as a function of the ratio γ_c/Γ. Unlike in the regime dominated by spontaneous decay, a projective spin measurement does not suffice to saturate the QCRB for CSS when collective dephasing becomes relevant. (c) Scaling of the minimal frequency estimation uncertainty of the QCRB for CSS relative to the SQL as function of the ensemble size N in the regime dominated by collective dephasing ($\Gamma = 0$). (d) Corresponding ratio of the optimal interrogation times of the QCRB for CSS T_{QCRB} and of CSS with a projective spin measurement T_{CSS}.

a GHZ-like protocol that saturates the OQI for small ensembles and closely approximates it for intermediate ensemble sizes. The observed 2.25 dB gain over the SQL arises from an unequal superposition of the two maximal Dicke states, which counteracts spontaneous decay during the free evolution time and can be generated by a minor modification of the GHZ state. Furthermore, the robustness of these protocols was shown through comprehensive Monte-Carlo simulations of atomic clocks, thereby paving the way for near-term implementations into experimental setups. Finally, we have investigated the susceptibility of the GHZ(-like) protocols to dephasing. While they remain robust to individual dephasing, approximating the OQI until the noise contributions from both decoherence processes become comparable, they exhibit a significantly higher susceptibility to collective dephasing, ultimately performing worse than the SQL.

GHZ(-like) states are an attractive experimental choice, since in a variation of the protocol involving the entanglement of Zeeman states of equal magnitude but opposite sign, they can be made first order magnetic field insensitive [4, 158], thus eliminate dephasing, the major source of decoherence [157]. Furthermore, the shorter optimum probe time compared to CSS reduces loss of contrast and time dilation shifts from motional heating of the ion crystal [12], thus improving the signal-to-noise ratio and the accuracy of such a clock. In addition to frequency metrology, the findings of this chapter can be applied to various precision measurements where phase estimation is limited by spontaneous decay.

3.10 Outlook

In the context of the comprehensive investigation of frequency metrology limited by spontaneous decay in this chapter, two primary open questions remain that are beyond the scope of this thesis.

First, as discussed before and shown in Fig. 3.2(b), while the heralded-uGHZ protocol approaches the OQI for small ensembles, it does not fully saturate it for $N > 4$. Consequently, the optimal states that do saturate the OQI have to be identified. For instance, the population distribution of the optimal input probe state for $N = 8$ is illustrated in Fig. 3.9(a). This state exhibits a uGHZ-like structure with an additional population in the Dicke state with $M = -1$. In particular, this state maintains a distinct separation in the distributions of each time-evolved Dicke state (cf. Sec. 3.7.6) even after the free evolution time, as depicted in Fig. 3.9(b). A detailed investigation of these optimal states could provide an intuitive physical explanation for their specific population distributions and the corresponding optimal measurements.

Second, the transition of the optimal Ramsey schemes, from GHZ-like protocols for small ensembles to SSS in the asymptotic limit, has to be examined. Specifically, the crossover from GHZ-like states, exhibiting a distinct separation of the Dicke states, to SSS with a binomial-like distribution (cf. Sec. 3.7.6) has to be investigated. Furthermore, it would be interesting to determine whether the OQI converges to the asymptotic limit like SSS, or if other optimal states can be identified in the transition regime. A first indication is provided by the evaluation of the QCRB for SSS, illustrated in Fig. 3.10. Here, the initial state corresponds to the optimal SSS determined with a projective measurement, while only the measurement is optimized. Already this simple approach reveals that SSS with a projective spin measurement are not optimal in the transition regime, suggesting the potential existence of superior

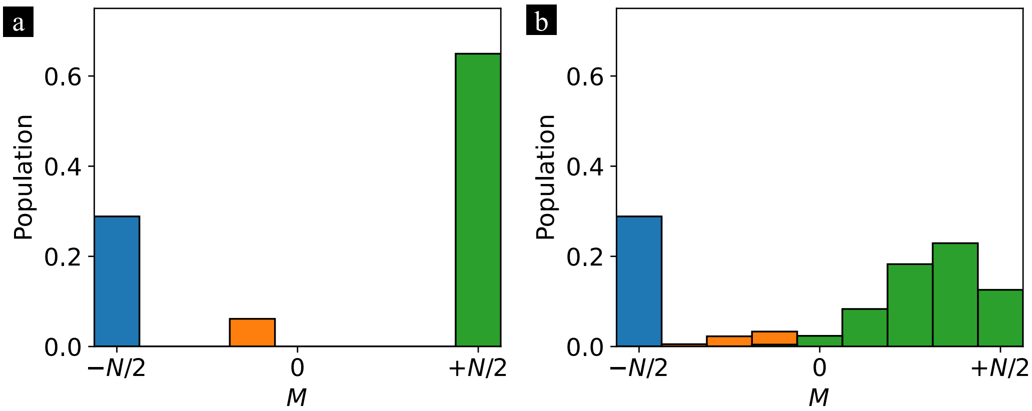

Figure 3.9: **Optimal initial state:** The population distribution of the optimal initial state for $N = 8$ at (a) $T = 0$ and (b) optimal interrogation time T_{min}. This state preserves a distinct separation of the three contributing Dicke states (depicted by different colors) during the free evolution time.

protocols. Overall, while the OQI appears to converge to the asymptotic limit for smaller ensembles than SSS, a comprehensive analysis requires the computation of the OQI for larger ensembles (cf. App. A).

Additionally, the model could be extended to incorporate further experimental noise processes. For instance, imperfections in initial state preparation or measurement errors could be taken into account. As explored in Refs. [5, 141], these effects can be modeled as decoherence processes – such as dephasing during the entangling gates. A simplified approach for implementing this in numerical simulations could involve an additional sampling stage that determines the success or failure of each Ramsey sequence.

Moreover, in the following, we address two particular questions raised by Shimon Kolkowitz during a discussion.

3.10.1 Incoherent pumping

Spontaneous decay describes the probabilistic transition of an excited atom to a lower energy state by emitting a photon (cf. Sec. 3.1). Conversely, incoherent pumping refers to the stochastic process where an atom absorbs a photon from an incoherent source, leading to a transition to a higher energy level. Hence, incoherent pumping can be interpreted as spontaneous excitation and thus represents the counterpart to spontaneous decay. Incoherent pumping can arise from the absorption of thermal photons present in cavity quantum electrodynamics (QED) due to its thermal fluctuations or field fluctuations. Additionally, blackbody radiation (BBR) is a ubiquitous source of incoherent pumping, characterized by the thermal electromagnetic radiation

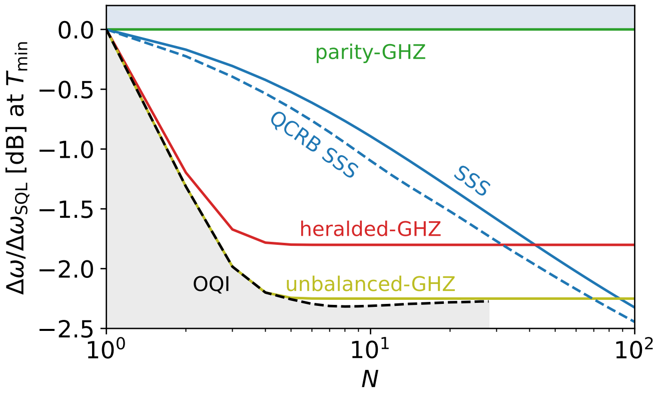

Figure 3.10: **QCRB of SSS:** Scaling of the relative frequency estimation uncertainty at the optimal interrogation time $T_{\min}$ with the ensemble size N. The ratio $\Delta\omega/\Delta\omega_{\mathrm{SQL}}$ is independent of the decay rate Γ due to the comparison with the SQL. The QCRB for SSS is shown to demonstrate that SSS with a projective spin measurement are suboptimal in the transition regime. While this suggests the potential for superior protocols, a comprehensive investigation is required.

emitted by all objects at non-zero temperatures. Rydberg atoms are particularly susceptible to incoherent pumping by blackbody radiation at room temperature, since the energy level spacing between adjacent Rydberg states often aligns with the peak intensity of the BBR spectrum. [12, 187–189]

In the following, we present the primary results, with detailed calculations provided in App. E.10. Considering a unitary phase evolution governed by the Hamiltonian $H = \omega S_z$, spontaneous decay with rate Γ and incoherent pumping with rate $\Gamma_\uparrow$, the dynamics of the system during the free evolution time T, represented by the quantum channel $\Lambda_{\phi,T}$, is described by a master equation of the form

$$\begin{aligned}\dot{\rho} &= -i\omega[S_z,\rho] + \frac{\Gamma}{2}\sum_{k=1}^{N}\left(2\sigma_-^{(k)}\rho\sigma_+^{(k)} - \sigma_+^{(k)}\sigma_-^{(k)}\rho - \rho\sigma_+^{(k)}\sigma_-^{(k)}\right)\\ &\quad + \frac{\Gamma_\uparrow}{2}\sum_{k=1}^{N}\left(2\sigma_+^{(k)}\rho\sigma_-^{(k)} - \sigma_-^{(k)}\sigma_+^{(k)}\rho - \rho\sigma_-^{(k)}\sigma_+^{(k)}\right)\\ &= -i\omega[S_z,\rho] + \frac{\Gamma}{2}\sum_{k=1}^{N}\left(2\sigma_-^{(k)}\rho\sigma_+^{(k)} - \sigma_{\mathrm{ee}}^{(k)}\rho - \rho\sigma_{\mathrm{ee}}^{(k)}\right)\\ &\quad + \frac{\Gamma_\uparrow}{2}\sum_{k=1}^{N}\left(2\sigma_+^{(k)}\rho\sigma_-^{(k)} - \sigma_{\mathrm{gg}}^{(k)}\rho - \rho\sigma_{\mathrm{gg}}^{(k)}\right).\end{aligned} \tag{3.98}$$

Importantly, the dissipative terms corresponding to spontaneous decay and incoherent pumping do not (super-)commute. Consequently, the dynamics cannot be separated and solved independently.

Analogous to our treatment of dephasing (cf. Sec. 3.8), we examine the crossover between the regimes dominated by either spontaneous decay or incoherent pumping. Specifically, we investigate the minimal frequency estimation uncertainty $\Delta\omega_{\mathrm{min}}$ relative to the SQL for a given ensemble size N as a function of the ratio $\Gamma_\uparrow/\Gamma$, as illustrated in Fig. 3.11. As before, we focus on small ensembles where the benefits of detecting and mitigating spontaneous decay events are more pronounced and the evaluation of the OQI remains feasible. In the regime where spontaneous decay is dominant, corresponding to ratios $\Gamma_\uparrow/\Gamma \ll 1$, the results of Sec. 3.7 are reproduced. Conversely, large ratios $\Gamma_\uparrow/\Gamma \gg 1$ represent the regime dominated by incoherent pumping. Indeed, this regime exhibits behavior precisely analogous to that observed for spontaneous decay. This feature can be explained through fundamental arguments: Although incoherent pumping and spontaneous decay are physically distinct processes, they are conceptually equivalent under an effective interchange of the clock basis $\{|\downarrow\rangle, |\uparrow\rangle\}$. Additionally, this equivalence is explicitly evident in Eq. (3.98), where the decoherence terms are identical except for the direction of the transitions. As a consequence, the results obtained for spontaneous decay are directly transferable to incoherent pumping. Furthermore, spontaneous decay and incoherent pumping have the same impact on the frequency estimation uncertainty for CSS, SSS and the parity-GHZ protocol. Interestingly, in the transition regime, the heralded-(u)GHZ protocols and the OQI exhibit a larger enhancement over the SQL compared to the regimes dominated by a single decoherence process. While the heralded-uGHZ protocol does not perfectly saturate the OQI for $N \geq 5$ in these regimes, it closely approaches it when $\Gamma \simeq \Gamma_\uparrow$. This can be explained as follows: In this regime, spontaneous decay events and incoherent pumping events induce quantum jumps in both directions with respect to the quantum number M. As these quantum jumps cannot be detected and mitigated for binomial(-like) distributions (cf. Sec. 3.7.6), CSS – which ultimately govern the SQL – exhibit increased susceptibility in the presence of both decoherence processes. In contrast, the specific measurement and estimation scheme of the heralded-(u)GHZ protocol enables the detection and mitigation of both types of quantum jumps, thus exhibiting greater resilience to the increased decoherence complexity. Furthermore, the GHZ state naturally becomes optimal for $\Gamma = \Gamma_\uparrow$, since both decoherence processes have the same impact, rendering an unbalanced population distribution disadvantageous.

3.10.2 Spontaneous decay events as erasure errors

As discussed in Sec. 3.7.6, only quantum jumps associated with decoherence processes affecting the populations are, in principle, detectable. Therefore, spontaneous decay events are potentially detectable, irrespective of the specific Ramsey sequence.

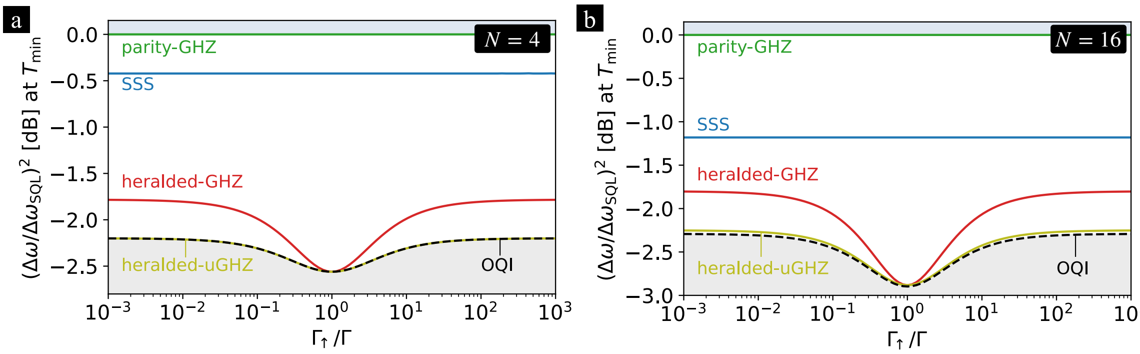

Figure 3.11: **Incoherent pumping:** Crossover between regimes limited by spontaneous decay with rate Γ and incoherent pumping with rate $\Gamma_\uparrow$. Minimal frequency estimation uncertainty $\Delta\omega_{\mathrm{min}}$, relative to the SQL, for (a) $N = 4$ and (b) $N = 16$ as a function of $\Gamma_\uparrow/\Gamma$. The ratio $\Delta\omega/\Delta\omega_{\mathrm{SQL}}$ is independent of the decoherence rates due to the comparison with the SQL.

However, the practicability and the experimental implementation of such detection strongly depend on the initial state and measurement, as elaborated in Sec. 3.7.6. Theoretically, detecting the emitted photons would allow for the identification of the decayed atoms. However, this would require a 4π-detector, which is unfortunately unrealistic in the contect of atomic clocks. Nevertheless, future experiments might enable the conversion of spontaneous decay events into erasure errors [190], building on recent proposals and demonstrations of error conversion techniques in various setups [191–198]. An erasure error refers to a noise process that takes the atom out of the clock space $\{|\uparrow\rangle, |\downarrow\rangle\}$ to an arbitrary third state $|-1\rangle$, which can be detected without perturbing the coherence within the clock space.[8] In the following, we explore the potential benefits of converting spontaneous decay events into erasure errors, building on the foundational concept introduced in Ref. [190] and applying this framework to spontaneous decay.

Due to the maximal entanglement inherent in GHZ(-like) states, even a single spontaneous decay event substantially degrades the coherence of the state, resulting in a complete loss of the imprinted phase information (cf. App. E.9). Therefore, for GHZ(-like) states, converting spontaneous decay events into erasure errors is ineffective. As a consequence, in the remainder of this section, we focus on the conventional Ramsey sequence employing CSS, as it allows for an analytical investigation.

Expressing the time evolved state $\rho_{\mathrm{in}}(\phi, T)$ as a mixture according to the framework of quantum trajectories and quantum jumps (cf. Eq. (3.91)) and employing the convexity of the QFI (cf. Sec. 3.5.2), the QFI of $\rho_{\mathrm{in}}(\phi, T)$ is bounded by

---

[8] While conceptually distinct, this is similar to atoms directly decaying to the state $|-1\rangle$. However, we focus on spontaneous decay within the clock space and subsequent error conversion.

$$\mathcal{F}_Q[\rho_{\mathrm{in}}(\phi, T)] \leq \sum_{k=0}^{N} p_k(\phi, T)\mathcal{F}_Q[\rho_k(\phi, T)], \tag{3.99}$$

where $\rho_k(\phi, T)$ denotes the state in the expansion involving k quantum jumps. Converting spontaneous decay events into erasure errors for CSS (cf. App. E.11), the frequency estimation uncertainty is determined accordingly by

$$(\Delta\omega(T))^2 \geq \frac{e^{\Gamma T} + 1}{2N\tau T}, \tag{3.100}$$

which is shown in Fig. 3.12(a). In the limit of $\Gamma \to 0$, or equivalently $T \to 0$, the frequency estimation uncertainty of CSS without error conversion is reproduced, as effectively no spontaneous decay events occur. In contrast, approaching T_{min}, error conversion facilitates a substantial enhancement, resulting in a significantly lower frequency estimation uncertainty. In particular, the gain increases for longer interrogation times $T \leq T_{\mathrm{min}}$, as the contribution of spontaneous decay becomes more pronounced. Furthermore, this scheme yields an optimal interrogation time approximately 25% longer than the excited-state lifetime t_{spont} of the atoms. As for the heralded-(u)GHZ protocols, the minimal frequency estimation uncertainty can be determined explicitly in terms of the Lambert-W function and is given by

$$(\Delta\omega_{\mathrm{min}})^2 \geq \frac{\Gamma}{2N\tau W(1/e)} = \frac{(\Delta\omega_{\mathrm{SQL}})^2}{2eW(1/e)}. \tag{3.101}$$

As a result, converting spontaneous decay events into erasure errors for CSS results in a constant enhancement of 1.8 dB, independent of the ensemble size N and equivalent to the heralded-GHZ protocol for $N \geq 5$, as illustrated in Fig. 3.12(b). Consequently, for small ensembles $N < 42$, this scheme achieves lower frequency estimation uncertainties than obtained with SSS (without error conversion).

In principle, the derived frequency estimation uncertainty represents a theoretical lower bound, and its saturability is not guaranteed – an aspect that is typical in local frequency estimation. Indeed, the convexity of the QFI for mixed states reflects the intrinsic uncertainty regarding the exact state of the system. However, converting spontaneous decay events into erasure errors effectively allows to determine the exact state within the mixture, thereby enabling the achievement of this lower bound in this particular scenario, thus yielding equality in the equations above.

At first glance, it might seem counterintuitive that the presented scheme performs below the OQI in certain regimes (cf. Fig. 3.12). However, this apparent discrepancy arises from the differing assumptions in both approaches. The OQI is evaluated within

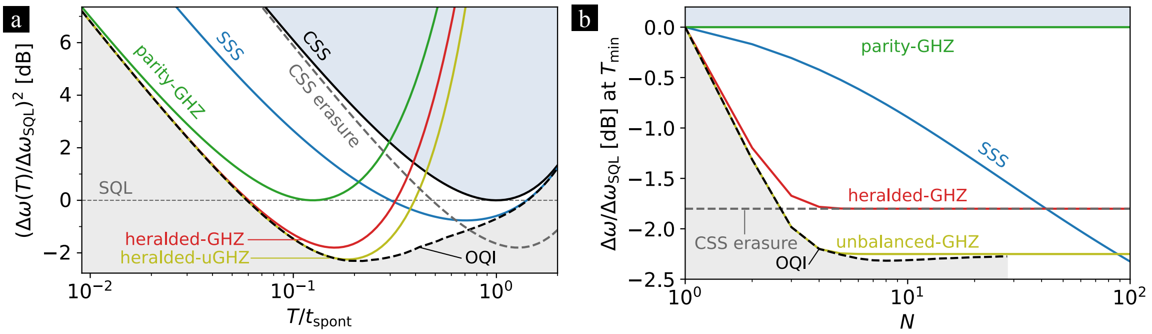

Figure 3.12: **Conversion of spontaneous decay events into erasure errors:** (a) Generic frequency estimation uncertainty $\Delta\omega(T)$ relative to the SQL for $N = 8$. The interrogation time is rescaled by the excited-state lifetime of the atoms $t_{\mathrm{spont}} = 1/\Gamma$. Conversion of spontaneous decay events into erasure errors for CSS (dashed gray) significantly reduces the susceptibility to the impact of spontaneous decay and thus achieves a lower frequency estimation uncertainty than the conventional Ramsey sequence (solid black). (b) Scaling of the relative frequency estimation uncertainty at the optimal interrogation time T_{min} with the ensemble size N. The ratio $\Delta\omega/\Delta\omega_{\mathrm{SQL}}$ is independent of the decay rate Γ due to the comparison with the SQL. Conversion of spontaneous decay events into erasure errors for CSS (dashed gray) results in a constant gain of 1.8 dB over the SQL, independent of N.

the master equation framework for decoherence processes (cf. Sec. 2.3.3), which exclusively considers the two clock basis states of the particles for the dynamics. In contrast, the presented scheme effectively leverages additional information by detecting spontaneous decay events through their conversion to erasure errors. Specifically, detecting the particles that decayed is effectively equivalent to using ancilla qubits. More intuitively, detecting the emitted photons – which is conceptually equivalent as discussed above – constitutes a measurement of environmental information, which, however, is explicitly traced out in the master equation approach and thus not accounted for in the OQI.

The presented concept can be readily extended to other initial states such as SSS, which, however, is beyond the scope of this outlook and typically requires numerical evaluation.

4

Bayesian frequency metrology limited by laser noise

4.1 Motivation and research problem

With state-of-the-art clock lasers reaching coherence times of several seconds [88], the excited-state lifetime of various clock candidates becomes the limiting time scale and spontaneous decay emerges as the dominant constraint (cf. Chapter 3). Nevertheless, the excited-state lifetimes of several clock candidates remain far beyond the regime of laser coherence times, ranging from minutes (Sr-atoms) to years (Yb^+-ions) [27]. Moreover, the impressive level of laser coherence is often degraded during propagation from the cavity to the location of the qubits. Consequently, many experimental setups are currently – and will likely remain – limited by laser noise.

Naively, frequency fluctuations and the associated laser noise could be regarded as a purely technical problem. However, stabilizing the laser is precisely the central objective of an atomic clock, making frequency fluctuations the primary measurand [11]. Disregarding laser noise as a mere technical issue would thus contradict the fundamental concept of atomic clocks and render the problem trivial. In principle, one might further ask how laser noise can impose a limiting factor although, by definition, it is the measurand – the quantity to be stabilized. To be precise, only the component of laser noise that cannot be corrected through interrogation of the atomic reference ultimately limits clock stability. Since Ramsey protocols have a finite range within which they can unambiguously interpret frequency fluctuations, errors arise when laser noise exceeds this range, fundamentally constraining stability. In the worst case, the feedback loop passes to an adjacent Ramsey fringe, resulting in the clock running systematically wrong and severely degrading the clock stability. Consequently, frequency metrology limited by laser noise features a trade-off: while longer interrogation times improve stability, they also amplify the impact of laser frequency fluctuations, imposing inherent limitations. Additionally, dead time in clock operation leads to undetected aliased frequency deviations, further degrading performance. Investigating the impact of frequency fluctuations is therefore essential for advancing next-generation clocks. To address this challenge, various approaches have been developed to account for frequency noise and to determine optimal interrogation schemes for specific experimental setups [91, 92, 199, 200]. In this endeavor, a particularly promising framework is the application of Bayesian estimation theory to frequency metrology – denoted as Bayesian frequency metrology – which incorporates laser noise directly into the theoretical model and leverages prior knowledge of frequency fluctuations for estimation [140, 141, 151, 201].

In recent years, operationally motivated echo protocols and variational quantum circuits have attracted significant interest, as they allow for a diverse range of interrogation schemes [5, 128, 139–143, 202–208]. In particular, these approaches have the potential to generate a high degree of entanglement while maintaining resilience to noise [5, 139–143] and thus represent a promising class of protocols for entanglement enhanced quantum frequency metrology. One-axis-twisting (OAT) [125] interactions serve as a versatile tool for implementing such protocols as they give rise to a variety of entangled states, ranging from spin-squeezed states (SSS) to GHZ states, and facilitate variational classes of generalized Ramsey protocols [5, 139–143]. Furthermore, OAT interactions are accessible in several setups as in ion traps via Mølmer-Sørensen gates [126–128], in tweezer arrays via Rydberg interactions [62, 129] or Bose-Einstein condensates via elastic collisions [130–133].

This chapter presents a progress report on frequency metrology tailored to optical atomic clocks employing Ramsey interrogation schemes primarily limited by laser noise. Specifically, we focus on single-ensemble clocks in which the atomic reference is periodically interrogated using the same protocol in each clock cycle. The objective is to outline potential advancements and challenges across various Ramsey interrogation schemes, effectively providing a theoretical guide for clock operation on different experimental platforms. In particular, we systematically examine a broad range of ensemble sizes and regimes defined by interrogation duration and dead time. To incorporate frequency fluctuations into the theoretical model, we employ a Bayesian framework for single-ensemble clocks, where the atomic reference is periodically interrogated using the same protocol in each clock cycle, while more general schemes are addressed in the outlook. To establish a theoretical foundation, we review Bayesian estimation theory and the corresponding fundamental bounds on clock stability. Additionally, we incorporate previous findings on clocks limited by laser noise, such as those in Refs. [91, 92], within the Bayesian framework and extend them in certain regimes. Building on pioneering work on variational quantum circuits in

Refs. [140–142], we identify optimal Ramsey schemes for various experimental platforms.

This chapter is structured in four parts. In the following, we provide a brief overview of each part and outline the primary results:

- Theoretical framework: To start with, Bayesian phase estimation theory is introduced in Sec. 4.2 and a hierachy of lower bounds on the estimation uncertainty is collected in Sec. 4.3, drawing an analogy to the local (frequentist) approach. In particular, the ultimate lower bound is derived, denoted as the optimal quantum interferometer (OQI), which represents the primary benchmark in this work. Additionally, in Sec. 4.4 the linear estimation strategy is discussed and the optimal Bayesian estimator is determined. In Sec. 4.5, we explicitly connect Bayesian phase estimation theory to frequency metrology by introducing the Allan deviation and establishing a relation between interrogation time and prior knowledge of the phase. Furthermore, we discuss general trade-offs in the context of Bayesian frequency metrology.

- Sec. 4.6: This section aims to saturate the ultimate lower bound imposed by the optimal quantum interferometer (OQI). Initially, the standard protocols, utilizing coherent spin states (CSS), spin-squeezed states (SSS) and GHZ states, are compared to the OQI. While GHZ states saturate the OQI at short interrogation times and SSS perform close to it at intermediate durations, substantial potential for enhancement remains across a broad range of interrogation times, particularly at long durations. To address this, especially considering small ensemble sizes characteristic of ion traps and tweezer arrays, we introduce generalized Ramsey protocols based on variational quantum circuits and identify optimal interrogation schemes. We demonstrate that in this regime, even low-depth quantum circuits suffice to approximate the OQI, which is crucial for maintaining reasonable operational complexity and thus enabling near-term experimental implementation. While the required circuit depth to achieve OQI stability increases with N, the performance gain diminishes with complexity, leading to a trade-off between reduced instability and increased experimental overhead, further motivating a focus on low circuit-complexity approaches.

- Sec. 4.7: To validate theoretical predictions on clock stability, we perform Monte Carlo simulations of the full feedback loop in an atomic clock, from which we can infer its long-term stability as quantified by the Allan deviation. In this context, fringe hops emerge as a significant limitation. In particular, for small ensembles

($N \lesssim 20$), characteristic of ion traps, fringe hops impose a stricter constraint on clock stability than the coherence time limit (CTL) of the local oscillator. As a consequence, for long interrogation times, variational protocols provide marginal to no advantage over SSS, while GHZ states remain optimal at short interrogation times. In contrast, for ensembles sizes in the regime of tweezer arrays ($N \gtrsim 20$), fringe hops and the CTL impose comparable limitations on clock stability at long interrogation times. Consequently, variational Ramsey protocols provide a substantial improvement over SSS. Nevertheless, the variation in stability across different clock runs – due to the stochastic nature of atomic clocks – and the relative reduction in enhancement with increasing circuit depth further supports the focus on low-depth quantum circuits.

- Sec. 4.8: We investigate the trade-off between quantum projection noise (QPN), the coherence time limit (CTL) and dead time effects by incorporating dead time into atomic clock operation within the framework of Bayesian frequency metrology. While clock stability for short dead times or small ensembles closely resembles the dead time-free scenario, dead time effects become increasingly significant with growing ensemble size or dead time, ultimately limiting clock performance. Following a general analysis, we examine specific examples with state-of-the-art parameters relevant to different experimental platforms, such as ion traps, tweezer arrays and lattice clocks. While GHZ states and SSS remain optimal for ion traps utilizing only a few ions, the potential gain from variational quantum circuits in tweezer arrays with several tens of atoms is substantially diminished. Specifically, SSS perform close to the optimal quantum interferometer (OQI) across a wide range of interrogation times, whereas variational quantum circuits offer an enhancement only at long interrogation times. However, this improvement is significantly reduced compared to the dead time-free case. Additionally, in the presence of dead time, fringe hops remain the dominant limitation in this regime, whereas in the dead time-free case, they constrain clock stability only at the same level as the CTL. As a consequence, SSS emerge as the preferred choice due to their robustness and practicality. For lattice clocks with hundreds or thousands of atoms, dead time effects strictly constrain clock stability and thus CSS suffice to approximate the OQI.

4.2 Bayesian phase estimation

The fundamental principles of atomic clocks and Ramsey interferometry are introduced in Sec. 3.2 and illustrated in Fig. 3.1, establishing the connection between frequency metrology and phase estimation theory.

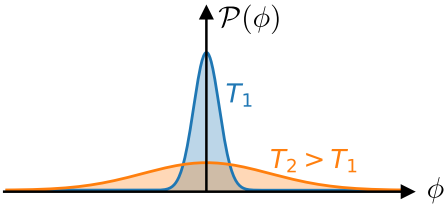

Figure 4.1: **Prior broadening:** Qualitative broadening of the prior distribution $\mathcal{P}(\phi)$ with longer interrogation times T, resulting from increased local oscillator noise.

In local (or frequentist) phase estimation (cf. Sec. 3.4.1), we have assumed that the phase ϕ is tightly centered around a fixed working point ϕ_0, such that $(\phi - \phi_0)^2 \ll 1$, and that the estimator is locally unbiased. Furthermore, probabilities are defined as the infinite-sample limit of an event. However, these assumptions are often not valid in the context of optical atomic clocks limited by laser noise. When the finite coherence time of the laser becomes the dominant limitation on clock stability, fluctuations in the accumulated phase during the free interrogation time become relevant and in principle can take arbitrary values $-\infty < \phi < \infty$. Additionally, these fluctuations require phase estimation based on single measurements to ensure unambiguous determination of ϕ, as the phase may change significantly between measurements of consecutive cycles, potentially preventing a unique estimation or assignment. This constraint makes asymptotic estimation, i.e. the collection and averaging of large amounts of data, impossible.

These phase fluctuations over different clock cycles, arising from the frequency noise of the local oscillator, can be modeled by a phase distribution $\mathcal{P}(\phi)$, depending on the particular noise profile. As the interrogation time T increases, the LO noise grows, causing the distribution to broaden, as illustrated in Fig. 4.1. To quantify the impact of these phase fluctuations and the resulting limitations to the phase estimation uncertainty, a commonly used cost function is the average mean squared error, defined as

$$\begin{aligned}(\Delta\phi)^2 &= \int_{-\infty}^{+\infty} \mathrm{d}\phi\, \mathcal{P}(\phi) \sum_x P(x|\phi)\, [\phi - \phi_{\mathrm{est}}(x)]^2 \\ &= \int_{-\infty}^{+\infty} \mathrm{d}\phi\, \mathcal{P}(\phi) (\Delta\phi_{\mathrm{QPN}})^2.\end{aligned} \tag{4.1}$$

It corresponds to the mean squared error (MSE) of the estimated phase $\phi_{\mathrm{est}}(x)$ with respect to the true phase value ϕ – the typical cost function of local phase estimation[1]

---

[1] For clarity, in this chapter we refer to the MSE $(\Delta\phi(T))^2$ (cf. Eq. (3.13)) as $(\Delta\phi_{\mathrm{QPN}})^2$, since it solely originates from the measurement and estimation uncertainty, and is therefore primarily governed by quantum projection noise (QPN).

$(\Delta\phi_{\mathrm{QPN}})^2$ – averaged over the phase distribution $\mathcal{P}(\phi)$. The average mean squared error reflects a global approach – extending local (frequentist) phase estimation – by incorporating all possible values of ϕ, which additionally makes unbiasedness redundant. Moreover, this approach is well-suited for arbitrary signals and estimation strategies, as it assesses the overall performance by averaging over the entire phase distribution, eliminating the need for specific assumptions about the signal structure or the estimation method. In general, for a proper estimation strategy, further information about the phase is gained through the measurement. Consequently, the average mean squared error is smaller than the variance $(\delta\phi)^2$ of the prior phase distribution $\mathcal{P}(\phi)$ and thus, ultimately is bounded by $0 \leq (\Delta\phi)^2 \leq (\delta\phi)^2$. In the limit of narrow phase distributions, where $\mathcal{P}(\phi)$ approximates a delta distribution centered at the optimal working point ϕ_0, the average mean squared error reduces to the MSE. Due to its global averaging, it is always lower bounded by the MSE evaluated at the optimal working point ϕ_0, where the MSE attains its maximum.

As argued above, local (frequentist) phase estimation is poorly suited in the regime where phase fluctuations around the optimal working point impose a substantial limitation. Although the accumulated phase is fixed for each interrogation sequence, it varies over different clock cycles and thus can be treated as a random variable, with the prior distribution $\mathcal{P}(\phi)$ reflecting the knowledge on the phase prior to any measurement. Consequently, Bayesian estimation theory represents the more appropriate framework. In Bayesian phase estimation, the posterior knowledge of ϕ, represented by the posterior distribution $P(\phi|x)$ and from which the estimator is ultimately determined, is updated according to Bayes theorem

$$P(\phi|x) = \frac{\mathcal{P}(\phi)P(x|\phi)}{P(x)} \tag{4.2}$$

based on the statistical model $P(x|\phi)$ and the prior distribution $\mathcal{P}(\phi)$. The marginal likelihood $P(x) = \int \mathrm{d}\phi\, \mathcal{P}(\phi)P(x|\phi)$ represents the probability of observing outcome x, averaged over all possible values of ϕ. Thus, it essentially provides a normalization of the posterior distribution. The interplay between prior information and measurement data already becomes evident at this stage. If $\mathcal{P}(\phi)$ varies slowly compared to $P(x|\phi)$, for example in the case of a flat prior or in the asymptotic limit of large ensembles, it has minimal influence on the posterior knowledge, and the statistical model primarily governs the inference strategy. Conversely, if the prior is sharply peaked, prior information dominates the estimation process and significantly shapes the posterior distribution.

Using Bayes theorem, Eq. (4.1) can be expressed in terms of the posterior distribution according to

$$(\Delta\phi)^2 = \sum_x P(x) \int_{-\infty}^{+\infty} \mathrm{d}\phi \, P(\phi|x) \, [\phi - \phi_{\text{est}}(x)]^2 \,. \tag{4.3}$$

In the remainder of this work, we estimate the accumulated phase within the framework of Bayesian estimation theory and quantify the phase estimation uncertainty based on this cost function. Furthermore, we review corresponding Bayesian bounds, to which we compare the performance of the investigated Ramsey protocols. As a consequence, we denote Eq. (4.3) – and thus likewise Eq. (4.1) due to its equivalence – as the Bayesian mean squared error (BMSE) throughout this work, following the literature such as Refs. [5, 140–142, 209, 210].

For the primary investigations in this chapter, we assume a unitary phase evolution through the quantum channel

$$\Lambda_{\phi,T}[\rho_{\text{in}}] = \mathcal{R}_z(\phi)\rho_{\text{in}}\mathcal{R}_z^{\dagger}(\phi) \tag{4.4}$$

with rotation $\mathcal{R}_z(\phi) = e^{-i\phi S_z}$, where $S_{x,y,z}$ denote the collective spin operators of N two level systems. Consequently, the quantum channel – and thus the statistical model $P(x|\phi)$ – is 2π-periodic with respect to the phase, i.e. $\Lambda_{\phi,T} = \Lambda_{\phi+2\pi,T}$. In this case, it is common to use a periodic cost function. However, in the context of atomic clocks, we explicitly adopt a global definition of the phase spanning $-\infty < \phi < \infty$, since $\phi + 2\pi k$ (with $k \in \mathbb{Z}$) originates from a different frequency deviation ω than ϕ, and thus has a distinct physical interpretation. This distinction proves particularly useful to quantify the coherence time limit of the local oscillator (cf. Sec. 4.3) and to discuss fringe hops (cf. Sec. 4.7) within the Bayesian framework. Furthermore, we assume a Gaussian prior distribution

$$\mathcal{P}(\phi) = \frac{1}{\sqrt{2\pi(\delta\phi)^2}} \exp\left(-\frac{\phi^2}{2(\delta\phi)^2}\right) \tag{4.5}$$

with zero mean and width $\delta\phi$, which is a reasonable approximation for the full feedback loop of an atomic clock [92], as we will motivate in Sec. 4.5.2.

4.3 Bounds in Bayesian phase estimation theory

The goal of Bayesian estimation is to minimize the cost function – the Bayesian mean squared error (BMSE). For a given prior distribution $\mathcal{P}(\phi)$, there are three control parameters to optimize: the initial state ρ_{in}, the measurement $\{\Pi_x\}$ and the estimation strategy $\phi_{\text{est}}(x)$. Based on these control parameters and building on

Refs. [68, 140, 151, 161, 162, 169, 200, 209, 211–221], we collect a hierarchy of lower bounds for the BMSE, analogous to the local estimation approach. The discussion in this section remains general, allowing for arbitrary prior distributions $\mathcal{P}(\phi)$ and quantum channels $\Lambda_{\phi,T}$, while specific assumptions and asymptotic results will be explicitly noted. In the following, we present the relevant bounds and key properties, while detailed proofs are provided in App. F.

4.3.1 Bayesian Cramér-Rao Bound (BCRB)

For a given initial state ρ_{in} and measurement $\{\Pi_x\}$, the Bayesian Cramér-Rao bound (BCRB) $(\Delta\phi_{\text{BCRB}})^2$ represents a lower bound on the BMSE $(\Delta\phi)^2$ and thus, implicates an optimization over all possible estimators ϕ_{est}. Assuming standard regularity conditions (cf. Eq. (3.24))

$$\sum_x \frac{\mathrm{d}P(x|\phi)}{\mathrm{d}\phi} = \frac{\mathrm{d}}{\mathrm{d}\phi}\sum_x P(x|\phi) = 0 \tag{4.6}$$

and vanishing of the prior at the boundaries

$$\lim_{\phi\to\pm\infty} \mathcal{P}(\phi) = 0, \tag{4.7}$$

the BCRB results from the van Trees inequality [211] and reads [212]

$$(\Delta\phi)^2 \geq (\Delta\phi_{\text{BCRB}})^2 = \min_{\phi_{\text{est}}}(\Delta\phi)^2 = \frac{1}{\overline{\mathcal{F}}+\mathcal{I}}. \tag{4.8}$$

Here, the measurement contribution is represented by the Fisher information averaged over the prior distribution

$$\begin{aligned}\overline{\mathcal{F}} \equiv \overline{\mathcal{F}}[\Lambda_{\phi,T}[\rho_{\text{in}}],\{\Pi_x\}] &= \int \mathrm{d}\phi\,\mathcal{P}(\phi)\mathcal{F}[\Lambda_{\phi,T}[\rho_{\text{in}}],\{\Pi_x\}] \\ &= \int \mathrm{d}\phi\,\mathcal{P}(\phi)\sum_x \frac{1}{P(x|\phi)}\left(\frac{\mathrm{d}P(x|\phi)}{\mathrm{d}\phi}\right)^2\end{aligned} \tag{4.9}$$

and

$$\mathcal{I} = \int \mathrm{d}\phi\,\frac{1}{\mathcal{P}(\phi)}\left(\frac{\mathrm{d}\mathcal{P}(\phi)}{\mathrm{d}\phi}\right)^2 \tag{4.10}$$

denotes the information contained in the prior knowledge, given by the Fisher information of the prior distribution. While $\mathcal{I} \geq 0$, the average Fisher information $\overline{\mathcal{F}}$ is upper bounded by its maximal value $\mathcal{F}_{\max} = \mathcal{F}[\Lambda_{\phi,T}[\rho_{\text{in}}],\{\Pi_x\}]$ achieved at the optimal working point ϕ_0, i.e. $\overline{\mathcal{F}} \leq \mathcal{F}_{\max}$. Hence, from Eq. (4.8) it is evident that the

BCRB in turn is lower bounded by the Cramér-Rao bound (CRB), the corresponding bound in local phase estimation

$$(\Delta\phi_{\mathrm{BCRB}})^2 \geq (\Delta\phi_{\mathrm{CRB}})^2 = \frac{1}{\mathcal{F}_{\mathrm{max}}}. \tag{4.11}$$

In contrast to the local approach, the optimal estimation strategy in the Bayesian framework can be derived explicitly as we will show in Sec. 4.4.

As a direct consequence of the convexity of the (classical) Fisher information (cf. Eq. (3.28)), mixing quantum states cannot increase the average Fisher information $\overline{\mathcal{F}}$ and thus does not decrease the BMSE.

For a Gaussian prior distribution, the prior information simplifies to $\mathcal{I} = (\delta\phi)^{-2}$. Moreover, while $\overline{\mathcal{F}}$ typically increases with the ensemble size, the prior information $\mathcal{I}$ is independent of N. Consequently, in the asymptotic limit of large N, the prior knowledge primarily contributes in the averaging of the Fisher information and we obtain $(\Delta\phi_{\mathrm{BCRB}})^2 \simeq \overline{\mathcal{F}}^{-1}$.

4.3.2 Bayesian Quantum Cramér-Rao Bound (BQCRB)

The Bayesian quantum Cramér-Rao bound (BQCRB) extends the (classical) Bayesian Cramér-Rao bound (BCRB) by including the optimization over all measurements $\{\Pi_x\}$. For a given initial state ρ_{in}, the BQCRB

$$(\Delta\phi_{\mathrm{BQCRB}})^2 = \min_{\{\Pi_x\}} (\Delta\phi_{\mathrm{BCRB}})^2 = \min_{\{\Pi_x\},\phi_{\mathrm{est}}} (\Delta\phi)^2 \tag{4.12}$$

provides a lower bound on the BCRB and thus establishes the hierachy

$$(\Delta\phi)^2 \geq (\Delta\phi_{\mathrm{BCRB}})^2 \geq (\Delta\phi_{\mathrm{BQCRB}})^2. \tag{4.13}$$

Naively, one might suggest to simply replace the average Fisher information $\overline{\mathcal{F}}$ in Eq. (4.8) by the average quantum Fisher information $\overline{\mathcal{F}_Q} = \int \mathrm{d}\phi\, \mathcal{F}_Q(\Lambda_{\phi,T}[\rho_{\mathrm{in}}])$. In general, however, the optimal measurement depends on ϕ and thus, this approach would effectively correspond to averaging over a set of measurements, each optimized for a particular phase value ϕ. By restricting the measurements – without loss of optimality – to the class of projection-valued measures (PVM) $\Pi_x = |x\rangle\langle x|$, with orthonormal eigenstates $|x\rangle$ of the observable X with eigenvalue x, satisfying $\langle x|x'\rangle = \delta_{x,x'}$, the BQCRB can be expressed as [151]

$$(\Delta\phi_{\mathrm{BQCRB}})^2 = (\delta\phi)^2 - \mathrm{Tr}\big(\overline{\rho} L^2\big). \tag{4.14}$$

Here, the double minimization over the measurement $\{\Pi_x\}$ and estimator ϕ_{est} is combined in a single quantity $L = \sum_x \Pi_x \phi_{\text{est}}(x)$. The optimal L is determined by the implicit equation

$$\overline{\rho}' = \frac{1}{2}\left(\overline{\rho}L + L\overline{\rho}\right), \tag{4.15}$$

where $\overline{\rho} = \int \mathrm{d}\phi\, \mathcal{P}(\phi)\Lambda_{\phi,T}[\rho_{\text{in}}]$ denotes the average state and $\overline{\rho}' = \int \mathrm{d}\phi\, \mathcal{P}(\phi)\Lambda_{\phi,T}[\rho_{\text{in}}]\phi$. The corresponding optimal measurement basis and estimator are given by the eigenbasis and eigenvalues of the operator L, respectively.

Interestingly, Eq. (4.14) and Eq. (4.15) have a similar structure as the quantum Fisher information (QFI) in local phase estimation (cf. Sec. 3.5.2). Indeed, assuming a unitary phase evolution according to Eq. (4.4) and a Gaussian prior distribution as defined in Eq. (4.5), the BQCRB can be related to the QFI $\mathcal{F}_Q[\overline{\rho}]$ of the average state $\overline{\rho}$ by [214]

$$(\Delta\phi_{\text{BQCRB}})^2 = (\delta\phi)^2\left[1 - (\delta\phi)^2\mathcal{F}_Q[\overline{\rho}]\right]. \tag{4.16}$$

In this case, the optimal measurement corresponds to the symmetric logarithmic derivative (SLD) of the QFI approach associated with $\mathcal{F}_Q[\overline{\rho}]$, and the optimal Bayesian estimator can be determined explicitly (cf. Sec. 4.4.). Evaluating the BQCRB thus becomes computationally equivalent to calculating the QFI of the average state $\overline{\rho}$. Indeed, the relation between the BMSE and the QFI in Eq. (4.16) is an interesting mathematical coincidence that is worth pointing out. Although this relation is only valid in the special case of single-parameter estimation and Gaussian prior distributions, it connects two conceptually different problems: On the one hand, global phase estimation, where the parameter range is characterized by the prior distribution, and on the other hand, local phase estimation based on a probe state that has been averaged over the prior distribution.

In analogy to classical phase estimation – despite optimizing over all possible measurements – mixing quantum states cannot enhance the estimation precision due to the convexity of the QFI (cf. Eq. (3.41)).

4.3.3 Optimal Quantum Interferometer (OQI)

As in the local approach, the optimal quantum interferometer (OQI) represents the ultimate lower bound of the BMSE, completing the hierachy

$$(\Delta\phi)^2 \geq (\Delta\phi_{\text{BCRB}})^2 \geq (\Delta\phi_{\text{BQCRB}})^2 \geq (\Delta\phi_{\text{OQI}})^2. \tag{4.17}$$

The OQI simultaneously optimizes over all three control parameters: the initial state ρ_{in}, measurement $\{\Pi_x\}$ and estimator ϕ_{est}:

$$\begin{aligned}(\Delta\phi_{\text{OQI}})^2 &= \min_{\rho_{\text{in}}}(\Delta\phi_{\text{BQCRB}})^2 = \min_{\rho_{\text{in}},\{\Pi_x\}}(\Delta\phi_{\text{BCRB}})^2 \\ &= \min_{\rho_{\text{in}},\{\Pi_x\},\phi_{\text{est}}}(\Delta\phi)^2.\end{aligned} \tag{4.18}$$

Unfortunately, no general expressions for the OQI sensitivity for arbitrary ensemble sizes are available, instead, they require complex numerical optimization procedures. In this context, we present an iterative optimization algorithm that facilitates efficient computation for small ensembles. Furthermore, we introduce the coherence time limit (CTL) and examine the asymptotic regime of large ensembles ($N \gg 1$).

Iterative optimization algorithm— In the following, we outline an algorithm introduced in Refs. [151, 170], which iteratively optimizes the initial probe state ρ_{in} and measurement $\{\Pi_x\}$, and enables an efficient computation for ensembles with up to several hundreds of particles. However, numerical optimization becomes challenging as the ensemble size $N \gg 1$ increases and approaches the asymptotic limit. This closely resembles the algorithm presented in Sec. 3.5.3 within the local framework, but is specifically tailored to Bayesian phase estimation theory.

For a given input probe state ρ_{in}, the optimal projective measurement and estimation strategy L can be determined according to the previous discussion on the BQCRB (cf. Sec. 4.3.2). Conversely, for a given L, the optimal ρ_{in} can be evaluated as follows: Rewriting the BMSE by identifying $L = \sum_x \Pi_x \phi_{\text{est}}(x)$ yields

$$(\Delta\phi)^2 = (\delta\phi)^2 + \operatorname{Tr}\left(\int \mathrm{d}\phi\, \mathcal{P}(\phi)\Lambda_{\phi,T}[\rho_{\text{in}}](L^2 - 2\phi L)\right). \tag{4.19}$$

Defining the adjoint quantum channel $\Lambda^\dagger_{\phi,T}$ as in the local approach (cf. Eq. (3.63)), i.e. through $\operatorname{Tr}(\Lambda_{\phi,T}[\rho]A) = \operatorname{Tr}\left(\rho\Lambda^\dagger_{\phi,T}[A]\right)$ for arbitrary operators A, the BMSE becomes

$$(\Delta\phi)^2 = (\delta\phi)^2 + \operatorname{Tr}\left(\rho_{\text{in}}\int \mathrm{d}\phi\, \mathcal{P}(\phi)\Lambda^\dagger_{\phi,T}[L^2 - 2\phi L]\right). \tag{4.20}$$

Consequently, the optimal input probe state $\rho_{\text{in}} = |\psi_{\text{in}}\rangle\langle\psi_{\text{in}}|$ is pure and corresponds to the eigenvector $|\psi_{\text{in}}\rangle$ of the operator $\int \mathrm{d}\phi\, \mathcal{P}(\phi)\Lambda^\dagger_{\phi,T}[L^2 - 2\phi L]$ associated with its most negative eigenvalue. In the iterative algorithm, starting from an arbitrary state, repeatedly the optimal measurement and the corresponding optimal probe state are determined iteratively until the BMSE converges to the OQI.

Coherence time limit (CTL)— Considering a 2π-periodic quantum channel with respect to the phase ϕ (cf. Eq. (4.4)), the OQI allows for unambiguous phase estimation within the range $[-\pi, +\pi]$. However, for sufficiently broad prior distributions, the phase ϕ may exceed this invertible regime and an estimation error of $(2\pi)^2$ is accumulated, associated with transitions between adjacent Ramsey fringes. Although the Bayesian framework naturally accounts for this crossover, it is nevertheless instructive to examine their contribution separately. For a Gaussian prior distribution, the estimation error associated with these events can be modeled by

$$(\Delta\phi_{\mathrm{OQI}}^{\mathrm{CTL}})^2 = 4\pi^2 \left[1 - \mathrm{erf}\left(\frac{\pi}{\sqrt{2}\delta\phi}\right)\right], \tag{4.21}$$

where $\mathrm{erf}(z)$ denotes the error function. In the context of an atomic clock, in this regime of long interrogation times, the coherence time of the local oscillator will become relevant and ultimately limits the clock stability. Consequently, we will denote Eq. (4.21) as the coherence time limit (CTL) of the OQI.

Asymptotic limit— In the asymptotic limit ($N \gg 1$), assuming unitary phase evolution as described by Eq. (4.4) and restricting to the invertible range $[-\pi, +\pi]$, it has been shown for arbitrary prior distributions that the ultimate lower bound is given by [209, 214–216]

$$(\Delta\phi_{\pi\mathrm{HL}})^2 = \frac{\pi^2}{N^2}. \tag{4.22}$$

In the absence of decoherence, this asymptotic limit reflects Heisenberg scaling with an additional factor of π, and is therefore referred to as the π-corrected Heisenberg limit (πHL). Intuitively, the πHL can be interpreted as the maximal estimation error associated with estimating a phase within $[-\pi, +\pi]$ using $N + 1$ evenly spaced measurement outcomes. Additionally taking into account the estimation error outside of the invertible range, as modeled by Eq. (4.21), the overall asymptotic estimation error for the OQI reads

$$\begin{aligned}(\Delta\phi_{\mathrm{OQI}}^{\mathrm{asym}})^2 &= (\Delta\phi_{\pi\mathrm{HL}})^2 + (\Delta\phi_{\mathrm{OQI}}^{\mathrm{CTL}})^2 \\ &= \frac{\pi^2}{N^2} + 4\pi^2 \left[1 - \mathrm{erf}\left(\frac{\pi}{\sqrt{2}\delta\phi}\right)\right].\end{aligned} \tag{4.23}$$

This result combines the fundamental limit set by the πHL with the contributions from phase estimation errors associated with transitions between Ramsey fringes, offering a comprehensive characterization of the OQI performance in the asymptotic regime. Notably, this bound can be saturated asymptotically by the phase operator based interferometer (POI) [140, 200, 215–221] (cf. App. F.3.3).

4.4 Estimators

Based on a statistical model $P(x|\phi)$ – defined by an initial state ρ_{in}, free evolution $\Lambda_{\phi,T}$ and measurement $\{\Pi_x\}$ according to Eq. (3.2) – various estimation strategies can be applied. In this chapter, we focus on two such strategies: the linear estimator and the optimal Bayesian estimator. The linear estimator is renowned for its simplicity and is both theoretically and experimentally commonly used and well understood. It often arises naturally in a local approach (i.e. for a narrow prior distribution and linear error propagation), where it is the standard choice (cf. Sec. 3.5.1). In contrast, the optimal Bayesian estimator – as the name suggests – achieves the best possible performance in Bayesian phase estimation. Explicit derivations are provided in App. F.

4.4.1 Linear estimator

The linear estimator is defined by

$$\phi_{\text{est}}^{\text{linear}}(x) = a \cdot x, \tag{4.24}$$

with scaling factor $a \in \mathbb{R}$. As discussed in detail in Sec. 3.5.1 and App. D.3, it originates from the method of moments in local phase estimation theory. In this context, assuming an unbiased estimator and small deviations from the optimal working point ϕ_0, the signal can be approximated linearly and the phase estimation uncertainty arises from quantum projection noise (QPN) (cf. Eq. (3.32))

$$\Delta\phi_{\text{QPN}} = \frac{\Delta X(\phi)}{|\partial_\phi \langle X(\phi)\rangle|}\bigg|_{\phi=\phi_0}. \tag{4.25}$$

This local result is obtained in the limit of narrow prior distributions ($\delta\phi \to 0$) around the optimal working point ϕ_0 and by choosing the particular scaling factor $a = \left(\partial_\phi \langle X(\phi)\rangle|_{\phi=\phi_0}\right)^{-1}$, corresponding to the inverse slope of the signal at ϕ_0.

In the Bayesian framework, however, this approach is poorly suited. First, the assumption of narrow prior distributions fails for realistic fluctuations of the phase, as discussed before. Second, the prior information explicitly influences the cost function and thus, the scaling factor a likewise has to depend on the prior distribution. For an arbitrary prior distribution with zero mean $\int \mathrm{d}\phi\, \mathcal{P}(\phi)\phi = 0$ and variance $(\delta\phi)^2 = \int \mathrm{d}\phi\, \mathcal{P}(\phi)\phi^2$, the optimal scaling factor and corresponding BMSE are given by

$$a = \frac{\int \mathrm{d}\phi\, \mathcal{P}(\phi)\phi \langle X(\phi)\rangle}{\int \mathrm{d}\phi\, \mathcal{P}(\phi) \langle X^2(\phi)\rangle} \tag{4.26}$$

$$(\Delta\phi)^2 = (\delta\phi)^2 - \frac{\left[\int \mathrm{d}\phi\, \mathcal{P}(\phi)\phi \langle X(\phi)\rangle\right]^2}{\int \mathrm{d}\phi\, \mathcal{P}(\phi) \langle X^2(\phi)\rangle}. \tag{4.27}$$

As in the local approach, the linear estimator and its estimation error depend only on the first and second moments of the observable X, which typically are easier to evaluate than the full statistical model $P(x|\phi)$. This simplicity makes the linear estimator a practical choice for phase estimation. Nevertheless, despite its advantages and reliable performance in several situations, the linear estimation strategy generally does not saturate the BCRB and thus is not optimal.

4.4.2 Optimal Bayesian estimator

In contrast to local phase estimation, where the Cramér-Rao bound can generally only be approximated in the infinite-sample limit using the maximum-likelihood estimator [6], the optimal estimator in Bayesian phase estimation can be derived explicitly [200]

$$\phi_{\text{est}}^{\text{opt}}(x) = \int \mathrm{d}\phi\, P(\phi|x)\phi, \tag{4.28}$$

saturating the BCRB with single shot measurements. This estimator corresponds to the average phase with respect to the posterior distribution $P(\phi|x)$, which can be expressed in terms of the statistical model $P(x|\phi)$ and prior distribution $\mathcal{P}(\phi)$ according to Bayes theorem Eq. (4.2). As a consequence, the optimal Bayesian estimator can be highly non-linear. The associated BMSE is given by

$$(\Delta\phi)^2 = (\delta\phi)^2 - \sum_x \frac{\left[\int \mathrm{d}\phi\, \mathcal{P}(\phi)P(x|\phi)\phi\right]^2}{P(x)}. \tag{4.29}$$

Although this resembles the structure of Eq. (4.27), the BMSE for the optimal Bayesian estimator explicitly depends on the statistical model, rather than merely on the first and second moments of the observable. Additionally, for the optimal Bayesian estimator, Eq. (4.3) reduces to the average posterior variance. Since the optimal Bayesian estimator saturates the BCRB, and thus minimizes the BMSE with respect to all estimation strategies, it is commonly referred to as the minimal mean squared error (MMSE) estimator. However, we continue to use the term ‘optimal Bayesian estimator’ throughout this work for consistency and clarity.

4.5 Bayesian frequency metrology

While the general relationship between frequency metrology and phase estimation was introduced in Sec. 3.2, here we establish an explicit connection within the Bayesian framework through the Allan deviation and by relating the interrogation time to the prior width. Furthermore, we discuss the resulting trade-offs qualitatively in the context of frequency metrology.

4.5.1 Clock stability and Allan deviation

The long-term stability of an atomic clock is quantified by the Allan deviation $\sigma_y(\tau)$ [11, 84–86], introduced in detail in Sec. 2.1, characterizing the fluctuations of fractional frequency deviations $y(t) = \omega(t)/\omega_0$ averaged over $\tau \gg T_C = T + T_D$. Here, the total cycle duration T_C accounts for the interrogation time T and any potential dead time T_D, arising from preparation steps and application of the feedback. In local frequency metrology – assuming short interrogation times leading to narrow prior distributions – the Allan deviation is well approximated by (cf. Sec. 3.4.3)

$$\sigma_y(\tau) = \frac{1}{\omega_0} \frac{\Delta\phi_{\mathrm{QPN}}}{T} \sqrt{\frac{T_C}{\tau}}. \tag{4.30}$$

In this context, clock stability is determined by the cost function in the local approach, the phase estimation uncertainty $\Delta\phi_{\mathrm{QPN}}$– which is commonly simply referred to as quantum projection noise (QPN) – characterizing the uncertainty associated with the measurement process.

However, the BMSE in Bayesian frequency metrology – which leverages Bayesian phase estimation strategies tailored to frequency metrology and directly includes the frequency fluctuations into the theoretical model – incorporates both measurement uncertainty and prior knowledge, preventing a straightforward substitution of $\Delta\phi_{\mathrm{QPN}}$ by $\Delta\phi$. To isolate the measurement contribution from the prior knowledge $\mathcal{I}$, we introduce the effective measurement uncertainty motivated by the Bayesian Cramér-Rao Bound (BCRB) in Eq. (4.8) and following Refs. [92, 140]

$$\Delta\phi_M = \left(\frac{1}{(\Delta\phi)^2} - \mathcal{I} \right)^{-1/2} = \left(\frac{1}{(\Delta\phi)^2} - \frac{1}{(\delta\phi)^2} \right)^{-1/2}, \tag{4.31}$$

where $\mathcal{I} = (\delta\phi)^{-2}$ for a Gaussian distribution. Hence, $\Delta\phi_M$ quantifies the quality of the measurement process in a single interrogation cycle. According to the discussion of the BCRB in Sec. 4.3.1, the effective measurement uncertainty is lower bounded by the average Fisher information $(\Delta\phi_M)^2 \geq 1/\overline{\mathcal{F}}$ and thus, a connection to the local approach can be established, yielding

$$(\Delta\phi_M)^2 \geq \frac{1}{\overline{\mathcal{F}}} \geq (\Delta\phi_{\mathrm{CRB}})^2 = \frac{1}{\mathcal{F}_{\max}}. \tag{4.32}$$

As a consequence, the clock stability in local frequency metrology – quantified by Eq. (4.30) – emerges in the limit of narrow prior distributions ($\delta\phi \ll 1$) or equivalently short interrogation times ($T \ll 1$).

With the effective measurement uncertainty, the Allan deviation in the framework of Bayesian frequency metrology is expressed as

$$\sigma_y(\tau) = \frac{1}{\omega_0} \frac{\Delta\phi_M}{T} \sqrt{\frac{T_C}{\tau}}. \tag{4.33}$$

Consequently, the three key quantities for quantifying the sensitivity and ultimately the clock stability in Bayesian frequency metrology are the prior width $\delta\phi$, the BMSE $\Delta\phi$, and the effective measurement uncertainty $\Delta\phi_M$. In the following, we will examine their relation in a qualitative discussion.

4.5.2 Qualitative scaling

Due to noise in the local oscillator, the phase diffusion grows with Ramsey dark time. Thus, the prior width $\delta\phi$ of the relative phase will be monotonically increasing with the interrogation time T (cf. Fig. 4.1). At first glance, one might assume that $\delta\phi$ is solely determined by the characteristics of the free running LO frequency. However, it depends even more strongly on the noise of the stabilized frequency and therefore on the details of interrogation, estimation and feedback. Although the prior phase distribution can generally vary over different clock cycles, it becomes stationary if the feedback loop stabilizes the LO reliably to the atomic reference. In this case, the residual noise can be considered to be white – to a good approximation – and thus can be modeled by a normal distribution characterized by the spread $\delta\phi$ (cf. Eq. (4.5)).

For a given finite $\delta\phi$, the interrogation protocol and estimation strategy can be optimized to minimize the estimation error $\Delta\phi$. At the same time, the effective measurement uncertainty, Eq. (4.31), and thus also the Allan deviation, Eq. (4.33), are minimized. Consequently, $\Delta\phi$ will ultimately determine the stabilized frequency noise, which in turn affects $\delta\phi$. Therefore, in order to reflect the closed feedback loop of the atomic clock, $\Delta\phi$ has to be optimized iteratively for suitably chosen $\delta\phi$, as detailed in Sec. 4.5.3.

The average error in phase estimation $\Delta\phi$ depends on the prior width $\delta\phi$ as well as the particular interrogation sequence and estimation strategy. As discussed before, $\Delta\phi \leq \delta\phi$ and thus the estimation error $\Delta\phi$ is reduced compared to the prior width $\delta\phi$, since a proper Ramsey protocol increases the information about the phase. Here, equality $\Delta\phi = \delta\phi$ corresponds to a worst case scenario in which the effective measurement variance diverges $\Delta\phi_M \to \infty$. This case represents an ineffective interrogation scheme, where the information gained through measurement and estimation fails to improve the characterization of residual noise. Conversely, a hypothetical perfect phase estimation (precluded by quantum mechanics due to its intrinsic indeterminism) would result in a vanishing estimation error $\Delta\phi \to 0$. Likewise, the effective measurement uncertainty would also vanish $\Delta\phi_M \to 0$, since this scenario implies a perfect measurement.

The form of the Allan deviation in Eq. (4.33) suggests that the stability can be improved by increasing the interrogation time T. However, this is only true as long as the coherence time limit (CTL) of the LO remains negligible and quantum projection noise $\Delta\phi_{\mathrm{QPN}}$ of the measurement dominates the effective measurement uncertainty. In general, three regimes can be distinguished based on the relation between the prior width $\delta\phi$ and QPN $\Delta\phi_{\mathrm{QPN}}$:

(i) Considering small prior widths $\delta\phi \ll 1$, the measurement and estimation protocol cannot significantly improve the knowledge of the phase distribution, since $\Delta\phi_{\mathrm{QPN}} \gg \delta\phi$ and thus $\Delta\phi \simeq \delta\phi$. In this case, $\Delta\phi_M \simeq \Delta\phi_{\mathrm{QPN}}$ and the local form of the Allan deviation, Eq. (4.30), is reproduced.

(ii) With increasing interrogation time T, the prior width surpasses QPN $\delta\phi > \Delta\phi_{\mathrm{QPN}}$. Nevertheless, in this regime, the information gain on the phase distribution resulting from the measurement and estimation strategy leads to $\Delta\phi \ll \delta\phi$ and thus $\Delta\phi_M < \delta\phi$. Hence, the optimal working point of the atomic clock is located in this region.

(iii) At long interrogation times, the coherence time of the local oscillator will become relevant and ultimately limits the clock stability. Here, the phase noise exceeds the domain of the measurement scheme where an unambiguous estimation is possible, giving $\Delta\phi_M \gg \delta\phi \simeq \Delta\phi \gg \Delta\phi_{\mathrm{QPN}}$.

Consequently, the Allan deviation features a trade-off between increased stability achieved through long interrogation times and the limitations imposed by the coherence time of the local oscillator, which are characterized by the coherence time limit (CTL). Fortunately, as previously discussed, this trade-off is inherently addressed within the framework of Bayesian frequency metrology. In terms of clock stability, this trade-off gives rise to an optimal interrogation time $T_{\min}$ at which the minimal Allan deviation $\sigma_{\min}$ is achieved. While $\sigma_{\min}$ accounts for the bias in phase estimation for phases beyond the invertible range of the Ramsey sequence (via the CTL), it nevertheless remains restricted to a single clock cycle and neglects cumulative effects that might arise in a full feedback loop. The most prominent of these effects are fringe hops, which are discussed in detail in Sec. 4.7 as they can only appear within the full feedback loop.

4.5.3 Interrogation time and prior width

In the previous section, we linked the clock stability at interrogation time T – characterized by the Allan deviation – with Bayesian phase estimation with prior width $\delta\phi$, described by the BMSE. Furthermore, we qualitatively discussed that the prior width increases with the interrogation time. To complete the connection between Bayesian phase estimation and frequency metrology, this section aims to establish an explicit relation between $\delta\phi$ and T. This relation serves as a bridge between the frequency fluctuations of the laser in an experiment and a theoretical representation in terms of a Gaussian prior distribution with a specific width. Establishing this connection is essential for modeling experiments accurately and ensuring the applicability of theoretical predictions to realistic scenarios.

State-of-the-art clock lasers are characterized by the spectral noise density $S_y(f) = \sum_\alpha h_\alpha f^\alpha$, which can be modeled by a power law [12, 83, 84, 87], where $\alpha = 0, -1, -2$ corresponds to white, flicker and random walk frequency noise, respectively (see Sec. 2.2 for a comprehensive overview). Accordingly, the Allan variance of the free-running LO can be expressed as $\sigma^2_{y,\mathrm{LO}}(\tau) = \tilde{h}_\alpha \tau^{-1-\alpha}$. To compare different local oscillators, a single timescale is defined characterizing the stability. As discussed in Sec. 2.2.2, we implicitly define the laser coherence time Z following Ref. [92] by

$$\sigma_{y,\mathrm{LO}}(Z_C) 2\pi\nu_0 Z = 1 \text{ rad}. \tag{4.34}$$

Here, $\sigma_{y,\mathrm{LO}}(Z_C)$ denotes the Allan deviation of the local oscillator averaging over a single cycle duration $Z_C = Z + T_D$ with dead time T_D.

In Ref. [92], it was demonstrated that the prior width of the full feedback loop can be approximated by the power law

$$(\delta\phi)^2 \simeq \chi(\alpha) \left(\frac{T}{Z}\right)^{1-\alpha} \tag{4.35}$$

depending solely on the ratio of interrogation time T and coherence time of the local oscillator Z, and the numerically determined factor $\chi(\alpha) = 1, 1.7, 2$ for $\alpha = 0, -1, -2$. This approximation was derived in the limit of large ensembles and long interrogation times using the conventional Ramsey protocol in the framework of local phase estimation, and was successfully applied in Refs. [91, 140]. However, in the full feedback loop of an atomic clock, the prior width $\delta\phi$ and estimation error $\Delta\phi$ mutually influence each other. Therefore, $\delta\phi$ has to be adjusted iteratively to account for the closed feedback loop dynamics, as motivated in the previous section and detailed in App. A. This iterative procedure is employed in Sec. 4.7, where realistic Monte Carlo simulations of the full feedback loop of an atomic clock are performed. Nevertheless, Eq. (4.35) remains a convenient approximation for general investigations and is thus adopted in Sec. 4.6.

In the following, motivated by state-of-the-art clock lasers [88], we assume a local oscillator predominantly limited by flicker frequency noise. Additionally, we neglect systematic shifts in the atomic transition frequency ω_0. Moreover, we will assume the atomic excited-state lifetime t_{spont} to be substantially longer than the clock cycle duration T_C, such that $t_{\mathrm{spont}} \gg T_C$.

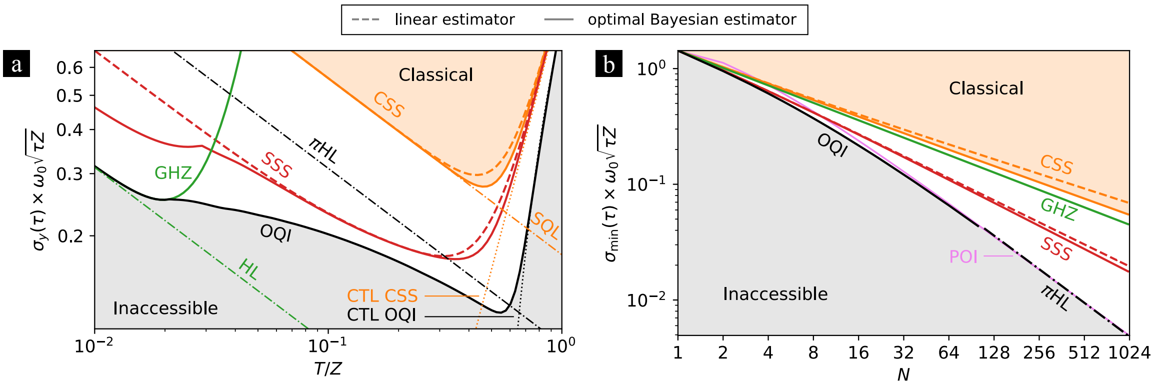

Figure 4.2: **Sensitivity of standard protocols in Bayesian frequency metrology:** (a) Generic scaling of the dimensionless Allan deviation $\sigma_y(\tau) \times \omega_0\sqrt{\tau Z}$ with the interrogation time T for the example of $N = 32$, rescaled by the averaging time τ, laser coherence time Z and transition frequency ω_0. Stabilities for the CSS (orange), SSS (red) and GHZ (green) protocols are compared to the performance of the OQI (black). For CSS and SSS, both the linear (dashed) and optimal Bayesian estimator (solid) are depicted. The gray shaded area represents the inaccessible stability region set by the OQI limit, while the orange shaded area indicates achievable stabilities using uncorrelated atoms. Dotted lines correspond to the CTL for OQI (black) and for CSS and SSS with the linear estimator (orange). Additionally, benchmarks such as the SQL (orange), HL (green), and πHL (black) are included as dashed-dotted lines. (b) Scaling of the dimensionless minimal Allan deviation $\sigma_{\min} \times \omega_0\sqrt{\tau Z}$ with the ensemble size N. In addition to the standard protocols, the POI performance (violet) is presented. For the OQI and POI, numerical optimization is performed for $N \leq 100$, while the asymptotic behavior, represented by the πHL (black dashed-dotted), is shown for $N > 100$.

4.6 Optimal Ramsey protocols in Bayesian frequency metrology

In this section, we aim to saturate the OQI in the context of atomic clocks. We begin by analyzing standard protocols and compare their performance to the OQI. Afterwards, we introduce variational classes of quantum circuits and investigate the associated optimal Ramsey protocols.

4.6.1 Standard protocols

To start with, we examine the effective measurement uncertainty and corresponding clock stability of standard Ramsey protocols (see App. G for detailed derivations). Specifically, we focus on coherent spin states (CSS), spin-squeezed states (SSS), and GHZ states, as well as the ultimate lower bound defined by the optimal quantum interferometer (OQI). For all Ramsey schemes, the dependence of clock stability on the interrogation time T reflects the three regimes discussed in Sec. 4.5.2, representing a trade-off between enhanced stability achieved through longer interrogation times and the coherence time limit. These distinct regimes are depicted in Fig. 4.2(a), which illustrates the generic dependence of stability on interrogation time. Furthermore, the scaling of the minimal Allan deviation $\sigma_{\min}$ with ensemble size N at the optimal interrogation time $T_{\min}$ is presented in Fig. 4.2(b). These figures are based on the work of Kaubruegger et al. [140] and are adapted here within the framework defined above. In particular, emphasis is placed on comparing the linear and optimal Bayesian estimation strategies across different protocols, with performance benchmarked against the OQI. To enable comparability between various setups, the achievable Allan deviations $\sigma_y(\tau)$ are rescaled with respect to the atomic transition frequency ω_0, the total averaging time τ and the laser coherence time Z. This rescaling ensures that the results are transferable to specific experimental parameters.

Coherent Spin States (CSS)— The conventional clock protocol employs Ramsey interferometry with coherent spin states (CSS) [115–117] – introduced in detail in Sec. 2.3.7 – as initial states, a collective projective spin measurement and a linear estimation strategy. In this scenario, the effective measurement uncertainty can be evaluated analytically as [92]

$$(\Delta\phi_M^{\mathrm{CSS}})^2 = \frac{\cosh((\delta\phi)^2)}{N} + \sinh\big((\delta\phi)^2\big) - (\delta\phi)^2. \tag{4.36}$$

For short interrogation times $T/Z \ll 1$, leading to narrow prior widths $\delta\phi \ll 1$, the conventional standard quantum limit (SQL) $\Delta\phi_{\mathrm{SQL}} = 1/\sqrt{N}$ is recovered. Conversely, for long interrogation times $T/Z \sim 1$, frequency fluctuations of the local oscillator dominate and the first term in Eq. (4.36) becomes negligible. This regime defines the coherence time limit (CTL) for CSS with a linear estimator,

$$(\Delta\phi_{\mathrm{CTL}}^{\mathrm{CSS}})^2 = \sinh\big((\delta\phi)^2\big) - (\delta\phi)^2. \tag{4.37}$$

Hence, the stability reflects a trade-off between these two regimes, as illustrated in Fig. 4.2(a), determining the minimal Allan deviation $\sigma_{\min}$. As the ensemble size N increases, the first term in Eq. (4.36) decreases, leading to shorter optimal interrogation times $T_{\min}$ to achieve $\sigma_{\min}$.

For the optimal Bayesian estimator, an explicit evaluation of the conditional probabilities $P(x|\phi)$ is required, as discussed in Sec. 4.4. Although $P(x|\phi)$ can be determined analytically for the CSS, the integrals in Eq. (4.29) generally have to be evaluated numerically. For short interrogation times, the narrow prior phase distribution allows for a good approximation by linearizing the signal. Thus, the optimal

Bayesian estimator reproduces the linear estimator in this regime. In contrast, for interrogation times in the region of the minimal Allan deviation, higher-order contributions of the sinusoidal signal become relevant and the curvature of the signal has to be considered. In this case, the optimal Bayesian estimator approximates the *arcsin* estimator, which directly inverts the signal and thus allows to estimate the phase unambiguously in the range $[-\pi/2, +\pi/2]$. This results in an extended dynamic range compared to the linear estimator, which cannot account for any non-linearity of the signal and thus exhibits a higher minimal instability. As a consequence, the optimal Bayesian estimator improves the scaling of $\Delta\phi_M$ with the ensemble size N to $\mathcal{O}(N^{-0.47})$, compared to $\mathcal{O}(N^{-0.42})$ for the linear estimator, as shown in Fig. 4.2(b). While the choice of an estimator has limited impact for small ensembles, the stability gain from the optimal Bayesian estimator becomes significant for large ensembles $N \gg 1$. Importantly, this improvement arises solely from classical post-processing of the measurement outcomes, while the quantum circuit remains unchanged. Nevertheless, the CTL prevents both estimation strategies from achieving the SQL of $1/\sqrt{N}$.

Spin-Squeezed States (SSS)— Extending the conventional Ramsey protocol with a single one-axis-twisting (OAT) interaction [125] for state preparation, various entangled states can be generated (see Sec 2.3.9 for a comprehensive overview). Here, OAT interactions are denoted by $\mathcal{T}_{\mathbf{k}}(\mu) = \exp\left(-i\frac{\mu}{2}S_{\mathbf{k}}^2\right)$ with twisting stength μ around axis $\mathbf{k}$, where $S_{\mathbf{k}} = k_1 S_x + k_2 S_y + k_3 S_z$ is the spin projection along direction $\mathbf{k}$. In particular, for small twisting strengths μ, one-axis-twisting generates spin-squeezed states (SSS) by shearing the initial CSS around the twisting axis, characterized by a squeezing parameter $\xi < 1$. Using the linear estimator, the effective measurement uncertainty is given by

$$(\Delta\phi_M^{\mathrm{SSS}})^2 = \frac{\left\langle S_y^2\right\rangle}{\left\langle S_x\right\rangle^2}\cosh\big((\delta\phi)^2\big) + \frac{\left\langle S_x^2\right\rangle}{\left\langle S_x\right\rangle^2}\sinh\big((\delta\phi)^2\big) - (\delta\phi)^2, \tag{4.38}$$

with expectation values provided in App. G.2. SSS show enhanced stability compared to CSS due to reduced fluctuations in the measured spin observable. However, the gain comes at the cost of smaller dynamic range, as the minimal Allan deviation is achieved at shorter interrogation times compared to CSS (cf. Fig. 4.2(a)). This is a direct consequence of SSS sharing the same coherence time limit as CSS, since $\left\langle S_y^2\right\rangle / \left\langle S_x\right\rangle^2 \ll 1$ and $\left\langle S_x^2\right\rangle / \left\langle S_x\right\rangle^2 \simeq 1$ for large prior widths $\delta\phi$ and corresponding optimal twisting strengths. Similar to the conventional Ramsey protocol, SSS with the optimal Bayesian estimator achieve a slightly extended dynamic range at long interrogation times. For large ensembles $N \gg 1$, the asymptotic scaling of the effective measurement uncertainty with the optimal Bayesian estimator approximates

$\mathcal{O}(N^{-2/3})$, depicted in Fig. 4.2(b), reflecting the scaling observed in decoherence-free local phase estimation [6, 125]. In contrast, the linear estimator exhibits a scaling $\mathcal{O}(N^{-0.63})$. Furthermore, the optimal Bayesian estimation strategy offers a remarkable advantage at short interrogation times, where $\delta\phi \lesssim 1/N$, as shown in Fig. 4.2(a). In this regime, the estimator becomes highly non-linear, allowing for substantially stronger twisting strengths μ, resulting in stronger squeezing and enhanced stability. However, as $\delta\phi$ approaches $1/N$, the scaling of the Allan deviation with the interrogation time T stagnates and converges towards the stability achieved with the linear estimator.

GHZ States— The maximally entangled Greenberger-Horne-Zeilinger (GHZ) state $|\mathrm{GHZ}\rangle = \left[|{\downarrow}\rangle^{\otimes N} + |{\uparrow}\rangle^{\otimes N}\right]/\sqrt{2}$ [121] represents an equal superposition of the collective ground and excited states. The corresponding Ramsey sequence, initially proposed by Wineland et al. [122], is referred to as the GHZ protocol.[2] During the free evolution time, the accumulated phase is amplified by a factor of N due to the maximal entanglement of the GHZ state. Subsequently, the parity Π is measured, resulting in a binary outcome ±1 that indicates whether the number of atoms in the ground state is even or odd. Since a binary outcome inevitably results in a linear estimator, both estimation strategies coincide and result in the effective measurement uncertainty

$$(\Delta\phi_M^{\mathrm{GHZ}})^2 = \frac{e^{N^2(\delta\phi)^2}}{N^2} - (\delta\phi)^2. \tag{4.39}$$

However, the optimal Bayesian estimator allows to avoid a parity measurement and perform a conventional projective spin measurement instead. In this case, the optimal Bayesian estimator effectively maps even and odd numbers of atoms in the ground state to the parity ±1, thereby mimicking a parity measurement and achieving the same sensitivity (cf. App. G.3). This strategy was essentially employed in a different framework in Ref. [157]. Both measurement and estimation strategies are optimal, since Eq. (4.39) aligns with the BQCRB for GHZ states. For short interrogation times, where $\delta\phi \lesssim 1/N$, the GHZ protocol achieves the conventional Heisenberg limit (HL) $\Delta\phi_{\mathrm{HL}} = 1/N$, as illustrated in Fig. 4.2(a), which corresponds to the OQI in a decoherence-free local phase estimation scenario. However, the sensitivity of the GHZ protocol decreases N-times faster than that of CSS as the prior width increases. For a parity measurement, this is attributed to the N-times increased oscillation frequency of the sinusoidal signal, yielding an accordingly reduced dynamic range. Ultimately, the resulting ambiguities in phase estimation cause the GHZ protocol to be effectively insensitive to phases $\phi \gtrsim 1/N$. Consequently, the optimal interrogation time scales approximately as $1/(NZ)$, leading to a scaling of the effective measurement uncertainty of $\mathcal{O}(N^{-1/2})$, equivalent to the SQL (cf. Fig. 4.2(b)). While the minimal Allan deviation of the GHZ protocol provides only a minor improvement over CSS and is outperformed by SSS, its shorter optimal interrogation time offers practical advantages. For instance, reduced probe times mitigate contrast losses and time dilation shifts caused by motional heating in ion crystals, thus improving the signal-to-noise ratio and the accuracy of such a clock [12].

---

[2] In Chapter 3, we referred to this protocol as parity-GHZ protocol. However, within the Bayesian framework, the parity-GHZ protocol already saturates the BQCRB of the GHZ state (cf. App. G.3) and thus, a distinction between different GHZ protocols is redundant.

OQI— As discussed in Sec. 4.3, the OQI requires numerical optimization, as no analytical expressions are available for arbitrary ensemble sizes. Instead, we investigate the general scaling based on Fig. 4.2. For short interrogation times $T/Z \ll 1$, where $\delta\phi \lesssim 1/N$, the OQI is saturated by the GHZ protocol, achieving the Heisenberg limit $\sigma_{\mathrm{HL}}(\tau) = 1/(N\sqrt{T\tau})$, as shown in Fig. 4.2(a). As the interrogation time increases and $\delta\phi \gtrsim N$, a characteristic *plateau* emerges in which the Allan deviation decreases only marginally with T. This plateau shifts to shorter interrogation times as the ensemble size N increases, reflecting the coherence time limit of the GHZ protocol. Beyond this plateau, as the interrogation time increases further, the scaling of the Allan deviation with T converges back to $1/\sqrt{T}$, ultimately reaching its minimum $\sigma_{\min}$ at $T_{\min}$. In the limit of large ensembles ($N \gg 1$), this minimum is determined by the π-corrected Heisenberg limit. While the OQI significantly outperforms SSS at $T_{\min}$, SSS perform close to the OQI in the transition regime, especially for small ensembles. The relative gain of the OQI over SSS at $T_{\min}$ increases with the ensemble size, as illustrated in Fig. 4.2(b). In the asymptotic limit $N \gg 1$, the POI, introduced in Sec. 4.3 and further detailed in App. F.3, is optimal, saturating the πHL. In this regime, the OQI scales as $\mathcal{O}(N^{-0.97})$, closely approaching Heisenberg scaling. At long interrogation times, the stability ultimately converges to the coherence time limit.

In the following, we essentially distinguish between two different regimes concerning the ensemble size N: The first regime covers systems ranging from $N = 1$ to some tens of atoms, as relevant for ion traps [16–18] or tweezer arrays [19–22]. The remainder of this section primarily focuses on bridging the gap between SSS and the OQI by identifying Ramsey protocols of increasing complexity that approximate the OQI within this regime. In contrast, for large ensembles ($N \gtrsim 100$), the regime of lattice clocks is reached and the asymptotic scaling is approximated [12, 23–26]. In this regime, dead time typically emerges as the dominant limitation [91], as discussed in detail in Sec. 4.8.

4.6.2 Variational Ramsey protocols

Recent advances in quantum information have inspired the development of variational quantum circuits as versatile tools for implementing interferometers with setup-specific quantum gates. Typically, each layer in these circuits comprises an entanglement-generating interaction and (single qubit) rotations that provide geometric flexibility. One-axis twisting (OAT) [125] interactions have gathered significant attention, as they can be implemented in several experimental platforms [62, 126–133] and corresponding circuits represent a natural extension of spin-squeezed states (SSS). Combined with collective rotations, OAT interactions form the building blocks of several variational quantum circuits [5, 139–143]. While Ref. [5] offers a unified framework for generalized echo protocols in local phase estimation, encompassing numerous previously documented approaches [128, 143, 202–208], this chapter investigates variational classes specifically tailored to Bayesian frequency metrology.

In general, any variational Ramsey protocol can be expressed as

$$P(x|\phi) = \mathrm{Tr}\left(|x_M\rangle\langle x_M|\,\Lambda_{\phi,T}[\rho_{\mathrm{in}}]\right) \tag{4.40}$$

$$\rho_{\mathrm{in}} = \mathcal{U}_{\mathrm{prep}}\,|\psi_0\rangle\langle\psi_0|\,\mathcal{U}_{\mathrm{prep}}^{\dagger} \tag{4.41}$$

$$|x_M\rangle\langle x_M| = \mathcal{U}_{\mathrm{meas}}^{\dagger}\,|M\rangle\langle M|\,\mathcal{U}_{\mathrm{meas}}, \tag{4.42}$$

with arbitrary unitary preparation and measurement operations $\mathcal{U}_{\mathrm{prep}}$ and $\mathcal{U}_{\mathrm{meas}}$, respectively. While $\mathcal{U}_{\mathrm{prep}}$ generates the initial state by acting on the ground state $|\psi_0\rangle = |{\downarrow}\rangle^{\otimes N}$, $\mathcal{U}_{\mathrm{meas}}$ effectively determines the measurement X by transforming the Dicke states $|M\rangle$, with spin $S = N/2$ and eigenvalue M of S_z, into the effective measurement basis states $|x_M\rangle$.[3] Since any alternative choice of $|\psi_0\rangle$ and Dicke basis $\{|M\rangle\langle M|\}$ can be incorporated into $\mathcal{U}_{\mathrm{prep}}$ and $\mathcal{U}_{\mathrm{meas}}$ by additional transformations, fixing $|\psi_0\rangle$ and $\{|M\rangle\langle M|\}$ does not limit the generality of the protocol. The unitaries $\mathcal{U}_{\mathrm{prep}}$ and $\mathcal{U}_{\mathrm{meas}}$ are constructed from n and m layers of the variational circuit, respectively. Consequently, n effectively determines the level of entanglement in the initial state, while m governs the measurement strategy and dynamic range, ultimately determining the minimal Allan deviation σ_{min}.

Previous results— Pioneering work on Bayesian variational Ramsey protocols was conducted in Refs. [140, 142]. These studies introduced a variational class constrained to be invariant under the x-parity transformation, resulting in an antisymmetric signal. Each layer of the quantum circuit consisted of two OAT interactions applied along orthogonal directions, combined with a collective rotation about one of these axes. While this choice provided a diverse class of entanglement-generating unitaries in each layer, it imposed significant geometric constraints. Nevertheless, the quality of phase estimation was not compromised, as the main objective was to saturate the OQI in the asymptotic limit of deep circuits. The analysis primarily focused on ensembles with several tens of qubits and employed linear estimation strategies. Kaubruegger et al. demonstrated that the minimal Allan deviation σ_{min} could be achieved with sufficiently deep circuits. However, this approach had two key drawbacks: the reliance on deep circuits due to restricted geometric flexibility, and the inclusion of two OAT interactions per layer, which are experimentally more challenging to implement than collective rotations.

---

[3] In this chapter, we restrict the analysis to the subspace with maximal spin $S = N/2$, as the system exhibits permutational invariance and the unitary dynamics, described by Eq. (4.4), preserves this symmetry.

Thurtell et al. in Ref. [141] addressed these limitations by proposing a variational class where each layer comprises a single OAT interaction around the z-axis combined with global rotations. These rotations are designed to effectively transform the OAT interaction with respect to an arbitrary axis, thereby eliminating geometric constraints. This approach reduced both the circuit depth and the number of OAT interactions, while achieving results comparable to those in Ref. [140]. Nevertheless, a considerable number of OAT interactions remained necessary. Moreover, the analysis was conducted within the framework of general Bayesian phase estimation and thus, did not consider the trade-off with respect to the interrogation time in frequency metrology.

Variational quantum circuits— In the following, we aim to approximate the OQI within the framework of Bayesian estimation tailored to frequency metrology. Instead of exploring the convergence towards the OQI with many layers for state preparation and measurement, we focus on variational quantum circuits with minimal depth. We primarily consider small ensembles relevant to ion traps and additionally investigate the transition toward tweezer arrays, which have been predominantly studied in Refs. [140,141]. Given the high degree of controllability achievable in these systems, this represents the regime where near-term experimental implementation is most likely. Moreover, variational protocols are less favorable in setups with many atoms, such as in lattice clocks, as we will discuss below. In contrast to earlier studies – relying on linear estimation strategies – we employ the optimal Bayesian estimator to fully exploit the potential of variational Ramsey protocols. This choice is motivated by the substantial improvements observed for the standard protocols, including enhanced squeezing for SSS at short interrogation times, an extended dynamic range for CSS and SSS, and an effective reduction in the circuit depth required to implement the GHZ protocol. Additionally, by using the optimal Bayesian estimator, we ensure saturation of the BCRB for any given initial state and measurement and thus minimizing the required circuit depth. A comprehensive comparison with the linear estimation strategy is provided in Sec. 4.7.3.

Building on the advancements in Refs. [140, 141], we define the variational class of generalized Ramsey protocols considered in this work, as illustrated in Fig. 4.3(a), by

$$\begin{aligned} \mathcal{U}_{\text{prep}} &= \mathcal{R}_{\mathbf{n}}\Big[\bigotimes_{j=1}^{n}\mathcal{T}_j\Big]\mathcal{R}_{\frac{\pi}{2}} \\ \mathcal{U}_{\text{meas}} &= \mathcal{R}_{\mathbf{m}}\Big[\bigotimes_{j=n+1}^{n+m}\mathcal{T}_j\Big]\mathcal{R}_{\mathbf{n}}^{\dagger}, \end{aligned} \tag{4.43}$$

where we introduced the abbreviations $\mathcal{T}_j = \mathcal{T}_{\mathbf{k}_j}(\mu_j)$ and $\mathcal{R}_{\frac{\pi}{2}} = \mathcal{R}_y\left(-\frac{\pi}{2}\right)$. The $\pi/2$-pulse $\mathcal{R}_{\frac{\pi}{2}}$ in $\mathcal{U}_{\text{en}}$ generates the CSS polarized in x-direction $|+\rangle^{\otimes N} = (|\uparrow\rangle + |\downarrow\rangle)^{\otimes N}/\sqrt{2}^N = \mathcal{R}_{\frac{\pi}{2}}|\downarrow\rangle^{\otimes N}$. The rotations $\mathcal{R}_{\mathbf{n}}$ and $\mathcal{R}_{\mathbf{m}}$ result in an effective phase evolution around an arbitrary axis $\mathbf{n}$, $S_{\mathbf{n}} = \mathcal{R}_{\mathbf{n}}^{\dagger}S_z\mathcal{R}_{\mathbf{n}}$, and an effective measurement of $S_{\mathbf{m}} = \mathcal{R}_{\mathbf{m}}^{\dagger}S_z\mathcal{R}_{\mathbf{m}}$, respectively. Similarly, each one-axis-twisting $\mathcal{T}_{\mathbf{k}}(\mu) = \mathcal{R}_{\mathbf{k}}^{\dagger}\mathcal{T}_z(\mu)\mathcal{R}_{\mathbf{k}}$ can be expressed as an OAT with respect to the z-axis and a rotation $\mathcal{R}_{\mathbf{k}}$. The resulting variational classes are not restricted by any geometric constraints.

For a given protocol class $[n, m]$, the quantum circuit contains $n+m$ OAT interactions with associated twisting strengths μ_j. Together with the rotations $\mathcal{R}_{\mathbf{n}}, \mathcal{R}_{\mathbf{m}}, \mathcal{R}_{\mathbf{k}_j}$, which ensure geometric generality and are each characterized by two variational parameters, the total number of variational parameters is $4 + 3(n + m)$. Notably, the particular choice of the CSS $|+\rangle^{\otimes N}$ as the initial state allows us to fix the first OAT of $\mathcal{U}_{\text{prep}}$ along the z-axis without losing any generality. This simplification reduces the total number of variational parameters by two.

The variational class defined in Eq. (4.43) contains the standard Ramsey protocols as limiting cases. Coherent spin states (CSS) are recovered in the $[0, 0]$-protocol, while spin-squeezed states (SSS) are implemented within the $[1, 0]$-class. The GHZ protocol emerges as a special case, either within the $[1, 0]$-class using the optimal Bayesian estimator, as discussed in the previous section, or as part of the $[1, 1]$-class, as implemented in Ref. [128].

Ramsey signals— The standard protocols, namely CSS, SSS and GHZ protocols, exhibit sinusoidal signals. While CSS and SSS have a dynamic range of $[-\pi/2, +\pi/2]$, allowing for unbiased phase estimation within this interval, the phase is imprinted N times faster for the GHZ state, leading to a correspondingly N times smaller dynamic range. In contrast, variational quantum circuits with multiple layers for state

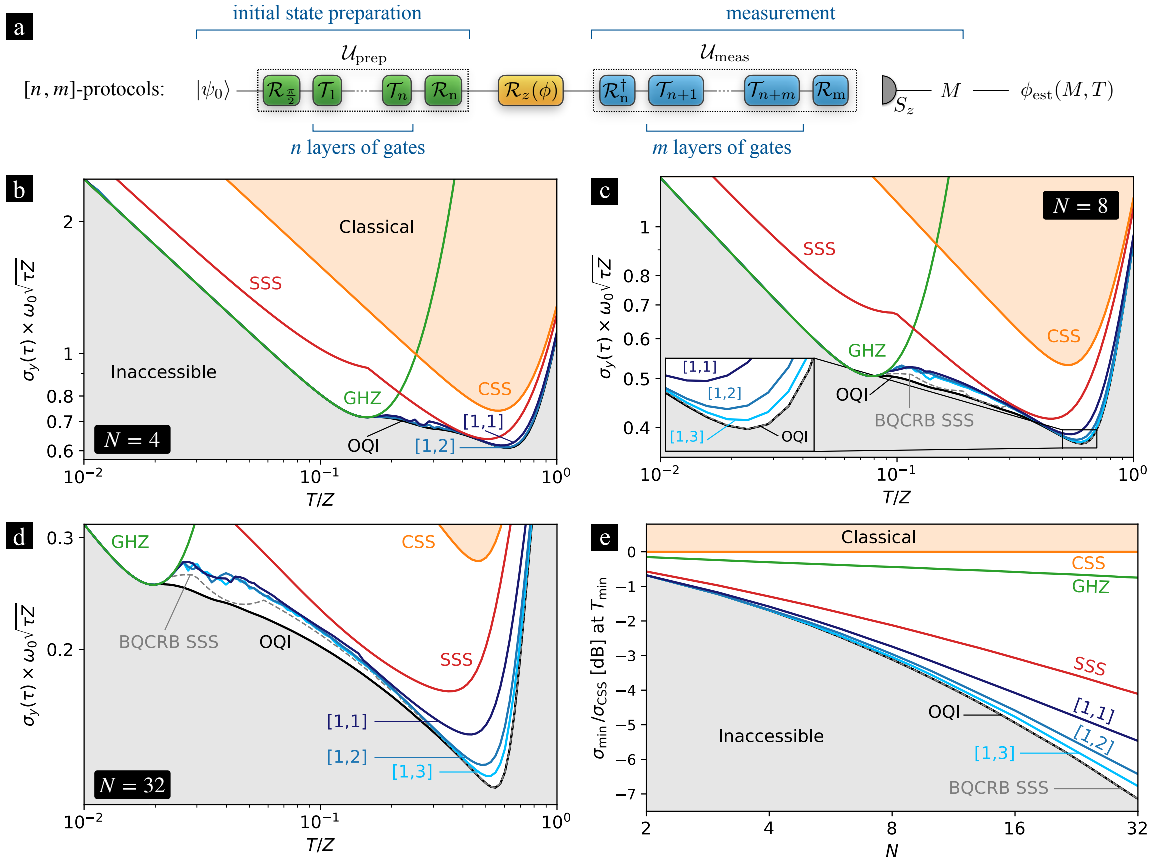

Figure 4.3: **Variational Ramsey protocols in Bayesian frequency metrology:** (a) Visualization of the variational Ramsey protocols defined in Eq. (4.43). The $\pi/2$-pulse $\mathcal{R}_{\frac{\pi}{2}} = \mathcal{R}_y(-\pi/2)$ generates the coherent spin state (CSS) polarized in x-direction from the ground state $|\psi_0\rangle = |{\downarrow}\rangle^{\otimes N}$. Entanglement in the initial state and measurement is introduced via one-axis-twisting (OAT) interactions, denoted by $\mathcal{T}_j = \mathcal{T}_{\mathbf{k}_j}(\mu_j)$ with twisting strength μ_j around axis $\mathbf{k}_j$. During the free evolution time T, the phase ϕ is imprinted onto the initial state via a rotation around the z-axis. The rotations $\mathcal{R}_{\mathbf{n}}$ and $\mathcal{R}_{\mathbf{m}}$ result in an effective phase evolution around an arbitrary axis $\mathbf{n}$, $S_{\mathbf{n}} = \mathcal{R}_{\mathbf{n}}^\dagger S_z \mathcal{R}_{\mathbf{n}}$, and an effective measurement of $S_{\mathbf{m}} = \mathcal{R}_{\mathbf{m}}^\dagger S_z \mathcal{R}_{\mathbf{m}}$, respectively. Finally, the phase is estimated based on measurement outcome M of observable S_z. (b-d) Approximating the OQI using variational $[1,m]$-classes (blue) for (a) $N = 4$, (b) $N = 8$ and (c) $N = 32$. For comparison, the standard protocols are shown as they naturally emerge as specific quantum circuits within the variational classes. Additionally, the BQCRB of SSS is shown (dashed gray). With increasing N, the complexity of the variational circuits required to approach OQI performance increases. (e) Scaling of the gain in clock stability compared to CSS at the optimal interrogation time T_{min} with N.

preparation and measurement can generate arbitrary signal shapes. In particular, the variational classes introduced above impose no restrictions on the geometry, and therefore the signal shape is not constrained.

Generic Ramsey signals for the $[1, 1]$ and $[1, 2]$ protocols are illustrated in Fig. 4.4(a) for $N = 8$ at interrogation time $T/Z = 0.1$. The signals, associated with the optimal variational parameters, are compared for both the linear and optimal Bayesian estimation strategies.

In principle, the estimation strategy does not affect the signal directly, as it is determined solely by the initial state, free evolution dynamics and measurement. However, the choice of the estimator influences the optimization of the variational parameters, which in turn affects the signal. Consequently, the linear estimation strategy typically yields anti-symmetric signals, at least within the range of the prior distribution. In contrast, the optimal Bayesian estimator can become highly nonlinear. As a result, corresponding signals often exhibit strongly non-sinusoidal shapes, lacking symmetry and any apparent relation to the phase. While this may initially seem counterintuitive, this approach ultimately achieves low phase estimation uncertainties when combined with the corresponding estimator, as we will explore in detail in the next section. An example has already been discussed in Sec. 4.6.1 for the GHZ protocol, where the optimal Bayesian estimator can effectively mimic a parity measurement, while the signal itself vanishes. A similar behavior is observed for the optimal $[1, 2]$ protocol with optimal Bayesian estimator in Fig. 4.4(a).

4.6.3 Optimal protocols

For fixed ensemble size N, circuit depth $[n, m]$ and prior phase width $\delta\phi$, the optimization of the quantum circuits introduced above is performed over all variational parameters. To enable a general discussion, we adopt the power-law scaling of the prior width with interrogation time T, as defined in Eq. (4.35). Results for exemplary ensemble sizes N as well as the scaling of the stability with N are presented in Fig. 4.3. The variational protocols are primarily compared to the OQI, as its saturation is the central goal of this section. Additionally, comparisons to standard Ramsey protocols are provided where relevant to highlight specific advantages and limitations.

General results— We begin by examining the general behavior and scaling of the variational classes, with a particular focus on the number of layers n and m. While $[n, 0]$-protocols yield collective spin measurements with sinusoidal signals, increasing m allows for arbitrary signal shapes, since no geometric constraints are imposed, as discussed in the previous section and illustrated in Fig. 4.4(a). As for the standard Ramsey protocols, variational protocols exhibit a clear trade-off between enhanced

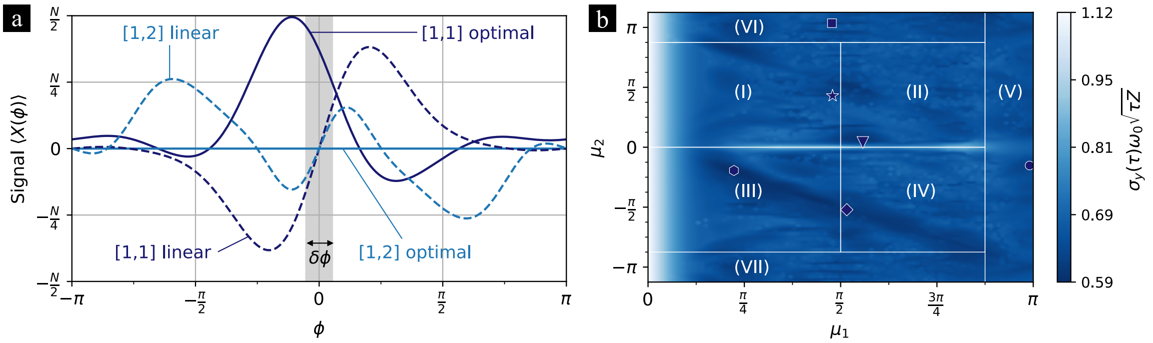

Figure 4.4: **Optimal Ramsey signals and optimization landscape:** (a) Comparison of signals $\langle X(\phi)\rangle$ of the optimal $[1,1]$ and $[1,2]$ protocols for the linear (dashed) and optimal Bayesian estimator (solid), for $N = 8$ at an interrogation time of $T/Z = 0.1$. The gray shaded region represents the spread of the prior distribution, with its width $\delta\phi$ corresponding to the specific interrogation time. (b) Optimization landscape in the μ_1-μ_2-plane for the $[1,1]$ class for $N = 8$ at an interrogation time of $T/Z = 0.1$. The Allan deviation $\sigma_y(\tau)$ is rescaled by the averaging time τ, coherence time Z and transition frequency ω_0. Darker areas correspond to better stability. The optimization areas (I-VII) are separated by white lines, while local minima within these regions are illustrated by symbols. In theory, the lowest instability is achieved by the protocol indicated by the hexagon in area (III), while the other local minima result in a comparable clock stability. Accordingly, the signal in (a) for the $[1,1]$-class with the optimal Bayesian estimator corresponds to the hexagon.

stability for increasing interrogation times and the coherence time limit of the local oscillator.

At long interrogation times close to the minimal Allan deviation $\sigma_{\min}$, the OQI is saturated by the BQCRB of SSS for any ensemble size N. Within the variational framework, this can be implemented using the $[1, m]$-classes, as the optimal measurement of the BQCRB is approximated in the limit $m \gg 1$. Increasing the number of entangling layers n yields $\sigma_{\min}$ comparable to that of the corresponding $[1, m]$-protocols, consistent with findings in Ref. [141]. Consequently, to extend the dynamic range and approximate the OQI at long interrogation times requires to increase m.

In contrast, at short interrogation times, the dynamic range is negligible, and increasing the entanglement depth of the initial state, effectively determined by n, becomes beneficial. However, GHZ states are already optimal in this regime and saturate the Heisenberg limit. Thus, $n = 1$ remains sufficient.

At the plateau of the OQI, where GHZ states become ineffective, the $[1, m]$-classes generally do not saturate the OQI. This regime becomes broader for larger ensembles, since the dynamic range of GHZ states reduces with N. Here, achieving the OQI requires asymptotically deep quantum circuits, which, however, is unfavorable, as discussed before. Even in the limit of $n + m \gg 1$, as considered in Refs. [140, 142], the variational class only gradually approximates the OQI with increasing complexity. Furthermore, in the plateau regime, the optimal variational parameters strongly depend on the prior width, causing substantial variations in the interferometer sequence. As a consequence, even minor modifications in the interrogation time can lead to profound changes in the form of both the signals and the associated estimation strategies. In particular, as the regime of GHZ states is exceeded, the twisting strengths decrease significantly, effectively reducing the degree of entanglement to adapt to increased LO noise. Interestingly, this susceptibility diminishes with increasing circuit complexity m. This can be interpreted as follows: For low depth quantum circuits, the variational space is limited and thus, the optimal states and measurements have to be extremely well tailored to a specific prior width to ensure a sufficiently high degree of entanglement and dynamic range at the same time. As the variational complexity increases, the variational space grows and reduces the susceptibility to small variations in the prior width. Additionally, this dependence gives rise to a large number of local minima, as illustrated in Fig. 4.4(b), making global optimization tedious and facilitating numerical errors, indicated by the non-smooth curves.

As a consequence, we focus on approximating the OQI in all regimes except the plateau using variational $[1, m]$-classes and strive for a minimal circuit depth m.

Protocol complexity and ensemble size— For the simplest case, $N = 2$, the GHZ protocol is optimal across most interrogation times because the critical prior width, $\delta\phi \sim 1/N$, is relatively large. Consequently, the region between the plateau and the minimal Allan deviation is narrow. In this transitional regime, SSS achieve the OQI, while the minimal Allan deviation (ADEV) as well as the plateau of the OQI are saturated by the simplest non-trivial variational class, the $[1, 1]$-protocols. Hence, standard protocols are sufficient to saturate the OQI across a wide range of interrogation times.

For $N = 4$, illustrated in Fig. 4.3(b), the plateau of the OQI already broadens significantly. SSS perform close to the OQI and the variational protocols over a narrow range of interrogation times in the transition regime. The $[1, 1]$-protocols remain optimal for a broad range of interrogation times, closely approaching the OQI at the plateau and at the minimal ADEV. Increasing the circuit complexity, the $[1, 2]$-class approximates the OQI.

For $N = 8$, depicted in Fig. 4.3(c), the discrepancy between low-depth quantum circuits and the OQI at the plateau becomes more pronounced. Even the BQCRB of SSS, effectively represented by $[1, m]$-classes for $m \gg 1$, approximates the OQI only closely. In the transition regime, where the OQI scaling reverts to $\sim 1/\sqrt{T}$, SSS approximate both the variational classes and the OQI, but the deviation grows with N, as discussed in Sec. 4.6.1. At the minimal ADEV, $[1,1]$-protocols substantially extend the dynamic range, but nevertheless leave a noticeable gap to the OQI, which is largely closed by $[1,2]$-classes. Increasing the variational complexity further, the $[1,3]$-class approximates the OQI in the vicinity of σ_{min}, but does not fully saturate it. Consequently, already for $N=8$ relatively deep quantum circuits are required to saturate the OQI entirely. Since the gain diminishes with increasing m, and in order to keep the quantum circuit comparably simple, we do not increase the circuit depth further.

As N increases, this trend continues, as shown for $N=32$ in Fig. 4.3(d). In this case, even the BQCRB of SSS exhibits significant deviations from the OQI at the plateau. In contrast, in the scaling regime of $\sim 1/\sqrt{T}$, and particularly at the minimal Allan deviation, the BQCRB saturates the OQI. The overall minimum is approximated by increasing m, but diminishing gains make deeper circuits less advantageous. Hence, we restrict our analysis to variational classes $[1,m]$ with $m \leq 3$ as before. In general, the variational complexity required to saturate the OQI grows with N (cf. Fig. 4.3(e)). These results align with the asymptotic analysis of OQI saturation in Refs. [140–142].

For large ensemble sizes ($N \gtrsim 100$), reaching the regime of optical lattice clocks, atom number fluctuations during interrogation become relevant [12]. Variational Ramsey protocols – optimized for fixed N – are highly sensitive to such fluctuations, making them less favorable in this regime. Instead, the POI emerges as a robust alternative, saturating the OQI in the limit of large N.

In summary, for systems with small ensembles N, such as ion traps and tweezer arrays, low-depth variational classes are sufficient to approximate the OQI. These protocols generally achieve optimal performance across all interrogation times, except at the OQI plateau. Already the simplest variational protocols from the $[1,1]$-class significantly enhance the stability at long interrogation times, particularly in the regime of the minimal Allan deviation. The circuit depth of $[1,m]$ protocols required to actually saturate the OQI at long interrogation times increases with N. However, the performance gain diminishes with m, presenting a trade-off between reduced instability and increasing complexity. To maintain a reasonable balance between dynamic range and circuit depth, we restrict our analysis to $m \leq 3$, acknowledging that the OQI can be fully saturated in the limit of deep circuits $m \gg 1$, as quantified by the BQCRB of SSS.

4.7 Application in the full feedback loop of an atomic clock

The Bayesian approach captures key aspects of atomic clock operation, including finite prior information, single-shot measurements, and the trade-off between enhanced stability achieved through longer interrogation times and the coherence time limit of the local oscillator. However, it models only a single clock cycle and neglects cumulative effects that arise in a full feedback loop. In particular, in the regime where the invertible domain of the main fringe is exceeded by the prior distribution and thus an unambiguous phase estimation is no longer possible, so called *fringe hops* might occur. In this scenario, the feedback loop passes to an adjacent Ramsey fringe resulting in the clock running systematically wrong and consequently degrading the clock stability. Whether fringe hops or the coherence time limit impose the dominant constraint depends on the specific Ramsey protocol and interrogation time. Since fringe hops are a feature only emerging in the context of a full feedback loop, they are not captured by the theoretical model presented above. While existing approaches, such as those in Refs. [91, 222], provide rough estimates for the effects of fringe hops based on single cycle properties, they are typically limited to sinusoidal signals and lack general applicability. A rigorous treatment of fringe hops requires modeling the complete feedback loop, as pursued in Ref. [199], but adapting this framework to variational Ramsey protocols lies beyond the scope of this work. Instead, we perform realistic Monte Carlo simulations of the full feedback loop to validate our theoretical predictions on clock stability. These numerical simulations reflect the basic principles of atomic clock operation (cf. Sec. 3.2). Further implementation details are provided in App. A and Ref. [3]. The prior width in the full feedback loop is determined iteratively, as discussed in Sec. 4.5.3 and App. A.

To start with, in Sec. 4.7.1 we examine the limitations imposed by fringe hops and discuss the associated deviations between theoretical predictions and numerical simulations. In Sec. 4.7.2, we investigate the clock stability within the full feedback loop of an atomic clock for various Ramsey protocols and ensemble sizes, identifying the protocols that perform best in the respective regimes. Furthermore, in Sec. 4.7.3, we compare the linear estimation strategy with the optimal Bayesian estimator, focusing particularly on variational quantum circuits and the limitations imposed by fringe hops.

4.7.1 Limitation due to fringe hops

Results of numerical simulations, presented in Fig. 4.5, show good agreement with theoretical predictions across a wide range of interrogation times. However, significant deviations arise in two regimes.

First, for small ensembles at long interrogation times, fringe hops limit the clock stability rather than the coherence time limit. As a result, the minimal Allan deviation σ_{min} is not achieved for the standard protocols and variational classes. Instead, the best stability is observed at $T_{\text{sim}} < T_{\text{min}}$, lying within the transition regime between the plateau of the OQI and σ_{min}. However, as N increases, T_{sim} approaches the coherence time limit at T_{min}, resulting in improved stability. In particular, for $N \gtrsim 20$, fringe hops and the coherence time limit spoil the stability at the same level and thus, the minimal Allan deviation is achieved for the standard protocols and variational classes. Notably, GHZ protocols remain limited by fringe hops regardless of N due to their inherently narrow dynamic range which decreases with the ensemble size.

Second, deviations arise in the regime of the plateau of the OQI, which primarily can be explained by three arguments: (i) Similar to long interrogation times, fringe hops can occur in this regime. For instance, for $\delta\phi \lesssim 1/N$, the optimal variational protocols resemble the GHZ protocol. However, as argued before, fringe hops prevent GHZ protocols to achieve its minimal Allan deviation. Likewise, the optimal variational protocols may not attain the theoretical prediction as $\delta\phi \sim 1/N$. In this regime, $m \neq 0$ typically generates highly non-sinusoidal signals with reduced dynamic range compared to CSS and SSS (cf. Fig. 4.4(a)), resulting in severe limitations due to fringe hops. (ii) As described in the previous section, in the regime of the OQI plateau, the optimal variational parameters are highly sensitive to small changes in the interrogation time, where this susceptibility diminishes with the circuit complexity m. With increasing ensemble size, this limitation increases, since the plateau gets broader with N. Although the prior width is determined iteratively, modeling the actual prior distribution solely based on the width remains a simplified parametrization of the prior knowledge. Furthermore, this iterative evaluation of the prior width relies on a fixed interrogation sequence (cf. App. A), which may not capture the true prior width of variational protocols sufficiently accurate. Consequently, the optimization can lead to variational protocols that are more susceptible to the true residual noise than predicted by the model, resulting in deviations between theoretical predictions and numerical simulations. (iii) Additionally, the assumption of a Gaussian prior distribution for the residual noise in each cycle may not reproduce the true dynamics appropriately. In particular, for small ensembles, the number of possible measurement outcomes is small and thus, the central limit theorem justifies this assumption to a reasonable level only in the asymptotic limit of many repetitions. Consequently, corresponding deviations reduce with increasing N.

As a consequence, stability can be compromised in both regimes. To address these limitations, we simulate the clock performance of several protocols for a fixed interrogation time T and variational class $[n, m]$, corresponding to distinct local minima in the parameter landscape (cf. Fig. 4.4(b)), and select the protocol that achieves the best stability. Consequently, the best-performing protocol identified in simulations may differ from the theoretical optimum, leading to deviations between simulation and theory. To give an example, the variational protocol associated with the hexagon in area (III) in Fig. 4.4(b) achieves the lowest Allan deviation in theory, while it is limited by fringe hops in the numerically simulated full feedback loop. Instead, the protocol corresponding to the circle in area (V) performs best in numerical simulations, resulting in a significant deviation to theoretical prediction. Moreover, the sensitivity landscape typically features numerous local minima and thus, it is not feasible to simulate all emerging protocols. In extreme cases, fringe hops may affect all simulated protocols, leading to complete stability loss. Hence, we show the least complex variational class $[1, m]$ that achieves theoretical predictions at the OQI plateau. At long interrogation times, we include simulation results of deeper quantum circuits where a substantial gain is observed.

4.7.2 Clock stability

Overall, numerical simulations align closely with theoretical predictions across a wide range of interrogation times. However, as discussed in the previous section, fringe hops impose the primary limitation at the OQI plateau. Additionally, for ensembles with $N \lesssim 20$ and long interrogation times, fringe hops limit the clock stability rather than the coherence time limit of the local oscillator. As a consequence, the minimal Allan deviation σ_{min} is not achieved for small ensembles, and variational protocols provide marginal to no advantage over SSS in this regime. In particular, we distinguish between three regimes based on the ensemble size:

(i) For very small ensembles with $N \lesssim 4$ (cf. Fig. 4.5(a)), the GHZ protocol saturates the ultimate lower limit – represented by the OQI – for short interrogation times, while at long interrogation times – approaching the fringe hop limit T_{sim} – SSS become optimal. Hence, variational protocols provide an advantage over standard protocols only in the regime of the OQI plateau. In this regime, typically the simplest $[1, 1]$-class already is sufficient to saturate the OQI. However, the optimal protocols vary significantly with interrogation time, increasing their susceptibility to fringe hops. Furthermore, the OQI plateau is relatively narrow for $N \lesssim 4$. Given the trade-off between potential stability gains and the experimental challenges involved in implementing more complex Ramsey protocols, the GHZ protocol at short interrogation times and SSS at longer interrogation times remain the preferable choices for ensembles with $N \lesssim 4$.

(ii) For intermediate ensembles with $4 < N \lesssim 20$ (cf. Fig. 4.5(b)), fringe hops continue to impose the fundamental limitation at long interrogation times. Furthermore, the regime of the OQI plateau expands, which in turn increases the region where variational protocols provide an advantage over SSS. Nevertheless, $[1, m]$ protocols remain fragile to fringe hops in this regime and additionally do not suffice to actually saturate the OQI. At long interrogation times approaching T_{sim}, which itself approximates T_{min} with increasing N, variational protocols offer improved stability compared to SSS. In this regime, again the simplest $[1, 1]$-class is sufficient to achieve a relevant improvement, while the additional benefit of $[1, m]$ protocols with $m > 1$ is negligible when considering the fluctuations over independent clock runs. However, to achieve a gain compared to SSS at long interrogation times requires $T \sim T_{\mathrm{sim}}$. For practical implementation in an experiment, Ref. [92] suggests to choose an interrogation time slightly shorter than T_{sim}, effectively providing a safety margin against fringe hops. As a result, similar to $N \lesssim 4$, variational protocols for $N \lesssim 20$ effectively enhance clock stability primarily within the OQI plateau regime, which remains less favorable in experimental settings, while GHZ states and SSS are beneficial at short and long interrogation times, respectively.

(iii) As the ensemble size increases to $N \gtrsim 20$ (cf. Fig. 4.5(c)), the limitations imposed by fringe hops and the coherence time limit become comparable. In this regime, variational protocols succeed to achieve σ_{min}, resulting in a substantial gain in stability over SSS. Furthermore, as N grows, increasing the circuit complexity m of the $[1, m]$ protocols provides relevant gains in stability.

To conclude, variational protocols for clocks with only a few atoms, characteristic of ion traps, primarily enhance stability within the OQI plateau. However, this regime is less favorable due to the strong dependence of variational parameters on interrogation time and increased susceptibility to fringe hops. In contrast, for clocks with several tens of atoms, typical of tweezer arrays, variational Ramsey protocols offer a significant improvement in clock stability, particularly at long interrogation times. Here, low-depth quantum circuits are sufficient, as the benefits diminish with increasing m, resulting in a trade-off between increased complexity and extended dynamic range.

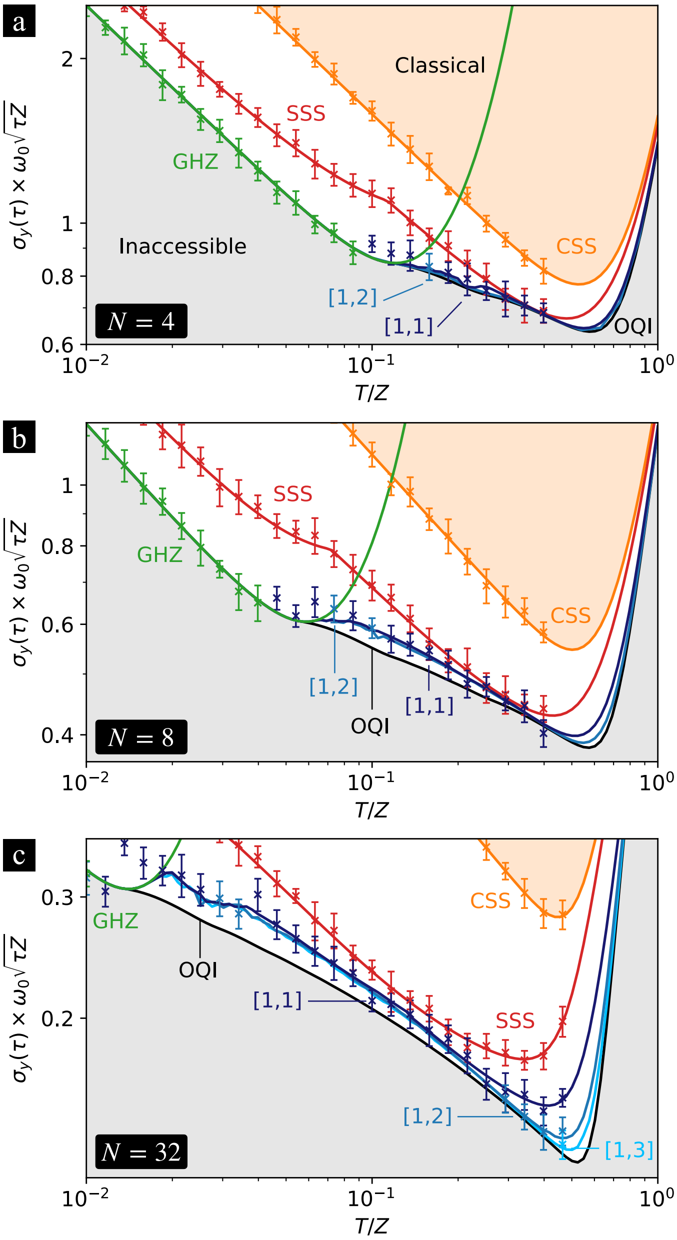

Figure 4.5: **Monte Carlo simulations of Ramsey protocols in Bayesian frequency metrology:** Numerical simulations of the full feedback loop in an atomic clock compared to the theoretical predictions of the Allan deviation for ensemble sizes (a) $N = 4$, (b) $N = 8$ and (c) $N = 32$. The variational Ramsey protocols $[n, m]$ consist of n and m layers of one-axis-twisting interactions for state preparation and measurement, respectively. Symbols represent the mean clock stability, while error bars indicate fluctuations over independent clock runs, arising from the stochastic nature of the Monte Carlo simulations. Fringe hops limit stability in the plateau regime and at long interrogation times, as discussed in the main text. The associated prior width is obtained iteratively. Further details on the numerical simulations are provided in App. A.

4.7.3 Comparison of linear and optimal Bayesian estimation

In Sec. 4.6.1, we observed that the optimal Bayesian estimator achieves significant improvements over the linear estimator in several regimes for standard protocols. For instance, it provides a larger dynamic range at long interrogation times and enables stronger spin-squeezed states at short interrogation times due to its non-linearity. Nevertheless, the linear estimator delivers equivalent results at interrogation times where the signal can be linearized within the extent of the prior distribution, which typically corresponds to $T/Z \ll 1$. Moreover, the linear estimator simplifies numerical studies (see Sec. 4.4) and has delivered remarkable results in previous works [91, 92], including applications in variational Ramsey interferometry [140–142]. Therefore, we compare the performance of the linear and optimal Bayesian estimators in the context of variational interrogation protocols to determine whether the potential advantages of the optimal Bayesian estimator, while significant in some regimes for standard protocols, translate into meaningful improvements in the case of variational quantum circuits.

In Fig. 4.6, we compare theoretical predictions of clock stability for optimized variational $[1, m]$ protocols employing both estimation strategies. Surprisingly, the linear estimator effectively achieves the same stability as the optimal Bayesian estimator. In particular, the optimal Bayesian estimator does not extend the dynamic range at long interrogation times and correspondingly does not enhance the minimal Allan deviation, while offering only a marginal enhancement in the plateau regime of the OQI, where GHZ protocols become ineffective. However, this gain is negligible, especially when considering the stability issues in this regime discussed in the previous sections. Consequently, in theory, the optimal Bayesian estimator does not provide a relevant improvement over the linear estimator, which is consistent with findings in Ref. [142] for exclusively anti-symmetric signals (cf. Supplementary Discussion S9 in Ref. [142]).

While theoretical predictions offer valuable insights, their validation in realistic scenarios is essential for a comprehensive analysis, as discussed before. Fig. 4.6 additionally presents numerical simulations of the full feedback loop. The standard protocols perform as predicted by theory, exhibiting the same limitation imposed by fringe hops at long interrogation times, as observed with the optimal Bayesian estimator. For larger ensemble sizes $N \gtrsim 20$, where the coherence time limit and fringe hops constrain clock stability at the same level, the reduced dynamic range of the linear estimator for sinusoidal signals becomes relevant. As a result, the optimal Bayesian estimator achieves higher stabilities for CSS and SSS, as discussed in Sec. 4.6.1. Again, variational protocols are constrained by fringe hops in two distinct regimes. (i) At the OQI plateau, the susceptibility to fringe hops is significantly enhanced for the linear estimator compared to the optimal Bayesian estimator, as indicated by larger deviations between theoretical predictions and numerical simulations, as well as broader regions where deeper quantum circuits are required to achieve theoretical predicitions. However, given the strong variation in optimal Ramsey schemes and the emergence of fringe hops, operating a clock in these regimes may be experimentally unfavorable anyway, as discussed in previous sections. Thus, the stronger limitation imposed by fringe hops in this regime is of minor practical relevance. (ii) For $N \lesssim 20$, clock stability is limited by fringe hops at the same level for both estimation strategies, leading to comparable maximal interrogation times T_{sim} (cf. Fig. 4.6(a) and (b)). In contrast to the optimal Bayesian estimator, for larger ensembles with $N \gtrsim 20$, fringe hops remain the dominant limitation when using the linear estimation strategy. As a consequence, the minimal Allan deviation σ_{min} is not achieved for $[1, m]$ protocols, as illustrated in Fig. 4.6(c). Therefore, in clocks with a few tens of atoms – typically realized in tweezer arrays – the linear estimation strategy causes fringe hops to impose a stricter constraint on clock stability than the coherence time of the local oscillator, ultimately resulting in reduced stability.

In summary, the optimal Bayesian estimator guarantees to saturate the BCRB, thereby maximizing the use of the measurement data. Whether the linear estimation strategy can achieve comparable performance depends strongly on the particular interrogation scheme and must be evaluated for each specific scenario. For variational Ramsey protocols, as considered in this work, the optimal Bayesian estimator proves to be less susceptible to fringe hops and therefore achieves higher stability. While this difference may be negligible in the regime of the OQI plateau, where these protocols are potentially unfavorable for experimental implementation, the critical ensemble size at which fringe hops and the coherence time limit constrain the clock stability at the same level is larger when using the linear estimation strategy.

Moreover, it is important to note that the estimation strategy primarily affects the classical post-processing of the measurement outcome. Consequently, the complexity of the Ramsey sequence remains unchanged for both estimation strategies. The quantum circuit itself is only indirectly influenced, as the choice of estimator affects the optimal variational parameters. Typically, the optimal Bayesian estimator leads to smaller total twisting strengths $\mu = \sum_j |\mu_j|$, particularly for variational classes $[1, m]$ with $m > 1$. Hence, the linear estimation strategy effectively requires larger twisting strengths to compensate for the non-linearity of the optimal Bayesian estimator. As a result, quantum circuits employing the optimal Bayesian estimator achieve shorter gate durations, which may be of practical interest.

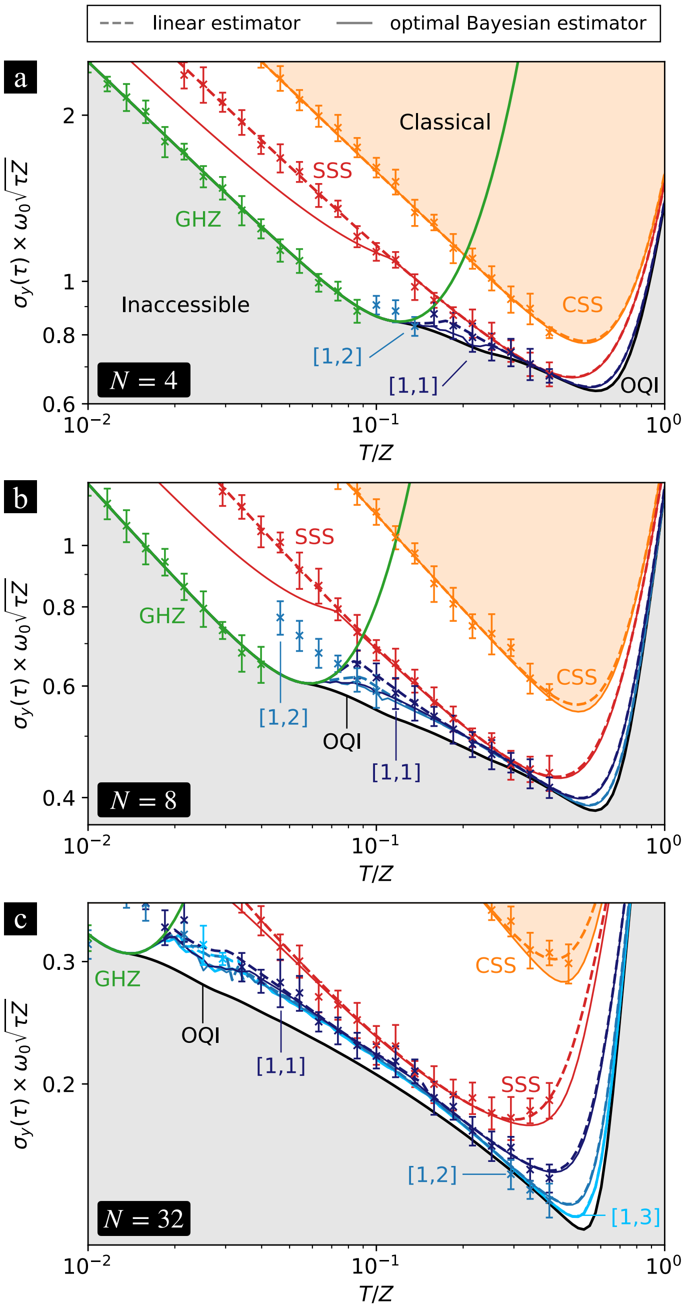

Figure 4.6: **Comparison of the linear and optimal Bayesian estimation strategy:** Numerical simulations of the full feedback loop in an atomic clock with a linear estimation strategy for ensemble sizes (a) $N = 4$, (b) $N = 8$ and (c) $N = 32$ characterized by the Allan deviation. The variational Ramsey protocols $[n, m]$ consist of n and m layers of one-axis-twisting interactions for state preparation and measurement, respectively. Lines depict theoretical predictions with the linear (dashed) and optimal Bayesian estimator (solid). Symbols represent the mean clock stability, while error bars indicate fluctuations over independent clock runs, arising from the stochastic nature of the process. Fringe hops limit stability in the plateau regime and at long interrogation times, as discussed in the main text. Further details on the numerical simulations are provided in App. A

4.8 Dead time

In the previous sections, we extensively discussed the trade-off between quantum projection noise (QPN) – which decreases with the interrogation time T (cf. Eq. (4.30)) – and the coherence time limit (CTL) of the local oscillator, which constraints clock stability at long interrogation times. Here, we extend the discussion to account for the effect of dead time T_D in atomic clock operation. Dead time typically arises from processes such as probe preparation, measurement and the application of feedback. During this period, frequency fluctuations of the local oscillator remain unmonitored by the Ramsey interrogation and therefore cannot be measured or corrected. The cumulative effect of this lack of information degrades the long-term stability of the atomic clock, a phenomenon first described by G. J. Dick [223, 224], therefore commonly referred to as the Dick effect. The contribution of the Dick effect to the clock stability is directly inferred from the spectral noise density $S_y(f)$ of the local oscillator and is given by [224, 225]

$$\sigma^2_{y,\mathrm{Dick}}(\tau) = \frac{1}{\tau}\frac{T_C^2}{T^2}\sum_{k=1}^{\infty} S_y\left(\frac{k}{T_C}\right)\frac{\sin^2(\pi k T/T_C)}{\pi^2 k^2}, \tag{4.44}$$

where $T_C = T_D + T$ is the clock cycle duration. The impact of the Dick effect diminishes with longer interrogation times T, as it depends on the ratio T/T_C which decreases when the relative contribution of dead time is reduced. Taking dead time into account, the overall clock stability is determined by the interplay between QPN, CTL and Dick noise. Specifically, it is characterized by the total Allan deviation

$$\sigma_{y,\mathrm{tot}}(\tau) = \sqrt{\sigma^2_{y,\mathrm{QPN}}(\tau) + \sigma^2_{y,\mathrm{CTL}}(\tau) + \sigma^2_{y,\mathrm{Dick}}(\tau)}, \tag{4.45}$$

where QPN and the CTL are combined in the Bayesian framework as $\sigma^2_y(\tau) = \sigma^2_{y,\mathrm{QPN}}(\tau) + \sigma^2_{y,\mathrm{CTL}}(\tau)$. While the Bayesian approach generally does not permit a strict separation of QPN and CTL contributions – except in specific cases such as the OQI or for CSS and SSS with a linear estimator (cf. Sec. 4.6.1) – it is, nevertheless, advantageous to treat them formally as independent components in order to discuss their general scaling quantitatively. The trade-off characterized by $\sigma_{y,\mathrm{tot}}(\tau)$ has been thoroughly studied for CSS and SSS with a linear estimator in Ref. [91], where QPN was characterized using local phase estimation theory, while the CTL was modeled via a stochastic differential equation describing the stabilized frequency of the local oscillator. In contrast, this chapter adopts the discussion to the Bayesian framework, which offers an intuitive and comprehensive approach to addressing these effects. Additionally, for comparison we include the ultimate lower bound on clock stability represented by the OQI. After analyzing the general scaling of $\sigma_{y,\mathrm{tot}}(\tau)$ for standard protocols, we consider various experimental platforms and discuss the effect of dead times characteristic of each setup. Furthermore, we explore the potential benefits of variational quantum circuits in these regimes.

4.8.1 Dead time in Bayesian frequency metrology

In addition to the contribution described by Eq.(4.44), dead time affects Bayesian frequency metrology in two distinct ways. First, and most notably, it modifies the scaling of the Allan deviation associated with QPN and the CTL as a function of the interrogation time T. Instead of the ideal $\sim 1/\sqrt{T}$ scaling, dead time reduces it to $\sim \sqrt{T_C/T^2}$, as apparent in Eq. (4.33). Second, dead time broadens the prior distribution of the phase due to unmonitored frequency fluctuations during T_D. Among these two effects, the modified scaling with T has a substantially larger impact, whereas the broadening of the prior distribution introduces only a relatively minor correction. Nevertheless, incorporating the implicit broadening is crucial for accurate modeling and for identifying optimal Ramsey protocols and estimation strategies, as the prior width strongly influences the optimal interrogation sequence, as explored in previous sections.

Although the prior width could, in principle, be adjusted iteratively to include dead time as for $T_D = 0$, this approach is computationally demanding. Moreover, our goal is to establish a direct connection between scenarios with ($T_D > 0$) and without ($T_D = 0$) dead time. Since the additional frequency fluctuations during dead time are unmonitored by the Ramsey interrogation, the broadening of the prior distribution during dead time and during the Ramsey sequence T are independent processes. Treating the broadening of the phase distribution during dead time as a phase diffusion process, the modified prior distribution $\mathcal{P}(\phi) = (\mathcal{P}_D * \mathcal{P}_T)(\phi)$ is obtained by a convolution of the initial prior distribution $\mathcal{P}_T(\phi)$, resulting from the Ramsey interrogation time T with corresponding width $\delta\phi_T$ (cf. Sec. 4.5.3), and the distribution $\mathcal{P}_D(\phi)$ associated with dead time. In this context, $\mathcal{P}_D(\phi)$ effectively acts as a Green's function [160]. Although local oscillator noise in general is correlated, the additional noise introduced during dead time within the full feedback loop is well approximated as white noise in the asymptotic limit of many clock cycles. Consequently, $\mathcal{P}_D(\phi)$ is modeled as a Gaussian distribution with zero mean and width $\delta\phi_D$. As a result, the modified prior distribution $\mathcal{P}(\phi)$ remains Gaussian with zero mean and variance

$$(\delta\phi)^2 = (\delta\phi_D)^2 + (\delta\phi_T)^2. \tag{4.46}$$

To fully incorporate the impact of dead time into the Bayesian framework, we now relate the broadening of the phase distribution – characterized by $\delta\phi_D$ – to the dead time T_D, akin to the dead time-free case in Sec. 4.5.3. Rather than deriving a comprehensive model for arbitrary scenarios, we establish a relation $\delta\phi_D(T_D)$ that primarily aims to accurately predict behavior in the vicinity of the minimal Allan deviation σ_{min} at interrogation time T_{min}. To this end, the broadening of the prior width during dead time can be effectively modeled by translating the additional frequency fluctuations into hypothetical phase shifts, as if they had occurred during a Ramsey interrogation of duration T_D. In this context, the associated prior width is given by (cf. App. A)

$$(\delta\phi_D)^2 \simeq 2\left(\frac{T_D}{Z}\right)^{1-\alpha}, \tag{4.47}$$

reflecting a power-law dependence, analogous to Eq. (4.35). Here, the parameter α again characterizes the nature of the frequency noise, with values $\alpha = 0, -1, -2$ corresponding to white, flicker and random walk frequency noise, respectively.

As a consequence, adjusting the prior width according to Eq. (4.46) extends the Bayesian framework to incorporate dead time within the clock cycle, accounting for both the Ramsey interrogation time T and the dead time T_D. Therefore, aside from adapting the prior width to reflect dead time T_D, the findings from the previous sections remain directly applicable. Therefore, the primary remaining task is to analyze the impact of the Dick effect $\sigma_{y,\text{Dick}}(\tau)$ on overall clock stability.

4.8.2 General results

In general, the total clock stability reflects a trade-off between quantum projection noise (QPN), the coherence time limit (CTL) and the Dick effect, as described by Eq. (4.45). While the CTL emerges at long interrogation times, limiting the clock stability as T approaches the laser coherence time Z, both QPN and Dick noise decrease monotonically with the interrogation time T. Unlike QPN, which reduces with larger ensembles, the CTL and Dick noise are independent of N. As a result, whether the minimal Allan deviation σ_{min} – achieved at optimal interrogation time T_{min} – arises from a trade-off between QPN and the CTL or between the Dick effect and the CTL depends on the particular dead time, ensemble size and Ramsey protocol [91].

For short dead times or small ensembles, QPN typically dominates Dick noise, leading to behavior that closely resembles the dead time-free case (cf. $N = 8$ in Fig. 4.7(a)). Here, the clock stability is primarily determined by a trade-off between QPN and the CTL and, therefore, depends on the ensemble size as well as the choice of Ramsey sequence. However, as dead time increases or QPN decreases, at some point, QPN is reduced to the level of Dick noise. Since Dick noise typically decreases more slowly with the interrogation time than QPN, first, it becomes dominant at long interrogation times, limiting the minimal Allan deviation σ_{min} (cf. $N = 32$ in Fig. 4.7(a)). Reducing QPN further, by either increasing the ensemble size or adapting the Ramsey interrogation, improves σ_{min} only marginally. In the regime where dead time effects strictly dominate over QPN – as is the case for large ensembles or long dead times – no further improvements in clock stability are possible, as Dick noise is independent of the particular Ramsey sequence and ensemble size. Therefore, we can define a lower limit σ_{lim} on the clock stability, at corresponding interrogation time T_{lim}, which is characterized by a trade-off between Dick noise and the CTL. Since the CTL is protocol-dependent, σ_{lim} in general differs for distinct Ramsey protocols and is primarily determined by their respective dynamic range.

Fig. 4.7(b) illustrates the scaling of σ_{min} with the ensemble size N for the standard Ramsey protocols. For small ensembles – where QPN dominates – clock stability improves as N increases, as in the ideal scenario ($T_D = 0$). However, as the ensemble size grows, Dick noise becomes relevant, reducing the N-scaling and causing the clock stability to converge to σ_{lim}. Unfortunately, explicit expressions for σ_{lim} can only be derived for protocols where QPN and CTL are separable, such as for the OQI or CSS and SSS with a linear estimator. Otherwise, the convergence towards σ_{lim} with N has to be evaluated numerically. As argued before, CSS and SSS with a linear estimator exhibit the same CTL and, consequently, identical lower limits. A similar behavior is observed for both protocols using the optimal Bayesian estimator, which, however, achieves an improved σ_{lim} due to the larger dynamic range (cf. Sec. 4.6.1). GHZ protocols – already highly susceptible to local oscillator noise in dead time-free scenarios – are further constrained by dead time, making them suitable only for small ensembles and short dead times. In the asymptotic limit, the performance of the POI again saturates the OQI.

To characterize the transition between the regimes dominated by either QPN or Dick noise, we define a critical ensemble size N_{crit}, at which the Allan deviation $\sigma_y(\tau)$ (cf. Eq. (4.33)) – arising from QPN and the CTL – saturates σ_{lim} at T_{lim}. Beyond N_{crit}, Dick noise dominates over QPN and thus spoils the N-scaling of σ_{min}, which ultimately converges towards σ_{lim} without substantial improvements as N increases. Since N_{crit} depends explicitly on QPN, it differs for distinct Ramsey protocols and estimation strategies, as generically illustrated in Fig. 4.7(c). For instance, N_{crit} for SSS is substantially smaller than for CSS, since they exhibit the same CTL, but SSS feature significantly smaller QPN. Consequently, the required ensemble size to approach σ_{lim} is substantially smaller for SSS compared to CSS, with a reduction of up to two orders of magnitude for short T_D, while still maintaining a significant difference even at long dead times. In contrast, the difference between OQI and SSS is relatively small, amounting to less than one order of magnitude for short dead times and becoming effectively negligible as T_D increases.

For a particular dead time T_D, the lower limit σ_{lim} is determined solely by the CTL of the Ramsey protocol and the estimation strategy, essentially reflecting the dynamic range. Consequently, CSS and SSS achieve the same lower limit for a specific estimator. Moreover, as shown in Fig. 4.7(d), the enhancement of σ_{lim} achieved by the OQI compared to CSS or SSS is relatively minor. Interestingly, increasing the dynamic range of CSS and SSS by substituting the linear by the optimal Bayesian estimation strategy yields a greater gain than the advantage provided by the OQI over CSS or SSS with the optimal Bayesian estimator. As a result, CSS and SSS already perform close to the OQI in the regime limited by dead time.

As T_D increases, the potential enhancement of σ_{lim} diminishes further. This can be understood as follows: In general, dead time shifts T_{min} – achieving the minimal Allan deviation σ_{min} – to longer interrogation times. This is shown in Fig. 4.7(e) and primarily results from the impact of $\sigma_{y,\text{Dick}}$ (cf. Fig. 4.7(a)). However, in this regime, the difference in the CTL for distinct Ramsey schemes decreases with increasing T (cf. Fig. 4.2(a)), thereby reducing the advantage associated with a larger dynamic range. While the OQI allows unbiased phase estimation over $[-\pi, +\pi]$, the optimal Bayesian strategy for CSS and SSS resembles the *arcsin* estimator and thus covers the range $[-\pi/2, +\pi/2]$ (cf. Sec. 4.6.1). As a result, the OQI and CSS or SSS with optimal Bayesian estimator exhibit a similar behavior, where the corresponding gain only marginally reduces with T_D. In contrast, the deviation between the linear and optimal Bayesian estimators for CSS and SSS diminishes substantially with T_D, since the corresponding N_{crit} becomes smaller, leading to a reduced gain in dynamic range for the optimal Bayesian estimator, as discussed in Sec. 4.6.1.

To summarize, for small ensembles N or short dead times T_D, clock stability is primarily limited by QPN, closely resembling the dead time-free case. However, as N or T_D increases, the Dick effect becomes the dominant noise and ultimately limits the clock stability. Beyond the critical ensemble size N_{crit}, which decreases with T_D, the minimal Allan deviation σ_{min} converges to the lower limit σ_{lim}. In this regime, further improvements in clock stability by increasing the ensemble size or adapting the Ramsey sequence are marginal. As a consequence, clocks with large ensembles ($N \gg 1$) limited by Dick noise approximate the lower limit σ_{lim} sufficiently well by employing CSS or SSS.

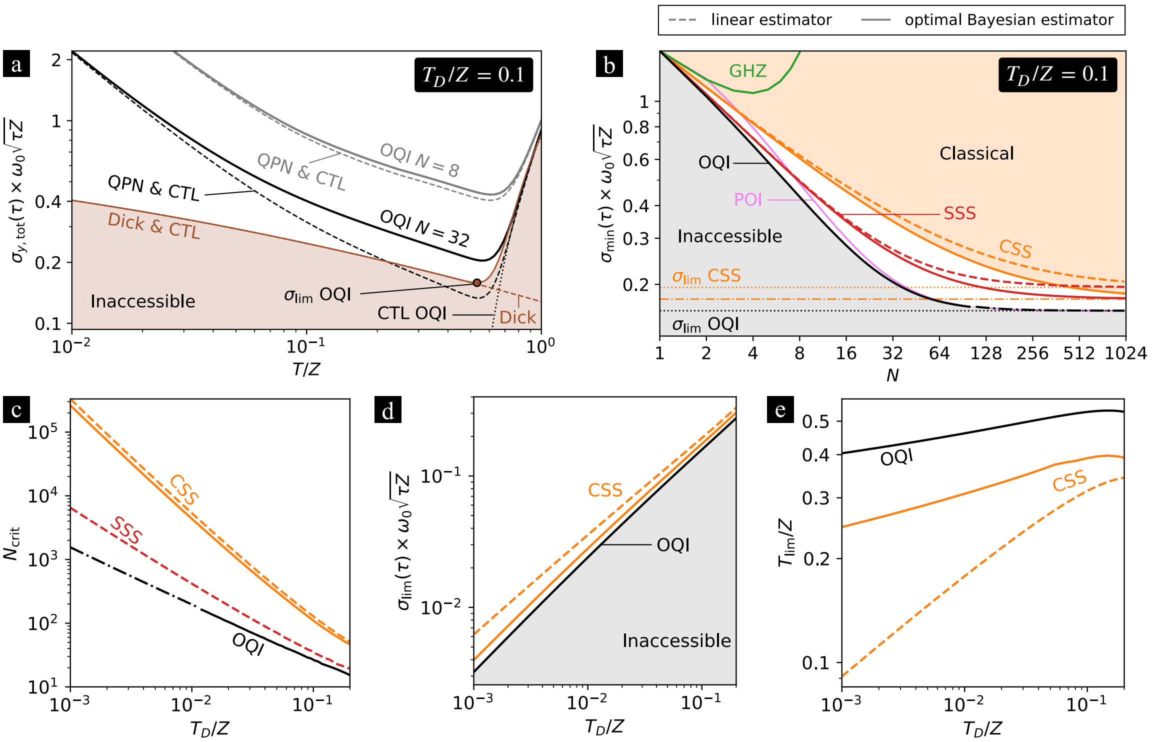

Figure 4.7: **Dead time effects:** (a) Generic scaling of the dimensionless total Allan deviation $\sigma_{y,\mathrm{tot}}(\tau) \times \omega_0\sqrt{\tau Z}$ with the interrogation time T for dead time $T_D/Z = 0.1$. The total stability (solid) of the OQI for $N = 8$ (gray) and $N = 32$ (black) is shown in comparison to the trade-off between QPN and CTL (dashed). The N-independent lower limit σ_{lim} (symbol) is imposed by a trade-off (solid brown) between Dick noise (dashed brown) and CTL (dotted black). Consequently, the brown shaded area is inaccessible. (b) Scaling of the total dimensionless minimal Allan deviation $\sigma_{\mathrm{min}} \times \omega_0\sqrt{\tau Z}$ with the ensemble size N for $T_D/Z = 0.1$. GHZ protocols (green) achieve no gain compared to CSS. For CSS (orange) and SSS (red), both the linear (dashed) and optimal Bayesian estimator (solid) are depicted. The gray shaded area represents the inaccessible stability region set by the OQI (black), while the orange shaded area indicates achievable stabilities using uncorrelated atoms. Dotted lines correspond to the lower limit σ_{lim} for the OQI and CSS with linear estimator, while the dashed dotted line denotes the lower limit for CSS using the optimal Bayesian estimator. SSS exhibit the same lower limit as discussed in the main text and seen from the convergence. The POI (violet) saturates the OQI for $N \gtrsim 50$. For the OQI and POI, numerical optimization is performed for $N \leq 100$, while the asymptotic behavior, represented by the πHL (black dashed-dotted), is shown for $N > 100$. (c) Critical ensemble size N_{crit} as a function of the dead time T_D/Z for the OQI (black), CSS (orange) and SSS (red). Again, dashed lines correspond to the linear estimator, while solid lines represent the optimal Bayesian estimator. The evaluation of the SSS with optimal Bayesian estimator requires the computation of the conditional probabilities (cf. Sec. 4.4) and thus is unfeasible for large N. For $N \gtrsim 100$, the asymptotic OQI, imposed by the πHL (black dashed-dotted), is shown. (d) Scaling of the total dimensionless lower limit $\sigma_{\mathrm{lim}} \times \omega_0\sqrt{\tau Z}$ with dead time for the OQI (black) and CSS (orange). For the CSS, linear (dashed) and optimal Bayesian estimator (solid) are displayed, while SSS achieve the same limits. (e) Corresponding interrogation times T_{lim}, effectively characterizing the dynamic range. SSS result in the same σ_{lim} and T_{lim} as CSS (cf. discussion in the main text).

4.8.3 Setup specific dead times

Building on the general discussion of dead time effects on clock stability in standard protocols, this section focuses on examining specific examples relevant to particular experimental setups, such as ion traps, tweezer arrays and lattice clocks, ranging from a few to thousands of atoms.

In general, atomic clock operation involves three key time scales: the laser coherence time Z, the dead time T_D and the interrogation time T. In a given experimental setup, Z and T_D are primarily independent but fixed, defining a specific ratio T_D/Z. In contrast, T remains an adjustable parameter, which is implicitly constrained by Z. As a consequence, findings on clock stability cannot be trivially rescaled with respect to various laser coherence times Z – as in the dead time-free scenario – or dead times T_D, since a modification of Z or T_D results in a change of the ratio T_D/Z, which in turn has a substantial impact on the clock stability, as discussed in the previous section.

In experimental settings, the dead time T_D and interrogation time T commonly are expressed in terms of the dimensionless duty cycle

$$\eta = \frac{T}{T_C} = \frac{T}{T + T_D}, \tag{4.48}$$

which quantifies the relative contribution of the interrogation time T to the total duration of the clock cycle $T_C = T_D + T$. Hence, a larger duty cycle η corresponds to a reduced relative impact of dead time. However, it is important to emphasize that, implicitly, a specific ratio between T_D and Z is always assumed.

While the laser coherence time Z is independent of the atomic reference, dead time strongly depends on the particular experimental platform. To address this, we investigate the clock stability for typical dead times across the three predominant regimes: ion traps, tweezer arrays and lattice clocks. Each of these platforms exhibits distinct time scale dynamics and operational characteristics that significantly influence clock performance. Ion traps provide the highest degree of control, including rapid cooling and no need for reloading due to deep trap depths, resulting in relatively short dead times [12]. Although recent advancements in Coulomb crystals have facilitated multi-ion clocks [17, 18], ion traps remain inherently limited in scalability, typically operating with only a few ions. In contrast, optical lattice clocks employ large ensembles of hundreds to thousands of atoms, enabling high precision at the cost of experimental challenges such as atom number fluctuations and interatomic collisions [12]. Furthermore, these systems exhibit substantially longer dead times due to processes such as loading the lattice and cooling the atoms [23–26]. Additionally, dead time has a particularly pronounced impact on clock stability in lattice clocks, as QPN is typically suppressed well below the Dick effect, as discussed in the previous section. Tweezer arrays bridge between these two contrary approaches, offering a balance between the high control in ion traps and the scalability inherent in lattice clocks [19–22]. By incorporating ensembles of several tens of atoms, they offer a promising compromise between precision, scalability and operational efficiency.

In the following, we investigate the clock stability for representative dead times T_D and laser coherence times Z across these three distinct regimes. As discussed before, this is equivalently expressed by fixing the ratio T_D/Z. Starting with ion traps, which feature relatively short dead times, we explicitly examine the interplay between laser coherence time Z, dead time T_D and interrogation time T – or equivalently the duty cycle η – using state-of-the-art parameter values to develop an intuitive understanding of the relationship between these time scales. Subsequently, we progressively increase the dead time for setups representing tweezer arrays and lattice clocks, illustrating how dead time increasingly constrains clock performance and how the optimal Ramsey protocols change accordingly.

Besides the experimental platform, dead time is also affected by the particular interrogation sequence. In practice, the preparation time required for different quantum states – particularly entangled states – can vary significantly depending on the specific initial state. Likewise, the measurement time can vary substantially between different measurement strategies, especially for correlated measurement transformations as pursued for the variational Ramsey protocols. For instance, the conventional Ramsey protocol – utilizing coherent spin states (CSS) and a projective spin measurement – can be performed relatively quickly, as it relies on standard collective rotations of the spin system. In contrast, spin-squeezed states (SSS) already require non-linear interactions or measurement-based feedback for state preparation, which introduce additional time overheads. While the variational $[1, m]$ protocols – investigated in the previous sections – have comparable state preparation times to SSS, as they are also generated by a single OAT interaction, each additional layer of the quantum circuit implementing the effective measurement involves interaction times that scale with the corresponding twisting strength. The OQI, which represents the ultimate lower bound and currently lacks a specific experimental implementation, potentially requires even more demanding resources. As a consequence, for a particular experimental setup, dead times arising from state preparation and measurement have to be considered for each interrogation scheme. However, the resulting dead times are highly individual for each experimental setup and are thus challenging to quantify in general. To nevertheless provide theoretical insight, we compare different Ramsey protocols assuming a fixed dead time for each experimental platform, independent of the protocol complexity. While the results derived in the following provide general insight, this assumption should be kept in mind, as it may lead to an overestimation of the performance of highly entangled states in practical scenarios.

Ion traps— In ion traps, dead times of about $T_D = 100$ ms are routinely implemented in experiments. Moreover, state-of-the-art clock lasers achieve laser coherence times Z of several seconds. In practice, however, this impressive level of coherence is often not entirely maintained as the laser propagates between the reference cavity used for pre-stabilization – which not necessarily is located close to the trap or even in the same laboratory – and the ions. While optical path-length stabilization should, in principle, preserve coherence all the way to the ions, experimental imperfections – such as phase noise within the vacuum chamber – typically lead to a degradation of this quality. Therefore, we assume a laser coherence time of $Z = 2$ s at the location of the ions. Hence, in this exemplary scenario we obtain a ratio $T_D/Z = 0.05$. Furthermore, Fig. 4.5 demonstrates that fringe hops limit the clock stability at interrogation times around $T_{\text{sim}} \sim 0.4 - 0.5 \times Z$. Consequently, the maximal achievable duty cycle, given by $\eta_{\max} = T_{\text{sim}}/(T_{\text{sim}} + T_D)$, is on the order of 90%.

As discussed in the previous section, for small ensembles and short dead times, clock stability typically resembles the dead time-free scenario ($T_D = 0$), as illustrated in Fig. 4.8(a) for $N = 8$ and $T_D/Z = 0.05$. In this case, QPN remains the primary limitation, while the Dick effect has only a marginal impact, leading to a behavior similar to that shown in Fig. 4.5(b). In comparison, however, in the presence of dead time the plateau of the OQI is substantially less pronounced and thus, fringe hops impose a less stringent limitation in this regime. As in the $T_D = 0$ case, SSS approximate the OQI in the transition region between the plateau and $\sigma_{\min}$. At long interrogation times, fringe hops remain the primary constraint, limiting the interrogation time to $T_{\text{sim}} < T_{\min}$. Furthermore, variational protocols effectively provide no significant enhancement in clock stability around T_{sim}. As a result, for optical atomic clocks based on ion traps, GHZ states and SSS approach the OQI over a broad range of interrogation times, while the deviation from the OQI or variational classes within the plateau are reduced compared to the dead time-free scenario.

Tweezer arrays— For tweezer arrays, we consider a representative case with $N = 32$ in Fig. 4.8(b), assuming an increased dead time of $T_D/Z = 0.1$. Within the framework of the previous example, this corresponds to an absolute dead time of $T_D = 200$ ms and a maximal achievable duty cycle of approximately $\eta_{\max} = 80\%$. As already evident in Fig. 4.7(a), dead time imposes a significant limitation on clock stability in this regime. While GHZ states are essentially ineffective, SSS already perform close to the OQI for short and intermediate interrogation times. In this regime, variational protocols only provide marginal improvements in stability, whereas a noticeable enhancement is observed primarily for $[1, m]$ protocols in the vicinity of $T_{\min}$. However, this gain is significantly smaller than in the dead time-free case, and unlike the $T_D = 0$ scenario, fringe hops constrain clock stability at interrogation times $T_{\text{sim}} \lesssim T_{\min}$. When additionally considering a safety margin for fringe hops, as discussed in Sec. 4.7, the improvement becomes effectively negligible when accounting for the increased complexity. Consequently, SSS emerge as a robust Ramsey sequence, achieving clock stabilities close to the OQI in this regime.

Interestingly, for short interrogation times, deviations between theoretical predictions and numerical simulations appear. These discrepancies stem from the assumed prior width in the presence of dead time, which is intended to provide a reliable model primarily for interrogation times in the vicinity of $\sigma_{\min}$.

Crossover regime— Typically, the boundaries between different platforms with respect to the ensemble size N are not sharply defined. To explore the transition between tweezer arrays and lattice clocks, we examine the case of $N = 100$ in Fig. 4.7(c), with an increased dead time $T_D/Z = 0.2$. In the example above, this corresponds to $T_D = 400$ ms and an associated maximal duty cycle of approximately $\eta_{\max} = 65\%$. Such an increase in dead times is characteristic of lattice clocks, as discussed before, but can also result from various processes such as the overhead of operating multiple tweezer arrays simultaneously, the potential need for reloading due to shallower trap depths or extended cooling times. Moreover, inhomogeneous interactions may be relevant, as addressed in Ref. [140].

As the ensemble size N increases, variational classes are no longer favorable, as discussed in previous sections. A key characteristic of this regime is that dead time becomes the dominant limitation. However, while CSS have not yet fully converged to the lower bound σ_{lim}, SSS already provide a close approximation. As a result, SSS perform close to the OQI across all interrogation times, except at $T_{\min}$, where their limited dynamic range becomes apparent. Additionally, the choice of estimation strategy for standard protocols gains importance, as the optimal Bayesian estimator yields significantly higher clock stability at long interrogation times compared to the linear estimator.

Lattice clocks— Finally, we investigate the regime of lattice clocks with large ensembles $N \gg 1$, where QPN is reduced well below the Dick noise. Fig. 4.8(d) illustrates the case of $N = 1000$ with $T_D/Z = 0.2$. In this regime, both CSS and SSS closely approximate the lower limit σ_{lim}. Consequently, at long interrogation times both protocols achieve comparable clock stability, as already indicated in Fig. 4.7, whereas SSS provide a significant advantage at short interrogation times. Furthermore, the optimal Bayesian estimator results in a substantially higher stability in the vicinity of T_{min} compared to the linear estimation strategy. Notably, deviations from theoretical predictions and numerical simulations appear for the SSS at short interrogation times due to the choice of prior width (cf. Sec. 4.8.1). Additionally, since SSS introduce correlations between atoms, unlike CSS, numerical approximations are required to simulate the full feedback loop for $N \gg 1$, which can further contribute to discrepancies.

As a result, in the regime of large ensembles dominated by dead time, effectively no quantum enhancement is achieved at the optimal interrogation time. To exploit the benefits of entanglement, dead time effects have to be mitigated – for example through dead time-free interrogation schemes, as discussed in Sec. 4.10.

In summary, for small ensembles – representing ion traps – the behavior closely resembles the dead time-free case. Here, standard protocols as GHZ states or SSS already achieve clock stabilities comparable to the OQI for a wide range of interrogation times. As the ensemble size N or dead time T_D increases, Dick noise becomes the dominant limitation, effectively reducing the potential enhancement offered by variational quantum circuits compared to SSS. In particular, dead time results in SSS performing close to the OQI for a variety of scenarios. In the regime of large ensembles $N \gg 1$, characteristic for lattice clocks, CSS likewise converge to the lower limit σ_{lim} at long interrogation times and thus, are sufficient to approximate the OQI. As a consequence, dead time significantly constraints clock stability, where the degree of limitation increases with the ensemble size.

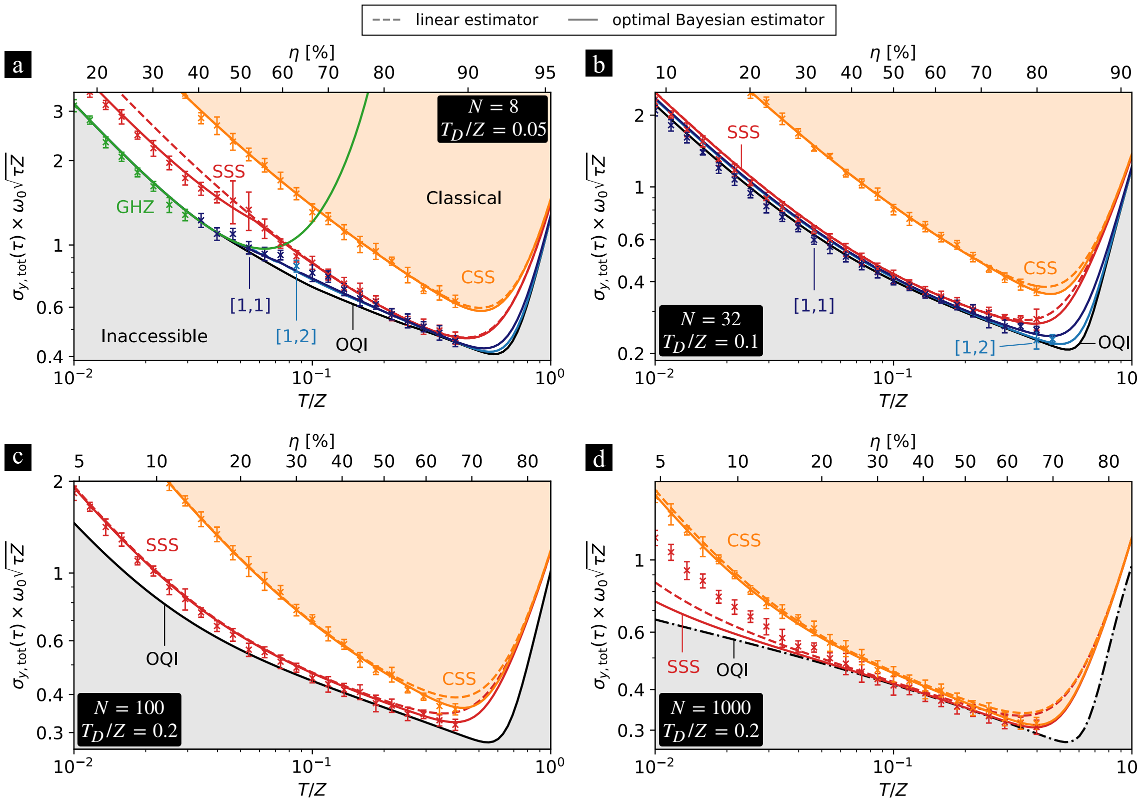

Figure 4.8: **Dead times characteristic for specific experimental setups:** Theoretical predictions and numercial simulations of various Ramsey protocols for (a) $N = 8$ and $T_D/Z = 0.05$, (b) $N = 32$ and $T_D/Z = 0.1$, (c) $N = 100$ and $T_D/Z = 0.2$, (d) $N = 1000$ and $T_D/Z = 0.2$. The variational Ramsey protocols $[n, m]$ consist of n and m layers of one-axis-twisting interactions for state preparation and measurement, respectively. Theory curves (lines) are displayed for the linear (dashed) and optimal Bayesian estimator (solid). Symbols represent numerical simulations in the full feedback loop of an atomic clock employing the optimal Bayesian estimation strategy. In both cases, the total Allan deviation is rescaled with respect to the atomic transition frequency ω_0, total averaging time τ and laser coherence time Z. The lower x-axis represents the interrogation time T relative to Z, while the upper x-axis denotes the dimensionless duty cycle η. The gray shaded area represents the inaccessible stability region set by the OQI limit (black), while the orange shaded area indicates achievable stabilities using uncorrelated atoms. For (a) $N = 8$ and (b) $N = 32$ the performance of variational quantum circuits (blue) is shown in addition to the standard protocols, namely GHZ states (green), CSS (orange) and SSS (red). For $N = 1000$, the asymptotic regime is reached and thus, the OQI is approximated by the πHL.

4.9 Conclusion

At this point, we briefly summarize the primary conclusion of this chapter, while referring to the outline at the end of Sec. 4.1 for a comprehensive overview of the insights and results. In general, the clock stability features a trade-off between quantum projection noise (QPN), the coherence time limit (CTL) and dead time effects. Additionally, fringe hops impose further constraints on stability within the full feedback loop of an atomic clock.

For small ensembles comprising a few atoms – as encountered in ion traps – fringe hops limit clock stability at long interrogation times. Consequently, in this regime, GHZ states and spin-squeezed states (SSS) approximate the optimal quantum interferometer (OQI) across a broad range of interrogation times. In contrast, variational protocols offer an advantage primarily within the plateau of the OQI. However, this regime is less favorable due to the strong dependence of variational parameters on interrogation time and the increased susceptibility to fringe hops. Moreover, in the presence of dead times typical for ion traps, the behavior closely resembles the dead time-free case, as QPN dominates the Dick effect.

For ensembles consisting of several tens of atoms – characteristic of tweezer arrays – variational clock protocols provide a significant improvement compared to SSS at long interrogation times. In this regime, fringe hops and the CTL constrain clock stability at a comparable level, enabling the achievement of the minimal Allan deviation. Moreover, low-depth quantum circuits $[1, m]$ are sufficient as the benefits diminish with increasing m, leading to a trade-off between increased complexity and extended dynamic range. However, as dead time increases, Dick noise becomes the primary limitation, substantially reducing the potential enhancement offered by variational quantum circuits compared to SSS. In particular, the limitation due to dead time results in SSS performing close to the OQI in a variety of scenarios.

In the regime of lattice clocks with large ensembles $N \gg 1$, QPN is reduced well below dead time effects. Consequently, any further improvements in stability by increasing the complexity of the Ramsey sequence are marginal, and coherent spin states (CSS) converge to the lower limit at long interrogation times, proving sufficient to approximate the OQI. As a result, effectively no quantum enhancement is achieved in this regime.

Overall, the optimal Ramsey protocols – and correspondingly the highest achievable clock stability – strongly depend on the specific parameters of the experimental setup. Although variational quantum circuits promise substantial enhancements in idealized scenarios, practical constraints as fringe hops and dead time effects limit these improvements. As a result, variational Ramsey protocols offer a significant advantage only in the regime of tweezer arrays primarily limited by QPN. In contrast, standard protocols utilizing GHZ states, CSS and SSS provide robust interrogation schemes, closely approaching the OQI in a variety of scenarios.

4.10 Outlook

This chapter provided a comprehensive overview of potential advancements and challenges across a broad range of scenarios in frequency metrology tailored to optical atomic clocks primarily limited by laser noise. Nevertheless, open questions remain and require further investigation.

Open questions— From a theoretical perspective, a rigorous treatment of the full feedback loop, as pursued in Ref. [199], within a Bayesian framework would ultimately be desirable. In particular, such a model of atomic clock operation could provide deeper insights into the following aspects:

(i) Currently, the connection between the Allan deviation, characterizing clock stability, and the Bayesian cost function – the Bayesian mean squared error (BMSE) – is based on mere heuristic arguments. In particular, this relation is motivated by analogy with the local approach and guided by fundamental bounds, however, no formal derivation exists. In a model of the full feedback loop, the effective measurement variance, defined in Eq. (4.31), should – ideally – emerge naturally in the evaluation of the Allan deviation and result in Eq. (4.33).

(ii) The prior phase distribution is typically modeled as a Gaussian distribution, with its width determined heuristically – either by a general approach or an iterative procedure. While this approximation yields reliable results in several situations, this parametrization, nevertheless, might not capture the true prior distribution sufficiently well in certain regimes, resulting in severe limitations. This issue might be particularly relevant for highly non-classical interrogation schemes, small ensemble sizes or in regimes where the optimal Ramsey protocol is highly susceptible to small changes in the prior width – as at the OQI plateau. Consequently, a generalized prior distribution could potentially enable a more accurate model of the actual frequency fluctuations – reflected in variations of the accumulated phase – and thereby reduce discrepancies between theoretical predictions and numerical simulations or experiments. Furthermore, it would facilitate the identification of optimal interrogation schemes tailored to the true prior distribution.

(iii) A promising approach involves full Bayesian propagation of the phase distribution throughout the entire clock run [201,210], rather than treating individual clock cycles in isolation. In this approach, the phase distribution is updated iteratively after each Ramsey sequence based on the measurement outcome, thereby enabling explicit tracking of frequency (or phase) fluctuations. Crucially, a global treatment of the phase over $-\infty < \phi < +\infty$ is required. Although restricting the phase to the periodic 2π interval accounts for ambiguities arising from transitions between adjacent fringes, it prevents their explicit resolution and thus ultimately limits the detection and potential mitigation of fringe hops.

Incorporating experimental limitations— Moreover, the concepts developed in this chapter can be extended to incorporate additional experimental limitations, enabling more detailed modeling of experiments. This, in turn, facilitates a deeper understanding of the underlying limiting processes and supports the identification of optimal Ramsey protocols tailored to specific experimental parameters. To this end, relevant decoherence processes – such as spontaneous decay or dephasing – can be included based on the concepts presented in Chapter 3. While numerical optimization in the context of local (frequentist) phase estimation with decoherence already is a fundamental challenge on its own – as discussed in detail in Chapter 3 – additionally introducing the averages over the prior phase distribution, inherent in Bayesian estimation theory, further increases the complexity. Consequently, incorporating decoherence effects directly into the theoretical framework of Bayesian phase estimation – as pursued in this chapter – would combine the numerical challenges of both approaches. Furthermore, the resulting optimal protocols may change substantially and thus would require a thorough investigation, similar to the discussion of dead time. However, this is beyond the scope of this progress report on frequency metrology limited by laser noise. Instead, we briefly review the literature considering decoherence effects. In particular, the additional effects of dephasing have already been examined in the Bayesian framework. For instance, Ref. [151] considers additional collective dephasing that is not associated with laser noise. Since collective dephasing is phenomenologically similar to the treatment of laser noise within the Bayesian framework, it affects stability in much the same way. The impact of uncorrelated single-atom dephasing in the Bayesian framework has been explored in Ref. [140], where it was observed that for moderate dephasing strengths the overall behavior remains qualitatively unchanged, although stability is naturally degraded. However, the benefit provided by variational quantum circuits – or more complex Ramsey schemes in general – over SSS diminishes substantially as the dephasing strength increases, leading to a behavior akin to that observed for dead time. A comparable pattern was reported in Ref. [141] for correlated single-atom dephasing. Furthermore, finite pulse durations – especially for clock species with ultra-narrow clock transitions yielding long interaction times – as well as gate imperfections – for state preparation and measurement – might be considered. Specifically, noise affecting the twisting operations has been considered in Refs. [5, 141]. As expected, deeper quantum circuits, which generally require stronger total twisting strengths, exhibit higher susceptibility to noise. Ref. [226] demonstrates that the potential improvements in clock stability through spin squeezing are significantly reduced if the squeezing is non-unitary. It further highlights that contrast loss during the squeezing process is less detrimental to clock stability than during the Ramsey dark time.

Overall, these observations reinforce the conclusions of this work: Standard protocols with low complexity – employing coherent spin states (CSS), GHZ states and spin-squeezed states (SSS) in particular – achieve stabilities compatible with the ultimate limit across a wide range of scenarios, whereas deeper quantum circuits – generating arbitrary states and measurements – offer a significant advantage only in very specific parameter regimes. This is consistent with a well-established observation in quantum sensing: In general, no single interrogation scheme is universally optimal. Instead, there exists an optimal protocol for a given application and its specific system parameters.

Strategies to overcome laser noise— In the framework of this chapter, laser noise constrains clock stability in three distinct ways: through the laser coherence time limit (CTL), the emergence of fringe hops and dead time effects. In addition to ongoing technological improvements in laser stability [88, 227, 228], several interrogation schemes have been proposed and demonstrated to address these limitations. However, these strategies go beyond the scope of this work, which focuses on conventional single-ensemble clock operation with identical interrogations of the atomic reference in each clock cycle. They include adaptive schemes [201, 210, 229, 230] and multi-ensemble strategies. For instance, dynamical decoupling sequences [231] and synchronous differential clock comparisons [232–235] have been demonstrated to extend interrogation times well beyond the laser coherence time. Other approaches involve active feedback and feedforward on the laser [236, 237], or cascaded clock operation that allows for increasingly long interrogation times [64, 237–240]. As proposed by Rosenband and Leibrandt in Ref. [241], partitioning atoms into multiple ensembles with distinct interrogation times can exponentially improve clock stability relative to the atom number. Furthermore, synchronous out-of-phase interrogations expand the invertible phase range and enhance the dynamic range [222, 242]. Moreover, dead time free clock operation can be achieved by asynchronously interrogating at least two atomic ensembles [29, 237, 243, 244]. Although these approaches extend beyond the scope of the present work, many of their underlying principles can be integrated with the Ramsey protocols discussed in this chapter, potentially mitigating the limitations imposed by laser noise and enabling longer interrogation times.

As a result, a variety of interrogation schemes have been developed to overcome the limitations imposed by laser noise. Nevertheless, a fundamental comparison that addresses the core questions of optimal scheme selection and efficient resource utilization across specific operational regimes is still lacking.

Zero-dead-time (ZDT) clocks— Finally, we discuss a specific aspect of zero-dead-time (ZDT) clocks, which can be readily investigated using the methods established in this chapter. To this end, we consider a setup comprising two ensembles[4], each with an identical atom number, operated within the same experiment. Indeed, such setups have already been experimentally realized across all three regimes discussed in this chapter – namely ion traps [245,246], tweezer arrays [64,247] and lattice clocks [29, 244]. To begin with, we consider coherent spin states (CSS) and a linear estimation strategy. The central question is whether it is advantageous to interrogate both ensembles simultaneously – effectively utilizing a total number of N atoms – or to implement a zero-dead-time clock scheme, with $N/2$ atoms per ensemble. This scenario reflects a fundamental trade-off: On the one hand, simultaneous interrogation reduces quantum projection noise (QPN) by leveraging the effective larger atom number and on the other hand, the ZDT approach eliminates dead time effects. Which of the two schemes offers better stability generally depends on the specific total atom number N, interrogation duration T and dead time T_D, as illustrated in Fig. 4.9(a). For the representative example with $N = 20$ atoms in total, the ZDT clock outperforms the conventional scheme at short interrogation times. However, at longer interrogation times, performance depends more sensitively on the actual dead time, particularly when approaching the minimal Allan deviation. As a consequence, we can identify a critical dead time $T_{D,\text{crit}}$ at which both approaches achieve equivalent stability at their respective optimal interrogation durations. Hence, for dead times shorter than the critical dead time ($T_D < T_{D,\text{crit}}$), the conventional clock scheme – despite incorporating dead time – is advantageous. Conversely, for longer dead times $T_D > T_{D,\text{crit}}$, the ZDT approach demonstrates superior stability. As expected from the results obtained in this chapter and illustrated in Fig. 4.9(b), the critical dead time decreases for larger ensembles, since the Dick effect becomes a relevant limitation on clock stability at shorter dead times due to reduced QPN. As a result, considering typical dead times for each experimental platform (cf. Sec. 4.8.3), conventional

---

[4] Note that this concept can be readily generalized to configurations with more than two ensembles.

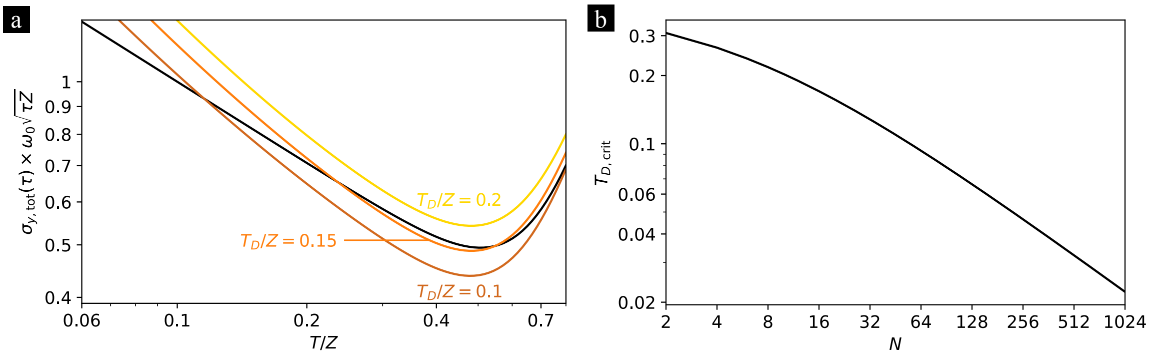

Figure 4.9: **Zero-dead-time clock:** (a) Generic scaling of the dimensionless total Allan deviation $\sigma_{y,\mathrm{tot}}(\tau) \times \omega_0\sqrt{\tau Z}$ with the interrogation time T relative to the coherence time Z for CSS and a linear estimation strategy. Colored lines represent conventional clock operation with $N = 20$ atoms and different dead times, whereas the black line depicts the zero-dead-time clock scheme with $N/2 = 10$ in each ensemble interrogated asynchronously. (b) Critical dead time $T_{D,\mathrm{crit}}$ as a function of the ensemble size N for CSS and a linear estimation strategy.

clock operation remains advantageous in ion traps, where QPN imposes the primary limitation. In contrast, the ZDT scheme is preferred in lattice clocks, where dead time effects dominate. In the transition regime – characteristic of tweezer arrays – the optimal strategy strongly depends on specific experimental parameters and thus represents the crossover between the two approaches.

Increasing the complexity of the Ramsey sequence – by adapting the initial state, the measurement or the estimation strategy – a similar qualitative behavior is observed. However, the critical dead time decreases further with the complexity of the quantum circuit, as dead time becomes the dominant limitation at progressively shorter dead times, as examined in Sec. 4.8.

5

Summary

Frequency metrology constitutes a cornerstone of modern precision measurements, playing a pivotal role in advancing fundamental research and technology. In particular, optical atomic clocks represent the most precise measurement devices to date, achieving stabilities at the level of 10^{-18} and below. Current efforts to further improve their stability involve exploring the use of entanglement in atomic systems to reduce quantum projection noise and surpass the standard quantum limit (SQL) imposed by uncorrelated atoms. Unfortunately, decoherence and noise processes limit the sensitivity in realistic scenarios and present a substantial obstacle in frequency metrology, impairing the precision of measurements by compromising the coherence of quantum systems essential for achieving entanglement-based enhancement. Consequently, frequency metrology inherently reflects a trade-off between achieving entanglement-enhanced sensitivity and maintaining robustness against decoherence and noise processes. Indeed, this fundamental challenge precisely defines the central objective of this thesis.

Specifically, we have considered single-ensemble clocks in which the atomic reference is periodically interrogated utilizing identical Ramsey protocols in each clock cycle. After providing a comprehensive theoretical foundation for atomic clock operation in Chapter 2 – primarily intended for future (graduate) students – we investigated regimes limited by decoherence processes in Chapter 3 – with a particular focus on spontaneous decay – and by laser noise in Chapter 4. As these two regimes are somewhat orthogonal, they are most effectively studied within distinct theoretical frameworks, namely local and Bayesian frequency metrology, respectively, which are introduced in detail at the beginning of each chapter.

In Chapter 3, we investigated the impact of spontaneous decay to frequency metrology, motivated by recent advancements in laser technology with coherence times of state-of-the-art clock lasers entering the regime of the excited-state lifetime of various clock candidates. This is particularly relevant as the finite lifetime of qubits in the excited state represents a fundamental limit rather than an external noise source.

Surprisingly – and in contrast to dephasing – we demonstrated that maximally entangled GHZ states provide a substantial enhancement compared to the SQL in the presence of spontaneous decay. In particular, we identified a protocol with quantum operations of low complexity and a highly nonlinear estimator that achieves this remarkable improvement. This is realized by a measurement and estimation scheme that implicitly allows to identify spontaneous decay events based on the measurement outcomes, while the estimation strategy explicitly excludes these cases at the end of the Ramsey sequence. Thus, it effectively implements an error detection and mitigation scheme tailored to frequency metrology limited by spontaneous decay.

In addition, we presented a variation of this protocol utilizing a GHZ-like initial state – with an unequal superposition of the two maximal Dicke states attributing a higher weight to the excited state to counteract spontaneous decay during the free evolution time – which achieves the ultimate lower limit for ensembles with several tens of atoms and outperforms spin-squeezed states (SSS) for up to 80 atoms. We validated the robustness of these protocols in realistic scenarios through comprehensive Monte-Carlo simulations of atomic clocks, thereby paving the way for near-term implementations into experimental setups. Moreover, we provided a detailed interpretation of why GHZ(-like) protocols remain optimal in the presence of spontaneous decay. Finally, we have examined the susceptibility of the GHZ(-like) protocols to dephasing.

Chapter 4 presented progress in frequency metrology tailored to optical atomic clocks primarily limited by laser noise, which currently is – and will likely remain – the dominant constraint in many experimental setups. We consolidated and extended previous findings on atomic clocks limited by laser noise and variational quantum circuits to establish a comprehensive theoretical framework for this regime. In particular, we focused on approaching the ultimate lower limit in stability via low-depth quantum circuits based on one-axis twisting operations across a variety of scenarios – including different experimental platforms, ensemble sizes and regimes characterized by a wide range of interrogation durations and dead times.

In general, clock stability reflects a trade-off between quantum projection noise (QPN), the coherence time limit (CTL) and dead time effects. Furthermore, fringe hops impose additional constraints on stability within the full feedback loop of an atomic clock. The optimal Ramsey protocols – and correspondingly the highest achievable clock stabilities – generally depend strongly on the specific parameters of the experimental setup. Although variational quantum circuits promise substantial enhancements in idealized scenarios, practical constraints as fringe hops and dead time effects limit these advantages.

In realistic scenarios, small ensembles comprising a few atoms – characteristic for ion traps – are limited by fringe hops at long interrogation times and thus, GHZ states and spin-squeezed states (SSS) approximate the ultimate lower bound across a broad range of interrogation times. Furthermore, variational Ramsey protocols are generally unfavorable for large ensembles – entering the regime of lattice clocks – due to the inherent particle number fluctuations. As a result, they offer a significant advantage only for intermediate ensemble sizes of several tens of atoms – as encountered in tweezer arrays – in the regime primarily limited by QPN. In this regime, low-depth quantum circuits $[1, m]$ are sufficient to approach the ultimate limit as the benefits diminish with increasing m, leading to a trade-off between increased complexity and extended dynamic range.

In the presence of dead times typical for ion traps, the behavior closely resembles the dead time-free case for small ensembles, since QPN dominates the Dick effect. In contrast, Dick noise becomes the primary limitation for tweezer arrays as dead time increases, substantially reducing the potential enhancement offered by variational quantum circuits compared to SSS. For large ensembles in the regime of lattice clocks, QPN is reduced well below dead time effects. As a consequence, increasing the complexity of the Ramsey sequence is redundant and coherent spin states (CSS) ultimately approach the lower limit at long interrogation times.

Finally, we briefly outlined clock schemes beyond the single-ensemble approach that have the potential to address the primary limitations discussed in this chapter – namely the laser coherence time limit (CTL), the emergence of fringe hops and dead time effects. Although these approaches extend beyond the scope of the present work, many of their underlying principles can be integrated with the Ramsey protocols discussed in this thesis.

As a closing statement, we hope that the results of this thesis will serve as a reference of clock stability in current setups and provide guidance for implementing optimal entanglement-enhanced Ramsey protocols in future clocks for a variety of experimental regimes. Although this work is tailored to frequency metrology in atomic clocks, the developed concepts extend to a general application in frequency metrology and Ramsey interferometry, including implementations in atom interferometry and magnetometry.

A

Numerical routines

In this appendix, we present the numerical methods employed throughout this thesis. In particular, we discuss the optimization of Ramsey interrogation schemes in App. A.1 and the Monte Carlo simulations of the full feedback loop in atomic clocks in App. A.2, which are performed to validate the theoretical predictions developed in this work. Furthermore, we present the procedure to determine the iterated prior width and to incorporate dead time noise into the prior phase distribution in App. A.3.

The numerical studies are implemented in the widely used programming language *Python* [248]. As is generally known, native *Python* can be comparatively slow when operations on arrays are implemented using explicit loops. However, this limitation is effectively addressed by the *NumPy* [249] library, which internally leverages optimized *C* and *Fortran* routines for numerical computations, enabling efficient memory management and vectorized operations that significantly reduce the overhead associated with native *Python* loops. A particularly useful library for quantum systems – especially for spin systems – is the *Quantum Toolbox in Python* (*QuTiP*) [250]. It provides comprehensive tools to represent a variety of quantum states and operators, perform quantum mechanical calculations and simulate dynamics in both closed and open quantum systems.

Naturally, it is advantageous to evaluate the quantities of interest analytically wherever possible to reduce the computational overhead of numerical computations. In addition, repeated computational steps – whether within optimization routines or clock simulations – are outsourced or precomputed to improve efficiency and ensure that iterative procedures exhibit minimal computational complexity.

A.1 Optimization

To perform numerical optimization of the cost functions introduced in this thesis, we utilize the *Python* library *SciPy* [251], which provides a dedicated package for optimization routines. For comparably simple optimization problems – involving only one or two parameters or when profound prior information about the optimal region is available – we employ the *minimize* function, which implements standard local optimization algorithms. In more complex scenarios, characterized by several parameters and a large number of local minima, global optimization techniques becomes necessary. In such cases, we adopt a *differential evolution* approach.

In the following sections, we reformulate the cost functions to enable efficient numerical evaluation and discuss specific limitations inherent to the numerical routines used in the context of local and Bayesian frequency metrology.

A.1.1 Local frequency metrology

In Chapter 3, we investigate local frequency metrology in the presence of decoherence processes during the Ramsey dark time. The treatment of such non-unitary dynamics requires to consider the full 2^N-dimensional Hilbert space. However, by assuming permutational invariance (cf. Sec 2.3.1), it is sufficient to restrict the analysis to the subspace spanned by the permutational invariant Dicke states. The dimension of this permutational invariant subspace scales as $\mathcal{O}(N^2)$ and thus offers a significant reduction compared to the exponential scaling of the full Hilbert space, enabling comprehensive numerical studies. An efficient implementation of this subspace is provided by the *QuTiP* module *Permutational Invariant Quantum Solver* (*PIQS*) [99].

Efficient expressions for the cost functions— In a systematic optimization procedure, the initial state and the measurement are iteratively adjusted in each optimization step. For the method of moments (cf. Eq. 3.32), the variance $(\Delta X(\phi, T))^2$ of the observable X and the slope of the signal $\partial_\phi \langle X(\phi, T)\rangle$ are required. While the evaluation of the variance is straightforward, the slope can be directly computed according to

$$\begin{aligned}
\partial_\phi \langle X(\phi, T)\rangle &= \partial_\phi \operatorname{Tr}\left(X\mathcal{R}_z(\phi)\Lambda_T[\rho_{\text{in}}]\mathcal{R}_z^\dagger(\phi)\right)\\
&= \partial_\phi \operatorname{Tr}\left(\mathcal{R}_z^\dagger(\phi)X\mathcal{R}_z(\phi)\Lambda_T[\rho_{\text{in}}]\right)\\
&= i\operatorname{Tr}\left(\mathcal{R}_z^\dagger(\phi)[S_z, X]\mathcal{R}_z(\phi)\Lambda_T[\rho_{\text{in}}]\right)\\
&= i\operatorname{Tr}\left([S_z, X]\Lambda_{\phi,T}[\rho_{\text{in}}]\right),
\end{aligned} \tag{A.1}$$

where we assumed that the phase imprint $\mathcal{R}_z(\phi)$ (super-)commutes with the dynamics arising from the decoherence processes $\Lambda_T[\rho_{\text{in}}]$ (cf. App. C.1).

As the method of moments is not optimal in general, it is often advantageous to consider the (classical) Fisher information (cf. Sec. 3.5.1) as a cost function for optimization. With

$$\begin{aligned}\partial_\phi P(x|\phi) &= \partial_\phi \operatorname{Tr}\left(|x\rangle\langle x|\, \mathcal{R}_z(\phi)\Lambda_T[\rho_{\text{in}}]\mathcal{R}_z^\dagger(\phi)\right) \\ &= -i \operatorname{Tr}\left(|x\rangle\langle x|\, [S_z, \Lambda_{\phi,T}[\rho_{\text{in}}]]\right),\end{aligned} \tag{A.2}$$

the (classical) Fisher information takes the numerically more tractable form

$$\mathcal{F}[\rho_{\text{in}}(\phi,T), \{\Pi_x\}] = -\sum_x \frac{\operatorname{Tr}\left(|x\rangle\langle x|\, [S_z, \Lambda_{\phi,T}[\rho_{\text{in}}]]\right)^2}{\operatorname{Tr}\left(|x\rangle\langle x|\, \Lambda_{\phi,T}[\rho_{\text{in}}]\right)}. \tag{A.3}$$

This quantity has to be optimized with respect to the phase ϕ to determine the optimal working point ϕ_0 (cf. Sec. 3.5.1). Although the apparent minus sign might appear confusing, the (classical) Fisher information remains positive as the numerator yields another minus sign.

Expressing the cost functions in this form enables efficient numerical implementation. In contrast, explicit evaluations based on the fundamental definitions typically result in substantially longer computational runtimes, which in turn restrict the accessible ensemble sizes and the complexity of the quantum operations that can be considered.

Limitations— Although the *PIQS* package provides an efficient implementation for permutational invariant quantum systems – resulting in a quadratic scaling of the Hilbert space dimension – the time evolution remains computationally challenging.

In principle, for a fixed interrogation time T, the time evolution is identical across all optimization steps and can therefore be evaluated once in advance. However, this requires the explicit computation of the matrix exponential $e^{\mathcal{L}T}$ of the Liouvillian $\mathcal{L}$, which contains $\mathcal{O}(N^8)$ elements (cf. App. C.2). Unfortunately, for spontaneous decay and individual dephasing, the time evolution is non-trivial as the dynamics is non-diagonal in the Dicke basis. Consequently, evaluating the general solution $e^{\mathcal{L}T}$ becomes unfeasible on a standard PC already for relatively small ensemble sizes ($N \gtrsim 20$) due to its computational complexity of $\mathcal{O}(N^{12})$.[1] Interestingly, the *mesolve* function of *QuTiP* offers an efficient computation for the explicit time evolution of a given state [250], thereby allowing to study larger ensembles. However, this approach requires the evaluation of the time evolution in every optimization step, which ultimately limits numerical studies to $N \lesssim 30$ as pursued in Chapter 3, particularly in the case of the optimal quantum interferometer (OQI).

---

[1] In general, for a system of Hilbert space dimension n, diagonalization – and thus evaluation of the matrix exponential – has complexity $\mathcal{O}(n^3)$. In the specific case of the permutational invariant subspace, the matrix representation of the Liouvillian $\mathcal{L}$ has dimension $\mathcal{O}(N^4)$ (cf. App. C.2) and thus results in an overall complexity of $\mathcal{O}(N^{12})$.

It is important to emphasize that this limitation originates from evaluating the dynamics in the Dicke basis, which is suboptimal for spontaneous decay and individual dephasing. A significant reduction in computational cost could be achieved by evaluating the dynamics in a basis in which the Liouvillian is diagonal, as demonstrated in Refs. [97, 98]. While such an approach would allow for the investigation of significantly larger ensembles – and thereby address the aspects discussed in Sec. 3.10 – this is beyond the scope of this thesis. Notably, this direction is currently being pursued by our master student Marius Burgath.

A.1.2 Bayesian frequency metrology

In Chapter 4, we restrict the analysis to the subspace with maximal spin $S = N/2$, which is fully symmetric under particle exchange. This symmetry is preserved by the unitary dynamics described in Eq. (4.4). The corresponding Hilbert subspace has dimension $N + 1$ and therefore scales linearly with the ensemble size. Moreover, it is sufficient to consider pure initial states, as mixing quantum states does not enhance the sensitivity (cf. Sec. 4.3). These simplifications enable comprehensive numerical investigations. In particular, the evaluation of the optimal quantum interferometer (OQI) can be performed up to the regime where the asymptotic scaling is reached. Nevertheless, numerical evaluation becomes computationally demanding for large ensembles $N \gg 1$, especially when considering complex quantum circuits.

In Bayesian phase estimation, averaging over the prior phase distribution requires evaluating an integral, as discussed in detail in Sec. 4.2. Fortunately, this integration can be performed analytically by reformulating the expressions for the Bayesian mean squared error (BMSE) utilizing the linear and optimal Bayesian estimation strategies, as shown below.

Linear estimator— For any operator $A = \sum_{M,M'} A_{M,M'} |M\rangle\langle M'|$ and an arbitrary input state $|\psi_{\text{in}}\rangle = \sum_M (\psi_{\text{in}})_M |M\rangle$ represented in the Dicke basis $|M\rangle$, the expectation values can be expressed as

$$\begin{aligned} \langle A(\phi)\rangle &= \langle\psi_{\text{in}}|\, \mathcal{R}_z^\dagger(\phi) A \mathcal{R}_z(\phi)\, |\psi_{\text{in}}\rangle \\ &= \sum_{M,M'} (\psi_{\text{in}})^*_M A_{M,M'} (\psi_{\text{in}})_{M'} e^{i(M-M')\phi}. \end{aligned} \tag{A.4}$$

Assuming a Gaussian prior distribution $\mathcal{P}(\phi)$ with zero mean and variance $(\delta\phi)^2$, we use the integrals

$$\int \mathrm{d}\phi \mathcal{P}(\phi) e^{ia\phi} = e^{-\frac{1}{2}a^2(\delta\phi)^2} \tag{A.5}$$

$$\int \mathrm{d}\phi \mathcal{P}(\phi) \phi e^{ia\phi} = ia(\delta\phi)^2 e^{-\frac{1}{2}a^2(\delta\phi)^2} \tag{A.6}$$

to obtain

$$\int \mathrm{d}\phi \mathcal{P}(\phi)\phi \langle X(\phi)\rangle = \sum_{M,M'} (\psi_{\mathrm{in}})^*_M X_{M,M'} (\psi_{\mathrm{in}})_{M'} i(\delta\phi)^2 (M-M') e^{-\frac{1}{2}(M-M')^2(\delta\phi)^2} \tag{A.7}$$

$$\int \mathrm{d}\phi \mathcal{P}(\phi) \langle X^2(\phi)\rangle = \sum_{M,M'} (\psi_{\mathrm{in}})^*_M (X^2)_{M,M'} (\psi_{\mathrm{in}})_{M'} e^{-\frac{1}{2}(M-M')^2(\delta\phi)^2}. \tag{A.8}$$

Defining the matrices B and C by

$$B_{M,M'} = i(\delta\phi)^2(M-M') e^{-\frac{1}{2}(M-M')^2(\delta\phi)^2} X_{M,M'} \tag{A.9}$$

$$C_{M,M'} = e^{-\frac{1}{2}(M-M')^2(\delta\phi)^2} (X^2)_{M,M'} \tag{A.10}$$

and writing $\psi_{\mathrm{in}} = ((\psi_{\mathrm{in}})_{-N/2}, \ldots, (\psi_{\mathrm{in}})_{+N/2})^T$, the BMSE for the linear estimation strategy (cf. Eq. (4.27)) takes the compact form

$$(\Delta\phi)^2 = (\delta\phi)^2 - \frac{(\psi^\dagger_{\mathrm{in}} B \psi_{\mathrm{in}})^2}{\psi^\dagger_{\mathrm{in}} C \psi_{\mathrm{in}}} \tag{A.11}$$

and is thus determined by simple scalar products.

Optimal Bayesian estimator— Similarly, for a projective measurement $\{|x\rangle\langle x|\}$, represented by $|x\rangle = \sum_M x_M |M\rangle$ with coefficients $x_M \in \mathbb{C}$, and an arbitrary state $|\psi\rangle$, the conditional probabilities can be expressed as

$$\begin{aligned} P(x|\phi) &= |\langle x| \mathcal{R}_z(\phi) |\psi_{\mathrm{in}}\rangle|^2 \\ &= \langle x| \mathcal{R}_z(\phi) |\psi_{\mathrm{in}}\rangle\langle\psi_{\mathrm{in}}| \mathcal{R}^\dagger_z(\phi) |x\rangle \\ &= \sum_{M,M'} x^*_M e^{-iM\phi} (\psi_{\mathrm{in}})_M (\psi_{\mathrm{in}})^*_{M'} e^{iM'\phi} x_{M'} \\ &= \sum_{M,M'} y^*_M e^{i(M'-M)\phi} y_{M'}, \end{aligned} \tag{A.12}$$

where we defined $y_M = x_M (\psi_{\mathrm{in}})^*_M$. Using the integrals from Eq. (A.5) and Eq. (A.6), we obtain

$$\int \mathrm{d}\phi \mathcal{P}(\phi) P(x|\phi)\phi = \sum_{M,M'} y^*_M y_{M'} i(\delta\phi)^2 (M-M') e^{-\frac{1}{2}(M-M')^2(\delta\phi)^2} \tag{A.13}$$

$$\int \mathrm{d}\phi \mathcal{P}(\phi) P(x|\phi) = \sum_{M,M'} y^*_M y_{M'} e^{-\frac{1}{2}(M-M')^2(\delta\phi)^2}. \tag{A.14}$$

Defining the matrices D and E by

$$D_{M,M'} = i(\delta\phi)^2(M - M')e^{-\frac{1}{2}(M-M')^2(\delta\phi)^2} \tag{A.15}$$

$$E_{M,M'} = e^{-\frac{1}{2}(M-M')^2(\delta\phi)^2} \tag{A.16}$$

and writing $\mathbf{y} = (y_{-N/2}, \dots, y_{+N/2})^T$, the BMSE for the optimal Bayesian estimator (cf. Eq. (4.29)) is given by

$$(\Delta\phi)^2 = (\delta\phi)^2 - \sum_{\mathbf{y}} \frac{(\mathbf{y}^\dagger D\mathbf{y})^2}{\mathbf{y}^\dagger E\mathbf{y}}, \tag{A.17}$$

where the summation over $\mathbf{y}$ effectively iterates over the measurement basis $|x\rangle$, resulting in a summation over simple scalar products.

A.2 Monte Carlo clock simulation

To validate theoretical predictions on clock stability and to assess the robustness of the presented Ramsey schemes in realistic scenarios, we perform comprehensive numerical Monte Carlo simulations of the full feedback loop in an atomic clock throughout this thesis. This appendix provides a brief overview of the methods used to simulate an atomic clock, primarily aligning with Ref. [3].

The core *Python* implementation of the Monte Carlo simulation was originally developed by Ian D. Leroux, focusing on different feedback strategies in the context of conventional Ramsey interferometry utilizing coherent spin states (CSS), as described in Ref. [92]. This initial implementation was tailored to single-ensemble clocks, where the atomic reference is periodically interrogated using the same protocol in each clock cycle.

In subsequent years, Marius Schulte adapted these routines. On the one hand, the routines where extended to incorporate the simulation of spin-squeezed states (SSS), with primary results published in Ref. [91]. On the other hand, the performance of the code was substantially increased by transforming it into *Cython* [252] code. *Cython* combines the development efficiency of *Python* with the execution speed of *C*. By extending the *Python* language and allowing direct compilation into *C*, even modest use of type declarations and minor code adjustments typically lead to considerable performance gains – an essential advantage for atomic clock simulations involving vast numbers of causally connected cycles.

In recent years, we implemented several additional modifications. The feedback loop was generalized to incorporate a wide range of interrogation strategies, from basic schemes such as applying corrections only after several clock cycles, to advanced multi-ensemble approaches utilizing dynamical decoupling or cascaded clocks, which, however, are beyond the scope of this thesis. Here, we outline a minimal working example representative of the implementation used to obtain the results throughout this thesis – which are published in Refs. [1, 2] – focusing on single-ensemble clock operation with identical Ramsey protocols in each cycle. In this context, the initial implementation was extended to support the simulation of arbitrary Ramsey schemes.

Overall, the Monte Carlo simulation implements the basic principles of an atomic clock, as introduced in Sec. 1.2 and Sec. 3.2, and follows the framework described in Sec. 2.4. In the following, we briefly outline the main aspects of the Monte Carlo simulations: the feedback loop, the local oscillator, the atomic reference and the servo. Finally, we discuss the evaluation of the long-term-stability in atomic clocks.

A.2.1 Feedback loop

In general, the Monte Carlo simulation is implemented in terms of frequencies ν rather than angular frequencies ω or relative frequencies y. Specifically, we consider frequency deviations $\nu(t) = \nu_0 - \nu_{\mathrm{LO}}(t)$ (cf. Eq. 3.1) of the local oscillator (LO) frequency ν_{LO} with respect to the atomic transition frequency ν_0.[2]

Each clock cycle k comprises two frequency values, representing the average frequency deviation during dead time T_D

$$\nu_{\mathrm{deadtime},k} = \frac{1}{T_D} \int_{(k-1)T_C}^{(k-1)T_C+T_D} \mathrm{d}t' \nu(t') \tag{A.18}$$

and during the Ramsey interrogation T

$$\nu_k = \frac{1}{T} \int_{(k-1)T_C+T_D}^{kT_C} \mathrm{d}t' \nu(t'), \tag{A.19}$$

where $T_C = T_D + T$ denotes the total duration of the clock cycle. Since frequency fluctuations during dead time are not monitored, we primarily focus on the frequency deviations ν_k during the Ramsey interrogation, while $\nu_{\mathrm{deadtime},k}$ is updated in each clock cycle accordingly. To distinguish between different frequency deviations during clock cycle k, representing specific aspects of the feedback loop, we use superscripts for ν_k in the following.

As ν_k denotes the averaged frequency deviation of the LO with respect to the atomic reference at the end of the interrogation time in cycle k, prior to the measurement, it is essential for the atomic interrogation. In particular, this frequency reflects stabilization in preceding cycles ($j < k$), but still incorporates the intrinsic (new) noise introduced during the current cycle k. At the end of the Ramsey sequence,

---

[2] Although angular frequencies ω are typically used throughout this thesis, here we adapt the notation to align with the implementation.

ν_k is estimated as ν_k^{est} based on the measurement outcome. Finally, to complete the feedback loop, the servo applies a correction ν_k^{corr} based on this frequency estimate. The resulting stabilized clock frequency is given by

$$\nu_k^{\mathrm{clock}} = \nu_k - \nu_k^{\mathrm{corr}}. \tag{A.20}$$

Although the free-running LO frequency is not directly accessible in practice due to continuous stabilization, it is convenient to generate the trace of average frequency deviations associated with the free running local oscillator, denoted by ν_k^{free}, in advance (cf. App. A.2.2). The actual LO frequency ν_k in the presence of feedback is related to ν_k^{free} through

$$\nu_k = \nu_k^{\mathrm{free}} - \nu_{k-1}^{\mathrm{tot-corr}}, \tag{A.21}$$

where the total (or cumulated) correction applied up to cycle k is defined as

$$\nu_k^{\mathrm{tot-corr}} = \sum_{j=1}^{k} \nu_j^{\mathrm{corr}}. \tag{A.22}$$

Accordingly, the clock frequency can be expressed as

$$\nu_k^{\mathrm{clock}} = \nu_k^{\mathrm{free}} - \nu_k^{\mathrm{tot-corr}}. \tag{A.23}$$

In summary, each clock cycle k consists of the following steps:

(i) Compute the frequency deviation during interrogation: $\nu_k = \nu_k^{\mathrm{free}} - \nu_{k-1}^{\mathrm{tot-corr}}$

(ii) Estimate the frequency deviation based on a particular Ramsey sequence: ν_k^{est}

(iii) Evaluate the total servo correction based on the estimate: $\nu_k^{\mathrm{tot-corr}}$

(iv) Correct the LO to obtain the clock frequency: $\nu_k^{\mathrm{clock}} = \nu_k^{\mathrm{free}} - \nu_k^{\mathrm{tot-corr}}$

The generation of the free-running LO frequency trace, as well as the implementation of the atomic reference and the servo, are detailed in the following sections.

A.2.2 Local Oscillator Noise

Throughout this work and in the Monte Carlo simulations, we assume clock operation with identical interrogation sequences in each clock cycle. In particular, both the dead time T_D and the interrogation time T are fixed during a single clock run. As a result, the sequence of average frequency deviations associated with the free-running local oscillator ν_k^{free}, where k labels the clock cycle, can be generated in advance for a given spectral noise density $S_y(f)$ or local oscillator Allan deviation $\sigma_{y,\mathrm{LO}}(\tau)$. Specifically, we focus on three standard types of noise: white frequency noise, flicker frequency noise and random walk frequency noise.

In principle, these frequency traces can be generated via a Fourier transformation of the desired spectral noise in the frequency domain. However, this approach becomes computationally expensive for long traces involving many clock cycles ($m \gg 1$). While white and random walk frequency noise can be generated using standard techniques [84], flicker frequency noise is efficiently generated by a sum of multiple damped random walks [92].

The main routine used to generate the frequency trace of the free-running local oscillator takes the Allan deviation at unit averaging time as input. Specifically, for white frequency noise (WN), flicker frequency noise (FN) and random walk frequency noise (RWN), the respective input parameters are the Allan deviations $\sigma_{\nu,\mathrm{WN}}(\tau = 1\ \mathrm{s})$, $\sigma_{\nu,\mathrm{FN}}(\tau = 1\ \mathrm{s})$ and $\sigma_{\nu,\mathrm{RWN}}(\tau = 1\ \mathrm{s})$, respectively. Importantly, these values specify the Allan deviation in terms of absolute frequency deviations ν. A representative example is shown in Fig. 2.2.

A.2.3 Reference

In each clock cycle k, the atomic reference is interrogated according to a specific Ramsey sequence. The frequency deviation ν_k gives rise to the accumulated phase $\phi_k = 2\pi\nu_k T$ during the free evolution time (Ramsey dark time). At the end of the Ramsey protocol, a measurement x_k is performed and the frequency deviation ν_k is estimated as $\nu_k^{\mathrm{est}} = \phi_k^{\mathrm{est}}/2\pi T$, where ϕ_k^{est} denotes the phase estimation of ϕ_k. While different estimation strategies are discussed in the main text, here, we focus on sampling measurement outcomes x based on the conditional probability distribution $P(x|\phi)$. To this end, we distinguish between several scenarios in the following, for which distinct sampling techniques are convenient.

Binomial distributions— An efficient method to sample Bernoulli trials is inverse transform sampling [253]. For a single qubit with statistical model $P(x|\phi)$, this procedure is implemented as follows: A random number p is drawn from the uniform distribution over the interval $[0, 1]$. If $p \leq P(x = +\frac{1}{2}|\phi)$, the qubit is measured in the excited state $|{\uparrow}\rangle$, otherwise, it is measured in the ground state $|{\downarrow}\rangle$. For N independent qubits, this process is repeated to generate a sampled measurement outcome of the ensemble, resulting in a binomial distribution (cf. Sec. 2.3.6).

Although this technique can, in principle, be generalized to arbitrary probability distributions [253], we primarily employ it to sample measurements of the conventional Ramsey protocol, which uses coherent spin states and projective spin measurements, naturally yielding binomial statistics.

Analytical distributions— If the conditional probabilities are known analytically, they can be efficiently evaluated in each clock cycle for a specific phase ϕ_k. A measurement outcome for an arbitrary statistical model $P(x|\phi)$ can be sampled using the *choices* method from the *random* package in *Python* [254], which takes the possible measurement outcomes and associated probabilities as input.

Exact numerical distributions— If no analytical expressions for the conditional probabilities are available, they have to be evaluated numerically in each clock cycle and can then be sampled using the methods describe above. In particular, it is useful to distinguish between two scenarios:

(i) We assume pure states $|\psi_{\text{in}}\rangle$ in the fully symmetric subspace, a unitary time evolution $\mathcal{R}_z(\phi) = e^{-i\phi S_z}$ and arbitrary projective measurements within this subspace – represented by a projection-valued measure (PVM) $\{|x\rangle\langle x|\}$. Specifically, we represent input states $|\psi_{\text{in}}\rangle = \sum_M (\psi_{\text{in}})_M |M\rangle$ and measurement basis states $|x\rangle = \sum_M x_M |M\rangle$ in the Dicke basis $|M\rangle$ with total spin $S = N/2$. Consequently, the conditional probabilities can be expressed as

$$\begin{aligned} P(x|\phi) &= |\langle x| \mathcal{R}_z(\phi) |\psi_{\text{in}}\rangle|^2 \\ &= |\sum_M x_M^* e^{-i\phi M} (\psi_{\text{in}})_M|^2 \\ &= |\mathbf{x}^\dagger (\mathbf{r} \circ \psi_{\text{in}})|^2, \end{aligned} \tag{A.24}$$

where $\circ$ denotes the Hadamard product (elementwise multiplication) and the vectors $\mathbf{x}$, $\mathbf{r}$ and ψ_{in} have coefficients x_M, $r_M = e^{-i\phi M}$ and $(\psi_{\text{in}})_M$, respectively.

(ii) We consider mixed states $\rho_{\text{in}}(T)$ and arbitrary projective measurements – represented by a projection-valued measure (PVM) $\{|x\rangle\langle x|\}$. Furthermore, we assume that the dynamics can be decomposed into a non-unitary quantum channel $\rho_{\text{in}}(T) = \Lambda_T[\rho_{\text{in}}]$ and a unitary phase evolution according to $\mathcal{R}_z(\phi)$, which commute. In the Dicke basis $|S, M\rangle$, the evolved state and the measurement are represented as $\rho_{\text{in}}(T) = \sum_{SM,S'M'} C_{SM,S'M'} |S, M\rangle\langle S', M'|$ and $\Pi_x = \sum_{SM,S'M'} A_{SM,S'M'} |S, M\rangle\langle S', M'|$, respectively. Hence, the conditional probabilities can be expressed as

$$\begin{aligned} P(x|\phi) &= \mathrm{Tr}\big(|x\rangle\langle x| \mathcal{R}_z(\phi)\rho_{\text{in}}(T)\mathcal{R}_z^\dagger(\phi)\big) \\ &= \sum_{SM,S'M'} A_{S'M',SM} e^{-i\phi(M-M')} C_{SM,S'M'}. \end{aligned} \tag{A.25}$$

By defining the matrix B with elements $B_{SM,S'M'} = e^{-i\phi(M-M')}$ and using that $\Pi_x = \Pi_x^\dagger$, which implies $A_{S'M',SM} = A^*_{SM,S'M'}$, we obtain

$$P(x|\phi) = \sum_{SM,S'M'} A^*_{SM,S'M'} B_{SM,S'M'} C_{SM,S'M'}. \tag{A.26}$$

Consequently, the conditional probability $P(x|\phi)$ is given by a sum over the matrix elements of the Hadamard product $A^* \circ B \circ C$, with coefficients defined above.

Note that these implementations are computationally significantly faster than evaluating the conditional probabilities directly in *QuTiP*, as they take advantage of efficient *numpy* array operations.

Gaussian approximation— In general, numerical evaluation of the conditional probabilities becomes computationally demanding with increasing ensemble size, as argued in App. A.1. However, if the statistical model $P(x|\phi)$ is well centered around its mean value $\langle X(\phi)\rangle$ for a given phase ϕ, characterized by a small variance $(\Delta X(\phi))^2$, the statistics can be approximated by a Gaussian distribution with corresponding mean value and variance. Consequently, this approximation effectively reflects an application of the central limit theorem. The random variable associated with the observable X is then distributed as

$$X \sim \mathcal{N}(\langle X(\phi)\rangle, (\Delta X(\phi))^2), \tag{A.27}$$

where $\mathcal{N}(\mu, \sigma^2)$ denotes a Gaussian (or normal) distribution with mean μ and variance σ^2.

However, this approximation is generally not suitable for states with populations exhibiting strict separation – such as the GHZ state, which comprises a superposition of the collective ground and excited states. In contrast, it applies particularly well to binomial-like distributions, as encountered for coherent spin states (CSS) and spin-squeezed states (SSS). Indeed, Ramsey protocols utilizing CSS and SSS emerge as robust and effective interrogation schemes in a variety of scenarios, particularly in the regime of large ensembles, as examined throughout this thesis. In the case of CSS and SSS, we obtain

$$\langle X(\phi)\rangle = \langle S_x\rangle \sin(\phi) + \langle S_y\rangle \cos(\phi) \tag{A.28}$$

$$(\Delta X(\phi))^2 = (\Delta S_x)^2 \sin^2(\phi) + (\Delta S_y)^2 \cos^2(\phi). \tag{A.29}$$

Specifically, the x and y components are independent, since $\langle S_x S_y + S_y S_x\rangle = 0$, and thus, S_x and S_y can be treated as independent random variables. Consequently, since X effectively constitutes a sum of random variables, it is distributed as

$$X \sim \mathcal{N}(\langle S_x\rangle \sin(\phi), (\Delta S_x)^2 \sin^2(\phi)) + \mathcal{N}(\langle S_y\rangle \cos(\phi), (\Delta S_y)^2 \cos^2(\phi)). \tag{A.30}$$

Additionally using that $\langle S_y\rangle = 0$, measurement outcomes can be sampled based on

$$X \sim [\langle S_x\rangle + \Delta S_x \mathcal{N}] \sin(\phi) + \Delta S_y \mathcal{N} \cos(\phi), \tag{A.31}$$

where $\mathcal{N}$ denotes a standard-normally distributed random variable with zero mean and unit variance.

Pre-evaluating the distribution— In scenarios where an exact numerical evaluation of the conditional probabilities is computationally unfeasible and the Gaussian approximation does not apply – for instance for intermediate ensemble sizes in the presence of decoherence – the statistical model $P(x|\phi)$ can be evaluated in advance for each measurement outcome x over a discrete set of phase values $\{\phi^{(1)}, \ldots, \phi^{(l)}\}$. In each clock cycle k, the phase bin $\phi^{(j)}$ that is closest to the actual phase ϕ, imprinted onto the atomic reference, is identified and the corresponding precomputed conditional probability is used to sample the measurement outcome. Hence, this approach effectively constitutes a lookup table.

Although the selected phase bin $\phi^{(j)}$ typically does not exactly match the actual phase ϕ, the resulting approximation error is negligible relative to dominant physical noise sources such as quantum projection noise and frequency fluctuations. In particular, for Ramsey protocols with phase evolution represented by a 2π-periodic unitary rotation, even relatively small values of l are typically sufficient to ensure accurate sampling.

A.2.4 Servo

The servo determines the correction applied to steer the local oscillator towards the atomic transition frequency. Specifically, the servo evaluates the total correction $\nu_k^{\text{tot}-\text{corr}}$ based on the frequency estimate ν_k^{est}, resulting from the Ramsey interrogation, as well as the corrections applied in previous clock cycles $\{\nu_{k-1}^{\text{tot}-\text{corr}}, \nu_{k-2}^{\text{tot}-\text{corr}}, \ldots\}$.

The implementation of the clock simulation incorporates two common servo types: the double-integrating servo and the general linear integrator. Both approaches are described in detail in Ref. [92] and are further outlined in Sec. 2.4. For the Monte Carlo simulations performed in this thesis, we primarily employ the general linear predictor – taking into account the past 50 frequency estimates – which provides reliable performance in several scenarios. However, the weights in the linear superposition of previous corrections, as presented in Ref. [92], are not universally optimal, as they rather represent a general approach. Hence, at specific interrogation times – where numerical simulations substantially deviate from numerical simulations – it might be advantageous to employ the double-integrating servo to reduce discrepancies.

A.2.5 Long-term stability

The (overlapping) Allan deviation is evaluated by adapting the *Python* package *Allantools* [255]. Although the Allan deviation $\sigma_y(\tau)$ depends on the total averaging time τ, clock stability is typically characterized by a single value, assuming that the Allan deviation scales as $\sim 1/\sqrt{\tau}$ for $\tau \gg 1$ s. This behavior is described by Eq. (3.23) in

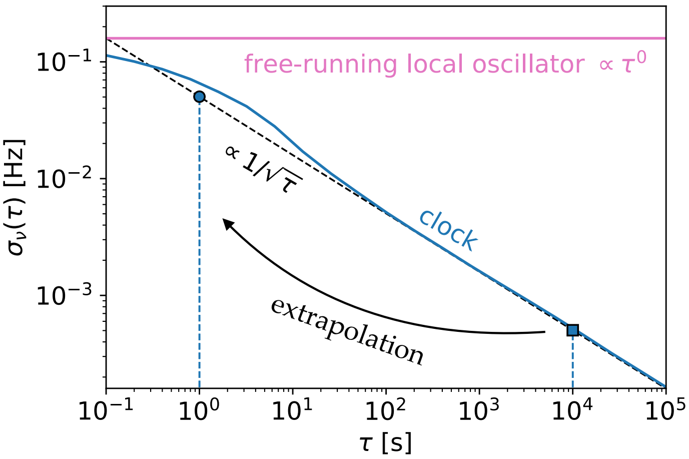

Figure A.1: **Long term stability:** The Allan deviation $\sigma_\nu(\tau)$ as a function of the averaging time τ for the free-running local oscillator (pink) and a clock with $N = 100$ atoms (blue). The clock is stabilized using a conventional Ramsey scheme based on coherent spin states, a projective spin measurement and a linear estimation strategy. The local oscillator is limited by flicker frequency noise with Allan deviation $\sigma_{\nu,\mathrm{FN}}(\tau = 1\text{ s}) = \frac{1}{2\pi}$ Hz, corresponding to a coherence time of $Z = 1$ s. The interrogation time $T/Z = 0.1$ is in the regime where quantum projection noise is the dominant constraint and we assume zero dead time $T_D = 0$. The Allan deviation at $\tau = 1$ s (circle) is extrapolated from the asymptotic regime $\tau/T \gg 1$ using the expected $\tau^{-1/2}$ scaling. Here, the Allan deviation is evaluated at 10^4 clock cycles (square) for a simulation where 10^6 cycles were performed in total.

local frequency metrology and by Eq. (4.33) in Bayesian frequency metrology. Conventionally, clock stability is quantified by the Allan deviation at unit averaging time $\sigma_y(\tau = 1\text{ s})$. Equivalently, the Allan deviation can be rescaled with the total averaging time, i.e. $\sigma_y(\tau)\sqrt{\tau}$.

However, due to the delayed feedback in clock operation, significant deviations between theoretical predictions and simulations (or experiments) arise at short averaging times $\tau \sim 1$ s, as illustrated in Fig. A.1. The expected long-term-stability $\sigma_y(\tau) \propto 1/\sqrt{\tau}$ is recovered only for sufficiently long averaging times $\tau \gg 1$ s. Therefore, stability is evaluated at $\tau \gg 1$ s and then extrapolated to its hypothetical value at $\tau = 1$ s based on the scaling $\sigma_y(\tau) \propto 1/\sqrt{\tau}$.

Since clock operation involves stochastic processes – such as random frequency fluctuations of the local oscillator and quantum projection noise in the measurement outcomes – results vary across different clock runs. To ensure robust stability estimates, each configuration – defined by fixed ensemble size N, interrogation time T, dead time T_D, and Ramsey sequence – is simulated over 10 independent clock runs. Accordingly, the data points shown in the respective figures represent mean values, while error bars indicate standard deviations. To include a protocol in the results, we impose the stringent criterion that no fringe hops occur across 10^8 total clock cycles, as even a single fringe hop leads to a complete loss of clock stability.

Furthermore, if frequency fluctuations of the local oscillator constitute the dominant noise source, the clock stability can be analyzed within a general framework. In particular, by rescaling the Allan deviation with the local oscillator coherence time Z and the atomic transition frequency ν_0, the resulting stability effectively becomes independent of the specific clock parameters, as pursued in Chapter. 4. Likewise, if decoherence processes impose the primary limitation, the stability can be rescaled with the corresponding decoherence rate, allowing for an equally general treatment, as presented in Chapter 3.

A.3 Prior width

In this appendix, we outline the iterative determination of the prior width and the incorporation of dead time noise into the prior phase distribution, as discussed in Chapter 4.

A.3.1 Iterative prior width

Eq. (4.35) provides a good approximation for the prior phase width $\delta\phi$ in the regime of large ensembles N and long interrogation times T, as demonstrated in Refs. [91, 92, 140]. However, as discussed in the main text, the prior width $\delta\phi$ and estimation error $\Delta\phi$ mutually influence each other in the full feedback loop of an atomic clock. Moreover, any model of the prior width can only capture the true residual noise to a certain degree. Consequently, an on-device optimization, as utilized in Ref. [142], would most accurately reflect the experimental conditions and thus, yield the best results. However, this approach has several disadvantages. First, it precludes theoretical predictions and *ab initio* studies of clock stability, making it impossible to exclude protocols prone to fringe hops, for instance. Second, it is exceptionally demanding in terms of experimental time. While the variational parameters need only be optimized for individual clock runs, evaluating the Allan deviation as a cost function requires a sufficiently long averaging time τ for each optimization step to achieve the long-term scaling according to $1/\sqrt{\tau}$. Unlike Bayesian phase estimation, which can focus on single interrogation cycles, on-device optimization for clock stability must account for time-varying frequency deviations ν across different clock cycles. As a result, on-device optimization using the Allan deviation as a cost function is impractical.

To overcome these challenges, we focus on modeling the prior knowledge according to a Gaussian distribution, as defined in Eq. (4.5), and iteratively adjust the prior width $\delta\phi$ to account for the closed feedback loop dynamics. The general strategy involves simulating the full feedback loop multiple times and using the results from previous simulations to estimate the prior width for the subsequent iteration stage. This procedure is repeated until convergence is achieved. In each iteration stage, the frequency deviation ν_k at the end of the Ramsey dark time is recorded and the associated mean value is interpolated as a function of the interrogation time at a fixed ensemble size. However, application of this iterative method to the variational protocols would lead to the same issues discussed above. Therefore, it is advantageous to use fixed and robust protocols, such as CSS and SSS, to ensure consistency. Additionally, comparing results across protocols would be cumbersome, as each protocol yields a distinct prior width and corresponding OQI. Instead, we approximate the prior width $\delta\phi$ for a fixed ensemble size through the following iterative stages:

- Stage 0 (Initialization): Start with a heuristic prior width, where $\delta\phi$ is interpolated linearly on a log-log scale between $(\delta\phi)^2 = (T/Z)^{4/3}N^{-1/4}$ for $T/Z = 0.01$ and the value given by Eq. (4.35) for $T/Z = 1$. Using this prior width, simulate the CSS protocol with the optimal Bayesian estimator and record the resulting frequency deviations $\{\nu_k\}$.

- Stage 1 (Refinement): Use the recorded $\{\nu_k\}$ from the previous simulation to determine the corresponding prior phase distribution. Fit this distribution to a Gaussian, as described by Eq. (4.5), to obtain an updated prior width $\delta\phi$. Plot $\delta\phi$ as a function of interrogation time and fit it with a fifth-order polynomial. Exclude prior widths for interrogation times where fringe hops limit stability and additionally add the value from Eq. (4.35) at $T/Z = 1$. Simulate the SSS protocol with the updated prior width.

- Stages $2, 3, \ldots$ (Iteration): Repeat the refinement process.

Convergence is typically achieved after stage 3, even for small ensembles, as the prior width from stage 4 introduces only negligible adjustments. This convergence is generically illustrated in Fig. A.2(a). Hence, the prior width from stage 3 is adopted to model a realistic atomic clock scenario used in Sec. 4.7 and Sec. 4.8.3. While this iterative approach provides a reasonable approximation of the closed feedback loop dynamics, it remains a simplification. Consequently, deviations between theoretical predictions and numerical simulations may still arise, as discussed above and in the main text.

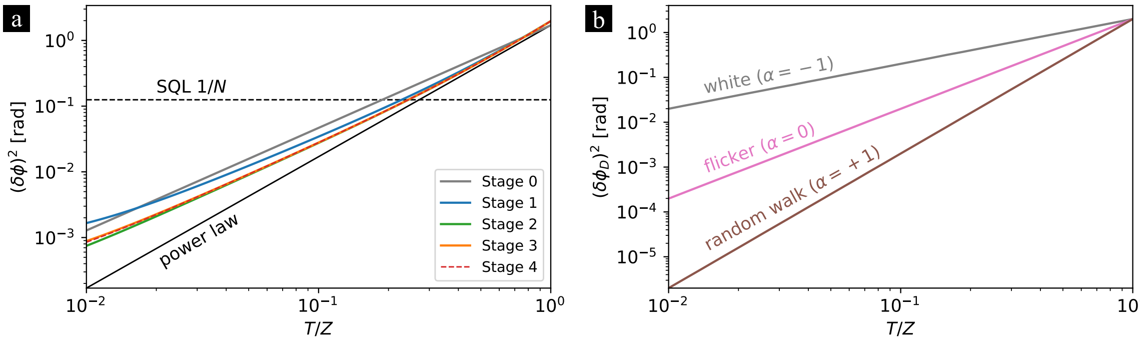

Figure A.2: **Variance of the prior phase distribution:** (a) Convergence of the prior variance $(\delta\phi)^2$ in the iterative approach for $N = 8$. The distinct iteration stages are illustrated by colored lines. Additionally, the power law scaling Eq. (4.35) and the SQL $1/N$ are shown for comparison. (b) Additional noise due to dead time characterized by the associated prior variance $(\delta\phi_D)^2$ given in Eq. (4.47) for white (gray), flicker (pink) and random walk frequency noise (brown). Mean values are averaged over 10 independent runs.

A.3.2 Prior width and dead time

As discussed in the main text, the additional noise introduced during dead time can be approximated as white noise in the asymptotic limit of many clock cycles. The corresponding prior width $\delta\phi_D$ is determined by simulating the uncorrected frequency trace of the free-running local oscillator and quantifying the noise accumulated during the cycle duration T_D. Specifically, the new frequency deviations $\nu_k^{\text{new}} = \nu_k^{\text{free}} - \nu_{k-1}^{\text{free}}$ are recorded for each cycle k, representing the differences between consecutive cycles. Using the recorded values $\{\nu_k^{\text{new}}\}$, the phase distribution associated with a hypothetical phase shift during T_D is evaluated, and the corresponding prior width $\delta\phi_D$ is extracted. Simulations confirm the power-law scaling predicted by Eq. (4.47), as illustrated in Fig. A.2(b).

B

Rotations of Collective Spin Operators and States

In this appendix we investigate how collective spin operators and states transform under collective rotations.

Arbitrary rotations of spin operators— A common transformation in the framework of generalized Ramsey protocols is the rotation $\mathcal{R}_{\mathbf{n}}(\theta)$ of a spin $S_{\mathbf{m}}$ around an arbitrary axis $\mathbf{n}$ by an angle θ. As a reminder, the notation $S_{\mathbf{m}} = m_1 S_x + m_2 S_y + m_3 S_z$ represents the projection of the spin vector $\mathbf{S}$ along a particular direction $\mathbf{m}$, $|\mathbf{m}| = 1$. In the following, we derive an expression for the rotated spin operator

$$S_{\mathbf{m}}(\theta) = \mathcal{R}_{\mathbf{n}}^{\dagger}(\theta) S_{\mathbf{m}} \mathcal{R}_{\mathbf{n}}(\theta) = e^{i\theta S_{\mathbf{n}}} S_{\mathbf{m}} e^{-i\theta S_{\mathbf{n}}} \tag{B.1}$$

where the explicit dependence on the rotation angle θ denotes the transformed spin operator. Differentiation with respect to θ yields

$$\partial_\theta S_{\mathbf{m}}(\theta) = i e^{i\theta S_{\mathbf{n}}} \left[S_{\mathbf{n}}, S_{\mathbf{m}}\right] e^{-i\theta S_{\mathbf{n}}}. \tag{B.2}$$

Evaluation for each individual spin component S_x, S_y, S_z results in the coupled differential equations

$$\begin{aligned} \partial_\theta S_x(\theta) &= n_2 S_z(\theta) - n_3 S_y(\theta) \\ \partial_\theta S_y(\theta) &= -n_1 S_z(\theta) + n_3 S_x(\theta) \\ \partial_\theta S_z(\theta) &= n_1 S_y(\theta) - n_2 S_x(\theta). \end{aligned} \tag{B.3}$$

Rewriting this in matrix notation

$$\partial_\theta \begin{pmatrix} S_x(\theta) \\ S_y(\theta) \\ S_z(\theta) \end{pmatrix} = \begin{pmatrix} 0 & -n_3 & n_2 \\ n_3 & 0 & -n_1 \\ -n_2 & n_1 & 0 \end{pmatrix} \begin{pmatrix} S_x(\theta) \\ S_y(\theta) \\ S_z(\theta) \end{pmatrix} = \begin{pmatrix} n_1 \\ n_2 \\ n_3 \end{pmatrix} \times \begin{pmatrix} S_x(\theta) \\ S_y(\theta) \\ S_z(\theta) \end{pmatrix} \tag{B.4}$$

shows that $\partial_\theta \mathbf{S}(\theta) = \mathbf{n} \times \mathbf{S}(\theta)$ and thus, the rotation of the spin in Eq. (B.1) is equivalent to a rotation of the axis $\mathbf{m}$ around $\mathbf{n}$ by the angle θ. Consequently, according to the Rodrigues rotation formula [256], the rotation of the spin results in[1]

$$S_{\mathbf{m}}(\theta) = (\mathbf{n}^T\mathbf{m})\mathbf{n}^T\mathbf{S} + \cos(\theta)\, \left[\mathbf{m}^T - (\mathbf{n}^T\mathbf{m})\mathbf{n}^T\right] \mathbf{S} - \sin(\theta)\, (\mathbf{n} \times \mathbf{m})^T\mathbf{S}. \tag{B.5}$$

Equivalently, this expression can be derived explicitly by using Eq. (2.73). Considering the particular example of $\mathbf{n} = \mathbf{e}_x$ and $\mathbf{m} = \mathbf{e}_z$, resembling the effective measurement of the conventional Ramsey protocol (cf. Sec. 2.3.7), the transformation is given by

$$S_z(\theta) = S_z \cos(\theta) + S_y \sin(\theta) \tag{B.6}$$

and thus, the second Ramsey $\frac{\pi}{2}$-pulse is equivalent to measuring S_y instead of S_z.

To implement spin systems numerically, it is necessary to choose a particular basis. Typically, the eigenstates of S_z are chosen, but in principle, any other spin projection $S_{\mathbf{m}}$ works equally well. The following discussion can therefore be generalized to any alternative basis. To determine several properties numerically – as expectation values or probabilities of particular events – it is advantageous to express arbitrary spin operators and states in terms of the preferred quantization axis.

Rotations of spin operators— Considering spin operators, we aim to determine the rotation axis $\mathbf{v}$ and angle α such that

$$S_{\mathbf{n}} = \mathcal{R}_{\mathbf{v}}^\dagger(\alpha) S_z \mathcal{R}_{\mathbf{v}}(\alpha). \tag{B.7}$$

To generate an arbitraty axis $\mathbf{n}$ by appropriately rotating $\mathbf{e}_z$, it suffices to choose the rotation axis $\mathbf{v}$ to lie in the x-y-plane. With $\mathbf{v} = (v_1, v_2, 0)^T$ and using Eq. (B.5), the right hand side becomes

$$\mathcal{R}_{\mathbf{v}}^\dagger(\alpha) S_z \mathcal{R}_{\mathbf{v}} = \cos(\alpha) S_z - \sin(\alpha)\, [v_2 S_x - v_1 S_y]\,. \tag{B.8}$$

---

[1] The difference in the sign of the sine, compared to the usual rotation formula, comes from the choice of defining a rotation $\mathcal{R}_{\mathbf{n}}(\theta) = e^{-i\theta S_{\mathbf{n}}}$ with a negative sign.

Hence, we have to choose

$$\alpha = \arccos(n_3) \qquad \text{and} \qquad \mathbf{v} = \begin{pmatrix} v_1 \\ v_2 \\ v_3 \end{pmatrix} = \frac{1}{\sqrt{n_1^2 + n_2^2}} \begin{pmatrix} n_2 \\ -n_1 \\ 0 \end{pmatrix}. \tag{B.9}$$

These are indeed the proper rotation angle and axis, as can be verified by noting that $\sin(\arccos(n_3)) = \sqrt{1 - n_3^2} = \sqrt{n_1^2 + n_2^2}$. Consequently, to express any spin operator $S_{\mathbf{n}}$ in terms of S_z, a rotation $\mathcal{R}_{\mathbf{v}}(\alpha)$ has to be applied with angle α and axis $\mathbf{v}$ as derived above.

Rotations of spin states— Considering spin states, we aim to determine the rotation axis $\mathbf{w}$ and angle β such that

$$|S, M\rangle_{\mathbf{m}} = \mathcal{R}_{\mathbf{w}}(\beta) \, |S, M\rangle_z \tag{B.10}$$

where $|S, M\rangle_{\mathbf{m}}$ denotes the eigenstate of $S_{\mathbf{m}}$ with eigenvalue M and total spin S. We rewrite the eigenvalue equation $S_{\mathbf{m}} \, |S, M\rangle_{\mathbf{m}} = M \, |S, M\rangle_{\mathbf{m}}$ according to

$$\begin{aligned} M \, |S, M\rangle_{\mathbf{m}} &= S_{\mathbf{m}} \, |S, M\rangle_{\mathbf{m}} &\text{(B.11)} \\ &= S_{\mathbf{m}} \mathcal{R}_{\mathbf{w}}(\beta) \, |S, M\rangle_z &\text{(B.12)} \\ &= \mathcal{R}_{\mathbf{w}}(\beta) \mathcal{R}_{\mathbf{w}}^{\dagger}(\beta) S_{\mathbf{m}} \mathcal{R}_{\mathbf{w}}(\beta) \, |S, M\rangle_z &\text{(B.13)} \end{aligned}$$

and thus, the appropriate rotation $\mathcal{R}_{\mathbf{w}}(\beta)$ is defined by the relation

$$\mathcal{R}_{\mathbf{w}}^{\dagger}(\beta) S_{\mathbf{m}} \mathcal{R}_{\mathbf{w}}(\beta) = S_z, \tag{B.14}$$

which is equivalent to

$$S_{\mathbf{m}} = \mathcal{R}_{\mathbf{w}}(\beta) S_z \mathcal{R}_{\mathbf{w}}^{\dagger}(\beta). \tag{B.15}$$

Comparing this with Eq. (B.7) shows that effectively $\mathcal{R}_{\mathbf{w}}(\beta) = \mathcal{R}_{\mathbf{v}}^{\dagger}(\beta)$ when substituting $\mathbf{n}$ by $\mathbf{m}$. Hence, spin states transform according to the adjoint of the rotation applied to spin operators. This distinction can be accounted for by either flipping the sign of the rotation angle ($\beta = -\alpha$), effectively reversing the rotation direction, or flipping the rotation axis ($\mathbf{w} = -\mathbf{v}$).

C

Decoherence processes

In the first part of this appendix, App. C.1, we demonstrate that the individual terms of the master equation are independent and can therefore be treated separately. In the second part, App. C.2, we derive general solutions for the respective contributions to the master equation.

The dynamics of the system during the Ramsey interrogation time T considering a unitary phase evolution, spontaneous decay with rate Γ, individual dephasing with rate γ and collective dephasing with rate γ_c is governed by the master equation Eq. (3.4). For simplicity, we introduce the following notation for the distinct terms

$$\mathcal{L}_\phi[\rho] = -i\omega[S_z, \rho] \tag{C.1}$$

$$\mathcal{L}_\Gamma[\rho] = \frac{\Gamma}{2}\sum_{k=1}^{N} 2\sigma_-^{(k)}\rho\sigma_+^{(k)} - \sigma_{\mathrm{ee}}^{(k)}\rho - \rho\sigma_{\mathrm{ee}}^{(k)} \tag{C.2}$$

$$\mathcal{L}_\gamma[\rho] = -\frac{\gamma}{2}\sum_{k=1}^{N} \sigma_{\mathrm{ee}}^{(k)}\rho\sigma_{\mathrm{gg}}^{(k)} + \sigma_{\mathrm{gg}}^{(k)}\rho\sigma_{\mathrm{ee}}^{(k)} \tag{C.3}$$

$$\mathcal{L}_{\gamma_c}[\rho] = \frac{\gamma_c}{2} 2S_z\rho S_z - \rho_\phi S_z^2 - S_z^2\rho. \tag{C.4}$$

Hence, the master equation Eq. (3.4) reads

$$\dot{\rho} = \mathcal{L}_\phi[\rho] + \mathcal{L}_\Gamma[\rho] + \mathcal{L}_\gamma[\rho] + \mathcal{L}_{\gamma_c}[\rho]. \tag{C.5}$$

C.1 Independence of the processes

In the following we show, that the four terms of the master equation (super-)commute pairwise.[1]

- $[\mathcal{L}_\phi, \mathcal{L}_\Gamma] = 0$:

$$\begin{aligned}
\mathcal{L}_\phi[\mathcal{L}_\Gamma[\rho]] &= -i\frac{\omega\Gamma}{4}\sum_{j,k=1}^{N}\left[\sigma_z^{(j)}, 2\sigma_-^{(k)}\rho\sigma_+^{(k)} - \sigma_{\mathrm{ee}}^{(k)}\rho - \rho\sigma_{\mathrm{ee}}^{(k)}\right] \\
&= -i\frac{\omega\Gamma}{4}\sum_{j,k=1}^{N}\left[\sigma_z^{(j)}, 2\sigma_-^{(k)}\rho\sigma_+^{(k)}\right] - \left[\sigma_z^{(j)}, \sigma_{\mathrm{ee}}^{(k)}\rho\right] - \left[\sigma_z^{(j)}, \rho\sigma_{\mathrm{ee}}^{(k)}\right] \\
&= -i\frac{\omega\Gamma}{4}\sum_{j,k=1}^{N} 2\left[\sigma_z^{(j)}, \sigma_-^{(k)}\rho\sigma_+^{(k)}\right] - \sigma_{\mathrm{ee}}^{(k)}\left[\sigma_z^{(j)}, \rho\right] - \underbrace{\left[\sigma_z^{(j)}, \sigma_{\mathrm{ee}}^{(k)}\right]}_{=0}\rho \\
&\quad - \rho\underbrace{\left[\sigma_z^{(j)}, \sigma_{\mathrm{ee}}^{(k)}\right]}_{=0} - \left[\sigma_z^{(j)}, \rho\right]\sigma_{\mathrm{ee}}^{(k)} \\
&= -i\frac{\omega\Gamma}{4}\sum_{j,k=1}^{N}\left(2\sigma_-^{(k)}\left[\sigma_z^{(j)}, \rho\right]\sigma_+^{(k)} - \sigma_{\mathrm{ee}}^{(k)}\left[\sigma_z^{(j)}, \rho\right] - \left[\sigma_z^{(j)}, \rho\right]\sigma_{\mathrm{ee}}^{(k)}\right)
\end{aligned}$$

where we used

$$\begin{aligned}
\left[\sigma_z^{(j)}, \sigma_-^{(k)}\rho\sigma_+^{(k)}\right] &= \sigma_-^{(k)}\left[\sigma_z^{(j)}, \rho\right]\sigma_+^{(k)} + \sigma_-^{(k)}\rho\underbrace{\left[\sigma_z^{(j)}, \sigma_+^{(k)}\right]}_{=2\delta_{jk}\sigma_+^{(k)}} + \underbrace{\left[\sigma_z^{(j)}, \sigma_-^{(k)}\right]}_{=-2\delta_{jk}\sigma_-^{(k)}}\rho\sigma_+^{(k)} \\
&= \sigma_-^{(k)}\left[\sigma_z^{(j)}, \rho\right]\sigma_+^{(k)}.
\end{aligned}$$

$$\mathcal{L}_\Gamma[\mathcal{L}_\phi[\rho]] = -i\frac{\omega\Gamma}{4}\sum_{j,k=1}^{N}\left(2\sigma_-^{(k)}\left[\sigma_z^{(j)}, \rho\right]\sigma_+^{(k)} - \sigma_{\mathrm{ee}}^{(k)}\left[\sigma_z^{(j)}, \rho\right] - \left[\sigma_z^{(j)}, \rho\right]\sigma_{\mathrm{ee}}^{(k)}\right)$$

---

[1] In principle, the following calculations can be shortened by restricting to single-particle operators for independent sums and concentrating on the relevant terms where commutation is non-trivial. Nevertheless, we will explicitly carry out the calculations at this point for clarity and completeness.

- $[\mathcal{L}_\phi, \mathcal{L}_\gamma] = 0$:

$$\begin{aligned}
\mathcal{L}_\phi[\mathcal{L}_\gamma[\rho]] &= i\frac{\omega\gamma}{4}\sum_{j,k=1}^{N}\left[\sigma_z^{(j)}, \sigma_{\text{ee}}^{(k)}\rho\sigma_{\text{gg}}^{(k)} + \sigma_{\text{gg}}^{(k)}\rho\sigma_{\text{ee}}^{(k)}\right] \\
&= i\frac{\omega\gamma}{4}\sum_{j,k=1}^{N}\sigma_{\text{ee}}^{(k)}\rho\underbrace{\left[\sigma_z^{(j)}, \sigma_{\text{gg}}^{(k)}\right]}_{=0} + \underbrace{\left[\sigma_z^{(j)}, \sigma_{\text{ee}}^{(k)}\right]}_{=0}\rho\sigma_{\text{gg}}^{(k)} + \sigma_{\text{ee}}^{(k)}\left[\sigma_z^{(j)}, \rho\right]\sigma_{\text{gg}}^{(k)} \\
&\quad + \sigma_{\text{gg}}^{(k)}\rho\underbrace{\left[\sigma_z^{(j)}, \sigma_{\text{ee}}^{(k)}\right]}_{=0} + \underbrace{\left[\sigma_z^{(j)}, \sigma_{\text{gg}}^{(k)}\right]}_{=0}\rho\sigma_{\text{ee}}^{(k)} + \sigma_{\text{gg}}^{(k)}\left[\sigma_z^{(j)}, \rho\right]\sigma_{\text{ee}}^{(k)} \\
&= i\frac{\omega\gamma}{4}\sum_{j,k=1}^{N}\left(\sigma_{\text{ee}}^{(k)}\left[\sigma_z^{(j)}, \rho\right]\sigma_{\text{gg}}^{(k)} + \sigma_{\text{gg}}^{(k)}\left[\sigma_z^{(j)}, \rho\right]\sigma_{\text{ee}}^{(k)}\right)
\end{aligned}$$

$$\mathcal{L}_\gamma[\mathcal{L}_\phi[\rho]] = i\frac{\omega\gamma}{4}\sum_{j,k=1}^{N}\left(\sigma_{\text{ee}}^{(k)}\left[\sigma_z^{(j)}, \rho\right]\sigma_{\text{gg}}^{(k)} + \sigma_{\text{gg}}^{(k)}\left[\sigma_z^{(j)}, \rho\right]\sigma_{\text{ee}}^{(k)}\right)$$

- $[\mathcal{L}_\phi, \mathcal{L}_{\gamma_c}] = 0$:

$$\begin{aligned}
\mathcal{L}_\phi[\mathcal{L}_{\gamma_c}[\rho]] &= -i\frac{\omega\gamma_c}{16}\sum_{j,k,l=1}^{N}\left[\sigma_z^{(j)}, 2\sigma_z^{(k)}\rho\sigma_z^{(l)} - \rho\sigma_z^{(k)}\sigma_z^{(l)} - \sigma_z^{(k)}\sigma_z^{(l)}\rho\right] \\
&= -i\frac{\omega\gamma_c}{16}\sum_{j,k,l=1}^{N} 2\sigma_z^{(j)}\sigma_z^{(k)}\rho\sigma_z^{(l)} - 2\sigma_z^{(k)}\rho\sigma_z^{(l)}\sigma_z^{(j)} - \sigma_z^{(j)}\rho\sigma_z^{(k)}\sigma_z^{(l)} \\
&\quad - \rho\sigma_z^{(k)}\sigma_z^{(l)}\sigma_z^{(j)} - \sigma_z^{(j)}\sigma_z^{(k)}\sigma_z^{(l)}\rho - \sigma_z^{(k)}\sigma_z^{(l)}\rho\sigma_z^{(j)}
\end{aligned}$$

$$\begin{aligned}
\mathcal{L}_{\gamma_c}[\mathcal{L}_\phi[\rho]] &= -i\frac{\omega\gamma_c}{16}\sum_{j,k,l=1}^{N} 2\sigma_z^{(k)}\left[\sigma_z^{(j)}, \rho\right]\sigma_z^{(l)} - \left[\sigma_z^{(j)}, \rho\right]\sigma_z^{(k)}\sigma_z^{(l)} - \sigma_z^{(k)}\sigma_z^{(l)}\left[\sigma_z^{(j)}, \rho\right] \\
&= -i\frac{\omega\gamma_c}{16}\sum_{j,k,l=1}^{N} 2\sigma_z^{(k)}\sigma_z^{(j)}\rho\sigma_z^{(l)} - 2\sigma_z^{(k)}\rho\sigma_z^{(j)}\sigma_z^{(l)} - \sigma_z^{(j)}\rho\sigma_z^{(k)}\sigma_z^{(l)} \\
&\quad - \rho\sigma_z^{(j)}\sigma_z^{(k)}\sigma_z^{(l)} - \sigma_z^{(k)}\sigma_z^{(l)}\sigma_z^{(j)}\rho - \sigma_z^{(k)}\sigma_z^{(l)}\rho\sigma_z^{(j)}
\end{aligned}$$

which are the same when renaming the summation indices j, k, l.

- $[\mathcal{L}_\Gamma, \mathcal{L}_\gamma] = 0$:

$$\begin{aligned}
\mathcal{L}_\Gamma[\mathcal{L}_\gamma[\rho]] &= -\frac{\Gamma\gamma}{4}\sum_{j,k=1}^{N} 2\sigma_-^{(k)}\left(\sigma_{\mathrm{ee}}^{(j)}\rho\sigma_{\mathrm{gg}}^{(j)} + \sigma_{\mathrm{gg}}^{(j)}\rho\sigma_{\mathrm{ee}}^{(j)}\right)\sigma_+^{(k)} \\
&\quad - \sigma_{\mathrm{ee}}^{(k)}\left(\sigma_{\mathrm{ee}}^{(j)}\rho\sigma_{\mathrm{gg}}^{(j)} + \sigma_{\mathrm{gg}}^{(j)}\rho\sigma_{\mathrm{ee}}^{(j)}\right) - \left(\sigma_{\mathrm{ee}}^{(j)}\rho\sigma_{\mathrm{gg}}^{(j)} + \sigma_{\mathrm{gg}}^{(j)}\rho\sigma_{\mathrm{ee}}^{(j)}\right)\sigma_{\mathrm{ee}}^{(k)} \\
&= -\frac{\Gamma\gamma}{4}\sum_{k=1}^{N}\Big[2\underbrace{\sigma_-^{(k)}\sigma_{\mathrm{ee}}^{(k)}}_{=\sigma_-^{(k)}}\rho\underbrace{\sigma_{\mathrm{gg}}^{(k)}\sigma_+^{(k)}}_{=0} + 2\underbrace{\sigma_-^{(k)}\sigma_{\mathrm{gg}}^{(k)}}_{=0}\rho\underbrace{\sigma_{\mathrm{ee}}^{(k)}\sigma_+^{(k)}}_{=\sigma_+^{(k)}} \\
&\quad - \underbrace{\sigma_{\mathrm{ee}}^{(k)}\sigma_{\mathrm{ee}}^{(k)}}_{=\sigma_{\mathrm{ee}}^{(k)}}\rho\sigma_{\mathrm{gg}}^{(k)} - \underbrace{\sigma_{\mathrm{ee}}^{(k)}\sigma_{\mathrm{gg}}^{(k)}}_{=0}\rho\sigma_{\mathrm{ee}}^{(k)} - \sigma_{\mathrm{ee}}^{(k)}\rho\underbrace{\sigma_{\mathrm{gg}}^{(k)}\sigma_{\mathrm{ee}}^{(k)}}_{=0} - \sigma_{\mathrm{gg}}^{(k)}\rho\underbrace{\sigma_{\mathrm{ee}}^{(k)}\sigma_{\mathrm{ee}}^{(k)}}_{=\sigma_{\mathrm{ee}}^{(k)}}\Big] \\
&\quad - \frac{\Gamma\gamma}{4}\sum_{j\neq k}\Big[\sigma_{\mathrm{ee}}^{(j)}\Big(2\sigma_-^{(k)}\rho\sigma_+^{(k)} - \sigma_{\mathrm{ee}}^{(k)}\rho - \rho\sigma_{\mathrm{ee}}^{(k)}\Big)\sigma_{\mathrm{gg}}^{(j)} \\
&\quad + \sigma_{\mathrm{gg}}^{(j)}\Big(2\sigma_-^{(k)}\rho\sigma_+^{(k)} - \sigma_{\mathrm{ee}}^{(k)}\rho - \rho\sigma_{\mathrm{ee}}^{(k)}\Big)\sigma_{\mathrm{ee}}^{(j)}\Big] \\
&= \frac{\Gamma\gamma}{4}\sum_{k=1}^{N}\left[\sigma_{\mathrm{ee}}^{(k)}\rho\sigma_{\mathrm{gg}}^{(k)} + \sigma_{\mathrm{gg}}^{(k)}\rho\sigma_{\mathrm{ee}}^{(k)}\right] \\
&\quad - \frac{\Gamma\gamma}{4}\sum_{j\neq k}\Big[\sigma_{\mathrm{ee}}^{(j)}\Big(2\sigma_-^{(k)}\rho\sigma_+^{(k)} - \sigma_{\mathrm{ee}}^{(k)}\rho - \rho\sigma_{\mathrm{ee}}^{(k)}\Big)\sigma_{\mathrm{gg}}^{(j)} \\
&\quad + \sigma_{\mathrm{gg}}^{(j)}\Big(2\sigma_-^{(k)}\rho\sigma_+^{(k)} - \sigma_{\mathrm{ee}}^{(k)}\rho - \rho\sigma_{\mathrm{ee}}^{(k)}\Big)\sigma_{\mathrm{ee}}^{(j)}\Big]
\end{aligned}$$

$$\begin{aligned}
\mathcal{L}_\gamma[\mathcal{L}_\Gamma[\rho]] &= -\frac{\Gamma\gamma}{4}\sum_{j,k=1}^{N} \sigma_{\mathrm{ee}}^{(j)}\left(2\sigma_-^{(k)}\rho\sigma_+^{(k)} - \sigma_{\mathrm{ee}}^{(k)}\rho - \rho\sigma_{\mathrm{ee}}^{(k)}\right)\sigma_{\mathrm{gg}}^{(j)} \\
&\quad + \sigma_{\mathrm{gg}}^{(j)}\left(2\sigma_-^{(k)}\rho\sigma_+^{(k)} - \sigma_{\mathrm{ee}}^{(k)}\rho - \rho\sigma_{\mathrm{ee}}^{(k)}\right)\sigma_{\mathrm{ee}}^{(j)} \\
&= -\frac{\Gamma\gamma}{4}\sum_{k=1}^{N}\Big[2\underbrace{\sigma_{\mathrm{ee}}^{(k)}\sigma_-^{(k)}}_{=0}\rho\underbrace{\sigma_+^{(k)}\sigma_{\mathrm{gg}}^{(k)}}_{=\sigma_+^{(k)}} + 2\underbrace{\sigma_{\mathrm{gg}}^{(k)}\sigma_-^{(k)}}_{=\sigma_-^{(k)}}\rho\underbrace{\sigma_+^{(k)}\sigma_{\mathrm{ee}}^{(k)}}_{=0} \\
&\quad - \underbrace{\sigma_{\mathrm{ee}}^{(k)}\sigma_{\mathrm{ee}}^{(k)}}_{=\sigma_{\mathrm{ee}}^{(k)}}\rho\sigma_{\mathrm{gg}}^{(k)} - \underbrace{\sigma_{\mathrm{gg}}^{(k)}\sigma_{\mathrm{ee}}^{(k)}}_{=0}\rho\sigma_{\mathrm{ee}}^{(k)} - \sigma_{\mathrm{ee}}^{(k)}\rho\underbrace{\sigma_{\mathrm{ee}}^{(k)}\sigma_{\mathrm{gg}}^{(k)}}_{=0} - \sigma_{\mathrm{gg}}^{(k)}\rho\underbrace{\sigma_{\mathrm{ee}}^{(k)}\sigma_{\mathrm{ee}}^{(k)}}_{=\sigma_{\mathrm{ee}}^{(k)}}\Big] \\
&\quad - \frac{\Gamma\gamma}{4}\sum_{j\neq k}\Big[\sigma_{\mathrm{ee}}^{(j)}\left(2\sigma_-^{(k)}\rho\sigma_+^{(k)} - \sigma_{\mathrm{ee}}^{(k)}\rho - \rho\sigma_{\mathrm{ee}}^{(k)}\right)\sigma_{\mathrm{gg}}^{(j)} \\
&\quad + \sigma_{\mathrm{gg}}^{(j)}\left(2\sigma_-^{(k)}\rho\sigma_+^{(k)} - \sigma_{\mathrm{ee}}^{(k)}\rho - \rho\sigma_{\mathrm{ee}}^{(k)}\right)\sigma_{\mathrm{ee}}^{(j)}\Big] \\
&= \frac{\Gamma\gamma}{4}\sum_{k=1}^{N}\left[\sigma_{\mathrm{ee}}^{(k)}\rho\sigma_{\mathrm{gg}}^{(k)} + \sigma_{\mathrm{gg}}^{(k)}\rho\sigma_{\mathrm{ee}}^{(k)}\right] \\
&\quad - \frac{\Gamma\gamma}{4}\sum_{j\neq k}\Big[\sigma_{\mathrm{ee}}^{(j)}\left(2\sigma_-^{(k)}\rho\sigma_+^{(k)} - \sigma_{\mathrm{ee}}^{(k)}\rho - \rho\sigma_{\mathrm{ee}}^{(k)}\right)\sigma_{\mathrm{gg}}^{(j)} \\
&\quad + \sigma_{\mathrm{gg}}^{(j)}\left(2\sigma_-^{(k)}\rho\sigma_+^{(k)} - \sigma_{\mathrm{ee}}^{(k)}\rho - \rho\sigma_{\mathrm{ee}}^{(k)}\right)\sigma_{\mathrm{ee}}^{(j)}\Big]
\end{aligned}$$

- $[\mathcal{L}_\Gamma, \mathcal{L}_{\gamma_c}] = 0$:

$$\begin{aligned}
\mathcal{L}_\Gamma[\mathcal{L}_{\gamma_c}[\rho]] &= \frac{\Gamma\gamma_c}{16}\sum_{j,k,l=1}^{N} 2\sigma_-^{(j)}\left(2\sigma_z^{(k)}\rho\sigma_z^{(l)} - \rho\sigma_z^{(k)}\sigma_z^{(l)} - \sigma_z^{(k)}\sigma_z^{(l)}\rho\right)\sigma_+^{(j)} \\
&\quad - \sigma_{\mathrm{ee}}^{(j)}\left(2\sigma_z^{(k)}\rho\sigma_z^{(l)} - \rho\sigma_z^{(k)}\sigma_z^{(l)} - \sigma_z^{(k)}\sigma_z^{(l)}\rho\right) \\
&\quad - \left(2\sigma_z^{(k)}\rho\sigma_z^{(l)} - \rho\sigma_z^{(k)}\sigma_z^{(l)} - \sigma_z^{(k)}\sigma_z^{(l)}\rho\right)\sigma_{\mathrm{ee}}^{(j)} \\
&= \frac{\Gamma\gamma_c}{16}\sum_{j,k,l=1}^{N} 4\sigma_-^{(j)}\sigma_z^{(k)}\rho\sigma_z^{(l)}\sigma_+^{(j)} - 2\sigma_-^{(j)}\rho\sigma_z^{(k)}\sigma_z^{(l)}\sigma_+^{(j)} \\
&\quad - 2\sigma_-^{(j)}\sigma_z^{(k)}\sigma_z^{(l)}\rho\sigma_+^{(j)} - 2\sigma_{\mathrm{ee}}^{(j)}\sigma_z^{(k)}\rho\sigma_z^{(l)} + \sigma_{\mathrm{ee}}^{(j)}\rho\sigma_z^{(k)}\sigma_z^{(l)} + \sigma_{\mathrm{ee}}^{(j)}\sigma_z^{(k)}\sigma_z^{(l)}\rho \\
&\quad - 2\sigma_z^{(k)}\rho\sigma_z^{(l)}\sigma_{\mathrm{ee}}^{(j)} + \rho\sigma_z^{(k)}\sigma_z^{(l)}\sigma_{\mathrm{ee}}^{(j)} + \sigma_z^{(k)}\sigma_z^{(l)}\rho\sigma_{\mathrm{ee}}^{(j)}
\end{aligned}$$

$$\begin{aligned}
\mathcal{L}_{\gamma_c}[\mathcal{L}_\Gamma[\rho]] = \frac{\Gamma\gamma_c}{16} \sum_{j,k,l=1}^{N} & 2\sigma_z^{(k)} \left(2\sigma_-^{(j)}\rho\sigma_+^{(j)} - \sigma_{\text{ee}}^{(j)}\rho - \rho\sigma_{\text{ee}}^{(j)}\right)\sigma_z^{(l)} \\
& - \left(2\sigma_-^{(j)}\rho\sigma_+^{(j)} - \sigma_{\text{ee}}^{(j)}\rho - \rho\sigma_{\text{ee}}^{(j)}\right)\sigma_z^{(k)}\sigma_z^{(l)} \\
& - \sigma_z^{(k)}\sigma_z^{(l)}\left(2\sigma_-^{(j)}\rho\sigma_+^{(j)} - \sigma_{\text{ee}}^{(j)}\rho - \rho\sigma_{\text{ee}}^{(j)}\right) \\
= \frac{\Gamma\gamma_c}{16} \sum_{j,k,l=1}^{N} & 4\sigma_z^{(k)}\sigma_-^{(j)}\rho\sigma_+^{(j)}\sigma_z^{(l)} - 2\sigma_z^{(k)}\sigma_{\text{ee}}^{(j)}\rho\sigma_z^{(l)} - 2\sigma_z^{(k)}\rho\sigma_{\text{ee}}^{(j)}\sigma_z^{(l)} \\
& - 2\sigma_-^{(j)}\rho\sigma_+^{(j)}\sigma_z^{(k)}\sigma_z^{(l)} + \sigma_{\text{ee}}^{(j)}\rho\sigma_z^{(k)}\sigma_z^{(l)} + \rho\sigma_{\text{ee}}^{(j)}\sigma_z^{(k)}\sigma_z^{(l)} \\
& - 2\sigma_z^{(k)}\sigma_z^{(l)}\sigma_-^{(j)}\rho\sigma_+^{(j)} + \sigma_z^{(k)}\sigma_z^{(l)}\sigma_{\text{ee}}^{(j)}\rho + \sigma_z^{(k)}\sigma_z^{(l)}\rho\sigma_{\text{ee}}^{(j)}
\end{aligned}$$

The terms without $\sigma_\pm$ operators are equal since only σ_z and σ_{ee} appear which commute independent of the index. For the remaining terms, we have to distinguish between all five cases:

$$\begin{aligned}
[\mathcal{L}_\Gamma, \mathcal{L}_{\gamma_c}][\rho] &= \frac{\Gamma\gamma_c}{16}\Big[\sum_{j,k,l}\cdots\Big] \\
&= \frac{\Gamma\gamma_c}{16}\Big[\sum_{j=k=l}\cdots \sum_{k=l,j\neq k}\cdots + \sum_{j=k,j\neq l}\cdots + \sum_{j=l,j\neq k}\cdots + \sum_{j\neq k,k\neq l,l\neq j}\cdots\Big]
\end{aligned}$$

(i) $j = k = l$:

$$\begin{aligned}
\frac{\Gamma\gamma_c}{16}\sum_{k=1}^{N}\Big[&4\sigma_-^{(k)}\rho\sigma_+^{(k)} - 2\sigma_-^{(k)}\rho\sigma_+^{(k)} - 2\sigma_-^{(k)}\rho\sigma_+^{(k)} - 4\sigma_-^{(k)}\rho\sigma_+^{(k)} \\
&+ 2\sigma_-^{(k)}\rho\sigma_+^{(k)} + 2\sigma_-^{(k)}\rho\sigma_+^{(k)}\Big] = 0
\end{aligned}$$

(ii) $k = l$, $j \neq k$:

$$\begin{aligned}
\frac{\Gamma\gamma_c}{16}\sum_{\substack{j,k=1\\ j\neq k}}^{N}\Big[&4\sigma_-^{(j)}\sigma_z^{(k)}\rho\sigma_z^{(k)}\sigma_+^{(j)} - 2\sigma_-^{(j)}\rho\sigma_+^{(j)} - 2\sigma_-^{(j)}\rho\sigma_+^{(j)} \\
&- 4\underbrace{\sigma_z^{(k)}\sigma_-^{(j)}}_{=\sigma_-^{(j)}\sigma_z^{(k)}}\rho\underbrace{\sigma_+^{(j)}\sigma_z^{(k)}}_{=\sigma_z^{(k)}\sigma_+^{(j)}} + 2\sigma_-^{(j)}\rho\sigma_+^{(j)} + 2\sigma_-^{(j)}\rho\sigma_+^{(j)}\Big] = 0
\end{aligned}$$

(iii) $j = k$, $j \neq l$:

$$\begin{aligned}
\frac{\Gamma\gamma_c}{16}\sum_{\substack{j,l=1\\ j\neq l}}^{N}\Big[&4\sigma_-^{(j)}\rho\sigma_z^{(l)}\sigma_+^{(j)} - 2\sigma_-^{(j)}\rho\underbrace{\sigma_z^{(j)}\sigma_z^{(l)}\sigma_+^{(j)}}_{=\sigma_z^{(l)}\sigma_+^{(j)}} - 2\sigma_-^{(j)}\sigma_z^{(l)}\rho\sigma_+^{(j)} \\
&+ 4\sigma_-^{(j)}\rho\underbrace{\sigma_+^{(j)}\sigma_z^{(l)}}_{=\sigma_z^{(l)}\sigma_+^{(j)}} - 2\sigma_-^{(j)}\rho\underbrace{\sigma_+^{(j)}\sigma_z^{(l)}}_{=\sigma_z^{(l)}\sigma_+^{(j)}} + 2\underbrace{\sigma_z^{(j)}\sigma_z^{(l)}\sigma_-^{(j)}}_{=-\sigma_z^{(l)}\sigma_-^{(j)}=-\sigma_-^{(j)}\sigma_z^{(l)}}\rho\sigma_+^{(j)}\Big]
\end{aligned}$$

(iv) $j = l$, $j \neq k$:

$$\frac{\Gamma\gamma_c}{16}\sum_{\substack{j,k=1\\ j\neq k}}^{N}\Big[4\sigma_-^{(j)}\sigma_z^{(k)}\rho\sigma_+^{(j)} - 2\sigma_-^{(j)}\rho\sigma_z^{(k)}\sigma_+^{(j)} - 2\underbrace{\sigma_-^{(j)}\sigma_z^{(k)}\sigma_z^{(j)}}_{=\sigma_-^{(j)}\sigma_z^{(k)}}\rho\sigma_+^{(j)}$$
$$+ 4\underbrace{\sigma_z^{(k)}\sigma_-^{(j)}}_{=\sigma_-^{(j)}\sigma_z^{(k)}}\rho\sigma_+^{(j)} + 2\sigma_-^{(j)}\rho\underbrace{\sigma_+^{(j)}\sigma_z^{(k)}\sigma_z^{(j)}}_{=-\sigma_+^{(j)}\sigma_z^{(k)}} - 2\underbrace{\sigma_z^{(k)}\sigma_-^{(j)}}_{=\sigma_-^{(j)}\sigma_z^{(k)}}\rho\sigma_+^{(j)}\Big]$$

(v) $j \neq k$, $k \neq l$, $j \neq l$:

$$\frac{\Gamma\gamma_c}{16}\sum_{\substack{j,k,l=1\\ j\neq k, k\neq l, j\neq l}}^{N}\Big[4\sigma_-^{(j)}\sigma_z^{(k)}\rho\sigma_z^{(l)}\sigma_+^{(j)} - 2\sigma_-^{(j)}\rho\sigma_z^{(k)}\sigma_z^{(l)}\sigma_+^{(j)} - 2\sigma_-^{(j)}\sigma_z^{(k)}\sigma_z^{(l)}\rho\sigma_+^{(j)}$$
$$- 4\underbrace{\sigma_z^{(k)}\sigma_-^{(j)}}_{=\sigma_-^{(j)}\sigma_z^{(k)}}\rho\underbrace{\sigma_+^{(j)}\sigma_z^{(l)}}_{=\sigma_z^{(l)}\sigma_+^{(j)}} + 2\sigma_-^{(j)}\rho\underbrace{\sigma_+^{(j)}\sigma_z^{(k)}\sigma_z^{(l)}}_{=\sigma_z^{(k)}\sigma_z^{(l)}\sigma_+^{(j)}} + 2\underbrace{\sigma_z^{(k)}\sigma_z^{(l)}\sigma_-^{(j)}}_{=\sigma_-^{(j)}\sigma_z^{(k)}\sigma_z^{(l)}}\rho\sigma_+^{(j)}\Big] = 0$$

While cases (i), (ii) and (v) vanish independently, cases (iii) and (iv) add to zero when renaming the indices $k \leftrightarrow l$.

- $[\mathcal{L}_\gamma, \mathcal{L}_{\gamma_c}] = 0$:
  Here it is advantageous to use the form $\mathcal{L}_\gamma[\rho] = \frac{\gamma}{4}\sum_{j=1}^{N}\sigma_z^{(j)}\rho\sigma_z^{(j)} - \rho$.

$$\begin{aligned}
\mathcal{L}_\gamma[\mathcal{L}_{\gamma_c}[\rho]] &= \frac{\gamma\gamma_c}{32}\sum_{j,k,l=1}^{N}\sigma_z^{(j)}\left(2\sigma_z^{(k)}\rho\sigma_z^{(l)} - \rho\sigma_z^{(k)}\sigma_z^{(l)} - \sigma_z^{(k)}\sigma_z^{(l)}\rho\right)\sigma_z^{(j)}\\
&\quad - \left(2\sigma_z^{(k)}\rho\sigma_z^{(l)} - \rho\sigma_z^{(k)}\sigma_z^{(l)} - \sigma_z^{(k)}\sigma_z^{(l)}\rho\right)\\
&= \frac{\gamma\gamma_c}{32}\sum_{j,k,l=1}^{N}2\sigma_z^{(j)}\sigma_z^{(k)}\rho\sigma_z^{(l)}\sigma_z^{(j)} - \sigma_z^{(j)}\rho\sigma_z^{(k)}\sigma_z^{(l)}\sigma_z^{(j)} - \sigma_z^{(j)}\sigma_z^{(k)}\sigma_z^{(l)}\rho\sigma_z^{(j)}\\
&\quad - 2\sigma_z^{(k)}\rho\sigma_z^{(l)} + \rho\sigma_z^{(k)}\sigma_z^{(l)} + \sigma_z^{(k)}\sigma_z^{(l)}\rho
\end{aligned}$$

$$\begin{aligned}
\mathcal{L}_{\gamma_c}[\mathcal{L}_\gamma[\rho]] &= \frac{\gamma\gamma_c}{32}\sum_{j,k,l=1}^{N}2\sigma_z^{(k)}\left(\sigma_z^{(j)}\rho\sigma_z^{(j)} - \rho\right)\sigma_z^{(l)} - \left(\sigma_z^{(j)}\rho\sigma_z^{(j)} - \rho\right)\sigma_z^{(k)}\sigma_z^{(l)}\\
&\quad - \sigma_z^{(k)}\sigma_z^{(l)}\left(\sigma_z^{(j)}\rho\sigma_z^{(j)} - \rho\right)\\
&= \frac{\gamma\gamma_c}{32}\sum_{j,k,l=1}^{N}2\sigma_z^{(k)}\sigma_z^{(j)}\rho\sigma_z^{(j)}\sigma_z^{(l)} - 2\sigma_z^{(k)}\rho\sigma_z^{(l)} - \sigma_z^{(j)}\rho\sigma_z^{(j)}\sigma_z^{(k)}\sigma_z^{(l)}\\
&\quad + \rho\sigma_z^{(k)}\sigma_z^{(l)} - \sigma_z^{(k)}\sigma_z^{(l)}\sigma_z^{(j)}\rho\sigma_z^{(j)} + \sigma_z^{(k)}\sigma_z^{(l)}\rho
\end{aligned}$$

While the terms with two σ_z operators are equal, for those with four σ_z operators we again have to distinguish between all five cases:

$$
\begin{aligned}
[\mathcal{L}_\gamma, \mathcal{L}_{\gamma_c}][\rho] &= \frac{\gamma\gamma_c}{32} \sum_{j,k,l=1}^{N} 2\sigma_z^{(j)}\sigma_z^{(k)}\rho\sigma_z^{(l)}\sigma_z^{(j)} - \sigma_z^{(j)}\rho\sigma_z^{(k)}\sigma_z^{(l)}\sigma_z^{(j)} - \sigma_z^{(j)}\sigma_z^{(k)}\sigma_z^{(l)}\rho\sigma_z^{(j)} \\
&\quad - 2\sigma_z^{(k)}\sigma_z^{(j)}\rho\sigma_z^{(j)}\sigma_z^{(l)} + \sigma_z^{(j)}\rho\sigma_z^{(j)}\sigma_z^{(k)}\sigma_z^{(l)} + \sigma_z^{(k)}\sigma_z^{(l)}\sigma_z^{(j)}\rho\sigma_z^{(j)} \\
&= \frac{\gamma\gamma_c}{32} \sum_{k=1}^{N} \left[2\rho - \sigma_z^{(k)}\rho\sigma_z^{(k)} - \sigma_z^{(k)}\rho\sigma_z^{(k)} - 2\rho + \sigma_z^{(k)}\rho\sigma_z^{(k)} + \sigma_z^{(k)}\rho\sigma_z^{(k)}\right] \\
&\quad + \frac{\gamma\gamma_c}{32} \sum_{\substack{j,k=1 \\ j\neq k}}^{N} \Big[2\sigma_z^{(j)}\sigma_z^{(k)}\rho\sigma_z^{(k)}\sigma_z^{(j)} - \sigma_z^{(j)}\rho\sigma_z^{(j)} - \sigma_z^{(j)}\rho\sigma_z^{(j)} \\
&\quad - 2\underbrace{\sigma_z^{(k)}\sigma_z^{(j)}}_{=\sigma_z^{(j)}\sigma_z^{(k)}}\rho\underbrace{\sigma_z^{(j)}\sigma_z^{(k)}}_{=\sigma_z^{(k)}\sigma_z^{(j)}} + \sigma_z^{(j)}\rho\sigma_z^{(j)} + \sigma_z^{(j)}\rho\sigma_z^{(j)}\Big] \\
&\quad + \sum_{\substack{j,l=1 \\ j\neq l}}^{N} \Big[2\rho\sigma_z^{(l)}\sigma_z^{(j)} - \sigma_z^{(j)}\rho\underbrace{\sigma_z^{(j)}\sigma_z^{(l)}\sigma_z^{(j)}}_{=\sigma_z^{(l)}} - \sigma_z^{(l)}\rho\sigma_z^{(j)} \\
&\quad - 2\rho\underbrace{\sigma_z^{(j)}\sigma_z^{(l)}}_{=\sigma_z^{(l)}\sigma_z^{(j)}} + \sigma_z^{(j)}\rho\sigma_z^{(l)} + \underbrace{\sigma_z^{(j)}\sigma_z^{(l)}\sigma_z^{(j)}\rho\sigma_z^{(j)}}_{=\sigma_z^{(l)}}\Big] \\
&\quad + \sum_{\substack{j,k=1 \\ j\neq k}}^{N} \Big[2\sigma_z^{(j)}\sigma_z^{(k)}\rho - \sigma_z^{(j)}\rho\sigma_z^{(k)} - \underbrace{\sigma_z^{(j)}\sigma_z^{(k)}\sigma_z^{(j)}}_{=\sigma_z^{(k)}}\rho\sigma_z^{(j)} \\
&\quad - 2\sigma_z^{(k)}\sigma_z^{(j)}\rho + \sigma_z^{(j)}\rho\underbrace{\sigma_z^{(j)}\sigma_z^{(k)}\sigma_z^{(j)}}_{=\sigma_z^{(k)}} + \sigma_z^{(k)}\rho\sigma_z^{(j)}\Big] \\
&\quad + \frac{\gamma\gamma_c}{32} \sum_{\substack{j,k=1 \\ j\neq k, k\neq l, j\neq l}}^{N} \Big[2\sigma_z^{(j)}\sigma_z^{(k)}\rho\sigma_z^{(l)}\sigma_z^{(j)} - \sigma_z^{(j)}\rho\sigma_z^{(k)}\sigma_z^{(l)}\sigma_z^{(j)} - \sigma_z^{(j)}\sigma_z^{(k)}\sigma_z^{(l)}\rho\sigma_z^{(j)} \\
&\quad - 2\underbrace{\sigma_z^{(k)}\sigma_z^{(j)}}_{=\sigma_z^{(j)}\sigma_z^{(k)}}\rho\underbrace{\sigma_z^{(j)}\sigma_z^{(l)}}_{=\sigma_z^{(l)}\sigma_z^{(j)}} + \sigma_z^{(j)}\rho\underbrace{\sigma_z^{(j)}\sigma_z^{(k)}\sigma_z^{(l)}}_{=\sigma_z^{(k)}\sigma_z^{(l)}\sigma_z^{(j)}} + \underbrace{\sigma_z^{(k)}\sigma_z^{(l)}\sigma_z^{(j)}}_{=\sigma_z^{(j)}\sigma_z^{(k)}\sigma_z^{(l)}}\rho\sigma_z^{(j)}\Big] \\
&= 0
\end{aligned}
$$

C.2 Time evolution

Since the individual contributions to the master equation in Eq. (C.5) (super-)commute pairwise, as demonstrated above, the dynamics of the associated processes can be solved separately.

Solution methods— In general, we aim to solve a master equation of the form $\dot{\rho} = \mathcal{L}[\rho]$, governed by the Lindblad (super-)operator $\mathcal{L}$, also known as the Liouvillian. Here, we outline a generic solution strategy for a two-level system, which can be readily extended to arbitrary ensemble sizes. Considering the state

$$\rho = \rho_{\text{ee}}|\uparrow\rangle\langle\uparrow| + \rho_{\text{eg}}|\uparrow\rangle\langle\downarrow| + \rho_{\text{ge}}|\downarrow\rangle\langle\uparrow| + \rho_{\text{gg}}|\downarrow\rangle\langle\downarrow|, \tag{C.6}$$

the master equation yields four – potentially coupled – differential equations

$$\dot{\rho}_{ee} = \langle\uparrow|\,\dot{\rho}\,|\uparrow\rangle = \langle\uparrow|\,\mathcal{L}[\rho]\,|\uparrow\rangle \tag{C.7}$$

$$\dot{\rho}_{eg} = \langle\uparrow|\,\dot{\rho}\,|\downarrow\rangle = \langle\uparrow|\,\mathcal{L}[\rho]\,|\downarrow\rangle \tag{C.8}$$

$$\dot{\rho}_{ge} = \langle\downarrow|\,\dot{\rho}\,|\uparrow\rangle = \langle\downarrow|\,\mathcal{L}[\rho]\,|\uparrow\rangle \tag{C.9}$$

$$\dot{\rho}_{gg} = \langle\downarrow|\,\dot{\rho}\,|\downarrow\rangle = \langle\downarrow|\,\mathcal{L}[\rho]\,|\downarrow\rangle\,, \tag{C.10}$$

which can be solved using standard techniques. Alternatively, the formal solution is given by

$$\rho(T) = e^{\mathcal{L}T}[\rho]. \tag{C.11}$$

Since the super-operator $\mathcal{L}$ acts linearly on the space of density matrices, it can be represented as a matrix acting on the vectorized density matrix $\vec{\rho}$. Hence, the master equation can be expressed as

$$\dot{\vec{\rho}} = \mathcal{L}\vec{\rho}. \tag{C.12}$$

For a two level system, $\mathcal{L}$ is represented by a 4×4 matrix and Eq. (C.12) is explicitly given by

$$\begin{pmatrix} \dot{\rho}_{ee} \\ \dot{\rho}_{eg} \\ \dot{\rho}_{ge} \\ \dot{\rho}_{gg} \end{pmatrix} = \begin{pmatrix} \langle\uparrow|\,\mathcal{L}[|\uparrow\rangle\langle\uparrow|]\,|\uparrow\rangle & \langle\uparrow|\,\mathcal{L}[|\uparrow\rangle\langle\downarrow|]\,|\uparrow\rangle & \langle\uparrow|\,\mathcal{L}[|\downarrow\rangle\langle\uparrow|]\,|\uparrow\rangle & \langle\uparrow|\,\mathcal{L}[|\downarrow\rangle\langle\downarrow|]\,|\uparrow\rangle \\ \langle\uparrow|\,\mathcal{L}[|\uparrow\rangle\langle\uparrow|]\,|\downarrow\rangle & \langle\uparrow|\,\mathcal{L}[|\uparrow\rangle\langle\downarrow|]\,|\downarrow\rangle & \langle\uparrow|\,\mathcal{L}[|\downarrow\rangle\langle\uparrow|]\,|\downarrow\rangle & \langle\uparrow|\,\mathcal{L}[|\downarrow\rangle\langle\downarrow|]\,|\downarrow\rangle \\ \langle\downarrow|\,\mathcal{L}[|\uparrow\rangle\langle\uparrow|]\,|\uparrow\rangle & \langle\downarrow|\,\mathcal{L}[|\uparrow\rangle\langle\downarrow|]\,|\uparrow\rangle & \langle\downarrow|\,\mathcal{L}[|\downarrow\rangle\langle\uparrow|]\,|\uparrow\rangle & \langle\downarrow|\,\mathcal{L}[|\downarrow\rangle\langle\downarrow|]\,|\uparrow\rangle \\ \langle\downarrow|\,\mathcal{L}[|\uparrow\rangle\langle\uparrow|]\,|\downarrow\rangle & \langle\downarrow|\,\mathcal{L}[|\uparrow\rangle\langle\downarrow|]\,|\downarrow\rangle & \langle\downarrow|\,\mathcal{L}[|\downarrow\rangle\langle\uparrow|]\,|\downarrow\rangle & \langle\downarrow|\,\mathcal{L}[|\downarrow\rangle\langle\downarrow|]\,|\downarrow\rangle \end{pmatrix} \begin{pmatrix} \rho_{ee} \\ \rho_{eg} \\ \rho_{ge} \\ \rho_{gg} \end{pmatrix}. \tag{C.13}$$

More generally, for a system with Hilbert space dimension n, $\mathcal{L}$ is represented by a $n^2 \times n^2$-matrix. In this form, the solution of Eq. (C.12) is obtained via the corresponding matrix exponential $\vec{\rho}(T) = e^{\mathcal{L}T}\vec{\rho}$.

Unitary phase evolution— The unitary phase evolution described in Eq. (C.1) results in a collective rotation by an angle $\phi = \omega T$ around the z-axis, as described by Eq. (3.6). This rotation acts independently and identically on all qubits and thus, it is sufficient to solve the dynamics for a single qubit. Consequently, it is convenient to examine the dynamics in the single-particle basis. In particular, we consider the generic state defined in Eq. (C.6) and examine the dynamics based on the evolution of the matrix elements. The unitary phase evolution results in (cf. Sec. 2.3.5)

$$\rho_{ee}(\phi) = \langle\uparrow|\,\rho(\phi)\,|\uparrow\rangle = \rho_{ee} \tag{C.14}$$

$$\rho_{eg}(\phi) = \langle\uparrow|\,\rho(\phi)\,|\downarrow\rangle = \rho_{eg}e^{-i\phi} \tag{C.15}$$

$$\rho_{ge}(\phi) = \langle\downarrow|\,\rho(\phi)\,|\uparrow\rangle = \rho_{ge}e^{i\phi} \tag{C.16}$$

$$\rho_{gg}(\phi) = \langle\downarrow|\,\rho(\phi)\,|\downarrow\rangle = \rho_{gg}. \tag{C.17}$$

Hence, only the coherences ρ_{eg} and ρ_{ge} accumulate the phase ϕ, while the populations ρ_{ee} and ρ_{gg} remain unchanged.

Spontaneous decay— The dynamics associated with spontanteous decay, described by the Lindblad operator in Eq. (C.2), is likewise independent and identical for all qubits. The corresponding single particle master equation reads

$$\dot\rho = \frac{\Gamma}{2}\left(2\sigma_-\rho\sigma_+ - \sigma_{\mathrm{ee}}\rho - \rho\sigma_{\mathrm{ee}}\right). \tag{C.18}$$

Accordingly, the time evolution of the matrix elements is determined by

$$\dot\rho_{ee} = \langle\uparrow|\,\dot\rho\,|\uparrow\rangle = -\Gamma\rho_{ee} \qquad \Rightarrow \qquad \rho_{ee}(t) = \rho_{ee}e^{-\Gamma t} \tag{C.19}$$

$$\dot\rho_{eg} = \langle\uparrow|\,\dot\rho\,|\downarrow\rangle = -\frac{\Gamma}{2}\rho_{eg} \qquad \Rightarrow \qquad \rho_{eg}(t) = \rho_{eg}e^{-\frac{\Gamma t}{2}} \tag{C.20}$$

$$\dot\rho_{ge} = \langle\downarrow|\,\dot\rho\,|\uparrow\rangle = -\frac{\Gamma}{2}\rho_{ge} \qquad \Rightarrow \qquad \rho_{ge}(t) = \rho_{ge}e^{-\frac{\Gamma t}{2}} \tag{C.21}$$

$$\dot\rho_{gg} = \langle\downarrow|\,\dot\rho\,|\downarrow\rangle = \Gamma\rho_{ee} \qquad \Rightarrow \qquad \rho_{gg}(t) = \rho_{gg} + \rho_{ee}\left[1 - e^{-\Gamma t}\right]. \tag{C.22}$$

As a result, for spontaneous decay, the population decays from the excited to the ground state, while the coherences diminish with T.

Individual dephasing— Likewise, individual dephasing, described by Eq. (C.3), acts independently and identically on all qubits. With the master equation for a single particle

$$\dot\rho = -\frac{\gamma}{2}\left(\sigma_{\mathrm{ee}}\rho\sigma_{\mathrm{gg}} + \sigma_{\mathrm{gg}}\rho\sigma_{\mathrm{ee}}\right), \tag{C.23}$$

the evolution of the matrix elements results in

$$\dot{\rho}_{ee} = 0 \qquad \Rightarrow \qquad \rho_{ee}(t) = \rho_{ee} \tag{C.24}$$

$$\dot{\rho}_{eg} = -\frac{\gamma}{2}\rho_{eg} \qquad \Rightarrow \qquad \rho_{eg}(t) = \rho_{eg} e^{-\frac{\gamma t}{2}} \tag{C.25}$$

$$\dot{\rho}_{ge} = -\frac{\gamma}{2}\rho_{ge} \qquad \Rightarrow \qquad \rho_{ge}(t) = \rho_{ge} e^{-\frac{\gamma t}{2}} \tag{C.26}$$

$$\dot{\rho}_{gg} = 0 \qquad \Rightarrow \qquad \rho_{gg}(t) = \rho_{gg}. \tag{C.27}$$

Thus, in the case of individual dephasing, the coherences decrease, while the populations remain unchanged.

Collective dephasing— In contrast to spontaneous decay and individual dephasing, collective dephasing – as its name suggests – represents a collective decoherence process. The master equation of the system is governed by Eq. (C.4) and thus, Dicke states (cf. Sec. 2.3.1) represent a more convenient basis. As a consequence, we typically consider collective dephasing separately. The matrix elements evolve according to

$$\dot{\rho}_{S,M;S',M'} = \langle S, M|\, \dot{\rho}\, |S', M'\rangle \tag{C.28}$$

$$= \frac{\gamma_c}{2}\left(2MM' - M^2 - (M')^2\right)\rho_{S,M;S',M'} \tag{C.29}$$

$$= -\frac{\gamma_c}{2}(M - M')^2 \rho_{S,M;S',M'} \tag{C.30}$$

$$\Rightarrow \rho_{S,M;S',M'}(t) = \rho_{S,M;S',M'} \exp\left(-\frac{\gamma_c t}{2}(M - M')^2\right). \tag{C.31}$$

Hence, as for individual dephasing, the populations remain unchanged, while the coherences decrease. Furthermore, no coherences between blocks with $S \neq S'$ are created, which allows to employ the reduced Dicke basis, introduced in Sec. 2.3.1.

D

Derivations of bounds in local phase estimation

In this appendix, we present a collection of proofs from the literature, such as Refs. [6, 161–170], for the lower bounds on the phase estimation uncertainty, as defined in Eq. (3.13), in the context of local phase estimation theory and the fundamental properties of the (quantum) Fisher information. In particular, to ensure a self-consistent understanding of the proofs, we first explicitly restate the assumptions and results from the main text before providing the proof.

D.1 Cramér-Rao Bound (CRB)

Assuming a locally unbiased estimator at ϕ_0, i.e.

$$\overline{\phi}_{\text{est}}|_{\phi=\phi_0} = \sum_x P(x|\phi_0)\phi_{\text{est}}(x) = \phi_0 \tag{D.1}$$

$$\frac{\mathrm{d}\overline{\phi}_{\text{est}}}{\mathrm{d}\phi}\Big|_{\phi=\phi_0} = \sum_x \frac{\mathrm{d}P(x|\phi)}{\mathrm{d}\phi}\Big|_{\phi=\phi_0}\phi_{\text{est}}(x) = 1, \tag{D.2}$$

and standard regularity conditions

$$\sum_x \frac{\mathrm{d}P(x|\phi)}{\mathrm{d}\phi} = \frac{\mathrm{d}}{\mathrm{d}\phi}\sum_x P(x|\phi) = 0, \tag{D.3}$$

the CRB reads

$$(\Delta\phi(T))^2 \geq (\Delta\phi_{\text{CRB}}(T))^2 = \min_{\phi_{\text{est}}}(\Delta\phi(T))^2 = \frac{1}{\mathcal{F}[\Lambda_{\phi,T}[\rho_{\text{in}}],\{\Pi_x\}]}, \tag{D.4}$$

with Fisher information [171, 172] defined by

$$\mathcal{F}[\Lambda_{\phi,T}[\rho_{\text{in}}],\{\Pi_x\}] = \sum_x \frac{1}{P(x|\phi)}\left(\frac{\mathrm{d}P(x|\phi)}{\mathrm{d}\phi}\right)^2. \tag{D.5}$$

Proof: The proof is based on Refs. [161, 162, 164, 165]. The product of the phase estimation uncertainty $(\Delta\phi(T))^2$ and the Fisher information $\mathcal{F}(\phi)$ can be rewritten as follows

$$\begin{aligned}(\Delta\phi(T)^2 \cdot &\mathcal{F}[\Lambda_{\phi,T}[\rho_{\text{in}}], \{\Pi_x\}] \\ &= \left(\sum_x P(x|\phi)\,[\phi_{\text{est}}(x)-\phi]^2\right)\left(\sum_x \frac{1}{P(x|\phi)}\left[\frac{\mathrm{d}P(x|\phi)}{\mathrm{d}\phi}\right]^2\right) \\ &= \left(\sum_x\left[\sqrt{P(x|\phi)}(\phi_{\text{est}}(x)-\phi)\right]^2\right)\left(\sum_x\left[\frac{1}{\sqrt{P(x|\phi)}}\frac{\mathrm{d}P(x|\phi)}{\mathrm{d}\phi}\right]^2\right).\end{aligned} \tag{D.6}$$

Application of the Cauchy-Schwarz inequality results in

$$\begin{aligned}(\Delta\phi(T))^2 \cdot \mathcal{F}[\Lambda_{\phi,T}[\rho_{\text{in}}], \{\Pi_x\}] &\geq \left(\sum_x [\phi_{\text{est}}(x)-\phi]\,\frac{\mathrm{d}P(x|\phi)}{\mathrm{d}\phi}\right)^2 \\ &= \left(\sum_x \frac{\mathrm{d}P(x|\phi)}{\mathrm{d}\phi}\phi_{\text{est}}(x) - \phi\sum_x \frac{\mathrm{d}P(x|\phi)}{\mathrm{d}\phi}\right)^2.\end{aligned} \tag{D.7}$$

While the first term gives 1, since the estimator is locally unbiased and thus Eq. (D.2) holds, the second term vanishes due to the regularity condition Eq. (D.3). Hence, the right hand side gives unity and we obtain the CRB Eq. (D.4). □

From this derivation we conclude that saturation of the CRB is equivalent to saturation of the Cauchy-Schwarz inequality, which is obtained for

$$f(\phi)\sqrt{P(x|\phi)}(\phi_{\text{est}}(x)-\phi) = \frac{1}{\sqrt{P(x|\phi)}}\frac{\mathrm{d}P(x|\phi)}{\mathrm{d}\phi} \tag{D.8}$$

with f being an arbitrary function of ϕ, independent of the measurement outcome x.

D.2 Fisher information

D.2.1 Convexity

Assuming that the state $\rho_{\text{in}}(\phi,T)$ represents an arbitrary mixture

$$\rho_{\text{in}}(\phi,T) = \sum_k p_k\rho_k(\phi,T), \tag{D.9}$$

with weights $p_k \geq 0$ satisfying $\sum_k p_k = 1$, the associated Fisher information is convex

$$\mathcal{F}[\rho_{\text{in}}(\phi,T), \{\Pi_x\}] \leq \sum_k p_k\,\mathcal{F}[\rho_k(\phi,T), \{\Pi_x\}], \tag{D.10}$$

where $\mathcal{F}[\rho_k(\phi, T), \{\Pi_x\}]$ denotes the Fisher information of state ρ_k.

Proof: The proof is based on Refs. [163,164]. For a mixed state as defined in Eq. (D.9), the conditional probability $P(x|\phi)$ is a superposition of the likelihoods $P_k(x|\phi)$ corresponding to the states $\rho_k(\phi, T)$, since

$$\begin{aligned} P(x|\phi) &= \mathrm{Tr}\left(\rho_{\mathrm{in}}(\phi, T)\Pi_x\right) = \mathrm{Tr}\left(\sum_k p_k \rho_k(\phi, T)\Pi_x\right) && \text{(D.11)} \\ &= \sum_k p_k \,\mathrm{Tr}\left(\Pi_x \rho_k(\phi, T)\right) = \sum_k p_k P_k(x|\phi). && \text{(D.12)} \end{aligned}$$

Accordingly, the Fisher information associated with ρ_k is given by

$$\mathcal{F}[\rho_k(\phi, T), \{\Pi_x\}] = \sum_x \frac{p_k}{P_k(x|\phi)} \left[\frac{\mathrm{d}P_k(x|\phi)}{\mathrm{d}\phi}\right]^2. \tag{D.13}$$

With this notation, the convexity of the Fisher information can be demonstrated by by employing the Cauchy-Schwarz inequality:

$$\begin{aligned} \left[\frac{\mathrm{d}P(x|\phi)}{\mathrm{d}\phi}\right]^2 &= \left[\sum_k p_k \frac{\mathrm{d}P_k(x|\phi)}{\mathrm{d}\phi}\right]^2 = \left[\sum_k \sqrt{p_k P_k(x|\phi)} \sqrt{\frac{p_k}{P_k(x|\phi)}} \frac{\mathrm{d}P_k(x|\phi)}{\mathrm{d}\phi}\right]^2 \\ &\leq \left(\sum_k p_k P_k(x|\phi)\right) \left(\sum_k \frac{p_k}{P_k(x|\phi)} \left[\frac{\mathrm{d}P_k(x|\phi)}{\mathrm{d}\phi}\right]^2\right) && \text{(D.14)} \\ &= P(x|\phi) \sum_k p_k \,\mathcal{F}[\rho_k(\phi, T), \{\Pi_x\}]. \end{aligned}$$

Dividing by $P(x|\phi)$ and summation over x finally results in Eq. (D.10). ☐

D.2.2 Additivity

Assuming a separable time evolved state with N independent systems $\rho_{\mathrm{in}}(\phi, T) = \bigotimes_{j=1}^{N} \rho_{\mathrm{in}}^{(j)}(\phi, T)$, where $\rho_{\mathrm{in}}^{(j)}(\phi, T)$ denotes the state of the j-th system, and independent measurements $\Pi_x = \bigotimes_{j=1}^{N} \Pi_{x_j}^{(j)}$, with measurement outcomes x_j and POVMs $\Pi_{x_j}^{(j)}$ for each system, the Fisher information is additive

$$\mathcal{F}[\rho_{\mathrm{in}}(\phi, T), \{\Pi_x\}] = \sum_{j=1}^{N} \mathcal{F}[\rho_{\mathrm{in}}^{(j)}(\phi, T), \{\Pi_x^{(j)}\}], \tag{D.15}$$

where $\mathcal{F}[\rho_{\mathrm{in}}^{(j)}(\phi, T), \{\Pi_x^{(j)}\}]$ denotes the Fisher information of the j-th system.

Proof: The proof follows Ref. [164]. For a separable time evolved state and independent measurements, the conditional probability factorizes according to $P(x|\phi) =$

$\prod_{j=1}^{N} P_j(x_j|\phi)$, where $P^{(j)}(x_j|\phi) = \mathrm{Tr}\Big(\Pi_{x_j}^{(j)} \rho_{\mathrm{in}}^{(j)}(\phi, T)\Big)$ denotes the likelihood of the j-th system. Hence, we obtain

$$\begin{aligned}
\mathcal{F}[\rho_{\mathrm{in}}(\phi,T),\{\Pi_x\}] &= \sum_{x_1,\dots,x_N} \frac{1}{P^{(1)}(x_1|\phi)\cdots P^{(N)}(x_N|\phi)} \left[\frac{\mathrm{d}P^{(1)}(x_1|\phi)\cdots P^{(N)}(x_N|\phi)}{\mathrm{d}\phi}\right]^2 \\
&= \sum_{x_1,\dots,x_N} P^{(1)}(x_1|\phi)\cdots P^{(N)}(x_N|\phi) \\
&\quad \times \sum_{j,k=1}^{N} \frac{1}{P^{(j)}(x_j|\phi)P^{(k)}(x_k|\phi)} \frac{\mathrm{d}P^{(j)}(x_j|\phi)}{\mathrm{d}\phi} \frac{\mathrm{d}P^{(k)}(x_k|\phi)}{\mathrm{d}\phi},
\end{aligned} \tag{D.16}$$

where we have applied the product rule. Here, it is instructive to distinguish between the two cases, namely $j = k$ and $j \neq k$. For $j = k$, the expression becomes

$$\begin{aligned}
&\sum_{j=1}^{N} \sum_{x_1,\dots,x_N} P^{(1)}(x_1|\phi)\cdots P^{(N)}(x_N|\phi) \frac{1}{[P^{(j)}(x_j|\phi)]^2} \left[\frac{\mathrm{d}P^{(j)}(x_j|\phi)}{\mathrm{d}\phi}\right]^2 \\
&= \sum_{j=1}^{N} \sum_{x_j} \frac{1}{P^{(j)}(x_j|\phi)} \left[\frac{\mathrm{d}P^{(j)}(x_j|\phi)}{\mathrm{d}\phi}\right]^2 \left[\sum_{x_1,\dots,x_{j-1},x_{j+1},\dots,x_N} \prod_{k\neq j} P^{(k)}(x_k|\phi)\right] \\
&= \sum_{j=1}^{N} \mathcal{F}[\rho_{\mathrm{in}}^{(j)}(\phi,T),\{\Pi_x^{(j)}\}],
\end{aligned} \tag{D.17}$$

where we introduced the Fisher information of the j-th system

$$\mathcal{F}[\rho_{\mathrm{in}}^{(j)}(\phi,T),\{\Pi_x^{(j)}\}] = \sum_{x_j} \frac{1}{P^{(j)}(x_j|\phi)} \left[\frac{\mathrm{d}P^{(j)}(x_j|\phi)}{\mathrm{d}\phi}\right]^2 \tag{D.18}$$

and used that the last bracket in Eq. (D.17) equals 1 due to the normalization of the conditional probabilities. Conversely, for $j \neq k$, we find

$$\begin{aligned}
&\sum_{j\neq k} \sum_{x_1,\dots,x_N} P^{(1)}(x_1|\phi)\cdots P^{(N)}(x_N|\phi) \sum_{j,k=1}^{N} \frac{1}{P^{(j)}(x_j|\phi)P^{(k)}(x_k|\phi)} \frac{\mathrm{d}P^{(j)}(x_j|\phi)}{\mathrm{d}\phi} \frac{\mathrm{d}P^{(k)}(x_k|\phi)}{\mathrm{d}\phi} \\
&= \sum_{j\neq k} \left[\sum_{x_j} \frac{\mathrm{d}P^{(j)}(x_j|\phi)}{\mathrm{d}\phi}\right] \left[\sum_{x_k} \frac{\mathrm{d}P^{(k)}(x_k|\phi)}{\mathrm{d}\phi}\right] \\
&\times \left[\sum_{x_1,\dots,x_{j-1},x_{j+1},\dots,x_{k-1},x_{k+1},\dots x_N} \prod_{k\neq l\neq j} P^{(l)}(x_l|\phi)\right].
\end{aligned} \tag{D.19}$$

While the last bracket equals 1, as before, the first and second bracket vanish as a result of the regularity condition Eq. (D.3). Thus, the terms for $j \neq k$ vanish, yielding Eq. (D.15). □

D.3 Method of moments

In this appendix, we outline the linear estimation strategy based on the method of moments, following Refs. [6, 164, 167]. Suppose an observable X with known mean value $\langle X(\phi, T)\rangle$ and variance $(\Delta X(\phi, t))^2$. Furthermore, assume n measurements of X with results $x_1, \dots, x_n$, defining the random variable $X_n = \frac{1}{n}\sum_{j=1}^{n} x_j$ which takes the mean value of the measurement outcomes. Although the conditional probabilities are inaccessible and thus the ML estimator cannot be employed, the central limit theorem nevertheless provides the probability distribution of X_n in the asymptotic limit of many repetitions $n \to \infty$ given by $X_n \overset{n\to\infty}{\sim} \mathcal{N}(\langle X(\phi, T)\rangle, (\Delta X(\phi, T))^2/n)$, representing a Gaussian distribution with mean $\langle X(\phi, T)\rangle$ and variance $(\Delta X(\phi, t))^2/n$. However, this only works sufficiently well if $\partial_\phi \langle X(\phi, T)\rangle \gg \partial_\phi(\Delta X(\phi, T))^2$, implying that the changes of $P(x|\phi)$ are primarily captured in the shift of the mean value. Conveniently, in this asymptotic limit, the concept of the ML estimation strategy can be applied to X_n, as we know its asymptotic probability distribution. Obviously, the distribution of X_n is maximized for $X_n = \langle X(\phi, T)\rangle$. Introducing the function $f(\phi) = \langle X(\phi, T)\rangle$ corresponding to the signal, the estimator associated with the method of moments $\phi_{\text{est}}^{\text{mom}}$ is thus the value of the parameter for which $f(\phi_{\text{est}}^{\text{mom}}) = X_n$. By inversion of the signal, we obtain $\phi_{\text{est}}^{\text{mom}} = f^{-1}(X_n)$. For instance, for a sinusoidal signal of the form $f(\phi) = \langle X(\phi, T)\rangle = b\sin(c(\phi - \phi_0))$, the corresponding estimator reads $\phi_{\text{est}}^{\text{mom}}(X_n) = \frac{1}{c}\arcsin(X_n/b) + \phi_0$. However, this inversion is possible only in the regime where $f(\phi) = \langle X(\phi, T)\rangle$ is monotone. As argued before, in local phase estimation the phase ϕ is tightly centered around the optimal working point ϕ_0, i.e. $(\phi - \phi_0)^2 \ll 1$. Hence, in this regime, the signal $\langle X(\phi, T)\rangle$ can typically be linearized around ϕ_0. In particular, we approximate the signal to first order as $\langle M\rangle_\phi = f(\phi) \simeq \frac{1}{a}(\phi - \phi_0)$, where the scaling factor $a = (\partial_\phi \langle X(\phi, T)\rangle|_{\phi=\phi_0})^{-1}$ reflects the inverse slope of the signal at the optimal working point ϕ_0. Consequently, the estimator associated with the method of moments is defined as

$$\phi_{\text{est}}^{\text{mom}}(X_n) = aX_n + \phi_0 = \frac{X_n}{\partial_\phi \langle X(\phi, T)\rangle|_{\phi=\phi_0}} + \phi_0. \tag{D.20}$$

In the limit $n \to \infty$, X_n converges to the mean value $X_n \overset{n\to\infty}{\to} \langle X(\phi, T)\rangle$. As a consequence, $\phi_{\text{est}}^{\text{mom}} \overset{n\to\infty}{\to} \phi$ and thus, the estimator $\phi_{\text{est}}^{\text{mom}}$ becomes asymptotically unbiased. Furthermore, both sides of the condition for saturation of the CRB Eq. (D.8) vanish, and thus, the CRB is asymptotically saturated and $\phi_{\text{est}}^{\text{mom}}$ becomes efficient. With $P(X_n|\phi) = \mathcal{N}(\langle X(\phi, T)\rangle, (\Delta X(\phi, T))^2/n)$, the Fisher information for the state

$\Lambda_{\phi,T}[\rho_{\text{in}}]$ and measurement $\{\Pi_{x,n}\}$, describing the observable X_n, is given by

$$\begin{aligned}\mathcal{F}[\Lambda_{\phi,T}[\rho_{\text{in}}], \{\Pi_{x,n}\}] &= \int \mathrm{d}X_n \sqrt{\frac{2\pi(\Delta X(\phi,T))^2}{n}} \exp\left(\frac{n(X_n - \langle X(\phi,T)\rangle)^2}{2(\Delta X(\phi,T))^2}\right) \\ &\quad \times \left[\sqrt{\frac{n}{2\pi(\Delta X(\phi,T))^2}} \exp\left(-\frac{n(X_n - \langle X(\phi,T)\rangle)^2}{2(\Delta X(\phi,T))^2}\right)\right]^2 \\ &= \int \mathrm{d}X_n \sqrt{\frac{n}{2\pi(\Delta X(\phi,T))^2}} \exp\left(-\frac{n(X_n - \langle X(\phi,T)\rangle)^2}{2(\Delta X(\phi,T))^2}\right) \\ &\quad \times \left[\frac{n(X_n - \langle X(\phi,T)\rangle)^2}{2(\Delta X(\phi,T))^2}\right]^2 \left[\frac{\mathrm{d}\langle X(\phi,T)\rangle}{\mathrm{d}\phi}\right]^2 \\ &= \left[\frac{\mathrm{d}\langle X(\phi,T)\rangle}{\mathrm{d}\phi}\right]^2 \frac{n}{(\Delta X(\phi,T))^2},\end{aligned} \tag{D.21}$$

where we approximated the sum $\sum_{X_n}$ by an integral $\int \mathrm{d}X_n$ due to the limit $n \gg 1$ and furthermore used the property of Gaussian distributions $\int \mathrm{d}x \frac{1}{\sqrt{2\pi\sigma^2}} x^2 e^{-x^2/2\sigma^2} = 1/\sigma^2$ to solve the integral. As a consequence, for $n \gg 1$, the sensitivity of $\phi_{\text{est}}^{\text{mom}}$ at ϕ_0 is given by

$$(\Delta\phi_{\text{mom}}(T))^2 = \left.\frac{(\Delta X(\phi,T))^2}{n\left(\partial_\phi \langle X(\phi,T)\rangle\right)^2}\right|_{\phi=\phi_0} \tag{D.22}$$

which reproduces the well-known form. Interestingly, Eq. (D.22) can equivalently be derived through error propagation (cf. Sec. 2.3.6). If we Taylor expand X_n around ϕ_0, we obtain

$$X_n \simeq \langle X(\phi_0,T)\rangle + \partial_\phi \langle X(\phi,T)\rangle\,|_{\phi=\phi_0} \cdot (\phi_{\text{est}}^{\text{mom}} - \phi) + \mathcal{O}\left[(\phi_{\text{est}}^{\text{mom}} - \phi)^2\right] \tag{D.23}$$

and thus

$$\frac{(X_n - \langle X(\phi_0,T)\rangle)^2}{\left(\partial_\phi \langle X(\phi,T)\rangle\,|_{\phi=\phi_0}\right)^2} = \left(\phi_{\text{est}}^{\text{mom}} - \phi\right)^2. \tag{D.24}$$

Identifying $(X_n - \langle X(\phi_0,T)\rangle)^2 = (\Delta X(\phi_0,T))^2/n$ and $\left(\phi_{\text{est}}^{\text{mom}} - \phi\right)^2 = (\Delta\phi_{\text{mom}}(T))^2$, we reproduce Eq. (D.22). The linear estimator and associated phase estimation uncertainty presented in the main text (cf. Sec. 3.5.1) are obtained for $n = 1$.

However, it is important to note that the method of moments with associated estimator Eq. (D.20) is only optimal for X_n, i.e. when only the mean and variance of the observable X_n are available. In general, assuming having access to the probability distributions of each individual measurement result, it is not optimal as we show below. With

$$\begin{aligned}\frac{\mathrm{d}\langle X(\phi,T)\rangle}{\mathrm{d}\phi} &= \sum_x x \frac{\mathrm{d}P(x|\phi)}{\mathrm{d}\phi} = \sum_x (x - \langle X(\phi,T)\rangle) \frac{\mathrm{d}P(x|\phi)}{\mathrm{d}\phi} \\ &= \sum_x \sqrt{P(x|\phi)}(x - \langle X(\phi,T)\rangle) \frac{1}{\sqrt{P(x|\phi)}} \frac{\mathrm{d}P(x|\phi)}{\mathrm{d}\phi},\end{aligned} \tag{D.25}$$

where we effectively added zero by $\sum_x \langle X(\phi,T)\rangle \frac{\mathrm{d}P(x|\phi)}{\mathrm{d}\phi}$ resulting from the regularity condition Eq. (D.3), we can apply the Cauchy-Schwarz inequality

$$\begin{aligned}\left[\frac{\mathrm{d}\,\langle X(\phi,T)\rangle}{\mathrm{d}\phi}\right]^2 &\leq \left[\sum_x P(x|\phi)(x-\langle X(\phi,T)\rangle)^2\right]\left[\sum_x \frac{1}{P(x|\phi)}\left(\frac{\mathrm{d}P(x|\phi)}{\mathrm{d}\phi}\right)^2\right]\\ &= (\Delta X(\phi,T))^2\,\mathcal{F}(\phi) \end{aligned} \tag{D.26}$$

and consequently, for a single measurement $n=1$, we obtain

$$(\Delta\phi_{\mathrm{CRB}}(T))^2 = \frac{1}{\mathcal{F}(\Lambda_{\phi,T}[\rho_{\mathrm{in}}],\{\Pi_x\})} \leq \frac{(\Delta X(\phi,T))^2}{(\partial_\phi\,\langle X(\phi,T)\rangle)^2} = (\Delta\phi_{\mathrm{mom}}(T))^2, \tag{D.27}$$

where $\{\Pi_x\}$ describes the measurement of the observable X.

D.4 Quantum Cramér-Rao Bound (QCRB)

For a given initial state ρ_{in}, the QCRB optimizes over all measurements $\{\Pi_x\}$ and estimation strategies ϕ_{est} and is given by

$$(\Delta\phi)^2 \geq (\Delta\phi_{\mathrm{CRB}})^2 \geq (\Delta\phi_{\mathrm{QCRB}})^2 = \frac{1}{\mathcal{F}_Q[\Lambda_{\phi,T}[\rho_{\mathrm{in}}]]}. \tag{D.28}$$

The quantum Fisher information (QFI) is expressed as

$$\mathcal{F}_Q[\rho] = \mathrm{Tr}\big(\rho L^2\big) \tag{D.29}$$

with symmetric logarithmic derivative (SLD) L implicitly defined by

$$\frac{\mathrm{d}\rho}{\mathrm{d}\phi} = \frac{1}{2}\left(\rho L + L\rho\right). \tag{D.30}$$

In analogy to the phase estimation uncertainty, the quantum Fisher information establishes an upper bound to the (classical) Fisher information by optimizing over all observables X (with associated POVMs $\{\Pi_x\}$), such that

$$\mathcal{F}_Q[\rho] = \max_{\{\Pi_x\}} \mathcal{F}[\rho,\{\Pi_x\}]. \tag{D.31}$$

Proof: The proof is based on Refs. [161, 162, 164, 168, 169]. Eigendecomposition of the state according to $\rho_{\mathrm{in}}(\phi,T) = \Lambda_{\phi,T}[\rho_{\mathrm{in}}] = \sum_k p_k\,|k\rangle\langle k|$, with $\langle j|k\rangle = \delta_{jk}$, $p_k \geq 0$ and $\sum_k p_k = 1$, allows for the explicit evaluation of the matrix elements of the SLD. Specifically, with

$$\langle j|\,\frac{\mathrm{d}\rho_{\mathrm{in}}(\phi,T)}{\mathrm{d}\phi}\,|k\rangle = \frac{1}{2}\,\langle j|\,\rho_{\mathrm{in}}(\phi,T)L + L\rho_{\mathrm{in}}(\phi,T)\,|k\rangle \tag{D.32}$$

$$= \frac{1}{2}\,\langle j|\,p_j L + p_k L\,|k\rangle = \frac{1}{2}(p_j+p_k)\,\langle j|\,L\,|k\rangle\,, \tag{D.33}$$

we obtain

$$\langle j|\, L \,|k\rangle = \frac{2\,\langle j|\, \frac{\mathrm{d}\rho_{\mathrm{in}}(\phi,T)}{\mathrm{d}\phi} \,|k\rangle}{p_j + p_k}. \tag{D.34}$$

Since $\rho_{\mathrm{in}}(\phi, T)$ is hermitian, the SLD L likewise is hermitian. For a measurement $\{\Pi_x\}$ associated to the observable X, with corresponding conditional probabilities $P(x|\phi) = \mathrm{Tr}(\Pi_x \rho_{\mathrm{in}}(\phi, T))$, the (classical) Fisher information is given by

$$\mathcal{F}[\rho_{\mathrm{in}}(\phi,T), \{\Pi_x\}] = \sum_x \frac{1}{\mathrm{Tr}(\Pi_x \rho_{\mathrm{in}}(\phi,T))} \left[\frac{\mathrm{d}\,\mathrm{Tr}(\Pi_x \rho_{\mathrm{in}}(\phi,T))}{\mathrm{d}\phi}\right]^2. \tag{D.35}$$

The numerator can be rewritten as

$$\begin{aligned}
\frac{\mathrm{d}\,\mathrm{Tr}(\Pi_x \rho_{\mathrm{in}}(\phi,T))}{\mathrm{d}\phi} &= \mathrm{Tr}\left(\Pi_x \frac{\mathrm{d}\rho_{\mathrm{in}}(\phi,T)}{\mathrm{d}\phi}\right) \\
&= \frac{1}{2}\,\mathrm{Tr}\left(\Pi_x L \rho_{\mathrm{in}}(\phi,T) + \Pi_x \rho_{\mathrm{in}}(\phi,T) L\right) \\
&= \frac{1}{2}\,\mathrm{Tr}\left(\Pi_x L \rho_{\mathrm{in}}(\phi,T) + \rho_{\mathrm{in}}(\phi,T) L \Pi_x\right) \\
&= \frac{1}{2}\,\mathrm{Tr}\left(\Pi_x L \rho_{\mathrm{in}}(\phi,T) + \rho_{\mathrm{in}}^{\dagger}(\phi,T) L^{\dagger} \Pi_x^{\dagger}\right) \\
&= \frac{1}{2}\,\mathrm{Tr}\left(\Pi_x L \rho_{\mathrm{in}}(\phi,T) + [\Pi_x L \rho_{\mathrm{in}}(\phi,T)]^{\dagger}\right) \\
&= \mathrm{Re}\,\mathrm{Tr}\left(\Pi_x L \rho_{\mathrm{in}}(\phi,T)\right) \\
&\leq |\,\mathrm{Tr}\left(\Pi_x L \rho_{\mathrm{in}}(\phi,T)\right)| \\
&= |\,\mathrm{Tr}\left(\sqrt{\rho_{\mathrm{in}}(\phi,T)}\sqrt{\Pi_x}\sqrt{\Pi_x} L \sqrt{\rho_{\mathrm{in}}(\phi,T)}\right)|,
\end{aligned} \tag{D.36}$$

where we used the cyclicity of the trace, the fact that $\rho_{\mathrm{in}}(\phi, T)$, Π_x and L are hermitian, and that $\rho_{\mathrm{in}}(\phi, T), \Pi_x \geq 0$. In a next step, we can apply the Cauchy-Schwarz inequality with respect to Hilbert-Schmidt matrix scalar products, i.e. $|\,\mathrm{Tr}\left(AB^{\dagger}\right)|^2 \leq \mathrm{Tr}\big(A^{\dagger}A\big)\,\mathrm{Tr}\big(B^{\dagger}B\big)$ with equality if and only if $A = \lambda B$, where $\lambda \in \mathbb{C}$. Hence,

$$\left[\frac{\mathrm{d}\,\mathrm{Tr}(\Pi_x \rho_{\mathrm{in}}(\phi,T))}{\mathrm{d}\phi}\right]^2 \leq |\,\mathrm{Tr}\left(\sqrt{\rho_{\mathrm{in}}(\phi,T)}\sqrt{\Pi_x}\sqrt{\Pi_x} L \sqrt{\rho_{\mathrm{in}}(\phi,T)}\right)|^2 \tag{D.37}$$

$$\leq \mathrm{Tr}\left(\rho_{\mathrm{in}}(\phi,T)\Pi_x\right)\mathrm{Tr}\left(\Pi_x L \rho_{\mathrm{in}}(\phi,T) L\right). \tag{D.38}$$

Finally, dividing by $P(x|\phi) = \mathrm{Tr}\left(\rho_{\mathrm{in}}(\phi,T)\Pi_x\right)$, summation over x and using $\sum_x \Pi_x = \mathbb{1}$, we derive

$$\begin{aligned}
\mathcal{F}[\rho_{\mathrm{in}}(\phi,T), \{\Pi_x\}] &\leq \sum_x \mathrm{Tr}\left(\Pi_x L \rho_{\mathrm{in}}(\phi,T) L\right) \\
&= \mathrm{Tr}\left(\Big[\sum_x \Pi_x\Big] L \rho_{\mathrm{in}}(\phi,T) L\right) \\
&= \mathrm{Tr}\big(\rho_{\mathrm{in}}(\phi,T) L^2\big) = \mathcal{F}_Q[\rho_{\mathrm{in}}(\phi,T)],
\end{aligned} \tag{D.39}$$

which yields the QCRB Eq. (D.28). □

D.5 Quantum Fisher information (QFI)

D.5.1 Convexity

For a mixed state $\rho_{\text{in}}(\phi,T)=\sum_k p_k\rho_k(\phi,T)$, as defined in Eq. (D.9), with weights $p_k\geq 0$ satisfying $\sum_k p_k=1$, the QFI is convex

$$\mathcal{F}_Q[\rho_{\text{in}}(\phi,T)]\leq\sum_k p_k\mathcal{F}_Q[\rho_k(\phi,T)]. \tag{D.40}$$

Proof: The proof follows Ref. [164]. The convexity of the QFI follows directly from the convexity of the classical Fisher information. For the measurement $\{\Pi_x\}$ describing the SLD L associated with $\rho_{\text{in}}(\phi,T)$, which corresponds to the optimal measurement, we have

$$\mathcal{F}_Q[\rho_{\text{in}}(\phi,T)]=\mathcal{F}[\rho_{\text{in}}(\phi,T),\{\Pi_x\}]\leq\sum_x p_k\mathcal{F}[\rho_k(\phi,T),\{\Pi_x\}]. \tag{D.41}$$

However, the optimal measurements for the states $\rho_k(\phi,T)$, given by $\{\Pi_{x,k}\}$ describing the corresponding SLDs L_k and yielding $\mathcal{F}_Q[\rho_k(\phi,T)]=\mathcal{F}[\rho_k(\phi,T),\{\Pi_{x,k}\}]$, generally do not coincide with $\{\Pi_x\}$ or L, respectively. Thus, $\mathcal{F}_Q[\rho_k(\phi,T)]\geq\mathcal{F}[\rho_k(\phi,T),\{\Pi_x\}]$ and we finally obtain Eq. (D.40). $\square$

D.5.2 Additivity

If we assume N independent systems $\rho_{\text{in}}(\phi,T)=\bigotimes_{j=1}^N\rho_{\text{in}}^{(j)}(\phi,T)$, the QFI is additive

$$\mathcal{F}_Q[\rho_{\text{in}}(\phi,T)]=\sum_{j=1}^N\mathcal{F}_Q[\rho_{\text{in}}^{(j)}(\phi,T)]. \tag{D.42}$$

Proof: The proof is based on Ref. [164]. With the SLD $L^{(j)}$ of the j-th system, differentiation of $\rho_{\text{in}}(\phi,T)$ with respect to ϕ using the product rule gives

$$\begin{aligned}\frac{\mathrm{d}\rho_{\text{in}}(\phi,T)}{\mathrm{d}\phi}&=\frac{\mathrm{d}}{\mathrm{d}\phi}\rho_{\text{in}}^{(1)}(\phi,T)\otimes\ldots\otimes\rho_{\text{in}}^{(N)}(\phi,T)\\&=\frac{\mathrm{d}\rho_{\text{in}}^{(1)}(\phi,T)}{\mathrm{d}\phi}\otimes\ldots\otimes\rho_{\text{in}}^{(N)}(\phi,T)\\&\quad+\rho_{\text{in}}^{(1)}(\phi,T)\otimes\frac{\mathrm{d}\rho_{\text{in}}^{(2)}(\phi,T)}{\mathrm{d}\phi}\otimes\ldots\otimes\rho_{\text{in}}^{(N)}(\phi,T)+\ldots\\&=\frac{1}{2}\left[L^{(1)}\rho_{\text{in}}^{(1)}(\phi,T)+\rho_{\text{in}}^{(1)}(\phi,T)L^{(1)}\right]\otimes\ldots\otimes\rho_{\text{in}}^{(N)}(\phi,T)+\ldots\\&=\frac{1}{2}\left[L^{(1)}\rho_{\text{in}}(\phi,T)+\rho_{\text{in}}(\phi,T)L^{(1)}\right]+\ldots\\&=\frac{1}{2}\left[\sum_{j=1}^N L^{(j)}\rho_{\text{in}}(\phi,T)+\rho_{\text{in}}(\phi,T)\sum_{j=1}^N L^{(j)}\right]\end{aligned} \tag{D.43}$$

and thus yields $L = \sum_{j=1}^{N} L^{(j)}$. Hence, the QFI becomes

$$\begin{aligned}
\mathcal{F}_Q[\rho_{\text{in}}(\phi, T)] &= \operatorname{Tr}\left(\rho_{\text{in}}(\phi, T) L^2\right) \\
&= \sum_{j=1}^{N} \operatorname{Tr}\left(\rho_{\text{in}}^{(j)}(\phi, T)(L^{(j)})^2\right) + \sum_{\substack{j,k=1 \\ j \neq k}}^{N} \operatorname{Tr}\left(\rho_{\text{in}}^{(j)}(\phi, T) L^{(j)} L^{(k)}\right) \\
&= \sum_{j=1}^{N} \mathcal{F}_Q[\rho_{\text{in}}^{(j)}(\phi, T)
\end{aligned} \tag{D.44}$$

and we obtain Eq. (D.42). The mixed terms $j \neq k$ vanish, since

$$\sum_{\substack{j,k=1 \\ j \neq k}}^{N} \operatorname{Tr}\left(\rho_{\text{in}}^{(j)}(\phi, T) L^{(j)} L^{(k)}\right) = \sum_{\substack{j,k=1 \\ j \neq k}}^{N} \operatorname{Tr}\left(\rho_{\text{in}}^{(j)}(\phi, T) L^{(j)}\right) \operatorname{Tr}\left(L^{(k)}\right), \tag{D.45}$$

and

$$\begin{aligned}
\operatorname{Tr}\left(\rho_{\text{in}}^{(j)}(\phi, T) L^{(j)}\right) &= \frac{1}{2} \operatorname{Tr}\left(\rho_{\text{in}}^{(j)}(\phi, T) L^{(j)} + L^{(j)} \rho_{\text{in}}^{(j)}(\phi, T)\right) \\
&= \operatorname{Tr}\left(\frac{\mathrm{d}\rho_{\text{in}}^{(j)}(\phi, T)}{\mathrm{d}\phi}\right) = \frac{\mathrm{d}}{\mathrm{d}\phi} \operatorname{Tr}\left(\rho_{\text{in}}^{(j)}(\phi, T)\right) = 0
\end{aligned} \tag{D.46}$$

due to normalization of the states $\rho_{\text{in}}^{(j)}(\phi, T)$. □

D.5.3 Unitary phase evolution

Assuming a general unitary phase evolution with generator G according to

$$\rho_{\text{in}}(\phi) = e^{-i\phi G} \rho_{\text{in}}\, e^{i\phi G} \tag{D.47}$$

and corresponding von Neumann equation

$$\frac{\mathrm{d}\rho}{\mathrm{d}\phi} = -i[G, \rho], \tag{D.48}$$

the quantum Fisher information (QFI) can be expressed as

$$\mathcal{F}_Q[\rho_{\text{in}}(\phi, T)] = 2 \sum_{\substack{j,k \\ p_j + p_k > 0}} \frac{(p_j - p_k)^2}{p_j + p_k} |\langle j| G |k\rangle|^2, \tag{D.49}$$

where p_k and $|k\rangle$ are the eigenvalues and eigenstates of $\rho_{\text{in}}(\phi, T)$, respectively. The associated optimal measurement is given by

$$L = 2i \sum_{\substack{j,k \\ p_j + p_k > 0}} \frac{p_j - p_k}{p_j + p_k} |j\rangle\langle j| G |k\rangle\langle k|\,. \tag{D.50}$$

Proof: The proof is based on Refs. [164, 168]. In the eigendecomposition $\rho_{\text{in}}(\phi, T) = \sum_k p_k \left|k\right\rangle\!\left\langle k\right|$ with eigenvalues $p_k > 0$, satisfying $\sum_k p_k = 1$, and eigenstates $\left|k\right\rangle$, respectively, we derive

$$\begin{aligned} \mathcal{F}_Q[\rho_{\text{in}}(\phi, T)] &= \mathrm{Tr}\big(\rho_{\text{in}}(\phi, T) L^2\big) = \sum_k p_k \left\langle k\right| L^2 \left|k\right\rangle \\ &= \sum_{j,k} p_k \left\langle k\right| L \left|j\right\rangle\!\left\langle j\right| L \left|k\right\rangle \\ &= \sum_{j,k} p_k |\left\langle j\right| L \left|k\right\rangle|^2 \\ &= \sum_{\substack{j,k \\ p_j + p_k > 0}} \frac{p_j + p_k}{2} |\left\langle j\right| L \left|k\right\rangle|^2, \end{aligned} \tag{D.51}$$

where we effectively reordered the weights p_k in the last step. Furthermore, with Eq. (D.34) and Eq. (D.48), we obtain

$$\begin{aligned} \mathcal{F}_Q[\rho_{\text{in}}(\phi, T)] &= \sum_{\substack{j,k \\ p_j + p_k > 0}} \frac{2}{p_j + p_k} |\left\langle j\right| \frac{\mathrm{d}\rho_{\text{in}}(\phi, T)}{\mathrm{d}\phi} \left|k\right\rangle|^2 \\ &= \sum_{\substack{j,k \\ p_j + p_k > 0}} \frac{2}{p_j + p_k} |(-i) \left\langle j\right| [G, \rho] \left|k\right\rangle|^2 \\ &= \sum_{\substack{j,k \\ p_j + p_k > 0}} \frac{2}{p_j + p_k} |(p_k - p_j) \left\langle j\right| G \left|k\right\rangle|^2 \\ &= 2 \sum_{\substack{j,k \\ p_j + p_k > 0}} \frac{(p_k - p_j)^2}{p_j + p_k} |\left\langle j\right| G \left|k\right\rangle|^2, \end{aligned} \tag{D.52}$$

which yields Eq. (D.49). Similarly, the matrix elements of the SLD are given by

$$\left\langle j\right| L \left|k\right\rangle = \frac{2 \left\langle j\right| \frac{\mathrm{d}\rho_{\text{in}}(\phi, T)}{\mathrm{d}\phi} \left|k\right\rangle}{p_j + p_k} = -2i \frac{(p_k - p_j)}{p_j + p_k} \left\langle j\right| G \left|k\right\rangle, \tag{D.53}$$

resulting in Eq. (D.50). □

D.5.4 Pure states

For pure states $\rho_{\text{in}}(\phi, T) = \left|\psi_\phi\right\rangle\!\left\langle \psi_\phi\right|$ and a unitary phase evolution according to Eq. (D.48), the QFI simplifies to

$$\mathcal{F}_Q[\rho_{\text{in}}(\phi, T)] = \mathcal{F}_Q[\left|\psi_\phi\right\rangle\!\left\langle \psi_\phi\right|] = 4(\Delta G)^2 \tag{D.54}$$

and thus is given by four times the variance of the generator G.
Proof: The proof follows Ref. [164]. For a pure state, we can express the derivative of the state with respect to the phase as

$$\frac{\mathrm{d}\rho_{\text{in}}(\phi,T)}{\mathrm{d}\phi} = |\psi_\phi\rangle\langle\dot{\psi}_\phi| + |\dot{\psi}_\phi\rangle\langle\psi_\phi| = \frac{1}{2}\left[|\psi_\phi\rangle\langle\psi_\phi|\, L + L\, |\psi_\phi\rangle\langle\psi_\phi|\right]. \tag{D.55}$$

Using that the mixed terms vanish as a consequence of the normalization of the state, i.e.

$$\langle\psi_\phi|\dot{\psi}_\phi\rangle + \langle\dot{\psi}_\phi|\psi_\phi\rangle = \frac{\mathrm{d}}{\mathrm{d}\phi}\langle\psi_\phi|\psi_\phi\rangle = \frac{\mathrm{d}}{\mathrm{d}\phi}1 = 0, \tag{D.56}$$

the SLD reads

$$L = 2\left[|\dot{\psi}_\phi\rangle\langle\psi_\phi| + |\psi_\phi\rangle\langle\dot{\psi}_\phi|\right]. \tag{D.57}$$

The corresponding QFI is given by

$$\begin{aligned}
\mathcal{F}_Q[|\psi_\phi\rangle\langle\psi_\phi|] &= \mathrm{Tr}\big(|\psi_\phi\rangle\langle\psi_\phi|\, L^2\big) \\
&= 4\,\mathrm{Tr}\Big(|\psi_\phi\rangle\langle\psi_\phi| \Big[|\dot{\psi}_\phi\rangle\langle\psi_\phi|\dot{\psi}_\phi\rangle\langle\psi_\phi| + |\dot{\psi}_\phi\rangle\langle\psi_\phi|\psi_\phi\rangle\langle\dot{\psi}_\phi| \\
&\qquad + |\psi_\phi\rangle\langle\dot{\psi}_\phi|\psi_\phi\rangle\langle\dot{\psi}_\phi| + |\psi_\phi\rangle\langle\dot{\psi}_\phi|\dot{\psi}_\phi\rangle\langle\psi_\phi|\Big]\Big) \\
&= 4\left(\langle\psi_\phi|\dot{\psi}_\phi\rangle^2 + |\langle\psi_\phi|\dot{\psi}_\phi\rangle|^2 + \langle\dot{\psi}_\phi|\psi_\phi\rangle^2 + \langle\dot{\psi}_\phi|\dot{\psi}_\phi\rangle\right) \\
&= 4\left(\langle\dot{\psi}_\phi|\dot{\psi}_\phi\rangle - |\langle\psi_\phi|\dot{\psi}_\phi\rangle|^2\right),
\end{aligned} \tag{D.58}$$

where we used the square of Eq. (D.56) in the last step. For a unitary dynamics according to Eq. (D.48), we obtain $|\dot{\psi}_\phi\rangle = -iG\,|\psi_\phi\rangle$ and thus

$$L = -2i\left(G\,|\psi_\phi\rangle\langle\psi_\phi| - |\psi_\phi\rangle\langle\psi_\phi|\, G\right) \tag{D.59}$$

$$\mathcal{F}_Q[|\psi_\phi\rangle\langle\psi_\phi|] = 4\left(\langle\psi_\phi|G^2|\psi_\phi\rangle - |\langle\psi_\phi|G|\psi_\phi\rangle|^2\right) = 4(\Delta G)^2, \tag{D.60}$$

which proves Eq. (D.54). □

Furthermore, since the QFI is convex and thus mixing states can only decrease the QFI, for an arbitrary state $\rho_{\text{in}}(\phi,T)$ and unitary dynamics with generator G, as described by Eq. (3.44), the QFI is bounded by

$$\mathcal{F}_Q[\rho_{\text{in}}(\phi,T)] \leq 4(\Delta G)^2, \tag{D.61}$$

with equality holding for pure states $\rho_{\text{in}}(\phi,T)$.
Proof: Here, we present a phenomenological proof, while a more comprehensive proof

is provided in Ref. [164]. For $p_k \geq 0$, we have $(p_j - p_k)^2 \leq (p_j + p_k)^2$. By reordering the weights p_k again, we obtain

$$\begin{aligned}\mathcal{F}_Q[\rho_{\text{in}}(\phi, T)] &= 2 \sum_{\substack{j,k \\ p_j+p_k>0}} \frac{(p_k - p_j)^2}{p_j + p_k} | \langle j| G |k\rangle |^2 \\ &\leq 2 \sum_{\substack{j,k \\ p_j+p_k>0}} (p_j + p_k) | \langle j| G |k\rangle |^2 = 4 \sum_{j,k} p_k | \langle j| G |k\rangle |^2 \\ &= 4 \sum_k p_k | \langle k| G^2 |k\rangle |^2 = 4 \left\langle G^2 \right\rangle .\end{aligned} \tag{D.62}$$

Hence, Eq. (D.61) holds when $\langle G\rangle = 0$. However, $\langle G\rangle \neq 0$ essentially represents a constant offset and thus, $\langle G\rangle = 0$ can be ensured by shifting the 'energy' according to $G \mapsto G - \langle G\rangle$. □

D.5.5 Decoherence-free scenario

In the ideal scenario, where no decoherence processes are present and thus the dynamics is entirely determined by the unitary evolution described by Eq. (D.47), the optimal input probe state is given by

$$|\psi_{\text{in}}\rangle = \frac{1}{\sqrt{2}} \left[|g_{\min}\rangle + e^{i\theta} |g_{\max}\rangle \right] \tag{D.63}$$

with eigenvectors $|g_{\min}\rangle$ and $|g_{\max}\rangle$ corresponding to the minimal and maximal eigenvalue $g_{\min}$ and $g_{\max}$ of G, respectively, and θ is an arbitrary phase. The associated QFI reads

$$\mathcal{F}_Q[|\psi_{\text{in}}\rangle] = (g_{\max} - g_{\min})^2. \tag{D.64}$$

Proof: The proof is based on Ref. [164]. As demonstrated in the previous sections, the Fisher information and quantum Fisher information (QFI) are convex and consequently, mixing states cannot improve the sensitivity. Therefore, we restrict to pure states $\rho_{\text{in}} = |\psi_{\text{in}}\rangle\langle\psi_{\text{in}}|$ as they are optimal if no decoherence is present and potentially would result in a mixed state. Furthermore, we have seen that the QFI of a pure state equals four times the variance of the generator G (cf. Eq. (D.54)). We thus only have to find the state for which the variance $(\Delta G)^2$ is maximized.

To start with, we decompose the generator G in its eigenbasis, expressed as $G = \sum_k g_k |g_k\rangle\langle g_k|$. For simplicity, we assume $g := g_{\max} = -g_{\min} \geq 0$ ensuring that $|g_k| \leq g$. This can always be achieved by a shift of the generator according to

$G \mapsto G - (g_{\min} + g_{\max})/2$, where the variance is invariant under such effective energy shifts. For an arbitrary state $|\psi_{\text{in}}\rangle = \sum_k p_k |g_k\rangle$, the QFI is given by

$$\begin{aligned} \mathcal{F}_Q[|\psi_{\text{in}}\rangle] &= 4(\Delta G)^2 = 4\left\langle G^2 \right\rangle - 4\left\langle G \right\rangle^2 \\ &\leq 4\left\langle G^2 \right\rangle = 4\left\langle \psi_{\text{in}} \right| G^2 \left| \psi_{\text{in}} \right\rangle = 4\sum_k |p_k|^2 g_k^2 \\ &\leq 4\sum_k |p_k|^2 g^2 = 4g^2 \sum_k |p_k|^2 = 4g^2. \end{aligned} \tag{D.65}$$

Equality of $\langle G^2 \rangle \leq g^2$ is only achieved for three states, namely $|\psi_{\text{in}}\rangle = |g_{\max}\rangle$, $|\psi_{\text{in}}\rangle = |g_{\min}\rangle$ and the state in Eq. (D.63). While the states $|\psi_{\text{in}}\rangle = |g_{\max}\rangle$ and $|\psi_{\text{in}}\rangle = |g_{\min}\rangle$ exhibit $\langle G \rangle^2 = g^2$, resulting in a vanishing variance $(\Delta G)^2$, the state in Eq. (D.63) features $\langle G \rangle^2 = 0$ and thus saturates Eq. (D.65). □

E

Calculations for protocols in local frequency metrology

E.1 Mapping the decoherence processes to the measurement

Separating the unitary phase evolution $\rho(\phi) = \Lambda_\phi[\rho] = \Lambda_{\phi,T=0}[\rho] = \mathcal{R}_z^\dagger(\phi)\rho\mathcal{R}_z(\phi)$ from the full dynamics $\Lambda_{\phi,T}$, described by Eq. (C.5), the effective time evolution $\Lambda_T = \Lambda_{\phi=0,T}$ is governed by the master equation

$$\dot{\rho} = \mathcal{L}_T[\rho] = \mathcal{L}_\Gamma[\rho] + \mathcal{L}_\gamma[\rho] + \mathcal{L}_{\gamma_c}[\rho] \tag{E.1}$$

with Lindblad operators $\mathcal{L}_\Gamma$, $\mathcal{L}_\gamma$ and $\mathcal{L}_{\gamma_c}$ defined in Eq. (C.2), Eq. (C.3) and Eq. (C.4), respectively. In this section we aim to map the decoherence processes onto the measurement X, thereby enabling a general treatment for a given measurement. In particular, we consider projective spin measurements (see App. E.1.1) and parity measurements (see App. E.1.2). This approach is particularly convenient for projective spin measurements, as both coherent spin states (CSS) and spin-squeezed states (SSS) utilize the same measurement scheme. Furthermore, it facilitates the derivation of lower bounds for specific measurements, following Ref. [149]. Interestingly, the bounds we derive within this approach already represent the ultimate lower bound, as they coincide with Eq. (3.65).

We can map the decoherence processes from the initial state to the observable X by exploiting the cyclicity of the trace

$$\partial_t \langle X(\phi, T)\rangle = \mathrm{Tr}\left(X\dot{\rho}(\phi)\right) = \mathrm{Tr}\left(X\mathcal{L}_T[\rho(\phi)]\right) = \mathrm{Tr}\left(\mathcal{L}_T^\dagger[X]\rho(\phi)\right) \tag{E.2}$$

with adjoint Lindblad (super-)operators

$$\mathcal{L}_T^\dagger[X] = \mathcal{L}_\Gamma^\dagger[X] + \mathcal{L}_\gamma^\dagger[X] + \mathcal{L}_{\gamma_c}^\dagger[X] \tag{E.3}$$

$$\mathcal{L}_\Gamma^\dagger[X] = \sum_{k=1}^N \mathcal{L}_\Gamma^{\dagger(k)}[X] = \frac{\Gamma}{2}\sum_{k=1}^N 2\sigma_+^{(k)} X \sigma_-^{(k)} - \sigma_{\mathrm{ee}}^{(k)} X - X\sigma_{\mathrm{ee}}^{(k)} \tag{E.4}$$

$$\mathcal{L}_\gamma^\dagger[X] = \sum_{k=1}^N \mathcal{L}_\gamma^{\dagger(k)}[X] = -\frac{\gamma}{2}\sum_{k=1}^N \sigma_{\mathrm{ee}}^{(k)} X \sigma_{\mathrm{gg}}^{(k)} + \sigma_{\mathrm{gg}}^{(k)} X \sigma_{\mathrm{ee}}^{(k)} \tag{E.5}$$

$$\mathcal{L}_{\gamma_c}^\dagger[X] = \frac{\gamma_c}{2}\left(2S_z X S_z - X S_z^2 - S_z^2 X\right). \tag{E.6}$$

For both projective spin measurements and parity measurements, the method of moments, defined in Eq. (3.32), is employed to determine the phase estimation uncertainty. Hence, we have to solve the differential equations for X and X^2.

E.1.1 Projective spin measurement

Here, we examine projective spin measurments. Without loss of generality, we assume a measurement of S_y. It is convenient to consider the Lindblad equations for the three decoherence processes separately.

$$\begin{aligned}\mathcal{L}_\Gamma^\dagger[S_y] &= \frac{\Gamma}{2}\sum_{k=1}^N 2\sigma_+^{(k)} S_y \sigma_-^{(k)} - \sigma_{\mathrm{ee}}^{(k)} S_y - S_y \sigma_{\mathrm{ee}}^{(k)} \\ &= \frac{\Gamma}{4}\sum_{j,k=1}^N \left(2\sigma_+^{(k)}\sigma_y^{(j)}\sigma_-^{(k)} - \sigma_{\mathrm{ee}}^{(k)}\sigma_y^{(j)} - \sigma_y^{(j)}\sigma_{\mathrm{ee}}^{(k)}\right)\end{aligned} \tag{E.7}$$

For $j \neq k$, the Pauli operators with different indices commute and thus the term vanishes since $\sigma_+\sigma_- = \sigma_{\mathrm{ee}}$. Furthermore, we have $\sigma_+\sigma_y = -i(\sigma_+\sigma_+ - \sigma_+\sigma_-) = i\sigma_{\mathrm{ee}}$, $\sigma_{\mathrm{ee}}\sigma_- = 0$, $\sigma_{\mathrm{ee}}\sigma_y = -i(\sigma_{\mathrm{ee}}\sigma_+ - \sigma_{\mathrm{ee}}\sigma_-) = -i\sigma_+$ and $\sigma_y\sigma_{\mathrm{ee}} = i\sigma_-$, and thus

$$\begin{aligned}\mathcal{L}_\Gamma^\dagger[S_y] &= \frac{\Gamma}{4}\sum_{k=1}^N \left(2\sigma_+^{(k)}\sigma_y^{(k)}\sigma_-^{(k)} - \sigma_{\mathrm{ee}}^{(k)}\sigma_y^{(k)} - \sigma_y^{(k)}\sigma_{\mathrm{ee}}^{(k)}\right) \\ &= -\frac{\Gamma}{4}\sum_{k=1}^N (-i)\left(\sigma_+^{(k)} - \sigma_-^{(k)}\right) = -\frac{\Gamma}{4}\sum_{k=1}^N \sigma_y^{(k)} = -\frac{\Gamma}{2} S_y.\end{aligned} \tag{E.8}$$

Similarly, we obtain

$$\begin{aligned}
\mathcal{L}_{\gamma}^{\dagger}[S_y] &= -\frac{\gamma}{2}\sum_{k=1}^{N}\left(\sigma_{\mathrm{ee}}^{(k)}S_y\sigma_{\mathrm{gg}}^{(k)}+\sigma_{\mathrm{gg}}^{(k)}S_y\sigma_{\mathrm{ee}}^{(k)}\right)\\
&= -\frac{\gamma}{4}\sum_{j,k=1}^{N}\left(\sigma_{\mathrm{ee}}^{(k)}\sigma_y^{(j)}\sigma_{\mathrm{gg}}^{(k)}+\sigma_{\mathrm{gg}}^{(k)}\sigma_y^{(j)}\sigma_{\mathrm{ee}}^{(k)}\right)\\
&= -\frac{\gamma}{4}\sum_{k=1}^{N}\left(\sigma_{\mathrm{ee}}^{(k)}\sigma_y^{(k)}\sigma_{\mathrm{gg}}^{(k)}+\sigma_{\mathrm{gg}}^{(k)}\sigma_y^{(k)}\sigma_{\mathrm{ee}}^{(k)}\right)\\
&= -\frac{\gamma}{4}\sum_{k=1}^{N}\sigma_y^{(k)} = -\frac{\gamma}{2}S_y.
\end{aligned} \tag{E.9}$$

In contrast, for collective dephasing, we employ the commutation relations of the spin operators

$$\begin{aligned}
S_yS_z &= S_zS_y + [S_y,S_z] = S_zS_y + iS_x\\
S_yS_z^2 &= S_zS_yS_z + iS_xS_z\\
&= S_z\left(S_zS_y + iS_x\right) + iS_zS_x + i[S_x,S_z]\\
&= S_z^2S_y + 2iS_zS_x + S_y,
\end{aligned} \tag{E.10}$$

yielding

$$\mathcal{L}_{\gamma_c}^{\dagger}[S_y] = \frac{\gamma_c}{2}\left(2S_zS_yS_z - S_yS_z^2 - S_z^2S_y\right) = -\frac{\gamma_c}{2}S_y. \tag{E.11}$$

In summary, the differential equation for the first moment is given by

$$\begin{aligned}
\partial_t\left\langle S_y(\phi,t)\right\rangle &= \mathrm{Tr}\Big(\mathcal{L}_T^{\dagger}[S_y]\rho(\phi)\Big)\\
&= \mathrm{Tr}\Big(\mathcal{L}_\Gamma^{\dagger}[S_y]\rho(\phi)\Big) + \mathrm{Tr}\big(\mathcal{L}_\gamma^{\dagger}[S_y]\rho(\phi)\big) + \mathrm{Tr}\big(\mathcal{L}_{\gamma_c}^{\dagger}[S_y]\rho(\phi)\big)\\
&= -\frac{\Gamma+\gamma+\gamma_c}{2}\left\langle S_y(\phi,t)\right\rangle
\end{aligned} \tag{E.12}$$

with solution

$$\left\langle S_y(\phi,T)\right\rangle = e^{-\frac{\Gamma+\gamma+\gamma_c}{2}T}\left\langle S_y(\phi)\right\rangle. \tag{E.13}$$

For the second moment, we proceed analogously.

$$\begin{aligned}
\mathcal{L}_\Gamma^{\dagger}[S_y^2] &= \frac{1}{4}\sum_{j,k,l=1}^{N}\mathcal{L}_\Gamma^{\dagger(k)}[\sigma_y^{(j)}\sigma_y^{(l)}]\\
&= \frac{1}{4}\sum_{k}\mathcal{L}_\Gamma^{\dagger(k)}[\underbrace{\sigma_y^{(k)}\sigma_y^{(k)}}_{=\mathbb{1}^{(k)}}] + \frac{1}{4}\sum_{k\neq j}\mathcal{L}_\Gamma^{\dagger(k)}[\sigma_y^{(j)}\sigma_y^{(k)}] + \frac{1}{4}\sum_{k\neq l}\mathcal{L}_\Gamma^{\dagger(k)}[\sigma_y^{(k)}\sigma_y^{(l)}]\\
&\quad + \frac{1}{4}\sum_{j\neq k,k\neq l,j\neq l}^{N}\mathcal{L}_\Gamma^{\dagger(k)}[\sigma_y^{(j)}\sigma_y^{(l)}]
\end{aligned} \tag{E.14}$$

The first and last term vanish, since the corresponding operators commute with the terms of the Lindblad (super-)operator. The second and third expression are identical apart from a relabeling of the indices $j \leftrightarrow l$. Hence,

$$\begin{aligned}\mathcal{L}_\Gamma[S_y^2] &= \frac{1}{2}\sum_{k\neq j}\mathcal{L}_\Gamma^{\dagger(k)}[\sigma_y^{(k)}\sigma_y^{(j)}]\\ &= \frac{1}{2}\sum_{k\neq j}\sigma_y^{(j)}\underbrace{\mathcal{L}_\Gamma^{\dagger(k)}[\sigma_y^{(k)}]}_{=-\frac{\Gamma}{2}\sigma_y^{(k)}}\\ &= -\frac{\Gamma}{4}\sum_{k\neq j}\sigma_y^{(j)}\sigma_y^{(k)}\end{aligned} \tag{E.15}$$

Explicitly expanding S_y^2 according to

$$S_y^2 = \frac{1}{4}\sum_{j,k}\sigma_y^{(j)}\sigma_y^{(k)} = \frac{1}{4}\sum_{k}\underbrace{\sigma_y^{(k)}\sigma_y^{(k)}}_{=\mathbb{1}^{(k)}} + \frac{1}{4}\sum_{j\neq k}\sigma_y^{(j)}\sigma_y^{(k)}, \tag{E.16}$$

which is equivalent to

$$\frac{1}{4}\sum_{j\neq k}\sigma_y^{(j)}\sigma_y^{(k)} = S_y^2 - \frac{N}{4}\mathbb{1}, \tag{E.17}$$

results in

$$\mathcal{L}_\Gamma^\dagger[S_y^2] = -\Gamma S_y^2 + \frac{N}{4}\Gamma\mathbb{1}. \tag{E.18}$$

For individual dephasing, the evaluation follows the same arguments, leading to

$$\mathcal{L}_\gamma^\dagger[S_y^2] = -\gamma S_y^2 + \frac{N}{4}\gamma\mathbb{1}. \tag{E.19}$$

For collective dephasing, again the commutation relations in Eq. (E.10) can be applied to obtain

$$\begin{aligned}\mathcal{L}_{\gamma_c}^\dagger[S_y^2] &= \frac{\gamma_c}{2}\left(2S_zS_y^2S_z - S_y^2S_z^2 - S_z^2S_y^2\right)\\ &= \frac{\gamma_c}{2}\left(2S_zS_y(S_zS_y + iS_x) - S_y(S_z^2S_y + 2iS_zS_x + S_y) - S_z^2S_y^2\right)\\ &= \frac{\gamma_c}{2}(2S_zS_yS_zS_y + 2iS_zS_yS_x - S_yS_z^2S_y\\ &\quad - 2iS_yS_zS_x - S_y^2 - S_z^2S_y^2)\\ &= \frac{\gamma_c}{2}(2S_z(S_zS_y + iS_x)S_y + 2iS_zS_yS_x - (S_z^2S_y + 2iS_zS_x + S_y)S_y\\ &\quad - 2i(S_zS_y + iS_x)S_x - S_y^2 - S_z^2S_y^2)\\ &= \frac{\gamma_c}{2}(2S_z^2S_y^2 + 2iS_zS_xS_y + 2iS_zS_yS_x - S_z^2S_y^2 - 2iS_zS_xS_y - S_y^2\\ &\quad - 2iS_zS_yS_x + 2S_x^2 - S_y^2 - S_z^2S_y^2)\\ &= \gamma_c(S_x^2 - S_y^2).\end{aligned} \tag{E.20}$$

Consequently, the differential equation for the second moment is given by

$$\begin{aligned}\partial_t \left\langle S_y^2(\phi,t)\right\rangle &= \mathrm{Tr}\Big(\mathcal{L}_T^\dagger[S_y^2]\rho(\phi)\Big)\\ &= \mathrm{Tr}\Big(\mathcal{L}_\Gamma^\dagger[S_y^2]\rho(\phi)\Big) + \mathrm{Tr}\big(\mathcal{L}_\gamma^\dagger[S_y^2]\rho(\phi)\big) + \mathrm{Tr}\big(\mathcal{L}_{\gamma_c}^\dagger[S_y^2]\rho(\phi)\big)\\ &= -(\Gamma+\gamma+\gamma_c)\left\langle S_y^2(\phi,t)\right\rangle + \gamma_c\left\langle S_x^2(\phi,t)\right\rangle + \frac{N}{4}(\Gamma+\gamma).\end{aligned} \tag{E.21}$$

Unfortunately, it is coupled to the differential equation for S_x^2. Similar to the calculations for the moments of S_y, we determine the differential equations for the moments of S_x.

$$\begin{aligned}\mathcal{L}_\Gamma^\dagger[S_x] &= \frac{\Gamma}{4}\sum_{j,k=1}^N 2\sigma_+^{(k)}\sigma_x^{(j)}\sigma_-^{(k)} - \sigma_{\mathrm{ee}}^{(k)}\sigma_x^{(j)} - \sigma_x^{(j)}\sigma_{\mathrm{ee}}^{(k)}\\ &= -\frac{\Gamma}{4}\sum_{k=1}^N \sigma_y^{(k)} = -\frac{\Gamma}{2}S_y,\end{aligned} \tag{E.22}$$

where we used $\sigma_+\sigma_x = (\sigma_+\sigma_+ + \sigma_+\sigma_-) = \sigma_{\mathrm{ee}}$, $\sigma_{\mathrm{ee}}\sigma_x = (\sigma_{\mathrm{ee}}\sigma_+ + \sigma_{\mathrm{ee}}\sigma_-) = \sigma_+$ and $\sigma_x\sigma_{\mathrm{ee}} = \sigma_-$. Similarly, we obtain

$$\begin{aligned}\mathcal{L}_\gamma^\dagger[S_x] &= -\frac{\gamma}{4}\sum_{j,k=1}^N \big(\sigma_{\mathrm{ee}}^{(k)}\sigma_x^{(j)}\sigma_{\mathrm{gg}}^{(k)} + \sigma_{\mathrm{gg}}^{(k)}\sigma_x^{(j)}\sigma_{\mathrm{ee}}^{(k)}\big)\\ &= -\frac{\gamma}{4}\sum_{k=1}^N \sigma_x^{(i)} = -\frac{\gamma}{2}S_x.\end{aligned} \tag{E.23}$$

With the commutation relations

$$\begin{aligned}S_xS_z &= S_zS_x + [S_x,S_z] = S_zS_x - iS_y\\ S_xS_z^2 &= S_zS_xS_z - iS_yS_z\\ &= S_z\left(S_zS_x - iS_y\right) - iS_zS_y - i[S_y,S_z]\\ &= S_z^2S_x - 2iS_zS_y + S_x,\end{aligned} \tag{E.24}$$

the Lindblad equation for collective dephasing is determined by

$$\begin{aligned}\mathcal{L}^{\dagger}_{\gamma_c}[S_x^2] &= \frac{\gamma_c}{2}\left(2S_zS_x^2S_z - S_x^2S_z^2 - S_z^2S_x^2\right)\\ &= \frac{\gamma_c}{2}\left(2S_zS_x(S_zS_x - iS_y) - S_x(S_z^2S_x - 2iS_zS_y + S_x) - S_z^2S_x^2\right)\\ &= \frac{\gamma_c}{2}(2S_zS_xS_zS_x - 2iS_zS_xS_y - S_xS_z^2S_x\\ &\quad + 2iS_xS_zS_y - S_x^2 - S_z^2S_y^2)\\ &= \frac{\gamma_c}{2}(2S_z(S_zS_x - iS_y)S_x - 2iS_zS_xS_y - (S_z^2S_x - 2iS_zS_y + S_x)S_x\\ &\quad + 2i(S_zS_x - iS_y)S_y - S_x^2 - S_z^2S_x^2)\\ &= \frac{\gamma_c}{2}(2S_z^2S_x^2 - 2iS_zS_yS_x - 2iS_zS_xS_y - S_z^2S_x^2 + 2iS_zS_yS_x - S_x^2\\ &\quad + 2iS_zS_xS_y + 2S_y^2 - S_x^2 - S_z^2S_x^2)\\ &= \gamma_c(S_y^2 - S_x^2).\end{aligned} \tag{E.25}$$

Therefore, we obtain

$$\partial_t \left\langle S_x^2(\phi,t)\right\rangle = -(\Gamma+\gamma+\gamma_c)\left\langle S_x^2(\phi,t)\right\rangle + \gamma_c\left\langle S_y^2(\phi,t)\right\rangle + \frac{N}{4}(\Gamma+\gamma). \tag{E.26}$$

This coupled linear differential equations of first order are solved by

$$\left\langle S_x^2(\phi,T)\right\rangle = \frac{N}{4}\left[1 - e^{-(\Gamma+\gamma)T}\right] + e^{-(\Gamma+\gamma+\gamma_c)T}\left[\cosh(\gamma_c T)\left\langle S_x^2(\phi)\right\rangle + \sinh(\gamma_c T)\left\langle S_y^2(\phi)\right\rangle\right] \tag{E.27}$$

$$\left\langle S_y^2(\phi,T)\right\rangle = \frac{N}{4}\left[1 - e^{-(\Gamma+\gamma)T}\right] + e^{-(\Gamma+\gamma+\gamma_c)T}\left[\sinh(\gamma_c T)\left\langle S_x^2(\phi)\right\rangle + \cosh(\gamma_c T)\left\langle S_y^2((\phi)\right\rangle\right]. \tag{E.28}$$

To determine the phase estimation uncertainty, we additionally have to include the unitary phase evolution according to

$$X(\phi) = \mathcal{R}_z^{\dagger}(\phi)X\mathcal{R}_z(\phi), \tag{E.29}$$

which directly follows from Eq. (3.6), resulting in

$$S_x(\phi) = \mathcal{R}_z^{\dagger}(\phi)S_x\mathcal{R}_z(\phi) = S_x\cos(\phi) - S_y\sin(\phi) \tag{E.30}$$

$$S_y(\phi) = \mathcal{R}_z^{\dagger}(\phi)S_y\mathcal{R}_z(\phi) = S_y\cos(\phi) + S_x\sin(\phi) \tag{E.31}$$

$$S_x^2(\phi) = \mathcal{R}_z^{\dagger}(\phi)S_x^2\mathcal{R}_z(\phi) = S_x^2\cos^2(\phi) - (S_xS_y + S_yS_x)\sin(\phi)\cos(\phi) + S_y^2\sin^2(\phi) \tag{E.32}$$

$$S_y^2(\phi) = \mathcal{R}_z^{\dagger}(\phi)S_y^2\mathcal{R}_z(\phi) = S_y^2\cos^2(\phi) + (S_xS_y + S_yS_x)\sin(\phi)\cos(\phi) + S_x^2\sin^2(\phi). \tag{E.33}$$

As a consequence, the slope of the signal reads

$$\partial_\phi \left\langle S_y(\phi,T)\right\rangle = e^{-\frac{\Gamma+\gamma+\gamma_c}{2}T}\left[-\left\langle S_y\right\rangle\sin(\phi) + \left\langle S_x\right\rangle\cos(\phi)\right], \tag{E.34}$$

where the expectation values $\langle\cdot\rangle$ are evaluated with respect to the initial state ρ_{in}, i.e. $\langle A\rangle = \mathrm{Tr}(A\rho_{\mathrm{in}})$ for arbitrary operators A. Finally, using that the optimal working point is $\phi_0 = 0$, which is the case for CSS and SSS and can be ensured otherwise by a shift of the signal, the phase estimation uncertainty is given by

$$\begin{aligned}(\Delta\phi(T))^2 &= \left.\frac{\left\langle S_y^2(\phi,T)\right\rangle - \left\langle S_y(\phi,T)\right\rangle^2}{(\partial_\phi \left\langle S_y^2(\phi,T)\right\rangle)^2}\right|_{\phi=\phi_0}\\ &= \frac{1}{e^{-(\Gamma+\gamma+\gamma_c)T}\left\langle S_x\right\rangle^2}\bigg(\frac{N}{4}\left[1-e^{-(\Gamma+\gamma)T}\right]\\ &\quad + e^{-(\Gamma+\gamma+\gamma_c)T}\left[\sinh(\gamma_c T)\left\langle S_x^2\right\rangle + \cosh(\gamma_c T)\left\langle S_y^2\right\rangle\right] - e^{-(\Gamma+\gamma+\gamma_c)T}\left\langle S_y\right\rangle^2\bigg)\\ &= \frac{\frac{N}{4}e^{\gamma_c T}\left[e^{(\Gamma+\gamma)T}-1\right] + \sinh(\gamma_c T)\left\langle S_x^2\right\rangle + \cosh(\gamma_c T)\left\langle S_y^2\right\rangle - \left\langle S_y\right\rangle^2}{\left\langle S_x\right\rangle^2}. \end{aligned} \tag{E.35}$$

Coherent spin states (CSS)— In principle, any coherent spin state (CSS) can be considered. However, since the phase evolution corresponds to a rotation around the z-axis and we measure the spin along the y-direction, the CSS has to be polarized in a direction mutually orthogonal to both axes. The CSS polarized in x-direction $(|\uparrow\rangle + |\downarrow\rangle)^{\otimes N}/\sqrt{2}^N$ has expectation values (cf. Sec. 2.3.7)

$$\langle S_x\rangle = \frac{N}{2},\quad \langle S_y\rangle = \langle S_x S_y\rangle = \langle S_y S_x\rangle = 0,\quad \left\langle S_x^2\right\rangle = \frac{N^2}{4},\quad \left\langle S_y^2\right\rangle = \frac{N}{4}. \tag{E.36}$$

Thus, the phase estimation uncertainty reads

$$\begin{aligned}(\Delta\phi(T))^2 &= \frac{\frac{N}{4}e^{\gamma_c T}\left[e^{(\Gamma+\gamma)T}-1\right] + \sinh(\gamma_c T)\frac{N^2}{4} + \cosh(\gamma_c T)\frac{N}{4}}{\frac{N^2}{4}}\\ &= \frac{e^{\gamma_c T}\left[e^{(\Gamma+\gamma)T}-1\right] + N\sinh(\gamma_c T) + \cosh(\gamma_c T)}{N}.\end{aligned} \tag{E.37}$$

To derive the results of the main text, it is instructive to consider collective dephasing separately:

$$(\Delta\phi(T))^2|_{\gamma_c=0} = \frac{e^{(\Gamma+\gamma)T}}{N} \tag{E.38}$$

$$(\Delta\phi(T))^2|_{\Gamma=\gamma=0} = \frac{N\sinh(\gamma_c T) + \cosh(\gamma_c T)}{N} = \frac{(N+1)e^{\gamma_c T} - (N-1)e^{-\gamma_c T}}{2N}. \tag{E.39}$$

The frequency estimation uncertainty for spontaneous decay and individual dephasing is given by

$$(\Delta\omega(T))^2|_{\gamma_c=0} = \frac{e^{(\Gamma+\gamma)T}}{N\tau T}. \tag{E.40}$$

Minimization with respect to the interrogation time T by

$$0 \overset{!}{=} \partial_T (\Delta\omega(T))^2|_{\gamma_c=0} = \frac{e^{(\Gamma+\gamma)T}}{N\tau} \frac{(\Gamma+\gamma)T - 1}{T^2} \tag{E.41}$$

results in

$$T_{\text{CSS}} = \frac{1}{\Gamma+\gamma} \tag{E.42}$$

$$(\Delta\omega_{\text{CSS}})^2 = \frac{e(\Gamma+\gamma)}{\tau N}. \tag{E.43}$$

As argued in the main text, this result represents the standard quantum limit (SQL).

Spin-squeezed states (SSS)— Spin-squeezed states (SSS) generated by one-axis-twisting (OAT) have properties [125]

$$\langle S_x \rangle = \frac{N}{2} \cos^{N-1}\left(\frac{\mu}{2}\right) \tag{E.44}$$

$$\langle S_y \rangle = 0 \tag{E.45}$$

$$\left\langle S_x^2 \right\rangle = \frac{N}{4}\left[N - \frac{1}{2}(N-1)A\right] \tag{E.46}$$

$$\left\langle S_y^2 \right\rangle = \frac{N}{4}\left\{1 + \frac{1}{4}(N-1)\left[A - \sqrt{A^2+B^2}\right]\right\} \tag{E.47}$$

$$A = 1 - \cos^{N-2}(\mu) \tag{E.48}$$

$$B = 4\sin\left(\frac{\mu}{2}\right)\cos^{N-2}\left(\frac{\mu}{2}\right) \tag{E.49}$$

where the twisting strength μ has to be optimized for each interrogation time T in order to minimize the phase estimation uncertainty described by Eq. (E.35).

Lower bound— A lower bound on the frequency estimation uncertainty considering spontaneous decay and individual dephasing can be determined following Ref. [149]. According to Eq. (E.35), the frequency estimation uncertainty reads

$$(\Delta\omega(T))^2 = \frac{\frac{N}{4}\left[e^{(\Gamma+\gamma)T} - 1\right] + (\Delta S_y)^2}{T\tau \langle S_x \rangle^2}. \tag{E.50}$$

Minimization with respect to the interrogation time T leads to the equation

$$\frac{N}{4}(\Gamma+\gamma)e^{(\Gamma+\gamma)T_{\min}} T_{\min} = \frac{N}{4}\left[e^{(\Gamma+\gamma)T_{\min}} - 1\right] + (\Delta S_y)^2 \tag{E.51}$$

and thus we obtain

$$(\Delta\omega_{\min})^2 = \frac{(\Gamma+\gamma)e^{(\Gamma+\gamma)T_{\min}}}{\tau N \left(\frac{\langle S_x \rangle}{N/2}\right)^2}. \tag{E.52}$$

Finally, using $e^{(\Gamma+\gamma)T_{\min}} \geq 1$ and $\langle S_x \rangle \leq N/2$, we find the lower bound Eq. (3.65), namely

$$(\Delta\omega_{\mathrm{asym}})^2 \geq \frac{\Gamma+\gamma}{N\tau}, \tag{E.53}$$

which gives a maximal improvement over the SQL of

$$\frac{(\Delta\omega_{\mathrm{asym}})^2}{(\Delta\omega_{\mathrm{SQL}})^2} \geq \frac{1}{e}. \tag{E.54}$$

For $\Gamma = 0$, this reproduces the result obtained in Ref. [149].

E.1.2 Parity measurement

This approach can analogously be applied to the parity measurement $\Pi = (-1)^N \sigma_x^{\otimes N}$. In particular, we focus on spontaneous decay and individual dephasing, since no explicit expressions can be derived for collective dephasing. With $\sigma_+\sigma_x = \sigma_{\mathrm{ee}}$, $\sigma_{\mathrm{ee}}\sigma_- = 0$, $\sigma_{\mathrm{ee}}\sigma_x = \sigma_+$ and thus $\sigma_x\sigma_{\mathrm{ee}} = \sigma_-$, we obtain

$$\begin{aligned}
\mathcal{L}_\Gamma^\dagger[\Pi] &= (-1)^N \frac{\Gamma}{2} \sum_{k=1}^{N} 2\sigma_+^{(k)}\sigma_x^{\otimes N}\sigma_-^{(k)} - \sigma_{\mathrm{ee}}^{(k)}\sigma_x^{\otimes N} - \sigma_x^{\otimes N}\sigma_{\mathrm{ee}}^{(k)} \\
&= (-1)^N \frac{\Gamma}{2} \sum_{k=1}^{N} -\sigma_x^{\otimes k-1} \otimes \sigma_+^{(k)} \otimes \sigma_x^{\otimes N-k} - \sigma_x^{\otimes k-1} \otimes \sigma_-^{(k)} \otimes \sigma_x^{\otimes N-k} \\
&= -(-1)^N \frac{\Gamma N}{2} \sigma_x^{\otimes N} = -\frac{\Gamma N}{2}\Pi
\end{aligned} \tag{E.55}$$

and similarly

$$\begin{aligned}
\mathcal{L}_\gamma^\dagger[\Pi] &= -(-1)^N \frac{\gamma}{2} \sum_{k=1}^{N} \sigma_{\mathrm{ee}}^{(k)}\sigma_x^{\otimes N}\sigma_{\mathrm{gg}}^{(k)} + \sigma_{\mathrm{gg}}^{(k)}\sigma_x^{\otimes N}\sigma_{\mathrm{ee}}^{(k)} \\
&= -(-1)^N \frac{\gamma}{2} \sum_{k=1}^{N} \sigma_x^{\otimes k-1} \otimes \sigma_+^{(k)} \otimes \sigma_x^{\otimes N-k} + \sigma_x^{\otimes k-1} \otimes \sigma_-^{(k)} \otimes \sigma_x^{\otimes N-k} \\
&= -(-1)^N \frac{\gamma N}{2} \sigma_x^{\otimes N} = -\frac{\gamma N}{2}\Pi,
\end{aligned} \tag{E.56}$$

where we used $\sigma_+\sigma_{\mathrm{gg}} = \sigma_+$, $\sigma_{\mathrm{gg}}\sigma_x = \sigma_-$ and $\sigma_-\sigma_{\mathrm{ee}} = \sigma_-$. Therefore, for the first moment we obtain the differential equation

$$\partial_t \langle \Pi(\phi, T) \rangle = \mathrm{Tr}\left(\mathcal{L}_\Gamma^\dagger[\Pi]\rho(\phi)\right) + \mathrm{Tr}\left(\mathcal{L}_\gamma^\dagger[\Pi]\rho(\phi)\right) = -\frac{\Gamma+\gamma}{2} N \langle \Pi(\phi, T) \rangle \tag{E.57}$$

with solution

$$\langle \Pi(\phi, T) \rangle = e^{-\frac{\Gamma+\gamma}{2}Nt} \langle \Pi(\phi) \rangle. \tag{E.58}$$

The unitary phase evolution is given by

$$\mathcal{R}_z^\dagger(\phi)\Pi\mathcal{R}_z(\phi) = (-1)^N \left(\cos(\phi)\sigma_x - \sin(\phi)\sigma_y\right)^{\otimes N}. \tag{E.59}$$

Hence,

$$\langle\Pi(\phi,T)\rangle = (-1)^N e^{-\frac{\Gamma+\gamma}{2}NT} \left\langle\left(\cos(\phi)\sigma_x - \sin(\phi)\sigma_y\right)^{\otimes N}\right\rangle. \tag{E.60}$$

Since $\Pi^2 = \mathbb{1}$, the second moment is trivially given by $\langle\Pi^2(\phi,T)\rangle = 1$. Consequently, the phase estimation uncertainty reads

$$\begin{aligned}(\Delta\phi(T))^2 &= \frac{\langle\Pi^2(\phi,T)\rangle - \langle\Pi(\phi,T)\rangle^2}{(\partial_\phi\langle\Pi(\phi,T)\rangle)^2}\Big|_{\phi=\phi_0} \\ &= \frac{1 - e^{-(\Gamma+\gamma)Nt}\langle\Pi(\phi)\rangle^2}{e^{-(\Gamma+\gamma)Nt}(\partial_\phi\langle\Pi(\phi)\rangle)^2}\Big|_{\phi=\phi_0} \\ &= \frac{e^{(\Gamma+\gamma)Nt} - \langle\Pi(\phi)\rangle^2}{(\partial_\phi\langle\Pi(\phi)\rangle_\phi)^2}\Big|_{\phi=\phi_0}.\end{aligned} \tag{E.61}$$

GHZ state— For the maximally entangled GHZ state [121]

$$|\mathrm{GHZ}\rangle = \frac{1}{\sqrt{2}}\left(|\downarrow\rangle^{\otimes N} + |\uparrow\rangle^{\otimes N}\right), \tag{E.62}$$

the expectation value of the parity operator is given by

$$\begin{aligned}\langle\Pi(\phi)\rangle &= (-1)^N \langle\mathrm{GHZ}|\left(\cos(\phi)\sigma_x - \sin(\phi)\sigma_y\right)^{\otimes N}|\mathrm{GHZ}\rangle \\ &= (-1)^N\frac{1}{2}\big[\langle\uparrow|\cos(\phi)\sigma_x - \sin(\phi)\sigma_y|\uparrow\rangle^N + \langle\uparrow|\cos(\phi)\sigma_x - \sin(\phi)\sigma_y|\downarrow\rangle^N \\ &\quad + \langle\downarrow|\cos(\phi)\sigma_x - \sin(\phi)\sigma_y|\uparrow\rangle^N + \langle\downarrow|\cos(\phi)\sigma_x - \sin(\phi)\sigma_y|\downarrow\rangle^N\big] \\ &= (-1)^N\frac{1}{2}\left[\left(\cos(\phi) + i\sin(\phi)\right)^N + \left(\cos(\phi) - i\sin(\phi)\right)^N\right] \\ &= (-1)^N\frac{1}{2}\left[e^{iN\phi} + e^{-iN\phi}\right] \\ &= (-1)^N\cos(N\phi),\end{aligned} \tag{E.63}$$

where we used $\sigma_x|\uparrow\rangle = |\downarrow\rangle$, $\sigma_x|\downarrow\rangle = |\uparrow\rangle$, $\sigma_y|\uparrow\rangle = i|\downarrow\rangle$ and $\sigma_y|\downarrow\rangle = -i|\uparrow\rangle$, and accordingly

$$\partial_\phi\langle\Pi(\phi)\rangle = (-1)^{N+1}N\sin(N\phi). \tag{E.64}$$

Consequently, the phase estimation uncertainty is determined by

$$(\Delta\phi(\phi,T))^2 = \frac{e^{(\Gamma+\gamma)NT} - \langle\Pi(\phi)\rangle^2}{(\partial_\phi\langle\Pi(\phi)\rangle)^2} = \frac{e^{(\Gamma+\gamma)NT} - \cos^2(N\phi)}{N^2\sin^2(N\phi)}, \tag{E.65}$$

which is minimal for $\phi_0 = \pi/2N$, yielding

$$(\Delta\phi(T))^2 = \frac{e^{(\Gamma+\gamma)NT}}{N^2}. \tag{E.66}$$

Hence, the frequency estimation uncertainty is given by

$$(\Delta\omega(T))^2 = \frac{e^{(\Gamma+\gamma)NT}}{\tau N^2 T}. \tag{E.67}$$

Minimization with respect to the interrogation time T by

$$0 \overset{!}{=} \partial_T (\Delta\omega(T))^2 = \frac{e^{(\Gamma+\gamma)NT}}{N^2\tau} \frac{N(\Gamma+\gamma)T - 1}{T^2} \tag{E.68}$$

results in

$$T_{\mathrm{parity-GHZ}} = \frac{1}{N}\frac{1}{\Gamma+\gamma} \tag{E.69}$$

$$(\Delta\omega_{\mathrm{parity-GHZ}})^2 = \frac{(\Gamma+\gamma)e}{N\tau}. \tag{E.70}$$

This minimal frequency estimation uncertainty is equivalent to the SQL, however it is achieved at a N-times shorter interrogation time.

Lower bound— Minimizing the frequency estimation uncertainty

$$(\Delta\omega(T))^2 = \frac{e^{(\Gamma+\gamma)Nt} - \langle \Pi(\phi)\rangle^2}{\tau T (\partial_\phi \langle \Pi(\phi)\rangle)^2}\Big|_{\phi=\phi_0} \tag{E.71}$$

with respect to the interrogation time T leads to the equation

$$(\Gamma+\gamma)NT_{\mathrm{min}} e^{(\Gamma+\gamma)NT_{\mathrm{min}}} = e^{(\Gamma+\gamma)NT_{\mathrm{min}}} - \langle \Pi(\phi)\rangle^2 \tag{E.72}$$

and thus we obtain

$$(\Delta\omega_{\mathrm{min}})^2 = \frac{(\Gamma+\gamma)N e^{(\Gamma+\gamma)NT_{\mathrm{min}}}}{\tau (\partial_\phi \langle \Pi(\phi)\rangle)^2}\Big|_{\phi=\phi_0}. \tag{E.73}$$

Finally, we derive the lower bound

$$(\Delta\omega_{\mathrm{min}})^2 \geq \frac{(\Gamma+\gamma)}{\tau N} \tag{E.74}$$

using $\partial_\phi \langle \Pi(\phi)\rangle |_{\phi=\phi_0} \leq N$ and $e^{(\Gamma+\gamma)NT_{\mathrm{min}}} \geq 1$. This bound is equal to the one derived for projective spin measurements Eq. (E.53) and additionally coincides with the asymptotic lower bound Eq. (3.65), yielding a maximal gain of $1/e$ over the SQL.

E.2 Coherent spin states (CSS)

Although we have already evaluated the frequency estimation uncertainty in the previous section, the time evolved state and the conditional probabilities are required to obtain the QCRB or CRB and to efficiently sample measurement outcomes in Monte Carlo simulations of the full feedback loop in an atomic clock.

In principle, any coherent spin state (CSS) can be considered. However, since the phase is imprinted by a rotation around the z-axis, the CSS has to point in the x-y-plane. Without loss of generality, we consider the conventional Ramsey scheme (cf. Sec. 2.3.5). Again, we focus on spontaneous decay and individual dephasing, since the Dicke basis becomes advantageous for addressing collective dephasing, as discussed in App. C.2.

The initial state is generated by a first $\pi/2$-pulse from the collective ground state

$$|\mathrm{CSS}\rangle = \mathcal{R}_y\left(-\tfrac{\pi}{2}\right)|\downarrow\rangle^{\otimes N} = \left[\frac{1}{\sqrt{2}}\left(|\downarrow\rangle + |\uparrow\rangle\right)\right]^{\otimes N} \tag{E.75}$$

which is polarized in x-direction and where we used $e^{i\frac{\pi}{4}\sigma_y} = \frac{1}{\sqrt{2}}(\mathbb{1} + i\sigma_y)$ according to Eq. (2.73). The state after the time evolution, according to the dynamics described by the master equation in Eq. (3.4), is given by

$$\rho_{\mathrm{CSS}}(\phi, T) = \frac{1}{2^N}\left[\left(2 - e^{-\Gamma T}\right)|\downarrow\rangle\langle\downarrow| + e^{-\frac{\Gamma+\gamma}{2}T}\left(e^{i\phi}|\downarrow\rangle\langle\uparrow| + e^{-i\phi}|\uparrow\rangle\langle\downarrow|\right) + e^{-\Gamma T}|\uparrow\rangle\langle\uparrow|\right]^{\otimes N}. \tag{E.76}$$

After the free evolution time T, a projective measurement of the spin component S_y is performed. This is accomplished by a second $\pi/2$-pulse – this time around the x-axis – followed by a measurement of S_z, since $S_y = \mathcal{R}_x^\dagger\left(\frac{\pi}{2}\right) S_z \mathcal{R}_x\left(\frac{\pi}{2}\right)$.

Conditional probabilities— With $e^{-i\frac{\pi}{4}\sigma_x} = \frac{1}{\sqrt{2}}(\mathbb{1} - i\sigma_x)$, the final state reads

$$\begin{aligned}
\rho^f_{\mathrm{CSS}}(\phi, T) &= \mathcal{R}_x\left(\frac{\pi}{2}\right)\rho_{\mathrm{CSS}}(\phi, T)\mathcal{R}_x^\dagger\left(\frac{\pi}{2}\right) \\
&= \frac{1}{2^N}\frac{1}{2^N}\Big[\left(2 - e^{-\Gamma t}\right)\left(|\downarrow\rangle\langle\downarrow| + i|\downarrow\rangle\langle\uparrow| - i|\uparrow\rangle\langle\downarrow| + |\uparrow\rangle\langle\uparrow|\right) \\
&\quad + e^{-\frac{\Gamma+\gamma}{2}t}\Big(e^{i\phi}\left(|\downarrow\rangle\langle\uparrow| + i|\downarrow\rangle\langle\downarrow| - i|\uparrow\rangle\langle\uparrow|\right) + |\uparrow\rangle\langle\downarrow| \\
&\quad + e^{-i\phi}\left(|\uparrow\rangle\langle\downarrow| + i|\uparrow\rangle\langle\uparrow| - i|\downarrow\rangle\langle\downarrow| + |\downarrow\rangle\langle\uparrow|\right)\Big) \\
&\quad + e^{-\Gamma t}\left(|\uparrow\rangle\langle\uparrow| + i|\uparrow\rangle\langle\downarrow| - i|\downarrow\rangle\langle\uparrow| + |\downarrow\rangle\langle\downarrow|\right)\Big]^{\otimes N} \\
&= \frac{1}{2^N}\Big[|\downarrow\rangle\langle\downarrow|\left(1 - e^{-\frac{\Gamma+\gamma}{2}t}\sin(\phi)\right) + |\downarrow\rangle\langle\uparrow|\left(i\left(1 - e^{-\Gamma t}\right) + e^{-\frac{\Gamma+\gamma}{2}t}\cos(\phi)\right) \\
&\quad + |\uparrow\rangle\langle\downarrow|\left(-i\left(1 - e^{-\Gamma t}\right) + e^{-\frac{\Gamma+\gamma}{2}t}\cos(\phi)\right) + |\uparrow\rangle\langle\uparrow|\left(1 + e^{-\frac{\Gamma+\gamma}{2}t}\sin(\phi)\right)\Big]^{\otimes N}.
\end{aligned} \tag{E.77}$$

Since the particles are identical and uncorrelated, it is sufficient to consider a single particle. The conditional probabilities are given by

$$P(\uparrow|\phi) = \frac{1}{2}\left[1 + e^{-\frac{\Gamma+\gamma}{2}T}\sin(\phi)\right] \tag{E.78}$$

$$P(\downarrow|\phi) = \frac{1}{2}\left[1 - e^{-\frac{\Gamma+\gamma}{2}T}\sin(\phi)\right], \tag{E.79}$$

yielding the binomial distribution

$$\begin{aligned} P(x = \frac{N}{2} - N_-|\phi) &= \binom{N}{N_-} P^{N-N_-}(\uparrow|\phi) \cdot P^{N_-}(\downarrow|\phi) \\ &= \frac{1}{2^N}\binom{N}{N_-}\left[1 + e^{-\frac{\Gamma+\gamma}{2}t}\sin(\phi)\right]^{N-N_-} \cdot \left[1 - e^{-\frac{\Gamma+\gamma}{2}t}\sin(\phi)\right]^{N_-} \end{aligned} \tag{E.80}$$

for measuring $x = \frac{N}{2} - N_-$, where N_- denotes the number of particles in the ground state $|\downarrow\rangle$.

QCRB— Since the particles are identical and uncorrelated, with the additivity of the QFI, we obtain

$$\mathcal{F}_Q[\rho_{\text{CSS}}(\phi, T)] = N\mathcal{F}_Q[\rho^{(1)}_{\text{CSS}}(\phi, T)] \tag{E.81}$$

with single particle time evolved state

$$\rho^{(1)}_{\text{CSS}}(\phi, T) = \frac{1}{2}\left[\left(2 - e^{-\Gamma T}\right)|\downarrow\rangle\langle\downarrow| + e^{-\frac{\Gamma+\gamma}{2}T}\left(e^{i\phi}|\downarrow\rangle\langle\uparrow| + e^{-i\phi}|\uparrow\rangle\langle\downarrow|\right) + e^{-\Gamma T}|\uparrow\rangle\langle\uparrow|\right]. \tag{E.82}$$

As a reminder, the QFI is defined by

$$\mathcal{F}_Q[\rho] = 2\sum_{\substack{j,k \\ p_j+p_k>0}} \frac{(p_j - p_k)^2}{p_j + p_k}|\langle j|G|k\rangle|^2, \tag{E.83}$$

where p_k and $|k\rangle$ are the eigenvalues and eigenstates of ρ.

It is instructive to determine the QFI of a generic 2×2-matrix, as it will also be required for the analysis of GHZ states. We assume a density matrix of the form

$$\rho^{(1)}_{\text{CSS}}(\phi, T) = a|\uparrow\rangle\langle\uparrow| + b|\uparrow\rangle\langle\downarrow| + b^*|\downarrow\rangle\langle\uparrow| + c|\downarrow\rangle\langle\downarrow| \doteq \begin{pmatrix} a & b \\ b^* & c \end{pmatrix} \tag{E.84}$$

with $a, b \in \mathbb{R}$ and $b \in \mathbb{C}$ defined by

$$a = \frac{1}{2}e^{-\Gamma T} \tag{E.85}$$

$$b = \frac{1}{2}e^{-\frac{\Gamma+\gamma}{2}T}e^{-i\phi} \tag{E.86}$$

$$c = \frac{1}{2}\left(2 - e^{-\Gamma T}\right). \tag{E.87}$$

With

$$0 \overset{!}{=} \det\Big(\rho^{(1)}_{\mathrm{CSS}}(\phi, T) - p\mathbb{1}\Big) = p^2 - p(a+c) + ac - |b|^2, \tag{E.88}$$

the eigenvalues $p_\pm$ are given by

$$p_\pm = \frac{1}{2}\left[a + c \pm \sqrt{(a+c)^2 - 4ac + 4|b|^2}\right] = \frac{1}{2}\left[a + c \pm \sqrt{(a-c)^2 + 4|b|^2}\right]. \tag{E.89}$$

The corresponding eigenvectors $\mathbf{v}_\pm$ are obtained by

$$0 \overset{!}{=} (\rho^{(1)}_{\mathrm{CSS}}(\phi, T) - p_\pm\mathbb{1})\mathbf{v}_\pm = \begin{pmatrix} a - p_\pm & b \\ b^* & c - p_\pm \end{pmatrix}\begin{pmatrix} d_\pm \\ e_\pm \end{pmatrix} = \begin{pmatrix} (a-p_\pm)d_\pm + be_\pm \\ b^* d_\pm + (c - p_\pm)e_\pm \end{pmatrix}, \tag{E.90}$$

yielding the condition

$$d_\pm = -\frac{c - p_\pm}{b^*}e_\pm = \frac{1}{2b^*}\left[a - c \pm \sqrt{(a-c)^2 + 4|b|^2}\right]. \tag{E.91}$$

Finally, the eigenvectors are given by

$$\mathbf{v}_\pm = \frac{1}{\mathcal{N}_\pm}\begin{pmatrix} d_\pm \\ 1 \end{pmatrix} \tag{E.92}$$

with normalization

$$\mathcal{N}_\pm^2 = |d_\pm|^2 + 1 = \frac{1}{4|b|^2}\left[a - c \pm \sqrt{(a-c)^2 + 4|b|^2}\right]^2 + 1. \tag{E.93}$$

In Dirac notation, the eigenvectors read

$$\mathbf{v}_+ \doteq |1\rangle = \frac{1}{\mathcal{N}_+}(d_+ |{\uparrow}\rangle + |{\downarrow}\rangle) \tag{E.94}$$

$$\mathbf{v}_+ \doteq |2\rangle = \frac{1}{\mathcal{N}_-}(d_- |{\uparrow}\rangle + |{\downarrow}\rangle). \tag{E.95}$$

Thus,

$$|\langle 1| S_z |2\rangle|^2 = \frac{1}{4(\mathcal{N}_+\mathcal{N}_-)^2}|d_+^* d_- - 1|^2 = \frac{1}{(\mathcal{N}_+\mathcal{N}_-)^2}, \tag{E.96}$$

since $d_+^* d_- = -1$. With

$$\begin{aligned}(\mathcal{N}_+\mathcal{N}_-)^2 &= |d_+ d_-|^2 + |d_+|^2 + |d_-|^2 + 1 = |d_+|^2 + |d_-|^2 + 2 \\ &= \frac{(a-c)^2 + 2|b|^2}{|b|^2} + 2 = \frac{(a-c)^2 + 4|b|^2}{|b|^2},\end{aligned} \tag{E.97}$$

where we used $|x+y|^2+|x-y|^2=2|x|^2+2|y|^2$, we obtain

$$|\langle 1|\, S_z\, |2\rangle\, |^2 = \frac{|b|^2}{(a-c)^2+4|b|^2}. \tag{E.98}$$

Finally, with $p_+ + p_- = a+c$ and $(p_+ - p_-)^2 = (a-c)^2+4|b|^2$, the QFI reads

$$\mathcal{F}_Q[\rho^{(1)}_{\text{CSS}}(\phi,T)] = 4\frac{(p_+-p_-)^2}{p_++p_-}|\langle 1|\, S_z\, |2\rangle\, |^2 = 4\frac{|b|^2}{a+c} = e^{-(\Gamma+\gamma)T} \tag{E.99}$$

and thus

$$\mathcal{F}_Q[\rho_{\text{CSS}}(\phi,T)] = Ne^{-(\Gamma+\gamma)T} \tag{E.100}$$

with associated QCRB

$$(\Delta\phi^{\text{CSS}}_{\text{QCRB}}(T))^2 = \frac{e^{(\Gamma+\gamma)T}}{N}. \tag{E.101}$$

Consequently, the QCRB is saturated by a projective spin measurement and linear estimation strategy. Additionally, this once again demonstrates that the QFI is independent of the phase ϕ.

E.3 Parity-GHZ protocol

The time evolved GHZ state is given by

$$\begin{aligned}\rho_{\text{GHZ}}(\phi,T) = \frac{1}{2}\Big(& |{\downarrow}\rangle\langle{\downarrow}|^{\otimes N} + e^{-\frac{\Gamma+\gamma+\gamma_c N}{2}NT}\Big[e^{iN\phi}\,|{\downarrow}\rangle\langle{\uparrow}|^{\otimes N} + e^{-iN\phi}\,|{\uparrow}\rangle\langle{\downarrow}|^{\otimes N}\Big] \\ &+ \big[e^{-\Gamma T}\,|{\uparrow}\rangle\langle{\uparrow}| + \big(1-e^{-\Gamma T}\big)\,|{\downarrow}\rangle\langle{\downarrow}|\big]^{\otimes N}\Big).\end{aligned} \tag{E.102}$$

Here, collective dephasing can be incorporated directly since the initial GHZ state is a superposition of the two maximal Dicke states, namely the collective ground and excited states $|{\downarrow}\rangle^{\otimes N}$ and $|{\uparrow}\rangle^{\otimes N}$, respectively.

After the free evolution time T, the parity $\Pi = (-1)^N\sigma_x^{\otimes N} = \mathcal{R}_y^\dagger\left(\frac{\pi}{2}\right)\sigma_z^{\otimes N}\mathcal{R}_y\left(\frac{\pi}{2}\right)$ is measured. Hence, with $e^{-i\frac{\pi}{4}\sigma_y} = \frac{1}{\sqrt{2}}(\mathbb{1}-i\sigma_y)$, the final state is given by

$$\begin{aligned}\rho^f_{\text{GHZ}}(\phi,T) = \frac{1}{2^{N+1}}\Big(& [|{\downarrow}\rangle\langle{\downarrow}| - |{\downarrow}\rangle\langle{\uparrow}| - |{\uparrow}\rangle\langle{\downarrow}| + |{\uparrow}\rangle\langle{\uparrow}|]^{\otimes N} \\ &+ e^{-\frac{\Gamma+\gamma+\gamma_c N}{2}NT}\Big[e^{i\phi N}\,[|{\downarrow}\rangle\langle{\downarrow}| + |{\downarrow}\rangle\langle{\uparrow}| - |{\uparrow}\rangle\langle{\downarrow}| - |{\uparrow}\rangle\langle{\uparrow}|]^{\otimes N} \\ &+ e^{-i\phi N}\,[|{\downarrow}\rangle\langle{\downarrow}| - |{\downarrow}\rangle\langle{\uparrow}| + |{\uparrow}\rangle\langle{\downarrow}| - |{\uparrow}\rangle\langle{\uparrow}|]^{\otimes N}\Big] \\ &+ \Big[e^{-\Gamma T}\,[|{\downarrow}\rangle\langle{\downarrow}| + |{\downarrow}\rangle\langle{\uparrow}| + |{\uparrow}\rangle\langle{\downarrow}| + |{\uparrow}\rangle\langle{\uparrow}|] \\ &+ \big(1-e^{-\Gamma T}\big)\,[|{\downarrow}\rangle\langle{\downarrow}| - |{\downarrow}\rangle\langle{\uparrow}| - |{\uparrow}\rangle\langle{\downarrow}| + |{\uparrow}\rangle\langle{\uparrow}|]\Big]^{\otimes N}\Big).\end{aligned} \tag{E.103}$$

The probability to measure N_- particles in the ground state thus reads

$$P(N_-|\phi) = \frac{1}{2^N}\binom{N}{N_-}\left[1 + (-1)^{N-N_-} e^{-\frac{\Gamma+\gamma+\gamma_c N}{2}NT}\cos(N\phi)\right]. \tag{E.104}$$

The parity has binary measurement outcomes $x = \pm 1$ which occur with conditional probabilities

$$P(x = +1|\phi) = \sum_{N_-\ \text{even}} P(N_-|\phi) = \sum_{k=0}^{\lfloor N/2 \rfloor} P(N_- = 2k|\phi) \tag{E.105}$$

$$P(x = -1|\phi) = \sum_{N_-\ \text{odd}} P(N_-|\phi) = \sum_{k=0}^{\lfloor N/2 \rfloor} P(N_- = 2k+1|\phi). \tag{E.106}$$

Naturally, out of the 2^N possibilities for measurement sequences $\{m_1, \ldots, m_N\}$, where $m_k \in \{\uparrow, \downarrow\}$ denotes the outcome of each particle, there exists an equal number of realizations where an even or odd number of particles is in the ground state. Therefore also $\sum_{N_-\ \text{even}} \binom{N}{N_-} = \sum_{N_-\ \text{odd}} \binom{N}{N_-} = 2^N/2$ and we obtain

$$P(x = \pm 1|\phi) = \frac{1}{2}\left[1 \pm (-1)^N e^{-\frac{\Gamma+\gamma+\gamma_c N}{2}NT}\cos(N\phi)\right]. \tag{E.107}$$

CRB— To ensure that the linear estimation scheme, which results in the phase estimation uncertainty described by Eq. (E.66), is optimal for a parity measurement and does not limit the sensitivity, we determine the CRB for the parity-GHZ protocol. With POVM $\{\Pi_x\}$ associated with the parity measurement, the (classical) Fisher information is given by

$$\begin{aligned}\mathcal{F}[\rho_{\text{GHZ}}(\phi, T), \{\Pi_x\}] &= \sum_{x=\pm 1} \frac{1}{P(x|\phi)}\left(\frac{\mathrm{d}P(x|\phi)}{\mathrm{d}\phi}\right)^2 \\ &= \frac{N^2}{2}\sum_{x=\pm 1} \frac{e^{-(\Gamma+\gamma+\gamma_c N)NT}\sin^2(N\phi)}{1 \pm (-1)^N e^{-\frac{\Gamma+\gamma+\gamma_c N}{2}NT}\cos(N\phi)}.\end{aligned} \tag{E.108}$$

The maximum is achieved at the optimal working point $\phi_0 = \pi/2N$ and thus, we obtain

$$\mathcal{F}[\rho_{\text{GHZ}}(\phi, T), \{\Pi_x\}] = N^2 e^{-(\Gamma+\gamma+\gamma_c N)NT}. \tag{E.109}$$

Consequently, the linear estimator is optimal for the parity-GHZ protocol since the corresponding phase estimation uncertainty, described by Eq. (E.66), saturates the CRB associated with Eq. (E.109).

Comparison to the scheme in Ref. [149]— Finally, we want to show that the interrogation scheme for the GHZ state presented in Ref. [149] is equivalent to the parity-GHZ protocol. In Ref. [149], the scheme is implemented using *controlled-NOT (CNOT) gates* $\mathcal{U}_{\text{CNOT}}$, representing a two-particle gate with transformation according to

$$\mathcal{U}_{\text{CNOT}}^{(1,2)} \left|\downarrow\right\rangle^{(1)} \otimes \left|\downarrow\right\rangle^{(2)} = \left|\downarrow\right\rangle^{(1)} \otimes \left|\downarrow\right\rangle^{(2)} \tag{E.110}$$

$$\mathcal{U}_{\text{CNOT}}^{(1,2)} \left|\downarrow\right\rangle^{(1)} \otimes \left|\uparrow\right\rangle^{(2)} = \left|\downarrow\right\rangle^{(1)} \otimes \left|\uparrow\right\rangle^{(2)} \tag{E.111}$$

$$\mathcal{U}_{\text{CNOT}}^{(1,2)} \left|\uparrow\right\rangle^{(1)} \otimes \left|\downarrow\right\rangle^{(2)} = \left|\uparrow\right\rangle^{(1)} \otimes \left|\uparrow\right\rangle^{(2)} \tag{E.112}$$

$$\mathcal{U}_{\text{CNOT}}^{(1,2)} \left|\uparrow\right\rangle^{(1)} \otimes \left|\uparrow\right\rangle^{(2)} = \left|\uparrow\right\rangle^{(1)} \otimes \left|\downarrow\right\rangle^{(2)} . \tag{E.113}$$

In particular, it flips the spin of the second particle if the first particle is in the excited state. Hence, a sequence of CNOT gates linking the first with each of the remaining particles is given by

$$\mathcal{U}_{\text{CNOT}} = \mathcal{U}_{\text{CNOT}}^{(1,2)} \otimes \mathcal{U}_{\text{CNOT}}^{(1,3)} \otimes \cdots \otimes \mathcal{U}_{\text{CNOT}}^{(1,N)} = \bigotimes_{i=2}^{N} \mathcal{U}_{\text{CNOT}}^{(1,k)}, \tag{E.114}$$

which flips the spin of all other particles if the first one is in the excited state. The scheme initially starts with the collective ground state $\left|\downarrow\right\rangle^{\otimes N}$ and performs a conventional $\pi/2$-pulse on the first particle, yielding

$$\left|\psi_0\right\rangle = \frac{1}{\sqrt{2}} \left(\left|\uparrow\right\rangle^{(1)} + \left|\downarrow\right\rangle^{(1)} \right) \otimes \left|\downarrow\right\rangle^{\otimes N-1} . \tag{E.115}$$

Applying a sequence of CNOT gates results in the GHZ state

$$\mathcal{U}_{\text{CNOT}} \left|\psi_0\right\rangle = \frac{1}{\sqrt{2}} \left(\left|\uparrow\right\rangle^{\otimes N} + \left|\downarrow\right\rangle^{\otimes N} \right) = \left|\text{GHZ}\right\rangle . \tag{E.116}$$

After the free evolution time, the preparation is reversed. Hence, first the sequence of CNOT gates is applied and afterwards a $\pi/2$-pulse is applied to the first particle. Finally, $\sigma_z^{(1)}$ is measured. Including the second Ramsey pulse in the measurement, we effectively measure

$$\mathcal{R}_y^{\dagger} \left(-\tfrac{\pi}{2}\right) \sigma_z \mathcal{R}_y \left(-\tfrac{\pi}{2}\right) = \sigma_x \tag{E.117}$$

of the first particle. Additionally, also the CNOT gates can be mapped to the measurement and we obtain

$$\begin{aligned}
&\mathcal{U}_{\mathrm{CNOT}}\,\big(\sigma_x^{(1)} \otimes \mathbb{1}^{\otimes N-1}\big)\mathcal{U}^{\dagger}_{\mathrm{CNOT}} \\
&\qquad = \mathcal{U}_{\mathrm{CNOT}}\left(\Big[\left|\uparrow\right\rangle\left|\downarrow\right\rangle^{(1)} + \left|\downarrow\right\rangle\left|\uparrow\right\rangle^{(1)}\Big] \otimes \big[\left|\uparrow\right\rangle\left|\uparrow\right\rangle + \left|\downarrow\right\rangle\left|\downarrow\right\rangle\big]^{\otimes N-1}\right)\mathcal{U}^{\dagger}_{\mathrm{CNOT}} \\
&\qquad = \left|\uparrow\right\rangle\left|\downarrow\right\rangle^{(1)} \otimes \big[\left|\downarrow\right\rangle\left|\uparrow\right\rangle + \left|\uparrow\right\rangle\left|\downarrow\right\rangle\big]^{\otimes N-1} \\
&\qquad\quad + \left|\downarrow\right\rangle\left|\uparrow\right\rangle^{(1)} \otimes \big[\left|\uparrow\right\rangle\left|\downarrow\right\rangle + \left|\downarrow\right\rangle\left|\uparrow\right\rangle\big]^{\otimes N-1} \\
&\qquad = \Big(\left|\uparrow\right\rangle\left|\downarrow\right\rangle^{(1)} + \left|\downarrow\right\rangle\left|\uparrow\right\rangle^{(1)}\Big) \otimes \sigma_x^{\otimes N-1} \\
&\qquad = \sigma_x^{\otimes N} \\
&\qquad = (-1)^N \Pi,
\end{aligned} \tag{E.118}$$

where we used $\mathcal{U}^{\dagger}_{\mathrm{CNOT}} = \mathcal{U}_{\mathrm{CNOT}}$ as can be easily seen from the definition. Hence, we obtain the parity measurement with an additional global phase $(-1)^N$ which does not contribute to the phase estimation uncertainty. Thus, both approaches are equivalent and yield the same results.

E.4 QCRB of the GHZ state

As a reminder, the time evolved GHZ state reads

$$\begin{aligned}
\rho_{\mathrm{GHZ}}(\phi, T) = \frac{1}{2}\Big(&\left|\downarrow\right\rangle\!\left\langle\downarrow\right|^{\otimes N} + e^{-\frac{\Gamma+\gamma+\gamma_c N}{2}NT}\left[e^{iN\phi}\left|\downarrow\right\rangle\!\left\langle\uparrow\right|^{\otimes N} + e^{-iN\phi}\left|\uparrow\right\rangle\!\left\langle\downarrow\right|^{\otimes N}\right] \\
&+ \left[e^{-\Gamma T}\left|\uparrow\right\rangle\!\left\langle\uparrow\right| + \left(1 - e^{-\Gamma T}\right)\left|\downarrow\right\rangle\!\left\langle\downarrow\right|\right]^{\otimes N}\Big).
\end{aligned} \tag{E.119}$$

Fortunately, this state is already almost diagonal, except for the subspace spanned by the maximal Dicke states $\left|\uparrow\right\rangle^{\otimes N}$ and $\left|\downarrow\right\rangle^{\otimes N}$, namely the four corners associated with $\left|\downarrow\right\rangle\!\left\langle\downarrow\right|^{\otimes N}$, $\left|\downarrow\right\rangle\!\left\langle\uparrow\right|^{\otimes N}$, $\left|\uparrow\right\rangle\!\left\langle\downarrow\right|^{\otimes N}$ and $\left|\uparrow\right\rangle\!\left\langle\uparrow\right|^{\otimes N}$. Hence, we only have to diagonalize an effective 2×2-matrix defined by

$$\begin{aligned}
\rho_{\mathrm{eff}} = \frac{1}{2}\Big(&\left[1 + \left(1 - e^{-\Gamma T}\right)^N\right]\left|\downarrow\right\rangle\!\left\langle\downarrow\right|^{\otimes N} + e^{-\frac{\Gamma+\gamma+\gamma_c N}{2}NT}\left[e^{iN\phi}\left|\downarrow\right\rangle\!\left\langle\uparrow\right|^{\otimes N} + e^{-iN\phi}\left|\uparrow\right\rangle\!\left\langle\downarrow\right|^{\otimes N}\right] \\
&+ e^{-\Gamma NT}\left|\uparrow\right\rangle\!\left\langle\uparrow\right|^{\otimes N}\Big) \\
\doteq \frac{1}{2}&\begin{pmatrix} e^{-\Gamma Nt} & e^{-\frac{\Gamma+\gamma+\gamma_c N}{2}Nt}e^{-iN\phi} \\ e^{-\frac{\Gamma+\gamma+\gamma_c N}{2}Nt}e^{iN\phi} & 1 + \left(1 - e^{-\Gamma t}\right)^N \end{pmatrix} = \begin{pmatrix} a & b \\ b^* & c \end{pmatrix}
\end{aligned} \tag{E.120}$$

with coefficients

$$a = \frac{1}{2} e^{-\Gamma N T} \tag{E.121}$$

$$b = \frac{1}{2} e^{-\frac{\Gamma+\gamma+\gamma_c N}{2} N T} e^{-iN\phi} \tag{E.122}$$

$$c = \frac{1}{2} \left[1 + \left(1 - e^{-\Gamma T} \right)^N \right]. \tag{E.123}$$

Since we already diagonalized a 2 × 2-matrix in App. E.2 for the CSS state, we can directly apply those results here. The eigenvectors are given by

$$|1\rangle = \frac{1}{\mathcal{N}_+} \left(d_+ |\uparrow\rangle^{\otimes N} + |\downarrow\rangle^{\otimes N} \right) \tag{E.124}$$

$$\left| 2^N \right\rangle = \frac{1}{\mathcal{N}_-} \left(d_- |\uparrow\rangle^{\otimes N} + |\downarrow\rangle^{\otimes N} \right) \tag{E.125}$$

with corresponding eigenvalues (cf. App. E.2). It is important to note that all other eigenvectors $|k\rangle$ are given by the $2^N - 2$ permutations of $|\uparrow\rangle^{N-N_-} |\downarrow\rangle^{N_-}$, where N_- denotes the number of particles in the ground state, and thus are orthogonal to $|1\rangle$ and $\left|2^N\right\rangle$. Furthermore, the action of the generator S_z does not change the states $|k\rangle$ for $k \neq 1, 2^N$ but only yields an additional factor $\frac{N}{2} - N_-$. Hence, the only non-vanishing term of the QFI is given by $| \langle 1 | S_z \left| 2^N \right\rangle | = N^2/(\mathcal{N}_+ \mathcal{N}_-)^2$ and, analogous to the CSS, we obtain the QFI

$$\begin{aligned} \mathcal{F}_Q[\rho_{\mathrm{GHZ}}(\phi, T)] &= 4 \frac{(p_+ - p_-)^2}{p_+ + p_-} | \langle 1 | S_z \left| 2^N \right\rangle |^2 = 4N^2 \frac{|b|^2}{a+c} \\ &= \frac{2N^2 e^{-(\Gamma+\gamma+\gamma_c N) N T}}{1 + e^{-\Gamma N T} + (1 - e^{-\Gamma T})^N} \end{aligned} \tag{E.126}$$

and associated QCRB

$$(\Delta\phi_{\mathrm{QCRB}}^{\mathrm{GHZ}}(T))^2 = \frac{e^{(\Gamma+\gamma+\gamma_c N) N T}}{2N^2} \left[1 + e^{-\Gamma N T} + \left(1 - e^{-\Gamma T} \right)^N \right]. \tag{E.127}$$

Indeed, the QCRB achieves a higher sensitivity than the parity-GHZ protocol (cf. Eq. (E.66)), since $\left(1 - e^{-\Gamma T}\right)^N + e^{-\Gamma N T} < 1$ for $N \geq 2$ and $T > 0$, and thus $(\Delta\phi_{\mathrm{QCRB}}^{\mathrm{GHZ}}(T))^2 < (\Delta\phi_{\mathrm{parity-GHZ}}(T))^2$. We show this by induction, using that e^{-x}

is monotonically decreasing for $x \geq 0$:

$$\begin{aligned}
&\text{conjecture:} && \left(1-e^{-\Gamma t}\right)^{N} < 1-e^{-\Gamma N t} \\
&N=2: && \left(1-e^{-\Gamma t}\right)^{2} = 1-\underbrace{e^{-\Gamma T}}_{>e^{-2\Gamma T}}\underbrace{-e^{-\Gamma t}+e^{-2\Gamma t}}_{<0} < 1-e^{-2\Gamma t} \\
&N \mapsto N+1: && \left(1-e^{-\Gamma t}\right)^{N+1} = \left(1-e^{-\Gamma t}\right)^{N}\left(1-e^{-\Gamma t}\right) \\
& && \qquad < \left(1-e^{-\Gamma N t}\right)\left(1-e^{-\Gamma t}\right) \\
& && \qquad = 1-e^{-\Gamma N t}-e^{-\Gamma t}+e^{-\Gamma(N+1)t} \\
& && \qquad = 1-\underbrace{e^{-\Gamma t}}_{>e^{-\Gamma(N+1)t}}+\underbrace{e^{-\Gamma(N+1)t}-e^{-\Gamma N t}}_{<0} \\
& && \qquad < 1-e^{-\Gamma(N+1)t}.
\end{aligned} \tag{E.128}$$

Consequently, the parity-GHZ protocol does not saturate the QCRB in the presence of spontaneous decay for $N \geq 2$ and $T > 0$.

E.5 GHZ transformation $\mathcal{U}_{\mathrm{GHZ}}$

In order to saturate the QCRB of the GHZ state and to assess the pertinent characteristics of the heralded-GHZ protocol, it is advantageous to employ the identity

$$\mathcal{U}_{\mathrm{GHZ}} = \frac{1}{\sqrt{2}} e^{-i\frac{\pi}{4E}} \left[\mathbb{1} + i^{N+E}\sigma_x^{\otimes N}\right] \tag{E.129}$$

with $E = 1$ ($E = 2$) for N even (odd), which was previously utilized in Ref. [128]. Application of $\mathcal{U}_{\mathrm{GHZ}}$ to the ground state $|{\downarrow}\rangle^{\otimes N}$ yields

$$|\psi_{\mathrm{in}}\rangle = \frac{1}{\sqrt{2}} e^{-i\frac{\pi}{4E}} \left(|{\downarrow}\rangle^{\otimes N} + i^{N+E}|{\uparrow}\rangle^{\otimes N}\right). \tag{E.130}$$

The exact GHZ state can be obtained by an additional trivial rotation around the z-axis according to

$$\begin{aligned}
|\mathrm{GHZ}\rangle &= e^{i\alpha}\mathcal{R}_{\mathbf{z}}(\theta_E)\mathcal{U}_{\mathrm{GHZ}}|{\downarrow}\rangle^{\otimes N} \\
&= \frac{1}{\sqrt{2}} e^{-i\frac{\pi}{4E}} e^{i\alpha}\mathcal{R}_{\mathbf{z}}(\theta_E)\left[|{\downarrow}\rangle^{\otimes N} + i^{N+E}|{\uparrow}\rangle^{\otimes N}\right] \\
&= \frac{1}{\sqrt{2}} e^{-i\frac{\pi}{4E}} e^{i\alpha} e^{i\frac{N\theta_E}{2}}\left[|{\downarrow}\rangle^{\otimes N} + e^{-iN\theta_E} i^{N+E}|{\uparrow}\rangle^{\otimes N}\right] \\
&= \frac{1}{\sqrt{2}} e^{-i\frac{\pi}{4E}} e^{i\alpha} e^{i\frac{N\theta_E}{2}}\left[|{\downarrow}\rangle^{\otimes N} + \left(e^{-i\frac{\pi}{2}}\right)^{N+E} i^{N+E}|{\uparrow}\rangle^{\otimes N}\right] \\
&= \frac{1}{\sqrt{2}}\left[|{\downarrow}\rangle^{\otimes N} + |{\uparrow}\rangle^{\otimes N}\right],
\end{aligned} \tag{E.131}$$

where $\theta_E = \frac{\pi}{2N}(N+E)$ and $\alpha = \frac{\pi}{4E} - \frac{\theta_E N}{2}$.

As the identity Eq. (E.129) is essential for the protocols investigated in the remainder of this appendix, we prove it here. The unitary $\mathcal{U}_{\mathrm{GHZ}}$ is defined in Eq. (3.77) by

$$\mathcal{U}_{\mathrm{GHZ}} = \begin{cases} \mathcal{T}_x(\pi) & \text{if } N \text{ is even} \\ \mathcal{R}_x\left(\frac{\pi}{2}\right)\mathcal{T}_x(\pi) & \text{if } N \text{ is odd} \end{cases} \tag{E.132}$$

which indicates that it is beneficial to distinguish between two cases, namely N even and odd. In particular, the identity Eq. (E.129) does not solely hold for the x-direction, but for arbitrary axes $\mathbf{k}$, as we show below.

N **even**— In the following we will prove that for N even, we obtain

$$\mathcal{T}_{\mathbf{k}}(\pi) = e^{-i\frac{\pi}{4}}\left[\mathbb{1} + i^{N+1}\sigma_{\mathbf{k}}^{\otimes N}\right] \tag{E.133}$$

with $\sigma_{\mathbf{k}} = k_1\sigma_x + k_2\sigma_y + k_3\sigma_z$ satisfying $\sum_j k_j^2 = 1$. To show this identity, we consider the product-eigenbasis $|s_1, \dots, s_N\rangle$ of the single particle operators $\sigma_{\mathbf{k}}^{(j)}$, where j denotes the index of the N particles with eigenvalues $s_j = \pm 1$. In particular, we primarily exploit the eigenvalue equations

$$\sigma_{\mathbf{k}}^{(j)}|s_1, \dots, s_N\rangle = s_j|s_1, \dots, s_N\rangle \tag{E.134}$$

$$S_{\mathbf{k}}|s_1, \dots, s_N\rangle = M|s_1, \dots, s_N\rangle \tag{E.135}$$

where $M = \frac{1}{2}\sum_{j=1}^N s_j$ denotes the eigenvalue of $S_{\mathbf{k}} = \frac{1}{2}\sum_{j=1}^N \sigma_{\mathbf{k}}^{(j)}$. Therefore,

$$\mathcal{T}_{\mathbf{k}}(\pi)|s_1, \dots, s_N\rangle = e^{-i\frac{\pi}{2}S_{\mathbf{k}}^2}|s_1, \dots, s_N\rangle = e^{-i\frac{\pi}{2}M^2}|s_1, \dots, s_N\rangle\,. \tag{E.136}$$

Since N is even, M is integer. For M even, we express $M = 2x$ with $x \in \mathbb{N}$. Consequently, $e^{-i\frac{\pi}{2}M^2} = e^{-2i\pi x^2} = 1^{x^2} = 1$. For M odd, we write $M = 2x + 1$ with $x \in \mathbb{N}$. Thus, $e^{-i\frac{\pi}{2}M^2} = e^{-2i\pi x^2}e^{-2i\pi x}e^{-i\frac{\pi}{2}} = 1^{x^2}1^x(-i) = -i$. Together, we obtain

$$\begin{aligned} e^{-i\frac{\pi}{2}M^2} &= \frac{1}{2}\left[\left(1 + (-1)^M\right) - \left(1 - (-1)^M\right)i\right] \\ &= \frac{1}{2}\left[(1 - i) + (-1)^M(1 + i)\right] \\ &= \frac{1 - i}{2}\left[1 + (-1)^M\frac{1 + i}{1 - i}\right] \\ &= e^{-i\frac{\pi}{4}}\frac{1}{\sqrt{2}}\left[1 + (-1)^M i\right]. \end{aligned} \tag{E.137}$$

Furthermore, with $N_\pm$ denoting the numbers of particles in the excited and ground states, respectively, we have

$$\begin{aligned}
\sigma_{\mathbf{k}}^{\otimes N} |s_1, \dots, s_N\rangle &= \left(\prod_{j=1}^{N} s_j\right) |s_1, \dots, s_N\rangle \\
&= (+1)^{N_+}(-1)^{N_-} |s_1, \dots, s_N\rangle \\
&= (-1)^{N_-} |s_1, \dots, s_N\rangle \\
&= (-1)^{\frac{N}{2}-M} |s_1, \dots, s_N\rangle \\
&= (-1)^{\frac{N}{2}}(-1)^{-M} |s_1, \dots, s_N\rangle \\
&= (-1)^{\frac{N}{2}}(-1)^{M} |s_1, \dots, s_N\rangle ,
\end{aligned} \tag{E.138}$$

where we used that M is integer in the last step. Since we considered an arbitrary state $|s_1, \dots, s_N\rangle$, by combining both terms we obtain the operator identity

$$\begin{aligned}
\mathcal{T}_{\mathbf{k}}(\pi) &= e^{-i\frac{\pi}{4}} \frac{1}{\sqrt{2}} \left[\mathbb{1} + (-1)^{\frac{N}{2}} i \sigma_{\mathbf{k}}^{\otimes N}\right] \\
&= e^{-i\frac{\pi}{4}} \frac{1}{\sqrt{2}} \left[\mathbb{1} + i^{N+1} \sigma_{\mathbf{k}}^{\otimes N}\right] ,
\end{aligned} \tag{E.139}$$

which is equivalent to Eq. (E.129). □

N **odd**— For N odd, no compact expression for $\mathcal{T}_{\mathbf{k}}(\pi)$ exists. This originates from M being half integer and thus prohibiting an analogous treatment as for N even. However, a similar identity is derived when extending the OAT interaction by an additional rotation by $\pi/2$ around axis $\mathbf{k}$, resulting in

$$\mathcal{R}_{\mathbf{k}}\left(\tfrac{\pi}{2}\right) \mathcal{T}_{\mathbf{k}}(\pi) = e^{-i\frac{\pi}{8}} \left[\mathbb{1} + i^{N+2} \sigma_{\mathbf{k}}^{\otimes N}\right] . \tag{E.140}$$

Similar to the case N even, we obtain

$$\begin{aligned}
\mathcal{R}_{\mathbf{k}}\left(\tfrac{\pi}{2}\right) \mathcal{T}_{\mathbf{k}}(\pi) |s_1, \dots, s_N\rangle &= e^{-i\frac{\pi}{2}S_{\mathbf{k}}} e^{-i\frac{\pi}{2}S_{\mathbf{k}}^2} |s_1, \dots, s_N\rangle \\
&= e^{-i\frac{\pi}{2}M} e^{-i\frac{\pi}{2}M^2} |s_1, \dots, s_N\rangle \\
&= e^{-i\frac{\pi}{2}\left(M^2+M\right)} |s_1, \dots, s_N\rangle \\
&= e^{i\frac{\pi}{8}} e^{-i\frac{\pi}{2}\left(M+\frac{1}{2}\right)^2} |s_1, \dots, s_N\rangle .
\end{aligned} \tag{E.141}$$

Since N is odd, M is half integer and thus $M + \frac{1}{2}$ is integer. Hence, by the same arguments as before, we can express this as

$$\begin{aligned}
e^{-i\frac{\pi}{2}\left(M+\frac{1}{2}\right)^2} &= e^{-i\frac{\pi}{4}} \frac{1}{\sqrt{2}} \left[1 + (-1)^{M+\frac{1}{2}} i\right] \\
&= e^{-i\frac{\pi}{4}} \frac{1}{\sqrt{2}} \left[1 + (-1)^{M} i^2\right] .
\end{aligned} \tag{E.142}$$

Therefore, with

$$\sigma_{\mathbf{k}}^{\otimes N}\left|s_1,\ldots,s_N\right\rangle=(-1)^{\frac{N}{2}}(-1)^M\left|s_1,\ldots,s_N\right\rangle, \tag{E.143}$$

we finally derive

$$\begin{aligned}\mathcal{R}_{\mathbf{k}}\left(\tfrac{\pi}{2}\right)\mathcal{T}_{\mathbf{k}}(\pi)&=e^{-i\frac{\pi}{8}}\frac{1}{\sqrt{2}}\left[\mathbb{1}+(-1)^{\frac{N}{2}}i^2\sigma_{\mathbf{k}}^{\otimes N}\right]\\&=e^{-i\frac{\pi}{8}}\frac{1}{\sqrt{2}}\left[\mathbb{1}+i^{N+2}\sigma_{\mathbf{k}}^{\otimes N}\right],\end{aligned} \tag{E.144}$$

which coincides with Eq. (E.129). □

E.6 Linear-GHZ protocol

In this section, we determine the final state and the moments associated with the observable

$$X=\mathcal{U}_{\mathrm{GHZ}}\,S_z\,\mathcal{U}_{\mathrm{GHZ}}^{\dagger} \tag{E.145}$$

and evaluate the phase estimation uncertainty of the linear-GHZ protocol.

Initial state and time evolution— Application of $\mathcal{U}_{\mathrm{GHZ}}$ to the ground state $|\downarrow\rangle^{\otimes N}$ yields

$$|\psi_{\mathrm{in}}\rangle=\frac{1}{\sqrt{2}}e^{-i\frac{\pi}{4E}}\left(|\downarrow\rangle^{\otimes N}+i^{N+E}|\uparrow\rangle^{\otimes N}\right). \tag{E.146}$$

The dynamics according to Eq. (3.4) leads to the time evolved state

$$\begin{aligned}\rho_{\mathrm{in}}(\phi,T)=\frac{1}{2}\Big(&|\downarrow\rangle\langle\downarrow|^{\otimes N}+e^{-\frac{\Gamma+\gamma}{2}NT}\left[(-i)^{N+E}e^{i\phi N}|\downarrow\rangle\langle\uparrow|^{\otimes N}+i^{N+E}e^{-i\phi N}|\uparrow\rangle\langle\downarrow|^{\otimes N}\right]\\&+\left[e^{-\Gamma T}|\uparrow\rangle\langle\uparrow|+\left(1-e^{-\Gamma T}\right)|\downarrow\rangle\langle\downarrow|\right]^{\otimes N}\Big).\end{aligned} \tag{E.147}$$

Final state— Applying the measurement transformation $\mathcal{U}_{\mathrm{GHZ}}$ of the observable X, as described in Eq.(E.145), to the time evolved state results in the final state $\rho_{\mathrm{in}}^f(\phi,T)=\mathcal{U}_{\mathrm{GHZ}}^{\dagger}\rho(\phi,T)\mathcal{U}_{\mathrm{GHZ}}$. With the action of $\mathcal{U}_{\mathrm{GHZ}}$ on the four terms in the time evolved state given by

$$\mathcal{U}_{\mathrm{GHZ}}^{\dagger}|\downarrow\rangle\langle\downarrow|^{\otimes N}\mathcal{U}_{\mathrm{GHZ}}=\frac{1}{2}\left[|\downarrow\rangle\langle\downarrow|^{\otimes N}+i^{N+E}|\downarrow\rangle\langle\uparrow|^{\otimes N}+(-i)^{N+E}|\uparrow\rangle\langle\downarrow|^{\otimes N}+|\uparrow\rangle\langle\uparrow|^{\otimes N}\right] \tag{E.148}$$

$$\mathcal{U}_{\mathrm{GHZ}}^{\dagger}|\downarrow\rangle\langle\uparrow|^{\otimes N}\mathcal{U}_{\mathrm{GHZ}}=\frac{1}{2}\left[|\downarrow\rangle\langle\uparrow|^{\otimes N}+i^{N+E}|\downarrow\rangle\langle\downarrow|^{\otimes N}+(-i)^{N+E}|\uparrow\rangle\langle\uparrow|^{\otimes N}+|\uparrow\rangle\langle\downarrow|^{\otimes N}\right] \tag{E.149}$$

$$\mathcal{U}_{\mathrm{GHZ}}^{\dagger}|{\uparrow}\rangle\langle{\downarrow}|^{\otimes N}\mathcal{U}_{\mathrm{GHZ}} = \frac{1}{2}\left[|{\uparrow}\rangle\langle{\downarrow}|^{\otimes N} + i^{N+E}|{\uparrow}\rangle\langle{\uparrow}|^{\otimes N} + (-i)^{N+E}|{\downarrow}\rangle\langle{\downarrow}|^{\otimes N} + |{\downarrow}\rangle\langle{\uparrow}|^{\otimes N}\right] \tag{E.150}$$

$$\begin{aligned}
&\mathcal{U}_{\mathrm{GHZ}}^{\dagger}\left(e^{-\Gamma T}|{\uparrow}\rangle\langle{\uparrow}| + \left(1-e^{-\Gamma T}\right)|{\downarrow}\rangle\langle{\downarrow}|\right)^{\otimes N}\mathcal{U}_{\mathrm{GHZ}} = \\
&\quad\frac{1}{2}\Big[\left(e^{-\Gamma T}|{\uparrow}\rangle\langle{\uparrow}| + \left(1-e^{-\Gamma T}\right)|{\downarrow}\rangle\langle{\downarrow}|\right)^{\otimes N} \\
&\quad + i^{N+E}\left(e^{-\Gamma T}|{\uparrow}\rangle\langle{\downarrow}| + \left(1-e^{-\Gamma T}\right)|{\downarrow}\rangle\langle{\uparrow}|\right)^{\otimes N} \\
&\quad + (-i)^{N+E}\left(e^{-\Gamma T}|{\downarrow}\rangle\langle{\uparrow}| + \left(1-e^{-\Gamma T}\right)|{\uparrow}\rangle\langle{\downarrow}|\right)^{\otimes N} \\
&\quad + \left(e^{-\Gamma T}|{\downarrow}\rangle\langle{\downarrow}| + \left(1-e^{-\Gamma T}\right)|{\uparrow}\rangle\langle{\uparrow}|\right)^{\otimes N}\Big],
\end{aligned} \tag{E.151}$$

the final state reads

$$\begin{aligned}
\rho_{\mathrm{in}}^{f}(\phi,T) = \frac{1}{4}\Big\{&|{\downarrow}\rangle\langle{\downarrow}|^{\otimes N} + i^{N+E}|{\downarrow}\rangle\langle{\uparrow}|^{\otimes N} + (-i)^{N+E}|{\uparrow}\rangle\langle{\downarrow}|^{\otimes N} + |{\uparrow}\rangle\langle{\uparrow}|^{\otimes N} \\
&+ e^{-\frac{\Gamma+\gamma+\gamma_c N}{2}NT}\Big((-i)^{N+E}e^{iN\phi} \\
&\quad\times\left[|{\downarrow}\rangle\langle{\uparrow}|^{\otimes N} + i^{N+E}|{\downarrow}\rangle\langle{\downarrow}|^{\otimes N} + (-i)^{N+E}|{\uparrow}\rangle\langle{\uparrow}|^{\otimes N} + |{\uparrow}\rangle\langle{\downarrow}|^{\otimes N}\right] \\
&+ i^{N+E}e^{-iN\phi}\left[|{\uparrow}\rangle\langle{\downarrow}|^{\otimes N} + i^{N+E}|{\uparrow}\rangle\langle{\uparrow}|^{\otimes N} + (-i)^{N+E}|{\downarrow}\rangle\langle{\downarrow}|^{\otimes N} + |{\downarrow}\rangle\langle{\uparrow}|^{\otimes N}\right]\Big) \\
&+ \left[e^{-\Gamma T}|{\uparrow}\rangle\langle{\uparrow}| + \left(1-e^{-\Gamma T}\right)|{\downarrow}\rangle\langle{\downarrow}|\right]^{\otimes N} \\
&+ i^{N+E}\left[e^{-\Gamma T}|{\uparrow}\rangle\langle{\downarrow}| + \left(1-e^{-\Gamma T}\right)|{\downarrow}\rangle\langle{\uparrow}|\right]^{\otimes N} \\
&+ (-i)^{N+E}\left[e^{-\Gamma T}|{\downarrow}\rangle\langle{\uparrow}| + \left(1-e^{-\Gamma T}\right)|{\uparrow}\rangle\langle{\downarrow}|\right]^{\otimes N} \\
&+ \left[e^{-\Gamma T}|{\downarrow}\rangle\langle{\downarrow}| + \left(1-e^{-\Gamma T}\right)|{\uparrow}\rangle\langle{\uparrow}|\right]^{\otimes N}\Big\}.
\end{aligned} \tag{E.152}$$

Moments— The signal is given by

$$\begin{aligned}
\langle X(\phi,T)\rangle &= \mathrm{tr}\left(X\rho_{\mathrm{in}}(\phi,T)\right) = \mathrm{tr}\left(S_z\rho_{\mathrm{final}}(\phi,T)\right) \\
&= \frac{N}{8}\Big(-1+1+e^{-\frac{\Gamma+\gamma+\gamma_c N}{2}Nt}\Big[(-i)^{N+E}e^{iN\phi}\left(-i^{N+E}+(-i)^{N+E}\right) \\
&\qquad + i^{N+E}e^{-iN\phi}\left(i^{N+E}-(-i)^{N+E}\right)\Big] + \left(2e^{-\Gamma t}-1\right) + \left(1-2e^{-\Gamma t}\right)\Big) \\
&= -\frac{N}{2}e^{-\frac{\Gamma+\gamma+\gamma_c N}{2}Nt}\cos(N\phi),
\end{aligned} \tag{E.153}$$

where we used $(-i)^{N+E} = (-1)^{N+E}i^{N+E} = -i^{N+E}$ since $N+E$ is always odd ($E=1$ for N even and $E=2$ for N odd). Furthermore,

$$\begin{aligned}
&\mathrm{Tr}\left(S_z\left[e^{-\Gamma T}|{\uparrow}\rangle\langle{\uparrow}| + \left(1-e^{-\Gamma T}\right)|{\downarrow}\rangle\langle{\downarrow}|\right]^{\otimes N}\right) = \\
&\quad\frac{1}{2}\underbrace{\mathrm{Tr}\left(e^{-\Gamma T}|{\uparrow}\rangle\langle{\uparrow}| + \left(1-e^{-\Gamma T}\right)|{\downarrow}\rangle\langle{\downarrow}|\right)^{N-1}}_{=1}\sum_{k=1}^{N}\mathrm{Tr}\left(e^{-\Gamma T}|{\uparrow}\rangle\langle{\uparrow}| - \left(1-e^{-\Gamma T}\right)|{\downarrow}\rangle\langle{\downarrow}|\right) \\
&\quad = \frac{N}{2}\left(2e^{-\Gamma t}-1\right)
\end{aligned} \tag{E.154}$$

and likewise for the last term in Eq. (E.152). Accordingly, the slope of the signal reads

$$\partial_\phi \left\langle X(\phi,T)\right\rangle = \frac{N^2}{2} e^{-\frac{\Gamma+\gamma+\gamma_c N}{2}Nt}\sin(N\phi). \tag{E.155}$$

Again, we have a symmetric signal with optimal working point $\phi_0 = \frac{\pi}{2N}$, maximizing the slope. With $S_z^2 = \frac{N}{4}\mathbb{1} + \frac{1}{4}\sum_{j\neq k}\sigma_z^{(j)}\sigma_z^{(k)}$, where the sum $\sum_{j\neq k}$ has $N(N-1)$ terms, the second moment is determined by

$$\begin{aligned}\left\langle X^2(\phi,T)\right\rangle &= \frac{N}{4} + \frac{N(N-1)}{16}\Big(1+1+e^{-\frac{\Gamma+\gamma+\gamma_c N}{2}Nt}\Big[(-i)^{N+E}e^{iN\phi}\left(i^{N+E}+(-i)^{N+E}\right) \\ &\quad + i^{N+E}e^{-iN\phi}\left((-i)^{N+E}+i^{N+E}\right)\Big] + \left(2e^{-\Gamma t}-1\right)^2 + \left(1-2e^{-\Gamma t}\right)^2\Big) \\ &= \frac{N}{4} + \frac{N(N-1)}{8}\left[1+\left(2e^{-\Gamma t}-1\right)^2\right] \\ &= \frac{N}{4}\left[1+(N-1)\left(1-2e^{-\Gamma t}+2e^{-2\Gamma t}\right)\right],\end{aligned} \tag{E.156}$$

where the last terms of Eq. (E.152) are evaluated analogously to Eq. (E.154).

Phase estimation uncertainty and estimator— According to the method of moments (cf. App. D.3), the phase estimation uncertainty is given by

$$\begin{aligned}(\Delta\phi_{\mathrm{linear-GHZ}}(T))^2 &= \frac{(\Delta X(\phi,T))^2}{(\partial_\phi\left\langle X(\phi,T)\right\rangle)^2}\Big|_{\phi=\phi_0} \\ &= \frac{e^{(\Gamma+\gamma+\gamma_c N)NT}}{N^3}\left[1+(N-1)\left(1-2e^{-\Gamma T}+2e^{-2\Gamma T}\right)\right]\end{aligned} \tag{E.157}$$

with associated linear estimator

$$\phi_{\mathrm{est}}(x) = \frac{x}{\partial_\phi\left\langle X(\phi,T)\right\rangle|_{\phi=\phi_0}} = \frac{2x}{N^2}e^{\frac{\Gamma+\gamma+\gamma_c N}{2}NT}. \tag{E.158}$$

For $N=2$, the linear-GHZ protocol saturates the QCRB. However, for $N>2$ the QCRB is not saturated and the SQL is asymptotically approximated (cf. Fig. 3.2(b)).

E.7 Heralded-GHZ protocol

The conditional probabilities can be directly inferred from the final state in Eq. (E.152) and read

$$P(x|\phi) = \frac{1}{4}\left[1+e^{-\Gamma NT}+\left(1-e^{-\Gamma T}\right)^N \mp 2e^{-\frac{\Gamma+\gamma}{2}NT}\cos(N\phi)\right] \tag{E.159}$$

if $x = \pm\frac{N}{2}$ and

$$P(x|\phi) = \frac{1}{4}\binom{N}{N_-}\left[e^{-\Gamma T(N-N_-)}\left(1-e^{-\Gamma T}\right)^{N_-} + e^{-\Gamma T N_-}\left(1-e^{-\Gamma T}\right)^{N-N_-}\right] \tag{E.160}$$

if $x = \frac{N}{2} - N_-$, where $N_- \in \{1, \ldots, N-1\}$ denotes the number of particles in the ground state $|\downarrow\rangle$. The conditional probabilities for $x \neq \pm\frac{N}{2}$ are symmetric in the sense that $P\left(x = +\frac{N}{2} - N_-|\phi\right) = P\left(x = +\frac{N}{2} - (N - N_-)|\phi\right)$. It is important to note that the phase information is solely encoded in the measurement outcomes of the maximal Dicke states, i.e. $x = \pm\frac{N}{2}$, which has profound implications, as discussed in detail in the main text (cf. Sec. 3.7.2). This motivates the highly nonlinear estimator

$$\phi_{\mathrm{est}}(x) = \begin{cases} \pm\frac{N}{2}\frac{1}{\partial_\phi \langle X(\phi,T)\rangle|_{\phi=\phi_0}} & \text{if } x = \pm\frac{N}{2} \\ 0 & \text{else} \end{cases} \tag{E.161}$$

introduced in Eq. (3.79). In this case, according to Eq. (3.13), the phase estimation uncertainty is given by

$$(\Delta\phi_{\mathrm{heralded-GHZ}}(T))^2 = \frac{N^2}{4}\frac{P\left(x = +\frac{N}{2}|\phi_0\right) + P\left(x = -\frac{N}{2}|\phi_0\right)}{\left(\partial_\phi \langle X(\phi,T)\rangle|_{\phi=\phi_0}\right)^2}. \tag{E.162}$$

With the conditional probabilities and the slope, determined in the previous section, we finally obtain

$$\phi_{\mathrm{est}}(x) = \begin{cases} \pm\frac{1}{N}\mathrm{e}^{\frac{(\Gamma+\gamma+\gamma_c N)}{2}NT} & \text{if } x = \pm\frac{N}{2} \\ 0 & \text{else} \end{cases} \tag{E.163}$$

and

$$(\Delta\phi_{\mathrm{heralded-GHZ}}(T))^2 = \frac{\mathrm{e}^{(\Gamma+\gamma)NT}}{2N^2}\left[1 + e^{-\Gamma NT} + \left(1 - e^{-\Gamma T}\right)^N\right], \tag{E.164}$$

which saturates the QCRB of the GHZ state described by Eq. (E.127).

Note that this measurement and estimation scheme, represented by X and the nonlinear estimator Eq. (E.163), can alternatively be imitated by the designed observable $\tilde{X} = \frac{N}{2}\mathcal{U}_{\mathrm{GHZ}}\left(|\uparrow\rangle\langle\uparrow|^{\otimes N} - |\downarrow\rangle\langle\downarrow|^{\otimes N}\right)\mathcal{U}_{\mathrm{GHZ}}^\dagger$. Interestingly, $\tilde{X}$ essentially corresponds to the SLD associated with the GHZ state $\rho_{\mathrm{GHZ}}(\phi, T)$, as described by Eq. (D.50) with eigenbasis determined in App. E.4.

Gain over SQL— Although the minimization of Eq. (E.164) with respect to the interrogation time T is generally not analytically possible, an explicit expression can be obtained for $\gamma = \gamma_c = 0$ and when neglecting the term $(1 - e^{-\Gamma T})^N$. This term is associated with the probability of N spontaneous decay events occurring during the interrogation time T (cf. App. E.9) and thus becomes increasingly unlikely with increasing N, as illustrated in Fig. 3.4(b). Here, we will derive Eq. (3.82). The frequency estimation uncertainty for the heralded-GHZ state – or equivalently the

QCRB of the GHZ state – in the limit $\gamma = \gamma_c = 0$ and if $(1-e^{-\Gamma T})^N$ can be neglected reads

$$(\Delta\omega_{\text{heralded}-\text{GHZ}}(T))^2 \simeq \frac{e^{\Gamma N T}+1}{2\tau N^2 T}. \tag{E.165}$$

Differentiation with respect to T

$$0 \overset{!}{=} \frac{1}{2\tau N^2}\frac{\Gamma N T e^{\Gamma N T} - \left[e^{\Gamma N T}+1\right]}{T^2} \tag{E.166}$$

yields the equation

$$\Gamma N T_{\text{min}} e^{\Gamma N T_{\text{min}}} = e^{\Gamma N T_{\text{min}}} + 1 \tag{E.167}$$

$$(\Gamma N T_{\text{min}} - 1) e^{\Gamma N T_{\text{min}}} = 1 \tag{E.168}$$

$$(\Gamma N T_{\text{min}} - 1) e^{\Gamma N T_{\text{min}} - 1} = \frac{1}{e}. \tag{E.169}$$

Although this equation is transcendent and thus has no closed solution, introducing the Lambert-W function [257], which can be efficiently evaluated numerically, nevertheless provides a formal solution. The Lambert-W function is defined as the inverse function of $x \mapsto xe^x$ and thus, $y = W(x)$ represents the formal solution of the equation $xe^x = y$. Consequently, Eq. (E.169) has the formal solution

$$\Gamma N T_{\text{min}} - 1 = W(1/e). \tag{E.170}$$

Rewriting Eq. (E.165), at T_{min} we obtain the minimal frequency estimation uncertainty

$$\begin{aligned}(\Delta\omega_{\text{heralded}-\text{GHZ}})^2 &\simeq \frac{1}{2\tau N^2}\frac{e^{\Gamma N T_{\text{min}}}+1}{T_{\text{min}}}\\ &= \frac{1}{2\tau N^2}\frac{(\Gamma N T_{\text{min}}-1)e^{\Gamma N T_{\text{min}}} + \Gamma N T_{\text{min}} - 1}{T_{\text{min}}(\Gamma N T_{\text{min}}-1)}\\ &= \frac{1}{2\tau N}\frac{\Gamma}{\Gamma N T_{\text{min}} - 1}\\ &= \frac{\Gamma}{\tau N}\frac{1}{2W(1/e)}\\ &= \frac{(\Delta\omega_{\text{SQL}})^2}{2eW(1/e)},\end{aligned} \tag{E.171}$$

where we used Eq. (E.168) in the second and Eq. (E.170) in the third step. Consequently, in this regime, the heralded-GHZ protocol $\Delta\omega_{\text{heralded}-\text{GHZ}}$ and the QCRB of the GHZ $\Delta\omega_{\text{QCRB}}^{\text{GHZ}}$ state achieve a constant gain of $\frac{1}{\sqrt{2eW(1/e)}} < 1$ compared to the SQL $\Delta\omega_{\text{SQL}}$, which corresponds to 1.8 dB (cf. Fig. 3.2(b)).

E.8 Heralded-uGHZ protocol

In this appendix, we discuss the heralded-uGHZ protocol. In particular, we start by evaluating the relevant properties for an arbitrary rotation angle θ. Based on the resulting phase estimation uncertainty, we determine the optimal rotation angle θ_{opt} and corresponding optimal uGHZ state. Furthermore, we specify the general results for θ_{opt}.

The heralded-uGHZ protocol is conceptually analogous to the heralded-GHZ protocol. Consequently, we primarily present the calculations, while details of individual steps that are not explicitly provided here are adopted from the linear-GHZ protocol (cf. Sec. E.6) and heralded-GHZ protocol (cf. Sec. E.7).

E.8.1 General uGHZ state

Initial state—

$$\begin{aligned} \mathcal{U}_{\mathrm{GHZ}}|\downarrow\rangle^{\otimes N} &= \frac{1}{\sqrt{2}} e^{-i\frac{\pi}{4E}} \left[\mathbb{1} + i^{N+E}\sigma_x^{\otimes N}\right] |\downarrow\rangle^{\otimes N} \\ &= \frac{1}{\sqrt{2}} e^{-i\frac{\pi}{4E}} \left[|\downarrow\rangle^{\otimes N} + i^{N+E}|\uparrow\rangle^{\otimes N}\right] \end{aligned} \tag{E.172}$$

$$\mathcal{R}_z(\theta)\mathcal{U}_{\mathrm{GHZ}}|\downarrow\rangle^{\otimes N} = \frac{1}{\sqrt{2}} e^{-i\frac{\pi}{4E}} \left[e^{i\frac{\theta N}{2}}|\downarrow\rangle^{\otimes N} + i^{N+E} e^{-i\frac{\theta N}{2}}|\uparrow\rangle^{\otimes N}\right] \tag{E.173}$$

$$\begin{aligned} |\psi_{\mathrm{in}}\rangle &= \mathcal{U}_{\mathrm{GHZ}}\mathcal{R}_z(\theta)\mathcal{U}_{\mathrm{GHZ}}|\downarrow\rangle^{\otimes N} \\ &= \frac{1}{\sqrt{2}} e^{-i\frac{\pi}{4E}} \left[\mathbb{1} + i^{N+E}\sigma_x^{\otimes N}\right] \frac{1}{\sqrt{2}} e^{-i\frac{\pi}{4E}} \left[e^{i\frac{\theta N}{2}}|\downarrow\rangle^{\otimes N} + i^{N+E} e^{-i\frac{\theta N}{2}}|\uparrow\rangle^{\otimes N}\right] \\ &= \frac{1}{2} e^{-i\frac{\pi}{2E}} \left[e^{i\frac{\theta N}{2}} \left(|\downarrow\rangle^{\otimes N} + i^{N+E}|\uparrow\rangle^{\otimes N}\right) + i^{N+E} e^{-i\frac{\theta N}{2}} \left(|\uparrow\rangle^{\otimes N} + i^{N+E}|\downarrow\rangle^{\otimes N}\right)\right] \\ &= \frac{1}{2} e^{-i\frac{\pi}{2E}} \left[\left(e^{i\frac{\theta N}{2}} + \left(i^{N+E}\right)^2 e^{-i\frac{\theta N}{2}}\right)|\downarrow\rangle^{\otimes N} + i^{N+E}\left(e^{i\frac{\theta N}{2}} + e^{-i\frac{\theta N}{2}}\right)|\uparrow\rangle^{\otimes N}\right] \\ &= e^{-i\frac{\pi}{2E}} \left[i \sin\left(\tfrac{\theta N}{2}\right)|\downarrow\rangle^{\otimes N} + i^{N+E}\cos\left(\tfrac{\theta N}{2}\right)|\uparrow\rangle^{\otimes N}\right] \end{aligned} \tag{E.174}$$

where we used that $\left(i^{N+E}\right)^2 = (-1)^{N+E} = -1$, since $E = 1$ for N even and $E = 2$ for N odd and thus $N + E$ is odd in both cases.

$$\begin{aligned} \rho_{\mathrm{in}} &= \sin^2\left(\tfrac{\theta N}{2}\right)|\downarrow\rangle\langle\downarrow|^{\otimes N} + \sin\left(\tfrac{\theta N}{2}\right)\cos\left(\tfrac{\theta N}{2}\right)\left[i(-i)^{N+E}|\downarrow\rangle\langle\uparrow|^{\otimes N} + (-i)i^{N+E}|\uparrow\rangle\langle\downarrow|^{\otimes N}\right] \\ &\quad + \cos^2\left(\tfrac{\theta N}{2}\right)|\uparrow\rangle\langle\uparrow|^{\otimes N} \\ &= \sin^2\left(\tfrac{\theta N}{2}\right)|\downarrow\rangle\langle\downarrow|^{\otimes N} + i^{N+E+1}\sin\left(\tfrac{\theta N}{2}\right)\cos\left(\tfrac{\theta N}{2}\right)\left[(-1)^{N+E}|\downarrow\rangle\langle\uparrow|^{\otimes N} - |\uparrow\rangle\langle\downarrow|^{\otimes N}\right] \\ &\quad + \cos^2\left(\tfrac{\theta N}{2}\right)|\uparrow\rangle\langle\uparrow|^{\otimes N} \\ &= \sin^2\left(\tfrac{\theta N}{2}\right)|\downarrow\rangle\langle\downarrow|^{\otimes N} - i^{N+E+1}\sin\left(\tfrac{\theta N}{2}\right)\cos\left(\tfrac{\theta N}{2}\right)\left[|\downarrow\rangle\langle\uparrow|^{\otimes N} + |\uparrow\rangle\langle\downarrow|^{\otimes N}\right] \\ &\quad + \cos^2\left(\tfrac{\theta N}{2}\right)|\uparrow\rangle\langle\uparrow|^{\otimes N} \end{aligned} \tag{E.175}$$

Hence, the initial state is GHZ-like with populations

$$P_{\text{in}}^{+}(\theta) = \text{Tr}\left(|{\uparrow}\rangle\langle{\uparrow}|^{\otimes N}\rho_{\text{in}}\right) = \cos^2\left(\tfrac{\theta N}{2}\right) \tag{E.176}$$

$$P_{\text{in}}^{-}(\theta) = \text{Tr}\left(|{\downarrow}\rangle\langle{\downarrow}|^{\otimes N}\rho_{\text{in}}\right) = \sin^2\left(\tfrac{\theta N}{2}\right). \tag{E.177}$$

Consequently, we refer to these states with $P_{\text{in}}^{+}(\theta) \neq P_{\text{in}}^{-}(\theta)$ as unbalanced GHZ (uGHZ) states. In particular, we obtain the following special cases:

- $\theta_{\uparrow} = 0$: $P_{\text{in}}^{+}(\theta) = 1$ and $P_{\text{in}}^{-}(\theta) = 0$. Thus, $\rho_{\text{in}} = |{\uparrow}\rangle\langle{\uparrow}|^{\otimes N}$ and $\mathcal{U}_{\text{GHZ}}^2$ simply transfers the population from the ground state to the excited state and consequently acts equivalent to a π-pulse around the x- or y-axis.
- $\theta_{\text{GHZ}} = \frac{\pi}{2N}$: $P_{\text{in}}^{+}(\theta) = P_{\text{in}}^{-}(\theta) = \frac{1}{2}$ resulting in the GHZ state and thus making the second $\mathcal{U}_{\text{GHZ}}$ transformation redundant.
- $\theta_{\downarrow} = \frac{\pi}{N}$: $P_{\text{in}}^{+}(\theta) = 0$ and $P_{\text{in}}^{-}(\theta) = 1$. Thus, $\rho_{\text{in}} = |{\downarrow}\rangle\langle{\downarrow}|^{\otimes N}$ and consequently $\mathcal{U}_{\text{GHZ}}\mathcal{R}_z(\theta_{\downarrow})\mathcal{U}_{\text{GHZ}}$ acts as the identity when applied to the ground state.

Note that the off-diagonal terms in the expression for the input state may not initially appear to be complex conjugates of each other. However, this is indeed the case, as demonstrated by

$$\left(i^{N+E+1}\right)^* = (-i)^{N+E+1} = (-1)^{N+E+1} i^{N+E+1} = i^{N+E+1}, \tag{E.178}$$

where we used the fact that $N + E + 1$ is even in all scenarios, since $N + E$ is odd in all cases, as discussed before.

Due to its GHZ-like nature, the same measurement and estimation strategy as for the heralded-GHZ protocol turns out to be optimal. Therefore, we denote the corresponding Ramsey scheme as heralded-uGHZ protocol.

Time evolution—

$$\begin{aligned}\rho_{\text{in}}(\phi, T) = {} & \sin^2\left(\tfrac{\theta N}{2}\right)|{\downarrow}\rangle\langle{\downarrow}|^{\otimes N} - i^{N+E+1} e^{-\frac{\Gamma+\gamma+\gamma_c N}{2}NT} \sin\left(\tfrac{\theta N}{2}\right)\cos\left(\tfrac{\theta N}{2}\right)\left[e^{i\phi N}|{\downarrow}\rangle\langle{\uparrow}|^{\otimes N}\right. \\ & \left. + e^{-i\phi N}|{\uparrow}\rangle\langle{\downarrow}|^{\otimes N}\right] + \cos^2\left(\tfrac{\theta N}{2}\right)\left[e^{-\Gamma T}|{\uparrow}\rangle\langle{\uparrow}| + \left(1 - e^{-\Gamma T}\right)|{\downarrow}\rangle\langle{\downarrow}|\right]^{\otimes N}\end{aligned} \tag{E.179}$$

Again, we can determine the populations

$$P_{\text{in}}^{+}(\theta, T) = \text{Tr}\left(|{\uparrow}\rangle\langle{\uparrow}|^{\otimes N}\rho_{\text{in}}(\phi, T)\right) = \cos^2\left(\tfrac{\theta N}{2}\right) e^{-N\Gamma T} \tag{E.180}$$

$$P_{\text{in}}^{-}(\theta, T) = \text{Tr}\left(|{\downarrow}\rangle\langle{\downarrow}|^{\otimes N}\rho_{\text{in}}(\phi, T)\right) = \sin^2\left(\tfrac{\theta N}{2}\right) + \cos^2\left(\tfrac{\theta N}{2}\right)\left(1 - e^{-\Gamma T}\right)^N. \tag{E.181}$$

To compensate for spontaneous decay during the Ramsey time T, the initial state has to give a higher weight to the collective excited state to obtain an equal distribution in the populations of the maximal Dicke states after T, associated with the rotation angle θ_{equal}. Consequently, $\theta_{\uparrow} = 0 < \theta_{\text{equal}} < \theta_{\text{GHZ}} = \pi/2N$. In particular, θ_{equal} is given by

$$\theta_{\text{equal}} = \frac{2}{N} \arctan\left(\sqrt{e^{-N\Gamma T} - (1-e^{-\Gamma T})^{N}}\right). \tag{E.182}$$

Final state—

$$\begin{aligned}
\rho_{\text{in}}^{f}(\phi,T) =& \, \mathcal{U}_{\text{GHZ}}^{\dagger}\, \rho_{\text{in}}(\phi,T)\, \mathcal{U}_{\text{GHZ}} \\
=& \, \frac{1}{2}\left[\mathbb{1} + (-i)^{N+E}\sigma_x^{\otimes N}\right] \rho_{\text{in}}(\phi,T) \left[\mathbb{1} + i^{N+E}\sigma_x^{\otimes N}\right] \\
=& \, \frac{1}{2}\sin^2\left(\tfrac{\theta N}{2}\right) \left[|{\downarrow}\rangle\langle{\downarrow}|^{\otimes N} + i^{N+E}|{\downarrow}\rangle\langle{\uparrow}|^{\otimes N} + (-i)^{N+E}|{\uparrow}\rangle\langle{\downarrow}|^{\otimes N} + |{\uparrow}\rangle\langle{\uparrow}|^{\otimes N}\right] \\
& - \frac{1}{2} i^{N+E+1} e^{-\frac{\Gamma+\gamma+\gamma_c N}{2}NT} \sin\left(\tfrac{\theta N}{2}\right)\cos\left(\tfrac{\theta N}{2}\right) \\
& \times \Big(e^{i\phi N}\left[|{\downarrow}\rangle\langle{\uparrow}|^{\otimes N} + i^{N+E}|{\downarrow}\rangle\langle{\downarrow}|^{\otimes N} + (-i)^{N+E}|{\uparrow}\rangle\langle{\uparrow}|^{\otimes N} + |{\uparrow}\rangle\langle{\downarrow}|^{\otimes N}\right] \\
& + e^{-i\phi N}\left[|{\uparrow}\rangle\langle{\downarrow}|^{\otimes N} + i^{N+E}|{\uparrow}\rangle\langle{\uparrow}|^{\otimes N} + (-i)^{N+E}|{\downarrow}\rangle\langle{\downarrow}|^{\otimes N} + |{\downarrow}\rangle\langle{\uparrow}|^{\otimes N}\right]\Big) \\
& + \frac{1}{2}\cos^2\left(\tfrac{\theta N}{2}\right)\Big[\left(e^{-\Gamma T}|{\uparrow}\rangle\langle{\uparrow}| + \left(1-e^{-\Gamma T}\right)|{\downarrow}\rangle\langle{\downarrow}|\right)^{\otimes N} \\
& + i^{N+E}\left(e^{-\Gamma T}|{\uparrow}\rangle\langle{\downarrow}| + \left(1-e^{-\Gamma T}\right)|{\downarrow}\rangle\langle{\uparrow}|\right)^{\otimes N} \\
& + (-i)^{N+E}\left(e^{-\Gamma T}|{\downarrow}\rangle\langle{\uparrow}| + \left(1-e^{-\Gamma T}\right)|{\uparrow}\rangle\langle{\downarrow}|\right)^{\otimes N} \\
& + \left(e^{-\Gamma T}|{\downarrow}\rangle\langle{\downarrow}| + \left(1-e^{-\Gamma T}\right)|{\uparrow}\rangle\langle{\uparrow}|\right)^{\otimes N}\Big]
\end{aligned} \tag{E.183}$$

Conditional probabilities—

$$\begin{aligned}
P\left(x = \pm\tfrac{N}{2}|\phi\right) =& \, \frac{1}{2}\left[\sin^2\left(\tfrac{\theta N}{2}\right) + \cos^2\left(\tfrac{\theta N}{2}\right)\left(e^{-N\Gamma T} + \left(1-e^{-\Gamma T}\right)^{N}\right)\right] \\
& \pm e^{-\frac{\Gamma+\gamma+\gamma_c N}{2}NT}\sin\left(\tfrac{\theta N}{2}\right)\cos\left(\tfrac{\theta N}{2}\right)\sin(N\phi)
\end{aligned} \tag{E.184}$$

and

$$\begin{aligned}
P\left(x = +\tfrac{N}{2} - N_{-}|\phi\right) =& \, \frac{1}{2}\cos^2\left(\tfrac{\theta N}{2}\right)\binom{N}{N_{-}} \\
& \times \left[e^{-\Gamma T(N-N_{-})}\left(1-e^{-\Gamma T}\right)^{N_{-}} + e^{-\Gamma T N_{-}}\left(1-e^{-\Gamma T}\right)^{N-N_{-}}\right]
\end{aligned} \tag{E.185}$$

for $1 \leq N_{-} \leq N-1$, where N_{-} denotes the number of particles in the ground state. Again, only the maximal outcomes provide information about the phase. Hence, it is advantageous to employ the flag estimator. Furthermore, the conditional probabilities for the non-maximal outcomes are symmetric in the sense that $P\left(x=+\frac{N}{2}-N_{-}|\phi\right)=P\left(x=+\frac{N}{2}-(N-N_{-})|\phi\right)$. As discussed before, for $\theta_{\mathrm{GHZ}}=\frac{\pi}{2N}$ we obtain the same result as for the heralded-GHZ protocol.

Signal and slope— The moments of the observable X can either be determined directly based on the final state $\rho_{\mathrm{in}}^{f}(\phi,T)$ or by using the conditional probabilities, since generally $\left\langle X^{k}(\phi,T)\right\rangle=\sum_{x}x^{k}P(x|\phi)$. Here, the approach utilizing the conditional probabilities is beneficial due to the symmetry of $P(x|\phi)$, resulting in

$$\begin{aligned}\langle X(\phi,T)\rangle&=\frac{N}{2}\left[P\left(x=\tfrac{N}{2}|\phi\right)-P\left(x=-\tfrac{N}{2}|\phi\right)\right]\\&=Ne^{-\frac{\Gamma+\gamma+\gamma_{c}N}{2}NT}\sin\left(\tfrac{\theta N}{2}\right)\cos\left(\tfrac{\theta N}{2}\right)\sin(N\phi).\end{aligned}\tag{E.186}$$

In contrast to the parity-GHZ protocol and heralded-GHZ protocol, this signal is anti-symmetric. The slope of the signal is given by

$$\partial_{\phi}\langle X(\phi,T)\rangle=N^{2}e^{-\frac{\Gamma+\gamma+\gamma_{c}N}{2}NT}\sin\left(\tfrac{\theta N}{2}\right)\cos\left(\tfrac{\theta N}{2}\right)\cos(N\phi),\tag{E.187}$$

which is maximized for the optimal working point $\phi_{0}=0$.

Estimator— The flag estimator for the heralded-uGHZ protocol is given by

$$\phi_{\mathrm{est}}(x)=\begin{cases}\pm\frac{e^{\frac{\Gamma+\gamma+\gamma_{c}N}{2}NT}}{2N\sin\left(\frac{\theta N}{2}\right)\cos\left(\frac{\theta N}{2}\right)} & \text{for } x=\pm\frac{N}{2}\\ 0 & \text{else.}\end{cases}\tag{E.188}$$

Phase estimation uncertainty— The phase estimation uncertainty at the optimal working point thus reads

$$(\Delta\phi_{\mathrm{heralded-uGHZ}}(T))^{2}=\frac{N^{2}}{4}\frac{P\left(x=+\frac{N}{2}|\phi_{0}\right)+P\left(x=-\frac{N}{2}|\phi_{0}\right)}{\left(\partial_{\phi}\langle X(\phi,T)\rangle|_{\phi=\phi_{0}}\right)^{2}}\tag{E.189}$$

$$=\frac{e^{(\Gamma+\gamma+\gamma_{c}N)NT}}{4N^{2}}\frac{\sin^{2}\left(\frac{\theta N}{2}\right)+\cos^{2}\left(\frac{\theta N}{2}\right)\left[e^{-N\Gamma T}+\left(1-e^{-\Gamma T}\right)^{N}\right]}{\sin^{2}\left(\frac{\theta N}{2}\right)\cos^{2}\left(\frac{\theta N}{2}\right)}\tag{E.190}$$

$$=\frac{e^{(\Gamma+\gamma+\gamma_{c}N)NT}}{4N^{2}}\left[\frac{1}{\cos^{2}\left(\frac{\theta N}{2}\right)}+\frac{e^{-N\Gamma T}+\left(1-e^{-\Gamma T}\right)^{N}}{\sin^{2}\left(\frac{\theta N}{2}\right)}\right].\tag{E.191}$$

QCRB— The QCRB for the uGHZ state can be evaluated analogously to the GHZ state. With modified coefficients

$$
\begin{aligned}
a &= \cos^2\left(\tfrac{\theta N}{2}\right) e^{-N\Gamma T} && \text{(E.192)}\\
b &= -i^{N+E+1} e^{-\frac{\Gamma+\gamma+\gamma_c N}{2} NT} \sin\left(\tfrac{\theta N}{2}\right) \cos\left(\tfrac{\theta N}{2}\right) e^{-i\phi N} && \text{(E.193)}\\
c &= \sin^2\left(\tfrac{\theta N}{2}\right) + \cos^2\left(\tfrac{\theta N}{2}\right) \left(1 - e^{-\Gamma T}\right)^N, && \text{(E.194)}
\end{aligned}
$$

the QCRB of the state $\rho_{\text{in}}(\phi, T)$ equals Eq. (E.191) and thus, the heralded-uGHZ protocol saturates the QCRB for arbitrary rotation angles θ.

E.8.2 Optimal uGHZ state

Optimal rotation angle— Based on the phase estimation uncertainty for a general uGHZ state with arbitrary θ, we can determine the optimal rotation angle θ_{opt}. Differentiation of the phase estimation uncertainty

$$
\begin{aligned}
&\partial_\theta (\Delta\phi_{\text{heralded}-\text{uGHZ}}(T))^2 = \\
&\quad -2\frac{e^{(\Gamma+\gamma+\gamma_c N)NT}}{4N^2}\frac{N}{2}\left[-\sin\left(\tfrac{\theta N}{2}\right)\frac{1}{\cos^3\left(\tfrac{\theta N}{2}\right)} + \cos\left(\tfrac{\theta N}{2}\right)\frac{e^{-N\Gamma T} + \left(1 - e^{-\Gamma T}\right)^N}{\sin^3\left(\tfrac{\theta N}{2}\right)}\right]\\
&\quad = -2\frac{e^{(\Gamma+\gamma+\gamma_c N)NT}}{4N^2}\frac{N}{2}\left[\frac{-\sin^4\left(\tfrac{\theta N}{2}\right) + \cos^4\left(\tfrac{\theta N}{2}\right)\left(e^{-N\Gamma T} + \left(1 - e^{-\Gamma T}\right)^N\right)}{\sin^3\left(\tfrac{\theta N}{2}\right)\cos^3\left(\tfrac{\theta N}{2}\right)}\right]
\end{aligned}
\tag{E.195}
$$

yields the equation

$$
\tan^4\left(\frac{\theta_{\text{opt}} N}{2}\right) = e^{-N\Gamma T} + \left(1 - e^{-\Gamma T}\right)^N. \tag{E.196}
$$

Hence, the optimal rotation angle is determined by

$$
\theta_{\text{opt}} = \frac{2}{N}\arctan\left(\sqrt[4]{e^{-N\Gamma T} + (1 - e^{-\Gamma T})^N}\right). \tag{E.197}
$$

Interestingly, the optimal rotation angle is different from the angle that provides an equal superposition of both maximal Dicke state after the free evolution time. In particular, $\theta_\uparrow = 0 < \theta_{\text{equal}} < \theta_{\text{opt}} < \theta_{\text{GHZ}} = \pi/2N$. As discussed in Sec. 3.7.3, the optimal rotation angle represents a trade-off between compensating for spontaneous decay by enhancing the weight of the collective excited state and the associated increase in decoherence due to spontaneous decay. Specifically, this trade-off is captured in Eq. (E.189), where the numerator effectively characterizes the noise, and the denominator represents the signal. In particular, the numerator becomes minimal for $\theta_\uparrow$, while the denominator is maximal for the GHZ state θ_{GHZ}. Ultimately, a compromise is found with the optimal rotation angle θ_{opt}, resulting in a smaller phase estimation uncertainty than for θ_{equal}.

In the following we will re-express all quantities determined above for the optimal rotation angle using the trigonometric identities

$$\sin^2(x) = \frac{\tan^2(x)}{1+\tan^2(x)} \tag{E.198}$$

$$\cos^2(x) = \frac{1}{1+\tan^2(x)}. \tag{E.199}$$

Initial state—

$$\begin{aligned}
\rho_{\text{in}} = {} & \frac{\sqrt{e^{-N\Gamma T} + \left(1-e^{-\Gamma T}\right)^N}}{1+\sqrt{e^{-N\Gamma T} + \left(1-e^{-\Gamma T}\right)^N}} |{\downarrow}\rangle\langle{\downarrow}|^{\otimes N} \\
& - i^{N+E+1} \frac{\sqrt[4]{e^{-N\Gamma T} + \left(1-e^{-\Gamma T}\right)^N}}{1+\sqrt{e^{-N\Gamma T} + \left(1-e^{-\Gamma T}\right)^N}} \left[|{\downarrow}\rangle\langle{\uparrow}|^{\otimes N} + |{\uparrow}\rangle\langle{\downarrow}|^{\otimes N} \right] \\
& + \frac{1}{1+\sqrt{e^{-N\Gamma T} + \left(1-e^{-\Gamma T}\right)^N}} |{\uparrow}\rangle\langle{\uparrow}|^{\otimes N}
\end{aligned} \tag{E.200}$$

$$P_{\text{in}}^{+} = \frac{1}{1+\sqrt{e^{-N\Gamma T} + \left(1-e^{-\Gamma T}\right)^N}} \tag{E.201}$$

$$P_{\text{in}}^{-} = \frac{\sqrt{e^{-N\Gamma T} + \left(1-e^{-\Gamma T}\right)^N}}{1+\sqrt{e^{-N\Gamma T} + \left(1-e^{-\Gamma T}\right)^N}} \tag{E.202}$$

Time evolution—

$$\begin{aligned}
\rho_{\text{in}}(\phi, T) = {} & \frac{\sqrt{e^{-N\Gamma T} + \left(1-e^{-\Gamma T}\right)^N}}{1+\sqrt{e^{-N\Gamma T} + \left(1-e^{-\Gamma T}\right)^N}} |{\downarrow}\rangle\langle{\downarrow}|^{\otimes N} \\
& - i^{N+E+1} e^{-\frac{\Gamma+\gamma+\gamma_c N}{2} NT} \frac{\sqrt[4]{e^{-N\Gamma T} + \left(1-e^{-\Gamma T}\right)^N}}{1+\sqrt{e^{-N\Gamma T} + \left(1-e^{-\Gamma T}\right)^N}} \\
& \times \left[e^{i\phi N} |{\downarrow}\rangle\langle{\uparrow}|^{\otimes N} + e^{-i\phi N} |{\uparrow}\rangle\langle{\downarrow}|^{\otimes N} \right] \\
& + \frac{1}{1+\sqrt{e^{-N\Gamma T} + \left(1-e^{-\Gamma T}\right)^N}} \left(e^{-\Gamma T} |{\uparrow}\rangle\langle{\uparrow}| + \left(1-e^{-\Gamma T}\right) |{\downarrow}\rangle\langle{\downarrow}| \right)^{\otimes N}
\end{aligned} \tag{E.203}$$

$$P_{\text{in}}^{+}(T)=\frac{e^{-N\Gamma T}}{1+\sqrt{e^{-N\Gamma T}+(1-e^{-\Gamma T})^N}} \tag{E.204}$$

$$P_{\text{in}}^{-}(T)=\frac{\sqrt{e^{-N\Gamma T}+(1-e^{-\Gamma T})^N}+\left(1-e^{-\Gamma T}\right)^N}{1+\sqrt{e^{-N\Gamma T}+(1-e^{-\Gamma T})^N}} \tag{E.205}$$

Conditional probabilities—

$$\begin{aligned} P\left(x=\pm\tfrac{N}{2}|\phi\right) &= \frac{1}{2}\underbrace{\frac{\sqrt{e^{-N\Gamma T}+(1-e^{-\Gamma T})^N}+e^{-N\Gamma T}+\left(1-e^{-\Gamma T}\right)^N}{1+\sqrt{e^{-N\Gamma T}+(1-e^{-\Gamma T})^N}}}_{=\sqrt{e^{-N\Gamma T}+(1-e^{-\Gamma T})^N}} \\ &\qquad \pm e^{-\frac{\Gamma+\gamma+\gamma_c N}{2}NT}\frac{\sqrt[4]{e^{-N\Gamma T}+(1-e^{-\Gamma T})^N}}{1+\sqrt{e^{-N\Gamma T}+(1-e^{-\Gamma T})^N}}\sin(N\phi) \\ &= \frac{1}{2}\sqrt{e^{-N\Gamma T}+(1-e^{-\Gamma T})^N} \\ &\qquad \pm e^{-\frac{\Gamma+\gamma+\gamma_c N}{2}NT}\frac{\sqrt[4]{e^{-N\Gamma T}+(1-e^{-\Gamma T})^N}}{1+\sqrt{e^{-N\Gamma T}+(1-e^{-\Gamma T})^N}}\sin(N\phi) \end{aligned} \tag{E.206}$$

and

$$\begin{aligned} P\left(x=+\tfrac{N}{2}-N_-|\phi\right) &= \frac{1}{2}\frac{1}{1+\sqrt{e^{-N\Gamma T}+(1-e^{-\Gamma T})^N}}\binom{N}{N_-} \\ &\qquad \times\left[e^{-\Gamma T(N-N_-)}\left(1-e^{-\Gamma T}\right)^{N_-}+e^{-\Gamma T N_-}\left(1-e^{-\Gamma T}\right)^{N-N_-}\right] \end{aligned} \tag{E.207}$$

for $1\leq N_-\leq N-1$. We can also determine the probability of measuring any outcome other than the maximal ones. This effectively reflects the probability that no phase information is obtained from the interrogation scheme, which is given by

$$\begin{aligned} P\left(x\neq\pm\tfrac{N}{2}|\phi,T\right) &= 1-P\left(x=+\tfrac{N}{2}|\phi,T\right)-P\left(x=-\tfrac{N}{2}|\phi,T\right) \\ &= 1-\sqrt{e^{-N\Gamma T}+(1-e^{-\Gamma T})^N}. \end{aligned} \tag{E.208}$$

Signal and slope—

$$\langle X(\phi,T)\rangle = Ne^{-\frac{\Gamma+\gamma+\gamma_c N}{2}NT}\frac{\sqrt[4]{e^{-N\Gamma T}+(1-e^{-\Gamma T})^N}}{1+\sqrt{e^{-N\Gamma T}+(1-e^{-\Gamma T})^N}}\sin(N\phi) \tag{E.209}$$

$$\partial_\phi \langle X(\phi, T)\rangle = N^2 e^{-\frac{\Gamma+\gamma+\gamma_c N}{2}NT} \frac{\sqrt[4]{e^{-N\Gamma T} + (1-e^{-\Gamma T})^N}}{1+\sqrt{e^{-N\Gamma T} + (1-e^{-\Gamma T})^N}} \cos(N\phi) \tag{E.210}$$

Estimator—

$$\phi_{\text{est}}(x) = \begin{cases} \pm\frac{e^{\frac{\Gamma+\gamma+\gamma_c N}{2}NT}}{2N} \frac{1+\sqrt{e^{-N\Gamma T}+(1-e^{-\Gamma T})^N}}{\sqrt[4]{e^{-N\Gamma T}+(1-e^{-\Gamma T})^N}} & \text{for } x = \pm\frac{N}{2} \\ 0 & \text{else} \end{cases} \tag{E.211}$$

Phase estimation uncertainty—

$$(\Delta\phi_{\text{heralded-uGHZ}}(T))^2 = \frac{e^{(\Gamma+\gamma+\gamma_c N)NT}}{4N^2} \left[1+\sqrt{e^{-N\Gamma T} + (1-e^{-\Gamma T})^N}\right]^2 \tag{E.212}$$

E.8.3 Gain over SQL

As for the heralded-GHZ protocol, the minimization of Eq. (E.212) with respect to the interrogation time T generally is not analytically possible, but an explicit expression can be obtained for $\gamma = \gamma_c = 0$ and when neglecting the term $(1 - e^{-\Gamma T})^N$. The concept is the same as for the heralded-GHZ protocol. However, due to the square in Eq. (E.212), it is convenient to optimize $\Delta\omega_{\text{heralded-uGHZ}}(T)$ with respect to the interrogation time. Differentiation of

$$\Delta\omega_{\text{heralded-uGHZ}}(T) \simeq \frac{e^{\frac{\Gamma NT}{2}} + 1}{2N\sqrt{\tau T}} \tag{E.213}$$

with respect to T leads to the equation

$$\begin{aligned} \frac{\Gamma N T_{\text{min}}}{2} e^{\frac{\Gamma N T_{\text{min}}}{2}} &= \frac{1}{2}\left[e^{\frac{\Gamma N T_{\text{min}}}{2}} + 1\right] \\ \left(\frac{\Gamma N T_{\text{min}}}{2} - \frac{1}{2}\right) e^{\frac{\Gamma N T_{\text{min}}}{2}} &= \frac{1}{2} \\ \left(\frac{\Gamma N T_{\text{min}}}{2} - \frac{1}{2}\right) e^{\frac{\Gamma N T_{\text{min}}}{2} - \frac{1}{2}} &= \frac{1}{2\sqrt{e}} \end{aligned} \tag{E.214}$$

and thus

$$\frac{\Gamma N T_{\text{min}}}{2} - \frac{1}{2} = W(1/2\sqrt{e}) \tag{E.215}$$

or equivalently

$$T_{\text{min}} = \frac{1 + 2W(1/2\sqrt{e})}{\Gamma N}. \tag{E.216}$$

Hence, the the minimal frequency estimation uncertainty is given by

$$\begin{aligned}
\Delta\omega_{\text{heralded}-\text{uGHZ}} &\simeq \frac{1}{2N\sqrt{\tau}} \frac{e^{\frac{\Gamma N T_{\min}}{2}}+1}{\sqrt{T_{\min}}} \\
&= \frac{1}{2N\sqrt{\tau}} \frac{\left(\frac{\Gamma N T_{\min}}{2}-\frac{1}{2}\right)e^{\frac{\Gamma N T_{\min}}{2}}+\left(\frac{\Gamma N T_{\min}}{2}-\frac{1}{2}\right)}{\sqrt{T_{\min}}\left(\frac{\Gamma N T_{\min}}{2}-\frac{1}{2}\right)} \\
&= \frac{\sqrt{\Gamma}}{2\sqrt{\tau N}} \frac{\frac{1}{2}+W(1/2\sqrt{e})}{\sqrt{1+W(1/2\sqrt{e})}W(1/2\sqrt{e})} \\
&= \sqrt{\frac{\Gamma}{\tau N}} \frac{\sqrt{1+2W(1/2\sqrt{e})}}{4W(1/2\sqrt{e})} \\
&= \Delta\omega_{\text{SQL}} \frac{\sqrt{1+2W(1/2\sqrt{e})}}{4\sqrt{e}W(1/2\sqrt{e})}
\end{aligned} \tag{E.217}$$

where we used Eq. (E.214), Eq. (E.215) and Eq. (E.216) in the second step. Consequently, in this regime, the heralded-uGHZ protocol $\Delta\omega_{\text{heralded}-\text{uGHZ}}$ achieves a constant gain of $\frac{\sqrt{1+2W(1/2\sqrt{e})}}{4\sqrt{e}W(1/2\sqrt{e})} < 1$ over the SQL $\Delta\omega_{\text{SQL}}$, which corresponds to 2.25 dB (cf. Fig. 3.2(b)).

E.9 Spontaneous decay events in GHZ(-like) states

In the preceding appendices, as well as throughout the main text, we have identified specific expressions in the conditional probabilities and estimation uncertainties with distinct numbers of spontaneous decay events. At this point, we aim to illustrate this association. To address this, we apply the framework of quantum trajectories and quantum jumps, as outlined generally in Sec. 2.3.3, to GHZ(-like) states in the presence of spontaneous decay. As a reminder, in this framework the time dynamics represents a mixture

$$\rho_{\text{in}}(\phi, T) = \sum_{k=0}^{\infty} p_k(T)\rho_k(T) \tag{E.218}$$

of normalized states

$$\rho_k(\phi, T) = \frac{\tilde{\rho}_k(\phi, T)}{\text{Tr}(\tilde{\rho}_k(\phi, T))} = \frac{\tilde{\rho}_k(\phi, T)}{p_k(\phi, T)} \tag{E.219}$$

with

$$\tilde{\rho}_k(\phi, T) = \int_0^T \mathrm{d}t_k \int_0^{t_k} \mathrm{d}t_{k-1} \ldots \int_0^{t_2} \mathrm{d}t_1\, \mathcal{G}(T, t_k)\mathcal{J}\mathcal{G}(t_k, t_{k-1})\mathcal{J} \ldots \mathcal{G}(t_2, t_1)\mathcal{J}\mathcal{G}(t_1, 0)\rho_{\text{in}} \tag{E.220}$$

and corresponding probabilities $p_k(\phi, T)$. In particular, the state $\tilde{\rho}_k(\phi, T)$ results from k quantum jumps within the interrogation time T and non-unitary dynamics in between. For spontaneous decay, the master equation can be expressed as

$$\begin{aligned}\dot{\rho} &= -i\omega[S_z, \rho] - \frac{\Gamma}{2}\sum_{k=1}^{N}\sigma_{\text{ee}}^{(k)}\rho - \rho\frac{\Gamma}{2}\sum_{k=1}^{N}\sigma_{\text{ee}}^{(k)} + \Gamma\sum_{k=1}^{N}\sigma_{-}^{(k)}\rho\sigma_{+}^{(k)} \\ &= -i\left(\omega S_z - i\frac{\Gamma}{2}\sum_{k=1}^{N}\sigma_{\text{ee}}^{(k)}\right)\rho + i\rho\left(\omega S_z\frac{\Gamma}{2}\sum_{k=1}^{N}\sigma_{\text{ee}}^{(k)}\right) + \Gamma\sum_{k=1}^{N}\sigma_{-}^{(k)}\rho\sigma_{+}^{(k)} \\ &= -iH_{\text{eff}}\rho + i\rho H_{\text{eff}}^{\dagger} + \Gamma\sum_{k=1}^{N}\sigma_{-}^{(k)}\rho\sigma_{+}^{(k)}\end{aligned} \tag{E.221}$$

with effective non-hermitian Hamiltonian

$$H_{\text{eff}} = \omega S_z - i\frac{\Gamma}{2}\sum_{k=1}^{N}\sigma_{\text{ee}}^{(k)}. \tag{E.222}$$

Hence, the continuous non-unitary time propagation $\mathcal{G}$ and the discrete quantum jumps $\mathcal{J}$, associated with actual decay events, are given by

$$\mathcal{G}(t, t_0)\rho = e^{-iH_{\text{eff}}(t-t_0)}\rho e^{iH_{\text{eff}}^{\dagger}(t-t_0)} \tag{E.223}$$

and

$$\mathcal{J}\rho = \Gamma\sum_{k=1}^{N}\sigma_{-}^{(k)}\rho\sigma_{+}^{(k)}, \tag{E.224}$$

respectively. Furthermore, at most N quantum jumps can occur, as this scenario would map the collective excited state $|\uparrow\rangle^{\otimes N}$ to the collective ground state $|\downarrow\rangle^{\otimes N}$. Thus, the mixture in Eq. (E.218) contains $N+1$ terms with $k \in \{0, \dots, N\}$.

To determine the aforementioned expressions associated with a particular number of spontaneous decay events for GHZ(-like) states, we consider the generic initial state

$$\rho_{\text{in}} = \rho_{\text{gg}}^{(N)}|\downarrow\rangle\langle\downarrow|^{\otimes N} + \rho_{\text{ge}}^{(N)}|\downarrow\rangle\langle\uparrow|^{\otimes N} + \rho_{\text{eg}}^{(N)}|\uparrow\rangle\langle\downarrow|^{\otimes N} + \rho_{\text{ee}}^{(N)}|\uparrow\rangle\langle\uparrow|^{\otimes N}. \tag{E.225}$$

The dynamics according to the master equation results in the time evolved state

$$\begin{aligned}\rho_{\text{in}}(T) = \rho_{\text{gg}}^{(N)}|\downarrow\rangle\langle\downarrow|^{\otimes N} &+ e^{-\frac{\Gamma NT}{2}}\left(\rho_{\text{ge}}^{(N)}e^{iN\phi}|\downarrow\rangle\langle\uparrow|^{\otimes N} + \rho_{\text{eg}}^{(N)}e^{-iN\phi}|\uparrow\rangle\langle\downarrow|^{\otimes N}\right) \\ &+ \rho_{\text{ee}}^{(N)}\left(e^{-\Gamma T}|\uparrow\rangle\langle\uparrow| + \left[1 - e^{-\Gamma T}\right]|\downarrow\rangle\langle\downarrow|\right)^{\otimes N}.\end{aligned} \tag{E.226}$$

To identify the individual terms in $\rho_{\text{in}}(\phi, T)$ with a certain number of quantum jumps, we have to evaluate the expansion described by Eq. (E.218). Of particular interest for the GHZ(-like) protocols investigated in this thesis is the 'no-jump' term with no spontaneous decay event, which is given by

$$\begin{aligned}\tilde{\rho}_0(\phi, T) &= \mathcal{G}(T,0)\rho_{\mathrm{in}} \\ &= \rho_{\mathrm{gg}}^{(N)}|{\downarrow}\rangle\langle{\downarrow}|^{\otimes N} + e^{-\frac{\Gamma N T}{2}}\left(\rho_{\mathrm{ge}}^{(N)} e^{iN\phi}|{\downarrow}\rangle\langle{\uparrow}|^{\otimes N} + \rho_{\mathrm{eg}}^{(N)} e^{-iN\phi}|{\uparrow}\rangle\langle{\downarrow}|^{\otimes N}\right) \\ &\quad + \rho_{\mathrm{ee}}^{(N)} e^{-\Gamma N T}|{\uparrow}\rangle\langle{\uparrow}|^{\otimes N},\end{aligned} \tag{E.227}$$

where $\phi = \omega T$. Consequently, the subspace of the maximal Dicke states in the time evolved state, which ultimately results in outcomes $x = \pm\frac{N}{2}$ for measurements of the observable X, is not solely governed by the no-jump dynamics, as the term $\rho_{\mathrm{ee}}^{(N)}\left(1 - e^{-\Gamma T}\right)^N |{\downarrow}\rangle\langle{\downarrow}|^{\otimes N}$ is not captured in $\tilde{\rho}_0(\phi, T)$. The probability of the no-jump dynamics is determined by

$$p_0(\phi, T) = \mathrm{Tr}(\tilde{\rho}_0(\phi, T)) = \rho_{\mathrm{gg}}^{(N)} + \rho_{\mathrm{ee}}^{(N)} e^{-\Gamma N T}. \tag{E.228}$$

Furthermore, it is interesting to note that the population of the collective excited state decreases, even in the absence of any decay events. This scenario can be understood through an analogy to Schrödinger's cat: the initial state represents a superposition of both the collective ground and excited states. As long as no measurement is performed, the exact state of the system remains unknown. However, as time elapses without any decay events occurring, the probability that the system was initially in the collective ground state increases.

In contrast, terms with $k > 0$ involve k spontaneous decay events. To understand the general structure of the terms, we examine $\tilde{\rho}_k(\phi, T)$ exemplarily for $k = 1, 2, 3$. With $\mathcal{J}|{\downarrow}\rangle\langle{\downarrow}|^{\otimes N} = \mathcal{J}|{\downarrow}\rangle\langle{\uparrow}|^{\otimes N} = \mathcal{J}|{\uparrow}\rangle\langle{\downarrow}|^{\otimes N} = 0$, we obtain

$$\begin{aligned}\tilde{\rho}_1(\phi, T) &= \int_0^T \mathrm{d}t_1 \mathcal{G}(T, t_1)\mathcal{J}\mathcal{G}(t_1, 0)\rho_{\mathrm{in}} \\ &= \rho_{\mathrm{ee}}^{(N)}\Gamma \int_0^T \mathrm{d}t_1 e^{-\Gamma N t_1} e^{-\Gamma(T-t_1)(N-1)} \sum_{j_1}^{N} |j_1\rangle\langle j_1| \\ &= \rho_{\mathrm{ee}}^{(N)} e^{-\Gamma T(N-1)}\Gamma \int_0^T \mathrm{d}t_1 e^{-\Gamma t_1} \sum_{j_1}^{N} |j_1\rangle\langle j_1|,\end{aligned} \tag{E.229}$$

where we introduced the notation

$$|j_1\rangle\langle j_1| = \sum_{j_1=1}^{N} \sigma_-^{(j_1)}|{\uparrow}\rangle|{\uparrow}\rangle^{\otimes N}\sigma_+^{(j_1)}. \tag{E.230}$$

In more general, we define

$$|j_1, \ldots, j_k\rangle\langle j_1, \ldots, j_k| = \sum_{\substack{j_1,\ldots,j_k=1 \\ \text{pairwise distinct}}}^{N} \sigma_-^{(j_k)} \ldots \sigma_-^{(j_1)}|{\uparrow}\rangle\langle{\uparrow}|^{\otimes N}\sigma_+^{(j_1)} \ldots \sigma_+^{(j_k)}. \tag{E.231}$$

The second term reads

$$
\begin{aligned}
\tilde{\rho}_2(\phi, T) &= \int_0^T \mathrm{d}t_2 \int_0^{t_2} \mathrm{d}t_1 \mathcal{G}(T, t_2)\mathcal{J}\mathcal{G}(t_2, t_1)\mathcal{J}\mathcal{G}(t_1, 0)\rho_{\mathrm{in}} \\
&= \rho_{\mathrm{ee}}^{(N)}\Gamma^2 \int_0^T \mathrm{d}t_2 \int_0^{t_2} \mathrm{d}t_1 e^{-\Gamma t_2(N-1)} e^{-\Gamma t_1} e^{-\Gamma(T-t_2)(N-2)} \sum_{\substack{j_1,j_2 \\ \text{pairwise distinct}}}^{N} |j_1, j_2\rangle\langle j_1, j_2| \\
&= \rho_{\mathrm{ee}}^{(N)} e^{-\Gamma T(N-2)}\Gamma^2 \int_0^T \mathrm{d}t_2 \int_0^{t_2} \mathrm{d}t_1 e^{-\Gamma(t_1+t_2)} \sum_{\substack{j_1,j_2 \\ \text{pairwise distinct}}}^{N} |j_1, j_2\rangle\langle j_1, j_2| \,.
\end{aligned}
\tag{E.232}
$$

This structure continues for the third term as well

$$
\begin{aligned}
\tilde{\rho}_3(\phi, T) &= \int_0^T \mathrm{d}t_3 \int_0^{t_3} \mathrm{d}t_2 \int_0^{t_2} \mathrm{d}t_1 \mathcal{G}(T, t_3)\mathcal{J}\mathcal{G}(t_3, t_2)\mathcal{J}\mathcal{G}(t_2, t_1)\mathcal{J}\mathcal{G}(t_1, 0)\rho_{\mathrm{in}} \\
&= \rho_{\mathrm{ee}}^{(N)}\Gamma^3 \int_0^T \mathrm{d}t_3 \int_0^{t_3} \mathrm{d}t_2 \int_0^{t_2} \mathrm{d}t_1 e^{-\Gamma t_3(N-2)} e^{-\Gamma(t_1+t_2)} e^{-\Gamma(T-t_3)(N-3)} \\
&\quad \times \sum_{\substack{j_1,j_2,j_3 \\ \text{pairwise distinct}}}^{N} |j_1, j_2, j_3\rangle\langle j_1, j_2, j_3| \\
&= \rho_{\mathrm{ee}}^{(N)} e^{-\Gamma T(N-3)}\Gamma^3 \int_0^T \mathrm{d}t_3 \int_0^{t_3} \mathrm{d}t_2 \int_0^{t_2} \mathrm{d}t_1 e^{-\Gamma(t_1+t_2+t_3)} \\
&\quad \times \sum_{\substack{j_1,j_2,j_3 \\ \text{pairwise distinct}}}^{N} |j_1, j_2, j_3\rangle\langle j_1, j_2, j_3|
\end{aligned}
\tag{E.233}
$$

and thus, in general, for arbitrary $k > 0$ we obtain

$$
\begin{aligned}
\tilde{\rho}_k(\phi, T) &= \int_0^T \mathrm{d}t_k \int_0^{t_k} \mathrm{d}t_{k-1} \ldots \int_0^{t_2} \mathrm{d}t_1 \, \mathcal{G}(T, t_k)\mathcal{J}\mathcal{G}(t_k, t_{k-1})\mathcal{J} \ldots \mathcal{G}(t_2, t_1)\mathcal{J}\mathcal{G}(t_1, 0)\rho_{\mathrm{in}} \\
&= \rho_{\mathrm{ee}}^{(N)} e^{-\Gamma T(N-k)}\Gamma^k \int_0^T \mathrm{d}t_k \int_0^{t_k} \mathrm{d}t_{k-1} \ldots \int_0^{t_2} \mathrm{d}t_1 \prod_{j=1}^{k} e^{-\Gamma t_j} \\
&\quad \times \sum_{\substack{j_1,\ldots,j_k \\ \text{pairwise distinct}}}^{N} |j_1, \ldots, j_k\rangle\langle j_1, \ldots, j_k| \,.
\end{aligned}
\tag{E.234}
$$

It is instructive to examine the summation over the jump terms in more detail. Essentially, it iterates over all distinct permutations with k particles in the ground state and $N - k$ particles in the excited state. These $\binom{N}{k}$ terms can be expressed in a compact form using the permutation operator $\mathcal{P}$, since $\mathcal{P}\left(|{\downarrow}\rangle\langle{\downarrow}|^{\otimes k} \otimes |{\uparrow}\rangle\langle{\uparrow}|^{\otimes N-k}\right)$ precisely generates these $\binom{N}{k}$ distinct variations of the state $|{\downarrow}\rangle\langle{\downarrow}|^{\otimes k} \otimes |{\uparrow}\rangle\langle{\uparrow}|^{\otimes N-k}$.

However, each permutation appears with a multiplicity factor $k!$, since Eq. (E.231) accounts for the specific sequence in which the k particles decay, even though the resulting state is the same. Overall, there are $k!$ possible sequences for this order. To give an example, for $N = 3$ and $k = 2$, the state $|\uparrow\rangle \otimes |\downarrow\rangle \otimes |\downarrow\rangle$ results from the two terms $\sigma_-^{(3)}\sigma_-^{(2)}|\uparrow\rangle\langle\uparrow|^{\otimes 3}\sigma_+^{(2)}\sigma_+^{(3)}$ and $\sigma_-^{(2)}\sigma_-^{(3)}|\uparrow\rangle\langle\uparrow|^{\otimes 3}\sigma_+^{(3)}\sigma_+^{(2)}$, both appearing in Eq. (E.231). Consequently, Eq. (E.231) alternatively can be expressed as

$$|j_1, \ldots, j_k\rangle\langle j_1, \ldots, j_k| = k!\mathcal{P}\left(|\downarrow\rangle\langle\downarrow|^{\otimes k} \otimes |\uparrow\rangle\langle\uparrow|^{\otimes N-k}\right). \tag{E.235}$$

Hence, the state with $k > 0$ decay events is given by

$$\begin{aligned}\tilde{\rho}_k(\phi, T) = {}& \rho_{\mathrm{ee}}^{(N)} e^{-\Gamma T(N-k)} k!\Gamma^k \\ & \times \int_0^T \mathrm{d}t_k \int_0^{t_k} \mathrm{d}t_{k-1} \ldots \int_0^{t_2} \mathrm{d}t_1 \prod_{j=1}^k e^{-\Gamma t_j} \mathcal{P}\left(|\downarrow\rangle\langle\downarrow|^{\otimes k} \otimes |\uparrow\rangle\langle\uparrow|^{\otimes N-k}\right) \\ = {}& \rho_{\mathrm{ee}}^{(N)} e^{-\Gamma T(N-k)} \mathcal{I}_k \mathcal{P}\left(|\downarrow\rangle\langle\downarrow|^{\otimes k} \otimes |\uparrow\rangle\langle\uparrow|^{\otimes N-k}\right).\end{aligned} \tag{E.236}$$

As a consequence, we have to evaluate the integrals

$$\mathcal{I}_k = k!\Gamma^k \int_0^{t_{k+1}} \mathrm{d}t_k \int_0^{t_k} \mathrm{d}t_{k-1} \ldots \int_0^{t_2} \mathrm{d}t_1 \prod_{j=1}^k e^{-\Gamma t_j}, \tag{E.237}$$

where we used the notation $t_{k+1} = T$. We conjecture that

$$\mathcal{I}_k = \left(1 - e^{-\Gamma t_{k+1}}\right)^k. \tag{E.238}$$

We prove this by induction. For $k = 1$, Eq. (E.238) is satisfied, since

$$\mathcal{I}_1 = \Gamma \int_0^{t_2} \mathrm{d}t_1 e^{-\Gamma t_1} = 1 - e^{-\Gamma t_2}. \tag{E.239}$$

For $k \mapsto k + 1$, we obtain

$$\begin{aligned}\mathcal{I}_{k+1} &= (k+1)!\Gamma^{k+1} \int_0^{t_{k+2}} \mathrm{d}t_{k+1} \int_0^{t_{k+1}} \mathrm{d}t_k \int_0^{t_k} \mathrm{d}t_{k-1} \ldots \int_0^{t_2} \mathrm{d}t_1 \prod_{j=1}^{k+1} e^{-\Gamma t_j} \\ &= (k+1)\Gamma \int_0^{t_{k+2}} \mathrm{d}t_{k+1} e^{-\Gamma t_{k+1}} \left(1 - e^{-\Gamma t_{k+1}}\right)^k \\ &= (k+1) \int_0^{1-e^{-\Gamma t_{k+2}}} \mathrm{d}x x^k \\ &= \left(1 - e^{-\Gamma t_{k+2}}\right)^{k+1},\end{aligned} \tag{E.240}$$

where we used the substitution $x = 1 - e^{-\Gamma t_{k+1}}$ with $\frac{\mathrm{d}x}{\mathrm{d}t_{k+1}} = \Gamma e^{-\Gamma t_{k+1}}$. Hence, Eq. (E.238) holds for arbitrary k.

Consequently, the terms for $k > 0$ in the expansion described by Eq. (E.218) are given by

$$\tilde{\rho}_k(\phi, T) = \rho_{\rm ee}^{(N)} e^{-\Gamma T(N-k)} \left(1 - e^{-\Gamma T}\right)^k \mathcal{P}\left(|{\downarrow}\rangle\langle{\downarrow}|^{\otimes k} \otimes |{\uparrow}\rangle\langle{\uparrow}|^{\otimes N-k}\right). \tag{E.241}$$

The corresponding probabilities of dynamics with $k > 0$ jumps are determined by

$$p_k(\phi, T) = \mathrm{Tr}(\tilde{\rho}_k(\phi, T)) = \rho_{\rm ee}^{(N)} \binom{N}{k} e^{-\Gamma T(N-k)} \left(1 - e^{-\Gamma T}\right)^k, \tag{E.242}$$

which are directly connected to the conditional probabilities of the GHZ(-like) protocols investigated in the previous sections. In particular, the scenario of N spontaneous decay events occurs with probability $p_N(\phi, T) = \rho_{\rm ee}^{(N)} \left(1 - e^{-\Gamma T}\right)^N$ and the system results to be in the collective ground state $|{\downarrow}\rangle^{\otimes N}$. Therefore, to be precise, the nonlinear estimator in Eq. (3.79) does not exclusively select the no-jump dynamics, but additionally takes the scenario involving N spontaneous decay events into account. However, the probability of this event becomes increasingly unlikely with increasing ensemble size N. In particular, this scenario can be effectively disregarded already for $N \geq 5$, as illustrated in Fig. 3.4(b).

To cross-check the result, we can verify the normalization of the time evolved state:

$$\begin{aligned}\sum_{k=0}^{N} p_k(\phi, T) &= \rho_{\rm gg}^{(N)} + \rho_{\rm ee}^{(N)} \sum_{k=0}^{N} \binom{N}{k} e^{-\Gamma T(N-k)} \left(1 - e^{-\Gamma T}\right)^k \\ &= \rho_{\rm gg}^{(N)} + \rho_{\rm ee}^{(N)} \left(e^{-\Gamma T} + 1 - e^{-\Gamma T}\right)^N = \rho_{\rm gg}^{(N)} + \rho_{\rm ee}^{(N)} = 1,\end{aligned} \tag{E.243}$$

where we used the binomial theorem.

E.10 Incoherent pumping

In this appendix, we derive the results presented for incoherent pumping and spontaneous decay in Sec. 3.10.1. Specifically, we begin in App. E.10.1 by demonstrating that the terms of the master equation for these two decoherence processes do not (super-)commute. Subsequently, we provide the simultaneous solution of the master equation in App. E.10.2. Furthermore, we map the decoherence process to projective spin measurements in App. E.10.3 and parity measurements in App. E.10.4 to determine the frequency estimation uncertainty for CSS, SSS and the parity-GHZ protocol. Finally, we examine the performance of the heralded-(u)GHZ protocols in App. E.10.5.

E.10.1 Non-commutativity of the master equation

The dynamics of the system during the Ramsey interrogation time T considering a unitary phase evolution, spontaneous decay with rate Γ and incoherent pumping with rate $\Gamma_\uparrow$ is governed by the master equation Eq. (3.98). As in App. C, we use the following notation for the distinct terms

$$\mathcal{L}_\phi[\rho] = -i\omega[S_z, \rho] \tag{E.244}$$

$$\mathcal{L}_\Gamma[\rho] = \frac{\Gamma}{2}\sum_{k=1}^{N} 2\sigma_-^{(k)}\rho\sigma_+^{(k)} - \sigma_{\mathrm{ee}}^{(k)}\rho - \rho\sigma_{\mathrm{ee}}^{(k)} \tag{E.245}$$

and additionally define

$$\mathcal{L}_\Gamma[\rho] = \frac{\Gamma_\uparrow}{2}\sum_{k=1}^{N} 2\sigma_+^{(k)}\rho\sigma_-^{(k)} - \sigma_{\mathrm{gg}}^{(k)}\rho - \rho\sigma_{\mathrm{gg}}^{(k)}. \tag{E.246}$$

Hence, the master equation can be expressed as

$$\dot{\rho} = \mathcal{L}_\phi[\rho] + \mathcal{L}_\Gamma[\rho] + \mathcal{L}_{\Gamma_\uparrow}[\rho]. \tag{E.247}$$

As for spontaneous decay, the term for incoherent pumping (super-)commutes with the unitary evolution since

$$\begin{aligned}
\mathcal{L}_\phi[\mathcal{L}_{\Gamma_\uparrow}[\rho]] &= -i\frac{\omega\Gamma_\uparrow}{4}\sum_{j,k=1}^{N}\left[\sigma_z^{(j)}, 2\sigma_+^{(k)}\rho\sigma_-^{(k)} - \sigma_{\mathrm{gg}}^{(k)}\rho - \rho\sigma_{\mathrm{gg}}^{(k)}\right] \\
&= -i\frac{\omega\Gamma_\uparrow}{4}\sum_{j,k=1}^{N}\left[\sigma_z^{(j)}, 2\sigma_+^{(k)}\rho\sigma_-^{(k)}\right] - \left[\sigma_z^{(j)}, \sigma_{\mathrm{gg}}^{(k)}\rho\right] - \left[\sigma_z^{(j)}, \rho\sigma_{\mathrm{gg}}^{(k)}\right] \\
&= -i\frac{\omega\Gamma_\uparrow}{4}\sum_{j,k=1}^{N} 2\left[\sigma_z^{(j)}, \sigma_+^{(k)}\rho\sigma_-^{(k)}\right] - \sigma_{\mathrm{gg}}^{(k)}\left[\sigma_z^{(j)}, \rho\right] - \underbrace{\left[\sigma_z^{(j)}, \sigma_{\mathrm{gg}}^{(k)}\right]}_{=0}\rho \\
&\quad - \rho\underbrace{\left[\sigma_z^{(j)}, \sigma_{\mathrm{gg}}^{(k)}\right]}_{=0} - \left[\sigma_z^{(j)}, \rho\right]\sigma_{\mathrm{gg}}^{(k)} \\
&= -i\frac{\omega\Gamma_\uparrow}{4}\sum_{j,k=1}^{N}\left(2\sigma_+^{(k)}\left[\sigma_z^{(j)}, \rho\right]\sigma_-^{(k)} - \sigma_{\mathrm{gg}}^{(k)}\left[\sigma_z^{(j)}, \rho\right] - \left[\sigma_z^{(j)}, \rho\right]\sigma_{\mathrm{gg}}^{(k)}\right),
\end{aligned} \tag{E.248}$$

where we used

$$\begin{aligned}
\left[\sigma_z^{(j)}, \sigma_+^{(k)}\rho\sigma_-^{(k)}\right] &= \sigma_+^{(k)}\left[\sigma_z^{(j)}, \rho\right]\sigma_-^{(k)} + \sigma_+^{(k)}\rho\underbrace{\left[\sigma_z^{(j)}, \sigma_-^{(k)}\right]}_{=-2\delta_{jk}\sigma_-^{(k)}} + \underbrace{\left[\sigma_z^{(j)}, \sigma_+^{(k)}\right]}_{=2\delta_{jk}\sigma_+^{(k)}}\rho\sigma_-^{(k)} \\
&= \sigma_+^{(k)}\left[\sigma_z^{(j)}, \rho\right]\sigma_-^{(k)},
\end{aligned} \tag{E.249}$$

and

$$\mathcal{L}_\Gamma[\mathcal{L}_\phi[\rho]] = -i\frac{\omega\Gamma}{4}\sum_{j,k=1}^{N}\left(2\sigma_+^{(k)}\left[\sigma_z^{(j)},\rho\right]\sigma_-^{(k)} - \sigma_{\mathrm{gg}}^{(k)}\left[\sigma_z^{(j)},\rho\right] - \left[\sigma_z^{(j)},\rho\right]\sigma_{\mathrm{gg}}^{(k)}\right). \tag{E.250}$$

In contrast, however, the terms for spontaneous decay and incoherent pumping do not (super-)commute. Evaluating $\mathcal{L}_\Gamma[\mathcal{L}_{\Gamma_\uparrow}[\rho]]$ and $\mathcal{L}_{\Gamma_\uparrow}[\mathcal{L}_\Gamma[\rho]]$, we focus on the terms for a single particle, as commutation for distinct particles is trivially satisfied. Hence, on the one hand for $\mathcal{L}_\Gamma[\mathcal{L}_{\Gamma_\uparrow}[\rho]]$ we obtain

$$\begin{aligned}&4\underbrace{\sigma_+^{(k)}\sigma_-^{(k)}}_{=\sigma_{\mathrm{ee}}^{(k)}}\rho\underbrace{\sigma_+^{(k)}\sigma_-^{(k)}}_{=\sigma_{\mathrm{ee}}^{(k)}}-2\underbrace{\sigma_+^{(k)}\sigma_{\mathrm{ee}}^{(k)}}_{=0}\rho\sigma_-^{(k)}-2\sigma_+^{(k)}\rho\underbrace{\sigma_{\mathrm{ee}}^{(k)}\sigma_-^{(k)}}_{=0}-2\underbrace{\sigma_{\mathrm{gg}}^{(k)}\sigma_-^{(k)}}_{=\sigma_-^{(k)}}\rho\sigma_+^{(k)}\\&+\underbrace{\sigma_{\mathrm{gg}}^{(k)}\sigma_{\mathrm{ee}}^{(k)}}_{=0}\rho+\sigma_{\mathrm{gg}}^{(k)}\rho\sigma_{\mathrm{ee}}^{(k)}-2\sigma_-^{(k)}\rho\underbrace{\sigma_+^{(k)}\sigma_{\mathrm{gg}}^{(k)}}_{=\sigma_+^{(k)}}+\sigma_{\mathrm{ee}}^{(k)}\rho\sigma_{\mathrm{gg}}^{(k)}+\rho\underbrace{\sigma_{\mathrm{ee}}^{(k)}\sigma_{\mathrm{gg}}^{(k)}}_{=0}\end{aligned} \tag{E.251}$$

and analogously for $\mathcal{L}_{\Gamma_\uparrow}[\mathcal{L}_\Gamma[\rho]]$

$$\begin{aligned}&4\underbrace{\sigma_-^{(k)}\sigma_+^{(k)}}_{=\sigma_{\mathrm{gg}}^{(k)}}\rho\underbrace{\sigma_-^{(k)}\sigma_+^{(k)}}_{=\sigma_{\mathrm{gg}}^{(k)}}-2\underbrace{\sigma_-^{(k)}\sigma_{\mathrm{gg}}^{(k)}}_{=0}\rho\sigma_+^{(k)}-2\sigma_-^{(k)}\rho\underbrace{\sigma_{\mathrm{gg}}^{(k)}\sigma_+^{(k)}}_{=0}-2\underbrace{\sigma_{\mathrm{ee}}^{(k)}\sigma_+^{(k)}}_{=\sigma_+^{(k)}}\rho\sigma_-^{(k)}\\&+\underbrace{\sigma_{\mathrm{ee}}^{(k)}\sigma_{\mathrm{gg}}^{(k)}}_{=0}\rho+\sigma_{\mathrm{ee}}^{(k)}\rho\sigma_{\mathrm{gg}}^{(k)}-2\sigma_+^{(k)}\rho\underbrace{\sigma_-^{(k)}\sigma_{\mathrm{ee}}^{(k)}}_{=\sigma_-^{(k)}}+\sigma_{\mathrm{gg}}^{(k)}\rho\sigma_{\mathrm{ee}}^{(k)}+\rho\underbrace{\sigma_{\mathrm{gg}}^{(k)}\sigma_{\mathrm{ee}}^{(k)}}_{=0}.\end{aligned} \tag{E.252}$$

Consequently, the (super-)commutator does not vanish since

$$[\mathcal{L}_{\Gamma_\uparrow},\mathcal{L}_\Gamma][\rho] = \frac{\Gamma\Gamma_\uparrow}{4}\sum_{k=1}^{N}4\sigma_{\mathrm{ee}}^{(k)}\rho\sigma_{\mathrm{ee}}^{(k)}+4\sigma_{\mathrm{gg}}^{(k)}\rho\sigma_{\mathrm{gg}}^{(k)}-4\sigma_-^{(k)}\rho\sigma_+^{(k)}-4\sigma_+^{(k)}\rho\sigma_-^{(k)} \neq 0 \tag{E.253}$$

and thus, the master equation has to be solved simultaneously for spontaneous decay and incoherent pumping.

E.10.2 Solution of the master equation

For a single particle, the master equation for spontaneous decay and incoherent pumping is given by

$$\dot{\rho} = \frac{\Gamma}{2}\left(2\sigma_-\rho\sigma_+ - \sigma_{\mathrm{ee}}\rho - \rho\sigma_{\mathrm{ee}}\right) + \frac{\Gamma_\uparrow}{2}\left(2\sigma_+\rho\sigma_- - \sigma_{\mathrm{gg}}\rho - \rho\sigma_{\mathrm{gg}}\right). \tag{E.254}$$

Hence, the time evolution for the matrix elements is determined by

$$\dot{\rho}_{\mathrm{ee}} = -\Gamma\rho_{\mathrm{ee}} + \Gamma_\uparrow\rho_{\mathrm{gg}} \tag{E.255}$$

$$\dot{\rho}_{\mathrm{eg}} = -\frac{\Gamma+\Gamma_\uparrow}{2}\rho_{\mathrm{eg}} \tag{E.256}$$

$$\dot{\rho}_{\mathrm{ge}} = -\frac{\Gamma+\Gamma_\uparrow}{2}\rho_{\mathrm{ge}} \tag{E.257}$$

$$\dot{\rho}_{\mathrm{gg}} = \Gamma\rho_{\mathrm{ee}} - \Gamma_\uparrow\rho_{\mathrm{gg}}. \tag{E.258}$$

While the coherences can be directly integrated, the coupled differential equations for the populations can be solved using standard techniques, finally resulting in

$$\rho_{\text{ee}}(t) = \frac{1}{\Gamma+\Gamma_\uparrow}\rho_{\text{ee}}(0)\left[\Gamma e^{-(\Gamma+\Gamma_\uparrow)t}+\Gamma_\uparrow\right] + \frac{\Gamma_\uparrow}{\Gamma+\Gamma_\uparrow}\rho_{\text{gg}}(0)\left[1-e^{-(\Gamma+\Gamma_\uparrow)t}\right] \tag{E.259}$$

$$\rho_{\text{eg}}(t) = \rho_{\text{eg}}(0)e^{-\frac{\Gamma+\Gamma_\uparrow}{2}t} \tag{E.260}$$

$$\rho_{\text{ge}}(t) = \rho_{\text{ge}}(0)e^{-\frac{\Gamma+\Gamma_\uparrow}{2}t} \tag{E.261}$$

$$\rho_{\text{gg}}(t) = \frac{\Gamma}{\Gamma+\Gamma_\uparrow}\rho_{\text{ee}}(0)\left[1-e^{-(\Gamma+\Gamma_\uparrow)t}\right] + \frac{1}{\Gamma+\Gamma_\uparrow}\rho_{\text{gg}}(0)\left[\Gamma+\Gamma_\uparrow e^{-(\Gamma+\Gamma_\uparrow)t}\right]. \tag{E.262}$$

E.10.3 Projective spin measurements

Following App. E.1.1, we map the decoherence process from the initial state to the observable X by defining the adjoint Lindblad (super-)operator

$$\mathcal{L}^\dagger_{\Gamma_\uparrow}[X] = \frac{\Gamma_\uparrow}{2}\sum_{k=1}^{N} 2\sigma_-^{(k)}\rho\sigma_+^{(k)} - \sigma_{\text{gg}}^{(k)}X - X\sigma_{\text{gg}}^{(k)}. \tag{E.263}$$

As before, we consider a measurement of S_y and thus have to determine

$$\begin{aligned}\mathcal{L}^\dagger_{\Gamma_\uparrow}[S_y] &= \frac{\Gamma_\uparrow}{2}\sum_{k=1}^{N} 2\sigma_-^{(k)}S_y\sigma_+^{(k)} - \sigma_{\text{gg}}^{(k)}S_y - S_y\sigma_{\text{gg}}^{(k)} \\ &= \frac{\Gamma_\uparrow}{4}\sum_{j,k=1}^{N}\left(2\sigma_-^{(k)}\sigma_y^{(j)}\sigma_+^{(k)} - \sigma_{\text{gg}}^{(k)}\sigma_y^{(j)} - \sigma_y^{(j)}\sigma_{\text{gg}}^{(k)}\right).\end{aligned} \tag{E.264}$$

Again, only the terms with $j = k$ contribute since $\sigma_-\sigma_+ = \sigma_{\text{gg}}$. Using $\sigma_-\sigma_y = -i(\sigma_-\sigma_+ - \sigma_-\sigma_-) = -i\sigma_{\text{gg}}$, $\sigma_{\text{gg}}\sigma_+ = 0$, $\sigma_{\text{gg}}\sigma_y = -i(\sigma_{\text{gg}}\sigma_+ - \sigma_{\text{gg}}\sigma_-) = i\sigma_-$ and $\sigma_y\sigma_{\text{gg}} = -i\sigma_+$, we obtain

$$\begin{aligned}\mathcal{L}^\dagger_{\Gamma}[S_y] &= \frac{\Gamma}{4}\sum_{k=1}^{N}\left(2\sigma_-^{(k)}\sigma_y^{(k)}\sigma_+^{(k)} - \sigma_{\text{gg}}^{(k)}\sigma_y^{(k)} - \sigma_y^{(k)}\sigma_{\text{gg}}^{(k)}\right) \\ &= -\frac{\Gamma}{4}\sum_{k=1}^{N}(-i)\left(\sigma_+^{(k)} - \sigma_-^{(k)}\right) = -\frac{\Gamma_\uparrow}{4}\sum_{k=1}^{N}\sigma_y^{(k)} = -\frac{\Gamma_\uparrow}{2}S_y.\end{aligned} \tag{E.265}$$

Additionally taking spontaneous decay into account (cf. App. E.1.1), the differential equation for the first moment is given by

$$\partial_t\left\langle S_y(\phi,t)\right\rangle = \text{Tr}\Big(\mathcal{L}^\dagger_{\Gamma}[S_y]\rho(\phi)\Big) + \text{Tr}\Big(\mathcal{L}^\dagger_{\Gamma_\uparrow}[S_y]\rho(\phi)\Big) = -\frac{\Gamma+\Gamma_\uparrow}{2}\left\langle S_y(\phi,t)\right\rangle \tag{E.266}$$

with solution

$$\left\langle S_y(\phi,T)\right\rangle = e^{-\frac{\Gamma+\Gamma_\uparrow}{2}T}\left\langle S_y(\phi)\right\rangle. \tag{E.267}$$

For the second moment, we proceed analogously.

$$\begin{aligned}\mathcal{L}^{\dagger}_{\Gamma_\uparrow}[S_y^2] &= \frac{1}{4}\sum_{j,k,l=1}^{N}\mathcal{L}^{\dagger(k)}_{\Gamma_\uparrow}[\sigma_y^{(j)}\sigma_y^{(l)}] \\ &= \frac{1}{4}\sum_{k}\mathcal{L}^{\dagger(k)}_{\Gamma_\uparrow}[\underbrace{\sigma_y^{(k)}\sigma_y^{(k)}}_{=\mathbb{1}^{(k)}}] + \frac{1}{4}\sum_{k\neq j}\mathcal{L}^{\dagger(k)}_{\Gamma_\uparrow}[\sigma_y^{(j)}\sigma_y^{(k)}] + \frac{1}{4}\sum_{k\neq l}\mathcal{L}^{\dagger(k)}_{\Gamma_\uparrow}[\sigma_y^{(k)}\sigma_y^{(l)}] \\ &+ \frac{1}{4}\sum_{j\neq k,k\neq l,j\neq l}^{N}\mathcal{L}^{\dagger(k)}_{\Gamma_\uparrow}[\sigma_y^{(j)}\sigma_y^{(l)}]\end{aligned} \tag{E.268}$$

The first and last term vanish, since the corresponding operators commute with the terms of the Lindblad (super-)operator. The second and third expression are identical apart from a relabeling of the indices $j \leftrightarrow l$. Hence,

$$\begin{aligned}\mathcal{L}_{\Gamma_\uparrow}[S_y^2] &= \frac{1}{2}\sum_{k\neq j}\mathcal{L}^{\dagger(k)}_{\Gamma_\uparrow}[\sigma_y^{(k)}\sigma_y^{(j)}] \\ &= \frac{1}{2}\sum_{k\neq j}\sigma_y^{(j)}\underbrace{\mathcal{L}^{\dagger(k)}_{\Gamma_\uparrow}[\sigma_y^{(k)}]}_{=-\frac{\Gamma_\uparrow}{2}\sigma_y^{(k)}} \\ &= -\frac{\Gamma_\uparrow}{4}\sum_{k\neq j}\sigma_y^{(j)}\sigma_y^{(k)}.\end{aligned} \tag{E.269}$$

Explicitly expanding S_y^2 according to

$$S_y^2 = \frac{1}{4}\sum_{j,k}\sigma_y^{(j)}\sigma_y^{(k)} = \frac{1}{4}\sum_{k}\underbrace{\sigma_y^{(k)}\sigma_y^{(k)}}_{=\mathbb{1}^{(k)}} + \frac{1}{4}\sum_{j\neq k}\sigma_y^{(j)}\sigma_y^{(k)}, \tag{E.270}$$

which is equivalent to

$$\frac{1}{4}\sum_{j\neq k}\sigma_y^{(j)}\sigma_y^{(k)} = S_y^2 - \frac{N}{4}\mathbb{1}, \tag{E.271}$$

yielding

$$\mathcal{L}^{\dagger}_{\Gamma_\uparrow}[S_y^2] = -\Gamma_\uparrow S_y^2 + \frac{N}{4}\Gamma\mathbb{1}. \tag{E.272}$$

As a result, the differential equation for the second moment is given by

$$\begin{aligned}\partial_t\left\langle S_y^2(\phi,t)\right\rangle &= \mathrm{Tr}\Big(\mathcal{L}^{\dagger}_{\Gamma}[S_y^2]\rho(\phi)\Big) + \mathrm{Tr}\Big(\mathcal{L}^{\dagger}_{\Gamma_\uparrow}[S_y^2]\rho(\phi)\Big) \\ &= -(\Gamma+\Gamma_\uparrow)\left\langle S_y^2(\phi,t)\right\rangle + \frac{N}{4}(\Gamma+\Gamma_\uparrow).\end{aligned} \tag{E.273}$$

Therefore, we obtain

$$\left\langle S_y^2(\phi,T)\right\rangle = \frac{N}{4}\left[1-e^{-(\Gamma+\Gamma_\uparrow)T}\right] + e^{-(\Gamma+\Gamma_\uparrow)T}\left\langle S_y^2((\phi)\right\rangle. \tag{E.274}$$

Consequently, incoherent pumping has the same effect on projective spin measurements as spontaneous decay and individual dephasing. Ultimately, the phase estimation uncertainty reads

$$(\Delta\phi(T))^2 = \frac{\frac{N}{4}\left[e^{(\Gamma+\Gamma_\uparrow)T}-1\right] + (\Delta S_y)^2}{\langle S_x\rangle^2}, \tag{E.275}$$

where the expectation value $\langle S_x\rangle$ and variance $(\Delta S_y)^2$ depend on the specific initial state. In particular, for CSS we obtain

$$(\Delta\phi_{\text{CSS}}(T))^2 = \frac{e^{(\Gamma+\Gamma_\uparrow)T}}{N} \tag{E.276}$$

$$T_{\text{CSS}} = \frac{1}{\Gamma+\Gamma_\uparrow} \tag{E.277}$$

$$(\Delta\omega_{\text{CSS}})^2 = \frac{e(\Gamma+\Gamma_\uparrow)}{\tau N}. \tag{E.278}$$

As argued in the main text, this result represents the standard quantum limit (SQL).

E.10.4 Parity measurement

We can proceed analogously for the parity measurement $\Pi = (-1)^N\sigma_x^{\otimes N}$. With $\sigma_-\sigma_x = \sigma_{\text{gg}}$, $\sigma_{\text{gg}}\sigma_+ = 0$, $\sigma_{\text{gg}}\sigma_x = \sigma_-$ and $\sigma_x\sigma_{\text{gg}} = \sigma_+$, we obtain

$$\begin{aligned}
\mathcal{L}^\dagger_{\Gamma_\uparrow}[\Pi] &= (-1)^N\frac{\Gamma_\uparrow}{2}\sum_{k=1}^{N} 2\sigma_-^{(k)}\sigma_x^{\otimes N}\sigma_+^{(k)} - \sigma_{\text{gg}}^{(k)}\sigma_x^{\otimes N} - \sigma_x^{\otimes N}\sigma_{\text{gg}}^{(k)} \\
&= (-1)^N\frac{\Gamma_\uparrow}{2}\sum_{k=1}^{N} -\sigma_x^{\otimes k-1}\otimes\sigma_-^{(k)}\otimes\sigma_x^{\otimes N-k} - \sigma_x^{\otimes k-1}\otimes\sigma_+^{(k)}\otimes\sigma_x^{\otimes N-k} \\
&= -(-1)^N\frac{\Gamma_\uparrow N}{2}\sigma_x^{\otimes N} = -\frac{\Gamma_\uparrow N}{2}\Pi.
\end{aligned} \tag{E.279}$$

Consequently, incoherent pumping also has the same effect as spontaneous decay and individual dephasing with regard to parity measurements, resulting in the phase estimation uncertainty

$$(\Delta\phi(T))^2 = \frac{e^{(\Gamma+\Gamma_\uparrow)Nt} - \langle\Pi(\phi)\rangle^2}{(\partial_\phi\langle\Pi(\phi)\rangle_\phi)^2}\Big|_{\phi=\phi_0}. \tag{E.280}$$

For a GHZ state, we finally determine

$$\begin{aligned}(\Delta\phi_{\mathrm{parity-GHZ}}(T))^2 &= \frac{e^{(\Gamma+\Gamma_\uparrow)NT}}{N^2} &\text{(E.281)}\\ T_{\mathrm{parity-GHZ}} &= \frac{1}{N}\frac{1}{\Gamma+\Gamma_\uparrow} &\text{(E.282)}\\ (\Delta\omega_{\mathrm{parity-GHZ}})^2 &= \frac{(\Gamma+\Gamma_\uparrow)e}{N\tau}. &\text{(E.283)}\end{aligned}$$

This minimal frequency estimation uncertainty is equivalent to the SQL, however it is achieved at a N-times shorter interrogation time.

E.10.5 Heralded-(u)GHZ protocol

For the protocols with GHZ(-like) states, we consider the initial state

$$\rho_{\mathrm{in}} = \rho_{\mathrm{gg}}^{(N)}|{\downarrow}\rangle\langle{\downarrow}|^{\otimes N} + \rho_{\mathrm{eg}}^{(N)}\left[|{\downarrow}\rangle\langle{\uparrow}|^{\otimes N} + |{\uparrow}\rangle\langle{\downarrow}|^{\otimes N}\right] + \rho_{\mathrm{ee}}^{(N)}|{\uparrow}\rangle\langle{\uparrow}|^{\otimes N}, \tag{E.284}$$

where we assume that $\rho_{\mathrm{eg}}^{(N)} = \rho_{\mathrm{ge}}^{(N)}$. The time evolved state is given by

$$\begin{aligned}\rho_{\mathrm{in}}(\phi,T) = {}& \frac{\rho_{\mathrm{gg}}^{(N)}}{\Gamma+\Gamma_\uparrow}\left(\left[\Gamma+\Gamma_\uparrow e^{-(\Gamma+\Gamma_\uparrow)T}\right]|{\downarrow}\rangle\langle{\downarrow}| + \Gamma_\uparrow\left[1-e^{-(\Gamma+\Gamma_\uparrow)T}\right]|{\uparrow}\rangle\langle{\uparrow}|\right)^{\otimes N}\\ &+ \rho_{\mathrm{eg}}^{(N)}e^{-\frac{\Gamma+\Gamma_\uparrow}{2}T}\left[e^{iN\phi}|{\downarrow}\rangle\langle{\uparrow}|^{\otimes N} + e^{-iN\phi}|{\uparrow}\rangle\langle{\downarrow}|^{\otimes N}\right] \qquad\text{(E.285)}\\ &+ \frac{\rho_{\mathrm{ee}}^{(N)}}{\Gamma+\Gamma_\uparrow}\left(\left[\Gamma e^{-(\Gamma+\Gamma_\uparrow)NT}+\Gamma_\uparrow\right]|{\uparrow}\rangle\langle{\uparrow}| + \Gamma\left[1-e^{-(\Gamma+\Gamma_\uparrow)T}\right]|{\downarrow}\rangle\langle{\downarrow}|\right)^{\otimes N}.\end{aligned}$$

Application of the measurement transformation $\mathcal{U}^\dagger_{\text{GHZ}}$ results in the final state

$$\begin{aligned}
\rho^f_{\text{in}}(\phi,T) = \frac{\rho^{(N)}_{\text{gg}}}{2}\frac{1}{\Gamma+\Gamma_\uparrow}\Bigg\{ & \left(\left[\Gamma+\Gamma_\uparrow e^{-(\Gamma+\Gamma_\uparrow)T}\right]|\downarrow\rangle\langle\downarrow| + \Gamma_\uparrow\left[1-e^{-(\Gamma+\Gamma_\uparrow)T}\right]|\uparrow\rangle\langle\uparrow|\right)^{\otimes N} \\
&+ (-i)^{N+E}\left(\left[\Gamma+\Gamma_\uparrow e^{-(\Gamma+\Gamma_\uparrow)T}\right]|\uparrow\rangle\langle\downarrow| + \Gamma_\uparrow\left[1-e^{-(\Gamma+\Gamma_\uparrow)T}\right]|\downarrow\rangle\langle\uparrow|\right)^{\otimes N} \\
&+ i^{N+E}\left(\left[\Gamma+\Gamma_\uparrow e^{-(\Gamma+\Gamma_\uparrow)T}\right]|\downarrow\rangle\langle\uparrow| + \Gamma_\uparrow\left[1-e^{-(\Gamma+\Gamma_\uparrow)T}\right]|\uparrow\rangle\langle\downarrow|\right)^{\otimes N} \\
&+ \left(\left[\Gamma+\Gamma_\uparrow e^{-(\Gamma+\Gamma_\uparrow)T}\right]|\uparrow\rangle\langle\uparrow| + \Gamma_\uparrow\left[1-e^{-(\Gamma+\Gamma_\uparrow)T}\right]|\downarrow\rangle\langle\downarrow|\right)^{\otimes N}\Bigg\} \\
&+ \frac{\rho^{(N)}_{\text{eg}}}{2}e^{-\frac{\Gamma+\Gamma_\uparrow}{2}NT} \\
&\times\Big[e^{iN\phi}\Big\{|\downarrow\rangle\langle\uparrow|^{\otimes N} + (-i)^{N+E}|\uparrow\rangle\langle\uparrow|^{\otimes N} + i^{N+E}|\downarrow\rangle\langle\downarrow|^{\otimes N} + |\uparrow\rangle\langle\downarrow|^{\otimes N}\Big\} \\
&+ e^{-iN\phi}\Big\{|\uparrow\rangle\langle\downarrow|^{\otimes N} + (-i)^{N+E}|\downarrow\rangle\langle\downarrow|^{\otimes N} + i^{N+E}|\uparrow\rangle\langle\uparrow|^{\otimes N} + |\downarrow\rangle\langle\uparrow|^{\otimes N}\Big\}\Big] \\
&+ \frac{\rho^{(N)}_{\text{ee}}}{2}\frac{1}{\Gamma+\Gamma_\uparrow}\Bigg\{\left(\left[\Gamma e^{-(\Gamma+\Gamma_\uparrow)T}+\Gamma_\uparrow\right]|\uparrow\rangle\langle\uparrow| + \Gamma\left[1-e^{-(\Gamma+\Gamma_\uparrow)T}\right]|\downarrow\rangle\langle\downarrow|\right)^{\otimes N} \\
&+ (-i)^{N+E}\left(\left[\Gamma e^{-(\Gamma+\Gamma_\uparrow)T}+\Gamma_\uparrow\right]|\downarrow\rangle\langle\uparrow| + \Gamma\left[1-e^{-(\Gamma+\Gamma_\uparrow)T}\right]|\uparrow\rangle\langle\downarrow|\right)^{\otimes N} \\
&+ i^{N+E}\left(\left[\Gamma e^{-(\Gamma+\Gamma_\uparrow)T}+\Gamma_\uparrow\right]|\uparrow\rangle\langle\downarrow| + \Gamma\left[1-e^{-(\Gamma+\Gamma_\uparrow)T}\right]|\downarrow\rangle\langle\uparrow|\right)^{\otimes N} \\
&+ \left(\left[\Gamma e^{-(\Gamma+\Gamma_\uparrow)T}+\Gamma_\uparrow\right]|\downarrow\rangle\langle\downarrow| + \Gamma\left[1-e^{-(\Gamma+\Gamma_\uparrow)T}\right]|\uparrow\rangle\langle\uparrow|\right)^{\otimes N}\Bigg\}.
\end{aligned}\tag{E.286}$$

From the final state, we can directly read off the conditional probabilities. In particular, only the conditional probabilities for the maximal Dicke states are required.

$$\begin{aligned}
P\left(x=\pm\tfrac{N}{2}|\phi\right) = \frac{\rho^{(N)}_{\text{gg}}}{2}\frac{1}{(\Gamma+\Gamma_\uparrow)^N}&\left[\left(\Gamma+\Gamma_\uparrow e^{-(\Gamma+\Gamma_\uparrow)T}\right)^N + \Gamma_\uparrow^N\left(1-e^{-(\Gamma+\Gamma_\uparrow)T}\right)^N\right] \\
&+ \frac{\rho^{(N)}_{\text{eg}}}{2}e^{-\frac{\Gamma+\Gamma_\uparrow}{2}NT}\left[e^{iN\phi}(\mp i)^{N+E} + e^{-iN\phi}(\pm i)^{N+E}\right] \\
&+ \frac{\rho^{(N)}_{\text{ee}}}{2}\frac{1}{(\Gamma+\Gamma_\uparrow)^N}\left[\left(\Gamma e^{-(\Gamma+\Gamma_\uparrow)T}+\Gamma_\uparrow\right)^N + \Gamma^N\left(1-e^{-(\Gamma+\Gamma_\uparrow)T}\right)^N\right]
\end{aligned}\tag{E.287}$$

Since $N+E$ is odd, this can be expressed as

$$\begin{aligned}
P\left(x=\pm\tfrac{N}{2}|\phi\right) = \frac{\rho^{(N)}_{\text{gg}}}{2}\frac{1}{(\Gamma+\Gamma_\uparrow)^N}&\left[\left(\Gamma+\Gamma_\uparrow e^{-(\Gamma+\Gamma_\uparrow)T}\right)^N + \Gamma_\uparrow^N\left(1-e^{-(\Gamma+\Gamma_\uparrow)T}\right)^N\right] \\
&+ \frac{\rho^{(N)}_{\text{ee}}}{2}\frac{1}{(\Gamma+\Gamma_\uparrow)^N}\left[\left(\Gamma e^{-(\Gamma+\Gamma_\uparrow)T}+\Gamma_\uparrow\right)^N + \Gamma^N\left(1-e^{-(\Gamma+\Gamma_\uparrow)T}\right)^N\right] \\
&\mp 2i^{N+E+1}\frac{\rho^{(N)}_{\text{eg}}}{2}e^{-\frac{\Gamma+\Gamma_\uparrow}{2}NT}\sin(N\phi).
\end{aligned}\tag{E.288}$$

Thus, the signal is determined by

$$\begin{aligned}\langle X(\phi,T)\rangle &= \frac{N}{2}\left[P\left(x=\tfrac{N}{2}|\phi\right)-P\left(x=-\tfrac{N}{2}|\phi\right)\right]\\ &= -4i^{N+E+1}\frac{N}{2}\frac{\rho_{\text{eg}}^{(N)}}{2}e^{-\frac{\Gamma+\Gamma_{\uparrow}}{2}NT}\sin(N\phi)\\ &= -i^{N+E+1}N\rho_{\text{eg}}^{(N)}e^{-\frac{\Gamma+\Gamma_{\uparrow}}{2}T}\sin(N\phi)\end{aligned} \tag{E.289}$$

and the slope is given by

$$\partial_{\phi}\langle X(\phi,T)\rangle = -i^{N+E+1}N^{2}\rho_{\text{eg}}^{(N)}e^{-\frac{\Gamma+\Gamma_{\uparrow}}{2}NT}\cos(N\phi), \tag{E.290}$$

which is maximized for the optimal working point $\phi_0 = 0$. Ultimately, the phase estimation uncertainty is obtained

$$\begin{aligned}(\Delta\phi(T))^{2} &= \frac{N^{2}}{4}\frac{P\left(x=+\frac{N}{2}|\phi\right)+P\left(x=-\frac{N}{2}|\phi\right)}{|\partial_{\phi}\langle X(\phi,T)\rangle|^{2}}\Bigg|_{\phi=\phi_0}\\ &= \frac{e^{(\Gamma+\Gamma_{\uparrow})NT}}{4N^{2}(\rho_{\text{eg}}^{(N)})^{2}}\frac{1}{(\Gamma+\Gamma_{\uparrow})^{N}}\left\{\rho_{\text{gg}}^{(N)}\left[\left(\Gamma+\Gamma_{\uparrow}e^{-(\Gamma+\Gamma_{\uparrow})T}\right)^{N}+\Gamma_{\uparrow}^{N}\left(1-e^{-(\Gamma+\Gamma_{\uparrow})T}\right)^{N}\right]\right.\\ &\quad\left.+\rho_{\text{ee}}^{(N)}\left[\left(\Gamma e^{-(\Gamma+\Gamma_{\uparrow})T}+\Gamma_{\uparrow}\right)^{N}+\Gamma^{N}\left(1-e^{-(\Gamma+\Gamma_{\uparrow})T}\right)^{N}\right]\right\}.\end{aligned} \tag{E.291}$$

Heralded-GHZ protocol— For the GHZ state, the matrix elements of the initial state are given by $\rho_{\text{gg}}^{(N)} = \rho_{\text{ee}}^{(N)} = \rho_{\text{eg}}^{(N)} = \frac{1}{2}$ and thus, the phase estimation uncertainty reads

$$\begin{aligned}(\Delta\phi_{\text{heralded}-\text{GHZ}}(T))^{2} = \frac{e^{(\Gamma+\Gamma_{\uparrow})NT}}{2N^{2}}\frac{1}{(\Gamma+\Gamma_{\uparrow})^{N}}\Big[&\left(\Gamma+\Gamma_{\uparrow}e^{-(\Gamma+\Gamma_{\uparrow})T}\right)^{N}\\ &+\left(\Gamma e^{-(\Gamma+\Gamma_{\uparrow})T}+\Gamma_{\uparrow}\right)^{N}+(\Gamma^{N}+\Gamma_{\uparrow}^{N})\left(1-e^{-(\Gamma+\Gamma_{\uparrow})T}\right)^{N}\Big].\end{aligned} \tag{E.292}$$

For $\Gamma_{\uparrow} = 0$, we reproduce the result without incoherent pumping, as given by Eq. (E.164). Furthermore, for $\Gamma = 0$, we obtain the analogous result with $\Gamma_{\uparrow}$ replacing Γ, which is further explained in the main text (cf. Sec. 3.10.1).

Heralded-uGHZ protocol— According to Eq. (E.175), the matrix elements for the uGHZ state are given by $\rho_{\text{gg}}^{(N)} = \sin^{2}\left(\frac{\theta N}{2}\right)$, $\rho_{\text{ee}}^{(N)} = \cos^{2}\left(\frac{\theta N}{2}\right)$ and $\rho_{\text{ge}}^{(N)} = \rho_{\text{eg}}^{(N)} =$

$-i^{N+E+1}\sin\left(\frac{\theta N}{2}\right)\cos\left(\frac{\theta N}{2}\right)$. Hence, the phase estimation uncertainty is determined by

$$\begin{aligned}(\Delta\phi(T))^2 &= \frac{e^{(\Gamma+\Gamma_\uparrow)NT}}{4N^2\sin^2\left(\frac{\theta N}{2}\right)\cos^2\left(\frac{\theta N}{2}\right)}\frac{1}{(\Gamma+\Gamma_\uparrow)^N} \\ &\times\Big\{\sin^2\left(\tfrac{\theta N}{2}\right)\left[\left(\Gamma+\Gamma_\uparrow e^{-(\Gamma+\Gamma_\uparrow)T}\right)^N+\Gamma_\uparrow^N\left(1-e^{-(\Gamma+\Gamma_\uparrow)T}\right)^N\right] \\ &+\cos^2\left(\tfrac{\theta N}{2}\right)\left[\left(\Gamma e^{-(\Gamma+\Gamma_\uparrow)T}+\Gamma_\uparrow\right)^N+\Gamma^N\left(1-e^{-(\Gamma+\Gamma_\uparrow)T}\right)^N\right]\Big\} \\ &= \frac{e^{(\Gamma+\Gamma_\uparrow)NT}}{4N^2}\frac{1}{(\Gamma+\Gamma_\uparrow)^N} \\ &\times\Big\{\frac{1}{\cos^2\left(\frac{\theta N}{2}\right)}\left[\left(\Gamma+\Gamma_\uparrow e^{-(\Gamma+\Gamma_\uparrow)T}\right)^N+\Gamma_\uparrow^N\left(1-e^{-(\Gamma+\Gamma_\uparrow)T}\right)^N\right] \\ &+\frac{1}{\sin^2\left(\frac{\theta N}{2}\right)}\left[\left(\Gamma e^{-(\Gamma+\Gamma_\uparrow)T}+\Gamma_\uparrow\right)^N+\Gamma^N\left(1-e^{-(\Gamma+\Gamma_\uparrow)T}\right)^N\right]\Big\}.\end{aligned} \tag{E.293}$$

As before, the optimal rotation angle θ_{opt} can be evaluated analytically to read

$$\theta_{\text{opt}} = \frac{2}{N}\arctan\left(\sqrt[4]{\frac{\left(\Gamma e^{-(\Gamma+\Gamma_\uparrow)T}+\Gamma_\uparrow\right)^N+\Gamma^N\left(1-e^{-(\Gamma+\Gamma_\uparrow)T}\right)^N}{\left(\Gamma+\Gamma_\uparrow e^{-(\Gamma+\Gamma_\uparrow)T}\right)^N+\Gamma_\uparrow^N\left(1-e^{-(\Gamma+\Gamma_\uparrow)T}\right)^N}}\right). \tag{E.294}$$

Using the trigonometric identities

$$\sin^2(x) = \frac{\tan^2(x)}{1+\tan^2(x)} \tag{E.295}$$

$$\cos^2(x) = \frac{1}{1+\tan^2(x)} \tag{E.296}$$

and rewriting $\theta_{\text{opt}} = \frac{2}{N}\arctan\left(\sqrt[4]{\frac{\beta}{\alpha}}\right)$, with

$$\alpha = \left(\Gamma+\Gamma_\uparrow e^{-(\Gamma+\Gamma_\uparrow)T}\right)^N+\Gamma_\uparrow^N\left(1-e^{-(\Gamma+\Gamma_\uparrow)T}\right)^N \tag{E.297}$$

$$\beta = \left(\Gamma e^{-(\Gamma+\Gamma_\uparrow)T}+\Gamma_\uparrow\right)^N+\Gamma^N\left(1-e^{-(\Gamma+\Gamma_\uparrow)T}\right)^N, \tag{E.298}$$

we can express the phase estimation uncertainty as

$$\begin{aligned}(\Delta\phi(T))^2 &= \frac{e^{(\Gamma+\Gamma_\uparrow)NT}}{4N^2}\frac{1}{(\Gamma+\Gamma_\uparrow)^N}\left[1+\tan^2\left(\tfrac{\theta_{\text{opt}}N}{2}\right)\right]\left[\alpha+\frac{\beta}{\tan^2\left(\frac{\theta_{\text{opt}}N}{2}\right)}\right] \\ &= \frac{e^{(\Gamma+\Gamma_\uparrow)NT}}{4N^2}\frac{1}{(\Gamma+\Gamma_\uparrow)^N}\left[1+\sqrt{\frac{\beta}{\alpha}}\right]\left[\alpha+\frac{\beta}{\sqrt{\frac{\beta}{\alpha}}}\right] \\ &= \frac{e^{(\Gamma+\Gamma_\uparrow)NT}}{4N^2}\frac{1}{(\Gamma+\Gamma_\uparrow)^N}\alpha\left[1+\sqrt{\frac{\beta}{\alpha}}\right]^2.\end{aligned} \tag{E.299}$$

Ultimately, we obtain

$$(\Delta\phi(T))^2 = \frac{e^{(\Gamma+\Gamma_\uparrow)NT}}{4N^2}\frac{\left(\Gamma+\Gamma_\uparrow e^{-(\Gamma+\Gamma_\uparrow)T}\right)^N+\Gamma_\uparrow^N\left(1-e^{-(\Gamma+\Gamma_\uparrow)T}\right)^N}{(\Gamma+\Gamma_\uparrow)^N}$$
$$\times\left[1+\sqrt{\frac{\left(\Gamma e^{-(\Gamma+\Gamma_\uparrow)T}+\Gamma_\uparrow\right)^N+\Gamma^N\left(1-e^{-(\Gamma+\Gamma_\uparrow)T}\right)^N}{\left(\Gamma+\Gamma_\uparrow e^{-(\Gamma+\Gamma_\uparrow)T}\right)^N+\Gamma_\uparrow^N\left(1-e^{-(\Gamma+\Gamma_\uparrow)T}\right)^N}}\right]^2 .$$

Again, for $\Gamma_\uparrow = 0$, we reproduce the result without incoherent pumping, as determined by Eq. (E.212). Although not directly apparent, for $\Gamma = 0$, we also obtain the analogous result with $\Gamma_\uparrow$ replacing Γ, as argued in the main text (cf. Sec. 3.10.1).

E.11 Spontaneous decay events as erasure errors

In the following, we derive the results presented in Sec. 3.10.2. Specifically, we apply the framework of quantum trajectories (cf. Sec. 3.7.4) to CSS in the presence of spontaneous decay in App. E.11.1. Furthermore, we convert quantum jumps into erasure errors and determine the frequency estimation uncertainty in App. E.11.2, following the fundamental approach introduced in Ref. [190].

E.11.1 Spontaneous decay events in CSS

Since the individual particles in a CSS are independent and identical, it is sufficient to study the dynamics of a single particle. Starting from the initial state

$$\rho^{(1)}_{\mathrm{CSS}} = \frac{1}{2}\left[|\downarrow\rangle\langle\downarrow| + |\downarrow\rangle\langle\uparrow| + |\uparrow\rangle\langle\downarrow| + |\uparrow\rangle\langle\uparrow|\right], \tag{E.300}$$

the mixture after free evolution time T consists of two terms, reflecting either the absence of any spontaneous decay events or the occurrence of exactly one. With the continuous non-unitary evolution $\mathcal{G}$ and discrete jumps $\mathcal{J}$, as defined in App. E.9, we obtain

$$\begin{aligned}\tilde{\rho}^{(1)}_0(\phi,T) &= \mathcal{G}(T,0)\rho^{(1)}_{\mathrm{CSS}}\\ &= \frac{1}{2}\left[|\downarrow\rangle\langle\downarrow| + e^{-\frac{\Gamma T}{2}}\left(e^{i\phi}|\downarrow\rangle\langle\uparrow| + e^{-i\phi}|\uparrow\rangle\langle\downarrow|\right) + e^{-\Gamma T}|\uparrow\rangle\langle\uparrow|\right] \qquad \text{(E.301)}\\ p^{(1)}_0(\phi,T) &= \frac{1}{2}\left[1+e^{-\Gamma T}\right] \qquad \text{(E.302)}\\ \rho^{(1)}_0(\phi,T) &= \frac{1}{1+e^{-\Gamma T}}\left[|\downarrow\rangle\langle\downarrow| + e^{-\frac{\Gamma T}{2}}\left(e^{i\phi}|\downarrow\rangle\langle\uparrow| + e^{-i\phi}|\uparrow\rangle\langle\downarrow|\right) + e^{-\Gamma T}|\uparrow\rangle\langle\uparrow|\right] \qquad \text{(E.303)}\end{aligned}$$

and

$$\begin{aligned}\tilde{\rho}_1^{(1)}(\phi,T) &= \int_0^T \mathrm{d}t_1 \mathcal{G}(T,t_1)\mathcal{J}\mathcal{G}(t_1,0)\rho_{\mathrm{CSS}}^{(1)} \\ &= \frac{1}{2}\Gamma \int_0^T \mathrm{d}t_1 e^{-\Gamma t_1} \left|\downarrow\right\rangle\left\langle\downarrow\right| \qquad \text{(E.304)} \\ &= \frac{1}{2}\left(1-e^{-\Gamma T}\right)\left|\downarrow\right\rangle\left\langle\downarrow\right| \end{aligned}$$

$$p_1^{(1)}(\phi,T) = \frac{1}{2}\left[1-e^{-\Gamma T}\right] \qquad \text{(E.305)}$$

$$\rho_1^{(1)}(\phi,T) = \left|\downarrow\right\rangle\left\langle\downarrow\right|. \qquad \text{(E.306)}$$

Consequently, the N-particle CSS after the free evolution time can be expressed as the mixture given by

$$\rho_{\mathrm{CSS}}(\phi,T) = \sum_{k=0}^{N} p_k(\phi,T)\rho_k(\phi,T) \qquad \text{(E.307)}$$

$$p_k(\phi,T) = \binom{N}{k}\left[p_0^{(1)}(\phi,T)\right]^{N-k}\left[p_1^{(1)}(\phi,T)\right]^{k} \qquad \text{(E.308)}$$

$$= \frac{1}{2^N}\binom{N}{k}\left[1+e^{-\Gamma T}\right]^{N-k}\left[1-e^{-\Gamma T}\right]^{k} \qquad \text{(E.309)}$$

$$\rho_k(\phi,T) = \frac{1}{\binom{N}{k}}\mathcal{P}\left(\left[\rho_0^{(1)}(\phi,T)\right]^{\otimes N-k}\otimes\left[\rho_1^{(1)}(\phi,T)\right]^{\otimes k}\right), \qquad \text{(E.310)}$$

where $\mathcal{P}$ denotes the permutation operator generating the $\binom{N}{k}$ permutations.

E.11.2 Conversion of spontaneous decay events into erasure errors

As argued in the main text, we aim to explore the advantages of converting spontaneous decay events into erasure errors. In this approach, the particles that decayed – characterized by the state $\rho_1^{(1)}$ – are effectively taken out of the clock space without perturbing the remaining particles. The corresponding state is given by

$$\rho_k(\phi,T) = \frac{1}{\binom{N}{k}}\mathcal{P}\left(\left[\rho_0^{(1)}(\phi,T)\right]^{\otimes N-k}\otimes\left|-1\right\rangle\left\langle-1\right|^{\otimes k}\right). \qquad \text{(E.311)}$$

As the k particles in the state $|-1\rangle\langle-1|$ no longer contribute in the Ramsey sequence, they can be traced out and we effectively obtain

$$\rho_k(\phi,T) = \left[\rho_0^{(1)}(\phi,T)\right]^{\otimes N-k}. \qquad \text{(E.312)}$$

Note, however, that $\rho_k(\phi,T)$ now represents a $N-k$-particle state.

Using Eq. (E.99) with $a = \frac{e^{-\Gamma T}}{1+e^{\Gamma T}}$, $c = \frac{1}{1+e^{\Gamma T}}$ and $b = \frac{e^{-\frac{\Gamma T}{2}}}{1+e^{\Gamma T}} e^{-i\phi}$, the QFI of the state $\rho_0^{(1)}$ is determined by

$$\mathcal{F}_Q[\rho_0^{(1)}(\phi, T)] = \frac{4e^{-\Gamma T}}{\left(1 + e^{-\Gamma T}\right)^2}. \tag{E.313}$$

Consequently, due to the additivity of the QFI, we obtain

$$\mathcal{F}_Q[\rho_k(\phi, T)] = (N-k)\mathcal{F}_Q[\rho_0^{(1)}(\phi, T)] = (N-k)\frac{4e^{-\Gamma T}}{\left(1 + e^{-\Gamma T}\right)^2}. \tag{E.314}$$

In the following, we prove that the QFI is saturated by a projective spin measurement with linear estimator. Applying the second $\pi/2$-pulse, given by $\mathcal{R}_x\left(\frac{\pi}{2}\right) = \frac{1}{\sqrt{2}}\left(\mathbb{1} - i\sigma_x\right)$, to the state $\rho_0^{(1)}(\phi, T)$, the final state reads

$$\begin{aligned} \rho_{0,f}^{(1)}(\phi, T) = \frac{1}{2}\frac{1}{1+e^{-\Gamma T}}\Big\{ & |{\downarrow}\rangle\langle{\downarrow}| - i|{\uparrow}\rangle\langle{\downarrow}| + i|{\downarrow}\rangle\langle{\uparrow}| + |{\uparrow}\rangle\langle{\uparrow}| \\ & + e^{-\frac{\Gamma T}{2}}\Big(e^{i\phi}\left[|{\downarrow}\rangle\langle{\uparrow}| - i\,|{\uparrow}\rangle\langle{\uparrow}| + i\,|{\downarrow}\rangle\langle{\downarrow}| + |{\uparrow}\rangle\langle{\downarrow}|\right] + \\ & + e^{-i\phi}\left[|{\uparrow}\rangle\langle{\downarrow}| - i\,|{\downarrow}\rangle\langle{\downarrow}| + i\,|{\uparrow}\rangle\langle{\uparrow}| + |{\downarrow}\rangle\langle{\uparrow}|\right]\Big) \\ & + e^{-\Gamma T}\left[|{\uparrow}\rangle\langle{\uparrow}| - i\,|{\downarrow}\rangle\langle{\uparrow}| + i\,|{\uparrow}\rangle\langle{\downarrow}| + |{\downarrow}\rangle\langle{\downarrow}|\right]\Big\}. \end{aligned} \tag{E.315}$$

Hence, we directly infer the signal

$$\langle S_z(\phi, T)\rangle = \frac{1}{2}\operatorname{tr}\left(\sigma_z \rho_{0,f}^{(1)}(\phi, T)\right) = \frac{1}{2}\frac{1}{1+e^{-\Gamma T}}e^{-\frac{\Gamma T}{2}}\sin(\phi), \tag{E.316}$$

while the second moment trivially reads $\langle S_z^2(\phi, T)\rangle = 1$, since $\sigma_z^2 = \mathbb{1}$. Consequently, we obtain the phase estimation uncertainty at optimal working point $\phi_0 = 0$ given by

$$(\Delta\phi(T))^2 = \left.\frac{\langle S_z^2(\phi, T)\rangle - \langle S_z(\phi, T)\rangle^2}{(\partial_\phi \langle S_z^2(\phi, T)\rangle)^2}\right|_{\phi=\phi_0} = \frac{1}{4}\frac{\left(1+e^{-\Gamma T}\right)^2}{e^{-\Gamma T}}, \tag{E.317}$$

which saturates the QFI.

Finally, we evaluate the QFI of the state $\rho_{\mathrm{CSS}}(\phi, T)$ within the framework in which spontaneous decay events have been converted into erasure errors. Utilizing the convexity of the QFI, we obtain

$$\begin{aligned}
\mathcal{F}_Q[\rho_{\mathrm{CSS}}(\phi,T)] &\leq \sum_{k=0}^{N} p_k(\phi,T)\mathcal{F}_Q[\rho_k(\phi,T)] \\
&= \sum_{k=0}^{N} p_k(\phi,T)(N-k)\mathcal{F}_Q[\rho_0^{(1)}(\phi,T)] \\
&= \frac{4e^{-\Gamma T}}{(1+e^{-\Gamma T})^2}\frac{1}{2^N}\sum_{k=0}^{N}(N-k)\binom{N}{k}\left[1+e^{-\Gamma T}\right]^{N-k}\left[1-e^{-\Gamma T}\right]^{k} \\
&= \frac{4e^{-\Gamma T}}{(1+e^{-\Gamma T})^2}\frac{1}{2^N}\left(N\sum_{k=0}^{N}\binom{N}{k}\left[1+e^{-\Gamma T}\right]^{N-k}\left[1-e^{-\Gamma T}\right]^{k}\right. \\
&\quad \left. -\sum_{k=0}^{N}k\binom{N}{k}\left[1+e^{-\Gamma T}\right]^{N-k}\left[1-e^{-\Gamma T}\right]^{k}\right) \qquad \text{(E.318)} \\
&= \frac{4e^{-\Gamma T}}{(1-e^{-\Gamma T})^2}N\left[1-\frac{1}{2}\left(1-e^{-\Gamma T}\right)\right] \\
&= \frac{4e^{-\Gamma T}}{(1-e^{-\Gamma T})^2}N\frac{1}{2}\left(1+e^{-\Gamma T}\right) \\
&= \frac{2Ne^{-\Gamma T}}{1+e^{-\Gamma T}},
\end{aligned}$$

where we used the binomial theorem and $\sum_{k=0}^{N}k\binom{N}{k}a^{N-k}b^k = bN(a+b)^{N-1}$ in Eq. (E.318). Accordingly, the frequency estimation uncertainty is given by

$$(\Delta\omega(T))^2 \geq \frac{1+e^{-\Gamma T}}{2N\tau Te^{-\Gamma T}} = \frac{e^{\Gamma T}+1}{2N\tau T}. \qquad \text{(E.319)}$$

This expression has the same structure as the frequency estimation uncertainty of the heralded-GHZ protocol in the limit where the N-jump contribution is disregarded (cf. Eq. (E.165)). Hence, the minimal frequency estimation uncertainty can be derived explicitly and expressed using the Lambert-W function. Differentiation with respect to T

$$0 \overset{!}{=} \partial_T(\Delta\omega(T))^2 = \frac{1}{2N\tau}\frac{\Gamma Te^{\Gamma T}-\left(e^{\Gamma T}+1\right)}{T^2} \qquad \text{(E.320)}$$

yields the transcendent equation

$$(\Gamma T_{\mathrm{min}}-1)e^{\Gamma T_{\mathrm{min}}} = 1, \qquad \text{(E.321)}$$

which is equivalent to

$$(\Gamma T_{\mathrm{min}}-1)e^{\Gamma T_{\mathrm{min}}-1} = \frac{1}{e}. \qquad \text{(E.322)}$$

With the formal solution $\Gamma T_{\text{min}} - 1 = W(1/e)$, we derive

$$\begin{aligned}
(\Delta\omega_{\text{min}})^2 &\geq \frac{1}{2N\tau}\frac{e^{\Gamma T_{\text{min}}}+1}{T_{\text{min}}} \\
&= \frac{1}{2N\tau}\frac{(\Gamma T_{\text{min}}-1)e^{\Gamma T_{\text{min}}} + (\Gamma T_{\text{min}}-1)}{(\Gamma T_{\text{min}}-1)T_{\text{min}}} \\
&= \frac{1}{2N\tau}\frac{\Gamma}{\Gamma T_{\text{min}}-1} \\
&= \frac{\Gamma}{2N\tau W(1/e)} \\
&= \frac{(\Delta\omega_{\text{SQL}})^2}{2eW(1/e)},
\end{aligned} \tag{E.323}$$

where we used Eq. (E.321) in the second step. Consequently, converting spontaneous decay events into erasure errors using the CSS results in a constant enhancement compared to the SQL, which, interestingly, is equivalent to the gain achieved by the heralded-GHZ protocol (cf. App. E.7).

F

Derivations of bounds and estimators in Bayesian phase estimation

In this appendix, we present a collection of proofs and derivations from the literature, such as Refs. [68, 140, 151, 161, 162, 169, 200, 209, 211–221], for the lower bounds on the BMSE, as defined in Eq. (4.1). Furthermore, we derive explicit expressions for the linear and optimal Bayesian estimators, as presented in Sec. 4.4.

F.1 Bayesian Cramér-Rao Bound (BCRB)

Assuming standard regularity conditions (cf. Eq. (D.3))

$$\sum_x \frac{\mathrm{d}P(x|\phi)}{\mathrm{d}\phi} = \frac{\mathrm{d}}{\mathrm{d}\phi}\sum_x P(x|\phi) = 0 \tag{F.1}$$

and vanishing of the prior at the boundaries

$$\lim_{\phi\to\pm\infty} \mathcal{P}(\phi) = 0, \tag{F.2}$$

the BCRB reads

$$(\Delta\phi)^2 \geq (\Delta\phi_{\mathrm{BCRB}})^2 = \min_{\phi_{\mathrm{est}}}(\Delta\phi)^2 = \frac{1}{\overline{\mathcal{F}}+\mathcal{I}}. \tag{F.3}$$

Here, the measurement contribution is represented by the Fisher information averaged over the prior distribution

$$\begin{aligned}\overline{\mathcal{F}} \equiv \overline{\mathcal{F}}[\Lambda_{\phi,T}[\rho_{\mathrm{in}}],\{\Pi_x\}] &= \int \mathrm{d}\phi\, \mathcal{P}(\phi)\mathcal{F}[\Lambda_{\phi,T}[\rho_{\mathrm{in}}],\{\Pi_x\}] \\ &= \int \mathrm{d}\phi\, \mathcal{P}(\phi)\sum_x \frac{1}{P(x|\phi)}\left(\frac{\mathrm{d}P(x|\phi)}{\mathrm{d}\phi}\right)^2\end{aligned} \tag{F.4}$$

and

$$\mathcal{I} = \int \mathrm{d}\phi \, \frac{1}{\mathcal{P}(\phi)} \left(\frac{\mathrm{d}\mathcal{P}(\phi)}{\mathrm{d}\phi} \right)^2 \tag{F.5}$$

denotes the information contained in the prior knowledge, given by the Fisher information of the prior distribution.

Proof: The proof is based on Refs. [211, 212]. By defining the function

$$f(\phi, x) = \sqrt{\mathcal{P}(\phi) P(x|\phi)} \, [\phi - \phi_{\mathrm{est}}(x)] \, , \tag{F.6}$$

the BMSE can be expressed as a squared norm

$$(\Delta\phi)^2 = \int \mathrm{d}\phi \sum_x f^2(\phi, x). \tag{F.7}$$

Furthermore, we define

$$g(\phi, x) = \frac{1}{\sqrt{\mathcal{P}(\phi) P(x|\phi)}} \frac{\mathrm{d}\mathcal{P}(\phi) P(x|\phi)}{\mathrm{d}\phi} \tag{F.8}$$

such that

$$\begin{aligned} \int \mathrm{d}\phi \sum_x g^2(\phi, x) &= \int \mathrm{d}\phi \sum_x \frac{1}{\mathcal{P}(\phi) P(x|\phi)} \left(\mathcal{P}(\phi) \frac{\mathrm{d}P(x|\phi)}{\mathrm{d}\phi} + P(x|\phi) \frac{\mathrm{d}\mathcal{P}(\phi)}{\mathrm{d}\phi} \right)^2 \\ &= \int \mathrm{d}\phi \, \mathcal{P}(\phi) \sum_x \frac{1}{P(x|\phi)} \left(\frac{\mathrm{d}P(x|\phi)}{\mathrm{d}\phi} \right)^2 \\ &\quad + \int \mathrm{d}\phi \, \frac{1}{\mathcal{P}(\phi)} \left(\frac{\mathrm{d}\mathcal{P}(\phi)}{\mathrm{d}\phi} \right)^2 \sum_x P(x|\phi) + 2 \int \mathrm{d}\phi \, \frac{\mathrm{d}\mathcal{P}(\phi)}{\mathrm{d}\phi} \sum_x \frac{\mathrm{d}P(x|\phi)}{\mathrm{d}\phi} \\ &= \overline{\mathcal{F}} + \mathcal{I}. \end{aligned} \tag{F.9}$$

In the last step, we introduced the average Fisher information $\overline{\mathcal{F}}$ and prior knowledge $\mathcal{I}$ defined in Eq. (F.4) and Eq. (F.5), respectively. Furthermore, the last term in Eq. (F.9) vanishes as a consequence of the regularity condition Eq. (F.1). Using partial integration, Eq. (F.2) and normalization of the probability distributions, we evaluate

$$\begin{aligned} \int \mathrm{d}\phi \sum_x f(\phi, x) g(\phi, x) &= \int \mathrm{d}\phi \sum_x [\phi - \phi_{\mathrm{est}}(x)] \, \frac{\mathrm{d}\mathcal{P}(\phi) P(x|\phi)}{\mathrm{d}\phi} \\ &= \left[\sum_x [\phi - \phi_{\mathrm{est}}(x)] \, \mathcal{P}(\phi) P(x|\phi) \right]_{-\infty}^{+\infty} - \int \mathrm{d}\phi \, \mathcal{P}(\phi) \sum_x P(x|\phi) \\ &= -1. \end{aligned} \tag{F.10}$$

Finally, application of the Cauchy-Schwarz inequality yields

$$\left(\int \mathrm{d}\phi \sum_x f(\phi,x)g(\phi,x)\right)^2 \leq \left(\int \mathrm{d}\phi \sum_x f^2(\phi,x)\right)\left(\int \mathrm{d}\phi \sum_x g^2(\phi,x)\right) \tag{F.11}$$

which – with the definitions from above – is equivalent to $1 \leq (\Delta\phi)^2\left[\overline{\mathcal{F}}+\mathcal{I}\right]$ and ultimately results in the van Trees inequality Eq. (F.3). □

F.2 Bayesian Quantum Cramér-Rao Bound (BQCRB)

By restricting the measurements – without loss of optimality – to the class of projection-valued measures (PVM) $\Pi_x = |x\rangle\langle x|$, with orthonormal eigenstates $|x\rangle$ of the observable X with eigenvalue x, satisfying $\langle x|x'\rangle = \delta_{x,x'}$, the BQCRB can be expressed as

$$(\Delta\phi_{\mathrm{BQCRB}})^2 = (\delta\phi)^2 - \mathrm{Tr}\big(\overline{\rho}L^2\big). \tag{F.12}$$

Here, the double minimization over the measurement $\{\Pi_x\}$ and estimator ϕ_{est} is combined in a single quantity $L = \sum_x \Pi_x\phi_{\mathrm{est}}(x)$. The optimal L is determined by the implicit equation

$$\overline{\rho}' = \frac{1}{2}\left(\overline{\rho}L + L\overline{\rho}\right), \tag{F.13}$$

where $\overline{\rho} = \int \mathrm{d}\phi\,\mathcal{P}(\phi)\Lambda_{\phi,T}[\rho_{\mathrm{in}}]$ denotes the average state and $\overline{\rho}' = \int \mathrm{d}\phi\,\mathcal{P}(\phi)\Lambda_{\phi,T}[\rho_{\mathrm{in}}]\phi$.
Proof: The proof follows Ref. [151]. We start by rewriting the BMSE as

$$\begin{aligned}(\Delta\phi)^2 &= \int \mathrm{d}\phi\,\mathcal{P}(\phi)\sum_x \mathrm{Tr}\left(\Lambda_{\phi,T}[\rho_{\mathrm{in}}]\Pi_x\right)\left[\phi-\phi_{\mathrm{est}}(x)\right]^2 \\ &= (\delta\phi)^2 + \mathrm{Tr}\left(\int \mathrm{d}\phi\,\mathcal{P}(\phi)\Lambda_{\phi,T}[\rho_{\mathrm{in}}]\sum_x \Pi_x\phi^2_{\mathrm{est}}(x)\right) \\ &\quad - 2\,\mathrm{Tr}\left(\int \mathrm{d}\phi\,\mathcal{P}(\phi)\phi\Lambda_{\phi,T}[\rho_{\mathrm{in}}]\sum_x \Pi_x\phi_{\mathrm{est}}(x)\right) \\ &= (\delta\phi)^2 + \mathrm{Tr}(\overline{\rho}L_2) - 2\,\mathrm{Tr}(\overline{\rho}'L_1),\end{aligned} \tag{F.14}$$

where $(\delta\phi)^2$ represents the variance of the prior distribution, $\overline{\rho} = \int \mathrm{d}\phi\,\mathcal{P}(\phi)\Lambda_{\phi,T}[\rho_{\mathrm{in}}]$ denotes the average state and $\overline{\rho}' = \int \mathrm{d}\phi\,\mathcal{P}(\phi)\Lambda_{\phi,T}[\rho_{\mathrm{in}}]\phi$. Furthermore, we have combined the measurement $\{\Pi_x\}$ and estimator ϕ_{est} by defining the operators $L_1 = \sum_x \Pi_x\phi_{\mathrm{est}}(x)$ and $L_2 = \sum_x \Pi_x\phi^2_{\mathrm{est}}(x)$.

In a first step, following Refs. [151, 161, 213], we demonstrate that – without loss of optimality – the measurement can be restricted to the class of projection-valued measures (PVM), i.e. projective von Neumann measurements $\Pi_x = |x\rangle\langle x|$, with orthonormal eigenstates $|x\rangle$, $\langle x|x'\rangle = \delta_{x,x'}$, of the observable X with eigenvalue x. We denote the projective strategy by $L_{1,2}^{\mathrm{PVM}}$, where $L_1^{\mathrm{PVM}} = L_1 = \sum_x \phi_{\mathrm{est}}(x)\,|x\rangle\langle x|$ effectively corresponds to the eigendecomposition. Based on Eq. (F.14), we have to show that $\mathrm{Tr}\big(\overline{\rho} L_2^{\mathrm{PVM}}\big) \leq \mathrm{Tr}(\overline{\rho} L_2)$ to prove that we do not lose any optimality by restricting to the projective strategy. Using that L_1 is hermitian and $\Pi_x \geq 0$, we can consider the inequality

$$\begin{aligned}\sum_x (\phi_{\mathrm{est}}(x) - L_1)\Pi_x(\phi_{\mathrm{est}}(x) - L_1) &\geq 0\\ \sum_x \phi_{\mathrm{est}}^2(x)\Pi_x - \sum_x \phi_{\mathrm{est}}(x)\Pi_x L_1 - L_1 \sum_x \phi_{\mathrm{est}}(x)\Pi_x + L_1 \sum_x \Pi_x L_1 &\geq 0 \qquad \text{(F.15)}\\ L_2 - L_1^2 &\geq 0\\ L_2 &\geq L_1^2, \qquad \text{(F.16)}\end{aligned}$$

where we have identified L_1 and L_2 in Eq. (F.15) and used the completeness relation $\sum_x \Pi_x = \mathbb{1}$. However, equality in Eq. (F.16) is achieved specifically for the projective strategy, since $L_2^{\mathrm{PVM}} = \sum_x \phi_{\mathrm{est}}^2(x)\,|x\rangle\langle x| = (L_1^{\mathrm{PVM}})^2$. Therefore, $\mathrm{Tr}\big(\overline{\rho} L_2^{\mathrm{PVM}}\big) \leq \mathrm{Tr}(\overline{\rho} L_2)$ and it is always optimal to choose the measurement to be projective.

In a second step, we derive the BQCRB Eq. (F.12). Choosing the projective strategy discussed above and accordingly labeling $L = L_1$ and thus $L_2 = L^2$, the BMSE reads

$$(\Delta\phi)^2 = (\delta\phi)^2 + \mathrm{Tr}\big(\overline{\rho} L^2\big) - 2\,\mathrm{Tr}(\overline{\rho}' L). \qquad \text{(F.17)}$$

Hence, the task of finding the optimal measurement and estimation reduces to the optimization of the operator L, containing both. Variation of L according to $L \mapsto L + \epsilon\delta L$ with infinitesimal parameter ϵ and hermitian δL yields

$$(\Delta\phi)^2 = (\delta\phi)^2 + \mathrm{Tr}\big(\overline{\rho}[L^2 + \epsilon L\delta L + \epsilon\delta L L + \epsilon^2 \delta L^2]\big) - 2\,\mathrm{Tr}(\overline{\rho}'[L + \epsilon\delta L]). \qquad \text{(F.18)}$$

Differentiation with respect to ϵ and evaluation at $\epsilon = 0$ results in

$$0 = \mathrm{Tr}([\overline{\rho} L + L\overline{\rho} - 2\overline{\rho}']\delta L). \qquad \text{(F.19)}$$

Since Eq. (F.19) must hold for any δL, it implies

$$\overline{\rho}' = \frac{1}{2}\left(L\overline{\rho} + \overline{\rho} L\right), \qquad \text{(F.20)}$$

reproducing Eq. (F.13). Substituting this expression for $\overline{\rho}'$ in Eq. (F.17), we find

$$\begin{aligned}(\Delta\phi)^2 &= (\delta\phi)^2 + \mathrm{Tr}\big(\overline{\rho}L^2\big) - 2\,\mathrm{Tr}(\overline{\rho}'L) \\ &= (\delta\phi)^2 + \mathrm{Tr}\big(\overline{\rho}L^2\big) - \mathrm{Tr}\big(\overline{\rho}L^2\big) - \mathrm{Tr}(L\overline{\rho}L) \\ &= (\delta\phi)^2 - \mathrm{Tr}\big(\overline{\rho}L^2\big),\end{aligned} \tag{F.21}$$

which corresponds to the BQCRB Eq. (F.12). □

F.2.1 Unitary phase evolution and Gaussian prior distribution

Assuming a unitary phase evolution according to Eq. (4.4) and a Gaussian prior distribution as defined in Eq. (4.5), the BQCRB can be related to the QFI $\mathcal{F}_Q[\overline{\rho}]$ of the average state $\overline{\rho}$ by

$$(\Delta\phi_{\mathrm{BQCRB}})^2 = (\delta\phi)^2\left[1 - (\delta\phi)^2\mathcal{F}_Q[\overline{\rho}]\right]. \tag{F.22}$$

Proof: The proof is based on Ref. [214]. The unitary phase evolution according to Eq. (4.4) corresponds to the von Neumann equation

$$\partial_\phi\Lambda_{\phi,T}[\rho_{\mathrm{in}}] = -i[S_z, \Lambda_{\phi,T}[\rho_{\mathrm{in}}]]. \tag{F.23}$$

Hence, we can rewrite $\overline{\rho}'$ as

$$\begin{aligned}\overline{\rho}' &= \int \mathrm{d}\phi\, \mathcal{P}(\phi)\phi\Lambda_{\phi,T}[\rho_{\mathrm{in}}] \\ &= -(\delta\phi)^2 \int \mathrm{d}\phi\, (\partial_\phi\mathcal{P}(\phi))\Lambda_{\phi,T}[\rho_{\mathrm{in}}] \\ &= -(\delta\phi)^2\, [\mathcal{P}(\phi)\Lambda_{\phi,T}[\rho_{\mathrm{in}}]]_{-\infty}^{+\infty} + (\delta\phi)^2 \int \mathrm{d}\phi\, \mathcal{P}(\phi)\partial_\phi\Lambda_{\phi,T}[\rho_{\mathrm{in}}] \qquad \text{(F.24)} \\ &= -i(\delta\phi)^2 \left[S_z, \int \mathrm{d}\phi\, \mathcal{P}(\phi)\Lambda_{\phi,T}[\rho_{\mathrm{in}}]\right] \\ &= -i(\delta\phi)^2\, [S_z, \overline{\rho}]\,, \qquad \text{(F.25)}\end{aligned}$$

where we exploited the property $\partial_\phi\mathcal{P}(\phi) = -(\delta\phi)^{-2}\phi\mathcal{P}(\phi)$ of a Gaussian prior distribution. Furthermore, we used partial integration in the second step and Eq. (F.2) as well as Eq. (F.23) in Eq. (F.24). With Eq. (F.13) and Eq. (F.25), we obtain

$$\frac{1}{2}\left(L\overline{\rho} + \overline{\rho}L\right) = -i(\delta\phi)^2\, [S_z, \overline{\rho}]\,. \tag{F.26}$$

Substituting $L := (\delta\phi)^2 L_{\mathrm{local}}$, the BQCRB Eq. (F.12) and the implicit equation Eq. (F.26) become

$$(\Delta\phi)^2 = (\delta\phi)^2\left[1 - (\delta\phi)^2\,\mathrm{Tr}\big(\overline{\rho}L_{\mathrm{local}}^2\big)\right] \tag{F.27}$$

$$\frac{1}{2}\left(L_{\mathrm{local}}\overline{\rho} + \overline{\rho}L_{\mathrm{local}}\right) = -i\,[S_z, \overline{\rho}]\,. \tag{F.28}$$

Comparison to the QFI approach in local phase estimation (cf. App. D.4) shows that L_{local} defines the symmetric logarithmic derivative (SLD) and thus, $\mathrm{Tr}(\overline{\rho} L_{\mathrm{local}}^2) = \mathcal{F}_Q[\overline{\rho}]$ corresponds to the quantum Fisher information of the average state $\overline{\rho}$, resulting in Eq. (F.22). □

F.3 Optimal Quantum Interferometer (OQI)

The optimal quantum interferometer (OQI) represents the ultimate lower bound of the BMSE. However, no general expressions for arbitrary ensemble sizes exist. In this appendix, we derive the explicit expressions for the specific scenarios discussed in the main text (cf. Sec. 4.3.3). In particular, we determine the coherence time limit (CTL) in App. F.3.1. Furthermore, we present an intuitive derivation of the π-corrected Heisenberg limit (πHL) in App. F.3.2, representing the ultimate lower bound in the asymptotic limit. Finally, we introduce the concept of the phase operator based interferometer (POI) in App. F.3.3, which saturates the πHL in the asymptotic regime.

F.3.1 Coherence time limit (CTL)

In the following, we derive Eq. (4.21). Considering a 2π-periodic quantum channel with respect to the phase ϕ as described by Eq. (4.4), the OQI allows for unambiguous phase estimation within the range $[-\pi, +\pi]$. Exceeding this invertible regime, an estimation error is accumulated which increases with the distance from the primary Ramsey fringe. In particular, an estimation error of $\epsilon_k = (2\pi k)^2$ is accumulated if the phase slips in the region $[-(2k+1)\pi, -(2k-1)\pi]$ or $[+(2k-1)\pi, +(2k+1)\pi]$ for $k \in \mathbb{N}$. The estimation error associated with these events can be modeled by

$$(\Delta\phi_{\mathrm{CTL}}^{\mathrm{OQI}})^2 = \sum_{k=1}^{\infty} \epsilon_k P_k, \tag{F.29}$$

which effectively represents the average of the estimation error ϵ_k weighted with its corresponding probability

$$P_k = \int_{-(2k+1)\pi}^{-(2k-1)\pi} \mathrm{d}\phi\, \mathcal{P}(\phi) + \int_{(2k-1)\pi}^{(2k+1)\pi} \mathrm{d}\phi\, \mathcal{P}(\phi). \tag{F.30}$$

Consequently, Eq. (F.29) constitutes an asymptotic limit for broad prior distributions. In the context of atomic clocks, this regime corresponds to long interrogation times, where the coherence time of the local oscillator will become relevant and ultimately limits the clock stability. Therefore, we will denote Eq. (4.21) as the coherence time limit (CTL) of the OQI. Assuming a Gaussian prior distribution as defined in Eq. (4.5), the probabilities P_k can be evaluated explicitly to read

$$\begin{aligned} P_k &= 2\int_{(2k-1)\pi}^{(2k+1)\pi} \mathrm{d}\phi\,\mathcal{P}(\phi) = 2\int_{0}^{(2k+1)\pi} \mathrm{d}\phi\,\mathcal{P}(\phi) - 2\int_{0}^{(2k-1)\pi} \mathrm{d}\phi\,\mathcal{P}(\phi) \\ &= \operatorname{erf}\left(\frac{(2k+1)\pi}{\sqrt{2}\delta\phi}\right) - \operatorname{erf}\left(\frac{(2k-1)\pi}{\sqrt{2}\delta\phi}\right), \end{aligned} \tag{F.31}$$

where we substituted $t = \frac{\phi}{\sqrt{2}\delta\phi}$ and introduced the error function $\operatorname{erf}(z) = \int_0^z \mathrm{d}t e^{-t^2}$. In the relevant regime of prior widths considered in Chapter 4, where typically only the adjacent fringes around $\phi = 0$ contribute, the prior distribution $\mathcal{P}(\phi)$ is effectively limited to the region $[-3\pi, +3\pi]$. As a result, the CTL simplifies significantly compared to the general form in Eq. (F.29), which accounts for contributions from all Ramsey fringes. Restricting to the error associated with the adjacent fringes around $\phi = 0$, the CTL reduces to

$$\begin{aligned} (\Delta\phi_{\mathrm{CTL}}^{\mathrm{OQI}})^2 &= 4\pi^2\left[\int_{-\infty}^{-\pi} \mathrm{d}\phi\,\mathcal{P}(\phi) + \int_{\pi}^{\infty} \mathrm{d}\phi\,\mathcal{P}(\phi)\right] = 4\pi^2\left[1 - \int_{-\pi}^{\pi} \mathrm{d}\phi\,\mathcal{P}(\phi)\right] \\ &= 4\pi^2\left[1 - \operatorname{erf}\left(\frac{\pi}{\sqrt{2}\delta\phi}\right)\right]. \end{aligned} \tag{F.32}$$

F.3.2 Asymptotic limit

With increasing ensemble size, the numerical algorithm presented in the main text becomes computationally challenging. However, in the asymptotic limit ($N \gg 1$), an explicit analytical expression for the OQI can be derived. Assuming unitary phase evolution as described by Eq. (4.4) and restricting to the invertible range $[-\pi, +\pi]$, it has been shown for arbitrary prior distributions [209, 214–216] that the ultimate lower bound is given by the π-corrected Heisenberg limit (πHL), as defined in Eq. (4.22). An intuitive derivation for Gaussian prior distributions is given in Ref. [214] and is reproduced here. Based on Eq. (F.22), the optimization of the BQCRB over all input probe states ρ_{in} is equivalent to optimizing the QFI over all averaged states $\overline{\rho}$. This averaging can be formally associated with a collective dephasing process, where the dephasing rate is identified with the variance of the prior distribution [151, 214]. By combining this perspective with the asymptotic result for collective dephasing derived in Ref. [68], the asymptotic OQI can be expressed as

$$(\Delta\phi_{\mathrm{OQI}})^2 \overset{N\gg1}{\simeq} (\delta\phi)^2\left[1 - \frac{1}{1 + \frac{\pi^2}{N^2(\delta\phi)^2}}\right] \overset{N\gg1}{\simeq} (\delta\phi)^2\left[1 - \left(1 - \frac{\pi^2}{N^2(\delta\phi)^2}\right)\right] = \frac{\pi^2}{N^2}, \tag{F.33}$$

where we used the expansion $\frac{1}{1+x} \overset{x \ll 1}{\simeq} 1 - x$. This result is valid for Gaussian prior distributions with widths $\delta\phi \ll N$, which encompasses all relevant widths in the asymptotic regime $N \gg 1$. It is therefore reasonable to expect that this result generalizes to arbitrary prior distributions, as the fundamental characteristics of the estimation problem in this regime remain largely unaffected by the specific shape of the prior [209, 214].

F.3.3 Phase operator based interferometer (POI)

Finally, we aim to identify the protocol that saturates the asymptotic limit of the OQI. As discussed above, simultaneously determining the optimal measurement, input probe state and estimation strategy is a highly non-trivial problem. However, assuming a flat prior distribution and a periodic cost function in the interval $[-\pi, +\pi]$, the concept of covariant measurements [162, 215] provides an explicit solution for the optimal measurement operator – the so-called phase operator [140, 200, 215–221]. The phase operator Φ is defined as

$$\begin{aligned} \Phi &= \sum_{s=-N/2}^{N/2} \phi_s \, |s\rangle\langle s| \\ \phi_s &= \frac{2\pi s}{N+1} \\ |s\rangle &= \frac{1}{\sqrt{N+1}} \sum_{M=-N/2}^{N/2} e^{-i\phi_s M} \, |M\rangle \end{aligned} \tag{F.34}$$

where ϕ_s are the eigenvalues with corresponding eigenstates $|s\rangle$, constructed from the eigenstates $|M\rangle$ of S_z with eigenvalue M and total spin $N/2$. An interferometer based on Φ is referred to as phase operator based interferometer (POI). Furthermore, under these assumptions, the optimal input states in the asymptotic regime ($N \gg 1$), known as *sine* states [140, 200, 215–221] and saturating the πHL, can also be explicitly determined by

$$|\psi_\Phi\rangle = \sqrt{\frac{2}{N+1}} \sum_{M=-N/2}^{N/2} \sin\left(\frac{\pi(M+1/2)}{N+1}\right) |M\rangle \,. \tag{F.35}$$

However, since the assumptions of a periodic cost function and flat prior distribution are contrary to the framework introduced in Sec. 4.2, namely a global BMSE with phases $-\infty < \phi < +\infty$ and Gaussian prior distributions, these measurements and states are not necessarily optimal in the approach pursued in Chapter 4. Therefore, the optimal initial states and measurements must be explicitly evaluated. Nevertheless, it is instructive to investigate the performance of the POI and compare it to the standard protocols as well as variational classes discussed in the main text. Notably, this scenario is contrary to the BQCRB, since the measurement is fixed by Φ, while we aim to optimize over all initial states. For a fixed prior width, the optimal state $|\psi_\Phi\rangle$ can be identified by adapting the iterative algorithm presented in Sec. 4.3.3 and building on methods from Ref. [140]: Starting with an arbitrary initial state $|\psi_{\text{in}}^{(0)}\rangle$, such as $|\psi_{\text{in}}^{(0)}\rangle = |s=0\rangle$, the optimal Bayesian estimator (cf. Sec. 4.4) $\phi_{est}^{(0)}(s)$ is computed. Based on $\phi_{est}^{(0)}(s)$, the subsequent input probe state $|\psi_{\text{in}}^{(1)}\rangle$ in the iterative algorithm is evaluated by selecting the eigenstate corresponding to the most negative eigenvalue of the operator $\int \mathrm{d}\phi\, \mathcal{P}(\phi)\Lambda_{\phi,T}^{\dagger}[L^2 - 2\phi L]$ defined in Eq. (4.20). This ensures that the state $|\psi_{\text{in}}^{(1)}\rangle$ is optimal for a given measurement and estimator. This process is repeated until convergence to the optimal state $|\psi_\Phi\rangle$ – tailored to the framework considered in Chapter 4 – is achieved. Numerical evaluation of this iterative algorithm shows that the POI saturates the OQI in the limit of large ensembles within the framework of Chapter 4, as discussed in the main text and depicted in Fig. 4.2(b).

F.4 Estimators

F.4.1 Linear estimator

With the linear estimator defined in Eq. (4.24) by $\phi_{\text{est}}^{\text{linear}}(x) = a \cdot x$, the BMSE is expressed as

$$\begin{aligned}(\Delta\phi)^2 &= (\delta\phi)^2 - 2a\int \mathrm{d}\phi\, \mathcal{P}(\phi)\phi \sum_x xP(x|\phi) + a^2 \int \mathrm{d}\phi\, \mathcal{P}(\phi) \sum_x x^2 P(x|\phi) \\ &= (\delta\phi)^2 - 2a\int \mathrm{d}\phi\, \mathcal{P}(\phi)\phi \left\langle X(\phi)\right\rangle + a^2 \int \mathrm{d}\phi\, \mathcal{P}(\phi) \left\langle X^2(\phi)\right\rangle .\end{aligned} \tag{F.36}$$

Here, the moments of the observable X are defined by $\langle X^n(\phi)\rangle = \sum_x x^n P(x|\phi)$. The optimal scaling factor a is determined by minimizing the BMSE. Differentiating Eq. (F.36) and solving for a yields

$$a = \frac{\int \mathrm{d}\phi\, \mathcal{P}(\phi)\phi \left\langle X(\phi)\right\rangle}{\int \mathrm{d}\phi\, \mathcal{P}(\phi) \left\langle X^2(\phi)\right\rangle}. \tag{F.37}$$

Hence, from Eq. (F.36), the corresponding BMSE is given by Eq. (4.27), i.e.

$$(\Delta\phi)^2 = (\delta\phi)^2 - \frac{\left[\int \mathrm{d}\phi\, \mathcal{P}(\phi)\phi \left\langle X(\phi)\right\rangle\right]^2}{\int \mathrm{d}\phi\, \mathcal{P}(\phi) \left\langle X^2(\phi)\right\rangle}. \tag{F.38}$$

Due to the linearity of the estimator, the scaling factor and BMSE only depend on the first and second moments of the observable X, rather than the full statistical model

$P(x|\phi)$. This dependence significantly simplifies practical computations, while retaining reliable performance in several situations. Nevertheless, the linear estimation strategy is not optimal in general.

F.4.2 Optimal Bayesian estimator

This derivation follows Ref. [200]. To start with, we expand Eq. (4.3) according to

$$(\Delta\phi)^2 = \sum_x P(x) \left[\int \mathrm{d}\phi \, P(\phi|x)\phi^2 - 2\phi_{\mathrm{est}}(x) \int \mathrm{d}\phi \, P(\phi|x)\phi + \phi_{\mathrm{est}}^2(x) \int \mathrm{d}\phi \, P(\phi|x) \right]. \tag{F.39}$$

As before, the first term results in the prior variance $(\delta\phi)^2$, while the last integral simplifies to unity due to the normalization of the posterior distribution. To minimize the BMSE, the optimal Bayesian estimator has to minimize the term in the brackets for each measurement outcome x, since $P(x) \geq 0$ and $\phi_{\mathrm{est}}(x)$ is independent for different x. Differentiating and solving for the estimator yields the optimal Bayesian estimator given in Eq. (4.28), namely $\phi_{\mathrm{est}}^{\mathrm{opt}}(x) = \int \mathrm{d}\phi \, P(\phi|x)\phi$. Thus, the optimal Bayesian estimator corresponds to the mean posterior phase. With this result, the BMSE becomes

$$(\Delta\phi)^2 = (\delta\phi)^2 - \sum_x P(x) \left(\phi_{\mathrm{est}}^{\mathrm{opt}}(x)\right)^2 . \tag{F.40}$$

Equivalently, the BMSE can be expressed in terms of the statistical model $P(x|\phi)$ and prior distribution $\mathcal{P}(\phi)$ according to Bayes theorem Eq. (4.2), resulting in Eq. (4.29). Unlike the linear estimator, the optimal Bayesian estimator as well as the corresponding BMSE depend explicitly on the statistical model, rather than just the first and second moments of the observable. While this dependence ensures optimality, it also increases computational complexity.

G

Calculations for protocols in Bayesian frequency metrology

In the following, we derive the sensitivities of the CSS, SSS and GHZ protocols introduced in Sec. 4.6.1.

G.1 Coherent Spin States (CSS)

For a measurement of the collective spin operator S_y and unitary phase evolution through a rotation around the z-axis, according to Eq. (4.4), the first and second moments of the observable are given by

$$\langle X(\phi)\rangle = \langle S_y(\phi)\rangle = \langle S_y\rangle \cos(\phi) + \langle S_x\rangle \sin(\phi) \tag{G.1}$$

$$\left\langle X^2(\phi)\right\rangle = \left\langle S_y^2(\phi)\right\rangle = \left\langle S_y^2\right\rangle \cos^2(\phi) + \langle S_yS_x + S_xS_y\rangle \sin(\phi)\cos(\phi) + \left\langle S_x^2\right\rangle \sin^2(\phi), \tag{G.2}$$

where the expectation values $\langle\cdot\rangle$ are evaluated with respect to the initial state $|\psi_{\text{in}}\rangle$ and thus are independent of the phase ϕ. Assuming a Gaussian prior distribution, as defined in Eq. (4.5), the integrals in Eq. (4.27) become

$$\int \mathrm{d}\phi\, \mathcal{P}(\phi)\phi \langle X(\phi)\rangle = \int \mathrm{d}\phi\, \mathcal{P}(\phi)\phi \left[\langle S_y\rangle \cos(\phi) + \langle S_x\rangle \sin(\phi)\right] = \langle S_x\rangle (\delta\phi)^2 e^{-(\delta\phi)^2/2} \tag{G.3}$$

$$\begin{aligned}\int \mathrm{d}\phi\, \mathcal{P}(\phi) \left\langle X^2(\phi)\right\rangle &= \int \mathrm{d}\phi\, \mathcal{P}(\phi) \big[\left\langle S_y^2\right\rangle \cos^2(\phi) + \langle S_yS_x + S_xS_y\rangle \sin(\phi)\cos(\phi) \\ &\qquad + \left\langle S_x^2\right\rangle \sin^2(\phi)\big] \\ &= e^{-(\delta\phi)^2} \left[\left\langle S_y^2\right\rangle \cosh\left((\delta\phi)^2\right) + \left\langle S_x^2\right\rangle \sinh\left((\delta\phi)^2\right)\right], \end{aligned} \tag{G.4}$$

where terms with odd integrands vanish directly. Thus, the optimal linear scaling factor, corresponding BMSE and effective measurement uncertainty are given by

$$\begin{aligned}
a &= \frac{\langle S_x\rangle\,(\delta\phi)^2 e^{(\delta\phi)^2/2}}{\langle S_y^2\rangle\cosh\left((\delta\phi)^2\right)+\langle S_x^2\rangle\sinh\left((\delta\phi)^2\right)}\\
(\Delta\phi)^2 &= (\delta\phi)^2\left[1-(\delta\phi)^2\frac{\langle S_x\rangle^2}{\langle S_y^2\rangle\cosh((\delta\phi)^2)+\langle S_x^2\rangle\sinh((\delta\phi)^2)}\right] \qquad \text{(G.5)}\\
(\Delta\phi_M)^2 &= \frac{\langle S_y^2\rangle}{\langle S_x\rangle^2}\cosh\big((\delta\phi)^2\big)+\frac{\langle S_x^2\rangle}{\langle S_x\rangle^2}\sinh\big((\delta\phi)^2\big)-(\delta\phi)^2.
\end{aligned}$$

For the conventional Ramsey protocol, a coherent spin state (CSS) polarized in x-direction is prepared by a $\pi/2$-pulse applied to the collective ground state

$$|\mathrm{CSS}\rangle=\mathcal{R}_y\left(-\tfrac{\pi}{2}\right)|{\downarrow}\rangle^{\otimes N}=|+\rangle^{\otimes N}=\left[\frac{1}{\sqrt{2}}(|{\downarrow}\rangle+|{\uparrow}\rangle)\right]^{\otimes N} \qquad \text{(G.6)}$$

which represents N uncorrelated atoms, each in an equal superposition of the ground and excited states. CSS and their properties are discussed in detail in Refs. [115–117], while a comprehensive overview is provided in Sec. 2.3.7. With expectation values

$$\langle S_x\rangle=\frac{N}{2},\qquad \langle S_y\rangle=\langle S_z\rangle=0,\qquad \langle S_x^2\rangle=\frac{N^2}{4}, \qquad \text{(G.7)}$$

$$\langle S_y^2\rangle=\frac{N}{4}=\langle S_z^2\rangle,\qquad \langle S_xS_y\rangle=0=\langle S_xS_z\rangle, \qquad \text{(G.8)}$$

we derive

$$a_{\mathrm{CSS}}=\frac{2e^{(\delta\phi)^2/2}}{\cosh((\delta\phi)^2)+N\sinh((\delta\phi)^2)} \qquad \text{(G.9)}$$

$$(\Delta\phi_{\mathrm{CSS}})^2=(\delta\phi)^2\left[1-(\delta\phi)^2\frac{N}{\cosh((\delta\phi)^2)+N\sinh((\delta\phi)^2)}\right] \qquad \text{(G.10)}$$

$$(\Delta\phi_M^{\mathrm{CSS}})^2=\frac{\cosh((\delta\phi)^2)}{N}+\sinh\big((\delta\phi)^2\big)-(\delta\phi)^2. \qquad \text{(G.11)}$$

Rewriting the first term, we recover the result from Ref. [92]

$$(\Delta\phi_M^{\mathrm{CSS}})^2=\frac{e^{(\delta\phi)^2}}{N}+\left(1-\frac{1}{N}\right)\sinh\big((\delta\phi)^2\big)-(\delta\phi)^2. \qquad \text{(G.12)}$$

G.2 Spin-Squeezed States (SSS)

The application of an one-axis-twisting (OAT) interaction $\mathcal{T}_z(\mu)=\exp\left(-i\frac{\mu}{2}S_z^2\right)$ with small twisting strength μ to the CSS, defined in Eq. (G.6), generates a spin-squeezed state (SSS). To align the minimal spin variance along the y-axis, an additional rotation $\mathcal{R}_x(\theta)$ around the x-axis by an angle θ is applied. Thus, the initial state reads

$$|\mathrm{SSS}\rangle = \mathcal{R}_x(\theta)\mathcal{T}_z(\mu)\,|\mathrm{CSS}\rangle\,. \tag{G.13}$$

These states are introduced and discussed in detail in Ref. [125], while a comprehensive overview is provided in Sec. 2.3.9. In comparison to CSS, the SSS differs primarily in its polarization and spin variances, while other properties remain unchanged. Hence, the optimal linear scaling factor, BMSE and effective measurement uncertainty are given by Eq. (G.5) with expectation values

$$\langle S_x\rangle = \frac{N}{2}\cos^{N-1}\left(\tfrac{\mu}{2}\right) \tag{G.14}$$

$$\left\langle S_x^2\right\rangle = \frac{N}{4}\left[N - \frac{1}{2}(N-1)A\right] \tag{G.15}$$

$$\left\langle S_y^2\right\rangle = \frac{N}{4}\left\{1 + \frac{1}{4}(N-1)\left[A - \sqrt{A^2+B^2}\right]\right\}, \tag{G.16}$$

where $A = 1 - \cos^{N-2}(\mu)$ and $B = 4\sin\left(\frac{\mu}{2}\right)\cos^{N-2}\left(\frac{\mu}{2}\right)$.

G.3 GHZ States

The GHZ state [121] is defined by

$$|\mathrm{GHZ}\rangle = \frac{1}{\sqrt{2}}\left[|\downarrow\rangle^{\otimes N} + |\uparrow\rangle^{\otimes N}\right], \tag{G.17}$$

which represents an equal superposition of the collective ground and excited states and thus, is maximally entangled. After the free evolution, the state reads

$$|\psi_\phi\rangle = \mathcal{R}_z\left(-\tfrac{\pi}{2N}\right)\mathcal{R}_z(\phi)\,|\mathrm{GHZ}\rangle = \frac{1}{\sqrt{2}}\left[e^{i\frac{N}{2}\phi - i\frac{\pi}{4}}|\downarrow\rangle^{\otimes N} + e^{-i\frac{N}{2}\phi + i\frac{\pi}{4}}|\uparrow\rangle^{\otimes N}\right], \tag{G.18}$$

where the additional rotation $\mathcal{R}_z\left(-\frac{\pi}{2N}\right)$ is applied to shift the optimal working point to $\phi_0 = 0$, since the prior is centered around $\phi = 0$. Equivalently, the prior distribution could be shifted by $\pi/2N$. The expectation value of the parity $\Pi = (-1)^N\sigma_x^{\otimes N}$ is given by

$$\langle\Pi(\phi)\rangle = (-1)^N\sin(N\phi). \tag{G.19}$$

Since $\sigma_x^2 = \mathbb{1}$, the second moment directly yields $\langle\Pi^2(\phi)\rangle = 1$. Hence, the integrals in Eq. (4.27) become

$$\int \mathrm{d}\phi\,\mathcal{P}(\phi)\phi\,\langle X(\phi)\rangle = (-1)^N\int \mathrm{d}\phi\,\mathcal{P}(\phi)\phi\sin(N\phi) = (-1)^N N(\delta\phi)^2 e^{-N^2(\delta\phi)^2/2} \tag{G.20}$$

$$\int \mathrm{d}\phi\,\mathcal{P}(\phi)\left\langle X^2(\phi)\right\rangle = 1. \tag{G.21}$$

Consequently, the corresponding optimal linear scaling factor, BMSE and effective measurement uncertainty are given by

$$a_{\mathrm{GHZ}} = (-1)^N N(\delta\phi)^2 e^{-N^2(\delta\phi)^2/2} \tag{G.22}$$

$$(\Delta\phi_{\mathrm{GHZ}})^2 = (\delta\phi)^2 \left[1 - N^2(\delta\phi)^2 e^{-N^2(\delta\phi)^2}\right] \tag{G.23}$$

$$(\Delta\phi_M^{\mathrm{GHZ}})^2 = \frac{e^{N^2(\delta\phi)^2}}{N^2} - (\delta\phi)^2. \tag{G.24}$$

Due to the binary nature of the parity measurement, the linear estimator is already optimal and thus saturates the BCRB and coincides with the optimal Bayesian estimator.

However, the parity measurement can also be mimicked by a projective spin measurement and application of the corresponding optimal Bayesian estimator: For N even, a Ramsey pulse is applied after the free evolution time, implemented by a rotation of $\pi/2$ around the x-axis, resulting in the final state

$$|\psi_f\rangle = \mathcal{R}_x\left(\tfrac{\pi}{2}\right)|\psi_\phi\rangle = \frac{1}{\sqrt{2}}\frac{1}{\sqrt{2}^N}\left[e^{i\frac{N}{2}\phi - i\frac{\pi}{4}}\left(|\downarrow\rangle - i|\uparrow\rangle\right)^{\otimes N} + e^{-i\frac{N}{2}\phi + i\frac{\pi}{4}}\left(|\uparrow\rangle - i|\downarrow\rangle\right)^{\otimes N}\right]. \tag{G.25}$$

For N odd, calculations are analogous with final rotation around the y-axis. Finally, a projective measurement of S_z is performed. Note that the final Ramsey pulse can equivalently be absorbed in the observable, leading to an effective measurement of S_y, as for the CSS and SSS protocol. The conditional probabilities are evaluated to read

$$P\left(x = +\tfrac{N}{2} - N_-|\phi\right) = \frac{1}{2^N}\binom{N}{N_-}\left[1 + (-1)^{\frac{N}{2}+N_-}\sin(N\phi)\right] \tag{G.26}$$

where N_- denotes the number of atoms in the ground state. Interestingly, the conditional probabilities for N_- and $N - N_-$ are equal (since N is even), resulting in a vanishing signal $\langle X(\phi)\rangle \equiv 0$. Nevertheless, with

$$P\left(x = +\tfrac{N}{2} - N_-\right) = \int \mathrm{d}\phi\, P(x|\phi)\,\mathcal{P}(\phi) = \frac{1}{2^N}\binom{N}{N_-}, \tag{G.27}$$

the optimal Bayesian estimator is given by

$$\phi_{\mathrm{est}}\left(x = +\tfrac{N}{2} - N_-\right) = \frac{1}{P(x)}\int \mathrm{d}\phi\, P(x|\phi)\,\mathcal{P}(\phi)\phi = (-1)^{\frac{N}{2}+N_-} N(\delta\phi)^2 e^{-N(\delta\phi)^2/2} \tag{G.28}$$

and an efficient estimation is possible. Consequently, the optimal estimation strategy distinguishes between even and odd numbers of atoms in the ground state and thus effectively mimics a parity measurement. Note that we performed the calculations for N even, ensuring that $N/2$ is integer and consequently $(-1)^{\frac{N}{2}} \in \mathbb{R}$. Analogous results are obtained for N odd.

As a final step, we determine the BQCRB for the GHZ state. Using Eq. (G.18), we find

$$\Lambda_{\phi,T}[\rho_{\text{in}}] = \frac{1}{2}\left[|{\downarrow}\rangle\langle{\downarrow}|^{\otimes N} + e^{iN\phi}|{\downarrow}\rangle\langle{\uparrow}|^{\otimes N} + e^{-iN\phi}|{\uparrow}\rangle\langle{\downarrow}|^{\otimes N} + |{\uparrow}\rangle\langle{\uparrow}|^{\otimes N}\right], \tag{G.29}$$

which leads to the average state

$$\overline{\rho} = \frac{1}{2}\left[|{\downarrow}\rangle\langle{\downarrow}|^{\otimes N} + e^{-N^2(\delta\phi)^2/2}\left(|{\downarrow}\rangle\langle{\uparrow}|^{\otimes N} + |{\uparrow}\rangle\langle{\downarrow}|^{\otimes N}\right) + |{\uparrow}\rangle\langle{\uparrow}|^{\otimes N}\right]. \tag{G.30}$$

Interestingly, Eq. (G.30) is no longer pure due to the averaging. As it effectively corresponds to a (real) 2x2-matrix, the QFI of $\overline{\rho}$ can be evaluated analogously to that of the GHZ state in the local approach (cf. App. E.4). Using Eq. (4.16), the BQCRB directly follows from

$$\mathcal{F}_Q[\overline{\rho}] = N^2 e^{-N^2(\delta\phi)^2} \tag{G.31}$$

and results in the same value as in Eq. (G.23).

Acknowledgements

This thesis marks the culmination of a long and rewarding journey – one that would not have been possible without the support, encouragement and contributions of many people. I am deeply grateful to each and every one of you.

First and foremost, I would like to express my sincere thanks to Klemens Hammerer. You have been an exceptional mentor throughout my entire academic journey, from my bachelor's thesis to this PhD. In the early days, you patiently answered every question – no matter how naive – and later became a vital sparring partner in many scientific discussions. You consistently gave me the freedom to pursue topics that sparked my curiosity, while providing clear, thoughtful and constructive guidance. I am especially grateful for the many inspiring conversations we shared, which helped me grow both scientifically and personally.

I would also like to thank Piet Schmidt for kindly agreeing to serve as a referee for this thesis. Your ongoing interest in my work and your valuable input – especially your experimental perspective – greatly enriched and shaped my research.

My thanks also go to Akimasa Miyake for agreeing to review this thesis and to Christian Ospelkaus for his continuous support over the years – from my early days as a bachelor student to ultimately chairing my defense. I truly appreciated your engagement throughout every stage of this path.

A heartfelt thank you goes to Birgit Gemmeke. Your help with countless administrative and bureaucratic matters over the years has been invaluable. Your patience, reliability and openness spared me many potential headaches and allowed me to focus on my research. I am also deeply grateful to the entire 'AG Hammerer'. The welcoming and collaborative atmosphere of the group made it more than just a workplace. I would like to thank Victor, Jan-Niclas, Michael, Florian, Maja, Ivan, Rui, Ruolin, Kasper, Erin, Julian, Patrik and Luis for countless insightful discussions, stimulating seminars, and many enjoyable moments. Special thanks go to my office mates – Victor, Maja and Erin – for making daily life in the office both productive and fun. I am also thankful to my colleagues in Braunschweig for their valuable input and the fresh perspectives they brought to our collaborations. In particular, I would like to thank Kai, Lennart and Fabian for the many engaging discussions and helpful contributions. I would also like to thank my bachelor and master students, Jonas Bettermann and Marius Burgath, for your dedication and the enthusiasm you brought to your projects. It was a real pleasure to work with you and to see your ideas come to life.

Last but by no means least, I want to thank my family and friends for their unwavering support throughout this time. Your encouragement and belief in me have meant more than I can express. I am especially grateful to Vanessa, Viviane and my parents – you were always there when it mattered most.

List of Figures

1.1 Basic principle of an atomic clock 6
1.2 Accuracy and stability 7

2.1 Allan deviation 13
2.2 Stability analysis of local oscillators 18
2.3 Visualization of states on the Bloch sphere 21
2.4 Block-diagonal structure in the Dicke basis 25
2.5 Wigner function 26
2.6 Energy level structure in a two level system 27
2.7 Conventional Ramsey interferometry 40
2.8 Quantum projection noise 42
2.9 One-axis-twisting interaction 52
2.10 Spin-squeezed states 53

3.1 Atomic clock and Ramsey interferometry 64
3.2 Enhancement of protocols with GHZ(-like) states compared to the SQL 85
3.3 Schematic illustration of the heralded-GHZ protocol 88
3.4 Optimal rotation angle and probability of no-jump dynamics 94
3.5 Monte-Carlo simulations of the full feedback loop in an atomic clock . 98
3.6 Separation of Dicke states and detection of spontaneous decay events 100
3.7 Crossover to dephasing 101
3.8 QCRB of CSS in the presence of collective dephasing 104
3.9 Optimal initial state 106
3.10 QCRB of SSS 107
3.11 Incoherent pumping 109
3.12 Conversion of spontaneous decay events into erasure errors 111

4.1 Prior broadening 117
4.2 Sensitivity of standard protocols in Bayesian frequency metrology . . 131
4.3 Variational Ramsey protocols in Bayesian frequency metrology 139
4.4 Optimal Ramsey signals and optimization landscape 141
4.5 Monte Carlo simulations of Ramsey protocols in Bayesian frequency metrology 148

4.6 Comparison of the linear and optimal Bayesian estimation strategy . 151
4.7 Dead time effects 157
4.8 Dead times characteristic for specific experimental setups 163
4.9 Zero-dead-time clock 169

A.1 Long term stability 187
A.2 Variance of the prior phase distribution 190

List of Tables

2.1 Noise contributions to the Allan variance 17

Bibliography

[1] T. Kielinski, P. O. Schmidt, and K. Hammerer. GHZ protocols enhance frequency metrology despite spontaneous decay. *Science Advances*, 10(43):eadr1439, 2024. URL: `https://www.science.org/doi/abs/10.1126/sciadv.adr1439`, `doi:10.1126/sciadv.adr1439`.

[2] T. Kielinski and K. Hammerer. Bayesian frequency metrology with optimal Ramsey interferometry in optical atomic clocks, 2025. URL: `https://arxiv.org/abs/2505.04287`, `arXiv:2505.04287`.

[3] T. Kielinski. Monte Carlo simulations of atomic clocks [Data set], 2025. URL: `https://data.uni-hannover.de/dataset/5dba3086-ff3a-4217-9d79-53c8c844fe3a`, `doi:10.25835/B7MMMMPU`.

[4] K. Dietze, L. Pelzer, L. Krinner, F. Dawel, J. Kramer, N. C. H. Spethmann, T. Kielinski, K. Hammerer, K. Stahl, J. Klose, S. Dörscher, C. Lisdat, E. Benkler, and P. O. Schmidt. Entanglement-enhanced optical ion clock, 2025. URL: `https://arxiv.org/abs/2506.11810`, `arXiv:2506.11810`.

[5] M. S. Scharnagl, T. Kielinski, and K. Hammerer. Optimal Ramsey interferometry with echo protocols based on one-axis twisting. *Phys. Rev. A*, 108:062611, Dec 2023. URL: `https://link.aps.org/doi/10.1103/PhysRevA.108.062611`, `doi:10.1103/PhysRevA.108.062611`.

[6] L. Pezzè, A. Smerzi, M. K. Oberthaler, R. Schmied, and P. Treutlein. Quantum metrology with nonclassical states of atomic ensembles. *Rev. Mod. Phys.*, 90:035005, Sep 2018. URL: `https://link.aps.org/doi/10.1103/RevModPhys.90.035005`, `doi:10.1103/RevModPhys.90.035005`.

[7] J. Ye and P. Zoller. Essay: Quantum sensing with atomic, molecular, and optical platforms for fundamental physics. *Phys. Rev. Lett.*, 132:190001, May 2024. URL: `https://link.aps.org/doi/10.1103/PhysRevLett.132.190001`, `doi:10.1103/PhysRevLett.132.190001`.

[8] M. A. Lombardi. *Time and Frequency*, page 783–801. Elsevier, 2003. URL: `http://dx.doi.org/10.1016/B0-12-227410-5/00780-8`, `doi:10.1016/b0-12-227410-5/00780-8`.

[9] J. Levine. Introduction to time and frequency metrology. *Review of Scientific Instruments*, 70(6):2567–2596, June 1999. URL: `http://dx.doi.org/10.1063/1.1149844`, `doi:10.1063/1.1149844`.

[10] C. Audoin and B. Guinot. *The measurement of time*. Cambridge University Press, Cambridge, England, September 2001.

[11] F. Riehle. *Frequency Standards: Basics and Applications*. Wiley, September 2003. URL: `http://dx.doi.org/10.1002/3527605991`, `doi:10.1002/3527605991`.

[12] A. D. Ludlow, M. M. Boyd, J. Ye, E. Peik, and P. O. Schmidt. Optical atomic clocks. *Rev. Mod. Phys.*, 87:637–701, Jun 2015. URL: `https://link.aps.org/doi/10.1103/RevModPhys.87.637`, `doi:10.1103/RevModPhys.87.637`.

[13] S. Colombo, E. Pedrozo-Peñafiel, and V. Vuletić. Entanglement-enhanced optical atomic clocks. *Applied Physics Letters*, 121(21):210502, November 2022. URL: `http://dx.doi.org/10.1063/5.0121372`, `doi:10.1063/5.0121372`.

[14] T. Udem, R. Holzwarth, and T. W. Hänsch. Optical frequency metrology. *Nature*, 416(6877):233–237, March 2002. URL: `http://dx.doi.org/10.1038/416233a`, `doi:10.1038/416233a`.

[15] J. Ye and S. T. Cundiff. *Femtosecond Optical Frequency Comb: Principle, Operation, and Applications*. Kluwer Academic Publishers, 2005. URL: `http://dx.doi.org/10.1007/b102450`, `doi:10.1007/b102450`.

[16] M. Steinel, H. Shao, M. Filzinger, B. Lipphardt, M. Brinkmann, A. Didier, T. Mehlstäubler, T. Lindvall, E. Peik, and N. Huntemann. Evaluation of a $^{88}\mathrm{Sr}^{+}$ optical clock with a direct measurement of the blackbody radiation shift and determination of the clock frequency. *Physical Review Letters*, 131(8):1079–7114, 2023. URL: `https://link.aps.org/doi/10.1103/PhysRevLett.131.083002`, `doi:10.1103/physrevlett.131.083002`.

[17] L. Pelzer, K. Dietze, V. J. Martínez-Lahuerta, L. Krinner, J. Kramer, F. Dawel, N. C. H. Spethmann, K. Hammerer, and P. O. Schmidt. Multi-ion frequency reference using dynamical decoupling. *Phys. Rev. Lett.*, 133:033203, Jul 2024. URL: `https://link.aps.org/doi/10.1103/PhysRevLett.133.033203`, `doi:10.1103/PhysRevLett.133.033203`.

[18] H. N. Hausser, J. Keller, T. Nordmann, N. M. Bhatt, J. Kiethe, H. Liu, I. M. Richter, M. von Boehn, J. Rahm, S. Weyers, E. Benkler, B. Lipphardt, S. Dörscher, K. Stahl, J. Klose, C. Lisdat, M. Filzinger, N. Huntemann, E. Peik, and T. E. Mehlstäubler. $^{115}\mathrm{In}^{+}$-$^{172}\mathrm{Yb}^{+}$ Coulomb crystal clock with 2.5×10^{-18} systematic uncertainty. *Phys. Rev. Lett.*, 134:023201, Jan 2025. URL: `https://link.aps.org/doi/10.1103/PhysRevLett.134.023201`, `doi:10.1103/PhysRevLett.134.023201`.

[19] I. S. Madjarov, A. Cooper, A. L. Shaw, J. P. Covey, V. Schkolnik, J. R. Williams, S. Johnson, M. A. Norcia, T. H. Yoon, S. A. Schaffer, A. O. Sushkov, M. Endres, and A. M. Kaufman. An atomic-array optical clock with single-atom readout. *Physical Review X*, 9(4):041052, 2019. URL: `https://link.aps.org/doi/10.1103/PhysRevX.9.041052`, `doi:10.1103/PhysRevX.9.041052`.

[20] M. A. Norcia, D. J. Young, W. J. Eckner, L. Anderegg, V. Schkolnik, and A. M. Kaufman. Second-scale coherence on an optical clock transition in a tweezer array. *Science*, 366(6461):93–97, 2019. URL: `http://dx.doi.org/10.1126/science.aay0644`, `doi:10.1126/science.aay0644`.

[21] A. W. Young, W. J. Eckner, W. R. Milner, D. Kedar, M. A. Norcia, E. Oelker, N. Schine, J. Ye, and A. M. Kaufman. Half-minute-scale atomic coherence and high relative stability in a tweezer clock. *Nature*, 588(7838):408–413, December 2020. URL: `http://dx.doi.org/10.1038/s41586-020-3009-y`, `doi:10.1038/s41586-020-3009-y`.

[22] A. L. Shaw, R. Finkelstein, R. B.-S. Tsai, P. Scholl, T. H. Yoon, J. Choi, and M. Endres. Multi-ensemble metrology by programming local rotations with atom movements. *Nat. Phys.*, 20(2):195–201, February 2024. URL: `http://dx.doi.org/10.1038/s41567-023-02323-w`, `doi:10.1038/s41567-023-02323-w`.

[23] M. Takamoto, I. Ushijima, M. Das, N. Nemitz, T. Ohkubo, K. Yamanaka, N. Ohmae, T. Takano, T. Akatsuka, A. Yamaguchi, and H. Katori. Frequency ratios of Sr, Yb, and Hg based optical lattice clocks and their applications. *Comptes Rendus. Physique*, 16(5):489–498, 2015. URL: `http://dx.doi.org/10.1016/j.crhy.2015.04.003`, `doi:10.1016/j.crhy.2015.04.003`.

[24] H. Katori, M. Takamoto, V. G. Pal'chikov, and V. D. Ovsiannikov. Ultrastable optical clock with neutral atoms in an engineered light shift trap. *Phys. Rev. Lett.*, 91:173005, Oct 2003. URL: `https://link.aps.org/doi/10.1103/PhysRevLett.91.173005`, `doi:10.1103/PhysRevLett.91.173005`.

[25] A. Al-Masoudi, S. Dörscher, S. Häfner, U. Sterr, and C. Lisdat. Noise and instability of an optical lattice clock. *Phys. Rev. A*, 92:063814, Dec 2015. URL: `https://link.aps.org/doi/10.1103/PhysRevA.92.063814`, `doi:10.1103/PhysRevA.92.063814`.

[26] H. Katori. Optical lattice clocks and quantum metrology. *Nature Photonics*, 5(4):203–210, March 2011. URL: `http://dx.doi.org/10.1038/nphoton.2011.45`, `doi:10.1038/nphoton.2011.45`.

[27] M. Abdel-Hafiz, P. Ablewski, A. Al-Masoudi, H. Álvarez Martínez, P. Balling, G. Barwood, E. Benkler, M. Bober, M. Borkowski, W. Bowden, R. Ciuryło, H. Cybulski, A. Didier, M. Doležal, S. Dörscher, S. Falke, R. M. Godun, R. Hamid, I. R. Hill, R. Hobson, N. Huntemann, Y. L. Coq, R. L. Targat, T. Legero, T. Lindvall, C. Lisdat, J. Lodewyck, H. S. Margolis, T. E. Mehlstäubler, E. Peik, L. Pelzer, M. Pizzocaro, B. Rauf, A. Rolland, N. Scharnhorst, M. Schioppo, P. O. Schmidt, R. Schwarz, Çağrı Şenel, N. Spethmann, U. Sterr, C. Tamm, J. W. Thomsen, A. Vianello, and M. Zawada. Guidelines for developing optical clocks with 10^{-18} fractional frequency uncertainty, 2019. URL: `https://arxiv.org/abs/1906.11495`, `arXiv:1906.11495`.

[28] E. Oelker, R. B. Hutson, C. J. Kennedy, L. Sonderhouse, T. Bothwell, A. Goban, D. Kedar, C. Sanner, J. M. Robinson, G. E. Marti, D. G. Matei, T. Legero, M. Giunta, R. Holzwarth, F. Riehle, U. Sterr, and J. Ye. Demonstration of 4.8×10^{-17} stability at 1 s for two independent optical clocks. *Nature Photonics*, 13(10):714–719, July 2019. URL: `http://dx.doi.org/10.1038/s41566-019-0493-4`, `doi:10.1038/s41566-019-0493-4`.

[29] M. Schioppo, R. C. Brown, W. F. McGrew, N. Hinkley, R. J. Fasano, K. Beloy, T. H. Yoon, G. Milani, D. Nicolodi, J. A. Sherman, N. B. Phillips, C. W. Oates, and A. D. Ludlow. Ultrastable optical clock with two cold-atom ensembles. *Nature Photonics*, 11(1):48–52, November 2016. URL: `http://dx.doi.org/10.1038/nphoton.2016.231`, `doi:10.1038/nphoton.2016.231`.

[30] T. Nicholson, S. Campbell, R. Hutson, G. Marti, B. Bloom, R. McNally, W. Zhang, M. Barrett, M. Safronova, G. Strouse, W. Tew, and J. Ye. Systematic evaluation of an atomic clock at 2×10^{-18} total uncertainty. *Nature Communications*, 6(1):6896, April 2015. URL: `http://dx.doi.org/10.1038/ncomms7896`, `doi:10.1038/ncomms7896`.

[31] B. J. Bloom, T. L. Nicholson, J. R. Williams, S. L. Campbell, M. Bishof, X. Zhang, W. Zhang, S. L. Bromley, and J. Ye. An optical lattice clock with accuracy and stability at the 10^{-18} level. *Nature*, 506(7486):71–75, January 2014. URL: `http://dx.doi.org/10.1038/nature12941`, `doi:10.1038/nature12941`.

[32] E. Pedrozo-Peñafiel, S. Colombo, C. Shu, A. F. Adiyatullin, Z. Li, E. Mendez, B. Braverman, A. Kawasaki, D. Akamatsu, Y. Xiao, and V. Vuletić. Entanglement on an optical atomic-clock transition. *Nature*, 588(7838):414–418, December 2020. URL: `http://dx.doi.org/10.1038/s41586-020-3006-1`, `doi:10.1038/s41586-020-3006-1`.

[33] A. Aeppli, K. Kim, W. Warfield, M. S. Safronova, and J. Ye. Clock with 8×10^{-19} systematic uncertainty. *Phys. Rev. Lett.*, 133:023401, Jul 2024. URL: `https://link.aps.org/doi/10.1103/PhysRevLett.133.023401`, `doi:10.1103/PhysRevLett.133.023401`.

[34] J. Keller, D. Kalincev, T. Burgermeister, A. P. Kulosa, A. Didier, T. Nordmann, J. Kiethe, and T. Mehlstäubler. Probing time dilation in Coulomb crystals in a high-precision ion trap. *Physical Review Applied*, 11(1):011002, January 2019. URL: `http://dx.doi.org/10.1103/PhysRevApplied.11.011002`, `doi:10.1103/physrevapplied.11.011002`.

[35] N. Aharon, N. Spethmann, I. D. Leroux, P. O. Schmidt, and A. Retzker. Robust optical clock transitions in trapped ions using dynamical decoupling. *New Journal of Physics*, 21(8):083040, August 2019. URL: `http://dx.doi.org/10.1088/1367-2630/ab3871`, `doi:10.1088/1367-2630/ab3871`.

[36] C. Sanner, N. Huntemann, R. Lange, C. Tamm, E. Peik, M. S. Safronova, and S. G. Porsev. Optical clock comparison for Lorentz symmetry testing. *Nature*, 567(7747):204–208, March 2019. URL: `http://dx.doi.org/10.1038/s41586-019-0972-2`, `doi:10.1038/s41586-019-0972-2`.

[37] Y. Huang, H. Guan, W. Bian, L. Ma, K. Liang, T. Li, and K. Gao. A comparison of two $^{40}\mathrm{Ca}^{+}$ single-ion optical frequency standards at the 5×10^{-17} level and an evaluation of systematic shifts. *Applied Physics B*, 123(5):166, May 2017. URL: `http://dx.doi.org/10.1007/s00340-017-6731-x`, `doi:10.1007/s00340-017-6731-x`.

[38] N. Dimarcq, M. Gertsvolf, G. Mileti, S. Bize, C. W. Oates, E. Peik, D. Calonico, T. Ido, P. Tavella, F. Meynadier, G. Petit, G. Panfilo, J. Bartholomew, P. Defraigne, E. A. Donley, P. O. Hedekvist, I. Sesia, M. Wouters, P. Dubé, F. Fang, F. Levi, J. Lodewyck, H. S. Margolis, D. Newell, S. Slyusarev, S. Weyers, J.-P. Uzan, M. Yasuda, D.-H. Yu, C. Rieck, H. Schnatz, Y. Hanado, M. Fujieda, P.-E. Pottie, J. Hanssen, A. Malimon, and N. Ashby. Roadmap towards the redefinition of the second. *Metrologia*, 61(1):012001, January 2024. URL: `http://dx.doi.org/10.1088/1681-7575/ad17d2`, `doi:10.1088/1681-7575/ad17d2`.

[39] M. Takamoto, I. Ushijima, N. Ohmae, T. Yahagi, K. Kokado, H. Shinkai, and H. Katori. Test of general relativity by a pair of transportable optical lattice clocks. *Nature Photonics*, 14(7):411–415, April 2020. URL: `http://dx.doi.org/10.1038/s41566-020-0619-8`, `doi:10.1038/s41566-020-0619-8`.

[40] C. W. Chou, D. B. Hume, T. Rosenband, and D. J. Wineland. Optical clocks and relativity. *Science*, 329(5999):1630–1633, September 2010. URL: `http://dx.doi.org/10.1126/science.1192720`, `doi:10.1126/science.1192720`.

[41] T. Bothwell, C. J. Kennedy, A. Aeppli, D. Kedar, J. M. Robinson, E. Oelker, A. Staron, and J. Ye. Resolving the gravitational redshift across a millimetre-scale atomic sample. *Nature*, 602(7897):420–424, February 2022. URL: `http://dx.doi.org/10.1038/s41586-021-04349-7`, `doi:10.1038/s41586-021-04349-7`.

[42] L. S. Dreissen, C.-H. Yeh, H. A. Fürst, K. C. Grensemann, and T. E. Mehlstäubler. Improved bounds on Lorentz violation from composite pulse Ramsey spectroscopy in a trapped ion. *Nature Communications*, 13(1):7314, November 2022. URL: `http://dx.doi.org/10.1038/s41467-022-34818-0`, `doi:10.1038/s41467-022-34818-0`.

[43] M. S. Safronova. The search for variation of fundamental constants with clocks. *Annalen der Physik*, 531(5):1800364, January 2019. URL: `http://dx.doi.org/10.1002/andp.201800364`, `doi:10.1002/andp.201800364`.

[44] B. M. Roberts, P. Delva, A. Al-Masoudi, A. Amy-Klein, C. Bærentsen, C. F. A. Baynham, E. Benkler, S. Bilicki, S. Bize, W. Bowden, J. Calvert, V. Cambier, E. Cantin, E. A. Curtis, S. Dörscher, M. Favier, F. Frank, P. Gill, R. M. Godun, G. Grosche, C. Guo, A. Hees, I. R. Hill, R. Hobson, N. Huntemann, J. Kronjäger, S. Koke, A. Kuhl, R. Lange, T. Legero, B. Lipphardt, C. Lisdat, J. Lodewyck, O. Lopez, H. S. Margolis, H. Álvarez Martínez, F. Meynadier, F. Ozimek, E. Peik, P.-E. Pottie, N. Quintin, C. Sanner, L. De Sarlo,

M. Schioppo, R. Schwarz, A. Silva, U. Sterr, C. Tamm, R. Le Targat, P. Tuckey, G. Vallet, T. Waterholter, D. Xu, and P. Wolf. Search for transient variations of the fine structure constant and dark matter using fiber-linked optical atomic clocks. *New Journal of Physics*, 22(9):093010, September 2020. URL: `http://dx.doi.org/10.1088/1367-2630/abaace`, `doi:10.1088/1367-2630/abaace`.

[45] A. Derevianko and M. Pospelov. Hunting for topological dark matter with atomic clocks. *Nature Physics*, 10(12):933–936, November 2014. URL: `http://dx.doi.org/10.1038/nphys3137`, `doi:10.1038/nphys3137`.

[46] M. S. Safronova, D. Budker, D. DeMille, D. F. J. Kimball, A. Derevianko, and C. W. Clark. Search for new physics with atoms and molecules. *Rev. Mod. Phys.*, 90:025008, Jun 2018. URL: `https://link.aps.org/doi/10.1103/RevModPhys.90.025008`, `doi:10.1103/RevModPhys.90.025008`.

[47] C. J. Kennedy, E. Oelker, J. M. Robinson, T. Bothwell, D. Kedar, W. R. Milner, G. E. Marti, A. Derevianko, and J. Ye. Precision metrology meets cosmology: Improved constraints on ultralight dark matter from atom-cavity frequency comparisons. *Phys. Rev. Lett.*, 125:201302, Nov 2020. URL: `https://link.aps.org/doi/10.1103/PhysRevLett.125.201302`, `doi:10.1103/PhysRevLett.125.201302`.

[48] T. Schuldt, M. Gohlke, M. Oswald, J. Wüst, T. Blomberg, K. Döringshoff, A. Bawamia, A. Wicht, M. Lezius, K. Voss, M. Krutzik, S. Herrmann, E. Kovalchuk, A. Peters, and C. Braxmaier. Optical clock technologies for global navigation satellite systems. *GPS Solutions*, 25(3), April 2021. URL: `http://dx.doi.org/10.1007/s10291-021-01113-2`, `doi:10.1007/s10291-021-01113-2`.

[49] T. D. Schmidt, T. Schuldt, G. Michalak, J. Surof, J. Poliak, G. Giorgi, C. Braxmaier, M. Meurer, and C. Günther. Optical technologies for future global navigation satellite systems. In *2023 IEEE/ION Position, Location and Navigation Symposium (PLANS)*. IEEE, April 2023. URL: `http://dx.doi.org/10.1109/PLANS53410.2023.10140082`, `doi:10.1109/plans53410.2023.10140082`.

[50] S. Droste, F. Ozimek, T. Udem, K. Predehl, T. W. Hänsch, H. Schnatz, G. Grosche, and R. Holzwarth. Optical-frequency transfer over a single-span 1840 km fiber link. *Phys. Rev. Lett.*, 111:110801, Sep 2013. URL: `https://link.aps.org/doi/10.1103/PhysRevLett.111.110801`, `doi:10.1103/PhysRevLett.111.110801`.

[51] C. Lisdat, G. Grosche, N. Quintin, C. Shi, S. Raupach, C. Grebing, D. Nicolodi, F. Stefani, A. Al-Masoudi, S. Dörscher, S. Häfner, J.-L. Robyr, N. Chiodo, S. Bilicki, E. Bookjans, A. Koczwara, S. Koke, A. Kuhl, F. Wiotte, F. Meynadier, E. Camisard, M. Abgrall, M. Lours, T. Legero, H. Schnatz, U. Sterr, H. Denker, C. Chardonnet, Y. Le Coq, G. Santarelli, A. Amy-Klein, R. Le Targat, J. Lodewyck, O. Lopez, and P.-E. Pottie. A clock network for geodesy and fundamental science. *Nature Communications*, 7(1):12443, August 2016. URL: `http://dx.doi.org/10.1038/ncomms12443`, `doi:10.1038/ncomms12443`.

[52] J. Grotti, S. Koller, S. Vogt, S. Häfner, U. Sterr, C. Lisdat, H. Denker, C. Voigt, L. Timmen, A. Rolland, F. N. Baynes, H. S. Margolis, M. Zampaolo, P. Thoumany, M. Pizzocaro, B. Rauf, F. Bregolin, A. Tampellini, P. Barbieri, M. Zucco, G. A. Costanzo, C. Clivati, F. Levi, and D. Calonico. Geodesy and metrology with a transportable optical clock. *Nature Physics*, 14(5):437–441, February 2018. URL: `http://dx.doi.org/10.1038/s41567-017-0042-3`, `doi:10.1038/s41567-017-0042-3`.

[53] T. E. Mehlstäubler, G. Grosche, C. Lisdat, P. O. Schmidt, and H. Denker. Atomic clocks for geodesy. *Reports on Progress in Physics*, 81(6):064401, April 2018. URL: `http://dx.doi.org/10.1088/1361-6633/aab409`, `doi:10.1088/1361-6633/aab409`.

[54] J. Grotti, I. Nosske, S. Koller, S. Herbers, H. Denker, L. Timmen, G. Vishnyakova, G. Grosche, T. Waterholter, A. Kuhl, S. Koke, E. Benkler, M. Giunta, L. Maisenbacher, A. Matveev, S. Dörscher, R. Schwarz, A. Al-Masoudi, T. Hänsch, T. Udem, R. Holzwarth, and C. Lisdat. Long-distance chronometric leveling with a portable optical clock. *Physical Review Applied*, 21(6):L061001, June 2024. URL: `http://dx.doi.org/10.1103/PhysRevApplied.21.L061001`, `doi:10.1103/physrevapplied.21.l061001`.

[55] W. M. Itano, J. C. Bergquist, J. J. Bollinger, J. M. Gilligan, D. J. Heinzen, F. L. Moore, M. G. Raizen, and D. J. Wineland. Quantum projection noise: Population fluctuations in two-level systems. *Phys. Rev. A*, 47:3554–3570, May 1993. URL: `https://link.aps.org/doi/10.1103/PhysRevA.47.3554`, `doi:10.1103/PhysRevA.47.3554`.

[56] C. W. Gardiner and P. Zoller. *Quantum noise*. Springer Series in Synergetics. Springer, Berlin, Germany, 3 edition, August 2004.

[57] L. Pezzé and A. Smerzi. Entanglement, nonlinear dynamics, and the heisenberg limit. *Phys. Rev. Lett.*, 102:100401, Mar 2009. URL: https://link.aps.org/doi/10.1103/PhysRevLett.102.100401, doi:10.1103/PhysRevLett.102.100401.

[58] D. J. Wineland, J. J. Bollinger, W. M. Itano, F. L. Moore, and D. J. Heinzen. Spin squeezing and reduced quantum noise in spectroscopy. *Phys. Rev. A*, 46:R6797–R6800, Dec 1992. URL: https://link.aps.org/doi/10.1103/PhysRevA.46.R6797, doi:10.1103/PhysRevA.46.R6797.

[59] D. J. Wineland, J. J. Bollinger, W. M. Itano, and D. J. Heinzen. Squeezed atomic states and projection noise in spectroscopy. *Phys. Rev. A*, 50:67–88, Jul 1994. URL: https://link.aps.org/doi/10.1103/PhysRevA.50.67, doi:10.1103/PhysRevA.50.67.

[60] J. Franke, S. R. Muleady, R. Kaubruegger, F. Kranzl, R. Blatt, A. M. Rey, M. K. Joshi, and C. F. Roos. Quantum-enhanced sensing on optical transitions through finite-range interactions. *Nature*, 621(7980):740–745, August 2023. URL: http://dx.doi.org/10.1038/s41586-023-06472-z, doi:10.1038/s41586-023-06472-z.

[61] J. M. Robinson, M. Miklos, Y. M. Tso, C. J. Kennedy, T. Bothwell, D. Kedar, J. K. Thompson, and J. Ye. Direct comparison of two spin-squeezed optical clock ensembles at the 10^{-17} level. *Nature Physics*, 20(2):208–213, January 2024. URL: http://dx.doi.org/10.1038/s41567-023-02310-1, doi:10.1038/s41567-023-02310-1.

[62] W. J. Eckner, N. Darkwah Oppong, A. Cao, A. W. Young, W. R. Milner, J. M. Robinson, J. Ye, and A. M. Kaufman. Realizing spin squeezing with Rydberg interactions in an optical clock. *Nature*, 621(7980):734–739, August 2023. URL: http://dx.doi.org/10.1038/s41586-023-06360-6, doi:10.1038/s41586-023-06360-6.

[63] R. Finkelstein, R. B.-S. Tsai, X. Sun, P. Scholl, S. Direkci, T. Gefen, J. Choi, A. L. Shaw, and M. Endres. Universal quantum operations and ancilla-based read-out for tweezer clocks. *Nature*, 634(8033):321–327, October 2024. URL: http://dx.doi.org/10.1038/s41586-024-08005-8, doi:10.1038/s41586-024-08005-8.

[64] A. Cao, W. J. Eckner, T. Lukin Yelin, A. W. Young, S. Jandura, L. Yan, K. Kim, G. Pupillo, J. Ye, N. Darkwah Oppong, and A. M. Kaufman. Multi-qubit gates

and Schrödinger cat states in an optical clock. *Nature*, 634(8033):315–320, October 2024. URL: http://dx.doi.org/10.1038/s41586-024-07913-z, doi:10.1038/s41586-024-07913-z.

[65] A. Shaji and C. M. Caves. Qubit metrology and decoherence. *Physical Review A*, 76(3):032111, September 2007. URL: http://dx.doi.org/10.1103/PhysRevA.76.032111, doi:10.1103/physreva.76.032111.

[66] R. Demkowicz-Dobrzański, J. Kołodyński, and M. Guţă. The elusive Heisenberg limit in quantum-enhanced metrology. *Nature Communications*, 3(1):1063, September 2012. URL: http://dx.doi.org/10.1038/ncomms2067, doi:10.1038/ncomms2067.

[67] B. M. Escher, R. L. de Matos Filho, and L. Davidovich. General framework for estimating the ultimate precision limit in noisy quantum-enhanced metrology. *Nature Physics*, 7(5):406–411, March 2011. URL: http://dx.doi.org/10.1038/nphys1958, doi:10.1038/nphys1958.

[68] S. I. Knysh, E. H. Chen, and G. A. Durkin. True limits to precision via unique quantum probe, 2014. URL: https://arxiv.org/abs/1402.0495, arXiv:1402.0495.

[69] W. Thomson and P. G. Tait. *Elements of Natural Philosophy*. Cambridge University Press, June 2010. URL: http://dx.doi.org/10.1017/CBO9780511709708, doi:10.1017/cbo9780511709708.

[70] I. I. Rabi, S. Millman, P. Kusch, and J. R. Zacharias. The molecular beam resonance method for measuring nuclear magnetic moments. the magnetic moments of ${}_3\mathrm{Li}^6$, ${}_3\mathrm{Li}^7$ and ${}_9\mathrm{F}^{19}$. *Phys. Rev.*, 55:526–535, Mar 1939. URL: https://link.aps.org/doi/10.1103/PhysRev.55.526, doi:10.1103/PhysRev.55.526.

[71] N. F. Ramsey. A molecular beam resonance method with separated oscillating fields. *Physical Review*, 78(6):695–699, June 1950. URL: http://dx.doi.org/10.1103/PhysRev.78.695, doi:10.1103/physrev.78.695.

[72] Proceedings of the 13th CGPM. page 103, 1967. URL: http://dx.doi.org/10.59161/CGPM1967RES1E, doi:10.59161/cgpm1967res1e.

[73] Proceedings of the 27th CGPM. 2022. URL: http://dx.doi.org/10.59161/CGPM2022RES5E, doi:10.59161/CGPM2022RES5E.

[74] J. Tiedau, M. V. Okhapkin, K. Zhang, J. Thielking, G. Zitzer, E. Peik, F. Schaden, T. Pronebner, I. Morawetz, L. T. De Col, F. Schneider, A. Leitner, M. Pressler, G. A. Kazakov, K. Beeks, T. Sikorsky, and T. Schumm. Laser excitation of the Th-229 nucleus. *Phys. Rev. Lett.*, 132:182501, Apr 2024. URL: `https://link.aps.org/doi/10.1103/PhysRevLett.132.182501`, `doi:10.1103/PhysRevLett.132.182501`.

[75] H. Margolis. A brief history of timekeeping. *Physics World*, 31(11):27–30, November 2018. URL: `http://dx.doi.org/10.1088/2058-7058/31/11/36`, `doi:10.1088/2058-7058/31/11/36`.

[76] C. Orzel. *A brief history of timekeeping.* Oneworld Publications, London, England, February 2022.

[77] M. A. Lombardi, T. P. Heavner, and S. R. Jefferts. NIST primary frequency standards and the realization of the SI second. *NCSLI Measure*, 2(4):74–89, December 2007. URL: `http://dx.doi.org/10.1080/19315775.2007.11721402`, `doi:10.1080/19315775.2007.11721402`.

[78] J. Jespersen. *From sundials to atomic clocks.* Dover Publications, Mineola, NY, 2 edition, March 2003.

[79] M. Lombardi. First in a series on the evolution of time measurement: celestial, flow, and mechanical clocks. *IEEE Instrumentation & Measurement Magazine*, 14(4):45–51, August 2011. URL: `http://dx.doi.org/10.1109/MIM.2011.5961371`, `doi:10.1109/mim.2011.5961371`.

[80] T. N. Bandi. A comprehensive overview of atomic clocks and their applications. *Biology, Engineering, Medicine and Science Reports*, 9(1):01–10, January 2023. URL: `http://dx.doi.org/10.5530/bems.9.1.1`, `doi:10.5530/bems.9.1.1`.

[81] Atomic Clocks — nist.gov. `https://www.nist.gov/atomic-clocks`. [Accessed 01-11-2024].

[82] D. Howe. Frequency domain stability measurements: A tutorial introduction. *NASA STI/Recon Technical Report N*, 76:30543, 02 1976.

[83] J. Rutman and F. Walls. Characterization of frequency stability in precision frequency sources. *Proceedings of the IEEE*, 79(7):952–960, 1991. URL: `http://dx.doi.org/10.1109/5.84972`, `doi:10.1109/5.84972`.

[84] W. Riley and D. Howe. Handbook of frequency stability analysis, 2008-07-01 00:07:00 2008. URL: `https://tsapps.nist.gov/publication/get_pdf.cfm?pub_id=50505`.

[85] D. Allan. Statistics of atomic frequency standards. *Proceedings of the IEEE*, 54(2):221–230, 1966. URL: `http://dx.doi.org/10.1109/proc.1966.4634`, `doi:10.1109/proc.1966.4634`.

[86] D. W. Allan. Should the classical variance be used as a basic measure in standards metrology? *IEEE Transactions on Instrumentation and Measurement*, IM-36(2):646–654, 1987. URL: `http://dx.doi.org/10.1109/TIM.1987.6312761`, `doi:10.1109/TIM.1987.6312761`.

[87] J. A. Barnes, A. R. Chi, L. S. Cutler, D. J. Healey, D. B. Leeson, T. E. McGunigal, J. A. Mullen, W. L. Smith, R. L. Sydnor, R. F. C. Vessot, and G. M. R. Winkler. Characterization of frequency stability. *IEEE Transactions on Instrumentation and Measurement*, IM-20(2):105–120, 1971. URL: `http://dx.doi.org/10.1109/TIM.1971.5570702`, `doi:10.1109/TIM.1971.5570702`.

[88] D. G. Matei, T. Legero, S. Häfner, C. Grebing, R. Weyrich, W. Zhang, L. Sonderhouse, J. M. Robinson, J. Ye, F. Riehle, and U. Sterr. 1.5 μm lasers with sub-10 mHz linewidth. *Phys. Rev. Lett.*, 118:263202, Jun 2017. URL: `https://link.aps.org/doi/10.1103/PhysRevLett.118.263202`, `doi:10.1103/PhysRevLett.118.263202`.

[89] A. V. Oppenheim and G. C. Verghese. *Signals, Systems and Inference*. Pearson Education, Amsterdam, 2015.

[90] S. Miller and D. Childers. *Probability and Random Processes - With Applications to Signal Processing and Communications*. Academic Press, Amsterdam, Boston, 2012.

[91] M. Schulte, C. Lisdat, P. O. Schmidt, U. Sterr, and K. Hammerer. Prospects and challenges for squeezing-enhanced optical atomic clocks. *Nature Communications*, 11(1), November 2020. URL: `http://dx.doi.org/10.1038/s41467-020-19403-7`, `doi:10.1038/s41467-020-19403-7`.

[92] I. D. Leroux, N. Scharnhorst, S. Hannig, J. Kramer, L. Pelzer, M. Stepanova, and P. O. Schmidt. On-line estimation of local oscillator noise and optimisation of servo parameters in atomic clocks. *Metrologia*, 54(3):307–321, April 2017. URL: `http://dx.doi.org/10.1088/1681-7575/aa66e9`, `doi:10.1088/1681-7575/aa66e9`.

[93] R. P. Feynman, J. Vernon, Frank L., and R. W. Hellwarth. Geometrical representation of the Schrödinger equation for solving maser problems. *Journal of Applied Physics*, 28(1):49–52, 01 1957. URL: `http://dx.doi.org/10.1063/1.1722572`, `doi:10.1063/1.1722572`.

[94] R. H. Dicke. Coherence in spontaneous radiation processes. *Phys. Rev.*, 93:99–110, Jan 1954. URL: `https://link.aps.org/doi/10.1103/PhysRev.93.99`, `doi:10.1103/PhysRev.93.99`.

[95] B. A. Chase and J. M. Geremia. Collective processes of an ensemble of spin-1/2 particles. *Phys. Rev. A*, 78:052101, Nov 2008. URL: `https://link.aps.org/doi/10.1103/PhysRevA.78.052101`, `doi:10.1103/PhysRevA.78.052101`.

[96] B. Q. Baragiola, B. A. Chase, and J. Geremia. Collective uncertainty in partially polarized and partially decohered spin-$\frac{1}{2}$ systems. *Phys. Rev. A*, 81:032104, Mar 2010. URL: `https://link.aps.org/doi/10.1103/PhysRevA.81.032104`, `doi:10.1103/PhysRevA.81.032104`.

[97] S. Hartmann. Generalized Dicke states, 2016. URL: `https://arxiv.org/abs/1201.1732`, `arXiv:1201.1732`.

[98] F. Fröwis, M. Skotiniotis, B. Kraus, and W. Dür. Optimal quantum states for frequency estimation. *New Journal of Physics*, 16(8):083010, aug 2014. URL: `https://dx.doi.org/10.1088/1367-2630/16/8/083010`, `doi:10.1088/1367-2630/16/8/083010`.

[99] N. Shammah, S. Ahmed, N. Lambert, S. De Liberato, and F. Nori. Open quantum systems with local and collective incoherent processes: Efficient numerical simulations using permutational invariance. *Phys. Rev. A*, 98:063815, Dec 2018. URL: `https://link.aps.org/doi/10.1103/PhysRevA.98.063815`, `doi:10.1103/PhysRevA.98.063815`.

[100] M. Xu, D. A. Tieri, and M. J. Holland. Simulating open quantum systems by applying SU(4) to quantum master equations. *Phys. Rev. A*, 87:062101, Jun 2013. URL: `https://link.aps.org/doi/10.1103/PhysRevA.87.062101`, `doi:10.1103/PhysRevA.87.062101`.

[101] G. S. Agarwal. Relation between atomic coherent-state representation, state multipoles, and generalized phase-space distributions. *Phys. Rev. A*, 24:2889–2896, Dec 1981. URL: `https://link.aps.org/doi/10.1103/PhysRevA.24.2889`, `doi:10.1103/PhysRevA.24.2889`.

[102] J. P. Dowling, G. S. Agarwal, and W. P. Schleich. Wigner distribution of a general angular-momentum state: Applications to a collection of two-level atoms. *Phys. Rev. A*, 49:4101–4109, May 1994. URL: `https://link.aps.org/doi/10.1103/PhysRevA.49.4101`, `doi:10.1103/PhysRevA.49.4101`.

[103] A. Messiah. *Quantum Mechanics: Vol. II.* North-Holland Publishing, Oxford, England, December 1961.

[104] C. W. Gardiner and P. Zoller. *Quantum world of ultra-cold atoms and light - book II: The physics of quantum-optical devices.* Cold Atoms. Imperial College Press, London, England, June 2015.

[105] C. Gerry and P. Knight. *Introductory Quantum Optics.* Cambridge University Press, October 2004. URL: `http://dx.doi.org/10.1017/CBO9780511791239`, `doi:10.1017/cbo9780511791239`.

[106] D. A. Steck. *Quantum and Atom Optics.* Cambridge, June 2024.

[107] H. Carmichael. *An open systems approach to quantum optics.* Lecture Notes in Physics Monographs. Springer, Berlin, Germany, 1993 edition, May 1993.

[108] M. A. Nielsen and I. L. Chuang. *Quantum Computation and Quantum Information.* Cambridge University Press, Cambridge, England, December 2010.

[109] M. M. Wilde. *Quantum Information Theory.* Cambridge University Press, Cambridge, England, 2 edition, February 2017.

[110] D. Manzano. A short introduction to the Lindblad master equation. *AIP Advances*, 10(2), February 2020. URL: `http://dx.doi.org/10.1063/1.5115323`, `doi:10.1063/1.5115323`.

[111] A. Rivas and S. Huelga. *Open Quantum Systems.* SpringerBriefs in Physics. Springer, Berlin, Germany, 2012 edition, September 2011.

[112] C. A. Brasil, F. F. Fanchini, and R. d. J. Napolitano. A simple derivation of the Lindblad equation. *Revista Brasileira de Ensino de Física*, 35(1):01–09, March 2013. URL: `http://dx.doi.org/10.1590/S1806-11172013000100003`, `doi:10.1590/s1806-11172013000100003`.

[113] J. Dalibard, Y. Castin, and K. Mølmer. Wave-function approach to dissipative processes in quantum optics. *Phys. Rev. Lett.*, 68:580–583, Feb 1992. URL: `https://link.aps.org/doi/10.1103/PhysRevLett.68.580`, `doi:10.1103/PhysRevLett.68.580`.

[114] K. Mølmer, Y. Castin, and J. Dalibard. Monte Carlo wave-function method in quantum optics. *J. Opt. Soc. Am. B*, 10(3):524–538, Mar 1993. URL: `https://opg.optica.org/josab/abstract.cfm?URI=josab-10-3-524`, `doi:10.1364/JOSAB.10.000524`.

[115] F. T. Arecchi, E. Courtens, R. Gilmore, and H. Thomas. Atomic coherent states in quantum optics. *Phys. Rev. A*, 6:2211–2237, Dec 1972. URL: `https://link.aps.org/doi/10.1103/PhysRevA.6.2211`, `doi:10.1103/PhysRevA.6.2211`.

[116] J. M. Radcliffe. Some properties of coherent spin states. *Journal of Physics A: General Physics*, 4(3):313, may 1971. URL: `https://dx.doi.org/10.1088/0305-4470/4/3/009`, `doi:10.1088/0305-4470/4/3/009`.

[117] F. T. Hioe. Coherent states and Lie algebras. *Journal of Mathematical Physics*, 15(8):1174–1177, August 1974. URL: `http://dx.doi.org/10.1063/1.1666788`, `doi:10.1063/1.1666788`.

[118] R. F. Werner. Quantum states with Einstein-Podolsky-Rosen correlations admitting a hidden-variable model. *Phys. Rev. A*, 40:4277–4281, Oct 1989. URL: `https://link.aps.org/doi/10.1103/PhysRevA.40.4277`, `doi:10.1103/PhysRevA.40.4277`.

[119] O. Gühne and G. Tóth. Entanglement detection. *Physics Reports*, 474(1):1–75, 2009. URL: `https://www.sciencedirect.com/science/article/pii/S0370157309000623`, `doi:10.1016/j.physrep.2009.02.004`.

[120] R. Horodecki, P. Horodecki, M. Horodecki, and K. Horodecki. Quantum entanglement. *Rev. Mod. Phys.*, 81:865–942, Jun 2009. URL: `https://link.aps.org/doi/10.1103/RevModPhys.81.865`, `doi:10.1103/RevModPhys.81.865`.

[121] D. M. Greenberger, M. A. Horne, and A. Zeilinger. *Going Beyond Bell's Theorem*, page 69–72. Springer Netherlands, 1989. URL: `http://dx.doi.org/10.1007/978-94-017-0849-4_10`, `doi:10.1007/978-94-017-0849-4_10`.

[122] J. J. . Bollinger, W. M. Itano, D. J. Wineland, and D. J. Heinzen. Optimal frequency measurements with maximally correlated states. *Phys. Rev. A*, 54:R4649–R4652, Dec 1996. URL: `https://link.aps.org/doi/10.1103/PhysRevA.54.R4649`, `doi:10.1103/PhysRevA.54.R4649`.

[123] J. D. Macomber and R. Lynch. Squeezed spin states. *The Journal of Chemical Physics*, 83(12):6514–6519, 12 1985. `arXiv:https://pubs.aip.org/aip/jcp/article-pdf/83/12/6514/18956600/6514\_1\_online.pdf`, `doi:10.1063/1.449838`.

[124] G. S. Agarwal and R. R. Puri. Atomic states with spectroscopic squeezing. *Phys. Rev. A*, 49:4968–4971, Jun 1994. URL: `https://link.aps.org/doi/10.1103/PhysRevA.49.4968`, `doi:10.1103/PhysRevA.49.4968`.

[125] M. Kitagawa and M. Ueda. Squeezed spin states. *Phys. Rev. A*, 47:5138–5143, Jun 1993. URL: `https://link.aps.org/doi/10.1103/PhysRevA.47.5138`, `doi:10.1103/PhysRevA.47.5138`.

[126] J. Benhelm, G. Kirchmair, C. F. Roos, and R. Blatt. Towards fault-tolerant quantum computing with trapped ions. *Nature Physics*, 4(6):463–466, April 2008. URL: `http://dx.doi.org/10.1038/nphys961`, `doi:10.1038/nphys961`.

[127] R. Blatt and D. Wineland. Entangled states of trapped atomic ions. *Nature*, 453(7198):1008–1015, June 2008. URL: `http://dx.doi.org/10.1038/nature07125`, `doi:10.1038/nature07125`.

[128] D. Leibfried, M. D. Barrett, T. Schaetz, J. Britton, J. Chiaverini, W. M. Itano, J. D. Jost, C. Langer, and D. J. Wineland. Toward Heisenberg-limited spectroscopy with multiparticle entangled states. *Science*, 304(5676):1476–1478, 2004. URL: `https://www.science.org/doi/abs/10.1126/science.1097576`, `doi:10.1126/science.1097576`.

[129] J. A. Hines, S. V. Rajagopal, G. L. Moreau, M. D. Wahrman, N. A. Lewis, O. Marković, and M. Schleier-Smith. Spin squeezing by Rydberg dressing in an array of atomic ensembles. *Physical Review Letters*, 131(6):063401, August 2023. URL: `http://dx.doi.org/10.1103/PhysRevLett.131.063401`, `doi:10.1103/physrevlett.131.063401`.

[130] A. Sørensen, L.-M. Duan, J. I. Cirac, and P. Zoller. Many-particle entanglement with Bose–Einstein condensates. *Nature*, 409(6816):63–66, January 2001. URL: `http://dx.doi.org/10.1038/35051038`, `doi:10.1038/35051038`.

[131] J. Estève, C. Gross, A. Weller, S. Giovanazzi, and M. K. Oberthaler. Squeezing and entanglement in a Bose–Einstein condensate. *Nature*, 455(7217):1216–1219, October 2008. URL: `http://dx.doi.org/10.1038/nature07332`, `doi:10.1038/nature07332`.

[132] C. Gross, T. Zibold, E. Nicklas, J. Estève, and M. K. Oberthaler. Nonlinear atom interferometer surpasses classical precision limit. *Nature*, 464(7292):1165–1169, March 2010. URL: `http://dx.doi.org/10.1038/nature08919`, `doi:10.1038/nature08919`.

[133] M. F. Riedel, P. Böhi, Y. Li, T. W. Hänsch, A. Sinatra, and P. Treutlein. Atom-chip-based generation of entanglement for quantum metrology. *Nature*, 464(7292):1170–1173, March 2010. URL: `http://dx.doi.org/10.1038/nature08988`, `doi:10.1038/nature08988`.

[134] D. F. Walls and P. Zoller. Reduced quantum fluctuations in resonance fluorescence. *Phys. Rev. Lett.*, 47:709–711, Sep 1981. URL: `https://link.aps.org/doi/10.1103/PhysRevLett.47.709`, `doi:10.1103/PhysRevLett.47.709`.

[135] G. S. Agarwal and R. R. Puri. Cooperative behavior of atoms irradiated by broadband squeezed light. *Phys. Rev. A*, 41:3782–3791, Apr 1990. URL: `https://link.aps.org/doi/10.1103/PhysRevA.41.3782`, `doi:10.1103/PhysRevA.41.3782`.

[136] K. Wodkiewicz and J. H. Eberly. Coherent states, squeezed fluctuations, and the SU(2) and SU(1,1) groups in quantum-optics applications. *J. Opt. Soc. Am. B*, 2(3):458–466, Mar 1985. URL: `https://opg.optica.org/josab/abstract.cfm?URI=josab-2-3-458`, `doi:10.1364/JOSAB.2.000458`.

[137] A. R. U. Devi and Sudha. Spin squeezing and quantum correlations, 2010. URL: `https://arxiv.org/abs/1101.0308`, `arXiv:1101.0308`.

[138] J. Ma, X. Wang, C. Sun, and F. Nori. Quantum spin squeezing. *Physics Reports*, 509(2–3):89–165, December 2011. URL: `http://dx.doi.org/10.1016/j.physrep.2011.08.003`, `doi:10.1016/j.physrep.2011.08.003`.

[139] M. Schulte, V. J. Martínez-Lahuerta, M. S. Scharnagl, and K. Hammerer. Ramsey interferometry with generalized one-axis twisting echoes. *Quantum*, 4:268, May 2020. URL: `http://dx.doi.org/10.22331/q-2020-05-15-268`, `doi:10.22331/q-2020-05-15-268`.

[140] R. Kaubruegger, D. V. Vasilyev, M. Schulte, K. Hammerer, and P. Zoller. Quantum variational optimization of Ramsey interferometry and atomic clocks. *Phys. Rev. X*, 11:041045, Dec 2021. URL: `https://link.aps.org/doi/10.1103/PhysRevX.11.041045`, `doi:10.1103/PhysRevX.11.041045`.

[141] T. G. Thurtell and A. Miyake. Optimizing one-axis twists for variational Bayesian quantum metrology. *Phys. Rev. Res.*, 6:023179, May 2024. URL: `https://link.aps.org/doi/10.1103/PhysRevResearch.6.023179`, `doi:10.1103/PhysRevResearch.6.023179`.

[142] C. D. Marciniak, T. Feldker, I. Pogorelov, R. Kaubruegger, D. V. Vasilyev, R. van Bijnen, P. Schindler, P. Zoller, R. Blatt, and T. Monz. Optimal metrology with programmable quantum sensors. *Nature*, 603(7902):604–609, March 2022. URL: `http://dx.doi.org/10.1038/s41586-022-04435-4`, `doi:10.1038/s41586-022-04435-4`.

[143] J. Li, G. R. M. da Silva, S. Kain, and S. M. Shahriar. Generalized echo squeezing protocol with near-Heisenberg-limit sensitivity and strong robustness against detection noise and variation in squeezing parameter. *Physical Review A*, 107(3):032610, March 2023. URL: `http://dx.doi.org/10.1103/PhysRevA.107.032610`, `doi:10.1103/physreva.107.032610`.

[144] E. Peik, T. Schneider, and C. Tamm. Laser frequency stabilization to a single ion. *Journal of Physics B: Atomic, Molecular and Optical Physics*, 39(1):145–158, December 2005. URL: `http://dx.doi.org/10.1088/0953-4075/39/1/012`, `doi:10.1088/0953-4075/39/1/012`.

[145] P. P. Vaidyanathan. *The theory of linear prediction.* Synthesis Lectures on Signal Processing. Morgan & Claypool, San Rafael, CA, December 2007.

[146] N. Wiener. *Extrapolation, interpolation, and smoothing of stationary time series.* The MIT Press. MIT Press, London, England, March 1964.

[147] A. N. Kolmogorov. Interpolation and extrapolation of stationary sequences. *Izvestiya the Academy of Sciences of the USSR, Ser. Math.*, (5):3–14, 1941.

[148] D. Ulam-Orgikh and M. Kitagawa. Spin squeezing and decoherence limit in Ramsey spectroscopy. *Physical Review A*, 64(5):052106, October 2001. URL: `http://dx.doi.org/10.1103/PhysRevA.64.052106`, `doi:10.1103/physreva.64.052106`.

[149] S. F. Huelga, C. Macchiavello, T. Pellizzari, A. K. Ekert, M. B. Plenio, and J. I. Cirac. Improvement of frequency standards with quantum entanglement. *Physical Review Letters*, 79(20):3865–3868, November 1997. URL: `http://dx.doi.org/10.1103/PhysRevLett.79.3865`, `doi:10.1103/physrevlett.79.3865`.

[150] P. Sekatski, M. Skotiniotis, J. Kołodyński, and W. Dür. Quantum metrology with full and fast quantum control. *Quantum*, 1:27, September 2017. URL: `http://dx.doi.org/10.22331/q-2017-09-06-27`, `doi:10.22331/q-2017-09-06-27`.

[151] K. Macieszczak, M. Fraas, and R. Demkowicz-Dobrzański. Bayesian quantum frequency estimation in presence of collective dephasing. *New Journal of Physics*, 16(11):113002, oct 2014. URL: `https://dx.doi.org/10.1088/1367-2630/16/11/113002`, `doi:10.1088/1367-2630/16/11/113002`.

[152] C. Cohen-Tannoudji, J. Dupont-Roc, and G. Grynberg. *Atom-Photon Interactions: Basic Process and Appilcations*. Wiley, April 1998. URL: `http://dx.doi.org/10.1002/9783527617197`, `doi:10.1002/9783527617197`.

[153] M. O. Scully and M. S. Zubairy. *Quantum Optics*. Cambridge University Press, September 1997. URL: `http://dx.doi.org/10.1017/CBO9780511813993`, `doi:10.1017/cbo9780511813993`.

[154] V. Weisskopf and E. Wigner. Berechnung der natürlichen Linienbreite auf Grund der Diracschen Lichttheorie. *Zeitschrift für Physik*, 63(1–2):54–73, January 1930. URL: `http://dx.doi.org/10.1007/BF01336768`, `doi:10.1007/bf01336768`.

[155] P. W. Milonni. *The quantum vacuum*. Academic Press, San Diego, CA, January 1994.

[156] H.-P. Breuer and F. Petruccione. *The theory of open quantum systems*. Oxford University Press, London, England, June 2002.

[157] T. Monz, P. Schindler, J. T. Barreiro, M. Chwalla, D. Nigg, W. A. Coish, M. Harlander, W. Hänsel, M. Hennrich, and R. Blatt. 14-qubit entanglement: Creation and coherence. *Phys. Rev. Lett.*, 106:130506, Mar 2011. URL: `https://link.aps.org/doi/10.1103/PhysRevLett.106.130506`, `doi:10.1103/PhysRevLett.106.130506`.

[158] C. F. Roos, M. Chwalla, K. Kim, M. Riebe, and R. Blatt. 'Designer atoms' for quantum metrology. *Nature*, 443(7109):316–319, September 2006. URL: `http://dx.doi.org/10.1038/nature05101`, `doi:10.1038/nature05101`.

[159] U. Dorner. Quantum frequency estimation with trapped ions and atoms. *New Journal of Physics*, 14(4):043011, April 2012. URL: `http://dx.doi.org/10.1088/1367-2630/14/4/043011`, `doi:10.1088/1367-2630/14/4/043011`.

[160] C. Gardiner. *Stochastic Methods - A Handbook for the Natural and Social Sciences*. Springer Berlin Heidelberg, Wiesbaden, 2010.

[161] C. W. Helstrom. Quantum detection and estimation theory. *Journal of Statistical Physics*, 1(2):231–252, 1969. URL: http://dx.doi.org/10.1007/BF01007479, doi:10.1007/bf01007479.

[162] A. Holevo. *Probabilistic and Statistical Aspects of Quantum Theory*. Edizioni della Normale, 2011. URL: http://dx.doi.org/10.1007/978-88-7642-378-9, doi:10.1007/978-88-7642-378-9.

[163] M. Cohen. The Fisher information and convexity. *IEEE Transactions on Information Theory*, 14(4):591–592, July 1968. URL: http://dx.doi.org/10.1109/TIT.1968.1054175, doi:10.1109/tit.1968.1054175.

[164] L. Pezzè and A. Smerzi. Quantum theory of phase estimation, 2014. URL: https://arxiv.org/abs/1411.5164, arXiv:1411.5164.

[165] S. M. Kay. *Fundamentals of statistical processing, volume I*. Prentice Hall, Philadelphia, PA, March 1993.

[166] E. L. Lehmann and G. Casella. *Theory of Point Estimation*. Springer Texts in Statistics. Springer, New York, NY, 2 edition, September 2003.

[167] R. Berger and G. Casella. *Statistical Inference*. Duxbury Press, Florence, AL, 2 edition, June 2001.

[168] S. L. Braunstein and C. M. Caves. Statistical distance and the geometry of quantum states. *Phys. Rev. Lett.*, 72:3439–3443, May 1994. URL: https://link.aps.org/doi/10.1103/PhysRevLett.72.3439, doi:10.1103/PhysRevLett.72.3439.

[169] M. G. A. Paris. Quantum estimation for quantum technology. *International Journal of Quantum Information*, 07(supp01):125–137, January 2009. URL: http://dx.doi.org/10.1142/S0219749909004839, doi:10.1142/s0219749909004839.

[170] K. Macieszczak. Quantum Fisher information: Variational principle and simple iterative algorithm for its efficient computation, 2013. arXiv:1312.1356.

[171] R. A. Fisher. On the mathematical foundations of theoretical statistics. *Philosophical Transactions of the Royal Society of London. Series A, Containing Papers of a Mathematical or Physical Character*, 222(594–604):309–368, January 1922. URL: http://dx.doi.org/10.1098/rsta.1922.0009, doi:10.1098/rsta.1922.0009.

[172] R. A. Fisher. Theory of statistical estimation. *Mathematical Proceedings of the Cambridge Philosophical Society*, 22(5):700–725, July 1925. URL: `http://dx.doi.org/10.1017/S0305004100009580`, `doi:10.1017/s0305004100009580`.

[173] M. Sarovar and G. J. Milburn. Optimal estimation of one-parameter quantum channels. *Journal of Physics A: Mathematical and General*, 39(26):8487–8505, June 2006. URL: `http://dx.doi.org/10.1088/0305-4470/39/26/015`, `doi:10.1088/0305-4470/39/26/015`.

[174] A. Fujiwara and H. Imai. A fibre bundle over manifolds of quantum channels and its application to quantum statistics. *Journal of Physics A: Mathematical and Theoretical*, 41(25):255304, May 2008. URL: `http://dx.doi.org/10.1088/1751-8113/41/25/255304`, `doi:10.1088/1751-8113/41/25/255304`.

[175] A. Das, W. Gorecki, and R. Demkowicz-Dobrzanski. Universal time scalings of sensitivity in Markovian quantum metrology, 2024. URL: `https://arxiv.org/abs/2404.03954`, `doi:10.48550/ARXIV.2404.03954`.

[176] S. Zhou and L. Jiang. Asymptotic theory of quantum channel estimation. *PRX Quantum*, 2(1), March 2021. URL: `http://dx.doi.org/10.1103/PRXQuantum.2.010343`, `doi:10.1103/prxquantum.2.010343`.

[177] S. Zhou, M. Zhang, J. Preskill, and L. Jiang. Achieving the Heisenberg limit in quantum metrology using quantum error correction. *Nature Communications*, 9(1), January 2018. URL: `http://dx.doi.org/10.1038/s41467-017-02510-3`, `doi:10.1038/s41467-017-02510-3`.

[178] R. Demkowicz-Dobrzański, J. Czajkowski, and P. Sekatski. Adaptive quantum metrology under general Markovian noise. *Physical Review X*, 7(4), October 2017. URL: `http://dx.doi.org/10.1103/PhysRevX.7.041009`, `doi:10.1103/physrevx.7.041009`.

[179] J. Kołodyński and R. Demkowicz-Dobrzański. Efficient tools for quantum metrology with uncorrelated noise. *New Journal of Physics*, 15(7):073043, jul 2013. URL: `https://dx.doi.org/10.1088/1367-2630/15/7/073043`, `doi:10.1088/1367-2630/15/7/073043`.

[180] R. Demkowicz-Dobrzański and L. Maccone. Using entanglement against noise in quantum metrology. *Physical Review Letters*, 113(25), December 2014. URL: `http://dx.doi.org/10.1103/PhysRevLett.113.250801`, `doi:10.1103/physrevlett.113.250801`.

[181] S. Kurdziałek, W. Górecki, F. Albarelli, and R. Demkowicz-Dobrzański. Using adaptiveness and causal superpositions against noise in quantum metrology. *Physical Review Letters*, 131(9):090801, August 2023. URL: `http://dx.doi.org/10.1103/PhysRevLett.131.090801`, `doi:10.1103/physrevlett.131.090801`.

[182] T. Macrì, A. Smerzi, and L. Pezzè. Loschmidt echo for quantum metrology. *Phys. Rev. A*, 94:010102, Jul 2016. URL: `https://link.aps.org/doi/10.1103/PhysRevA.94.010102`, `doi:10.1103/PhysRevA.94.010102`.

[183] Z. Cai, R. Babbush, S. C. Benjamin, S. Endo, W. J. Huggins, Y. Li, J. R. McClean, and T. E. O'Brien. Quantum error mitigation. *Reviews of Modern Physics*, 95(4):045005, December 2023. URL: `http://dx.doi.org/10.1103/RevModPhys.95.045005`, `doi:10.1103/revmodphys.95.045005`.

[184] T. Gudjons, B. Hilbert, P. Seibert, and G. Werth. Precise lifetime determination of the metastable $3d^2D_{5/2}$ level in Ca^+ by "electron shelving". *Europhysics Letters (EPL)*, 33(8):595–598, March 1996. URL: `http://dx.doi.org/10.1209/epl/i1996-00384-1`, `doi:10.1209/epl/i1996-00384-1`.

[185] Y. Huang, H. Guan, M. Zeng, L. Tang, and K. Gao. $^{40}Ca^+$ ion optical clock with micromotion-induced shifts below 1×10^{-18}. *Physical Review A*, 99(1):011401, January 2019. URL: `http://dx.doi.org/10.1103/PhysRevA.99.011401`, `doi:10.1103/physreva.99.011401`.

[186] Y. Huang, B. Zhang, M. Zeng, Y. Hao, Z. Ma, H. Zhang, H. Guan, Z. Chen, M. Wang, and K. Gao. Liquid-nitrogen-cooled Ca^+ optical clock with systematic uncertainty of 3×10^{-18}. *Physical Review Applied*, 17(3):034041, March 2022. URL: `http://dx.doi.org/10.1103/PhysRevApplied.17.034041`, `doi:10.1103/physrevapplied.17.034041`.

[187] V. D. Ovsiannikov, A. Derevianko, and K. Gibble. Rydberg spectroscopy in an optical lattice: Blackbody thermometry for atomic clocks. *Phys. Rev. Lett.*, 107:093003, Aug 2011. URL: `https://link.aps.org/doi/10.1103/PhysRevLett.107.093003`, `doi:10.1103/PhysRevLett.107.093003`.

[188] L. Festa, N. Lorenz, L.-M. Steinert, Z. Chen, P. Osterholz, R. Eberhard, and C. Gross. Blackbody-radiation-induced facilitated excitation of Rydberg atoms in optical tweezers. *Phys. Rev. A*, 105:013109, Jan 2022. URL: `https://link.aps.org/doi/10.1103/PhysRevA.105.013109`, `doi:10.1103/PhysRevA.105.013109`.

[189] T. F. Gallagher and W. E. Cooke. Interactions of blackbody radiation with atoms. *Phys. Rev. Lett.*, 42:835–839, Mar 1979. URL: `https://link.aps.org/doi/10.1103/PhysRevLett.42.835`, `doi:10.1103/PhysRevLett.42.835`.

[190] P. Niroula, J. Dolde, X. Zheng, J. Bringewatt, A. Ehrenberg, K. C. Cox, J. Thompson, M. J. Gullans, S. Kolkowitz, and A. V. Gorshkov. Quantum sensing with erasure qubits. *Phys. Rev. Lett.*, 133:080801, Aug 2024. URL: `https://link.aps.org/doi/10.1103/PhysRevLett.133.080801`, `doi:10.1103/PhysRevLett.133.080801`.

[191] Y. Wu, S. Kolkowitz, S. Puri, and J. D. Thompson. Erasure conversion for fault-tolerant quantum computing in alkaline earth Rydberg atom arrays. *Nature Communications*, 13(1), August 2022. URL: `http://dx.doi.org/10.1038/s41467-022-32094-6`, `doi:10.1038/s41467-022-32094-6`.

[192] K. Sahay, J. Jin, J. Claes, J. D. Thompson, and S. Puri. High-threshold codes for neutral-atom qubits with biased erasure errors. *Phys. Rev. X*, 13:041013, Oct 2023. URL: `https://link.aps.org/doi/10.1103/PhysRevX.13.041013`, `doi:10.1103/PhysRevX.13.041013`.

[193] S. Ma, G. Liu, P. Peng, B. Zhang, S. Jandura, J. Claes, A. P. Burgers, G. Pupillo, S. Puri, and J. D. Thompson. High-fidelity gates and mid-circuit erasure conversion in an atomic qubit. *Nature*, 622(7982):279–284, October 2023. URL: `http://dx.doi.org/10.1038/s41586-023-06438-1`, `doi:10.1038/s41586-023-06438-1`.

[194] P. Scholl, A. L. Shaw, R. B.-S. Tsai, R. Finkelstein, J. Choi, and M. Endres. Erasure conversion in a high-fidelity Rydberg quantum simulator. *Nature*, 622(7982):273–278, October 2023. URL: `http://dx.doi.org/10.1038/s41586-023-06516-4`, `doi:10.1038/s41586-023-06516-4`.

[195] M. Kang, W. C. Campbell, and K. R. Brown. Quantum error correction with metastable states of trapped ions using erasure conversion. *PRX Quantum*, 4:020358, Jun 2023. URL: `https://link.aps.org/doi/10.1103/PRXQuantum.4.020358`, `doi:10.1103/PRXQuantum.4.020358`.

[196] J. D. Teoh, P. Winkel, H. K. Babla, B. J. Chapman, J. Claes, S. J. de Graaf, J. W. O. Garmon, W. D. Kalfus, Y. Lu, A. Maiti, K. Sahay, N. Thakur, T. Tsunoda, S. H. Xue, L. Frunzio, S. M. Girvin, S. Puri, and R. J. Schoelkopf. Dual-rail encoding with superconducting cavities. *Proceedings of the National Academy of Sciences*, 120(41), October 2023. URL: `http://dx.doi.org/10.1073/pnas.2221736120`, `doi:10.1073/pnas.2221736120`.

[197] A. Kubica, A. Haim, Y. Vaknin, H. Levine, F. Brandão, and A. Retzker. Erasure qubits: Overcoming the T_1 limit in superconducting circuits. *Phys. Rev. X*, 13:041022, Nov 2023. URL: `https://link.aps.org/doi/10.1103/PhysRevX.13.041022`, `doi:10.1103/PhysRevX.13.041022`.

[198] H. Levine, A. Haim, J. S. C. Hung, N. Alidoust, M. Kalaee, L. DeLorenzo, E. A. Wollack, P. Arrangoiz-Arriola, A. Khalajhedayati, R. Sanil, H. Moradinejad, Y. Vaknin, A. Kubica, D. Hover, S. Aghaeimeibodi, J. A. Alcid, C. Baek, J. Barnett, K. Bawdekar, P. Bienias, H. A. Carson, C. Chen, L. Chen, H. Chinkezian, E. M. Chisholm, A. Clifford, R. Cosmic, N. Crisosto, A. M. Dalzell, E. Davis, J. M. D'Ewart, S. Diez, N. D'Souza, P. T. Dumitrescu, E. Elkhouly, M. T. Fang, Y. Fang, S. Flammia, M. J. Fling, G. Garcia, M. K. Gharzai, A. V. Gorshkov, M. J. Gray, S. Grimberg, A. L. Grimsmo, C. T. Hann, Y. He, S. Heidel, S. Howell, M. Hunt, J. Iverson, I. Jarrige, L. Jiang, W. M. Jones, R. Karabalin, P. J. Karalekas, A. J. Keller, D. Lasi, M. Lee, V. Ly, G. MacCabe, N. Mahuli, G. Marcaud, M. H. Matheny, S. McArdle, G. McCabe, G. Merton, C. Miles, A. Milsted, A. Mishra, L. Moncelsi, M. Naghiloo, K. Noh, E. Oblepias, G. Ortuno, J. C. Owens, J. Pagdilao, A. Panduro, J.-P. Paquette, R. N. Patel, G. Peairs, D. J. Perello, E. C. Peterson, S. Ponte, H. Putterman, G. Refael, P. Reinhold, R. Resnick, O. A. Reyna, R. Rodriguez, J. Rose, A. H. Rubin, M. Runyan, C. A. Ryan, A. Sahmoud, T. Scaffidi, B. Shah, S. Siavoshi, P. Sivarajah, T. Skogland, C.-J. Su, L. J. Swenson, J. Sylvia, S. M. Teo, A. Tomada, G. Torlai, M. Wistrom, K. Zhang, I. Zuk, A. A. Clerk, F. G. S. L. Brandão, A. Retzker, and O. Painter. Demonstrating a long-coherence dual-rail erasure qubit using tunable transmons. *Phys. Rev. X*, 14:011051, Mar 2024. URL: `https://link.aps.org/doi/10.1103/PhysRevX.14.011051`, `doi:10.1103/PhysRevX.14.011051`.

[199] M. Fraas. An analysis of the stationary operation of atomic clocks. *Communications in Mathematical Physics*, 348(2):363–393, September 2016. URL: `http://dx.doi.org/10.1007/s00220-016-2761-1`, `doi:10.1007/s00220-016-2761-1`.

[200] R. Demkowicz-Dobrzański, M. Jarzyna, and J. Kołodyński. *Quantum Limits in Optical Interferometry*, page 345–435. Elsevier, 2015. URL: `http://dx.doi.org/10.1016/bs.po.2015.02.003`, `doi:10.1016/bs.po.2015.02.003`.

[201] C. Han, Z. Ma, Y. Qiu, R. Fang, J. Wu, C. Zhan, M. Li, J. Huang, B. Lu, and C. Lee. Atomic clock locking with Bayesian quantum parameter estimation: Scheme and experiment. *Phys. Rev. Appl.*, 22:044058, Oct 2024. URL:

https://link.aps.org/doi/10.1103/PhysRevApplied.22.044058, doi:10.1103/PhysRevApplied.22.044058.

[202] E. Davis, G. Bentsen, and M. Schleier-Smith. Approaching the Heisenberg limit without single-particle detection. *Phys. Rev. Lett.*, 116:053601, Feb 2016. URL: https://link.aps.org/doi/10.1103/PhysRevLett.116.053601, doi:10.1103/PhysRevLett.116.053601.

[203] F. Fröwis, P. Sekatski, and W. Dür. Detecting large quantum Fisher information with finite measurement precision. *Phys. Rev. Lett.*, 116:090801, Mar 2016. URL: https://link.aps.org/doi/10.1103/PhysRevLett.116.090801, doi:10.1103/PhysRevLett.116.090801.

[204] T. Macrì, A. Smerzi, and L. Pezzè. Loschmidt echo for quantum metrology. *Phys. Rev. A*, 94:010102, Jul 2016. URL: https://link.aps.org/doi/10.1103/PhysRevA.94.010102, doi:10.1103/PhysRevA.94.010102.

[205] S. P. Nolan, S. S. Szigeti, and S. A. Haine. Optimal and robust quantum metrology using interaction-based readouts. *Phys. Rev. Lett.*, 119:193601, Nov 2017. URL: https://link.aps.org/doi/10.1103/PhysRevLett.119.193601, doi:10.1103/PhysRevLett.119.193601.

[206] S. Colombo, E. Pedrozo-Peñafiel, A. F. Adiyatullin, Z. Li, E. Mendez, C. Shu, and V. Vuletić. Time-reversal-based quantum metrology with many-body entangled states. *Nature Physics*, 18(8):925–930, July 2022. URL: http://dx.doi.org/10.1038/s41567-022-01653-5, doi:10.1038/s41567-022-01653-5.

[207] S. C. Burd, R. Srinivas, J. J. Bollinger, A. C. Wilson, D. J. Wineland, D. Leibfried, D. H. Slichter, and D. T. C. Allcock. Quantum amplification of mechanical oscillator motion. *Science*, 364(6446):1163–1165, 2019. URL: https://www.science.org/doi/abs/10.1126/science.aaw2884, doi:10.1126/science.aaw2884.

[208] F. Anders, L. Pezzè, A. Smerzi, and C. Klempt. Phase magnification by two-axis countertwisting for detection-noise robust interferometry. *Phys. Rev. A*, 97:043813, Apr 2018. URL: https://link.aps.org/doi/10.1103/PhysRevA.97.043813, doi:10.1103/PhysRevA.97.043813.

[209] W. Górecki, R. Demkowicz-Dobrzański, H. M. Wiseman, and D. W. Berry. π-corrected Heisenberg limit. *Phys. Rev. Lett.*, 124:030501, Jan 2020.

URL: https://link.aps.org/doi/10.1103/PhysRevLett.124.030501, doi:10.1103/PhysRevLett.124.030501.

[210] S. Direkci, R. Finkelstein, M. Endres, and T. Gefen. Heisenberg-limited Bayesian phase estimation with low-depth digital quantum circuits, 2024. URL: https://arxiv.org/abs/2407.06006, arXiv:2407.06006.

[211] H. L. Van Trees. *Detection, estimation and modulation theory: Detection, estimation and linear modulation theory pt. 1*. John Wiley & Sons, Nashville, TN, January 1968.

[212] R. D. Gill and B. Y. Levit. Applications of the van Trees inequality: A Bayesian Cramér-Rao bound. *Bernoulli*, 1(1/2):59–79, 1995. URL: http://www.jstor.org/stable/3318681, doi:10.2307/3318681.

[213] S. Personick. Application of quantum estimation theory to analog communication over quantum channels. *IEEE Transactions on Information Theory*, 17(3):240–246, 1971. URL: http://dx.doi.org/10.1109/TIT.1971.1054643, doi:10.1109/TIT.1971.1054643.

[214] M. Jarzyna and R. Demkowicz-Dobrzański. True precision limits in quantum metrology. *New Journal of Physics*, 17(1):013010, jan 2015. URL: https://dx.doi.org/10.1088/1367-2630/17/1/013010, doi:10.1088/1367-2630/17/1/013010.

[215] V. Bužek, R. Derka, and S. Massar. Optimal quantum clocks. *Phys. Rev. Lett.*, 82:2207–2210, Mar 1999. URL: https://link.aps.org/doi/10.1103/PhysRevLett.82.2207, doi:10.1103/PhysRevLett.82.2207.

[216] D. W. Berry and H. M. Wiseman. Optimal states and almost optimal adaptive measurements for quantum interferometry. *Phys. Rev. Lett.*, 85:5098–5101, Dec 2000. URL: https://link.aps.org/doi/10.1103/PhysRevLett.85.5098, doi:10.1103/PhysRevLett.85.5098.

[217] G. Summy and D. Pegg. Phase optimized quantum states of light. *Optics Communications*, 77(1):75–79, 1990. URL: https://www.sciencedirect.com/science/article/pii/0030401890904645, doi:10.1016/0030-4018(90)90464-5.

[218] D. T. Pegg and S. M. Barnett. Unitary phase operator in quantum mechanics. *Europhysics Letters*, 6(6):483, jul 1988. URL: https://dx.doi.org/10.1209/0295-5075/6/6/002, doi:10.1209/0295-5075/6/6/002.

[219] B. C. Sanders and G. J. Milburn. Optimal quantum measurements for phase estimation. *Phys. Rev. Lett.*, 75:2944–2947, Oct 1995. URL: `https://link.aps.org/doi/10.1103/PhysRevLett.75.2944`, `doi:10.1103/PhysRevLett.75.2944`.

[220] R. Derka, V. Bužek, and A. K. Ekert. Universal algorithm for optimal estimation of quantum states from finite ensembles via realizable generalized measurement. *Phys. Rev. Lett.*, 80:1571–1575, Feb 1998. URL: `https://link.aps.org/doi/10.1103/PhysRevLett.80.1571`, `doi:10.1103/PhysRevLett.80.1571`.

[221] A. Luis and J. Peřina. Optimum phase-shift estimation and the quantum description of the phase difference. *Phys. Rev. A*, 54:4564–4570, Nov 1996. URL: `https://link.aps.org/doi/10.1103/PhysRevA.54.4564`, `doi:10.1103/PhysRevA.54.4564`.

[222] W. Li, S. Wu, A. Smerzi, and L. Pezzè. Improved absolute clock stability by the joint interrogation of two atomic ensembles. *Phys. Rev. A*, 105:053116, May 2022. URL: `https://link.aps.org/doi/10.1103/PhysRevA.105.053116`, `doi:10.1103/PhysRevA.105.053116`.

[223] G. J. Dick. Local oscillator induced instabilities in trapped ion frequency standards. *Proceedings of the 19th Annual Precise Time and Time Interval Systems and Applications Meeting December 1 - 3, Redondo Beach, California*, pages pp. 133–147, 1987.

[224] G. Dick, J. Prestage, C. Greenhall, and L. Maleki. Local oscillator induced degradation of medium-term stability in passive atomic frequency standards. *Proceedings of the 22th Annual Precise Time and Time Interval Systems and Applications Meeting, December 4 - 6, Virginia*, June 1990.

[225] G. Santarelli, C. Audoin, A. Makdissi, P. Laurent, G. Dick, and A. Clairon. Frequency stability degradation of an oscillator slaved to a periodically interrogated atomic resonator. *IEEE Transactions on Ultrasonics, Ferroelectrics and Frequency Control*, 45(4):887–894, July 1998. URL: `http://dx.doi.org/10.1109/58.710548`, `doi:10.1109/58.710548`.

[226] B. Braverman, A. Kawasaki, and V. Vuletić. Impact of non-unitary spin squeezing on atomic clock performance. *New Journal of Physics*, 20(10):103019, oct 2018. URL: `https://dx.doi.org/10.1088/1367-2630/aae563`, `doi:10.1088/1367-2630/aae563`.

[227] J. M. Robinson, E. Oelker, W. R. Milner, W. Zhang, T. Legero, D. G. Matei, F. Riehle, U. Sterr, and J. Ye. Crystalline optical cavity at 4 K with thermal-noise-limited instability and ultralow drift. *Optica*, 6(2):240–243, Feb 2019. URL: `https://opg.optica.org/optica/abstract.cfm?URI=optica-6-2-240`, `doi:10.1364/OPTICA.6.000240`.

[228] D. Kedar, J. Yu, E. Oelker, A. Staron, W. R. Milner, J. M. Robinson, T. Legero, F. Riehle, U. Sterr, and J. Ye. Frequency stability of cryogenic silicon cavities with semiconductor crystalline coatings. *Optica*, 10(4):464–470, Apr 2023. URL: `https://opg.optica.org/optica/abstract.cfm?URI=optica-10-4-464`, `doi:10.1364/OPTICA.479462`.

[229] M. Mullan and E. Knill. Optimizing passive quantum clocks. *Phys. Rev. A*, 90:042310, Oct 2014. URL: `https://link.aps.org/doi/10.1103/PhysRevA.90.042310`, `doi:10.1103/PhysRevA.90.042310`.

[230] J. Zhou, J. Huang, J. Wei, C. Han, and C. Lee. High-dynamic-range atomic clocks with dual Heisenberg-limited precision scaling, 2024. URL: `https://arxiv.org/abs/2411.14944`, `arXiv:2411.14944`.

[231] S. Dörscher, A. Al-Masoudi, M. Bober, R. Schwarz, R. Hobson, U. Sterr, and C. Lisdat. Dynamical decoupling of laser phase noise in compound atomic clocks. *Communications Physics*, 3(1):185, October 2020. URL: `http://dx.doi.org/10.1038/s42005-020-00452-9`, `doi:10.1038/s42005-020-00452-9`.

[232] N. V. Nardelli, X. Zhang, E. R. Clements, M. Kim, Y. S. Hassan, W. F. McGrew, K. Beloy, A. Ludlow, D. R. Leibrandt, D. H. Hume, and T. M. Fortier. Differential spectroscopy of atomic clocks for improved measurement instability. In *Conference on Lasers and Electro-Optics*, page STh4A.4. Optica Publishing Group, 2021. URL: `https://opg.optica.org/abstract.cfm?URI=CLEO_SI-2021-STh4A.4`, `doi:10.1364/CLEO_SI.2021.STh4A.4`.

[233] D. B. Hume and D. R. Leibrandt. Probing beyond the laser coherence time in optical clock comparisons. *Physical Review A*, 93(3):032138, March 2016. URL: `http://dx.doi.org/10.1103/physreva.93.032138`, `doi:10.1103/physreva.93.032138`.

[234] X. Zheng, J. Dolde, V. Lochab, B. N. Merriman, H. Li, and S. Kolkowitz. Differential clock comparisons with a multiplexed optical lattice clock. *Nature*, 602(7897):425–430, February 2022. URL: `http://dx.doi.org/10.1038/s41586-021-04344-y`, `doi:10.1038/s41586-021-04344-y`.

[235] E. R. Clements, M. E. Kim, K. Cui, A. M. Hankin, S. M. Brewer, J. Valencia, J.-S. Chen, C.-W. Chou, D. R. Leibrandt, and D. B. Hume. Lifetime-limited interrogation of two independent $^{27}\mathrm{Al}^{+}$ clocks using correlation spectroscopy. *Phys. Rev. Lett.*, 125:243602, Dec 2020. URL: https://link.aps.org/doi/10.1103/PhysRevLett.125.243602, doi:10.1103/PhysRevLett.125.243602.

[236] L. Pezzè and A. Smerzi. Heisenberg-limited noisy atomic clock using a hybrid coherent and squeezed state protocol. *Phys. Rev. Lett.*, 125:210503, Nov 2020. URL: https://link.aps.org/doi/10.1103/PhysRevLett.125.210503, doi:10.1103/PhysRevLett.125.210503.

[237] M. E. Kim, W. F. McGrew, N. V. Nardelli, E. R. Clements, Y. S. Hassan, X. Zhang, J. L. Valencia, H. Leopardi, D. B. Hume, T. M. Fortier, A. D. Ludlow, and D. R. Leibrandt. Improved interspecies optical clock comparisons through differential spectroscopy. *Nature Physics*, 19(1):25–29, November 2022. URL: http://dx.doi.org/10.1038/s41567-022-01794-7, doi:10.1038/s41567-022-01794-7.

[238] E. M. Kessler, P. Kómár, M. Bishof, L. Jiang, A. S. Sørensen, J. Ye, and M. D. Lukin. Heisenberg-limited atom clocks based on entangled qubits. *Phys. Rev. Lett.*, 112:190403, May 2014. URL: https://link.aps.org/doi/10.1103/PhysRevLett.112.190403, doi:10.1103/PhysRevLett.112.190403.

[239] J. Borregaard and A. S. Sørensen. Efficient atomic clocks operated with several atomic ensembles. *Physical Review Letters*, 111(9):090802, August 2013. URL: http://dx.doi.org/10.1103/physrevlett.111.090802, doi:10.1103/physrevlett.111.090802.

[240] W. Bowden, A. Vianello, I. R. Hill, M. Schioppo, and R. Hobson. Improving the Q factor of an optical atomic clock using quantum nondemolition measurement. *Phys. Rev. X*, 10:041052, Dec 2020. URL: https://link.aps.org/doi/10.1103/PhysRevX.10.041052, doi:10.1103/PhysRevX.10.041052.

[241] T. Rosenband and D. R. Leibrandt. Exponential scaling of clock stability with atom number, 2013. URL: https://arxiv.org/abs/1303.6357, arXiv:1303.6357.

[242] X. Zheng, J. Dolde, and S. Kolkowitz. Reducing the instability of an optical lattice clock using multiple atomic ensembles. *Physical Review X*, 14(1):011006, January 2024. URL: http://dx.doi.org/10.1103/PhysRevX.14.011006, doi:10.1103/physrevx.14.011006.

[243] G. W. Biedermann, K. Takase, X. Wu, L. Deslauriers, S. Roy, and M. A. Kasevich. Zero-dead-time operation of interleaved atomic clocks. *Phys. Rev. Lett.*, 111:170802, Oct 2013. URL: `https://link.aps.org/doi/10.1103/PhysRevLett.111.170802`, `doi:10.1103/PhysRevLett.111.170802`.

[244] M. Takamoto, T. Takano, and H. Katori. Frequency comparison of optical lattice clocks beyond the Dick limit. *Nature Photonics*, 5(5):288–292, April 2011. URL: `http://dx.doi.org/10.1038/nphoton.2011.34`, `doi:10.1038/nphoton.2011.34`.

[245] M. J. Zawierucha, T. Rehmert, J. Keller, T. E. Mehlstäubler, P. O. Schmidt, and F. Wolf. Deterministic preparation of a dual-species two-ion crystal. *Phys. Rev. A*, 110:013107, Jul 2024. URL: `https://link.aps.org/doi/10.1103/PhysRevA.110.013107`, `doi:10.1103/PhysRevA.110.013107`.

[246] K. Pyka, N. Herschbach, J. Keller, and T. E. Mehlstäubler. A high-precision segmented Paul trap with minimized micromotion for an optical multiple-ion clock. *Applied Physics B*, 114(1–2):231–241, July 2013. URL: `http://dx.doi.org/10.1007/s00340-013-5580-5`, `doi:10.1007/s00340-013-5580-5`.

[247] D. Bluvstein, H. Levine, G. Semeghini, T. T. Wang, S. Ebadi, M. Kalinowski, A. Keesling, N. Maskara, H. Pichler, M. Greiner, V. Vuletić, and M. D. Lukin. A quantum processor based on coherent transport of entangled atom arrays. *Nature*, 604(7906):451–456, April 2022. URL: `http://dx.doi.org/10.1038/s41586-022-04592-6`, `doi:10.1038/s41586-022-04592-6`.

[248] G. Van Rossum and F. L. Drake. *Python 3 Reference Manual.* CreateSpace, Scotts Valley, CA, 2009.

[249] C. R. Harris, K. J. Millman, S. J. van der Walt, R. Gommers, P. Virtanen, D. Cournapeau, E. Wieser, J. Taylor, S. Berg, N. J. Smith, R. Kern, M. Picus, S. Hoyer, M. H. van Kerkwijk, M. Brett, A. Haldane, J. F. del Río, M. Wiebe, P. Peterson, P. Gérard-Marchant, K. Sheppard, T. Reddy, W. Weckesser, H. Abbasi, C. Gohlke, and T. E. Oliphant. Array programming with NumPy. *Nature*, 585(7825):357–362, September 2020. URL: `http://dx.doi.org/10.1038/s41586-020-2649-2`, `doi:10.1038/s41586-020-2649-2`.

[250] N. Lambert, E. Giguère, P. Menczel, B. Li, P. Hopf, G. Suárez, M. Gali, J. Lishman, R. Gadhvi, R. Agarwal, A. Galicia, N. Shammah, P. Nation, J. R. Johansson, S. Ahmed, S. Cross, A. Pitchford, and F. Nori. QuTiP 5: The quantum toolbox in python. 2024. URL: `https://arxiv.org/abs/2412.04705`, `arXiv:2412.04705`.

[251] P. Virtanen, R. Gommers, T. E. Oliphant, M. Haberland, T. Reddy, D. Cournapeau, E. Burovski, P. Peterson, W. Weckesser, J. Bright, S. J. van der Walt, M. Brett, J. Wilson, K. J. Millman, N. Mayorov, A. R. J. Nelson, E. Jones, R. Kern, E. Larson, C. J. Carey, İ. Polat, Y. Feng, E. W. Moore, J. VanderPlas, D. Laxalde, J. Perktold, R. Cimrman, I. Henriksen, E. A. Quintero, C. R. Harris, A. M. Archibald, A. H. Ribeiro, F. Pedregosa, P. van Mulbregt, A. Vijaykumar, A. P. Bardelli, A. Rothberg, A. Hilboll, A. Kloeckner, A. Scopatz, A. Lee, A. Rokem, C. N. Woods, C. Fulton, C. Masson, C. Häggström, C. Fitzgerald, D. A. Nicholson, D. R. Hagen, D. V. Pasechnik, E. Olivetti, E. Martin, E. Wieser, F. Silva, F. Lenders, F. Wilhelm, G. Young, G. A. Price, G.-L. Ingold, G. E. Allen, G. R. Lee, H. Audren, I. Probst, J. P. Dietrich, J. Silterra, J. T. Webber, J. Slavič, J. Nothman, J. Buchner, J. Kulick, J. L. Schönberger, J. V. de Miranda Cardoso, J. Reimer, J. Harrington, J. L. C. Rodríguez, J. Nunez-Iglesias, J. Kuczynski, K. Tritz, M. Thoma, M. Newville, M. Kümmerer, M. Bolingbroke, M. Tartre, M. Pak, N. J. Smith, N. Nowaczyk, N. Shebanov, O. Pavlyk, P. A. Brodtkorb, P. Lee, R. T. McGibbon, R. Feldbauer, S. Lewis, S. Tygier, S. Sievert, S. Vigna, S. Peterson, S. More, T. Pudlik, T. Oshima, T. J. Pingel, T. P. Robitaille, T. Spura, T. R. Jones, T. Cera, T. Leslie, T. Zito, T. Krauss, U. Upadhyay, Y. O. Halchenko, and Y. Vázquez-Baeza. SciPy 1.0: fundamental algorithms for scientific computing in Python. *Nature Methods*, 17(3):261–272, February 2020. URL: `http://dx.doi.org/10.1038/s41592-019-0686-2`, `doi:10.1038/s41592-019-0686-2`.

[252] S. Behnel, R. Bradshaw, C. Citro, L. Dalcin, D. S. Seljebotn, and K. Smith. Cython: The best of both worlds. *Computing in Science & Engineering*, 13(2):31–39, 2011.

[253] L. Devroye. *Non-Uniform Random Variate Generation.* Springer New York, 1986. URL: `http://dx.doi.org/10.1007/978-1-4613-8643-8`, `doi:10.1007/978-1-4613-8643-8`.

[254] G. Van Rossum. *The Python Library Reference, release 3.8.2.* Python Software Foundation, 2020.

[255] A. E. Wallin, D. Price, C. G. Carson, F. Meynadier, Y. Xie, and E. Benkler. allantools: Python package for allan variance and related analyses. `https://allantools.readthedocs.io/en/latest/`, 2024.

[256] Rodrigues. Des lois géométriques qui régissent les déplacements d'un système solide dans l'espace, et de la variation des coordonnées provenant de ces

déplacements considérés indépendamment des causes qui peuvent les produire. *Journal de Mathématiques Pures et Appliquées*, pages 380–440, 1840. URL: `http://eudml.org/doc/234443`.

[257] *NIST Digital Library of Mathematical Functions*. `https://dlmf.nist.gov/`, Release 1.2.3 of 2024-12-15. F. W. J. Olver, A. B. Olde Daalhuis, D. W. Lozier, B. I. Schneider, R. F. Boisvert, C. W. Clark, B. R. Miller, B. V. Saunders, H. S. Cohl, and M. A. McClain, eds. URL: `https://dlmf.nist.gov/`.

ACADEMIC CURRICULUM VITAE

Personal Data

NAME: Timm Mirek Kielinski
BORN: 8 March 1997 in Hannover, Germany
ADDRESS: Meyenfeldstraße 9, 30419 Hannover

Education

In progress	Doktor der Naturwissenschaften, Dr. rer. nat. Leibniz Universität Hannover Thesis: *Frequency Metrology with Optimal Ramsey Interferometry for Optical Atomic Clocks* Supervisor: Prof. Dr. K. Hammerer
04/2021–present	PhD student at Institut für theoretische Physik, Leibniz Universität Hannover
03/2021	MASTER OF SCIENCE (PHYSICS) Leibniz Universität Hannover Thesis: *Quantum Strategies for Optical Atomic Clocks* Supervisor: Prof. Dr. K. Hammerer
10/2018–03/2021	Master studies at Leibniz Universität Hannover
11/2018	BACHELOR OF SCIENCE (PHYSICS) Leibniz Universität Hannover Thesis: *Nichtklassische Zustände in Atomuhren* Supervisor: Prof. Dr. K. Hammerer
10/2015–11/2018	Bachelor studies at Leibniz Universität Hannover
2007–2015	ABITUR St. Ursula Schule Hannover

Complete list of publications

T. Kielinski, P. O. Schmidt and K. Hammerer, *GHZ protocols enhance frequency metrology despite spontaneous decay.* [1]

T. Kielinski and K. Hammerer, *Bayesian frequency metrology with optimal Ramsey interferometry in optical atomic clocks.* [2] (submitted to Reports on Progress in Physics)

T. Kielinski, *Monte Carlo simulations of atomic clocks [Data set].* [3]

K. Dietze, L. Pelzer, L. Krinner, F. Dawel, J. Kramer, N. C. H. Spethmann, **T. Kielinski**, K. Hammerer, K. Stahl, J. Klose, S. Dörscher, C. Lisdat, E. Benkler and P. O. Schmidt, *Entanglement-enhanced optical ion clock.* [4] (submitted to Physical Review Letters)

M. S. Scharnagl, **T. Kielinski** and K. Hammerer, *Optimal Ramsey interferometry with echo protocols based on one-axis twisting.* [5]